

SANDIA REPORT

SAND89-0462 • UC-70

Unlimited Release

Printed April 1989

8524
RS-8232-2/168718

Wackey cy!

Systems Analysis, Long-Term Radionuclide Transport, and Dose Assessments, Waste Isolation Pilot Plant (WIPP), Southeastern New Mexico; March 1989

A. R. Lappin, R. L. Hunter, Editors
D. P. Garber, P. B. Davies, Associate Editors



8232-2/1068718



0000001 -

Prepared by
Sandia National Laboratories
Albuquerque, New Mexico 87185 and Livermore, California 94550
for the United States Department of Energy
under Contract DE-AC04-76DP00789



Issued by Sandia National Laboratories, operated for the United States Department of Energy by Sandia Corporation.

NOTICE: This report was prepared as an account of work sponsored by an agency of the United States Government. Neither the United States Government nor any agency thereof, nor any of their employees, nor any of their contractors, subcontractors, or their employees, makes any warranty, express or implied, or assumes any legal liability or responsibility for the accuracy, completeness, or usefulness of any information, apparatus, product or process disclosed, or represents that its use would not infringe privately owned rights. Reference herein to any specific commercial product, process, or service by trade name, trademark, manufacturer, or otherwise, does not necessarily constitute or imply its endorsement, recommendation, or favoring by the United States Government, any agency thereof or any of their contractors or subcontractors. The views and opinions expressed herein do not necessarily state or reflect those of the United States Government, any agency thereof or any of their contractors.

Printed in the United States of America. This report has been reproduced directly from the best available copy.

Available to DOE and DOE contractors from
Office of Scientific and Technical Information
PO Box 62
Oak Ridge, TN 37831

Prices available from (615) 576-8401, FTS 626-8401

Available to the public from
National Technical Information Service
U.S. Department of Commerce
5285 Port Royal Road
Springfield, VA 22161

NTIS price codes
Printed copy: A29
Microfiche copy: A01

SAND89—0462
Unlimited Release
Printed April 1989

Distribution
Category UC—70

SYSTEMS ANALYSIS,
LONG-TERM RADIONUCLIDE TRANSPORT, AND DOSE ASSESSMENTS,
WASTE ISOLATION PILOT PLANT (WIPP), SOUTHEASTERN NEW MEXICO;
MARCH 1989

A. R. Lappin and R. L. Hunter, Editors
D. P. Garber and P. B. Davies, Associate Editors
Sandia National Laboratories
Albuquerque, New Mexico

Contributors:

R. L. Beauheim
D. J. Borns
L. H. Brush
B. M. Butcher
T. Cauffman*
M. S. Y. Chu
L. S. Gomez
R. V. Guzowski**
H. J. Iuzzolino***
V. Kelley*
S. J. Lambert
M. G. Marietta
J. W. Mercer
E. J. Nowak
J. Pickens*
R. P. Rechard
M. Reeves*
K. L. Robinson
M. D. Siegel

*INTERA
**SAIC
***GEO-CENTERS, Inc.

ACKNOWLEDGEMENTS

The schedule for preparing this report was aggressive, and we could not have met it without extensive support from Tech. Reps., Inc., of Albuquerque. In particular, John Stikar, Technical Writer; Lorna Marchand, Technical Editor and several people in the Word Processing Department, headed by Debbie Rivard, stayed cheerful and efficient under a heavy load. Ron D. McCurley of New Mexico Engineering Research Institute and Jim Schreiber of SAIC assisted in preparing portions of Chapters 4.0 and 7.0.

EXECUTIVE SUMMARY

This report summarizes the current understanding of the expected long-term behavior of the Waste Isolation Pilot Plant (WIPP) repository and estimates long-term radionuclide doses in a series of six analyses investigating both undisturbed repository performance (Case I) and performance in response to a relatively high-consequence human intrusion (Case II). It is the result of an intensive effort over a short time. The U.S. Department of Energy (DOE) decided to have Sandia National Laboratories prepare this report as a result of a meeting held January 5, 1989. The conceptual model of the expected long-term behavior of the WIPP repository used in this report was formulated in early to mid January 1989, drawing on information and understanding developed over the past decade. Numerical modeling of ground-water flow, radionuclide transport, and doses to humans began January 20, 1989 and was completed March 20, 1989.

The report has several objectives:

1. To briefly summarize Sandia's current technical understanding of the major components of long-term performance of the WIPP repository. The following areas are specifically addressed:
 - a. the hydrology and geochemistry of the Salado Formation (Fm.), Rustler Fm., Dewey Lake Red Beds, and Bell Canyon Fm.;
 - b. the hydraulic characteristics of a pressurized brine reservoir assumed, on the basis of geophysical studies and nearby drillhole testing, to be present within fractured anhydrite of the Castile Fm. beneath a portion of the underground workings;
 - c. the expected waste-entombment behavior of rooms and panels, including structural, gas-generation, and brine-inflow effects;
 - d. the expected behavior of the sealing system;

- e. the expected properties and durability of borehole plugs assumed to be emplaced after penetration of the repository by hydrocarbon-exploration drilling;
 - f. radionuclide-transport mechanisms and properties of the Culebra Dolomite, the major pathway for ground-water transport of radionuclides from the WIPP to the biosphere.
2. To compare the current conceptual and numerical models in the technical areas listed above with those available at the time of the WIPP Final Environmental Impact Statement (FEIS) (DOE, 1980a).
 3. To document the parameter values now thought to be "representative" or "most likely" for use in numerical predictions of the long-term behavior of the repository. Where possible, the uncertainties in both data and resulting calculated long-term behavior of the repository are discussed.
 4. To describe, document, and interpret six sets of calculations estimating the potential health effects to individuals resulting from emplacement of CH-TRU wastes in the WIPP, hydrologic saturation of the repository as a result of either natural processes or human intrusion, direct and indirect exposure during and after drilling (where appropriate), and ground-water transport of radionuclides to a hypothetical stock well south of the WIPP site.

The calculations presented here investigate radionuclide transport and resulting health effects both during undisturbed performance of the WIPP repository and in response to a relatively high-consequence human intrusion into the repository. The human intrusion considered is drilling that results in a long-term interconnection of the repository, an underlying brine reservoir in the Castile Fm., and the overlying Culebra Dolomite. The Culebra Dolomite provides a relatively permeable pathway for ground-water transport of radionuclides to the hypothetical stock well.

This report compiles the results of ongoing evaluation of several areas of long-term performance of the WIPP repository. The understanding of factors

that affect long-term performance has changed in major ways since 1980. Several examples of these changes in understanding are described below.

1. It is now recognized that the Salado Fm., consisting of layered halites with numerous anhydrite and clay marker beds, is probably hydraulically saturated, with very low effective permeability in undisturbed regions. At the time of the WIPP FEIS, the Salado Fm. was thought to be hydraulically unsaturated, with sufficient gas permeability to dissipate any gases that might be generated by emplaced waste. Thus, the estimated far-field permeability of the Salado Fm. has decreased significantly since the time of the WIPP FEIS.
2. Current estimates of total gas-generation capacities resulting from degradation of emplaced waste and containers are smaller than similar estimates in the FEIS. The expected gas-generation potential dominated by microbial activity is significantly less (~600 moles/drum versus 2,000 moles/drum), but the expected gas generation by corrosion of drums and metallic wastes is greater (~900 moles/drum versus approximately zero). Gas-generation rates, total volume of gas generated, and the time periods over which gas generation might occur are currently uncertain and depend on the interaction of gas generation, brine inflow, and structural behavior of the repository.
3. The combination of somewhat reduced gas volumes from waste degradation and greatly decreased far-field permeability leads to the conclusion that the expected condition of the WIPP repository for a currently undefined period of time following closure will be dominated by gas at elevated pressure, with little or no free brine within the workings. Brine inflow during early stages of closure (i.e., before gas pressure builds up) will be less than the sorbing capacity of the design-basis salt/bentonite backfill. Room humidity is expected to be buffered between 60 and 70% relative humidity, in equilibrium with halite. Because of the limited brine permeability of the Salado Fm., it is possible that, in the absence of human intrusion, brine saturation of the WIPP may not occur within 10,000 years.

4. The volumes of gas potentially generated, even in the absence of free brine, may exceed the gas-storage capacity of the waste-emplacement rooms at their final state of closure under lithostatic pressure. Four possible locations or mechanisms for gas storage or relief of pressures are considered here: (1) expansion of the rooms, after closure, to something less than their original volume; (2) generation of a secondary zone of increased porosity due to fracturing around the waste-emplacement rooms, or gas storage in an incompletely removed disturbed-rock zone similar to that now known to exist around rooms during closure; (3) migration of gas along open fractures both within Marker Bed 139 (which underlies the waste-emplacement rooms and develops open fractures in response to excavation) and perhaps within stratigraphic contacts at and near the repository horizon; and (4) following transport through Marker Bed 139, migration of gas into the shafts and adjacent marker beds. It is not now possible to evaluate definitively the likelihood of the various gas storage and relief mechanisms; however, no dramatic consequence is expected. At the time of the FEIS, gas pressurization of the repository was examined and dismissed, because the far-field Salado permeability was thought to be sufficient to dissipate any gases that might be generated within the repository.

5. Because Castile brine is known to be present in hole WIPP-12 (one mile north of the center of the WIPP site) and is interpreted on the basis of geophysical studies to extend to the south, pressurized brine is assumed here to be present within the upper anhydrite of the Castile Fm. beneath a portion of the WIPP waste-emplacement panels. The properties of this brine reservoir are assumed to be the same as those interpreted from hydrologic testing of the WIPP-12 reservoir. The assumed Castile brine is of concern only in the event of human intrusion. The response of the overall containment system to penetration of a hypothetical brine pocket within the Salado Fm. was qualitatively evaluated in the FEIS, but no detailed calculations were performed.

6. In calculations of the WIPP response to human intrusion by a hydrocarbon-exploration borehole connecting an assumed Castile brine reservoir, the repository, the Culebra Dolomite, and the land surface, the results are

sensitive to assumptions about borehole plugging. It is assumed here that the borehole is plugged in accordance with current State of New Mexico regulations and that the permeability of the borehole plug increases to a constant value as the plug degrades, beginning 75 years after emplacement. Plugging of industry boreholes (as opposed to boreholes drilled by the WIPP Project) was not specifically addressed in the FEIS.

7. As in the FEIS, the Culebra Dolomite Member of the Rustler Fm. is considered to be the main pathway for ground-water transport. For purposes of modeling in the FEIS, the Rustler Fm. was assumed to behave as a porous medium for both ground-water flow and radionuclide transport, and the Culebra and Magenta Dolomites were combined as a single "Rustler aquifer." Available data and models now indicate that flow and transport within the Culebra Dolomite are affected by the presence of fractures over distances that vary with the interpreted Culebra properties and may be as great as a few kilometers. Both the time periods and the distances over which radionuclide transport is evaluated in this report differ from those considered in the WIPP FEIS. In the FEIS, the major emphasis was on evaluating ground-water transport to Malaga Bend on the Pecos River, ~26 km southwest of the center of the WIPP site. The emphasis here is on evaluating radionuclide transport to a much nearer location, a hypothetical Culebra stock well ~6 km south of the center of the site. In the FEIS, transport and dose calculations were extended well beyond one million years. In this report, because of the awareness that transport and dose calculations beyond 10,000 years are meaningless, calculations are extended to 10,000 years only. However, where appropriate, behavior beyond this time period is discussed qualitatively.

Evaluation of the performance of the WIPP repository under undisturbed conditions indicates that no radionuclides will be transported either to the Culebra Dolomite or to the land surface within 10,000 years. The calculations include both expected behavior (Case IA) and behavior in which radionuclide solubility and repository-seal permeability are increased from expected values (Case IB). These calculations assume both that the repository is saturated with brine 2,000 years after closure and that any migration or release of gases prior to this time does not affect the subsequent permeability of the

repository sealing system by more than two orders of magnitude. It is possible that the time period over which gas dominates undisturbed repository performance will exceed 2,000 years; if so, these calculations may be very conservative. No calculations of undisturbed performance were included in the FEIS.

Four sets of calculations presented here (Cases IIA through IID) examine the long-term (10,000-year) response of the WIPP to a human intrusion involving an underlying reservoir of pressurized brine within the Castile Fm. Both direct release to the surface and doses to a hypothetical farm family living 500 m downwind of the intrusion hole are calculated to be very low for Case II.

Case IIA assumes "expected" or "representative" characteristics for the repository, the breaching well, and the Culebra Dolomite. Critical variables include radionuclide solubility, waste permeability, borehole permeability, and transport properties within the Culebra Dolomite (matrix porosity, fracture spacing, matrix tortuosity, free-water diffusivity of radionuclides, and radionuclide distribution coefficient, K_d). The waste permeability enters directly into these calculations only to the extent that the assigned permeability for Cases IIA and IIC (10^{-13} m²) is assumed to allow mixing of Castile brine near the borehole, sufficient for these brines to reach the same radionuclide concentration as already exists within the repository. Thus, the radionuclide source term to the Culebra Dolomite for Cases IIA and IIC results from contamination of the entire Castile-brine and Salado-brine volumes by a full complement of radionuclides. For Case IIA, radium-226 is the only radionuclide reaching the stock well in any significant quantity in 10,000 years. The calculated 50-year dose commitment from one year of eating contaminated beef is 2.1×10^{-4} mrem for Case IIA at 10,000 years.

Case IIB assumes that waste emplaced at WIPP is compacted prior to emplacement, and that waste compaction reduces permeability sufficiently to prevent significant mixing of Castile brine within the repository. Thus, the only radionuclide source term into the Culebra Dolomite results from the flow of contaminated Salado brine to the borehole; the Castile brine merely acts as a carrier. If "expected" transport properties were assumed for Case IIB, the

resulting doses at 10,000 years would be reduced from the already extremely low values calculated in Case IIA.

Therefore, Case IIB assumes that, other than the elimination of brine circulation within the repository, flow and transport properties in the repository and geosphere are degraded. Specifically, radionuclide solubility is increased by two orders of magnitude, and borehole-plug permeability is increased by one order of magnitude. Analogous changes are made in the model of the Culebra Dolomite, which decrease the effectiveness of radionuclide retardation and increase the importance of fracture flow; i.e., matrix porosity, matrix tortuosity, free-water diffusivity, and distribution coefficients (K_{ds}) are all decreased, and fracture spacing is increased.

This combination of changes results in increased flow and transport within the Culebra Dolomite and in significant concentrations at the hypothetical Culebra stock well in less than 10,000 years. For this degraded-parameter case, first arrival of uranium at the stock well is calculated to occur in slightly more than 100 years. The maximum whole-body 50-year dose commitment from one year of beef ingestion is estimated to be 72 mrem in Case IIB, occurring 10,000 years after repository decommissioning.

Because of the mix of assumptions used, it is not possible in Case IIB to isolate the benefits of waste compaction. Therefore, Case IIC assumes the same flow and transport behavior outside the repository as Case IIB, but also assumes sufficient waste permeability to allow brine mixing within the repository. Thus, the differences between Case IIA and Case IIC are that radionuclide solubilities and flow and transport behavior outside the repository have been degraded in Case IIC and that brines are assumed to mix within the repository. As a result of the higher radionuclide input into the Culebra Dolomite, arrival time at the stock well is decreased slightly relative to results from Case IIB, from slightly >100 years to slightly <100 years. The maximum whole-body 50-year dose commitment from one year of beef ingestion is estimated to be 130 mrem in Case IIC, occurring ~1,350 years after repository decommissioning.

The ranges of radionuclide solubilities and flow and transport properties both within and outside the repository used in this report are based on incomplete data. The primary focus of research during the demonstration phase of the WIPP Project is to decrease the uncertainties in parameters important to long-term performance of the WIPP. However, the results of this research cannot be prejudged. Therefore, Case IID was run to examine the potential benefits that might be gained from engineering modification of the WIPP waste and backfill. This case assumes the same radionuclide solubilities as for Case IIA, but also assumes that permeability within the repository is reduced sufficiently to (1) eliminate mixing of Castile brines; and (2) limit the brine inflow from the Salado Fm. in such a way that the effective inflow is from a single room ($0.1 \text{ m}^3/\text{year}$), rather than from an entire waste-emplacement panel ($1.3 \text{ m}^3/\text{year}$), as assumed in Cases IIA through IIC. Flow and transport properties outside the repository are degraded in Case IID to the same values used in Cases IIB and IIC.

The results of Case IID indicate that, because of the assumed flow and transport properties outside the repository, first arrival of radionuclides at the hypothetical stock well is only slightly slower than in Case IIB, i.e., between 100 and 200 years. However, the peak concentrations and hence peak doses for Case IID are reduced from those calculated in Case IIB by two to three orders of magnitude. The maximum whole-body 50-year dose commitment from one year of beef ingestion is estimated to be 0.9 mrem in Case IID, occurring 10,000 years after repository decommissioning.

Thus, the calculations presented here indicate several things:

1. Undisturbed performance of the WIPP is not expected to result in any release of radionuclides either to the Culebra Dolomite or to the surface in well over 10,000 years, even assuming increased radionuclide solubilities and degraded flow and transport properties in the WIPP drifts and shafts.
2. If the "expected" or "representative" properties of waste, backfill, borehole plugs, and the Culebra Dolomite are supported by results obtained during the WIPP demonstration phase, the result will be a high degree of

confidence that the WIPP will be able to demonstrate compliance with applicable regulatory guidelines at the end of the WIPP performance assessment.

3. If the final estimates of the properties of waste, backfill, borehole plugs, and the Culebra are significantly "worse" than those properties concluded to be "expected" here, and if no significant modification is made to waste or backfill, significant releases to the hypothetical stock well might result.
4. If, however, the final estimates of the properties of waste, backfill, borehole plugs, and the Culebra are significantly "worse" than those properties concluded to be "expected" here it should be possible to gain a high degree of confidence in long-term repository performance by completing engineering modifications of the waste and backfill. At this time, it is not clear whether such modifications will be required.

The effort in this report to estimate the overall uncertainties about several areas of the long-term performance of the WIPP is a major step forward. The calculations in this report are based largely on data collected since the time of the FEIS. In some areas, however, required data remain either non-existent or highly uncertain. In most of these areas (e.g., gas generation rates under realistic conditions), great reduction in uncertainty is expected during the demonstration phase at the WIPP. In some areas, however, qualitative reduction in uncertainties as a result of reasonable amounts of additional work is not probable. For example, flow and transport behavior within the Culebra Dolomite has been the subject of intense effort over approximately the last five years. The preliminary indication is that, with the exception of additional boreholes in the region of the offsite pathways to reduce travel-time uncertainties, additional field work will not eliminate the existing uncertainties. Expert judgment will be used, even in the final WIPP performance assessment, to evaluate data uncertainties.

The results presented in this report reflect an approach that is distinct in two main ways from that which will be taken in WIPP performance assessment. First, the calculations presented here are deterministic (i.e., they assume a

probability of 1.0 for each calculation). This approach is physically unrealistic; in fact, the results calculated here are mutually exclusive, because each calculation assumes different repository and geosphere characteristics. Second, no calculation of 10,000-year doses from radionuclide transport or of doses following human intrusion are required by 40 CFR 191. Thus, the results of the calculations in this report are not intended to be directly compared with the performance standard in 40 CFR 191. Probabilistic calculations, which assign numerical probabilities to important input data and to each of several scenarios, will be conducted during the next four years as part of WIPP performance assessment and will culminate in a comparison with 40 CFR 191.

CONTENTS

	Page
1.0 INTRODUCTION, OBJECTIVES, AND SUMMARY OF RESULTS.....	1-1
1.1 Introduction and Objectives.....	1-1
1.2 Summary of Results.....	1-22
1.2.1 Changes in Understanding of Major Aspects of WIPP Performance Since 1980.....	1-22
1.2.2 Estimated Health Effects from Release of Radionuclides.	1-23
1.2.2.1 Releases at the Head of the Intrusion Well (Case II).....	1-23
1.2.2.2 Releases from a Stock Pond.....	1-26
2.0 GENERAL GEOLOGY OF THE WIPP SITE.....	2-1
3.0 HYDROLOGY AND GEOCHEMISTRY OF THE WIPP SITE.....	3-1
3.1 Introduction.....	3-1
3.2 Salado Formation.....	3-2
3.2.1 Salado Hydrology.....	3-4
3.2.1.1 Understanding and Assumptions Prior to Mining.	3-4
3.2.1.2 New Understanding Derived from WIPP Underground Experience.....	3-5
3.2.1.3 Current Brine-Inflow Model and Assumptions....	3-9
3.2.1.4 Uncertainties in the Present Understanding of Brine Inflow.....	3-10
3.2.1.5 Potential Drawbacks of Using Conservative Estimates for Brine Inflow.....	3-13
3.2.2 Chemistry of Intergranular Brines of the Salado Formation.....	3-14
3.3 Rustler Formation.....	3-23
3.3.1 Physical Hydrology.....	3-26
3.3.1.1 Unnamed Lower Member and Rustler/Salado Contact.....	3-28
3.3.1.2 Culebra Dolomite.....	3-34
3.3.1.3 Tamarisk Claystone.....	3-42
3.3.1.4 Magenta Dolomite.....	3-43

3.3.1.5	Forty-Niner Claystone.....	3-47
3.3.1.6	Hydraulic-Head Relations.....	3-49
3.3.2	Geochemical Variability of Rustler Fluids.....	3-55
3.3.2.1	Changes in Understanding Since the <u>FEIS</u>	3-58
3.3.2.2	Data Reliability.....	3-61
3.3.2.3	Sources of Data.....	3-63
3.3.2.4	Solute Data.....	3-63
3.3.2.5	Samples of Unknown Reliability.....	3-73
3.3.2.6	Data Variability.....	3-73
3.3.3	Hydrochemical Model for Culebra Ground Waters.....	3-74
3.3.3.1	Hydrochemical Facies of Culebra Ground Water..	3-75
3.3.3.2	Hydraulic Versus Geochemical Confinement.....	3-78
3.3.3.3	Steady-State Versus Transient Flow.....	3-89
3.3.3.4	Chemical Reaction Model for Composition of Culebra Ground Waters.....	3-92
3.3.3.5	Conclusion.....	3-96
3.3.4	Radionuclide Retardation in the Culebra Dolomite.....	3-97
3.3.4.1	Limitations in the Use of Distribution Coefficients (K_d).....	3-98
3.3.4.2	Geochemical Conditions in the Culebra Dolomite.....	3-101
3.3.4.3	Review of Available K_d Data.....	3-102
3.3.4.4	Extrapolation of K_d Values: General Principles.....	3-107
3.3.4.5	Procedure for Choice of Recommended K_d Values for Transport in the Culebra Dolomite.....	3-116
3.3.4.6	Use of K_d 's in Transport Equations.....	3-116
3.3.4.7	Conclusion.....	3-118
3.3.5	Numerical Ground-Water-Flow and Transport Model of the Culebra Dolomite.....	3-119
3.3.5.1	Modeling History.....	3-119
3.3.5.2	Limitations of Current Data Base.....	3-128
3.3.5.3	Limitations of Modeling Approach.....	3-128
3.4	Castile Formation, Including Brine Reservoirs.....	3-129
3.4.1	Castile Formation Hydrology in the <u>FEIS</u>	3-130
3.4.2	General Information on Castile Hydrology Developed Since the <u>FEIS</u>	3-133

3.4.3	Updated Interpretation of the Properties of the WIPP-12 Brine Reservoir.....	3-136
3.4.3.1	WIPP-12 Testing Program and Factors Limiting Interpretation.....	3-136
3.4.3.2	Conceptual Model of the WIPP-12 Brine Reservoir.....	3-140
3.4.3.3	Interpretive Approach and Results.....	3-144
3.5	Bell Canyon Formation and Dewey Lake Red Beds.....	3-149
3.5.1	Bell Canyon Formation.....	3-149
3.5.2	Dewey Lake and Shallower Units.....	3-151
4.0	CONDITION OF THE REPOSITORY IN THE ABSENCE OF HUMAN INTRUSION.....	4-1
4.1	Overview of the Disposal-Room Model.....	4-1
4.2	Gas-Production Rates, Potentials, and Periods.....	4-3
4.2.1	Processes that Produce Gas.....	4-4
4.2.2	Microbial Gas Production.....	4-5
4.2.3	Anoxic Corrosion.....	4-7
4.2.4	Discussion.....	4-11
4.3	Expected Brine Inflow to Waste Rooms and Panels Based on a Darcy-Flow Model.....	4-13
4.3.1	Brine-Inflow Volumes for Early-Time, Undisturbed Conditions.....	4-14
4.3.2	Brine-Inflow Rates for Long-Term Breach Conditions.....	4-20
4.4	Initial Inventory and Decay Chains.....	4-22
4.4.1	Radionuclides in the CH Inventory.....	4-23
4.4.2	Radionuclides Included in Transport Calculations.....	4-24
4.4.3	RH-TRU Inventory.....	4-26
4.5	Radionuclide Concentrations in Brines.....	4-27
4.5.1	Sources of Uncertainty.....	4-28
4.5.2	Radionuclide Concentrations Used in Transport Calculations.....	4-29
4.6	Radionuclide Sorption in the Waste Panels.....	4-30
4.6.1	Effects of Solution and Backfill Chemistry on Sorption.....	4-30
4.7	Structural Interaction of the Salado Formation and Repository.....	4-32
4.7.1	Understanding and Assumptions Prior to Mining.....	4-34
4.7.2	Experience Gained Underground.....	4-35
4.7.3	Generation and Character of the DRZ.....	4-35

4.7.4	Impact of the DRZ.....	4-41
4.7.4.1	Structural Effects.....	4-41
4.7.4.2	Hydrologic Effects.....	4-42
4.7.4.3	Gas and Brine Storage.....	4-45
4.7.5	Closure Mechanisms.....	4-46
4.8	Terminal Waste State.....	4-48
4.8.1	Void Volume (Porosity).....	4-49
4.8.2	Permeability.....	4-56
4.9	Expected State of the Design-Basis Drift and Shaft Seal and Backfill Systems.....	4-57
4.9.1	Room, Panel, and Drift Backfill.....	4-58
4.9.2	Drift and Panel Seal Systems.....	4-60
4.9.2.1	Sealing Marker Bed 139.....	4-62
4.9.3	Shaft Seal Systems.....	4-63
4.9.3.1	Lower Shaft Seal System.....	4-63
4.9.3.2	Seal and Backfill Material in Upper Shafts....	4-67
4.10	Possible Repository Response to Gas Generation and Total Volumes Generated.....	4-67
4.10.1	Slurry Formation within the Disposal Rooms.....	4-68
4.10.2	Potential Gas-Storage Volumes and Pressures Within and Surrounding the Repository.....	4-71
4.10.2.1	Excavated and Enclosed Volumes.....	4-71
4.10.2.2	Hypothetical Gas Pressures.....	4-77
4.10.2.3	Storage-Region Pressures from Combined Gas Generation and Creep Closure.....	4-82
4.10.3	Possible Paths and Mechanisms for Relief of Elevated Gas Pressures.....	4-85
4.10.4	Possible Resaturation Mechanisms.....	4-88
4.11	Possible Engineered Modifications of Waste and Backfill.....	4-89
4.11.1	Disposal-Room Assumptions for Cases IIB and IID.....	4-90
4.11.2	Other Engineered Modifications.....	4-93
4.11.2.1	Brine Control.....	4-94
4.11.2.2	Gas Control.....	4-96
5.0	EVALUATION OF PATHWAYS TO MAN.....	5-1
5.1	Overview.....	5-2

5.2	Approach to Calculating Releases (Case II).....	5-5
5.2.1	Removal of Cuttings to the Head of the Breaching Well..	5-5
5.2.2	Radionuclide Release at the Head of the Breaching Well (Case II).....	5-10
5.2.3	Radionuclide Release at a Stock Pond.....	5-13
5.3	Hypothetical Culebra Stock-Well Location.....	5-13
5.3.1	Uncertainties in Stock-Well Location.....	5-15
6.0	RADIONUCLIDE TRANSPORT IN THE ABSENCE OF HUMAN INTRUSION (CASE I)...	6-1
6.1	Narrative Description of Cases IA and IB.....	6-3
6.2	Results of NEFTRAN Calculations.....	6-6
7.0	RADIONUCLIDE TRANSPORT AFTER HUMAN INTRUSION INVOLVING A CASTILE BRINE RESERVOIR (CASE II).....	7-1
7.1	Narrative Description of Case II.....	7-1
7.2	Releases from the Head of an Intrusion Well (Case II).....	7-5
7.2.1	Release to the Surface in the Form of Cuttings and Drilling Mud.....	7-5
7.2.2	External Dose Received by Drill-Crew Member.....	7-6
7.2.3	Doses Received by a Hypothetical Farm Family Through Indirect Pathways.....	7-7
7.3	Post-Plugging Release to Culebra Dolomite and Resulting Doses.	7-12
7.3.1	Fluid Release to the Culebra Dolomite for Cases IIA, IIB, IIC, and IID.....	7-12
7.3.2	Contaminant Transport for Case IIA.....	7-18
7.3.3	Contaminant Transport for Case IIB.....	7-23
7.3.3.1	Stable Lead.....	7-23
7.3.3.2	Radionuclides.....	7-35
7.3.4	Contaminant Transport for Case IIC.....	7-38
7.3.5	Contaminant Transport for Case IID.....	7-52
7.3.6	Releases from a Stock Pond (Case II).....	7-64
7.3.7	Interpreting Predictions of Radiation Doses.....	7-71
7.3.8	Risk Associated with Environmental Radiation Standards.....	7-73

8.0	SUMMARY AND CONCLUSIONS.....	8-1
8.1	Hydrology and Geochemistry of the Salado Formation.....	8-1
8.2	Hydrology and Geochemistry of the Rustler Formation.....	8-2
8.2.1	Physical Hydrology.....	8-2
8.2.2	Geochemistry.....	8-4
8.2.3	Radionuclide Retardation in the Matrix of the Culebra Dolomite.....	8-6
8.2.4	Numerical Ground-Water-Flow and Transport Model of the Culebra Dolomite.....	8-6
8.3	Castile Formation and Shallower Units.....	8-7
8.4	Gas-Production Rates, Potentials, and Periods.....	8-8
8.5	Expected Brine Inflow to Waste Rooms and Panels Based on a Darcy-Flow Model.....	8-8
8.6	Initial Inventory and Decay Chains.....	8-9
8.7	Radionuclide Concentrations in Brines and Sorption in the Repository.....	8-10
8.8	Structural Interaction of the Salado Formation and Repository.	8-10
8.9	Terminal Waste State.....	8-11
8.10	Shaft Seal and Backfill Systems.....	8-12
8.11	Possible Repository Response to Gas Generation, and Total Volumes Generated.....	8-13
8.12	Possible Engineered Modifications of Waste and Backfill.....	8-14
8.13	Evaluation of Pathways to Man.....	8-15
8.14	Undisturbed Performance of the WIPP.....	8-16
8.15	Long-Term Performance of the WIPP in Response to Human Intrusion	8-17

APPENDICES

A.	UNPUBLISHED REFERENCE MEMOS	A-1
A.1	Drum (metal) corrosion, microbial decomposition of cellulose, reactions between drum-corrosion products and microbially generated gases, reactions between possible backfill constituents and gases and water Chemical reactions.....	A-3
A.2	Effects of microbial activity on repository chemistry, radionuclide speciation and solubilities in WIPP brines.....	A-31
A.3	Lab-scale microbial experiments.....	A-51

A.4	Dilatancy and Fracturing in the Disturbed Rock Zone and Its Contribution to the Total Observed Closure in WIPP Excavations.....	A-61
A.5	Numerical Brine Flow Modeling to an Isolated WIPP Disposal Room.....	A-69
A.6	Brine Flow to a Mined Room.....	A-83
A.7	Darcy Model for Brine Inflow to the WIPP; Evaluation of Data from the IT Brine Sampling Program.....	A-95
A.8	Increased Permeability Near Storage Rooms: Effect on Brine Inflow Computed With a Darcy Model.....	A-105
A.9	Preliminary Quantitative Estimates of TRU Waste and Waste Containers to be Emplaced in the WIPP.....	A-117
B.	SPECIFICATIONS FOR THE WIPP SEAL SYSTEM.....	B-1
B.1	Dimensions of Shaft- and Repository-Seal Components.....	B-1
C.	STANDARD DRILLING PROCEDURES USED IN THE DELAWARE BASIN.....	C-1
D.	NUMERICAL APPROACH TO CALCULATIONS DESCRIBING UNDISTURBED PERFORMANCE.....	D-1
D.1	Computer Model and Input.....	D-1
D.1.1	NEFTRAN.....	D-1
D.1.2	Generalized Network for the Undisturbed Case.....	D-7
D.2	Recommended Radionuclide-Distribution Coefficients for the Repository Seals, Drifts, and Shafts.....	D-9
D.2.1	Introduction.....	D-9
D.2.2	Estimated K_d values.....	D-14
D.2.3	Extrapolation of Experimental Data to Obtain Recommended K_d Values.....	D-15
D.2.4	Explanation of Recommended K_d Values.....	D-18
D.2.5	Conclusion.....	D-19
E.	NUMERICAL APPROACH TO CALCULATIONS DESCRIBING RADIONUCLIDE TRANSPORT AFTER HUMAN INTRUSION.....	E-1
E.1	Numerical Implementation of Post-Plugging Analysis.....	E-1
E.1.1	Modeling Approach.....	E-1
E.1.2	General Description of SWIFT II.....	E-1
E.1.3	Implementation of Brine-Reservoir and Borehole Submodels.....	E-2
E.1.3.1	Model Configuration.....	E-2
E.1.3.2	Influence Functions.....	E-4

E.1.3.3	Generalized Brine-Reservoir Response.....	E-6
E.1.3.4	Reservoir-Borehole-Aquifer Coupling.....	E-7
E.1.4	Assumptions About Repository Interactions and Source Term.....	E-10
E.1.5	Implementation of Flow and Transport in the Culebra.....	E-14
E.1.5.1	Use of a Stream Tube to Calculate Transport...	E-15
E.1.5.2	Lateral Dispersion.....	E-20
E.1.5.3	Source-Block Considerations.....	E-24
E.2	Input Parameters for Post-Plugging Analysis.....	E-25
E.2.1	Brine-Reservoir Parameters.....	E-25
E.2.1.1	Initial Reservoir Pressure.....	E-26
E.2.1.2	Reservoir Thickness.....	E-28
E.2.1.3	Reservoir Transmissivity.....	E-29
E.2.1.4	Reservoir Fluid Density.....	E-30
E.2.1.5	Reservoir Boundary.....	E-31
E.2.1.6	Reservoir Porosity.....	E-33
E.2.1.7	Reservoir Compressibility.....	E-34
E.2.2	Borehole Parameters.....	E-35
E.2.3	Repository Source-Term Parameters.....	E-37
E.2.4	Culebra Parameters.....	E-39
E.2.4.1	Regional Flow Field.....	E-39
E.2.4.2	Free-Water Diffusivity.....	E-43
E.2.4.3	Matrix Porosity.....	E-45
E.2.4.4	Matrix Tortuosity and Grain Density.....	E-48
E.2.4.5	Fracture Porosity.....	E-48
E.2.4.6	Matrix-Block Length.....	E-50
E.2.4.7	Longitudinal Dispersivity.....	E-51
E.2.4.8	Matrix and Fracture Distribution Coefficients (K_d 's).....	E-51
REFERENCES.....		R-1

FIGURES

	Page
1-1. Setting of the WIPP site relative to the northern Delaware Basin, showing selected geomorphic features and some boreholes.....	1-2
1-2. Approximate layout of the WIPP, showing both experimental (northern) and waste emplacement (southern) portions of the underground workings.....	1-3
1-3. Generalized stratigraphic column of the Delaware Mountain Group and younger sedimentary rocks at and near the WIPP site....	1-4
1-4. Hydrologic boreholes and wells at and near the WIPP site.....	1-6
3-1. Hydrostratigraphic column of the Rustler Fm. near the WIPP site..	3-24
3-2. Distribution of Rustler halite and transmissivities of the unnamed lower member and Rustler/Salado contact zone.....	3-29
3-3. Measured water levels and estimated freshwater heads of the unnamed lower member and Rustler/Salado contact zone.....	3-33
3-4. Distribution of Rustler halite and transmissivities of the Culebra Dolomite.....	3-37
3-5. Estimated freshwater heads in the Culebra Dolomite Member.....	3-40
3-6. Distribution of Rustler halite and Magenta transmissivity around the WIPP site.....	3-44
3-7. Water levels and estimated freshwater heads in the Magenta Dolomite Member.....	3-46
3-8. Estimated freshwater heads in the Forty-niner claystone.....	3-50
3-9. Cross section through the WIPP site showing hydraulic gradients between Rustler members.....	3-52

3-10.	Hydrologic boreholes and wells at and near the WIPP site.....	3-59
3-11.	Hydrochemical facies of the Culebra Dolomite.....	3-76
3-12.	Trilinear diagram for Culebra ground waters.....	3-77
3-13.	Stable-isotope compositions of ground waters from the Rustler Fm.	3-80
3-14.	Tritium and radiocarbon in Rustler and Dewey Lake ground waters..	3-82
3-15.	$^{87}\text{Sr}/^{86}\text{Sr}$ ratios in Ochoan and related rocks.....	3-85
3-16a.	δD values of the water of crystallization in gypsums as a function of depth.....	3-87
3-16b.	Ranges for gypsum and selenite δD values expected from crystallization or recrystallization.....	3-88
3-17.	$^{234}\text{U}/^{238}\text{U}$ activity ratios (ARs) in ground water from the Culebra Dolomite.....	3-91
3-18.	Relationship between apparent solubility product (log Q) for gypsum and ionic strength in Culebra water samples	3-94
3-19.	Relationship between apparent solubility product (log Q) for dolomite and ionic strength in Culebra water samples.....	3-95
3-20.	Effect of variation in carbonate alkalinity on the adsorption of Pu(IV) on goethite in 0.1 M NaNO_3 solution at pH = 8.6.....	3-109
3-21.	Effect of variation in pH on adsorption of PU(IV) onto goethite in 0.1 M NaNO_3 solution.	3-111
3-22.	Calculated K_d for sorption of U(VI) onto a goethite substrate as a function of pH at fixed total carbon concentration, in the presence of EDTA.....	3-112

3-23.	Effect of variable EDTA concentration and pH on calculated K_d for sorption of U(VI) onto goethite at a fixed partial pressure of CO ₂ and Ca concentration.....	3-113
3-24.	Variation in adsorption of U(VI) onto montmorillonite with constant amounts of clay, water, and total ionic strength and variable proportions of uranyl [U(VI)] ion and other cations.	3-115
3-25.	Approximate boundaries of ground-water flow and transport models in the WIPP region.....	3-121
3-26.	Deep boreholes that have encountered pressurized brine within the Castile Fm., northern Delaware Basin.....	3-131
3-27.	Horner-pressure plots for WIPP-12 Flow Tests 2 and 3.....	3-142
3-28.	Simulated and observed flow-rate history and pressure buildup for WIPP-12 Flow Test 2.....	3-146
3-29.	Simulated and observed flow-rate history and pressure buildup for WIPP-12 Flow Test 3.....	3-147
3-30.	Boreholes Cabin Baby-1 and DOE-2 relative to the distribution of known Bell Canyon sands at and near the WIPP site.....	3-150
4-1.	Salado Fm. permeabilities derived from in-situ experiments.....	4-15
4-2.	Cumulative brine-inflow volumes for a representative waste-emplacement room at permeabilities of 10^{-20} and 10^{-21} m ² , assuming lithostatic far-field pore pressure.....	4-17
4-3.	Time-dependent brine-inflow rates per meter of tunnel at permeabilities of 10^{-20} and 10^{-21} m ² , assuming lithostatic far-field pore pressure.....	4-18
4-4.	Comparison of calculated and measured Room D closures.....	4-36
4-5.	Schematic distribution of the DRZ around a representative waste room.....	4-38
4-6.	Schematic representation of processes acting in the DRZ.....	4-40

4-7.	Schematic distribution of fluid-flow behavior around a waste room.....	4-44
4-8.	Expected total room porosity as a function of time.....	4-53
4-9.	Schematic design of a WIPP panel seal.....	4-61
4-10.	Schematic design of a WIPP lower shaft seal system.....	4-65
4-11.	Excavated and enclosed areas of the WIPP repository.....	4-73
4-12.	Geologic cross section at the repository horizon.....	4-76
4-13.	Pressure history to initial closure of storage area, assuming no leakage.....	4-83
5-1.	Generalized pathways for possible radionuclide dose and health effects.....	5-4
5-2.	Schematic diagram of drill string for purposes of pathway evaluation.....	5-6
5-3.	Distribution of estimated brine densities within the Culebra Dolomite.....	5-14
5-4.	Particle travel paths and the location of the hypothetical Culebra stock well.....	5-16
6-1.	Schematic diagram of Cases IA and IB.....	6-2
7-1.	Schematic diagram illustrating the principal components of Case II	7-2
7-2.	Flow rates to the Culebra Dolomite from the breach borehole for Cases IIA, IIB, IIC, and IID.....	7-14
7-3.	Concentration profiles along the stream-tube centerline for stable Pb at 10,000 years, Case IIA.....	7-20

7-4.	Concentration profiles along the stream-tube centerline for the ^{238}Pu decay chain at 10,000 years, Case IIA.....	7-21
7-5.	Concentration profile along the stream-tube centerline for stable Pb at 10,000 years, Case IIB.....	7-24
7-6.	Breakthrough and boundary concentrations for stable Pb as a function of time, Case IIB.....	7-25
7-7.	Concentration profiles along the stream-tube centerline for the ^{240}Pu decay chain at 10,000 years, Case IIB.....	7-26
7-8.	Breakthrough and boundary concentrations for the ^{240}Pu decay chain, Case IIB.....	7-27
7-9.	Concentration profiles along the stream-tube centerline for the ^{239}Pu decay chain at 10,000 years, Case IIB.....	7-28
7-10.	Breakthrough and boundary concentrations for the ^{239}Pu decay chain, Case IIB.....	7-29
7-11.	Concentration profiles along the stream-tube centerline for the ^{238}Pu decay chain at 10,000 years, Case IIB.....	7-30
7-12.	Breakthrough and boundary concentrations for the ^{238}Pu decay chain, Case IIB.....	7-31
7-13.	Concentration profiles along the stream-tube centerline for the ^{241}Am decay chain at 10,000 years, Case IIB.....	7-32
7-14.	Breakthrough and boundary concentrations for the ^{241}Am decay chain, Case IIB	7-33
7-15.	Concentration profile along the stream-tube centerline for stable Pb at 10,000 years, Case IIC.....	7-39
7-16.	Breakthrough and boundary concentrations for stable Pb as a function of time, Case IIC.....	7-40
7-17.	Concentration profiles along the stream-tube centerline for the ^{240}Pu decay chain at 10,000 years, Case IIC.....	7-41

7-18.	Breakthrough and boundary concentrations for the ^{240}Pu decay chain, Case IIC.....	7-42
7-19.	Concentration profiles along the stream-tube centerline for the ^{239}Pu decay chain at 10,000 years, Case IIC.....	7-43
7-20.	Breakthrough and boundary concentrations for the ^{239}Pu decay chain, Case IIC.....	7-44
7-21.	Concentration profiles along the stream-tube centerline for the ^{238}Pu decay chain at 10,000 years, Case IIC.....	7-45
7-22.	Breakthrough and boundary concentrations for the ^{238}Pu decay chain, Case IIC	7-46
7-23.	Concentration profiles along the stream-tube centerline for the ^{241}Am decay chain at 10,000 years, Case IIC.....	7-47
7-24.	Breakthrough and boundary concentrations for the ^{241}Am decay chain, Case IIC	7-48
7-25.	Concentration profile along the stream-tube centerline for stable Pb at 10,000 years, Case IID.....	7-54
7-26.	Breakthrough and boundary concentrations for stable Pb as a function of time, Case IID.....	7-55
7-27.	Concentration profiles along the stream-tube centerline for the ^{240}Pu decay chain at 10,000 years, Case IID.....	7-56
7-28.	Breakthrough and boundary concentrations for the ^{240}Pu decay chain, Case IID.....	7-57
7-29.	Concentration profiles along the stream-tube centerline for the ^{239}Pu decay chain at 10,000 years, Case IID.....	7-58
7-30.	Breakthrough and boundary concentrations for the ^{239}Pu decay chain, Case IID.....	7-59
7-31.	Concentration profiles along the stream-tube centerline for the ^{238}Pu decay chain at 10,000 years, Case IID.....	7-60

7-32.	Breakthrough and boundary concentrations for the ^{238}Pu decay chain, Case IID	7-61
7-33.	Concentration profiles along the stream-tube centerline for the ^{241}Am decay chain at 10,000 years, Case IID.....	7-62
7-34.	Breakthrough and boundary concentrations for the ^{241}Am decay chain, Case IID	7-63
D-1.	Numerical flow-network input for simulation of Cases IA and IB...	D-8
E-1.	Schematic diagram of the brine-reservoir-breach release simulation.....	E-3
E-2.	Model area, WIPP-site boundary, breach-borehole and stock-well locations, and transport pathway.....	E-16
E-3.	Schematic illustration of streamlines in a unidirectional flow field perturbed by an injection well	E-17
E-4.	Calibrated transmissivity distribution from LaVenue et al.'s (1988) ground-water-flow model of the Culebra Dolomite.....	E-21
E-5.	Schematic illustration of intrusion borehole after plug emplacement.....	E-36
E-6.	Simulated flow field (Darcy velocities) for the Culebra Dolomite under undisturbed conditions.....	E-42

TABLES

		Page
1-1.	Summary of Changes Since 1980 in Understanding of Major Factors Potentially Affecting WIPP Long-Term Performance.....	1-7
1-2.	Description of and Input Parameters for Cases Analyzed in This Report.....	1-18
1-3.	Maximum Doses Received by a Member of the Drilling Crew (Case II)	1-25
1-4.	Maximum Doses Received by a Hypothetical Farmer Through Indirect Pathways (Case II)	1-25
1-5.	Maximum Doses Received by a Person Through the Contaminated-Beef Pathway.....	1-27
1-6.	Comparison of Radionuclide Concentrations from Natural and Man-Made Sources.....	1-28
2-1.	Generalized Stratigraphy of the Rustler Fm. at and near the WIPP Site.....	2-3
3-1.	Summary of Salado Permeability Measurements Made from the WIPP Underground Workings near the Waste-Disposal Horizon.....	3-7
3-2.	Summary of Salado Permeability Measurements in the Waste-Handling Shaft.....	3-7
3-3.	Summary of Salado Premeability Measurements Made from the Ground Surface.....	3-8
3-4.	Composition of "Standard" Intergranular Salado Brines.....	3-20
3-5.	Summary of Hydraulic Testing of the Unnamed Lower Member and Upper Salado Fm.....	3-31

3-6.	Hydraulic-Head Information for the Unnamed Lower Member and Upper Salado Fm.....	3-35
3-7.	Summary of Transmissivity Data for the Culebra Dolomite.....	3-38
3-8.	Hydraulic-Head Data for the Culebra Dolomite.....	3-41
3-9.	Summary of Transmissivity Data for the Magenta Dolomite.....	3-45
3-10.	Hydraulic-Head Data for the Magenta Dolomite.....	3-48
3-11.	Hydraulic-Head Data for the Forty-Niner Claystone.....	3-49
3-12.	Major Solutes in Ground Waters from the Rustler Formation.....	3-65
3-13.	Comparison of Radionuclide Distribution Coefficients for the Culebra Dolomite.....	3-100
3-14.	Sources of K_d Data Used to Estimate Values for Repository (Case I) and Culebra (Case II) Transport.....	3-103
3-15.	Sources of Additional K_d Data Used to Estimate Values for Culebra Dolomite in Cases I and II.....	3-105
3-16.	Nominal Compositions of Ground-Water/Brine Simulants Used in Batch K_d Experiments Summarized in Tables 3-14 and 3-15..	3-106
3-17.	Comparison of Transmissivity Data (m^2/s) for Culebra Modeling....	3-122
3-18.	Summary of Hydraulic Testing Activities at WIPP-12 from November 10, 1981 to March 7, 1983.....	3-137
3-19.	Ranges of Properties for Similar Reservoirs in the Northern Delaware Basin Summary of Interpreted Properties of the WIPP-12 Brine Reservoir and Estimated.....	3-148
4-1.	Summary of estimated gas-generation rates and potentials from WIPP waste and containers.....	4-19

4-2a.	CH-Waste Inventory (Initial Inventory).....	4-23
4-2b.	Modified Inventory Used in Calculations.....	4-25
4-3.	Simplified Radionuclide Chains Used in the Calculations.....	4-25
4-4.	Estimated Sorption Capacities of Bentonite Backfill and Iron Oxides.....	4-33
4-5.	Solid and Void Volumes in Waste.....	4-48
4-6.	Disposal-Room Parameters for Cases IIA and IIC.....	4-55
4-7.	Summary of Excavated and Enclosed Areas and Initial Volumes Within the WIPP Repository and Site, Not Considering Closure.....	4-75
4-8.	Gas-Storage Volumes and Calculated Pressures in Storage Area from Maximum Gas Potentials.....	4-81
4-9.	Disposal-Room Parameters for Cases IIB and IID.....	4-91
5-1.	Initial CH-TRU Waste Inventory, Defined on the Basis of Drum Equivalents.....	5-9
7-1.	Inventory Discharged to the Settling Pit (Cases IIA and IIB).....	7-6
7-2.	Maximum Dose Received by a Member of the Drilling Crew (Case II).	7-8
7-3.	Radionuclide Concentrations in the Dry Mud Pit (Case II).....	7-8
7-4.	Air Concentration (Ci/m^3) and Deposition Flux Values (Case II)...	7-9
7-5.	Soil Radionuclides Concentrations (Case II).....	7-10
7-6.	Soil-to-Plant and Forage-to-Food-Product Transfer Factors (Case II)	7-11

7-7.	50-Year Committed Dose Equivalent Factors (Case II).....	7-13
7-8.	Maximum Doses Received by a Hypothetical Farmer Through Indirect Pathways (Case II).....	7-13
7-9.	Radionuclide Concentrations in Culebra Brine at the Hypothetical Stock Well Location.....	7-65
7-10.	Water-to-Food Product Transfer Factors.....	7-67
7-11.	50-Year Committed Dose Equivalent Factors.....	7-67
7-12.	Sample Calculation for Np-237, Case IIC, 1345 Years.....	7-68
7-13.	Maximum Doses Received by a Person Through the Contaminated-Beef Pathway, 86 g/d Beef Ingestion.....	7-69
7-14.	Comparison of Estimated 50-Year CEDE's Using Data From Case IIC at 1,345 Years.....	7-70
C-1.	Specifications for Gas and Oil Exploratory Boreholes.....	C-4
D-1.	Nomenclature Used in Appendix D-1.....	D-3
D-2.	Numerical Parameters Input to NEFTRAN for Case IA.....	D-10
D-3.	Numerical Parameters Input to NEFTRAN for Case IB.....	D-11
D-4.	Retardation Factors for Use in Cases IA and IB.....	D-12
D-5.	Recommended K_d Values for Modeling Radionuclide Transport in Drifts, Seals, and Marker Bed 139.....	D-16
E-1.	Specifications for Repository Parameters Used in Case II Simulations.....	E-12
E-2.	Specifications for Intrusion Borehole for Case II Simulations....	E-13

E-3.	Characterization of the Waste Plume Within the Culebra Dolomite from Point of Release to Stock Well.....	E-19
E-4.	Parameter Base-Case and Range Values Selected for the Hypothetical Brine Reservoir.....	E-27
E-5.	Specification of Waste Radionuclide Species and their Initial ($t = 0$) Mass Inventory (Including Stable Lead) in the Repository for the Case II Simulations.....	E-38
E-6.	Parameter Base-Case and Range Values Selected for the Culebra Dolomite (Case II).....	E-40
E-7.	Estimated Free-Water Diffusion Coefficients for Radionuclide Transport in the Matrix of the Culebra Dolomite (cm^2/s).....	E-44
E-8.	Summary of Porosities Measured in Culebra Core Samples.....	E-46
E-9.	Summary of Formation Factors and Calculated Tortuosities from Culebra Core Samples.....	E-49
E-10.	Estimated Matrix K_d Values for Transport Calculations in the Culebra Dolomite (mL/g).....	E-53
E-11.	Estimated K_d Values for Clays of the Culebra Dolomite (mL/g).....	E-53
E-12.	Estimated K_a Values for Transport Calculations in the Fractures of the Culebra Dolomite.....	E-53

1.0 INTRODUCTION, OBJECTIVES, AND SUMMARY OF RESULTS

1.1 Introduction and Objectives

The Waste Isolation Pilot Plant (WIPP) in southeastern New Mexico (Figure 1-1) is designed for the receipt, handling, storage, and disposal of defense-generated transuranic (TRU) wastes. The WIPP underground workings (Figure 1-2) are currently being constructed at a depth of ~655 m (2,150 ft) in bedded halites in the lower portion of the Salado Formation (Fm.) (Figure 1-3).

The U.S. Environmental Protection Agency (EPA) has determined that the safe disposal of TRU wastes requires effective isolation of the waste from the accessible environment for thousands of years. The EPA has developed a standard for the performance of nuclear-waste repositories (40 CFR 191; EPA, 1985) that regulates the performance of a proposed repository on time scales that, in some cases, extend to 10,000 years. Although 40 CFR 191 Subpart B has been remanded to the EPA by the United States Court of Appeals for the First Circuit (Natural Resources Defense Council v. U.S. Environmental Protection Agency, 824 F.2d 1258 (1st Cir. 1987)), the WIPP Project will continue to respond to 40 CFR 191 as first promulgated until a new standard is in place (U.S. Department of Energy [DOE] and State of New Mexico, 1981, as amended 1987).

A nuclear-waste repository will have an unavoidable impact on the environment in which it is placed, even in the absence of human intrusion after decommissioning. Additional environmental impact and health effects may result from such human intrusion. Both unavoidable environmental impacts of the WIPP and potential radionuclide doses to individuals as a result of expected operations and human intrusion were considered in the WIPP Final Environmental Impact Statement (FEIS; DOE, 1980a).

In the nine years since the WIPP FEIS was written, there has been major growth in the understanding of the geologic and hydrologic behavior of the WIPP site (e.g., Lappin, 1988) and of the Salado Fm. adjacent to the WIPP

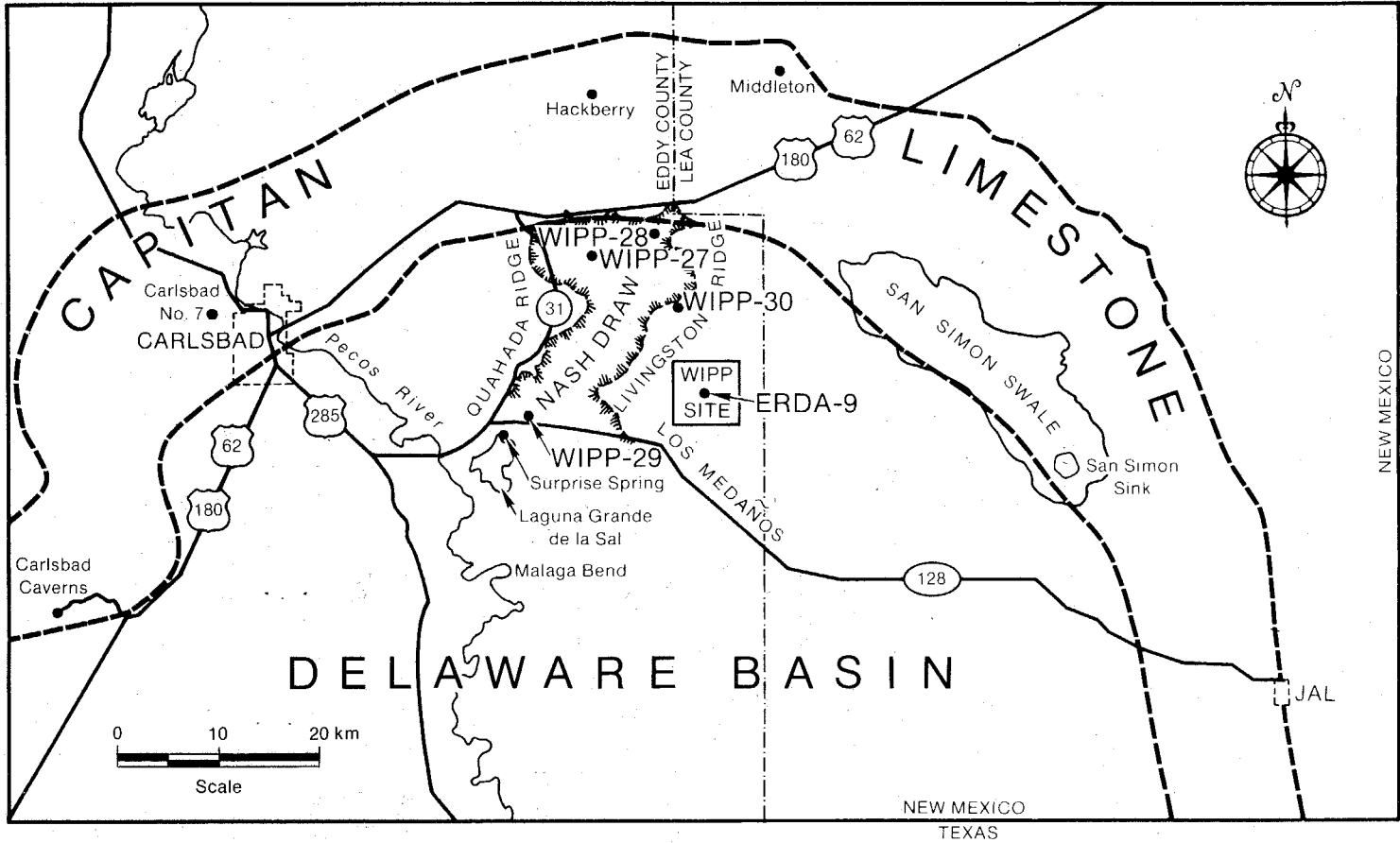
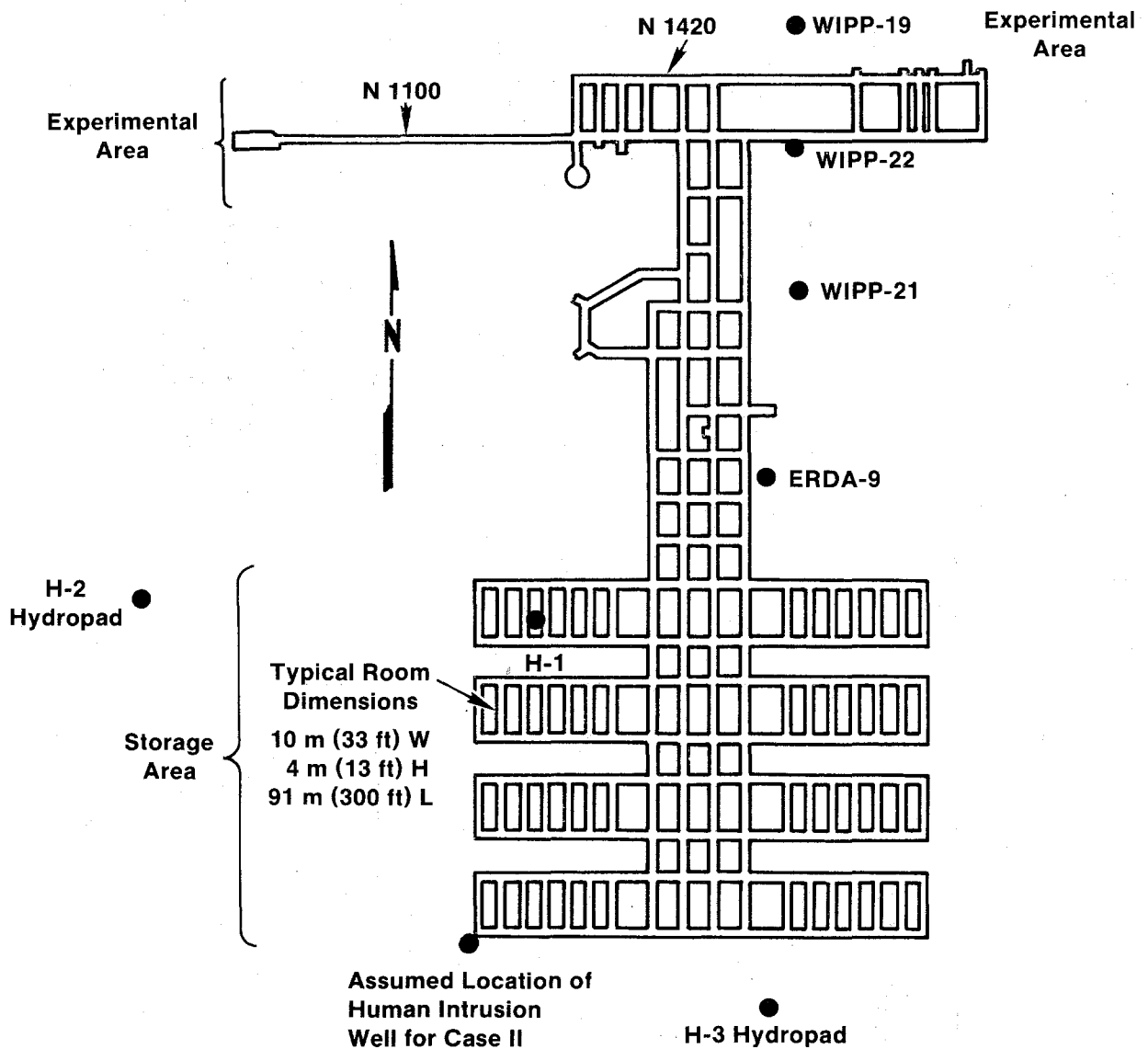


Figure 1-1. Setting of the WIPP site relative to the northern Delaware Basin, showing selected geomorphic features and some boreholes (after Lambert, 1983, Fig. VI-1).



TRI-6330-34-0

Figure 1-2. Approximate layout of the WIPP, showing both experimental (northern) and waste-emplacement (southern) portions of the underground workings.

SYSTEM	SERIES	GROUP	FORMATION	MEMBER
RECENT	RECENT		SURFICIAL DEPOSITS	
QUATERNARY	PLEISTOCENE		MESCALERO CALICHE	
			GATUNA	
TRIASSIC		DOCKUM	UNDIVIDED	
PERMIAN	OCHOAN		DEWEY LAKE RED BEDS	
			RUSTLER	Forty-niner
				Magenta Dolomite
				Tamarisk
				Culebra Dolomite
	unnamed			
	SALADO			
	CASTILE			
	GUADALUPIAN	DELAWARE MOUNTAIN	BELL CANYON	
			CHERRY CANYON	
BRUSHY CANYON				

TRI-6330-89-0

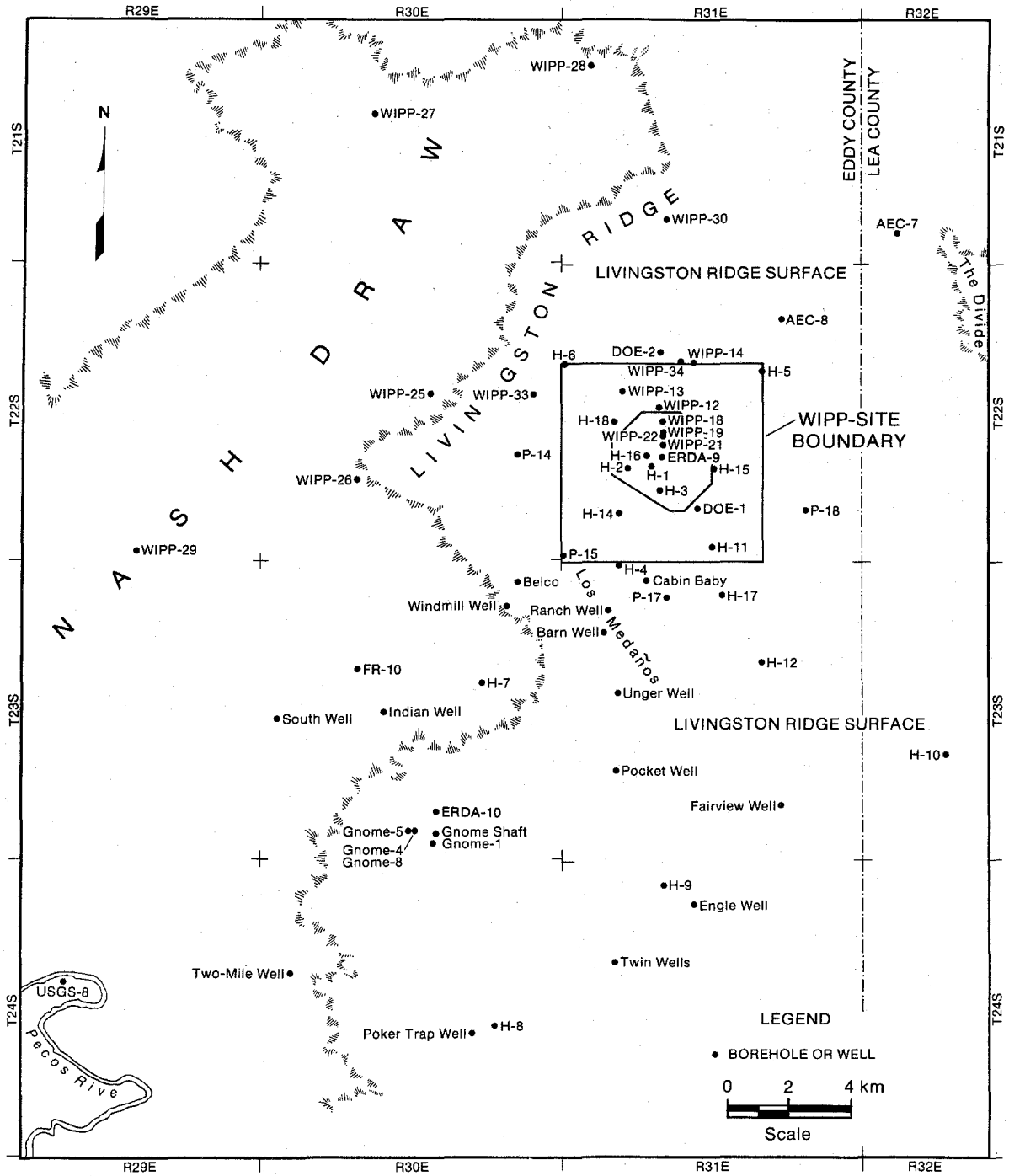
Figure 1-3. Generalized stratigraphic column of the Delaware Mountain Group and younger sedimentary rocks at and near the WIPP site (Beauheim, 1987c, Fig. 2-1).

underground workings (e.g., Tyler et al., 1988) (Table 1-1). Neither Lappin nor Tyler et al., however, directly considered the possible effects of new information and conceptual models on the long-term performance of the WIPP, nor did they consider the behavior of some features critical to long-term performance, such as the emplacement of borehole plugs in later exploration holes that might penetrate the WIPP.

Partly in response to the qualitative changes in the understanding of the expected behavior of the WIPP repository, the DOE decided in 1988 to prepare a Supplemental Environmental Impact Statement (SEIS) for the WIPP. The WIPP SEIS will specifically address those areas in which the conceptual, numerical, and regulatory understanding of the expected behavior of the WIPP repository have significantly improved since the WIPP FEIS was prepared.

This report has several objectives. First, it briefly summarizes Sandia's current technical understanding of in-situ behavior affecting the prediction of long-term performance of the WIPP repository. The following topics are included: (1) the hydrology and geochemistry of the Salado Fm., Rustler Fm., Dewey Lake Red Beds, and Bell Canyon Fm.; (2) the hydrology of brine assumed to be present within fractured anhydrite of the Castile Fm. beneath the repository; (3) the expected overall structural, gas-generation, and brine-inflow behavior of rooms or panels, filled with either as-designed or modified WIPP waste and backfill; (4) the expected design and behavior of the sealing system; and (5) the expected properties and durability of borehole plugs assumed to be emplaced after penetration of the repository during future hydrocarbon exploration. The locations of boreholes specifically named in the text are shown in Figure 1-4.

Second, this report compares the current conceptual and numerical models in the technical areas listed above with those available at the time of the WIPP FEIS (DOE, 1980a) (Table 1-1). Some changes in conceptual and numerical models may have minor impact on the expected behavior of the repository, even in 10,000 years. Other changes, such as the relationship between gas generation within the repository and far-field permeability of the Salado Fm., suggest qualitatively different behavior than was expected at the time of the WIPP FEIS.



TRI-6330-77-0

Figure 1-4. Hydrologic boreholes and wells at and near the WIPP site (Siegel, Lambert, and Robinson, 1989).

Table 1-1. Summary of Changes Since 1980 in Understanding of Major Factors Potentially Affecting WIPP Long-Term Performance

Assumptions and Treatment
In WIPP FEIS (DOE, 1980a)

Present Understanding and Potential Impact

Salado Brine Flow and Brine Permeability

- | | |
|---|--|
| a. "The Salado acts hydrologically as a confining bed, and does not contain circulating groundwater" (p. 7-87). In effect, it was assumed at this time that brine was present only in fluid inclusions and hydrous minerals. | a. Grain-boundary brines are compositionally distinct from fluid inclusions; Salado Fm. probably is hydrologically saturated (Section 3.2.1). |
| b. "From experimental data, the total volume of fluid drawn to any canister can be estimated crudely; it may lie between 0.1 and 20 liters, with 0.1 liter more likely" (p. 9-158). Brine flow was interpreted to result only from thermal gradients resulting from emplacement of heat-producing wastes. | b. Major contribution is flow of grain-boundary fluids as a result of pore-pressure gradients resulting from excavation; experimental results to date modeled assuming Darcy flow, which implies non-zero long-term inflow; uncertainties arising from possible stratigraphic effects, two-phase flow, and non-Darcy flow are not yet quantified. Darcy-flow model probably overpredicts brine inflow (Section 3.2.1), but still indicates that early brine saturation is highly improbable (Section 4.10.1); brine saturation is ultimately expected. |
| c. Because the <u>FEIS</u> concluded that the Salado Fm. did not contain circulating ground water, the question of far-field brine permeability was not considered further. | c. Far-field brine permeability is probably $<10^{-20}$ to 10^{-21} m ² and may be effectively zero in undisturbed region (see above). |

Table 1-1. Summary of Changes Since 1980 in Understanding of Major Factors Potentially Affecting WIPP Long-Term Performance (continued)

Assumptions and Treatment
In WIPP FEIS (DOE, 1980a)

Present Understanding and Potential Impact

Salado Gas Permeability and Gas-Storage Properties

- | | |
|---|--|
| a. Although no specific far-field permeability was assigned, parametric studies indicated that Salado gas permeability appeared to be sufficient to dissipate the volumes of gas potentially generated by waste. | a. Far-field permeability is probably $<10^{-20}$ to 10^{-21} m ² , and grain-boundary brines pressurized to between hydrostatic and lithostatic pressure; because gases would have to displace these brines, dissipating any significant volumes of gas generated within the repository (Section 3.2.1) would be very difficult. |
| b. "According to initial estimates ... there is little possibility of repository failure from overpressurization at gas-generation rates of less than 5 moles per year per drum. Since these conclusions depend on the gas permeability and the mechanical properties of the repository medium, they will be subject to some revision when data are available from the actual underground workings" (p. 9-156). | b. Combination of gas-generation rates (Section 4.2) and very low far-field permeability will probably result in gas pressures exceeding lithostatic load unless they are relieved by (1) room re-expansion; (2) gas storage in disturbed-rock zone adjacent to repository; (3) gas storage within Marker Bed 139 and along other stratigraphic contacts near the repository horizon; (4) a combination of gas migration up shafts and into adjacent marker beds (Section 4.10); or (5) engineering modification of the waste or backfill. Marker Bed 139 will be a relatively high-permeability path directly under excavations, except for seal locations, because of the development of open fractures (Sections 4.9, 6.0). |

Table 1-1. Summary of Changes Since 1980 in Understanding of Major Factors Potentially Affecting WIPP Long-Term Performance (continued)

Assumptions and Treatment
In WIPP FEIS (DOE, 1980a)

Present Understanding and Potential Impact

Salado Brine Geochemistry

- | | |
|--|---|
| a. Although only one analysis of Salado brine was included in the <u>FEIS</u> (a mine seep in the Duval mine, Table 7-19, p. 7-93), WIPP Brines "A" and "B" were defined for experimental purposes in other work conducted during the same period. Brine A is K and Mg-rich; Brine B is a high-NaCl brine. | a. Considerable variability of Salado brines has been found (Section 3.2.2). "Standard" brine identified is similar to <u>FEIS</u> brine B, but less rich in K and Mg, higher in Na, Cl, and B (Table 3-4); brine standard defined appears to be near saturation with respect to anhydrite, gypsum, and halite; brines collected within WIPP underground workings often evolve gas, thought to be mainly N ₂ . |
|--|---|

Radionuclide Solubility in Salado Brines

- | | |
|--|---|
| a. The <u>FEIS</u> assumed congruent dissolution of salt and waste, without assigning solubility limits directly to the waste radionuclides, i.e., "... the waste-dissolution rate was assumed to be the same as the rate at which the salt formation was dissolved." (p. K-20). | a. A wide range of effective radionuclide solubilities (10 ⁻³ to 10 ⁻⁹ Molar) (Section 4.5) is possible because of the wide range in local Eh, pH, possible organic complexes, and possible effects of particulates; present best-estimate solubility (10 ⁻⁶ M) is simple log-intermediate of range; sorption of radionuclides onto clays and iron corrosion products (Section 4.6) may be an effective mechanism, but it is not included numerically in calculations, because of the wide range of radionuclide solubilities. |
|--|---|

Table 1-1. Summary of Changes Since 1980 in Understanding of Major Factors Potentially Affecting WIPP Long-Term Performance (continued)

Assumptions and Treatment
In WIPP FEIS (DOE, 1980a)

Present Understanding and Potential Impact

Gas Generation Within WIPP Repository by Radiolysis, Bacteriological Activity, and Corrosion of Metals

- | | |
|---|--|
| a. Based on the data available in 1980, the interpretation was that the dominant gas developed by microbial activity would be CO ₂ (p. 9-153). The average rate of gas generation by all mechanisms (not including anoxic drum corrosion) was estimated to be 0.3 to 1.4 moles/drum (equivalent) per year, with lower and upper limits of 0.0005 and 2.8 moles/drum per year (Table 9-68, p. 9-155). A total gas-generation potential of 2,000 moles/drum was estimated by Molecke (1979). | a. Updated interpretation is that microbial action could produce CO ₂ , CH ₄ , H ₂ S, or N ₂ , although CO ₂ and N ₂ are most likely; wide range of gas compositions is possible depending on oxidation state; estimated rate for microbial action, 0.85 moles/drum/year is average of rates estimated in <u>FEIS</u> ; estimated total gas-generation potential from microbial activity reduced to 606 moles/drum, based on recent inventory estimates (Section 4.2). |
| b. Gas generation under anoxic conditions was considered possible, "at a maximum rate of 2 moles per year per drum." However, "under the dry conditions expected in a repository, the corrosion of steel is not expected to yield significant quantities of gas" (p. 9-154). | b. Anoxic corrosion of Fe is probably an important process in Mg-rich Salado brines; estimated rates of H ₂ generation by drum corrosion range from 0.26 to 2 moles/drum/year; average value 1.1 moles/drum/year is increased to 1.7 moles/drum/year to account for metallic waste; estimated total gas-generation potential from corrosion is 894 moles/drum; gas generation <u>rates</u> depend strongly on availability of free brine. |
| c. The total gas-generation potential estimated in work supporting the <u>FEIS</u> was 2,000 moles/drum. | c. Total estimated gas-generation potential is 1,480 moles/drum at rates as high as 2.55 moles/drum/year; net balance of microbial action and H ₂ O is not known, but assumed to be zero; ~100 m ³ of brine per room is required to complete anoxic corrosion. |

Table 1-1. Summary of Changes Since 1980 in Understanding of Major Factors Potentially Affecting WIPP Long-Term Performance (continued)

Assumptions and Treatment
In WIPP FEIS (DOE, 1980a)

Present Understanding and Potential Impact

Gas Generation Within WIPP Repository by Radiolysis, Bacteriological Activity, and Corrosion of Metals (continued)

- | | |
|--|---|
| d. The duration of gas generation was not specifically considered in the <u>FEIS</u> . | d. The estimated duration of gas generation is highly uncertain; microbial activity depends strongly on waste geometry, i.e., compaction; drum corrosion depends on availability of free brine or at least maintenance of humid conditions. |
|--|---|

Salado Structural and Hydrologic Behavior Near the Underground Workings

- | | |
|---|--|
| a. No credit was taken in the <u>FEIS</u> for structural or creep closure of the WIPP repository, i.e., "waste is assumed to be uniformly distributed throughout the volumes of the undisturbed disposal areas at the time a scenario begins" (p. K-23). | a. Mechanical closure of repository plays large role in reducing permeability and defining "final" structural state, but does not enter directly into numerical calculations; final porosity of design-basis waste and backfill is 0.16 to 0.25; final permeability is 0.1 Darcy (10^{-13} m ²) (Section 4.8); closure to "final" state is assumed to take ~60 years. |
| b. Mechanical closure of the repository was assumed to occur largely by a process of coherent creep, although the possibility of a dilatant zone around the underground workings was recognized, i.e., "... open volume in the repository will close, probably in 50 to 200 years. Closure to full salt density is expected because the air in a room and tunnel is ... not enough to maintain appreciable openings in the salt. Nevertheless, some volume may become available for storing evolved gas because of dilatancy ...: as the salt creeps into openings in the repository, it is at a reduced density" (p. 9-154). | b. Wall-closure rates measured in-situ are about three times those expected on basis of original model calculations; far-field process is still creep, but near-field region develops a disturbed rock zone (DRZ); DRZ development and extent is time-dependent; DRZ includes dilation, macroscopic fracturing, and development of a zone of increased permeability adjacent to underground workings; DRZ may retard final closure and may serve as both source and sink for brine (Sections 4.3, 4.7) and as sink for gas (Section 4.10); with the exception of Marker Bed 139, which is assumed to remain open (Sections 4.7, 6.1), it is assumed that the DRZ is eliminated in final stages of closure. |

Table 1-1. Summary of Changes Since 1980 in Understanding of Major Factors Potentially Affecting WIPP Long-Term Performance (continued)

Assumptions and Treatment
In WIPP FEIS (DOE, 1980a)

Present Understanding and Potential Impact

"Final" State of Waste-Emplacement Rooms and Panels

- a. The FEIS assumed that the waste would be dry and compacted prior to any breach; i.e., "as the salt flows under lithostatic pressure, ... open volume in the repository will close, probably in 50 to 200 years" (p. 9-154). However, in breaches involving fluid flow through the repository, a transmissivity of $3.9 \times 10^{-3} \text{ m}^2/\text{s}$ (permeability of $-4.7 \times 10^{-10} \text{ m}^2$) was assumed (p. 9-132).
- a. It is concluded that mechanical closure to near-final porosity and permeability will occur independent of brine inflow and gas generation; it is generally assumed that final structural state is not altered by brine or gas behavior (Section 4.8); calculations of undisturbed performance (Section 6.0) assume that repository immediately resaturates at end of assumed 2000-year gas-generation phase; however, mechanism and time required for resaturation are uncertain (Section 4.10); calculations of transport in event of human intrusion (Section 7.0) assume that gas is passively vented from repository and that one-phase brine flow is transport mechanism; possibility of two-phase flow is recognized (Section 3.2.1) but cannot be quantified at present.

Backfill

- a. FEIS discussed backfill only briefly. Use of crushed salt as a backfill material was assumed for purposes of controlling subsidence (p. 9-151).
- a. Design-basis backfill is assumed to be 70/30 salt/bentonite mixture in waste-emplacement areas and crushed salt elsewhere; major objective is control of free brine (Section 4.8); other options being considered include addition of getters to control gas pressures and use of grouts to control permeability (Section 4.11).

Table 1-1. Summary of Changes Since 1980 in Understanding of Major Factors Potentially Affecting WIPP Long-Term Performance (continued)

Assumptions and Treatment
In WIPP FEIS (DOE, 1980a)

Present Understanding and Potential Impact

Seals Within Repository

- a. FEIS discussed shaft sealing or plugging only briefly. It was stated that "the [shaft and borehole] plugs are to have long-term durability, low water permeability, resistance to groundwater attack, and physical and chemical compatibility with the surrounding rock. The plug materials are also required to bond to the surrounding rock ..." (p. 8-54).
- a. Design basis is for emplacement of multi-component seals at entrance to each waste-emplacement panel and at two locations within accessways (Section 4.9); major reliance for long-term containment is on compacted backfill, because grouts and cements in multi-component seals are assumed to degrade; it is assumed (Section 4.9) that Marker Bed 139 will be sealed only at seal locations; design-basis shaft sealing combines multi-component seals at base of shaft, in the Salado Fm. below the Rustler Fm., and in the Rustler Fm. (Section 4.9); however, it is assumed only that compaction of crushed salt in lower 200 m of shaft is effective (Section 4.9).

Borehole Plugging

- a. FEIS did not specifically discuss plugging of boreholes not present at the time of decommissioning. However, in modeling of breach scenarios 2a and 2b in the FEIS (the "U-tube" scenarios), hydraulic conductivities of 50 ft/day ($\sim 2 \times 10^{-11} \text{ m}^2$) and 5 ft/day ($\sim 2 \times 10^{-12} \text{ m}^2$) were assumed for two "failed" boreholes (p. 9-132).
- a. It is assumed that in the event of human intrusion by a hydrocarbon-exploration hole, the borehole is later plugged according to currently existing regulations (Section 7.0, Appendix C); grout and concrete used in plugs is assumed to degrade beginning 75 years after emplacement; degraded plug permeabilities of 10^{-12} and 10^{-11} m^2 are considered.

Hydrology of Castile Fm.: Presence and Character of Castile Brine Reservoir Beneath WIPP Underground Workings

- a. The presence of pressurized brines in anticlinal structures within the Castile Fm. was recognized, and brine was known to be present in hole ERDA-6 (Table 7-19, p. 7-93). Based on the apparent restriction of these brines to anticlinal structures, FEIS apparently concluded that Castile brine was unlikely to be present beneath the WIPP underground workings (p. 7-87).
- a. Pressurized brines are assumed to be present beneath WIPP waste-emplacement panels, based on data from drill holes and geophysical studies (Section 3.4); properties of brine occurrence are assumed to be those interpreted for the WIPP-12 reservoir (Section 3.4, Appendix E, Table 3-19).

Table 1-1. Summary of Changes Since 1980 in Understanding of Major Factors Potentially Affecting WIPP Long-Term Performance (continued)

Assumptions and Treatment
In WIPP FEIS (DOE, 1980a)

Present Understanding and Potential Impact

Hydrology of the Bell Canyon Fm. and Relationship of Bell Canyon and Rustler Heads

- | | |
|---|--|
| a. Although the possibility of downward flow was recognized, it was assumed for purposes of calculation that flow between the Bell Canyon Fm. (Delaware Mountain Group) and the Rustler Fm. would be upward (p. 9-130). | a. Based on interpretation of relative heads at holes Cabin Baby-1 and DOE-2, it is concluded that flow would be downward if Bell Canyon and Rustler Fms. were connected (Section 3.5.1) by an open borehole; because of low local permeability of Bell Canyon Fm., flow in this unit would be very slow and is not considered quantitatively. |
|---|--|

Rustler Physical Hydrology, Geochemistry, and Numerical Modeling

- | | |
|--|---|
| a. Three water-bearing zones within the Rustler Fm. were recognized: the Magenta Dolomite, Culebra Dolomite, and the "Rustler-Salado interface" (p. 7-87). | a. A total of 41 Culebra locations have been tested (Table 3-17); testing to date indicates presence of five water-producing units within Rustler Fm. (Section 3.3.1, Figure 3-1). |
| b. The Culebra Dolomite and Magenta Dolomite, though known to vary in permeability, were combined as a single "Rustler aquifer" and assigned a uniform hydraulic conductivity of 1 ft/day ($\sim 3.5 \times 10^{-6}$ m/s) east of Nash Draw for purposes of numerical modeling. In the model, hydraulic conductivity was assumed to be higher within Nash Draw, with a maximum value of 2.2×10^{-4} m/s (Figure K-7, p. K-15). | b. Culebra Dolomite is still interpreted to dominate flow near site; Culebra transmissivity varies by approximately three orders of magnitude within the WIPP site (10^{-7} to 10^{-4} m ² /s, Table 3-17); total range of reported transmissivities varies from $\leq 2 \times 10^{-7}$ m ² /s to $>10^{-3}$ m ² /s (Table 3-7); all measured transmissivities included as point values in model estimates of transmissivity distribution (Figure E-6); zone of relatively high transmissivities is present in southeastern portion of site. |

Table 1-1. Summary of Changes Since 1980 in Understanding of Major Factors Potentially Affecting WIPP Long-Term Performance (continued)

Assumptions and Treatment
In WIPP FEIS (DOE, 1980a)

Present Understanding and Potential Impact

Rustler Physical Hydrology, Geochemistry, and Numerical Modeling (continued)

- | | |
|--|--|
| c. For purposes of numerical modeling, the "Rustler aquifers" were assumed to behave as an isotropic porous medium with a uniform porosity of 0.10 (Table K-2, p. K-18). | c. Local flow and transport behavior is affected by fracturing where $T \geq 10^{-6} \text{ m}^2/\text{s}$; distances over which fracturing plays a role depend on local properties, especially in southeastern part of site (Section 7.3, Appendix E.2.4); under some conditions fractures may dominate transport out of the WIPP site (Section 7.3). Measured matrix porosities range from 0.03 to 0.3 (Table E-8). |
| d. Regional flow within the "Rustler aquifers" was assumed to be toward the southwest, with final discharge at Malaga Bend on the Pecos River (Figure K-5, p. K-13). The possibility that flow in the site area might be to the southeast was recognized (p. K-11). Modeling was conducted on the basis of equivalent freshwater heads. | d. Modern flow within Culebra Dolomite is interpreted to be largely north-south in site area, but dominated by flow in zone of relatively high transmissivity in southeastern portion of site; ultimate discharge point is not known; interpretation based on model that includes effects of variable brine density (Figure 5-3). |
| e. For purposes of numerical modeling, the Culebra and Magenta Dolomites were combined into a single unit, the "Rustler aquifers." It was concluded that "... Rustler Formation aquifers ... apparently do not communicate hydrologically with any of the aquifers below the Salado Formation or with the shallow-dissolution zone" (p. K-11). Although not specifically stated, steady-state flow directions and rates were also assumed. | e. Head potentials between units are known to be laterally variable (Section 3.3.1); limits to vertical flow are considered qualitatively (Section 3.3.3); present modeling assumes confined steady-state flow for 10,000 years (Section 7.3, Appendix E), except for disturbance by Castile brine reservoir; however, it is recognized that Rustler hydrologic setting is transient over 10,000 years (Section 3.3.3); where defined, relative head potentials and geochemistry within Rustler Fm. are not consistent with modern infiltration from surface at WIPP site. |

Table 1-1. Summary of Changes Since 1980 in Understanding of Major Factors Potentially Affecting WIPP Long-Term Performance (concluded)

Assumptions and Treatment
In WIPP FEIS (DOE, 1980a)

Present Understanding and Potential Impact

Rustler Physical Hydrology, Geochemistry, and Numerical Modeling (continued)

- | | |
|--|--|
| f. Although the Rustler brines were known to be variable (Table K-3, p. K-20), this variability could not be included in ground-water modeling. | f. Total range of TDS in Rustler brines at the WIPP site is estimated to be 4,000 to >300,000 mg/L (Section 3.3.2), Culebra waters range from ~10,000 to >200,000 mg/L (Table 3-12); careful and repetitive sampling of ground waters is needed. |
| g. Although not specifically stated, radionuclide retardation in the Rustler Fm. was estimated using a porous-medium approximation. Specific K_{ds} used include Pu, 2,100 mL/mg; U, 10 mL/mg; Np, 350 mL/mg (Table K-3, p. K-20). | g. Radionuclide retardation estimates in the Culebra Dolomite (Section 3.3.4) are reduced as a result of effects of variable ground-water composition, possible organic complexing, uncertainties in Eh and pH, competing ions, and the presence of discrete fractures within the Culebra Dolomite; ranges of K_{ds} considered here (Table 3-13) include Pu, 25 to 300 mL/g; U, 1 to 10 mL/g; Np, 1 to 10 mL/g. |
| h. Although the conclusion does not seem to be specifically stated, the Rustler aquifers appeared to be very effective in retarding radionuclide transport. | h. Even with fracturing and decreased K_{ds} , Culebra Dolomite is reliable given estimated "most likely" properties but not as favorable as in <u>FEIS</u> ; some calculations in this report, however, indicate that there are combinations of Culebra transport properties that, although unlikely, could lead to dominant fracture-flow effects over distances up to 5 km. |
-

Third, this report documents both parameter values now thought to be "representative" or "most likely" for use in numerical predictions of the long-term behavior of the repository and the estimated ranges of these parameters. When possible, the uncertainties in data and the resulting predictions of long-term behavior of the repository are discussed. The uncertainties in some parameters are included in the calculations reported here.

Finally, this report describes, documents, and interprets six sets of calculations of potential health effects to individuals, resulting from emplacement of TRU wastes in the WIPP, hydrologic saturation of the repository as a result of either natural processes or human intrusion, ground-water transport of radionuclides, and direct exposures resulting from drilling (where appropriate). Case IA calculates doses resulting from undisturbed performance, assuming the design-basis waste and backfill and expected waste solubilities and transport properties within the repository. Case IB also calculates undisturbed performance, assuming increased waste solubility and degraded flow and transport properties within the repository and in the geosphere. Case II examines repository performance following drilling through the repository and a Castile brine reservoir, using varying assumptions (Table 1-2) to examine the effects of uncertainties in transport properties of both waste and geosphere.

The deterministic calculations in this report are not a part of the WIPP performance assessment required by 40 CFR 191; they are not designed to show either compliance or lack of compliance with the EPA's standard for radioactive waste disposal (40 CFR 191), for two reasons. First, the calculations presented here are deterministic (i.e., they assume a probability of 1.0 for each calculation). This approach is physically unrealistic; in fact, the results calculated here are mutually exclusive, because each calculation assumes different repository and geosphere characteristics. Second, no calculation of 10,000-year doses from radionuclide transport or of doses following human intrusion are required by 40 CFR 191. Thus, the results of the calculations in this report are not intended to be directly compared with the performance standard in 40 CFR 191. Probabilistic calculations, which assign numerical probabilities to important input data and to each of

Table 1-2. Description of and Input Parameters for Cases Analyzed

Case	Description	Repository Parameters	Transport Parameter
IA	Undisturbed Performance	<p>EXPECTED</p> <p>Radionuclide Solubility 10^{-6} M</p>	<p>EXPECTED</p> <p>Lower-Shaft Permeability 10^{-20} m²</p> <p>Culebra Permeability 5×10^{-15} to 3×10^{-13} m²</p> <p>Culebra Matrix Porosity 0.16</p>
IB	Undisturbed Performance	<p>DEGRADED</p> <p>Radionuclide Solubility 10^{-4} M</p>	<p>DEGRADED</p> <p>Lower-Shaft Permeability 10^{-20} m²</p> <p>Marker Bed 139 Seal Permeability 4×10^{-17} m²</p> <p>Culebra Permeability 5×10^{-15} to 5×10^{-17} m²</p> <p>Culebra Matrix Porosity 0.07</p>
IIA	Response to Breach of Castile Brine Reservoir	<p>EXPECTED</p> <p>Radionuclide Solubility 10^{-6} M</p> <p>Waste/Backfill Permeability 10^{-13} m² Sufficient For Mixing^a</p> <p>Salado Brine Inflow 1.3 m³/panel/year</p>	<p>EXPECTED</p> <p>Long-Term Plug Permeability 10^{-12} m²</p> <p>Culebra Matrix Porosity 0.16</p> <p>Culebra Fracture Porosity 0.0015</p> <p>Culebra Fracture Spacing 2 m</p> <p>Culebra Free-Water Diffusivity 1×10^{-6} cm²/s</p> <p>Culebra K_d's Range 0.1 to 200 mL/g</p> <p>Culebra Matrix Tortuosity 0.15</p>
IIB	Response to Breach of Castile Brine Reservoir	<p>PERMEABILITY LIMITED</p> <p>SOLUBILITY DEGRADED</p> <p>Radionuclide Solubility 10^{-4} M</p> <p>Waste Precompaction Reduces Permeability Enough to Prohibit Mixing^b</p> <p>Salado Brine Inflow 1.3 m³/panel/year</p>	<p>DEGRADED</p> <p>Long-term Plug Permeability 10^{-11} m²</p> <p>Culebra Matrix Porosity 0.07</p> <p>Culebra Fracture Porosity 0.0015</p> <p>Culebra Fracture Spacing 7 m</p> <p>Culebra Free-water Diffusivity 5×10^{-7} cm²/s</p> <p>Culebra K_d's Range 0.05 to 100 mL/g</p> <p>Culebra Matrix Tortuosity 0.03</p>

Table 1-2. Description of and Input Parameters for Cases Analyzed (concluded)

Case	Description	Repository Parameters	Transport Parameter
IIC	Response to Breach of Castile Brine Reservoir	<p>DEGRADED</p> <p>Radionuclide Solubility 10^{-4} M</p> <p>Waste/Backfill Permeability 10^{-13} m² Sufficient for Mixing^a</p> <p>Salado Brine Inflow 1.3 m³/panel/year</p>	<p>DEGRADED</p> <p>Long-term Plug Permeability 10^{-11} m²</p> <p>Culebra Matrix Porosity 0.07</p> <p>Culebra Fracture Porosity 0.0015</p> <p>Culebra Fracture Spacing 7 m</p> <p>Culebra Free-Water Diffusivity 5×10^{-7} cm²/s</p> <p>Culebra K_d's Range 0.05 to 100 mL/g</p> <p>Culebra Matrix Tortuosity 0.03</p>
IID	Response to Breach of Castile Brine Reservoir	<p>PERMEABILITY LIMITED</p> <p>SOLUBILITY AS EXPECTED</p> <p>Radionuclide Solubility 10^{-6} M</p> <p>Waste/Backfill Permeability 10^{-16} m² Prohibits Mixing^b</p> <p>Salado Brine Inflow 0.1 m³/panel/year</p>	<p>DEGRADED</p> <p>Long-term Plug Permeability 10^{-11} m²</p> <p>Culebra Matrix Porosity 0.07</p> <p>Culebra Fracture Porosity 0.0015</p> <p>Culebra Fracture Spacing 7 m</p> <p>Culebra Free-Water Diffusivity 5×10^{-7} cm²/s</p> <p>Culebra K_d's Range 0.05 to 100 mL/g</p> <p>Culebra Matrix Tortuosity 0.03</p>

- a. Sufficient for mixing - it is assumed that Castile brine equilibrates to same radionuclide concentration as in repository at each time step.
- b. Because brine mixing is eliminated, only long-term source of radionuclides is from Salado brine flow through waste and backfill.

several scenarios, will be conducted during the next four years as part of WIPP performance assessment and will culminate in a comparison with 40 CFR 191.

The choice of Cases I and II for modeling here was influenced in part by the scenarios for WIPP performance-assessment modeling (Hunter, 1989), and in part by the calculations in the FEIS (DOE, 1980a), which also examined borehole intrusion. No human intrusion other than exploratory drilling is considered here, in line with the guidance contained in Appendix B of 40 CFR 191, which explicitly states that intrusion by inadvertent, intermittent exploratory boreholes can be the most severe intrusion scenario assumed by the implementing agencies in carrying out performance assessments. Four portions of Appendix B of the Standard contain suggestions and assumptions that guide the development of scenarios for human intrusion and assignment of probabilities to them:

Active institutional controls over disposal sites should be maintained for as long a period of time as is practicable after disposal; however, performance assessments that assess isolation of wastes from the accessible environment shall not consider any contributions from active institutional controls for more than 100 years after disposal.

... The Agency assumes that, as long as such passive institutional controls [as are described in Section 191.14(c)] endure and are understood, they: (1) can be effective in deterring systematic or persistent exploitation of these disposal sites; and (2) can reduce the likelihood of inadvertent, intermittent human intrusion to a degree to be determined by the implementing agency. However, the Agency believes that passive institutional controls can never be assumed to eliminate the chance of inadvertent and intermittent human intrusion into these disposal sites.

...The Agency believes that the most productive consideration of inadvertent intrusion concerns those realistic possibilities that may be usefully mitigated by repository design, site selection, or use of passive controls... Therefore, inadvertent and intermittent intrusion by exploratory drilling for resources...can be the most severe intrusion scenario assumed by the implementing agencies. Furthermore, the implementing agencies can assume that passive institutional controls or the intruders' own exploratory procedures are adequate for the intruders to soon detect, or be warned of, the incompatibility of the area with their activities.

...The implementing agencies should consider the effects of each particular disposal system's site, design, and passive institutional controls in judging the likelihood and consequences of such

inadvertent exploratory drilling. However, the Agency assumes that the likelihood of such inadvertent and intermittent drilling need not be taken to be greater than 30 boreholes per square kilometer of repository area per 10,000 years for geologic repositories in proximity to sedimentary rock formations (EPA, 1985, Appendix B).

To comply with 40 CFR 191.14, the DOE must designate the disposal site with "the most permanent markers, records, and other passive institutional controls practicable." The EPA's assumption that such controls "can be effective in deterring systematic or persistent exploitation of these disposal sites" for as long as they endure and are understood, in combination with the suggestion that exploratory boreholes can be the most severe human-intrusion scenarios, led Hunter (1989) to conclude in part that

No human intrusion of the repository will occur during the period of active institutional controls. Credit for active institutional controls can be taken only for 100 years after closure.

While passive institutional controls endure, no mineral exploitation will be carried out deliberately inside the controlled area, but reasonable, site-specific exploitation outside the controlled area may occur and should be considered in the performance assessment.

Intrusion of the repository leads to its detection. No mechanism for detection need be advanced, although this report describes several possible mechanisms. The EPA's use of the word "incompatibility" allows the conclusion that the intruders will plug and abandon their boreholes to avoid the effects of the repository, because incompatible means "incapable of association . . . , unsuitable for use together because of undesirable chemical or physiological effects, not both true"

While passive institutional controls endure, the number of exploratory boreholes assumed to be drilled inside the controlled area may be reduced below 30 boreholes/km² per 10,000 years (but not to zero), if there is reason to believe that the controls will be effective... [emphasis added].

The validity of the assumption that human intrusion will certainly occur at least once during the 10,000-year lifetime of the repository, even in the presence of enduring passive markers, has been debated. In light of the EPA's guidance in 40 CFR 191, however, the WIPP performance assessment is assuming that at least one borehole will intrude the repository, and that approach is echoed here.

Case II assumes that drilling of the borehole intruding the repository continues for at least 15 hours after the repository horizon is reached, that the Castile Fm. is penetrated, and that an occurrence of pressurized brine is encountered. Eventually, the borehole is plugged. After plug degradation, the pressurized brine drives the flow of radionuclide-contaminated brine up the borehole and into the Culebra Dolomite. (Calculation indicates that long-term pressure is not sufficient for flow to the surface.) Although this sequence of events reflects current practice in the hydrocarbon industry in the Delaware Basin, it may be a conservative interpretation of the wording in Appendix B of 40 CFR 191, which allows the DOE to assume that intruders "soon detect ... the incompatibility" of the repository with their activities. The meaning of "soon" is not given in Appendix B of 40 CFR 191. This report takes "soon" to mean at least 15 hours, the time that it takes to drill between the repository horizon and the Castile Fm., even though current technology would allow the drillers to detect the radioactivity within the repository within minutes of intruding it. This report cannot determine which interpretation is correct. If future guidance from the EPA to the DOE suggests that currently available technology, rather than current industrial practice, should guide the design of human-intrusion analyses, then the cases presented here would probably be greatly modified, and the doses to human beings would probably be substantially reduced.

1.2 Summary of Results

1.2.1 Changes in Understanding of Major Aspects of WIPP Performance Since 1980

The results of this report fall into three broad categories. First, the general geology of the WIPP site, largely independent of emplacement of waste at the WIPP, is described. These results, primarily developed in Chapter 3.0, demonstrate the improvement in understanding of the WIPP site that has taken place in the past ten years and provide a general framework for considering the long-term performance of the WIPP. They are summarized in condensed form in Table 1-1. In each area of interest listed in Table 1-1, the current understanding is also compared with the understanding at the time of FEIS

(DOE, 1980a). Each entry in Table 1-1 refers to the part of the report that discusses a specific topic in more detail.

Second, the expected behavior of the WIPP is described, with emphasis on the behavior of waste-emplacements rooms and panels, and with the exception of radionuclide transport. These results, largely developed in Chapter 4.0, form the conceptual connection between site-characterization knowledge, discussed in Chapter 3.0, and the numerical results describing expected radionuclide-transport behavior, discussed in Chapters 6.0 and 7.0. In addition, Chapter 4.0 discusses data uncertainties and transient behavior that are relevant to WIPP performance but are not included in calculations in Chapters 6.0 and 7.0. The results and conclusions of Chapter 4.0 are also summarized in Table 1-1.

Third, the numerical results of calculation of long-term radionuclide-transport behavior at the WIPP, both under undisturbed conditions and in response to human intrusion, are presented. Human intrusion is assumed to connect a reservoir of pressurized brine in the Castile Fm. with the WIPP repository. The six specific cases analyzed and the various numerical inputs assumed for each case are summarized in Table 1-2. The results of the radionuclide-transport calculations are summarized in Section 1.1.2 and in Tables 1-3, 1-4, and 1-5 (Section 1.2.2).

1.2.2 Estimated Health Effects from Release of Radionuclides

The possible human-exposure pathways for all cases considered here begin with release to the surface at the head of the intrusion well or at a stock well in the Culebra Dolomite located down gradient from the repository. In Cases IA and IB, no radionuclide migration to either the Culebra Dolomite or the surface occurs within 10,000 years under the assumed conditions. The two sections below summarize the results for the two general types of releases that are calculated in Case II.

1.2.2.1 Releases at the Head of the Intrusion Well (Case II). Releases at the head of the intrusion well comprise two possible parts. First, the borehole penetrates a repository panel, removing cuttings. Second, particles are eroded from the consolidated waste by the swirl of the drilling fluid.

Three drums of consolidated wastes are estimated to be removed in the form of cuttings and eroded material. The two components, cuttings and eroded material, comprise the total release to the surface at the head of the intrusion borehole.

All material (cuttings and particles eroded from the room contents by drilling fluid) is immediately deposited into a settling pond at the well head. An external radiation exposure may be received by the drilling crew; however, only the member of the crew who receives the maximum exposure is considered. A geologist who examines cutting chips for a period of one hour at a distance of one meter is assumed to be that individual. The same approach used in the FEIS (DOE, 1980a, p. 9-144) was used to calculate the external dose received by the geologist (Table 1-3). As in the FEIS, the chip samples are treated as point sources with no self-shielding effects.

The exposure rate from natural background radiation is ~0.01 milliroentgen per hour (mR/hr) (100 mrem/yr). Even though the estimated exposure rate from chip examination is eight times the background exposure rate, the incremental dose is only 0.08 mR/yr, because the exposure only lasts for one hour. One mR/hr is approximately equal to a biological effect of 1 mrem/hr if the quality factor is 1 for gamma rays.

After drilling operations cease, radioactive material remaining in the drilling-mud settling pond is available for transport through airborne or surface-water pathways. Doses to a hypothetical farm family living 500 m downwind from the settling pond were assessed in the FEIS. These pathways are not believed to be significant, because it is very doubtful that a farm (as opposed to a ranch) would ever exist at this location under such arid conditions and with such unsuitable topsoils; however, the dose estimates were repeated for completeness.

The pathways that result in doses to the hypothetical farm family must begin with particle transport from the mud pit by wind or surface-water erosion. Surface-water transport was not included in either the FEIS (DOE, 1980a, p. 9-145) or the calculations in this report, because there is no

Table 1-3. Maximum Doses Received by a Member of the Drilling Crew (Case II)

<u>Nuclide</u>	<u>mCi/chip</u>	<u>E (MeV)</u>	<u>n (gam-q/dis)</u>	<u>Ex (mR/hr-chip)</u>
Pu-238	35.0	0.099	8.0×10^{-5}	1.4×10^{-4}
Pu-239	4.0	0.0		
Pu-240	1.0	0.65	2.0×10^{-7}	6.5×10^{-8}
U-233	0.06	0.029	1.7×10^{-4}	1.5×10^{-7}
U-235	3.2×10^{-6}	0.143	0.11	
		0.185	0.54	
		0.204	0.05	3.0×10^{-7}
Am-241	7.1	0.06	0.36	0.077
Np-237	7.3×10^{-5}	0.0		
	Total			0.08 mR/hr-chip

Table 1-4. Maximum Doses Received by a Hypothetical Farmer Through Indirect Pathways (Case II)

<u>Committed Dose Equivalent After 1-Year Exposure (mrem/50 yr)</u>					
<u>Nuclide</u>	<u>Beef</u>	<u>Milk</u>	<u>Above-Surface Crops</u>	<u>Below-Surface Crops</u>	<u>Inhalation</u>
Am-241	3.04×10^{-12}	9.97×10^{-11}	8.81×10^{-8}	1.03×10^{-9}	2.62×10^{-1}
Np-237	8.23×10^{-17}	4.86×10^{-17}	4.20×10^{-15}	---	2.58×10^{-6}
Pu-238	1.69×10^{-13}	2.69×10^{-15}	3.30×10^{-10}	1.35×10^{-9}	4.37×10^{-1}
Pu-239	1.98×10^{-14}	3.15×10^{-16}	3.87×10^{-11}	1.58×10^{-10}	5.40×10^{-2}
Pu-240	4.94×10^{-15}	7.89×10^{-16}	9.68×10^{-12}	3.95×10^{-11}	1.35×10^{-2}
U-233	5.87×10^{-14}	6.22×10^{-13}	1.59×10^{-13}	7.29×10^{-12}	2.62×10^{-4}
U-235	2.93×10^{-18}	3.11×10^{-17}	7.95×10^{-18}	3.65×10^{-17}	1.19×10^{-8}
Total Ingested Dose:			4.87×10^{-10}		
Total Inhaled Dose:					7.66×10^{-1}

Note: Includes breathing rate of $2.7 \times 10^{-4} \text{ m}^3/\text{s}$.

integrated surface-water drainage from the WIPP site (Hunter, 1985). The pathways considered here are thus the same as those used in the FEIS. They include inhalation of contaminated air and ingestion of foods (meat, milk, and above- and below-surface food crops) produced on the farm. The estimated doses to an individual member of this farm family (Table 1-4) are assumed to be the same for all variants of Case II. The sum of 0.77 mrem primarily from inhalation of ^{238}Pu and ^{241}Am calculated for a person living on the hypothetical farm is the 50-year committed dose equivalent. The estimated 50-year committed dose from ingestion of contaminated food products is only 4.9×10^{-10} mrem. Table 1-5 compares the dry deposition flux of plutonium at the hypothetical farm with other radionuclide concentrations from natural and man-made sources. The dose calculations to the geologist and farm-family member presented here are conservative in that they take no credit for radioactive decay of the waste prior to drilling.

1.2.2.2 Releases from a Stock Pond. The starting point for calculations of doses arising from ingestion of contaminated beef is the hypothetical stock well in the Culebra Dolomite. The concentrations of the radionuclides at the stock well were highest at 10,000 years. These concentrations were used for the dose calculations. Some cases showed peak-arrival times for a few radionuclides before 10,000 years. Concentrations at these peak-arrival times were also calculated, but they resulted in lower doses than the 10,000-year concentrations with one exception.

The estimated doses calculated for a person consuming 86 g/d of beef contaminated by radionuclides from the stock pond are reported in Table 1-6. The 50-year committed effective dose equivalents (CEDE's) are 2.1×10^{-4} mrem for Case IIA at 10,000 years, 72 mrem for Case IIB at 10,000 years, 130 mrem for Case IIC at 1,345 years, and 0.91 mrem for Case IID at 10,000 years. These calculations were made for CEDE factors for radionuclides transported in a soluble chemical form. In the WIPP ground-water environment, radionuclides are usually found in relatively insoluble chemical forms. If CEDE's for these insoluble chemical forms are used, the highest estimated dose of 130 mrem (Case IIC) would decrease to 30 mrem, and estimated doses for other cases would also decrease.

Table 1-5. Comparison of Radionuclide Concentrations from Natural and Man-Made Sources

Dry deposition flux of plutonium	
at hypothetical farm	5 pCi/m ²
Worldwide Pu-239 fallout levels	2000 pCi/m ²
Experimental study areas	2 x 10 ⁶ to 4 x 10 ⁸ pCi/m ²
U.S. average natural alpha activity	3 x 10 ⁵ pCi/m ²
High natural radiation background areas	
Colorado	7 x 10 ⁶ pCi/m ²
Brazil	5 x 10 ⁷ pCi/m ²
U.S.S.R.	2 x 10 ⁸ pCi/m ²

Table 1-6. Maximum Doses Received by a Person Through the Contaminated-Beef Pathway

Committed Effective Dose Equivalent After 1-Year Exposure (mrem/50 yr)

	<u>Nuclide</u>	<u>mrem</u>	<u>Sum</u>
Case IIA			
	Ra-226	3.0×10^{-5}	
	Pb-210	1.8×10^{-4}	2.1×10^{-4}
Case IIB			
	Np-237	2.5	
	Pb-210	2.8×10^1	
	Pu-239	2.2×10^{-1}	
	Pu-240	1.1×10^{-1}	
	Ra-226	4.7	
	Th-229	3.3×10^{-1}	
	Th-230	1.2×10^{-3}	
	U-233	3.1×10^1	
	U-234	5.2	
	U-236	5.0×10^{-2}	7.2×10^1
Case IIC			
	Np-237	9.1	
	Pb-210	9.2	
	Pu-239	7.1×10^{-6}	
	Pu-240	1.4×10^{-5}	
	Ra-226	1.5	
	Th-229	1.3×10^{-1}	
	Th-230	4.3×10^{-4}	
	U-233	9.0×10^1	
	U-234	1.9×10^1	
	U-236	5.3×10^{-2}	1.3×10^2
Case IID			
	Np-237	7.8×10^{-2}	
	Pb-210	3.4×10^{-1}	
	Pu-239	1.8×10^{-4}	
	Pu-240	3.8×10^{-4}	
	Ra-226	5.7×10^{-2}	
	Th-229	1.4×10^{-3}	
	Th-230	1.5×10^{-5}	
	U-233	2.7×10^{-1}	
	U-234	1.7×10^{-1}	
	U-236	4.8×10^{-4}	9.1×10^{-1}

2.0 GENERAL GEOLOGY OF THE WIPP SITE

The WIPP site is located in southeastern New Mexico, in the northern portion of the Delaware Basin (Figure 1-1). The generalized stratigraphy in the vicinity of the WIPP from the Bell Canyon Fm. to the surface is summarized in Figure 1-3. Regional stratigraphic relationships and characteristics for all units of interest in the northern Delaware Basin were discussed in detail by Powers et al. (1978). The brief summary included here is intended only to provide a geologic framework for the units of specific interest.

The Delaware Basin became a distinct structure by the late Pennsylvanian Period or early Permian Period, ~280 million years ago. Approximately 250 million years ago, the reef now represented by the Capitan Limestone began to grow around the margins of the developing basin, and the sandstones, shales, and carbonates now making up the Delaware Mountain Group (DMG) were deposited within the basin. Most of the Capitan Limestone is relatively massive. Some portions of the unit are hydrologically active and locally support karst hydrology, including the formation of large cavities like Carlsbad Caverns. The Delaware Mountain Group, which is limited to the basin, contains three major subdivisions, the Brushy Canyon, Cherry Canyon, and Bell Canyon Fms. (in ascending stratigraphic order). Only the Bell Canyon Fm. is considered here, as it is the first regionally continuous water-bearing formation beneath the WIPP underground workings. The hydraulic behavior of the Bell Canyon Fm. is assumed to be more important to the long-term performance of the WIPP than that of any underlying units.

The Bell Canyon Fm. (the first unit beneath the WIPP that is a local target of hydrocarbon exploration) is divided into five informal members, the Hays sandstone, Olds sandstone, Ford shale, Ramsey sandstone, and Lamar limestone (in ascending stratigraphic order). The members vary in thickness and lithology. The Ramsey sandstone tends to be elongated and laterally discontinuous, in the nature of "channel sands." Individual sands are separated laterally by stratigraphically equivalent siltstones and shales. Near the WIPP site, the Bell Canyon Fm. consists of a layered sequence of

sandstones, shales and siltstones, and limestones 300 m or more in thickness (Powers et al., 1978).

Within the northern Delaware Basin, the sandstones and shales of the Bell Canyon Fm. are overlain by the thick-bedded sequence of anhydrites and halites of the Castile Fm., also of Permian age. The Castile Fm. near the WIPP site normally contains three relatively thick anhydrite/carbonate units and two thick halites. The anhydrites and halites contain abundant anhydrite and carbonate laminae, may be strongly deformed internally, and are locally variable in thickness. The thickness of the Castile Fm. near the WIPP site is ~400 m.

The Salado Fm., of Late Permian (Ochoan) age, is 530 to 610 m thick at and near the WIPP site and is generally bedded on a scale of 0.1 to 1 m. It contains 45 numbered "anhydrite" marker beds of variable thickness (MB 101 through MB 145 with increasing depth). Between marker beds, the Salado Fm. consists of layered halites of varying purity and accessory mineralogy; anhydrite (CaSO_4), clays, and polyhalite ($\text{K}_2\text{MgCa}_2(\text{SO}_4)_4 \cdot 2\text{H}_2\text{O}$) are dominant accessory minerals. The WIPP repository horizon is between MB 138 and MB 139.

The Salado Fm. is overlain by the Rustler Fm., also of Ochoan age. The Rustler Fm. contains five members (Table 2-1). Two, the Magenta and Culebra Dolomites, are gypsiferous dolomites with a variable concentration of vugs and fractures and local occurrence of silty zones. The other three members of the Rustler Fm. (unnamed member, Tamarisk Member, and Forty-niner Member in upward succession) consist of varying proportions of anhydrite, siltstone, claystone, and halite. The major mineralogical variability within the Rustler Fm. as a whole is in the degree of alteration of anhydrite to gypsum and the presence or absence of halite, both generally interpreted to result from evaporite dissolution. Some of this variability, however, may reflect original depositional patterns. The Rustler Fm. ranges from 83 to 130 m in thickness at the WIPP site, depending on the extent of evaporite dissolution and depositional variability.

Table 2-1. Generalized Stratigraphy of the Rustler Fm. at and near the WIPP Site (after Snyder, 1985)

<u>Age</u>	<u>Member</u>	<u>Approximate Thickness (m)</u>	<u>Generalized Character in "Unaltered" Sections</u>
Permian/ Ochoan	Forty-Niner	45±	Anhydrite Halite and Siltstone Anhydrite
	Magenta Dolomite	6 to 9	Thinly Laminated Gypsiferous Dolomite; Local Anhydrite
	Tamarisk	65±	Anhydrite Halite and Siltstone Anhydrite
	Culebra Dolomite	6 to 10	Finely Crystalline, Vuggy, Gypsiferous Dolomite; Local Siltstone
	Unnamed	44±	Alternating Halite, Siltstone, Anhydrite Laminated Siltstone

The Culebra Dolomite is the first laterally continuous unit above the repository horizon to display significant permeability. Barring direct breach to the surface, the Culebra Dolomite provides the most likely pathway between the repository and the subsurface accessible environment. The hydrology and fluid geochemistry of the Culebra Dolomite are complex. The unit displays wide ranges in hydraulic properties, local flow and transport mechanisms, and geochemistry. As a result of these factors, the Culebra Dolomite has received much study during WIPP site characterization.

The Rustler Fm. at the WIPP is overlain by the Dewey Lake Red Beds (the uppermost unit of the Ochoan Series), consisting largely of siltstones and claystones with subordinate sandstones. The unit is ~30 to 170 m thick at and near the WIPP site, varying at least in part as a result of post-depositional erosion. Where relatively thick and hydraulically unsaturated, the Dewey Lake Red Beds form a low-permeability buffer zone between the surface and relatively soluble carbonates and sulfates in the underlying Rustler Fm. In some areas, however, the unit is thinned by local erosion and is hydraulically saturated. Where sufficiently thin, the Dewey Lake may not present an

effective barrier to vertical fluid movement from the surface into the Rustler, depending on the local fluid pressures within and above the Rustler Fm. Where saturated, the Dewey Lake Red Beds may, in some areas, serve as a source of fluids to the underlying Rustler Fm. The depositional age of the Castile, Salado, and Rustler Fms., as well as the Dewey Lake Red Beds, ranges from ~245 million to 230 million years. Over approximately the eastern half of the WIPP site, the Dewey Lake Red Beds are overlain by the (undivided) Dockum Group of sandstones and shales of Triassic age.

The shallowest and youngest stratigraphic units at the WIPP site proper, except for recent surficial sands, are the Gatuña Fm., the Mescalero caliche, and the Berino soil. The Gatuña Fm., the upper part of which is ~600,000 years old, consists of siltstones, sands, and stream-laid conglomerates, deposited in a wetter climate than is now present in southeastern New Mexico. The Mescalero caliche, 510,000 to 410,000 years old, is relatively continuous near the WIPP site and supports the Livingston Ridge surface, on which the site is located (Figure 1-1). The Berino soil, ~250,000 years old, is a thin horizon and is much less widespread than either the Gatuña or the Mescalero (Bachman, 1985). Together, the Gatuña Fm., Mescalero caliche, and Berino soil indicate some of the variability of the climate in southeastern New Mexico over the past 600,000 years, but also indicate the relative structural stability of the Livingston Ridge surface over the past 400,000 to 500,000 years.

Localized gypsite-spring deposits, ~25,000 years old, occur along the eastern flank of Nash Draw, but the springs are not currently active. Around the northwestern margin of the Delaware Basin, packrat middens indicate that the climate ~10,500 years ago was wetter than that at present. The recent surficial windblown sands at and near the WIPP site are almost all stabilized by vegetation. South of the site, however, there is an area in which surficial dunes appear to be active. It is from these dunes that the area has derived its name, "Los Medaños."

3.0 HYDROLOGY AND GEOCHEMISTRY OF THE WIPP SITE

3.1 Introduction

This chapter summarizes the present conceptual and numerical understanding of the behavior of geologic formations at the WIPP site, generally independent of the presence of the WIPP underground workings. Separating information about the workings from information about the Salado Fm. (within which lie the repository workings) is not always possible, because much of the available information about the Salado has been derived from the WIPP. In the case of the Salado Fm., a distinction is maintained where possible between generic behavior, described in this section, and room- or panel-specific behavior, which is considered in detail in Chapter 4.0.

Section 3.2 discusses the overall hydrologic behavior and modeling of the Salado Fm., although the only setting considered is that immediately surrounding the WIPP. The near-field and far-field permeabilities of the Salado Fm. play a crucial role in controlling brine and gas flow into and out of the WIPP. Salado brine compositions, in combination with those of the Rustler and Castile Fms., will control the compositions of any brines and gases present within the repository after interaction with waste and backfill.

Section 3.3 discusses the Rustler Fm. Gathering data on the Rustler Fm. has been a major focus of WIPP site characterization, especially since the time of the FEIS (DOE, 1980a) (Table 1-1). Section 3.3.1 discusses the physical hydrology of the Rustler Fm., including the distribution of fractures and possible vertical fluid flow. Section 3.3.2 discusses the chemical variability of Rustler ground waters, with emphasis on the Culebra Dolomite. The variability of Culebra ground waters is critical in interpreting modern and ancient flow directions and may play a role in radionuclide migration. Section 3.3.3 discusses the relationship between the variability of Culebra waters, isotopic findings, and the apparent time dependence of the hydrologic setting of the Rustler Fm. over ~10,000 years, the same length of time considered in calculations presented in this report. Section 3.3.4 discusses radionuclide retardation in the Culebra Dolomite, especially the effects of

potential geochemical variability (Sections 3.2.2 and 3.3.2) on radionuclide sorption. Section 3.3.5 discusses the evolution of flow and transport modeling within the Culebra Dolomite from the time of FEIS to the present. Flow and transport models at the time of the FEIS were equivalent-porous-medium models based on equivalent freshwater heads. Current models treat flow and transport through a locally fractured medium; flow directions reflect variations in downhole pressure as a result of both altitudinal and fluid-density variations arising from the variability of Culebra brines (Section 3.3.2).

Section 3.4 discusses the hydrology of the Castile Fm., with special emphasis on the interpreted properties of the WIPP-12 brine reservoir. At the time of the FEIS, pressurized Castile brines were not expected beneath the WIPP (Table 1-1). However, as a result of data from hole WIPP-12 and geophysical studies, it is now assumed for purposes of calculation that the WIPP-12 reservoir underlies at least a portion of the WIPP waste-emplacement panels.

Section 3.5 briefly discusses the Bell Canyon Fm. and Dewey Lake Red Beds. Recent work in holes Cabin Baby-1 and DOE-2 indicates that if the Culebra Dolomite and the Bell Canyon Fm. were connected by a drillhole, the final direction of brine flow between them would be downward, rather than upward as assumed in the FEIS. Little has changed in the interpretation of the Dewey Lake Red Beds since the time of the FEIS.

3.2 Salado Formation

The following are the major conclusions of Section 3.2.

- The interpreted far-field permeability of the Salado Fm. is 10^{-20} to 10^{-21} m², based on brine-inflow measurements and testing. Ongoing work, however, indicates that this estimate may be too high. In fact, the effective far-field permeability in the absence of significant pressure gradients may be near zero, and Darcy-flow assumptions may not be appropriate.

- Experimental results have been modeled successfully with a one-phase (brine only), poroelastic, Darcy-flow model, assuming isotropy. Uncertainties in this model include potential stratigraphic effects, variations in storativity and fluid compressibility, detailed effects of borehole deformation, reliability of estimates of far-field pore pressures, and the possibility of two-phase flow. It has not been possible to distinguish in the field between flow in response to far-field Darcy permeability and flow in response to increased permeability of the Salado halite in that volume structurally disturbed by the presence of the WIPP itself. With the possible exception of two-phase flow, however, Darcy-flow calculations should be conservative, i.e., they should overestimate brine flow as a function of time.
- Earlier results from testing of the Salado Fm. in holes drilled from the surface are unreliable for several reasons, with the exception of an upper-bound permeability of <0.3 microdarcy estimated in hole DOE-2. Therefore, the results of testing from the surface are not included in estimates of far-field Salado permeability in this report. Similarly, high permeabilities interpreted from the results of gas-flow testing in the disturbed rock zone surrounding the underground workings (Section 4.7) are not considered in evaluating the estimated far-field permeability.
- Salado brine analyses indicate considerable vertical and lateral variability, although much of this variability may result from sampling difficulties. A reference Salado brine, defined for purposes of performance assessment, is high enough in Mg to support active anoxic corrosion of metals (Section 4.2) and appears to be in equilibrium with anhydrite, gypsum, and halite. Data are not available to estimate whether this brine is in equilibrium with magnesite ($MgCO_3$), polyhalite ($K_2MgCa_2(SO_4)_4$), quartz, or Salado clays.
- Microbial activity within the repository could decrease the oxidation potential (Eh), generate CO_2 , and decrease pH. Interactions between brine, grouts, and hydroxide getters such as KOH (Section 4.11) could lead to very basic conditions, i.e., very high pH, in the repository.

3.2.1 Salado Hydrology

This section discusses the present understanding of fluid flow within the Salado Fm., especially as influenced by the presence of the WIPP. Amounts and processes of brine inflow to and brine and gas egress from the repository play critical roles in its long-term behavior. For example, although the nature of the dependence of biological gas generation on brine inflow is not clear (Section 4.2), there is little doubt that the potential amount and rate of gas generation as a result of corrosion depend strongly on the amount of free brine within the repository (Sections 4.2, 4.3, 4.10). In addition, the amounts of brines that might be present control the possibility of slurry formation during closure (Section 4.10.1).

3.2.1.1 Understanding and Assumptions Prior to Mining. The WIPP FEIS (DOE, 1980a) was written prior to mining the underground workings; it was assumed that the final state of emplaced waste in the absence of human intrusion would be compacted and dry. It was also assumed that the gas permeability of the Salado Fm. was sufficient to dissipate the quantities of gas that were expected to be generated by the emplaced waste. These assumptions were based on the best available conceptual models and data for bedded salt. The increasing complexity in conceptual models and data that have resulted from underground experience at the WIPP is a normal and expected progression in research and development.

The brine-related studies that were completed prior to mining led to several specific conclusions. First, the only water in Salado halites was thought to be contained in fluid inclusions and hydrous minerals. No grain-boundary brines were thought to be present; i.e., the only grain-boundary fluid was thought to be gas. Second, brine influx from the Salado Fm. was thought to be stress- or temperature-gradient driven and small, with no long-term steady-state flow. Finally, because brine-inflow volumes were expected to be small, there was no perceived need for engineered backfill designed to control either brine or possible interactions between brine and waste.

Corresponding conclusions were drawn about the gas-generation and gas-transport properties of the waste and the Salado Fm. The far-field gas

permeability of the Salado Fm., based on results of gas-flow testing conducted from the surface, was assumed to be on the order of 10^{-18} to 10^{-17} m² (a few microdarcies). Because the interpreted far-field gas permeability of the Salado Fm. was sufficient to dissipate the quantities of gas that were expected to be generated by the emplaced waste, there was no concern about a potential buildup of gas pressure within the repository.

With the understanding of the WIPP site that was current in 1980, radionuclide migration from the WIPP was thought to be essentially zero in the absence of human intrusion.

3.2.1.2 New Understanding Derived from WIPP Underground Experience.

Information about the occurrence and movement of brine within the Salado Fm. and in-situ measurements of Salado permeabilities has yielded a new understanding of Salado hydrology. The presence and movement of brine in the Salado Fm. adjacent to the underground workings is evidenced by small "weeps" that commonly develop on the walls of an excavation shortly after it is mined. Rarely does the brine-flow rate to the walls exceed the evaporation rate resulting from mine ventilation. Growth of these weeps generally stops within a year after mining. Movement of brine in the Salado Fm. has been quantified by in-situ measurements of brine flow into sealed boreholes and by in-situ permeability measurements. Much of the information derived from underground experience has been summarized elsewhere (Tyler et al., 1988).

In-situ brine-flow experiments are one approach to measuring Salado permeability. Near-steady-state brine-flow rates into sealed boreholes, measured under carefully controlled conditions, are in the range of 5×10^{-8} to 1×10^{-7} liters per second (Nowak and McTigue, 1987). These rates have been used to calculate Salado permeabilities that are predominantly in the range of 10^{-21} to 10^{-20} m² (a few nanodarcies or 10^{-14} to 10^{-13} m/s conductivity) using a poroelastic Darcy-flow model. (McTigue and Nowak, 1987; Nowak et al., 1988).

Calculations from brine-flow experiments and more direct in-situ permeability measurements show that the far-field permeability of the Salado Fm. may be several orders of magnitude smaller than previously estimated. The

best direct measurements of far-field permeability within the Salado Fm. are in the range of 10^{-20} to 10^{-22} m² (10 nanodarcies or less; much smaller than a few microdarcies) (Peterson et al., 1987a; Saulnier and Avis, 1988; Tyler et al., 1988) (Tables 3-1 and 3-2). These values are consistent with values inferred from brine-inflow measurements (McTigue and Nowak, 1987; Nowak et al., 1988). Uncertainties in the application of these values to the WIPP arise from the lack of reliable measurements of stratigraphic effects and from the possible effects of borehole closure and fluid flow on calculated conductivities and measured far-field fluid pressures.

Previous measurements of Salado permeability, used in the FEIS, were made in boreholes drilled from the surface and are characterized by large uncertainties and known errors (Table 3-3). These uncertainties can be greatly reduced and the errors eliminated by careful in-situ measurements. Therefore, only in-situ measurements of brine flow and permeability are now considered to be valid for WIPP models.

The FEIS cited values for Salado permeability that were derived from drill-stem tests (DSTs) performed in ERDA-9 (Lambert and Mercer, 1978). These values have since been determined to be unreliable for two principal reasons. First, the purpose of the ERDA-9 DSTs was to detect pressurized brine, not to measure the permeability of the Salado Fm. As a result, pressure-stabilization periods preceding the tests were too short to allow adequate equilibration between borehole and formation pressures for quantitative testing and analysis. Individual test components were also too short to allow representative formation responses to develop. Thus, the pressure record developed during testing represented an inseparable superposition of pressure transients resulting from drilling and various test components. That pressure record cannot be interpreted to yield unique values of permeability. Second, the oilfield service company that performed the tests and analyses erred in the application of the analysis technique. Even though no flow was measured during the testing, an analytical approach that requires a low rate as an input parameter was misused to provide the reported results. The reported permeability values are, therefore, meaningless.

Table 3-1. Summary of Salado Permeability Measurements Made from the WIPP Underground Workings Near the Waste-Disposal Horizon (Peterson et al. 1987a, 1987b)

<u>Stratum</u>	<u>Permeability (m²)</u>
Predominantly Halite	10 ⁻²¹
Anhydritic MB139	10 ⁻²⁰
Predominantly Halite	<1.2 x 10 ⁻²⁰

Notes: Conversion factors:

Density of WIPP brine at 28°C = 1.2 x 10³ kg/m³
(1.2 g/cm³) (Stein and Krumhansl, 1986; Kaufman, 1960, p. 612).

Viscosity of WIPP brine at 28° = 1.6 x 10⁻³ Pa-s
(1.6 centipoise) (Kaufman, 1960, p. 622; Ezrokhi, 1952).

One darcy = 7.3 x 10⁻⁶ m/s (~10⁻⁵ m/s) = 9.9 x 10⁻¹³ m² (~10⁻¹² m²)

One nanodarcy = 7.3 x 10⁻¹⁵ m/s (~10⁻¹⁴ m/s) = 9.9 x 10⁻²² m² (~10⁻²¹ m²)

Table 3-2. Summary of Salado Permeability Measurements in the Waste-Handling Shaft (Saulnier and Avis, 1988)

<u>Depth (m)</u>	<u>Penetration (m from shaft wall)</u>	<u>Hydraulic Conductivity (m/s)</u>	<u>Permeability (m²)</u>
259	3.04 - 4.29 (halite)	2 x 10 ⁻¹⁴	3 x 10 ⁻²¹
	3.73 - 4.84 (halite)	1 x 10 ⁻¹³	1 x 10 ⁻²⁰
	5.13 - 6.24 (halite)	3 x 10 ⁻¹⁴	4 x 10 ⁻²¹
	5.66 - 7.92 (halite)	1 x 10 ⁻¹³	1 x 10 ⁻²⁰
	7.06 - 10.97 (halite)	3 x 10 ⁻¹⁴	4 x 10 ⁻²¹
402	1.64 - 2.90 (halite)	3 x 10 ⁻¹⁴	4 x 10 ⁻²¹
	3.73 - 4.84 (anhydrite)	3 x 10 ⁻¹⁴	4 x 10 ⁻²¹
	5.66 - 12.75 (polyhalite)	2 x 10 ⁻¹⁴	3 x 10 ⁻²¹

Table 3-3. Summary of Salado Permeability Measurements Made from the Ground Surface

Well	Depth Interval (m)	Hydraulic Conductivity (m/s)	Approximate Permeability (m ²)
ERDA-9 ¹	436.8 - 452.9	5 x 10 ⁻¹²	6 x 10 ⁻¹⁹ - 7 x 10 ⁻¹⁹
	613.9 - 638.3	2 x 10 ⁻¹¹ - 5 x 10 ⁻¹¹	3 x 10 ⁻¹⁸ - 6 x 10 ⁻¹⁸
	765.7 - 798.0	1 x 10 ⁻¹¹ - 2 x 10 ⁻¹¹	2 x 10 ⁻¹⁸
	765.7 - 799.5	2 x 10 ⁻¹¹ - 3 x 10 ⁻¹¹	2 x 10 ⁻¹⁸ - 3 x 10 ⁻¹⁸
	799.5 - 826.9	5 x 10 ⁻¹³ - 2 x 10 ⁻¹⁰	7 x 10 ⁻²⁰ - 2 x 10 ⁻¹⁷
	799.5 - 876.0	3 x 10 ⁻¹² - 5 x 10 ⁻¹¹	4 x 10 ⁻¹⁹ - 6 x 10 ⁻¹⁸
AEC-7 ²	554.4 - 584.9	0 - 2 x 10 ⁻¹¹	0 - 3 x 10 ⁻¹⁸
	676.4 - 706.8	9 x 10 ⁻¹¹ - 2 x 10 ⁻¹⁰	1 x 10 ⁻¹⁷ - 2 x 10 ⁻¹⁷
Cabin Baby-1 ³	230.7 - 828.3	<7 x 10 ⁻¹³ - <7 x 10 ⁻¹⁴	<8 x 10 ⁻²⁰ - <9 x 10 ⁻²¹
DOE-2 ⁴	669.0 - 703.7	<2 x 10 ⁻¹²	<3 x 10 ⁻¹⁹
	317.0 - 943.4	undefined	

1. Griswold (1977)
2. Peterson et al. (1981)
3. Beauheim et al. (1983)
4. Beauheim (1986)

Air-injection tests in AEC-7 (Peterson et al., 1981) also resulted in unreliable estimates of Salado permeability. Pretest conditions were poorly defined, and pressure-stabilization and test-component durations were too short to allow meaningful separation of the superimposed responses that were observed. Attempts to interpret the data resulted in inconsistent conclusions. Similar difficulties were encountered during attempts to interpret DSTs performed in the Salado Fm. at Cabin Baby-1 (Beauheim et al., 1983). Lack of knowledge of pretest conditions and test durations that were too short preclude reliable interpretation of the test data.

The most carefully controlled measurement of Salado permeability in a hole drilled from the surface was attempted at DOE-2 (Beauheim, 1986). Testing of the entire Salado Fm. was inconclusive, and testing of the interval from

Marker Bed 138 to Marker Bed 139 resulted only in an upper limit on permeability, indicating that Salado permeability could not be properly measured in holes drilled from the surface within a reasonable period of time. The times required to reach near-steady-state initial conditions would be prohibitively long. Consequently, all plans for future testing centered on holes drilled from WIPP shafts and underground workings.

Another important parameter for analysis of fluid and mechanical processes near the repository is lithostatic pressure in the Salado Fm. Various values for lithostatic pressure have been derived. Based on the integrated rock density measured in ERDA-9, Krieg (1984) reported a lithostatic pressure of 14.83 MPa at clay seam F in the upper portion of the repository horizon. Based on the average breakdown and reopening pressures from hydraulic fracturing tests at the repository horizon, Wawersik and Stone (1985) determined a range of isotropic in-situ stress from 14.28 to 17.9 MPa. Wawersik and Stone (1985) also reported a best estimate of instantaneous shut-in pressure for the same hydraulic fracturing tests of 16.62 MPa and a calculated lithostatic pressure of 14.9 MPa. The analyses contained in this report incorporate both previous and new calculations that use lithostatic pressure. The lithostatic pressures used in these calculations range from 14.0 to 15.0 MPa.

3.2.1.3 Current Brine-Inflow Model and Assumptions. A predictive model for brine inflow based on Darcy flow in a poroelastic medium has been developed from in-situ test data (Nowak et al., 1988). The brine-inflow rates calculated using this model are consistent with existing brine-inflow data and with the in-situ permeability measurements described above, and the model has been used to predict brine inflow to waste-disposal rooms (Nowak et al., 1988).

Several assumptions are inherent in the current brine-inflow model (Nowak et al., 1988; Nowak and McTigue, 1987; Appendix A.6). Salt surrounding the WIPP is assumed to be a homogeneous, isotropic medium that contains interconnected porosity extending outward without bound. Initial and far-field brine pressures are assumed in the calculations presented here to be lithostatic, with the differential between these pressures and atmospheric

pressure at the excavation wall providing the primary driving force for brine flow. The use of lithostatic initial and far-field pressures provides an upper bound on pore-pressure increases caused by excavation-related stresses. No back pressure from the room contents is assumed. Darcy's Law, along with elastic fluid and matrix compressibilities, is assumed to adequately describe the flow process. Inelastic volumetric deformation of the salt is neglected.

This model has been used to analyze brine-inflow rates to moisture-release experiments (Nowak and McTigue, 1987; Nowak, 1986) and brine-inflow rates to observation holes in the WIPP excavations (Nowak et al., 1988; Deal and Case, 1987; Appendix A.7). The results of these analyses are generally consistent with each other and with the available in-situ permeability measurements (Peterson et al., 1987a, 1987b), reinforcing the applicability of the Darcy-flow model for predicting long-term brine inflow.

3.2.1.4 Uncertainties in the Present Understanding of Brine Inflow. The flow of brine in low-permeability environments is a complex physical process that has been the subject of limited laboratory, in-situ, and theoretical research. Even though the current brine-inflow model is generally consistent with field observations, much work remains to evaluate additional flow mechanisms, system characteristics, and parameter uncertainties. Ongoing studies that will more thoroughly characterize Salado hydrology include the room-scale brine-inflow experiment, pore-pressure and in-situ permeability measurements, and model analyses of flow mechanisms. Several flow-mechanism and system-characterization uncertainties that are currently under investigation are discussed below.

Non-Darcy Flow. In low-permeability environments like the salt at WIPP, much of the pore fluid is near the mineral surfaces of the porous matrix. Under these conditions, interactions between the mineral surfaces and the fluid may change the fluid properties in such a way that the fluid no longer behaves as a Newtonian fluid (i.e., a fluid with viscosity independent of velocity gradient). In practical terms, this may result in reduced "effective conductivities" at low gradients or perhaps even in a threshold gradient, below which no fluid flow occurs.

Because measuring very low permeabilities in the laboratory is difficult, non-Darcy-flow behavior is not well understood, and consensus in the scientific community is yet to be reached concerning the exact physical processes involved and how to quantify this behavior (Neuzil, 1986). Most research on non-Darcy-flow behavior has focused only on clay materials (Swartzendruber, 1962; Olsen, 1966; Kutilek, 1972; Elnaggar et al., 1974), and almost no work has been done on salt materials. Because non-Darcy-flow processes tend to inhibit flow, the use of a Darcy model tends to overestimate flow rates (Remson, 1984). Therefore, the use of a Darcy model to predict brine inflow may over-estimate brine-inflow rates and conservatively predict brine quantities. Non-Darcy-flow behavior is being studied by quantifying the differences in pore-pressure response adjacent to an excavation for each model, so that the two models can be compared when adequate pore-pressure information is available from field tests.

Stratigraphic Effects. The current brine-inflow model assumes that the Salado Fm. in the vicinity of the WIPP excavation has homogeneous hydrologic properties. The Salado Fm. is not a homogeneous medium; it contains well-defined stratigraphic variations in mineralogy, texture, and physical properties. Most likely, there are also stratigraphic variations in hydrologic properties like permeability, porosity, and storage properties. There is also direct evidence of stratigraphic variation in hydrologic behavior. Distinct stratigraphic preferences are shown by brine seeps in the walls of the facility (Deal and Case, 1987; Stein and Krumhansl, 1986). Moist zones are associated with some of the coarsely crystalline halite layers during coring (Deal and Case, 1987). Notably higher gas-injection rates have been measured in Marker Bed 139 where it has been affected by stress relief fracturing (Stormont et al., 1987; Borns and Stormont, 1988). Thus, in addition to naturally occurring variation in hydraulic properties, the evolution of the disturbed rock zone will superimpose additional heterogeneity in the immediate vicinity of the excavation, because different lithologic units will respond to excavation-related stresses in different ways.

Current studies of the impact of stratigraphic heterogeneities in the field include direct in-situ measurements of brine-inflow rate and local-scale permeability in several stratigraphic horizons at various distances from the

excavation walls. In order to assess the potential impact of stratigraphic effects on brine-inflow predictions, numerical simulations will examine various descriptions of the flow-system heterogeneities.

Characterization of the Storage Parameter in Salt Environments. The standard form of the ground-water flow equation assumes linear elastic fluid and matrix behavior. In most natural systems, fluid compressibility is an easily defined constant. As noted by Bredehoeft (1988), however, the presence of gas associated with the brine in the salt at WIPP may cause higher compressibilities in the brine than if it were a pure liquid. If all the gas is in solution, then its effect on fluid compressibility is relatively small (Dodson and Standing, 1944), but if the gas comes out of solution, its effect on overall system compressibility can be large. Short of explicitly modeling the gas phase (discussed below), the presence of gas is best represented by examining an increased range of fluid compressibility.

In most natural aquifer materials, the porous matrix behaves in a linear elastic fashion. In contrast, salt deformation is dominated by inelastic processes under many conditions. Little is known about inelastic volumetric deformation in salt (Nowak et al., 1988; Appendix A.6), which introduces an element of uncertainty about the long-term compressibility of salt as it affects the storage parameter in the basic flow equation. Over an extended period of time, salt may have an additional component of inelastic deformation, and therefore, the "effective compressibility" may be larger than the elastic compressibility that is measured in the laboratory or using geophysical techniques. A similar increase in "effective compressibility" has been proposed as an explanation for measured porosity-depth profiles that are inconsistent with known elastic compressibilities for the geologic materials along the profiles (Neuzil, 1986). In order to bound the possible effects of inelastic volumetric behavior on estimates of brine inflow at WIPP, an increased range of matrix compressibility must be examined.

Fluid and matrix compressibility and porosity characterize the transient storage response of the rock to hydraulic stresses. Increasing the value of one or both of these parameters results in higher values for the storage parameter. Increasing the value of the storage parameter causes higher flux

at early and intermediate times and also increases the amount of time required for flow to attain steady-state conditions (Bredehoeft, 1988). Additional work will be necessary to characterize the effect of storage-related uncertainty on brine-inflow estimates for the WIPP.

Multi-Phase Flow. As noted above, naturally occurring gas is present in brine from the Salado Fm. Small amounts of gas are associated with many of the brine weeps that form on freshly mined surfaces. Gas is commonly exsolved from solution when brine samples are poured from one container to another. Gas is observed bubbling up through the brine in the observation boreholes in the floor of the WIPP mine. Gas has been encountered in some of the pressurized test intervals in the Salado Fm.

In a two-phase flow system, the gas component will come out of solution when fluid pressure drops below a critical value that is a function of composition, degree of saturation, and temperature. The gas-component phase change is accompanied by large increases in volume and an associated release of compressive energy. This type of phase change associated with a drop in fluid pressure provides the primary driving force in many multi-phase oil reservoirs (Muskat, 1949).

The exact role of gas in brine inflow at WIPP is yet to be determined. Gas may play a passive role of exsolving in inconsequential volumes near the mine face. If, in contrast, a large quantity of gas is coming out of solution at some distance into the salt, gas may play a more active role and contribute to the driving forces that move brine from the salt into the excavations. A more detailed analysis of the impact of gas on brine inflow will require both field measurements to characterize the pressure-volume behavior of the gas-brine system and numerical analyses of possible multi-phase behavior in the vicinity of an excavation.

3.2.1.5 Potential Drawbacks of Using Conservative Estimates for Brine Inflow. Brine inflow to the WIPP excavation is a complex process involving uncertainties in both flow mechanisms and parameter measurements. Various assumptions have been required to define the problem in a fashion that can be adapted to numerical, predictive models. Most of these assumptions are

conservative and overestimate brine inflow. Although this approach provides a conservative evaluation of brine inflow, it may complicate the assessment of interactions between brine inflow and other processes. Given the complexity of the brine-inflow process, this is the only tenable approach at this time.

The most important potential process interaction involving brine is the generation of gas from the waste materials that will be buried at the WIPP. If sufficient brine is present, the combination of microbial activity, canister corrosion, metal-waste corrosion, and radiolysis will produce large quantities of gas (Section 4.2). Enough gas may be generated to create a final repository state that consists of rooms that are unsaturated and that contain pore space occupied primarily by gas near lithostatic pressure. Given the current brine-inflow estimates, sufficient quantities of brine appear to be available to allow gas generation to occur; however, it is easy to forget that current estimates may be inherently high, not because of parameter-value selections, but because of fundamental model assumptions. If brine-inflow rates are significantly less than the current estimates, gas production may be limited by a restricted quantity of available brine, and the final repository state may be different. Therefore, in light of the important interactions between brine inflow and gas generation, brine inflow must be characterized as fully as possible, rather than characterized using an approach that results only in conservatively high estimates of the upper bound. Given the complexities of the low-permeability salt environment, accurate descriptions of brine inflow will require a much larger effort than estimating upper bound on inflow rates and will require work on fundamental flow mechanisms in addition to in-situ parameter measurements.

3.2.2 Chemistry of Intergranular Brines of the Salado Formation

This section discusses the compositions of Salado brines in the repository in the absence of interaction with waste, containers, and backfill. Initial brine composition is a critical starting point in evaluating potential radionuclide solubilities (Section 4.5) and the potential for sorption within the repository (Section 4.6). It also plays a direct role in evaluating the

potential for anoxic metal corrosion (Section 4.2) and possible variability of radionuclide retardation within the Culebra Dolomite in the event of human intrusion (Section 3.3.4).

Laboratory, modeling, and underground studies of repository and radionuclide chemistry will require the definition of standard brines of specified chemical composition. The selection of standard brines for these investigations will comprise several steps. Fluids that could enter WIPP disposal rooms after they are filled and sealed will be identified. Previous chemical analyses of these brines will be evaluated, and in some cases additional analyses will be made. The causes of chemical variations within each type of brine will be assessed. Finally, the sensitivity of repository and radionuclide chemistry to chemical variations within and between these brines will be determined. Evaluation of previous chemical analyses, additional analyses, and assessment of the causes of chemical variations might also aid in developing a hydrologic model for the Salado Fm.

Three types of brines could enter the repository. First, intergranular brines from the Salado Fm. at or near the repository horizon could enter the drifts and disposal rooms. These brines are currently seeping into the WIPP through the ribs and, to a lesser extent, the back and the floor, but rarely accumulate because of evaporation caused by ventilating the mine. After the repository is filled and sealed, however, the air trapped in voids will become saturated, and these brines could accumulate. Intragranular brines (fluid inclusions) that occur in the Salado Fm., in contrast, will not migrate in the absence of a large thermal gradient, and will not be considered in studies of repository and radionuclide chemistry. The second type of fluid occurs in isolated but occasionally large pockets in the underlying Castile Fm. These brines could enter the repository if an exploratory drillhole penetrates both a disposal room and a brine reservoir. Finally, fluids from overlying formations could seep down the shafts, along the drifts, and around or through the seals to the disposal rooms. Because most of the fluids in the overlying formations are undersaturated with respect to the minerals in the Salado Fm., they would dissolve salts from the backfill or the Salado Fm. In the process, they would become saturated brines. The composition of these brines could differ greatly, however, from the two other types of brines.

Because intergranular Salado brines had not been observed prior to the release of the FEIS (DOE, 1980a), this discussion focuses on the chemistry of these brines. The chemistry of fluids from the Rustler Fm. is described in Section 3.3.2.

Two groups are studying the chemistry of intergranular brines from the Salado Fm. Stein and Krumhansl (1986, 1988) collected and analyzed brines from five short (up to 20.3-cm [8-in]) floor holes and 24 short (up to 25.4-cm [10-in]) horizontal holes in the northern, experimental area of the WIPP underground workings. They referred to these samples of intergranular brines as "brine weeps." Stein and Krumhansl (1986, 1988) also collected and analyzed intergranular brines from 18 downholes in the northern area of the mine. They referred to these holes, which extended to depths of a few feet, as "floor holes." Stein and Krumhansl will collect and analyze additional brines from new horizontal holes (see below). Deal et al. (1989) collected brines from several drillholes that penetrate up to 15.2 m (50 ft) above the back or below the floor of the drifts, as well as from a few short (up to 0.9 m [3 ft]) horizontal holes and a floor seep. These holes are also located mainly in the northern part of the WIPP underground workings. This study is part of the ongoing Brine Sampling and Evaluation Program (BSEP), which is also monitoring the accumulation rates of brines in these holes (Deal and Case, 1987; Deal et al., 1989). Deal et al. (1989) sent their samples to the International Technology Corporation (IT) laboratory in Export, PA, and the United Nuclear Corporation Geotech (UNC) laboratory in Grand Junction, CO, for chemical analysis. In addition to the data reported by Deal et al. (1989), the WIPP performance assessment (PA) has evaluated unpublished BSEP results provided by Paul Drez and Jonathan Myers of IT. This group will continue to collect brine samples from these and additional holes and will send them to one or both of these laboratories for analysis.

The evaluation carried out for the WIPP PA to date has identified potentially important chemical variations within the available BSEP data. The concentrations of bromine (Br^-), chloride (Cl^-), and magnesium (Mg^{2+}) in brines collected from three BSEP upholes, for example, differ from the concentrations of these elements in brines from ten BSEP downholes. (Because most of the BSEP data on which these conclusions are based are still

unpublished, these variations cannot be illustrated in figures or tables here.) The concentrations of calcium (Ca^{2+}), potassium (K^+), sodium (Na^+), and sulfate (SO_4^{2-}), in contrast, are similar in both BSEP upholes and downholes. The BSEP has obtained data for boron (probably present mainly as H_3BO_3 and HB_4O_7^- or H_3BO_3 and $\text{B}(\text{OH})_4^-$, but referred to as B^{3+} here), but the concentrations of this element in upholes and downholes have not yet been compared. The WIPP PA is not evaluating the results reported by the BSEP for numerous minor and trace elements at this time, because these elements will probably not affect the studies of repository and radionuclide chemistry significantly. The differences between the concentrations of Br^- , Cl^- , and Mg^{2+} in BSEP upholes and downholes could result from different sampling artifacts associated with each type of hole. Samples collected from the upholes, for example, accumulate in containers suspended from the collars of the holes. As they trickle down through the DRZ, these brines probably change composition as a result of evaporation caused by passage of the mine air through small fractures induced by excavation of the drifts. As they evaporate, they could also change composition by reacting with minerals in the back. Brines collected from the downholes could be contaminated by material from the floor of the drifts during sampling. The differences between the concentrations of Br^- , Cl^- , and Mg^{2+} in BSEP upholes and downholes could also result from stratigraphic differences in intergranular Salado brines.

Potentially important chemical variations also exist between the data reported by Deal et al. (1989) and Drez and Myers of IT and the data obtained by Stein and Krumhansl (1986, 1988). The concentrations of Br^- and Cl^- in brines from BSEP upholes and downholes, for example, differ from the concentrations of these elements in samples collected by Stein and Krumhansl (1986, 1988) from 24 horizontal holes. The concentrations of Ca^{2+} , K^+ , Mg^{2+} , Na^+ , and SO_4^{2-} are similar in brines from the BSEP holes and the holes sampled by Stein and Krumhansl (1986, 1988). The differences between the concentrations of Br^- and Cl^- reported by Deal et al. (1989) and those obtained by Stein and Krumhansl (1986, 1988) could result from sampling artifacts like those discussed above or from stratigraphic differences. They could also result from differences in the sampling techniques or the method of shipping used by the two groups studying these brines, or they could result

from differences between the laboratory techniques used at the IT and UNC laboratories and those used by Stein and Krumhansl (1986, 1988).

The WIPP Project is attempting to determine the causes of the chemical variations observed in intergranular brines from the Salado Fm. A preliminary statistical model of the possible causal factors discussed above is providing guidance for an interlaboratory comparison study using synthetic brines of known composition and additional brine sampling and analysis by Stein and Krumhansl. The study will examine factors such as spatial variations in the chemistry of brines from a given stratigraphic horizon and temporal variations in brine chemistry and in the sampling, shipping, and analytical techniques used by each analytical laboratory. This additional sampling and analysis has two objectives. First, it will determine whether, at a given stratigraphic horizon within the drifts, there are significant differences in brine chemistry between the northern, experimental area of the WIPP, and the southern area, where waste will be emplaced. Very few brines from the southern area have been sampled and analyzed. Second, it will ascertain whether, at a given location within the mine, there are significant chemical differences between brines collected from different stratigraphic horizons within the drifts. Furthermore, laboratory studies of the possible effects of the sampling artifacts discussed above might indicate whether these processes contribute to observed variations in brine chemistry. The results of these additional studies, along with additional results from the ongoing BSEP, might lead to an improved understanding of the chemical variations discussed above.

Quantifying the causes of chemical variations in intergranular brines might in turn aid the development of a hydrologic model of the Salado Fm. Spatial and stratigraphic variations, for example, might constrain estimates of the advective or diffusive transport of brines or dissolved solids and gases through interconnected voids in the undisturbed rock and through fractures in the DRZ. At this time, however, it is unclear whether spatial or stratigraphic factors contribute to the observed variations in the chemistry of these brines.

A standard composition for intergranular Salado brines is being defined at this time, with the understanding that this composition might have to be

revised upon completion of additional studies of brine chemistry. This standard brine, discussed below, is the best available estimate of the "average" composition of intergranular Salado brines.

The standard brines (Table 3-4) were obtained in three steps. First, data were included from chemical analyses of 29 brine weeps (Stein and Krumhansl, 1986, 1988) and from brines from 12 holes (ten long downholes, one short floor hole, and one short horizontal hole) reported by Deal et al. (1989) and Drez and Myers of IT. Data for fluid inclusions (Stein and Krumhansl, 1986, 1988) were excluded, because intragranular brines will not migrate in the absence of a large thermal gradient. Data for the floor holes (Stein and Krumhansl, 1986, 1988) were also excluded, although the data for these holes might be included in the next standard brine, because they are similar to the brines from downholes sampled by the BSEP. Furthermore, the datum for SO_4^{2-} from Sample 19 of Stein and Krumhansl (1986, 1988) is excluded, because the reported value is so high that it is clearly erroneous. All data from the BTP holes (a subset of the BSEP holes) and upholes sampled by Deal et al. (1989) and Drez and Myers of IT were excluded, because the BTP holes are contaminated with fluids from the Rustler Fm. spread in the mine to control dust and/or from grout, and because fluids from the upholes probably changed composition by evaporation or reaction with minerals in the back during accumulation.

Second, for those holes that yielded sufficient brine for replicate analyses, the results for each element or chemical property have been averaged to obtain one value for each sampling date. If two laboratories analyzed samples obtained from a given hole on the same date and either or both of these laboratories carried out replicate analyses, all of the replicate results from both laboratories were averaged simultaneously to obtain one value for that hole on that date. For holes sampled more than once, the results for each element or chemical property from each sampling date were averaged to obtain one value for each hole.

Third, the results for each element or chemical property from the 41 holes considered were averaged to obtain an overall average for each element or chemical property in this standard brine. The values for each hole were not weighted for the integrated volume of brine that has accumulated in that hole

Table 3-4. Composition of "Standard" Intergranular Salado Brines

<u>Element or Chemical Property</u>	<u>PAB 1¹</u>	<u>PAB 2</u>	<u>Brine A²</u>	<u>Brine B³</u>
Alk. (mM) ⁴	13.7	13.8	-	-
Alk., ext. (mM) ⁵	14.8	15.7	-	-
B ³⁺ (mM) ⁶	152	148	20	20
Br ⁻ (mM)	13	13	10	10
Ca ²⁺ (mM)	10	9	20	20
Cl ⁻ (M)	6.04	6.02	5.35	4.93
Eh ⁷	-	-	-	-
K ⁺ (mM)	500	510	770	<5
Mg ²⁺ (M)	1.0	1.0	1.44	<0.005
Na ⁺ (M)	3.9	3.9	1.83	5.00
pH	6.0	6.1	6.5	6.5
SG ⁸	1.22	1.22	1.2	1.2
SO ₄ ²⁻ (mM)	160	170	40	40
TDS ⁹	385,000	378,000	306,000	297,000
TIC (mM) ¹⁰	0.37	-	10	10

1. Defined in Appendix A.

2. Standard brine developed by Molecke (1976, 1983) to simulate fluids equilibrated with K⁺- and Mg²⁺-bearing minerals in overlying potash-bearing zones prior to entering the WIPP.

Table 3-4. Composition of "Standard" Intergranular Salado Brines
(continued)

3. Standard brine developed by Molecke (1976, 1983) to simulate fluids entering a domal salt repository or relatively pure halite.
 4. Alkalinity reported as equivalent HCO_3^- , solutions titrated to pH = 4.5.
 5. Extended alkalinity reported as equivalent HCO_3^- , solutions titrated to pH = 2.5 to 3.0.
 6. Probably present mainly as H_3BO_3 .
 7. Eh not measured with an Eh electrode or calculated theoretically, but assumed to be similar to that of solutions in equilibrium with atmospheric oxygen (see, for example, Garrels and Christ, 1965, Figure 11.2)
 8. Specific gravity.
 9. Total dissolved solids.
 10. Total inorganic carbon unspecified for PAB 2 because it varied by a few orders of magnitude from sample to sample and was undetectable in several samples.
-

to date, for the most recently measured accumulation rate, or for any other such factor. The differences between PAB 1 and PAB 2 (Table 3-4) arise mainly from the fact that Drez and Myers of IT provided additional BSEP data after the definition of PAB 1.

Different methods could have been used to define a standard intergranular brine from the Salado Fm. and might be used in the future. The results of the interlaboratory comparison study, for example, might imply that data from one of the analytical laboratories should be excluded. Furthermore, it might be preferable to weight the data obtained for each hole for the volume of brine that has accumulated in that hole to date, for the most recently measured accumulation rate, or for some similar factor. This could, however, bias the results in favor of the BSEP data at the expense of the data from Stein and Krumhansl (1986, 1988). This is because the BSEP requires relatively large

volumes of brine for their chemical analyses and measures the accumulation rates of these brines on an ongoing basis, whereas Stein and Krumhansl (1986, 1988) analyzed relatively small volumes of brine and sampled their holes only once. The results of the ongoing investigation of brine chemistry, especially the statistical analysis of the causes of chemical variations, will ultimately determine the best method for defining the "average" composition of intergranular Salado brines.

Although PAB 2 is a preliminary estimate of the "average" composition of intergranular Salado brines at or near the stratigraphic horizon of the WIPP underground workings, a modeling study using the geochemical speciation and solubility code EQ3NR (Wolery, 1983; Jackson and Wolery, 1985) implies that this brine is at or near equilibrium with the major and minor minerals that make up most of the Salado Fm. (Stein [1985] characterized the mineralogy of the Salado Fm. at and near the stratigraphic horizon of the repository.) PAB 2 is at or near equilibrium with anhydrite (CaSO_4), basanite ($\text{CaSO}_4 \cdot 0.5\text{H}_2\text{O}$), gypsum ($\text{CaSO}_4 \cdot 2\text{H}_2\text{O}$), and halite (NaCl). Because the concentration of total inorganic carbon has not been determined reliably (Table 3-4), it is unclear whether PAB 2 is in equilibrium with magnesite (MgCO_3). Furthermore, the thermodynamic data base for EQ3NR does not include a solubility product for polyhalite ($\text{K}_2\text{MgCa}_2(\text{SO}_4)_4 \cdot 2\text{H}_2\text{O}$); it is thus unclear whether PAB 2 is in equilibrium with this mineral. Finally, it is unclear whether PAB 2 is in equilibrium with clay minerals and quartz (SiO_2), because the ion interaction parameters required to compute the activity coefficients for aluminum (Al^{3+}) and silicon (Si^{4+}) in brines, and hence the solubilities of clays and quartz in brines, have not been determined experimentally or incorporated into the EQ3NR data base.

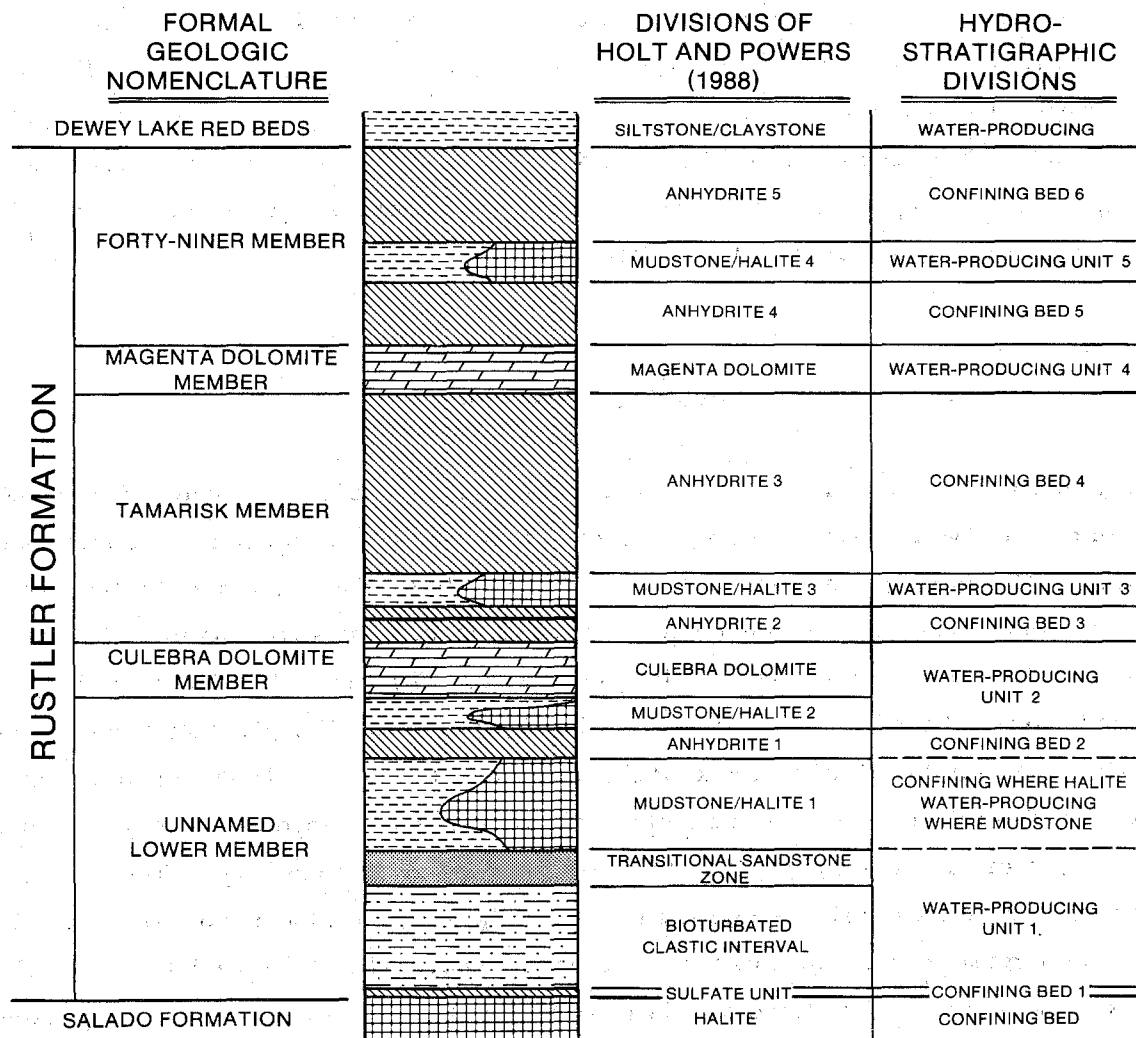
The standard brine PAB 2 represents the "average" composition of intergranular Salado brines prior to reactions with backfill additives, drums, waste boxes, or the radioactive or nonradioactive constituents of TRU waste. These reactions could change the composition and chemical properties, especially the Eh and pH, of PAB 2 or any other standard brine. Microbial activity and corrosion of metals will decrease the Eh of any brine present. Microbial activity, for example, could decrease the Eh to values characteristic of denitrification, the reduction of manganese(IV) oxides, the

reduction of iron(III) oxides, or even SO_4^{2-} reduction. The specific numerical values of Eh for any of these processes depend on pH, which cannot be predicted yet. Microbial production of carbon dioxide (CO_2) could decrease the pH of the brine to acidic values. Reactions between brine and the cements used in grouting some of the drums and in seals could increase the pH to basic values. Reactions between brine and three of the proposed backfill additives for the removal of CO_2 , calcium oxide (CaO), potassium hydroxide (KOH), and sodium hydroxide (NaOH), could increase the pH to very basic values. One objective of laboratory, modeling, and underground studies of repository chemistry will be to quantify the effects of reactions like these on the composition, Eh, and pH of any brine present.

3.3 Rustler Formation

The hydrologic data for the Rustler Fm. at the time of the FEIS (DOE, 1980a) were derived from testing performed at eight locations (Cooper and Glanzman, 1971; Mercer and Orr, 1979). Since that time, 33 additional well sites have been established and considerable testing (in some cases retesting) has been performed. Thus, the hydrology of the Rustler Fm. is much better understood today than at the time of the FEIS. The FEIS recognized three water-producing units within the Rustler Fm. (the Rustler-Salado contact zone, the Culebra Dolomite, and the Magenta Dolomite), but lumped the Magenta and Culebra together as a single "Rustler aquifer" during modeling. Today, five water-producing units are recognized: the lower siltstone portion of the unnamed lower member and the Rustler-Salado contact, the Culebra Dolomite, the Tamarisk claystone, the Magenta Dolomite, and the Forty-niner claystone (Figure 3-1). These water-producing units are separated by evaporitic confining beds. The hydrologic properties of each of these units, abstracted from Holt et al. (1989), are summarized below.

Some disagreement remains about the extent and significance of halite distribution and evaporite dissolution within the Rustler Fm. The detailed stratigraphic division of the Rustler Fm. shown in Figure 3-1 is updated from similar detailed divisions developed by Snyder (1985) and Lowenstein (1987). The distribution of Rustler halite indicated in Figures 3-2 (p. 3-29),



TRI-6330-91-0

Figure 3-1. Hydrostratigraphic column of the Rustler Fm. near the WIPP site (Holt et al., 1989).

3-4 (p. 3-37), and 3-6 (p. 3-44) is similar to halite-distribution patterns given by Snyder (1985) and Chaturvedi and Channell (1985), but is based on more-extensive and more-recent core examination.

In broad terms, Snyder (1985), Lowenstein (1987), and Chaturvedi and Channell (1985) interpreted the original distribution of halite within the Rustler Fm. to be laterally continuous within the region of the WIPP site and interpreted local absence of halite in a given stratigraphic interval where it is known to occur elsewhere as the result of evaporite dissolution. This interpretation tends to maximize the amount of Rustler dissolution. In contrast, Holt and Powers (1988) and Holt et al. (1989) concluded that much of the variability in distribution of Rustler halite is primary (depositional) and that Rustler dissolution has been limited in extent. The two differing interpretations have little impact on WIPP performance, because, as summarized by Lappin (1988), extrapolation of the maximum dissolution rates indicates no threat to the WIPP repository within 10,000 years. The two interpretations might, however, affect the amount of change in local Rustler flow and transport properties expected over the next 10,000 years. This question is not specifically addressed here; the current calculations of long-term performance (Chapters 6.0 and 7.0) do assume, however, current estimates of both "expected" and "degraded" Culebra properties.

Sections 3.3.2 and 3.3.3 discuss the geochemical variability of Rustler ground waters and the implications of the variability and isotopic studies in interpreting the transient hydrologic and geochemical setting of the WIPP site. The information in these sections plays little direct role in the long-term performance calculations of Chapters 6.0 and 7.0. However, the geochemical information contained in Section 3.3.2 plays a critical role in estimating radionuclide-retardation coefficients (K_d 's) in the Culebra Dolomite (Section 4.6). Similarly, interpretations in Section 3.3.3 play a major role in interpreting limited vertical ground-water movement within the Rustler Fm. (Section 3.3.1).

Radionuclide-transport calculations in the WIPP FEIS assumed porous-medium behavior and could not evaluate variations in ground-water composition (Table 1-1). Neither conclusion now appears adequate. Section 3.3.4

discusses the expected radionuclide distribution coefficients (K_d 's) within the Culebra Dolomite, largely independent of the presence of fractures. The expected effectiveness of radionuclide retardation within fractured portions of the Culebra Dolomite is contained in Chapter 7.0 and Appendix E.

3.3.1 Physical Hydrology

The following are the major conclusions of Section 3.3.1.

- There are five water-bearing zones within the Rustler Fm., rather than the three recognized at the time of the FEIS. In ascending order, these zones are the siltstone portion of the lower unnamed member and the Rustler/Salado contact; the Culebra Dolomite; the Tamarisk claystone; the Magenta Dolomite; and the Forty-niner claystone. At and near the WIPP site, the Culebra Dolomite dominates flow.
- The transmissivity of the lower claystone is generally $<6 \times 10^{-10}$ m²/s, except where dissolution of the upper Salado Fm. has occurred. Flow in this interval appears to be generally westward, except within Nash Draw, where it is southwesterly.
- The transmissivity of the Culebra Dolomite ranges over as much as six orders of magnitude at the WIPP site and in Nash Draw, from $<10^{-7}$ to $>10^{-3}$ m²/s. The variability is apparently a direct result of fracturing. Except in Nash Draw, the Culebra Dolomite appears to be effectively confined by Tamarisk anhydrite, gypsum, and siltstone in the unnamed member. Modern flow within the Culebra Dolomite is southerly near the site and southwesterly in Nash Draw. South of the site, flow is apparently to the west, although there is considerable uncertainty in actual flow directions, because of very gentle gradients and variable brine density.
- In general, Culebra tests indicating transmissivities between 10^{-6} and 10^{-4} m²/s show evidence of fracture flow. Effective fractures are not present in boreholes with lower transmissivity. In addition, perhaps because of very closely spaced fractures, tests indicating higher transmissivities do not show hydraulic effects of fracturing.

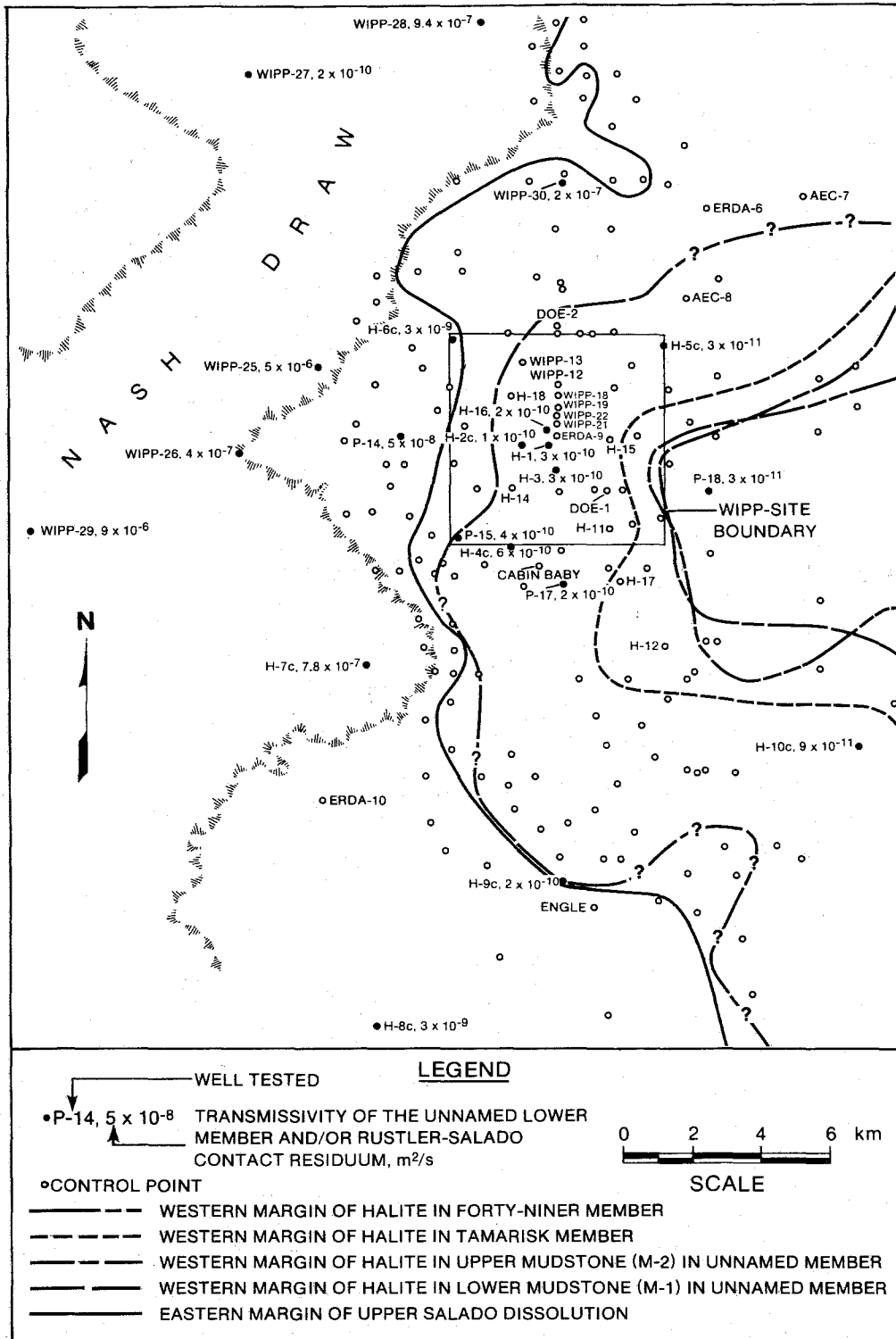
- Except in Nash Draw, the Tamarisk claystone is separated from the Magenta and Culebra Dolomites by intervening anhydrite and gypsum. The Tamarisk claystone has been tested at only four locations; at all four the transmissivity was too low to interpret. No hydraulic-head data are available from the Tamarisk Member.
- The transmissivity of the Magenta Dolomite is generally at least an order of magnitude below that of the Culebra Dolomite, i.e., generally $<10^{-7}$ m²/s east of Nash Draw. Modern regional flow within the Magenta Dolomite appears to be to the west near the site and to the southwest in Nash Draw, quite distinct from general flow directions within the Culebra Dolomite.
- The Forty-niner claystone, bounded above and below by relatively impermeable anhydrite, has been tested at only three locations, where its transmissivity is estimated to be 10^{-8} to 10^{-9} m²/s. Forty-niner transmissivity may be higher in Nash Draw, but it has not been tested there. Forty-niner heads estimated at H-3d, H-14, H-16, and DOE-2 are below those of the underlying Magenta Dolomite.
- Where there has been little evaporite dissolution, relative heads within the Rustler Fm. indicate vertical flow into the Culebra Dolomite from below and above, i.e., the Culebra is draining the Rustler system. However, the difference between hydraulic head potentials in the different units indicates that this drainage is very slow. At the site, the relative head potentials between the Magenta and Forty-niner Members indicate that there is no modern vertical recharge from the Dewey Lake Red Beds into any portion of the Rustler Fm. below the Forty-niner Member. West of the site, however, the decreasing difference between Magenta and Culebra heads may indicate a combination of westward and downward drainage of the Magenta Dolomite.
- In general, modern flow within the Rustler Fm. is toward the west and then parallel to the axis of Nash Draw. The notable exception is the Culebra Dolomite, in which flow near the site is to the south. With the exception of the Culebra, the flow directions would generally be interpreted to indicate recharge from the north and east. The units to the north and east are

deeper and are separated by thicker confining beds than at the site. These results, especially when combined with the geochemical variability of Culebra ground waters (Section 3.3.2) and isotopic interpretations (Section 3.3.3), indicate that modern flow directions within the Rustler Fm., specifically including the Culebra Dolomite, do not reflect flow from a modern recharge area to a modern discharge area, but rather reflect a recharge-and-discharge cycle.

3.3.1.1 Unnamed Lower Member and Rustler/Salado Contact. The unnamed lower member of the Rustler Fm. is composed of a layered sequence of clayey siltstone, gypsum/anhydrite, and halite. In the vicinity of the WIPP, the thickness of the unnamed lower member ranges from 24 m (78.8 ft) (at ERDA-6) to 46 m (150 ft) (at P-18). The siltstone water-producing unit within the unnamed lower member generally has a transmissivity of $\leq 6 \times 10^{-10} \text{ m}^2/\text{s}$. Where dissolution of the upper Salado Fm. has occurred, the transmissivity of the unnamed member is higher, and the "brine aquifer" present in the upper Salado residuum may be hydraulically continuous with the unnamed member siltstone. Hydraulic heads in the unnamed member and upper Salado Fm. indicate ground water flows westerly toward Nash Draw and southwesterly down the axis of Nash Draw.

From a hydrostratigraphic point of view, the bottom several feet of the unnamed member, consisting of anhydrite/gypsum, polyhalite, and halite, represent a confining bed indistinguishable hydraulically from the underlying Salado Fm. The lower siltstone unit of the unnamed member (the transition zone and bioturbated clastic interval of Holt and Powers [1988]) can be considered to be the lowermost Rustler water-producing zone, and the overlying halite and anhydrite/gypsum units act as another confining bed. The top unit of the unnamed member is composed of siltstone, mudstone, and claystone. At some locations south and east of the WIPP site, such as P-18, this unit also contains halite (Holt and Powers, 1988).

West and southwest of the WIPP site, where halite in the upper Salado and lower Rustler Fms. has been dissolved (Figure 3-2), a highly transmissive zone exists in the residuum of the upper Salado Fm. at the contact with the Rustler Fm.; Robinson and Lang (1938) referred to this zone as a "brine aquifer."



TRI-6330-92-0

Figure 3-2. Distribution of Rustler halite and transmissivities of the unnamed lower member and Rustler/Salado contact zone (Holt et al., 1989).

Brecciation of the unnamed lower member has been observed in Nash Draw, where the upper Salado Fm. has been dissolved (Holt and Powers, 1988), but the degree to which this brecciation may have enhanced transmissivity or decreased the effectiveness of the unnamed member confining beds is unclear. If the anhydrite, gypsum, polyhalite, and halite at the bottom of the Rustler Fm. are dissolved, however, the brine aquifer is probably hydraulically continuous (i.e., not separated by a confining bed) with the unnamed member siltstone. Where dissolution of the upper Salado Fm. has not occurred, no significant permeability is associated with the upper Salado Fm. and its contact with the Rustler Fm., and the lower siltstone provides the only water-producing unit in the lower Rustler and upper Salado Fms.

Mercer (1983) reported values of transmissivity for the "Rustler-Salado contact residuum" from 20 locations in the vicinity of the WIPP site. These values and an additional value (H-16) reported by Beauheim (1987c) are shown, along with the locations of the wells at which the measurements were made, in Figure 3-2. A summary of test information from these locations is presented in Table 3-5. Tests at H-8c, WIPP-25, WIPP-27, WIPP-28, and WIPP-29 were conducted over intervals contained entirely within the upper Salado Fm. (Table 3-5). Transmissivity values reported for these locations, although based on brine testing and therefore reliable, are not representative of the water-producing unit within the unnamed lower member of the Rustler Fm.

Test intervals at the other wells varied in length between 7 and 44 m (23 and 144 ft) with different stratigraphic coverages, but all included at least the lower 2 m (6.6 ft) of the Rustler Fm. and the upper 1 m (3.3 ft) of the Salado Fm. Most of the transmissivity values for the Rustler-Salado contact zone range from 3×10^{-11} to 6×10^{-10} m²/s. No correlation is evident between test-interval thicknesses and transmissivities. If the measured transmissivities are considered to be derived entirely from whatever portions of the lower siltstone of the unnamed member were included in the test intervals, the average hydraulic conductivity of the siltstone ranges from about 7×10^{-12} to 1×10^{-10} m/s. Transmissivities greater than 6×10^{-10} m²/s were measured at five locations. Dissolution of the upper Salado Fm. has occurred at four of these locations (H-6c, H-7c, P-14, and WIPP-26; Figure 3-2), and the test intervals included 4 to 12 m (13 to 39 ft) of the upper

Table 3-5. Summary of Hydraulic Testing of the Unnamed Lower Member and Upper Salado Fm. (Mercer and Orr, 1979; Mercer et al., 1981; Dennehy, 1982; Dennehy and Mercer, 1982; Mercer, 1983; Richey, 1986, 1987a; Beauheim, 1987a).

Well	Unnamed Lower Member Depth Interval (m)	Depth Interval Tested (m)	Completion Interval (m)	Transmissivity (m^2/s)	Comments
H-1	213-249 ^a	213-257	245-252	3×10^{-10}	
H-2c	197-233	226-242	226-242	1×10^{-10}	
H-3(b1)	212-250	244-265	248-255	3×10^{-10}	
H-4c	157-191	186-201	186-201	6×10^{-10}	
H-5c	282-317	312-328	312-328	3×10^{-11}	
H-6c	191-220	213-226	213-226	3×10^{-9}	top of Salado salt at 220 m
H-7c	84-116 ^a	109-128	109-128	7.8×10^{-7}	top of Salado salt at 123 m
H-8c	187-223	224-246 ^b	224-246	3×10^{-9}	top of Salado salt at 243 m
H-9c	206-241	239-249	239-249	2×10^{-10}	
H-10c	424-458	452-469	452-469	9×10^{-11}	
H-16	221-257	225-259	225-259	2×10^{-10}	
P-14	181-209	206-213	206-213	5×10^{-8}	top of Salado salt at 212 m
P-15	133-165	162-171	162-171	4×10^{-10}	
P-17	178-218	214-221	214-221	2×10^{-10}	
P-18	286-332	328-335	328-335	3×10^{-11}	
WIPP-25	144-172	176-185 ^b	176-185	5×10^{-6}	top of Salado salt at 183 m
WIPP-26	64-94	69-100	69-100	4×10^{-7}	top of Salado salt at 98 m
WIPP-27	97-127	130-140 ^b	130-140	2×10^{-10}	top of Salado salt at 155 m
WIPP-28	136-162	167-180 ^b	167-180	9.4×10^{-7}	top of Salado salt at 180 m
WIPP-29	13-44	66-76 ^b	66-76	9×10^{-6}	top of Salado salt at 77 m
WIPP-30	199-228	223-230	223-230	2×10^{-7}	

a. Revision of published depth by R.P. Snyder, USGS, personal communication

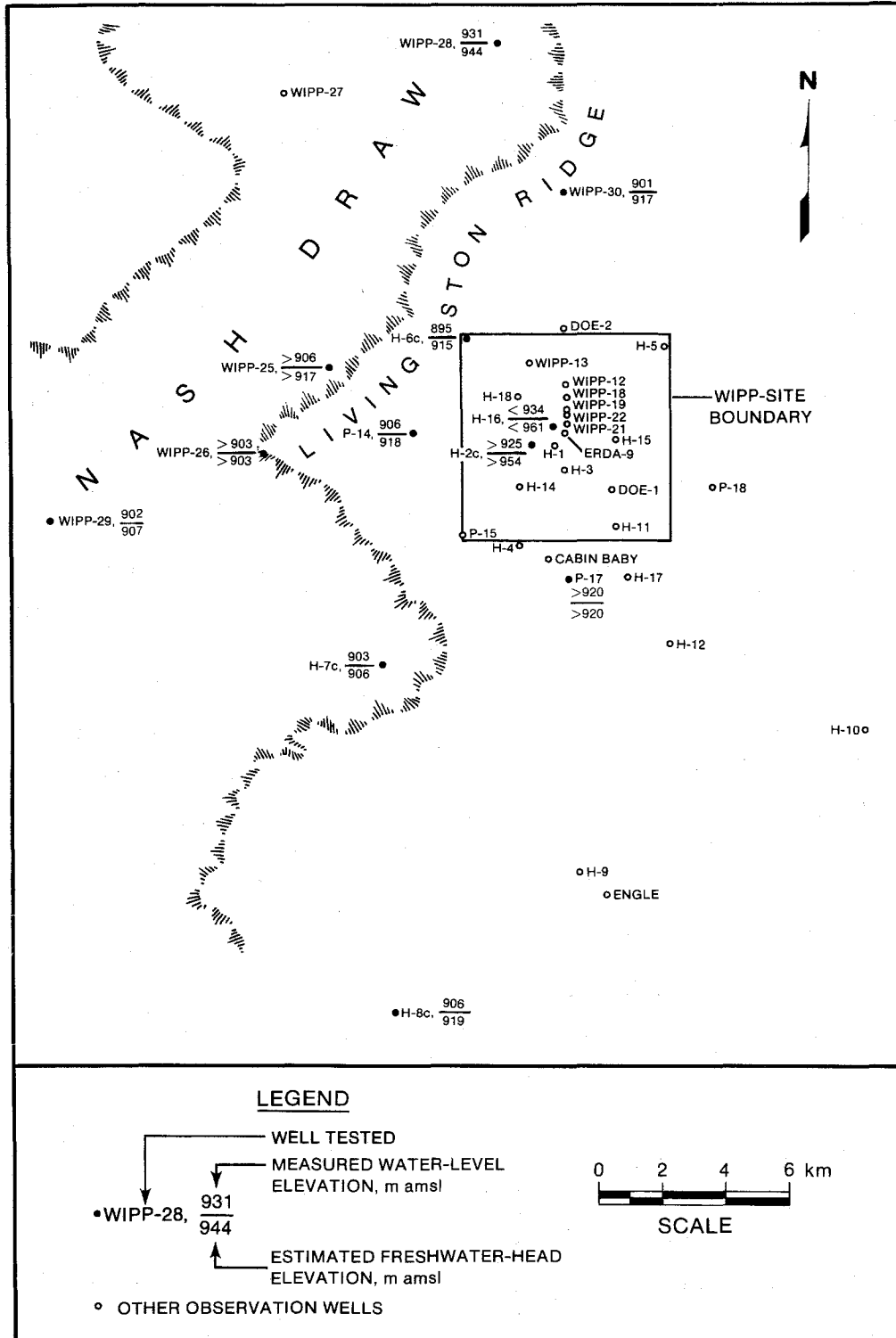
b. No Rustler tested

Salado Fm. and residuum, which probably contributed the increased transmissivity. Only the value from WIPP-30, $2 \times 10^{-7} \text{ m}^2/\text{s}$, cannot be explained by dissolution-related transmissivity enhancement.

Few measurements have been made of the stabilized water level or fluid pressure of the unnamed lower member or Rustler-Salado contact zone. Water levels take months or years to stabilize in wells completed in low-transmissivity zones like the unnamed member. Most of the wells in which the lower Rustler and upper Salado Fms. were tested did not remain completed to those zones long enough for water levels to stabilize, but were instead recompleted to allow testing and monitoring of overlying units. As a result, reliable water-level data are available only from those wells where unnamed member or Rustler-Salado transmissivities $>10^{-10} \text{ m}^2/\text{s}$ were measured.

Richey (1987b) presented water-level data collected from the Rustler-Salado contact zone by the USGS between 1977 and 1985. Stabilized water levels were attained only in wells H-6c, H-7c, H-8c, P-14, WIPP-28, and WIPP-30. Water levels appeared to be stabilizing in WIPP-25, WIPP-26, and WIPP-29 during their monitoring periods; the last measurements can be used as minimum water-level altitudes at those locations. Of the other wells where Rustler-Salado water levels were measured, only the data from H-2c are adequate to place a lower bound on the stabilized water-level altitude that is useful in understanding flow directions. A similarly useful upper bound can be placed on the stabilized water-level altitude at H-16 using fluid-pressure data (Beauheim, 1987c).

Water-level altitudes were measured in the 11 wells listed above (Figure 3-3). Drawing conclusions from these data is difficult, because the specific gravity of the Rustler-Salado water is different in each well. Converting the water-level altitudes to freshwater-head altitudes (the altitude at which a column of fresh water would stand while exerting the same pressure at the midpoint of the well-completion interval as the actual water in the well) provides a more useful basis for evaluating general directions of ground-water flow. Because of the dip of the Rustler Fm., however, freshwater-head altitudes calculated from the midpoints of the well-completion intervals do not share a common elevation datum, and therefore should be



TRI-6330-93-0

Figure 3-3. Measured water levels and estimated freshwater heads of the unnamed lower member and Rustler/Salado contact zone (Holt et al., 1989).

considered only qualitative indicators of potential flow directions. Moreover, any conversion to freshwater head is only as good as the estimate of the specific gravity (or fluid density) of the water in the well at the time of the water-level measurement. The freshwater-head altitudes shown in Figure 3-3 were estimated using specific-gravity data presented by Mercer (1983), Richey (1987a), and Beauheim (1987c). Most of the specific-gravity measurements were made at or near the time of the water-level measurements, and the freshwater-head estimates in those cases are probably accurate within 3 m. The times of the specific-gravity measurements at H-2c, P-14, WIPP-25, and WIPP-28 are unknown, however, making the freshwater-head estimates at those locations less certain. Table 3-6 summarizes the hydraulic-head data available for the unnamed lower member and upper Salado Fm.

Consideration of the estimated freshwater heads shown on Figure 3-3 indicates several things. First, the heads at the wells completed entirely in the upper Salado Fm. (H-8c, WIPP-25, WIPP-28, and WIPP-29) do not seem to differ significantly from the heads at the wells completed across the Rustler-Salado contact, indicating probable good hydraulic communication between the brine aquifer in the upper Salado residuum and the lower Rustler siltstone. Second, the heads are consistent with Mercer's (1983) interpretation that flow through the low-transmissivity sections of the Rustler-Salado is generally westerly or southwesterly across the WIPP site toward the sink represented by the high transmissivities in Nash Draw, while the flow within Nash Draw is generally southwesterly toward Malaga Bend on the Pecos River. Flow from the southeast (H-7c and H-8c) may be westerly toward the river or northwesterly toward the higher transmissivities within Nash Draw.

3.3.1.2 Culebra Dolomite. The Culebra Dolomite Member of the Rustler Fm. is a finely crystalline, locally argillaceous and arenaceous, vuggy dolomite ranging in thickness from 7 m (23 ft) (at DOE-1 and other locations) to 14 m (46 ft) (at H-7) near the WIPP. The Culebra Dolomite is generally considered to provide the most important potential ground-water-transport pathway for radionuclides that may escape from the WIPP to the accessible environment. Accordingly, the WIPP Project has devoted much attention to understanding the hydrogeology and hydraulic properties of the Culebra. One early observation, first documented by Mercer and Orr (1979), was that the transmissivity of the

Table 3-6. Hydraulic-Head Information for the Unnamed Lower Member and Upper Salado Fm.

<u>Well</u>	<u>Ground-Surface Elevation (m amsl)</u>	<u>Stabilized Depth to Water (m)</u>	<u>Depth to Middle of Completion Interval (m)</u>	<u>Borehole-Fluid Specific Gravity</u>	<u>Freshwater-Head Elevation (m amsl)</u>	<u>Depth to Middle of Culebra (m)</u>	<u>Freshwater-Head Elevation at Midpoint of Culebra (m amsl)</u>
H-2c	1030	<105	234	1.225	>954	193	>945
H-6c	1020	125	219	1.21	915	188	908
H-7c	964	61	118	1.048	906	78	904
H-8c	1046	140	235	1.13	919	183	913
H-16	1039	>105 ^a	242	1.2	<961	217	<956
P-14	1024	118	210	1.126	918	178	914
WIPP-25	979	<73	181	1.093	>917	140	>913
WIPP-26	961	<58	85	1.04	>903	60	>903
WIPP-28	1020	89	173	1.152	944	132	938
WIPP-29	907	5-9	71	1.072	903-907	8	896-903
WIPP-30	1045	144	226	1.202	917	196	911

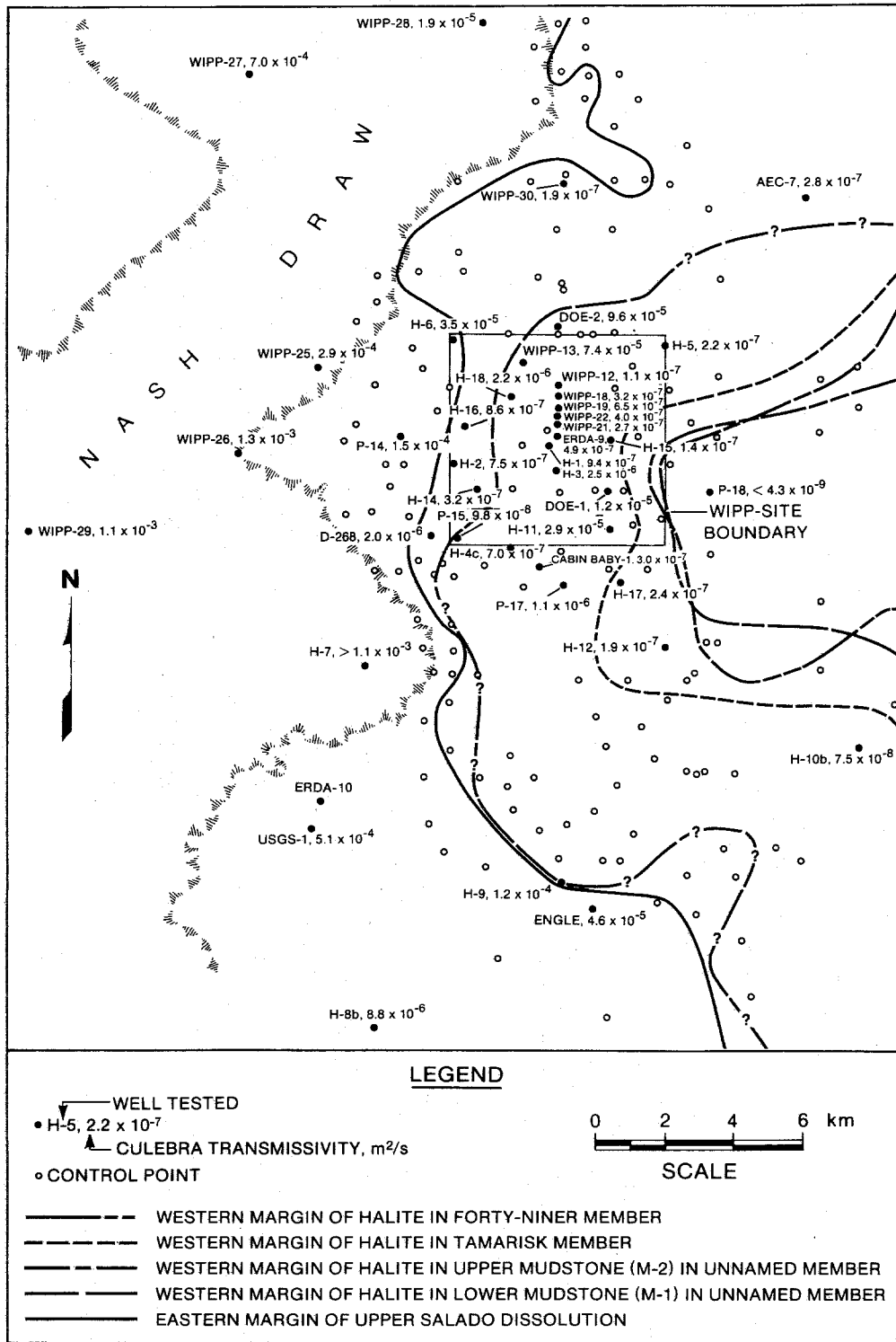
a. Converted from pressure data presented in Beauheim (1987c)

Culebra Dolomite varies by six orders of magnitude in the vicinity of the WIPP site. This variation in transmissivity appears to be the immediate result of differing degrees of fracturing within the Culebra Dolomite. The cause of the fracturing, however, has been a topic of speculation that is as yet unresolved.

The Culebra Dolomite is underlain by a siltstone/mudstone/claystone unit of the unnamed lower member, and overlain by an anhydrite unit of the Tamarisk Member (Figure 3-1), both of which have lower hydraulic conductivities than the Culebra Dolomite and serve to confine it hydraulically. The underlying siltstone likely provides a source of leakage to the Culebra, but the overlying anhydrite is relatively nonleaky. In Nash Draw, fracturing and possibly dissolution of the Tamarisk Member has probably made it less effective as a confining bed. Where the Culebra Dolomite is only 3 m (10 ft) below land surface at WIPP-29, it may be unconfined. The degree of confinement is unclear at H-7 and WIPP-26.

Mercer (1983) reported values for Culebra transmissivity at 20 locations. Beauheim (1987c) provided values for Culebra transmissivity at 15 new locations and new estimates at 7 locations for which values had previously been reported. Combined with testing performed for Project Gnome (Cooper and Glanzman, 1971) and other recent work performed at DOE-2 (Beauheim, 1986), H-3 (Beauheim, 1987a), H-11 (Saulnier, 1987), WIPP-13 (Beauheim, 1987b), AEC-7 (Beauheim, 1989a), and D-268 (Beauheim, 1989a), the Culebra has been tested at 41 locations in the vicinity of the WIPP (Table 3-7). Figure 3-4 shows these 41 locations, the most recent transmissivity values at each location, and the distribution of halite within the Rustler Fm. over the same area. In general, the highest Culebra transmissivities ($>10^{-4}$ m²/s) are found in areas where no halite is present in the Rustler Fm., and the lowest transmissivities ($\leq 2 \times 10^{-7}$ m²/s) are found in areas where halite is present in at least the Tamarisk and unnamed lower members of the Rustler Fm. Where halite is present only in the unnamed lower member, a wide range of transmissivities is found.

Culebra transmissivities of about 1×10^{-6} m²/s or greater appear to be related to fracturing. Where the transmissivity of the Culebra Dolomite is less than 10^{-6} m²/s, few or no open fractures have been observed in core, and



TRI-6330-94-0

Figure 3-4. Distribution of Rustler halite and transmissivities of the Culebra Dolomite (Holt et al., 1989).

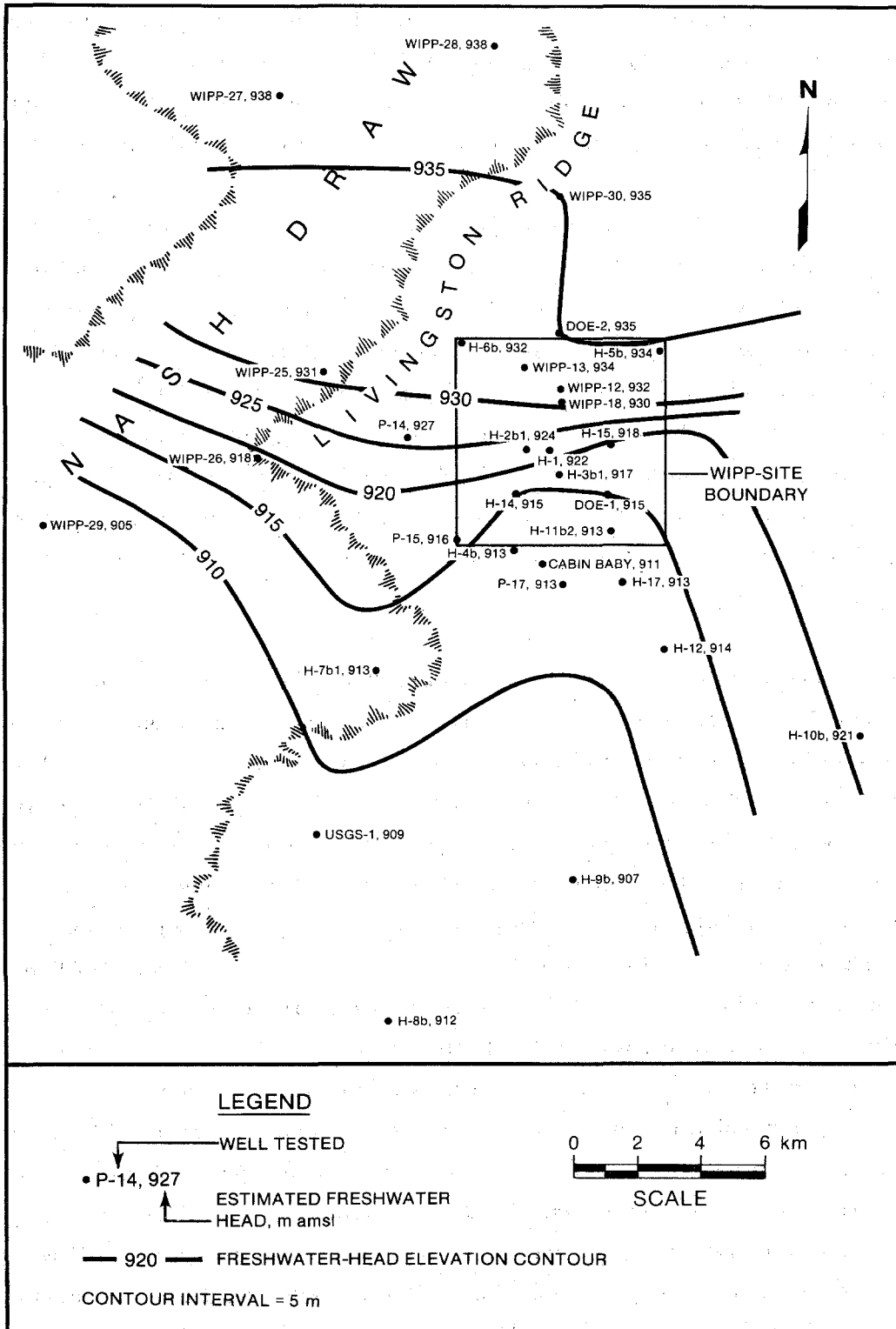
Table 3-7. Summary of Transmissivity Data for the Culebra Dolomite

Well	Culebra Depth Interval (m)	Transmissivity (m ² /s)	Reference
AEC-7	265-273	2.8 x 10 ⁻⁷	Beauheim (1989a)
Cabin Baby-1	153-161	3.0 x 10 ⁻⁷	Beauheim (1987c)
D-268	113-119	2.0 x 10 ⁻⁶	Beauheim (1989a)
DOE-1	250-257	1.2 x 10 ⁻⁵	Beauheim (1987c)
DOE-2	251-258	9.6 x 10 ⁻⁵	Beauheim (1986)
Engle	201-208	4.6 x 10 ⁻⁵	Beauheim (1987c)
ERDA-9	215-222	4.9 x 10 ⁻⁷	Beauheim (1987c)
H-1	206-213	9.4 x 10 ⁻⁷	Beauheim (1987c)
H-2	190-197	7.5 x 10 ⁻⁷	Beauheim (1989b)
H-3	205-212	2.5 x 10 ⁻⁶	Beauheim (1987a)
H-4c	149-157	7.0 x 10 ⁻⁷	Beauheim (1987c)
H-5	273-280	2.2 x 10 ⁻⁷	Mercer (1983)
H-6	150-156	3.5 x 10 ⁻⁵	Beauheim (1989b)
H-7	72-86	>1.1 x 10 ⁻³	Mercer (1983)
H-8b	179-187	8.8 x 10 ⁻⁶	Beauheim (1987c)
H-9	197-206	1.2 x 10 ⁻⁴	Beauheim (1989b)
H-10b	415-424	7.5 x 10 ⁻⁸	Mercer (1983)
H-11	223-230	2.9 x 10 ⁻⁵	Saulnier (1987)
H-12	251-259	1.9 x 10 ⁻⁷	Beauheim (1987c)
H-14	166-174	3.2 x 10 ⁻⁷	Beauheim (1987c)
H-15	262-269	1.4 x 10 ⁻⁷	Beauheim (1987c)
H-16	214-221	8.6 x 10 ⁻⁷	Beauheim (1987c)
H-17	215-223	2.4 x 10 ⁻⁷	Beauheim (1987c)
H-18	210-217	2.2 x 10 ⁻⁶	Beauheim (1987c)
P-14	175-181	1.5 x 10 ⁻⁴	Mercer (1983)
P-15	126-133	9.8 x 10 ⁻⁸	Beauheim (1987c)
P-17	170-178	1.1 x 10 ⁻⁶	Beauheim (1987c)
P-18	277-286	<4.3 x 10 ⁻⁹	Beauheim (1987c)
USGS-1	158-167	5.1 x 10 ⁻⁴	Cooper and Glanzman (1971)
WIPP-12	247-255	1.1 x 10 ⁻⁷	Beauheim (1987c)
WIPP-13	214-221	7.4 x 10 ⁻⁵	Beauheim (1987b)
WIPP-18	240-246	3.2 x 10 ⁻⁷	Beauheim (1987c)
WIPP-19	230-237	6.5 x 10 ⁻⁷	Beauheim (1987c)
WIPP-21	222-230	2.7 x 10 ⁻⁷	Beauheim (1987c)
WIPP-22	226-233	4.0 x 10 ⁻⁷	Beauheim (1987c)
WIPP-25	136-144	2.9 x 10 ⁻⁴	Mercer (1983)
WIPP-26	57-64	1.3 x 10 ⁻³	Mercer (1983)
WIPP-27	89-97	7.0 x 10 ⁻⁴	Mercer (1983)
WIPP-28	128-136	1.9 x 10 ⁻⁵	Mercer (1983)
WIPP-29	4-13	1.1 x 10 ⁻³	Mercer (1983)
WIPP-30	192-199	1.9 x 10 ⁻⁷	Beauheim (1987c)

the Culebra's hydraulic behavior during pumping or slug tests is that of a single-porosity medium. Where transmissivities are between 10^{-6} and at least 10^{-4} m²/s, open fractures are observed in core, and the hydraulic behavior of the Culebra Dolomite during pumping tests is that of a double-porosity medium.

Double-porosity media have two porosity sets that differ in permeability and storage volume. Typically, one porosity set is a fracture network, with higher permeability and lower storage, and the other is the primary porosity of the rock matrix, with lower permeability and higher storage. Where the transmissivity of the Culebra Dolomite is greater than 10^{-4} m²/s, Culebra core is heavily fractured, to the point of brecciation. Double-porosity hydraulic behavior is less apparent in these highly transmissive areas, perhaps because matrix-block size decreases as fracture frequency increases, decreasing the time lag observed between the hydraulic response of the fractures and that of the matrix.

In most wells completed in the Culebra Dolomite, water levels have been measured regularly since the wells were constructed. Because about 60 wells are currently or were once completed in the Culebra, abundant water-level data are available. Culebra water levels at and around the WIPP site have been affected, however, by continuous drainage into one or more WIPP shafts since the construction of the Exploratory Shaft (now the Construction and Salt-Handling Shaft) in late 1981, as well as by numerous pumping tests and water-quality sampling exercises conducted since 1980. Thus, defining the potentiometric surface of the Culebra Dolomite undisturbed by WIPP activities is difficult. LaVenue et al. (1988) thoroughly reviewed Culebra water-level data, fluid-density data, and WIPP-related hydraulic stresses and estimated the undisturbed freshwater-heads at 31 wells. These estimates (Table 3-8) are contoured in Figure 3-5. The freshwater-head contours indicate a southwesterly flow direction down Nash Draw, a southerly flow direction across the WIPP site, and an area of low gradients with apparently westerly flow south of the site. Davies (1989) reported that flow directions in this southern area of low hydraulic gradients are difficult to define reliably, because variations in fluid density within this part of the Culebra Dolomite may be as important as pressure differences in determining flow directions.



TRI-6330-95-0

Figure 3-5. Estimated freshwater heads in the Culebra Dolomite Member (LaVenue et al., 1988).

Table 3-8. Hydraulic-Head Data for the Culebra Dolomite

Well	Ground-Surface Altitude (m)	Freshwater- Head Altitude (m) ^a	Depth to Middle of Culebra (m)	Fluid Specific Gravity ^a	Depth to Middle of Magenta (m)	Freshwater- Head Altitude at Midpoint of Magenta (m)
Cabin Baby-1	1014	911	157			
DOE-1	1056	915	254			
DOE-2	1042	935	255	1.041	217	934
H-1	1036	922	210	1.022	176	921
H-2b1	1030	924	193	1.009	161	923
H-3b1	1033	917	208	1.036	174	916
H-4b	1016	913	155	1.016	118	913
H-5b	1068	934	277	1.102	243	930
H-6b	1020	932	188	1.039	153	931
H-7b	964	913	79			
H-8b	1047	912	183	1.000	145	912
H-9b	1038	907	202	1.001	164	907
H-10b	1124	921	419	1.047	386	919
H-11b2	1040	913	226			
H-12	1044	914	255			
H-14	1020	915	170	1.008	133	915
H-15	1061	918	266			
H-16	1039	916 ^b	217	1.04 ^c	184	915 ^b
H-17	1031	913	219			
P-14	1024	927	178			
P-15	1009	916	129			
P-17	1017	913	174			
USGS-1	1044	909	162			
WIPP-12	1058	932	251			
WIPP-13	1038	934	217			
WIPP-18	1053	930	243			
WIPP-25	979	931	140	1.008	96	931
WIPP-26	961	918	60			
WIPP-27	968	938	93	1.092	56	934
WIPP-28	1020	938	132	1.032	91	937
WIPP-29	907	905	8			
WIPP-30	1045	935	196	1.020	160	934

a. Data from LaVenue et al. (1988) except as noted

b. Lowered by drainage into WIPP shafts; converted from pressure data (Stensrud et al., 1988a)

c. Average of values from WIPP-19 and H-2a (Randall et al., 1988)

3.3.1.3 Tamarisk Claystone. The Tamarisk Member of the Rustler Fm. is composed of two anhydrite and gypsum units with a silty-claystone interbed in the lower half of the member (Figure 3-1). The anhydrite/gypsum units act as confining beds, and the claystone is the least productive of the Rustler water-producing units. Halite is found in association with the claystone interbed along the central and southern portions of the eastern boundary of the WIPP site and farther east (Figure 3-2 or 3-4). Near the WIPP, the Tamarisk Member ranges in thickness from 24 m (79 ft) (at H-2 and H-10) to 55 m (180 ft) (at P-18). The Tamarisk Member is entirely absent at WIPP-29 (Mercer, 1983).

Less is known about the hydraulic properties of the Tamarisk Member than about those of the other Rustler members. Hydraulic tests of the Tamarisk claystone have been attempted at only four locations: H-3b3 (1984 unpublished field notes), DOE-2 (Beauheim, 1986), H-14 (Beauheim, 1987c), and H-16 (Beauheim, 1987c). Testing at all four locations failed, because the transmissivities were apparently too low to measure over a period of several days. Based on the interpretation of similar tests performed successfully on the unnamed lower member at H-16, Beauheim (1987c) concluded that the transmissivity of the Tamarisk claystone is likely 10^{-11} m²/s or less. The transmissivity of the Tamarisk Member might be greater west of the WIPP site in Nash Draw, where dissolution of the upper Salado and Rustler Fms. has occurred, but no direct measurements have been made there.

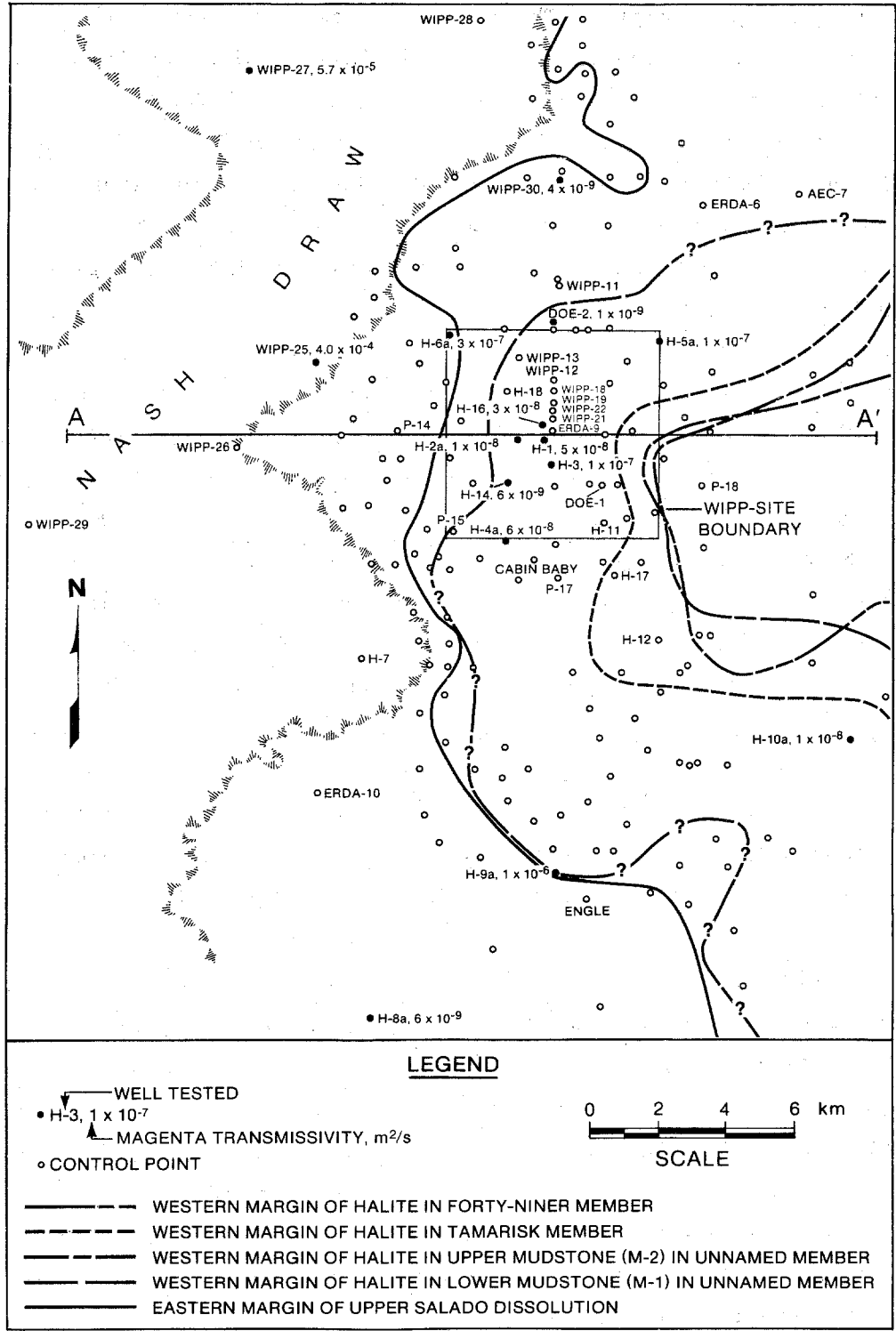
The undisturbed hydraulic head within the Tamarisk claystone has never been measured. The same low transmissivity that prevented successful hydraulic testing of the Tamarisk at H-3b3, DOE-2, H-14, and H-16 also prevented measurements of hydraulic heads at those locations. Fluid pressures have been measured within the Tamarisk interval of H-16 since August 1987 (Stensrud et al., 1988a, 1988b), but no pressure stabilization was achieved before the pressure began responding to the construction of the nearby Air-Intake Shaft. Tamarisk fluid pressures might be expected to be intermediate between those of the overlying Magenta and underlying Culebra Dolomites, but this supposition is unconfirmed.

3.3.1.4 Magenta Dolomite. The Magenta Dolomite Member of the Rustler Fm. is a gypsiferous and arenaceous dolomite ranging in thickness from 5 m (16 ft) (at WIPP-27) to 9 m (30 ft) (at H-9) in the vicinity of the WIPP. The Magenta Dolomite is absent at WIPP-29 and is unsaturated at H-7a and WIPP-26 (Mercer, 1983). Mercer (1983) also reported that the Magenta was unsaturated at WIPP-28, based on the apparent lack of a response to a bailing test. Subsequent water-level monitoring (Richey, 1987b) has indicated that the Magenta Dolomite is saturated at WIPP-28.

Hydraulic tests have been performed on the Magenta Dolomite at 16 locations (Mercer, 1983; Beauheim, 1986, 1987c). Most of the transmissivity values obtained from these tests (Figure 3-6, Table 3-9) are $\leq 10^{-7}$ m²/s. Relatively high values of transmissivity, 3×10^{-7} and 1×10^{-6} m²/s, are found at H-6a and H-9a, respectively. No halite is present in the Rustler Fm. at either of these locations, and the transmissivity of the Culebra Dolomite is also high at both. The two highest values of Magenta transmissivity, 4×10^{-4} and 6×10^{-5} m²/s, are found in Nash Draw at WIPP-25 and WIPP-27, respectively, where dissolution of the upper Salado Fm. has caused collapse and fracturing of the overlying Rustler Fm. Dissolution of the upper Salado Fm. has apparently not affected the Magenta at all locations where it has occurred, however, because the transmissivity of the Magenta Dolomite is very low at H-8 and could not be measured at WIPP-28 (Figure 3-6).

Between 1979 and 1981, stabilized water levels were measured in 13 wells completed in the Magenta Dolomite (Richey, 1987b). Figure 3-7 shows the altitudes of these stabilized water levels, along with estimated freshwater-head altitudes calculated using specific-gravity (or fluid-density) data (Mercer et al., 1981; Dennehy and Mercer, 1982; Mercer, 1983; Lambert and Robinson, 1984; Richey, 1986, 1987a). The contours of the freshwater-heads indicate a southwesterly flow direction within the Magenta Dolomite in the northern portion of Nash Draw and a generally westward flow direction toward Nash Draw over the rest of the region.

Figure 3-7 also shows freshwater heads estimated from pressure measurements at DOE-2, H-14, and H-16. The pressure measurements at DOE-2 and H-14 were reported by Beauheim (1986, 1987c) to represent upper bounds on the



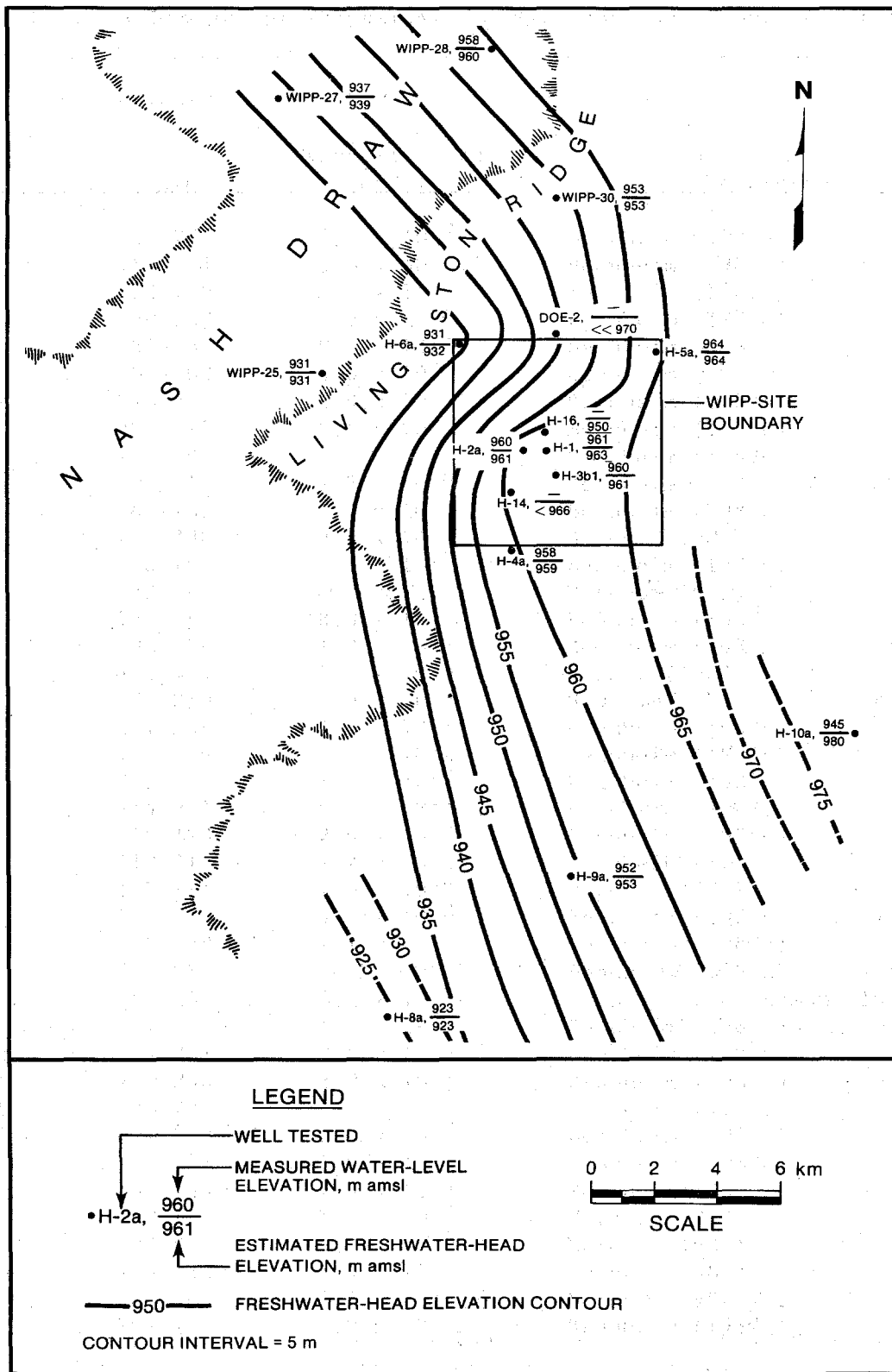
TRI-6330-96-0

Figure 3-6. Distribution of Rustler halite and Magenta transmissivity around the WIPP site (Holt et al., 1989).

Table 3-9. Summary of Transmissivity Data for the Magenta Dolomite

<u>Well</u>	<u>Magenta Depth Interval (m)</u>	<u>Transmissivity (m²/s)</u>	<u>Comments</u>
DOE-2	213-220	1 x 10 ⁻⁹	
H-1	172-180	5 x 10 ⁻⁸	
H-2a	157-166	1 x 10 ⁻⁸	
H-3b1	170-178	1 x 10 ⁻⁷	
H-4a	114-122	6 x 10 ⁻⁸	
H-5a	239-247	1 x 10 ⁻⁷	
H-6a	150-156	3 x 10 ⁻⁷	
H-8a	142-149	6 x 10 ⁻⁹	
H-9a	159-169	1 x 10 ⁻⁶	
H-10a	383-390	1 x 10 ⁻⁸	
H-14	129-137	6 x 10 ⁻⁹	
H-16	180-188	3 x 10 ⁻⁸	
WIPP-25	92-100	4.0 x 10 ⁻⁴	
WIPP-27	54-59	5.7 x 10 ⁻⁵	
WIPP-28	87-94	low	testing unsuccessful
WIPP-30	156-164	4 x 10 ⁻⁹	

stabilized formation pressures, while the pressure measurement at H-16 reflects drainage from the Magenta Dolomite into the nearby WIPP shafts since 1981 (Beauheim, 1987c). The estimated freshwater heads at DOE-2, H-14, and H-16 are in qualitative agreement, however, with the pattern of freshwater



TRI-6330-97-0

Figure 3-7. Water levels and estimated freshwater heads in the Magenta Dolomite Member (Holt et al., 1989).

heads derived from the water-level data. Table 3-10 summarizes the hydraulic-head data available for the Magenta Dolomite.

3.3.1.5 Forty-Niner Claystone. The Forty-niner Member of the Rustler Fm. is composed of two anhydrite and gypsum units separated by a silty claystone interbed. The anhydrite/gypsum units act as confining beds, while the claystone is a water-producing unit. Halite is found in association with this interbed east of the WIPP site (Figure 3-1). Near the WIPP, the thickness of the Forty-niner Member ranges from 7 m (23 ft) (at WIPP-27) to 23 m (76 ft) (at P-18). The Forty-niner Member is entirely absent at WIPP-29 (Mercer, 1983).

The claystone water-producing unit of the Forty-niner Member has been hydraulically tested at only three locations: DOE-2, H-14, and H-16 (Beauheim, 1986, 1987c). At these locations, the interbed thickness ranges from 3 to 5 m (10 to 16 ft). Transmissivities reported for the claystone interbed are 3×10^{-9} to 1×10^{-8} m²/s at DOE-2, 3×10^{-8} to 8×10^{-8} m²/s at H-14, and 5×10^{-9} to 6×10^{-9} m²/s at H-16. As for the other Rustler members, the transmissivity of the Forty-niner claystone might be higher west of the WIPP site in Nash Draw, but no direct measurements have been made there. Where the halite unit is found with the claystone east of the WIPP site, the transmissivity of the claystone may be less than where the halite is absent.

Testing of the Forty-niner anhydrites and gypsums alone has been attempted only in H-14 (Beauheim, 1987c). At H-14, a drillstem test was performed in the upper 8 m (26 ft) of the upper Forty-niner anhydrite. This test was qualitative and showed only that the transmissivity of the anhydrite must be several orders of magnitude lower than that of the Forty-niner claystone.

The hydraulic head of the Forty-niner claystone has been measured at wells H-3d, H-14, H-16, and DOE-2 (Table 3-11). Beauheim (1987c) summarized these observations and estimated static fluid pressures at the midpoint of the claystone. The greatest uncertainty in these estimates was attached to the measurement from DOE-2. Re-examination of the original data from DOE-2 (Beauheim, 1986) indicates that a "static" pressure 12 psi lower than that

Table 3-10. Hydraulic-Head Data for the Magenta Dolomite

Well	Ground-Surface Altitude (m)	Stabilized Depth to Water (m)	Depth to Middle of Magenta (m)	Borehole- Fluid Specific Gravity	Freshwater- Head Altitude (m)	Depth to Middle of Forty-Niner Claystone (m)	Freshwater- Head Altitude at Midpoint of Claystone (m)
DOE-2	1042	>>94 ^a	217	1.18	<<970	206	<<969 ^b
H-1	1036	75	176	1.021	963		
H-2a	1030	70	161	1.012	961		
H-3 ^{b1}	1033	73	174	1.010	961	164	961
H-4a	1016	58	118	1.017	959		
H-5a	1069	105	243	1.008	964		
H-6a	1020	89	153	1.007	932		
H-8a	1046	123	145	1.008	923		
H-9a	1038	86	164	1.006	953		
H-10a	1124	179	386	1.171	980		
H-14	1020	>67 ^c	133	1.2	<966	121	<965 ^b
H-16	1039	105 ^{d, e}	184	1.2	950 ^c	173	949 ^{b, d}
WIPP-25	979	48	96	1.010	931		
WIPP-27	968	31	56	1.078	939		
WIPP-28	1020	62	91	1.048	960		
WIPP-30	1045	92	160	1.01	953		

a. Converted from pressure data (Beauheim, 1986)

b. Assuming actual Magenta water specific gravity = 1.02

c. Converted from pressure data (Beauheim, 1987c)

d. Lowered by drainage into WIPP shafts

e. Converted from pressure data (Stensrud et al., 1988a)

Table 3-11. Hydraulic-Head Data for the Forty-Niner Claystone

<u>Well</u>	<u>Ground-Surface Altitude (m)</u>	<u>Depth to Middle of Forty-Niner Claystone (m)</u>	<u>Fluid Pressure at Middle of Claystone (kPa)</u>	<u>Freshwater- Head Altitude (m)</u>
DOE-2	1042	206	<1255 ^a	<964
H-3d	1033	164	821 ^b	953
H-14	1020	121	490 ^b	948
H-16	1039	173	793 ^b	947

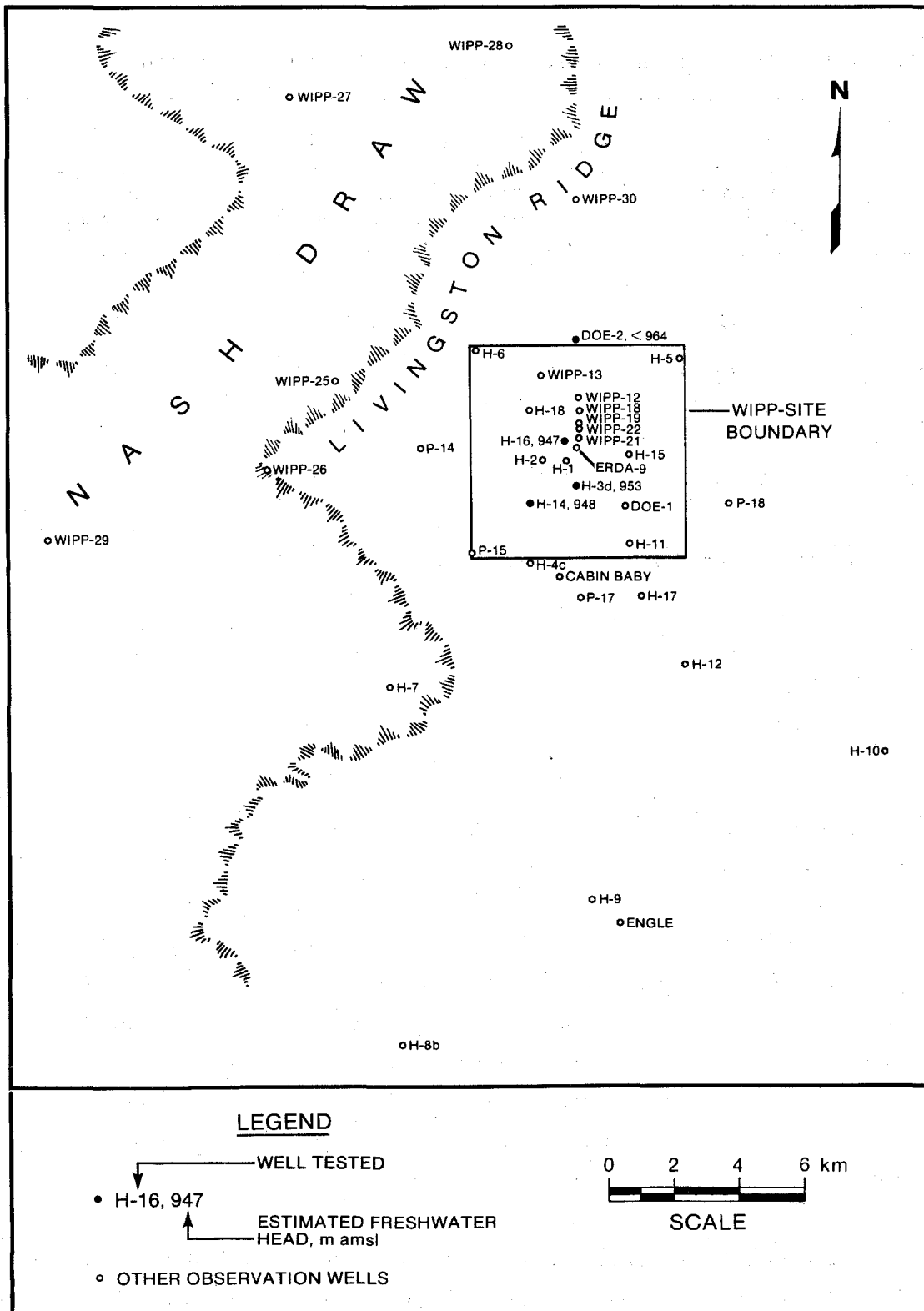
a. Data recalculated from Beauheim (1986)

b. Data from Beauheim (1987c)

reported by Beauheim (1987c) probably provides a more accurate upper bound on the Forty-niner head at that location.

Figure 3-8 shows the static fluid-pressure estimates at H-3d, H-14, H-16, and DOE-2 converted to freshwater heads. Firm conclusions cannot be drawn from so few data, but the data are not inconsistent with an assumption of southwesterly to westerly flow toward Nash Draw. The relatively low head at H-16 may, as suggested by Beauheim (1987c), be related more to localized drainage into the WIPP shafts than to the undisturbed regional head distribution.

3.3.1.6 Hydraulic-Head Relations. The hydraulic-head distributions of the unnamed lower member/upper Salado, Magenta Dolomite, and Forty-niner claystone (Figures 3-3, 3-7, and 3-8) all indicate westerly to southwesterly components to the ground-water flow in those units. Flow within the more transmissive Culebra Dolomite appears to be largely southerly (Figure 3-5). If these flow systems were at steady state, the observed hydraulic heads would



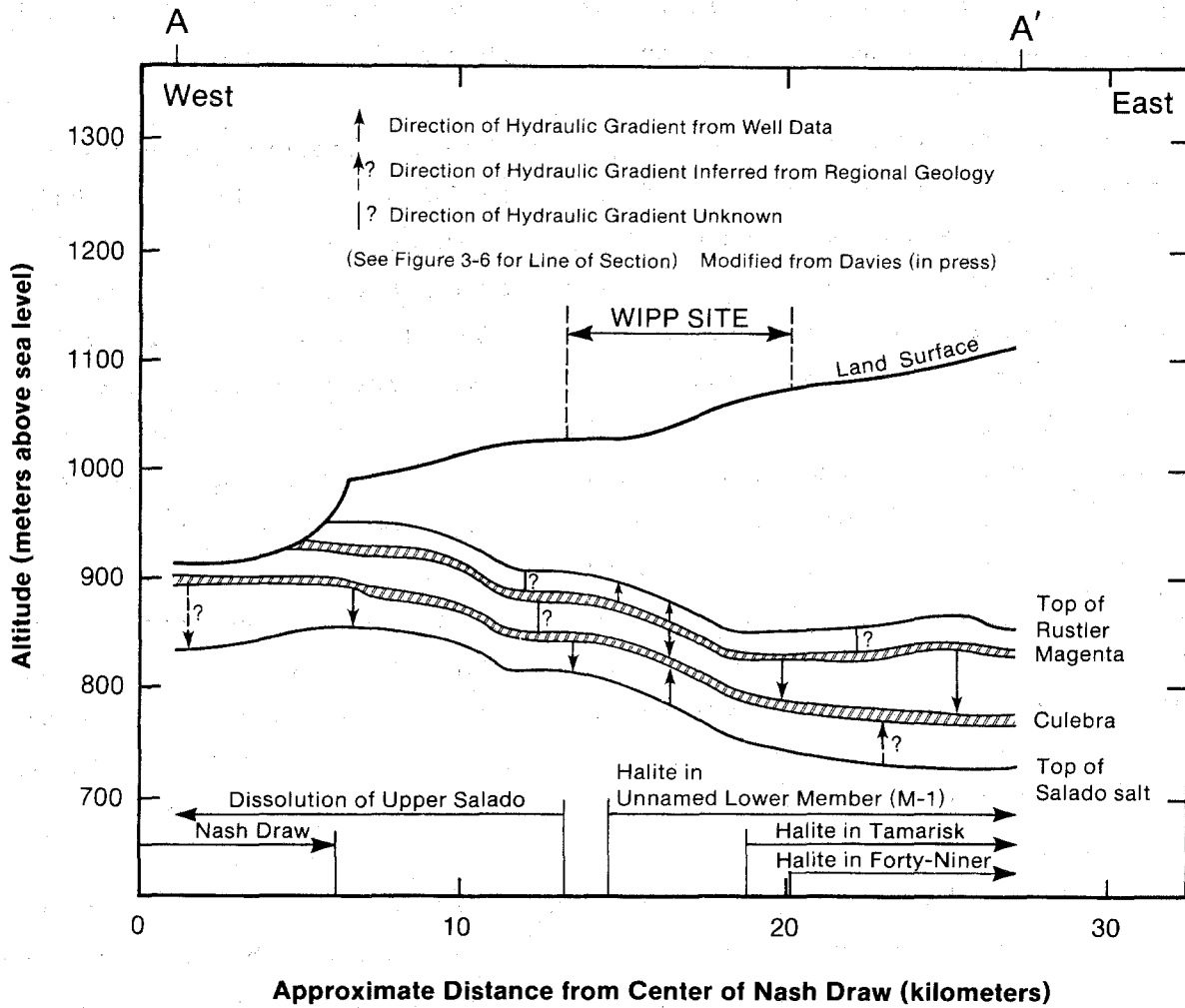
TRI-6330-98-0

Figure 3-8. Estimated freshwater heads in the Forty-niner claystone (Holt et al., 1989).

indicate that the systems' recharge areas must lie to the east or northeast. Because the Rustler dips to the east, however, its depth of burial increases, transmissivities of the water-producing units generally decrease, and the thickness and effectiveness of confining beds increase in that direction. All these factors argue against the existence of recharge areas to the east.

An alternative explanation for the present-day distribution of hydraulic heads within the Rustler Fm. was advanced by Lambert and Harvey (1987) (Section 3.3.3). Based on isotopic data from Rustler ground waters, they argued that the flow systems are not at steady state, but are instead draining following a late-Pleistocene recharge event. They thought that all Rustler members were recharged, perhaps from the present vicinity of Nash Draw, during a wetter pluvial period ~10,000 to 20,000 years ago. When the climate changed to its current semi-arid condition, the Rustler Fm. began draining to the west or southwest. The Culebra Dolomite, being the most transmissive of the Rustler water-producing units, has drained more quickly than the other units, and its present-day flow direction may reflect factors in addition to continued drainage. Davies (1989) used a numerical ground-water-flow model to simulate the recharge-and-discharge scenario proposed by Lambert and Harvey and found that the current distribution of heads is a plausible result of >10,000 years of drainage from the Rustler Fm.

If Lambert and Harvey's (1987) hypothesis of late-Pleistocene recharge and current discharge is correct, vertical hydraulic gradients within the Rustler Fm. should also reflect a recharge-and-discharge cycle. Figure 3-9 is a vertical east-west cross section through the center of the WIPP site showing the directions of the vertical hydraulic gradients between members of the Rustler Fm. Where no dissolution of either upper Salado or Rustler halite has occurred, from about the middle of the WIPP site to the east, hydraulic gradients from the unnamed member and Magenta Dolomite converge on the Culebra Dolomite. The Culebra Dolomite, being the most transmissive part of the Rustler Fm. in this vicinity, drains faster internally than the other water-producing units and probably also acts as a drain on the overall system. The gradients toward the Culebra Dolomite do not imply, however, that significant vertical leakage between units is occurring. Rather, the preservation of high hydraulic heads in the low-permeability Magenta and unnamed members



TRI-6330-88-0

Figure 3-9. Cross section through the WIPP site showing hydraulic gradients between Rustler members (Holt et al., 1989).

demonstrate the effectiveness of the confining beds separating them from the Culebra Dolomite. Davies (1989) reached similar conclusions based on numerical simulations of hypothetical drainage of high heads in the Rustler Fm.

The western portion of the WIPP site appears to be a transition region in which vertical hydraulic gradients change. In the region west of the site, where dissolution of the upper Salado Fm. has occurred, the Magenta head decreases to the point of unsaturation, and gradients are downward from the Culebra Dolomite to the unnamed member and upper Salado Fm. The increases in the transmissivities of the unnamed member and upper Salado Fm., Culebra Dolomite, and Magenta Dolomite, caused by dissolution west of the site, allow increased internal drainage from each of the members to the west and southwest. Dissolution of the upper Salado and subsidence of the Rustler Fm. may also have fractured the Rustler confining beds, allowing drainage between Rustler members.

Vertical hydraulic gradients between the Magenta Dolomite and Forty-niner claystone are upward in the central portion of the WIPP site. The two water-producing units are separated by an effective confining bed in this region, which likely prevents significant leakage. The origin of the head difference between the Magenta Dolomite and Forty-niner claystone is unclear, but the relative heads prevent overlying units from recharging the Magenta at the present time. No data are available to evaluate hydraulic gradients between the Magenta Dolomite and Forty-niner claystone east or west of the site.

The hydraulic-head data from the Magenta Dolomite and Forty-niner claystone near the site, indicating both the potential for upward flow from the Magenta Dolomite and the improbability of surficial recharge to Rustler carbonates near the site are consistent with interpretations summarized in Section 3.3.3. These interpretations indicate that, while the flow directions within the Rustler Fm. are transient on a time scale of ~10,000 years, vertical fluid flow within the Rustler Fm. near the site is and has been limited, and confined Rustler ground waters near the site have been isolated from the atmosphere for at least 12,000 to 16,000 years. Evaporite karst is not present at the WIPP site, contrary to some interpretations (e.g., Barrows,

1982). The presence of karst at the WIPP site would require that there be at least periodic recharge from the surface to the Rustler Fm. and that the Rustler units affected be hydraulically unconfined, at least near the recharge locations. One implicit implication of evaporite karst is that Rustler ground waters at the WIPP site would be modern.

Evaporite karst is present in southeastern New Mexico and accounts for the formation of Nash Draw, west of the WIPP site. In general, halites, anhydrites, and gypsums are removed in evaporite karst before limestones or dolomites are affected. As a result, because of the mechanical weakness of gypsum, evaporite karst structures are limited in area and depth and are distinct from the large, deep caverns that develop elsewhere in areas of limestone karst (Bachman, 1987). Shallow gypsum caves are present within Forty-niner anhydrites (converted to gypsum) within Nash Draw. In addition, the Magenta Dolomite appears to be unconfined or drained within Nash Draw (cf. Section 3.3.1).

The hydraulic-head data discussed in this section indicate, in contrast, that modern vertical recharge from the surface to any Rustler member below the Forty-niner claystone is not physically feasible in the immediate area of the WIPP site. In addition, the transmissivity of Rustler anhydrites near the site itself is too small for successful field measurement. The present data base of relative Magenta and Forty-niner heads is limited, however, and does not preclude the possibility of vertical drainage in areas where the Dewey Lake Red Beds are saturated south of the WIPP site.

Hole WIPP-33 (Figure 1-4) west of the WIPP site was drilled by the WIPP Project specifically to investigate the possibility of evaporite karst. The hole was drilled near the center of a surficial depression breaching the Mescalero Caliche. As summarized by Bachman (1985), the WIPP-33 structure apparently results from vertical fluid movement from the surface to the Forty-niner anhydrites at some time, i.e., it is the result of evaporite karst. Bachman also noted that the WIPP-33 structure is unique in the WIPP site area. As noted in Section 3.3.3, the deuterium content of gypsums from the Forty-niner Member at WIPP-33 is inconsistent with crystallization in the presence of modern meteoric water.

In summary, both the horizontal and vertical distributions of hydraulic heads within the Rustler Fm. are consistent with the hypothesis of Lambert and Harvey (1987) that the Rustler flow systems are not at steady state, but are instead in a transient discharge phase following a late-Pleistocene recharge event. Current flow directions are not representative of systems flowing from recharge to discharge areas.

3.3.2 Geochemical Variability of Rustler Fluids

The major conclusions of this section and Section 3.3.3 are listed here.

- The estimated variability of total dissolved solids (TDS) contents of Rustler ground waters in the WIPP region ranges from <3,000 to >300,000 mg/L. In many cases, even the best efforts at careful sampling and laboratory analysis leave the compositions uncertain. The uncertainty is in many cases but not always greater for holes in which transmissivity is limited.
- Near the site, TDS concentrations in Culebra waters range from ~10,000 mg/L to >200,000 mg/L. No Culebra ground waters at the site itself are suitable for stock consumption, let alone human consumption. In spite of several sampling attempts, the solute concentration of Culebra water at H-2, which may be near 10,000 mg/L, is not well known. However, H-2 is not on the flowpath considered in the human-intrusion case (Chapter 7.0).
- In general, Magenta waters are less saline than those in the underlying Culebra Dolomite, with TDS concentrations ranging from ~4,000 to 25,000 mg/L within the site boundary. Waters from the Rustler/Salado contact zone are quite saline; TDS concentrations are ~300,000 to 400,000 mg/L within the site boundary.
- Based on the variability of ground-water compositions, four hydrochemical facies are defined within the Culebra Dolomite. Dilute CaSO_4 waters south of the site (Facies B) lie directly downstream along the modern flow directions in the Culebra Dolomite from more saline and variable brines (Facies C). This is inconsistent with steady-state confined flow. The boundary

between Facies B and C is not precisely known, but it must lie south of a line joining P-17, H-12, and H-10.

- Hydraulic testing (Section 3.3.1) indicates that there is no effective vertical connection between the Culebra and Magenta Dolomites near the site on the time scale of hydraulic testing (a few months). Available isotopic results indicate that any vertical fluid flow on much longer time scales must be limited.
- Confined Rustler and Capitan ground waters have a stable-isotope character distinct from that of unconfined Capitan waters in Carlsbad Caverns and from other waters from alluvium and the Ogallala Fm. that are interpreted to represent modern precipitation in the northern Delaware Basin. These results indicate that the Rustler ground waters were recharged in a different climatic setting than that of the present time, but do not indicate either the time of this recharge or direction of ground-water flow at that time.
- Four radiocarbon ages calculated on samples from the WIPP area indicate that these waters (three from the Culebra Dolomite and one from the Dewey Lake Red Beds) were isolated from the atmosphere at least 12,000 to 16,000 years ago. Other analyzed waters reflect complex contamination from drilling fluids, lost-circulation materials, and the metabolic products of their degradation. The calculated radiocarbon ages represent minimal values, because some undetected contamination may still be present in all samples.
- The locations of the successful radiocarbon measurements effectively bracket the WIPP site, but do not imply any single flow direction, i.e., calculated ages do not increase in any one direction. All ground waters for which the radiocarbon measurements are interpretable have stable-isotopic character consistent with those of other confined Rustler waters.
- The radiocarbon measurements are all consistent with lack of significant vertical influx to the Culebra Dolomite near the WIPP site for $\geq 10,000$ years and isolation of confined Rustler waters from the atmosphere (and

vertical recharge) for $\geq 10,000$ years. Both stable-isotope variations and radiocarbon results are consistent with the presence of both "modern" waters and older waters within the Dewey Lake Red Beds.

- $^{87}\text{Sr}/^{86}\text{Sr}$ ratios of host rocks and veins within the Rustler Fm. are indistinguishable, implying an internal source for the solutes rather than extensive flow from external sources. Ratios within the Culebra and Magenta Dolomites are distinct from those of the surrounding parts of the Rustler Fm. and from ratios characteristic of surficial input. Ratios within the Dewey Lake Red Beds, in contrast, imply mixing of Rustler-type waters and surface waters, as reflected in the strontium isotopes of caliche and gypsite spring deposits.
- Flow from the surface to layers beneath the Dewey Lake is minimal, implying that the isotopic distinction of the Culebra and Magenta Dolomites is the result of lateral flow.
- The isotopic character of waters of hydration from essentially all vein gypsums analyzed from the Rustler Fm. and Dewey Lake Red Beds is consistent with crystallization in the presence of varying amounts of Rustler-type ground water, as distinct from the interpreted isotopic character of modern precipitation. Several of the analyzed gypsums could not have precipitated in equilibrium with any amount of modern water. Compositional relationships among gypsums analyzed from borehole WIPP-34 indicate vertical fluid flow in both directions from the Magenta Dolomite.
- Uranium-disequilibrium studies, specifically an eastward increase in $^{234}\text{U}/^{238}\text{U}$ activity ratios, imply that ground-water flow at the time of Rustler recharge ($\geq 12,000$ to $16,000$ years ago on the basis of radiocarbon studies) had an easterly component, in contrast to the modern southerly flow within the Culebra Dolomite (Section 3.3.1).
- Stable-isotope, radiocarbon, and uranium-disequilibrium data are consistent with four interpretations: (1) confined Rustler waters at and near the WIPP site were isolated both from the atmosphere and from any significant vertical recharge $\geq 12,000$ to $16,000$ years ago; (2) Rustler ground-water

flow at the time of recharge had an easterly component; (3) neither flow directions nor fluid compositions within the Culebra Dolomite are at steady-state; and (4) the time scale of change in flow directions is $\geq 10,000$ years.

3.3.2.1 Changes in Understanding Since the FEIS. When the FEIS (DOE, 1980a) was prepared, the only data on solutes in ground waters from the Rustler Fm. near the WIPP site (Lambert, 1978) were for seven Rustler samples (two Culebra, two Magenta, and three unspecified). Mercer and Orr's (1979) solute data for 15 Rustler samples (eight Culebra, three Magenta, and four Rustler/Salado) were not available in time to be included in the FEIS.

The FEIS stated that "total dissolved solids in well water sampled from the Rustler Fm. are at levels of 3000 to 60,000 ppm (Lambert, 1978)" (DOE, 1980a, Vol. 1, p. 7-89). In light of the data now available, this statement is misleading, if not incorrect, for two reasons. First, the total-dissolved-solids (TDS) concentrations in the Rustler Fm. (the three most-productive water-bearing zones) range from <3000 to $>300,000$ mg/L in the study area (Figure 3-10) and from ~ 4000 to $>300,000$ mg/L at the WIPP site. These ranges are much wider than the range given in the FEIS. Second, some of Lambert's (1978) Rustler samples were mislabeled, and some are now considered unreliable; that is, the TDS range in the FEIS is based on some incorrect data.

Variations in concentrations of dissolved solids in ground waters from the Rustler Fm. in the study area are discussed in more detail below. In brief, the data of Mercer and Orr (1979) showed a range of $\sim 4,000$ to $>300,000$ mg/L; additional data (Mercer, 1983) expanded the range slightly; and subsequent work has confirmed this wide range of ground-water compositions.

Because some of Lambert's (1978) Rustler data may be incorrect, those data do not support the range of TDS concentrations given in the FEIS. Specifically, data from five of Lambert's seven "Rustler" samples are questioned for three reasons. First, two stock wells--James Ranch (called Ranch Well in this report) and Fairview Well--were then thought to sample the Rustler Fm.; these wells are now known to sample the Dewey Lake Red Beds

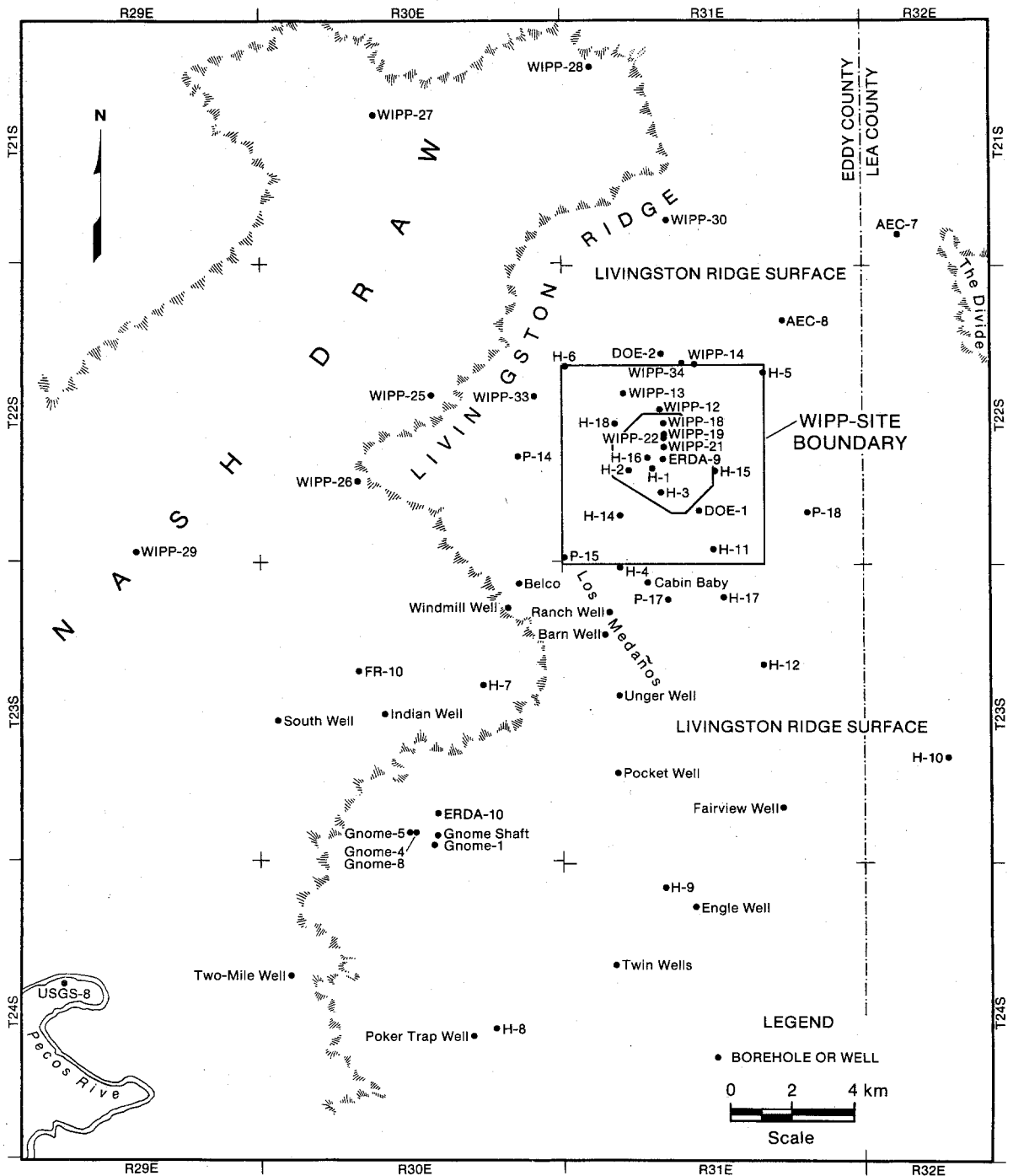


Figure 3-10. Hydrologic boreholes and wells at and near the WIPP site (Siegel, Lambert, and Robinson, 1989).

(Lambert and Harvey, 1987). Thus the lower end of the TDS concentration range in the FEIS (~3,000 mg/L) was based on Dewey Lake samples; fortuitously, the freshest samples from the Rustler Fm. have similar TDS concentrations. Second, samples from the Culebra and Magenta Dolomites at well H-3 were collected in August 1976 (USGS Multiple Station Listing). The data from these samples were rejected by Mercer and Orr (1979) and Mercer (1983) in favor of data from samples collected in 1977. Comparing the data from the August 1976 samples with data from more recent samples (discussed in more detail below) shows that the Magenta sample was probably contaminated, and the Culebra sample may have been slightly contaminated. Finally, the collector ring in the Duval mine shaft was located at the bottom of the Rustler Fm. Because the water may have come from any of the water-producing horizons in the shaft and may be a mix of waters from more than one horizon, the sample is of little geochemical significance.

Mercer (1983) published data from the U.S. Geological Survey (USGS) on samples collected from the Culebra and Magenta Dolomites and the Rustler/Salado contact zone between 1976 and 1980. He reported wide ranges of TDS concentrations in all three zones; his ranges are similar to those given below. Mercer observed that, in all three zones, TDS and the sum of the concentrations of potassium and magnesium correlate roughly with regions of restricted flow (low transmissivities) and the presence or absence of halite above or below the zone being considered.

Ramey (1985) also analyzed Mercer's (1983) data. He included a detailed study of the Culebra data, but added little to previous discussions of data from the Magenta Dolomite and the Rustler/Salado contact zone. More-recent interpretations of the Culebra data (including newer data) are discussed in Section 3.3.3.

Between 1976 and 1987, solutes were measured in ground-water samples from the Culebra and Magenta Dolomites and Rustler/Salado contact zone at more than 30 locations (hydropads or stock wells) at and near the WIPP site. An evaluation of the data for the major solutes (Na, K, Mg, Ca, Cl⁻, and SO₄²⁻) has shown that some of these samples were contaminated (or in some other way not representative of unperturbed ground water) and that some of the analytical

results were inaccurate (Robinson, 1988). At least some unreliable data can be recognized and excluded from further consideration.

The present understanding of the compositions of fluids from the Rustler Fm. thus comes from a much larger and more reliable data base than was available when the FEIS was prepared.

3.3.2.2 Data Reliability. Ground-water samples have been collected from the Culebra Dolomite at over 30 locations (hydropads or wells), from the Magenta Dolomite at 12 locations, and from the Rustler/Salado contact zone at 20 locations. Many locations have been sampled more than once, and in many instances, samples collected at the same time from a given site have been analyzed by more than one laboratory.

When more than one set of solute analyses for ground water from a stratigraphic zone at a location (hydropad or stock well) are available, there are often discrepancies between some or all of the sets of analyses. In some cases, samples collected at different times (ranging from a few weeks to several years apart) have significantly different compositions. In other cases, the results (for at least some, if not all, solutes) from different laboratories for samples collected at the same time differ significantly. Thus, in some cases, some analytical data are thought to be incorrect; in other cases, the analyses or the samples themselves may be the source of the discrepancies.

Faced with these varying data sets from some locations, the problem is to decide which data are the most reliable. At locations from which only one ground-water sample has been collected and analyzed, the problem is to determine whether that one data set is reliable.

Data may be incorrect for any or all of the following three reasons (Robinson, 1988), ignoring the possibility of typographical errors in source documents. First, a ground-water sample might not have been representative of unperturbed ground water, at least with respect to the parameters being measured. For example, the ground water around a borehole can be contaminated by drilling mud or brine or by additives used to control lost circulation

during drilling; such contamination can affect the concentrations of many major, minor, and trace solutes. Ground water can be contaminated by the well casing or the pump; for example, iron concentrations in many of these ground waters appear to be a function of the presence or absence of well casing and of the pumping rate used to collect the sample. Bringing ground water from aquifer depth and pressure to the ground surface at atmospheric pressure can cause some changes; for example, carbon dioxide may outgas, causing the pH of the solution to increase. Second, the concentration of some solutes in the ground-water sample might have changed between the time of collection and the time of analysis. For example, a sample could be stored for some time at too low a temperature; species that were at or close to saturation at aquifer temperature might precipitate (an irreversible process, on a laboratory time scale). Finally, the analysis of a parameter might be inaccurate. For example, an inappropriate analytical technique might have been used, or the analyst might have erred during the analysis or in calculating the results.

At many of the locations of interest, collecting a representative sample is difficult because of the uncertain histories and low productivities of the wells (cf. Section 3.3.1 for transmissivity data). When some of these wells were drilled, there were no plans to collect water samples from the Rustler aquifers. Thus, careful records were not always kept of the types or quantities of materials added to the borehole to aid in activities such as drilling, coring, controlling lost circulation, reconfiguring the well, and so forth. Even when contamination is known or suspected, the low productivities at many of the wells make it difficult or impossible to purge contaminants by pumping.

When representative samples are collected, the widely variable bulk compositions and concentrations of specific solutes of interest make the analysis of these solutes difficult. These are not drinking waters that can be reliably analyzed by EPA-approved methods. The appropriate method for a solute will depend on both the approximate concentration of that solute and on the bulk composition (the ionic strength and the concentrations of the other solutes) of the sample. Because budgetary constraints do not allow every analytical method to be validated for every WIPP sample, the data are often justified by indirect means (often by comparing with data from other

laboratories). Some data have been published before analytical difficulties could be identified and corrected.

3.3.2.3 Sources of Data. Mercer (1983) summarized the USGS analyses of samples collected by the USGS between 1976 and 1980.

Robinson (1988) included analyses by Sandia National Laboratories and its subcontractor, UNC Technical Services (formerly Bendix Field Engineering Corp., Grand Junction, CO; the designation UNC/Bendix will be used here), of samples collected by the USGS, Sandia, Hydro Geo Chem, and the WIPP Water Quality Sampling Program (WQSP) between 1979 and 1986. Robinson (1988) also included field data for samples collected by Sandia and Hydro Geo Chem between 1980 and 1984. UNC (1988) gave some more-recent, as-yet unpublished analyses of WQSP samples by UNC/Bendix.

Chapman (1988) included analyses by the New Mexico Bureau of Mines & Mineral Resources (NMBM&MR) of some samples collected by the WQSP for the New Mexico Environmental Evaluation Group (EEG).

A series of annual reports by WQSP personnel (Uhland and Randall, 1986; Uhland et al., 1987; Randall et al., 1988) includes field data for the WQSP samples and laboratory analyses of those samples by IT Analytical Services (ITAS). Data for WQSP samples collected in 1988 and 1989 have not yet been published and are not considered here.

3.3.2.4 Solute Data. Table 3-12 summarizes the data from the sources listed above; well locations are shown in Figure 3-10. Data were included in the table or rejected as described by Robinson (1988), whose approach includes evaluating both the representativeness of the samples with respect to the parameters of interest and the quality of the analyses.

The representativeness of the samples was evaluated in three ways. The method of collection was considered (bailing or swabbing versus pumping, pumping rate, volume of water pumped before sampling, etc.); field data were considered (when parameters were monitored periodically during a pumping test for purging of possible contaminants); and if possible, analyses of samples

collected during different hydrologic tests at the same hydropad and stratigraphic zone were compared (Robinson, 1988). The qualities of various sets of analytical data were evaluated by checking charge-balance errors, by considering any available supporting data from the laboratory (analysis of replicates, spiked samples, control samples, etc.), by comparing laboratory results for certain parameters with reliable field results for the same parameters, and by comparing results from different laboratories for samples collected at the same time from the same well and stratigraphic zone (Robinson, 1988).

Table 3-12 includes concentrations of the major solutes, TDS, and bicarbonate; field pH data; and density data. Concentrations of the major solutes (Na, K, Ca, Mg, Cl^- , and SO_4^{2-}) are presented as ranges that represent all data that are considered reliable. A single value, rather than a range, indicates that only one value is considered reliable. Concentrations were rounded to two significant figures; the lower number in a range was rounded down and the higher number was rounded up. Concentrations of TDS were calculated by summing the concentrations of the major solutes plus bicarbonate given in the table. Field values of HCO_3^- and pH are given, again as ranges when possible. Single values indicate either that only one value was considered reliable or that the same value was measured during each sampling episode. All HCO_3^- and pH data must be used with caution, however, because of the carbon-dioxide outgassing mentioned above (Siegel, Robinson, and Myers, 1989; Meijer et al.; 1987; Robinson, 1988). Densities or specific gravities are included for samples from most locations.

Table 3-12 considers samples from wells that were drilled specifically for the WIPP project. Data from the Culebra Dolomite at Engle Well are also included, but other data from stock wells are ignored for several reasons. Most of the stock wells lie south of the area of major interest for the WIPP; the reliability of many samples (collected before 1985) and analyses is difficult to evaluate; and few data are available for samples collected more recently. Bodine et al. (1989) and Randall et al. (1988) gave data from samples of Culebra ground water from Windmill Well, Indian Well, South Well, Mobley Ranch Well, the Gnome wells (also called USGS wells), Two-Mile Well, and Poker Trap Well.

Table 3-12. Major Solutes in Ground Waters From the Rustler Formation^[1]
 Part A: Samples from the Culebra Dolomite

Hydropad ^[2] (Wells)	Density ^[3] (g/cm ³)	TDS ^[4] (mg/L)	Na (mg/L)	K (mg/L)	Ca (mg/L)	Mg (mg/L)	Cl ⁻ (mg/L)	SO ₄ ²⁻ (mg/L)	HCO ₃ ⁻ ^[5] (mg/L)	pH ^[6]	Dates	Ref ^[7]
DOE-1	1.088	122000- 135000	41000- 46000	900- 1300	1400- 1800	1400- 1700	71000- 77000	6500- 7400	45- 46	7.1	4/85;7/86; 7/87	b,c,e, f,g
DOE-2 ^[8]	1.041	56000- 62000	17000- 19000	300- 420	1900- 2000	900- 1100	32000- 35000	3500- 4000	67 ^[8]	7.0 ^[8]	3/85;8/86	b,c,e, f
H-1 ^[9]	1.022	30000	9400	190	780	280	12000	7400	100	7.6	6/76	a
H-2 ^[10] (H-2A,B1,C)	1.009	see footnote										
H-3 (H-3B1,B2,B3)	1.036	50000- 58000	16000- 19000	360- 500	1200- 1600	670- 850	27000- 31000	4600- 5200	50- 52	7.3- 7.4	3/77;6/84; 2/85;12/85; 4/86;8/87	a,b,c, e,f,g
H-4 (H-4B,C)	1.016	19600- 22300	5800- 6300	180- 260	640- 700	400- 510	7400- 8200	5100- 6300	68- 75	7.6- 8.0	5/81;8/84; 7/85;11/86;9/87	b,c,e, f,g
H-5 (H-5B,C)	1.102	148000- 158000	52000- 55000	1100- 1400	1300- 1700	2100- 2300	84000- 90000	7000- 7900	50- 86	7.4- 7.9	6/81;10/81; 8/85;5/86	b,c,e, f
H-6 (H-6B,C)	1.039	52000- 61000	16000- 19000	340- 600	1700- 2200	900- 1200	30000- 34000	3300- 4000	90- 96	6.9- 7.2	5/81;9/85; 7/86;11/87	b,c,e, f,g
H-7 (H-7B1)	1.001	3000- 3400	160- 210	7.0- 7.7	540- 680	130- 140	300- 350	1700- 1900	120	7.0- 7.3	3/80;3/86; 2/87	a,c,d, e,g
H-8 (H-8B)	1.000	2500- 2900	51- 56	3.7- 4.6	520- 560	150- 170	30- 36	1700- 2000	93- 96	7.2- 7.3	1/86;2/87	b,c,e, g
H-9 (H-9B)	1.001	2800- 3200	140- 160	6.8- 7.6	560- 630	130- 150	170- 210	1700- 1900	110	7.3- 7.4	11/85;1/87	b,c,e, g
H-10 ^[9] (H-10B)	1.047	66000	21000	520	1600	1000	36000	5600	45	8.3	3/80	a
H-11 (H-11B3)	1.078	109000- 123000	37000- 44000	720- 990	1300- 1700	1300- 1600	63000- 67000	6100- 7200	54- 55	7.2- 7.3	6/85;6/86; 9/87	b,c,e, f,g

Table 3-12. Major Solutes in Ground Waters From the Rustler Formation^[1]
 Part A: Samples from the Culebra Dolomite (continued)

Hydropad ^[2] (Wells)	Density ^[3] (g/cm ³)	TDS ^[4] (mg/L)	Na (mg/L)	K (mg/L)	Ca (mg/L)	Mg (mg/L)	Cl ⁻ (mg/L)	SO ₄ ²⁻ (mg/L)	HCO ₃ ⁻ ^[5] (mg/L)	pH ^[6]	Dates	Ref ^[7]
H-12	1.093	139000- 146000	49000- 52000	1200- 1600	1600- 1800	1900- 2000	78000- 80000	7200- 8200	53- 62	7.2	8/85;1/87	c, e, g
H-14	1.008	15400- 16500	3300- 3400	190- 250	1700- 1800	480- 530	8200- 8600	1500- 1900	40	7.7	5/87	d, g
H-15	1.153	220000- 240000	82000- 84000	1400- 1800	1500- 2000	2300- 2700	130000- 140000	6300- 6600	41	~7	5/87	d, g
H-16	--	36000	12000	240	890	330	16000	6700	~70	--	8/87	d
H-17	1.103	154000- 155000	55000	1400	1500	1700	87000- 88000	7000	50	7.0	10/87	g
H-18	1.02 sg	24000	6800	240	980	510	12000	3700	53	7.6	11/87	g
P-14	1.017	22000- 26000	3700- 4400	38- 50	3500- 3900	740- 900	13000- 15000	1400- 1700	100- 110	6.8- 6.9	2/86;6/87	b, c, e, g
P-15 ^[9]	1.015	24000	6900	1700	770	63	11000	3200	~110	--	5/77	a
P-17	1.061	84000- 93000	28000- 30000	770- 1000	1500- 1700	1400- 1800	47000- 51000	5500- 7200	61- 64	7.5	3/86;12/86; 10/87	b, c, d, e, f, g
P-18 ^[11]	see footnote											
WIPP-13	1.043	62000- 69000	19000- 23000	340- 590	1400- 1800	1000- 1200	36000- 37000	4500- 5100	120	6.6	2/87	d, g
WIPP-19	1.07 sg	98000- 107000	30000- 34000	830- 850	1800- 1900	1900- 2400	58000- 62000	5000- 5400	84	7.0	7/87	d, g
WIPP-25 ^[12]	1.008	see footnote										
WIPP-26 ^[13]	1.012	see footnote										
WIPP-27	1.092	133000- 136000	39000- 40000	8100	3100- 3300	1900- 2000	77000- 79000	3800- 3900	120	6.4	8/80;9/80	a, c

Table 3-12. Major Solutes in Ground Waters From the Rustler Formation^[1]
 Part A: Samples from the Culebra Dolomite (continued)

Hydropad ^[2] (Wells)	Density ^[3] (g/cm ³)	TDS ^[4] (mg/L)	Na (mg/L)	K (mg/L)	Ca (mg/L)	Mg (mg/L)	Cl ⁻ (mg/L)	SO ₄ ²⁻ (mg/L)	HCO ₃ ⁻ ^[5] (mg/L)	pH ^[6]	Dates	Ref ^[7]
WIPP-28	1.032	46000- 47000	15000	480	1100- 1200	560	24000- 25000	4400	--	6.5	9/80	c
WIPP-29 ^[14]	1.213	see footnote										
WIPP-30	1.020	29000- 30000	8600	260	1100- 1200	460	14000- 15000	4100	~74	8.8	9/80	c
Engle Well	1.001	3000- 3300	180- 200	5- 10	570- 590	130- 160	220- 240	1800- 2000	70- 110	7.2- 7.4	3/85;12/87	b,c,e, g

Part B: Samples from the Rustler/Salado Contact Zone

Hydropad ^[2] (Wells)	Density ^[3] (g/cm ³)	TDS ^[4] (mg/L)	Na (mg/L)	K (mg/L)	Ca (mg/L)	Mg (mg/L)	Cl ⁻ (mg/L)	SO ₄ ²⁻ (mg/L)	HCO ₃ ⁻ ^[5] (mg/L)	pH ^[6]	Dates	Ref ^[7]
H-1 ^[9]	--	330000	56000	17000	13000	30000	210000	520	680	7.9	2/77	a
H-2 ^[9] (H-2C)	1.225	310000	66000	9100	9200	25000	200000	1300	200	5.9	2/77	a
H-3 ^[9] (H-3B1)	--	330000	59000	14000	18000	25000	210000	370	470	7.6	2/77	a
H-4 ^[9] (H-4C)	1.21	310000- 330000	64000- 66000	8000- 15000	8300- 8600	25000- 27000	200000- 210000	700- 1400	~1	--	3/79	a,c
H-5 ^[9] (H-5C)	1.26	370000- 410000	14000- 15000	16000- 21000	1700- 2100	76000- 82000	260000- 290000	1400- 2000	200	--	5/79	a,c
H-6 ^[9] (H-6C)	1.21	310000- 330000	79000- 80000	6600- 8000	4100- 4200	20000- 21000	200000- 210000	1400- 2000	~1	--	4/79	a,c
H-7 ^[9] (H-7C)	1.048	70000	22000	210	2600	910	41000	2900	43	6.8	3/80	a
H-8 ^[9] (H-8C)	1.129	124000	46000	660	1200	430	70000	5300	26	7.6	9/80	a

Table 3-12. Major Solutes in Ground Waters From the Rustler Formation^[1]
 Part B: Samples from the Rustler/Salado Contact Zone (continued)

<u>Hydropad^[2]</u> <u>(Wells)</u>	<u>Density^[3]</u> <u>(g/cm³)</u>	<u>TDS^[4]</u> <u>(mg/L)</u>	<u>Na</u> <u>(mg/L)</u>	<u>K</u> <u>(mg/L)</u>	<u>Ca</u> <u>(mg/L)</u>	<u>Mg</u> <u>(mg/L)</u>	<u>Cl⁻</u> <u>(mg/L)</u>	<u>SO₄²⁻</u> <u>(mg/L)</u>	<u>HCO₃⁻^[5]</u> <u>(mg/L)</u>	<u>pH^[6]</u>	<u>Dates</u>	<u>Ref^[7]</u>
H-9 ^[9] (H-9C)	1.20	330000	130000	1200	1300	870	190000	2600	29	7.0	5/80	a
H-10 ^[9] (H-10C)	1.20	310000	100000	4000	1500	11000	190000	3300	65	6.3	5/80	a
P-14 ^[9]	1.126	310000	120000	1300	570	1200	180000	10000	220	7.2	2/77	a
P-15 ^[15]	see footnote											
P-17 ^[9]	1.193	270000- 280000	23000	8800	15000	40000	180000- 190000	500- 1200	790	--	5/79	a,c
P-18 ^[16]	see footnote											
WIPP-25	--	330000	120000	3300	560	3300	190000	12000	130	7.4	7/80	c
WIPP-26	--	190000	69000	1200	1400	1700	110000	7500	270	7.7	7/80	c
WIPP-27 ^[17]	see footnote											
WIPP-28	1.18 sg	270000- 280000	97000	4300	600	3400	150000- 160000	17000	170	7.0	7/80	c
WIPP-29	--	110000- 111000	36000	1500	1100	2300	57000- 58000	12000	200	7.2	7/80	c
WIPP-30	--	310000- 320000	120000	2200	960	2800	180000- 190000	7400	620	7.5	7/80	c

Table 3-12. Major Solutes in Ground Waters From the Rustler Formation^[1]
 Part C: Samples from the Magenta Dolomite

Hydropad ^[2] (Wells)	Density ^[3] (g/cm ³)	TDS ^[4] (mg/L)	Na (mg/L)	K (mg/L)	Ca (mg/L)	Mg (mg/L)	Cl ⁻ (mg/L)	SO ₄ ²⁻ (mg/L)	HCO ₃ ⁻ ^[5] (mg/L)	pH ^[6]	Dates	Ref ^[7]
H-1 ^[9]	1.021	18900	5700	70	890	270	8000	3900	92	7.4	6/76	a
H-2 ^[9] (H-2A)	1.012	10300	2700	81	820	170	4100	2400	74	8.6	2/77	a
H-3 (H-3B1)	1.006 sg	7900- 9000	1500- 1700	34- 36	900- 1000	290- 330	3300- 3500	1800- 2400	45- 47	7.6- 8.0	7/85;9/86; 9/87	c, e, f, g
H-4 (H-4C)	1.02 sg	23400- 24200	7100- 7300	80- 100	610- 660	410- 500	8400- 8500	6700- 7100	70- 85	8.1- 8.4	11/86;10/87	c, f, g
H-5 (H-5C)	1.006 sg	6900- 7000	1500	34	550	170	1000- 1100	3600	56	8.0	10/86	c, f
H-6 (H-6C)	1.002- 1.003 sg	4200- 4600	640- 650	16- 18	500- 550	160- 170	420- 430	2400- 2700	51- 52	7.7- 7.8	10/86;11/87	c, f, g
H-8 ^[18] (H-8A)	1.008 --	9000 7200	2400 1800	84 59	870 560	17 10	3500 3000	2100 1700	~30 30	9.3 7.5	2/80 10/85	a e
H-9 ^[9] (H-9A)	1.004	5000	800	28	550	170	750	2700	~40	8.5	2/80	a
H-10 ^[9] (H-10A)	1.171	260000	93000	510	2500	2600	160000	2700	--	7.1	3/80	a
WIPP-25	1.004 sg	11700- 12100	2900	72	900- 920	260	4900- 5300	2500	180	6.9	9/80	c
WIPP-27	1.09 sg	144000- 149000	43000- 44000	8000- 10000	3600- 3700	2000- 2100	84000- 86000	2900- 3400	210- 220	6.4- 6.5	9/80(2x)	a, c
WIPP-30 ^[19]	see footnote											

Footnotes for Table 3-12.

1. Concentrations of major solutes are given as ranges that represent all the data -- from the sources listed in footnote 7 -- that are thought to be reliable. A single value, rather than a range, indicates that only one value is considered reliable. Data from these sources that are not considered reliable -- either because the sample is not considered representative of the unperturbed groundwater or because the analyses are thought to be in error -- have been excluded.
2. At multi-well hydropads, the sampled well(s) are shown in parentheses.
3. Values followed by the initials "sg" are specific gravities (unitless); all others are densities (g/cm^3). Data are from the following sources.
Culebra: Specific gravities are from Randall et al. (1988). Densities are those recommended by LaVenue et al. (1988, appendix F).
Magenta: Specific gravities are from Robinson (1988), Uhland and Randall (1986), Uhland et al. (1987), and Randall et al. (1988). Densities are from Mercer (1983, Table 10).
Rustler/Salado: Specific gravities are from Robinson (1988). Densities are from Mercer (1983, Tables 2 and 6) and Robinson (1988).
4. TDS = total-dissolved-solids concentrations; calculated by summing the concentrations of Na, K, Ca, Mg, Cl^- , SO_4^{2-} , and HCO_3^- given in this table.
5. Alkalinities measured in the field and expressed as mg/L HCO_3^- . A field value was not available from H-16 (Culebra); the value measured in the laboratory is given here. Reliable alkalinity data are not available for WIPP-28 (Culebra); the alkalinity continually decreased during a long-term pumping test (see Robinson, 1988, or Lambert and Robinson, 1984). Alkalinity was not determined in the H-10 (Magenta) sample.
6. pH values measured in the field.
7. References from which data (except some densities) were compiled:
 - a. Mercer, 1983
 - b. Chapman, 1988
 - c. Robinson, 1988
 - d. UNC, 1988
 - e. Uhland and Randall, 1986
 - f. Uhland et al., 1987
 - g. Randall et al., 1988
8. DOE-2 Culebra: the HCO_3^- and pH data are from the 3/85 sampling episode. The well was later acidized; in 8/86 the alkalinity was 150 mg/L and the pH was 6.3.
9. The following samples were collected by bailing. Because the representativeness of the samples cannot be evaluated, the data should be used with caution.
Culebra: H-1, H-10, P-15; Magenta: H-1, H-2, H-9, H-10;
Rustler/Salado: H-1, H-2, H-3, H-4, H-5, H-6, H-7, H-8, H-9, H-10, P-14, P-17.

10. H-2 Culebra: for reasons that are not understood, the quality of the Culebra water at H-2 has varied with time. Although some solutes have stayed fairly constant (SO_4^{2-} , 2900 - 3300; K, 90 - 120; Ca 670 - 750; Mg, 120 - 170 mg/L), Na and Cl^- have changed as follows:
In 2/77 (H-2B1): Na, 2100 mg/L; Cl^- , 2800 mg/L.
In 3/77 (H-2C): Na, 3600 mg/L; Cl^- , 4700 mg/L.
In 4/86 (H-2A): Na, 3500-3600 mg/L; Cl^- , 5200-5400 mg/L.
In 8/87 (H-2A): Na, 2600 mg/L; Cl^- , 4400-4800 mg/L.
During the four tests, other parameters were: HCO_3^- - 59, 62, 75, 54 mg/L; pH - 8.4, 8.2, 8.0, 7.8; TDS - 8900, 12500, 13000, 11000 mg/L. (references a,c,f,g in footnote 7).
The representativeness of these samples cannot be evaluated.
11. P-18 Culebra: Mercer (1983) reports solute data for a sample collected in 5/77. But because of the extremely low productivity of the well, there is reason to doubt that the sample collected was representative of the unperturbed groundwater (Lambert and Harvey, 1987). The data are not given here.
12. WIPP-25 Culebra: for reasons that are not understood, the quality of the Culebra water at WIPP-25 has varied with time.
In 8/80, parameters (mg/L) were: Na, 3200; K, 74; Ca, 900-910; Mg, 260; Cl^- , 5200-5300; SO_4^{2-} , 2500; HCO_3^- , 210; TDS, 12300-12500; pH, 6.9 (reference c in footnote 7).
In 2/86 and 4/87, parameters (mg/L) were: Na, 3100-3400; K, 100-120; Ca, 1100-1200; Mg, 310-340; Cl^- , 6100-6500; SO_4^{2-} , 2300-2400; HCO_3^- , 130; TDS, 13100-14100; pH, 7.2 (references c,e,g in footnote 7).
13. WIPP-26 Culebra: for reasons that are not understood, the quality of the Culebra water at WIPP-26 has varied with time.
In 8/80, parameters (mg/L) were: Na, 3600; K, 170; Ca, 1200-1300; Mg, 360; Cl^- , 6900-7200; SO_4^{2-} , 2500; HCO_3^- , 140; TDS, 14900-15300; pH, 6.9 (reference c in footnote 7).
In 11/85, parameters (mg/L) were: Na, 3800-4300; K, 340-360; Ca, 1200-1400; Mg, 370-430; Cl^- , 8400-8800; SO_4^{2-} , 2300-2500; HCO_3^- , 120; TDS, 16500-17900; pH, 7.1 (references b,c,e in footnote 7).
In 4/87, parameters (mg/L) were: Na 2900; K, 190; Ca, 1100; Mg, 330; Cl^- , 5800; SO_4^{2-} , 1900; HCO_3^- , 110; TDS, 12300; pH 7.0 (reference g in footnote 7).
14. WIPP-29 Culebra: probably because of the influence of nearby potash-mining activities, the quality of the Culebra water at WIPP-29 has varied with time.
In 8/80, parameters (mg/L) were: Na, 71000-79000; K, 16000; Ca, 800-1000; Mg, 5400-5700; Cl^- , 130000-140000; SO_4^{2-} , 13000-14000; HCO_3^- , 210-260; TDS, 236000-256000; pH, 6.1 (references a,c in footnote 7).
In 12/85, parameters (mg/L) were: Na, 90000-95000; K, 20000-24000; Ca, 630-680; Mg, 6300-6500; Cl^- , 170000-180000; SO_4^{2-} , 17000-20000; HCO_3^- , 160; TDS, 304000-326000; pH, 5.9 (references b,c,e in footnote 7).
In 3/87, parameters (mg/L) were: Na, 89000; K, 20000; Ca, 600; Mg, 5900; Cl^- , 150000-160000; SO_4^{2-} , 17000; HCO_3^- , 160; TDS, 283000-293000; pH, 6.2 (reference g in footnote 7).

15. P-15 Rustler/Salado: Mercer (1983) reports solute data for a sample collected in 4/79. But Lambert and Harvey (1987) showed that the sample was probably contaminated with Culebra water from the same well. The data are not given here.
16. P-18 Rustler/Salado: Mercer (1983) reports solute data for a sample collected in 5/79. But because of the extremely low productivity of the well, there is reason to doubt that the sample collected was representative of the unperturbed groundwater (Lambert and Harvey, 1987). The data are not given here.
17. WIPP-27 Rustler/Salado: Mercer (1983) reports solute data for a sample collected in 5/80. But because the well "ran dry" during a later pumping test and based on some subsequent field measurements of several solutes (chloride, divalent cations, sulfate), the 9/80 sample is not considered to be representative (Robinson, 1988). The data are not given here.
18. H-8 Magenta: the sample from 2/80 was collected by bailing; the sample from 10/85 was collected by pumping (however, the well quickly "ran dry"). Because of the extremely low productivity of the well, neither sample can be confidently stated to be representative. The data should be used with caution.
19. WIPP-30 Magenta: Mercer (1983) reports solute data for a sample collected in 9/80. But because of the low productivity of the well and based on some subsequent field measurements of several solutes (chloride, divalent cations, sulfate), the 9/80 sample is not considered to be representative (Robinson, 1988). The data are not given here.

3.3.2.5 Samples of Unknown Reliability. The reliability of the data for samples from some locations cannot be evaluated. These include some samples collected by bailing and samples from some wells at which the water quality appears to be changing with time.

At many locations, samples were collected first by the USGS by bailing or swabbing and later by other groups (such as Sandia, Hydro Geo Chem, or the WQSP) after long-term pumping tests. Comparing these data sets showed that many (but not all) of the bailed or swabbed samples appeared to be contaminated, perhaps by drilling fluid that was not completely removed by the bailing or swabbing process. At some locations, however, the only available data are the USGS analyses of samples they collected by bailing or swabbing. Because some, but not all, of the bailed or swabbed samples from other locations have been shown to be contaminated, there is no good way of evaluating the representativeness of most of these samples. The data are therefore included in Table 3-12, but warnings are given in the footnotes.

At several locations, the chemistries of water samples collected at different times are significantly different, but not necessarily because of difficulties in collecting apparently representative samples or because of analytical errors. These locations are discussed in more detail in the footnotes of Table 3-12.

3.3.2.6 Data Variability. Concentrations of dissolved solids in ground waters from three water-producing horizons of the Rustler Fm. vary widely in the study area (Figure 3-10). Specifically, TDS ranges from <3000 to >300,000 mg/L. Major solute ranges are Cl^- , ~30 to ~300,000 mg/L; SO_4^{2-} , ~400 to ~20,000 mg/L; Na, ~50 to >100,000 mg/L; K, ~4 to >20,000 mg/L; Ca, ~500 to ~18,000 mg/L; and Mg, ~10 to >80,000 mg/L.

The Culebra Dolomite shows variations similar to those of the Rustler Fm. overall, with TDS ranging from <3,000 mg/L to >300,000 mg/L in the study area. Within the WIPP site boundary (Figure 3-10), TDS concentrations in Culebra waters range from ~10,000 to >200,000 mg/L. Major solute ranges in Culebra waters from wells within the site boundary are Cl^- , <8,000 to >100,000 mg/L;

SO₄²⁻, ~1,500 to ~8,000 mg/L; Na, ~3,000 to ~80,000 mg/L; K, ~100 to ~1,500 mg/L; Ca, ~700 to ~2,000 mg/L; and Mg, ~100 to ~2,500 mg/L.

Waters from the Magenta Dolomite are generally fresher; TDS concentrations range from ~4,000 to >200,000 mg/L in the study area. The range in the Magenta is much narrower, ~4,000 to ~25,000 mg/L, if data from two wells are ignored: H-10, for which the quality of the sample cannot be evaluated, and WIPP-27, where the quality of the water is affected by potash-mining activities. Within the site boundary, the range is ~4,000 to ~25,000 mg/L.

Waters from the Rustler/Salado contact zone are the most saline, with TDS concentrations ranging from 70,000 to >300,000 mg/L in the study area. Within the site boundary, the range in TDS concentrations is much narrower, ~300,000 to ~400,000 mg/L.

3.3.3 Hydrochemical Model for Culebra Ground Waters

One goal of constructing an interpretive hydrochemical model for the Culebra Dolomite is to provide a conceptual basis for predicting the chemical and hydrologic response of the aquifer to the influx of brine and radionuclides from the repository. Several questions were addressed by a recent hydrochemical facies study of the Culebra (Siegel, Lambert, and Robinson, 1989):

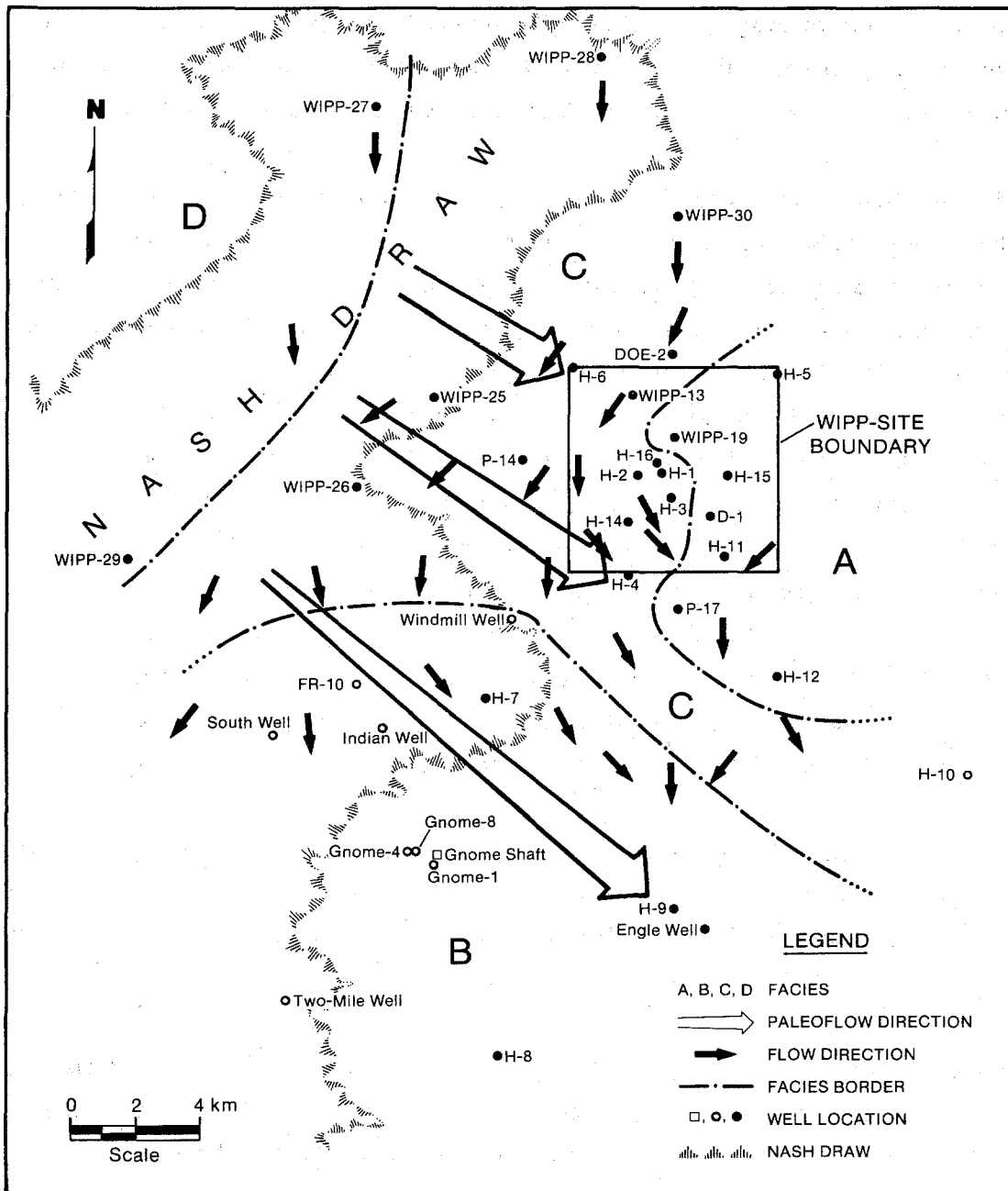
1. Is the spatial distribution of solutes consistent with the hydrologic flow directions predicted independently by hydrogeologic studies assuming steady-state, confined flow?
2. On what time scale can the Culebra Dolomite be considered confined; is it receiving modern recharge at the WIPP site?
3. On what time scale can the flow within the Culebra Dolomite be considered transient; has the north-south flow direction indicated by hydrologic data been constant throughout the Pleistocene Epoch?

4. What chemical reactions control the composition of waters in the Culebra Dolomite; how strongly chemically buffered is the rock/water system with respect to possible chemical changes that may be induced by the influx of wastes and brines into the aquifer as a result of a release?

This section reviews the current understanding of these subjects. Consistency of flow directions suggested by geochemical and hydrologic data can be further supported by demonstrating that the location and magnitude of solute fluxes from potential sources and to potential sinks produce the observed distribution of solutes in the postulated hydrologic flow field. An important part of this analysis is the identification of hydrochemical facies, water types that have similar chemistries and origins. Resolving the questions of modern recharge, transience, and confined flow requires examination of isotopic ratios and the distribution of diagnostic minerals in order to differentiate the independent histories of the solutes, water molecules, and mineral phases in the Culebra Dolomite. Evaluating the degree to which the Culebra aquifer is buffered against future chemical changes requires identifying the major sources and sinks of solutes in the Culebra Dolomite and an assessment of the degree of chemical equilibrium in the aquifer.

3.3.3.1 Hydrochemical Facies of Culebra Ground Water. Based on stratigraphic and hydrologic data and the major solute compositions described in Section 3.3.2 and by Siegel, Robinson, and Myers (1989), four hydrochemical facies are delineated (Figures 3-11 and 3-12).

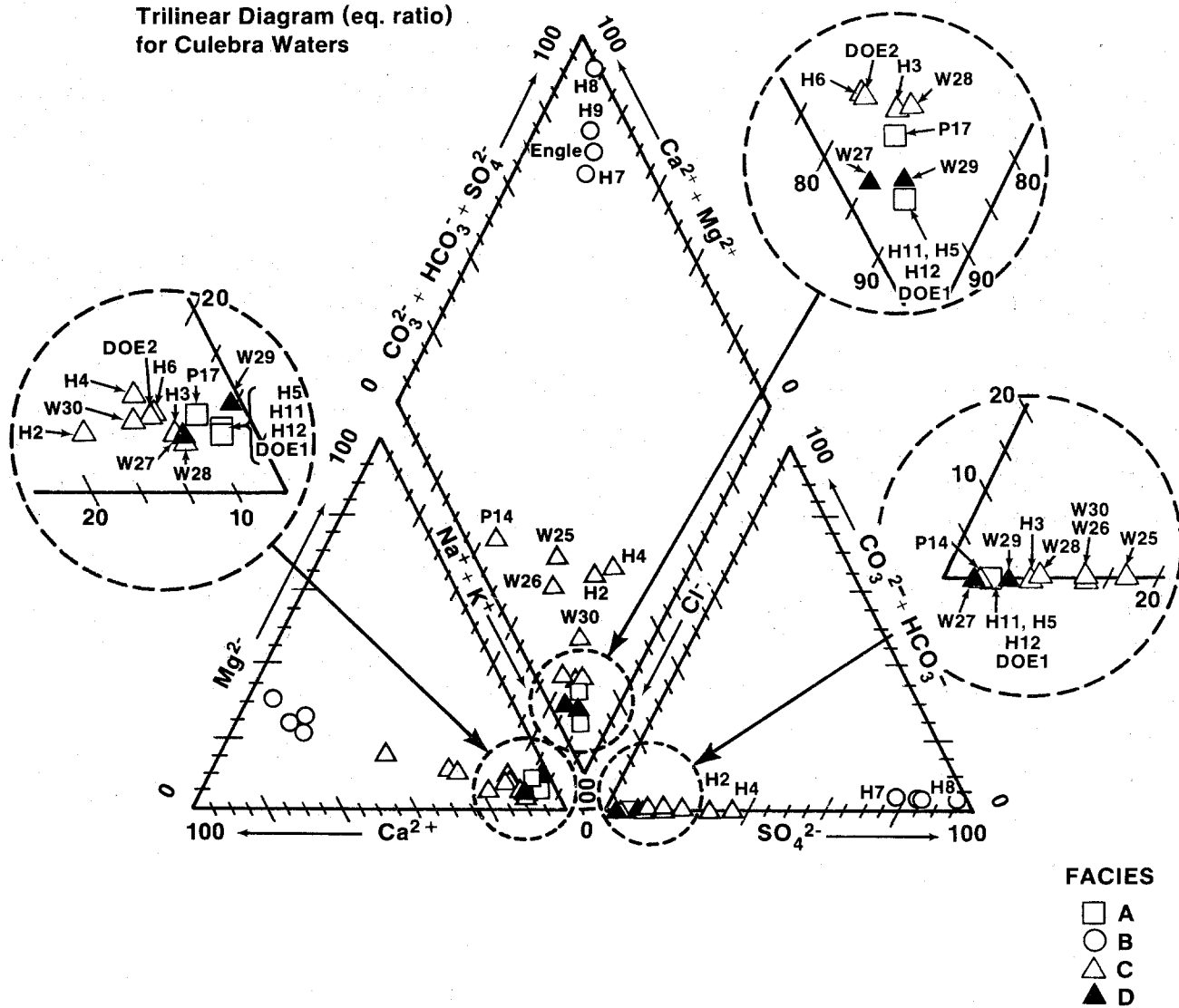
Zone A comprises a saline (about 2 to 3 molal) NaCl brine with a Mg/Ca molar ratio >1.2 . This water is found in the eastern third of the area shown in Figure 3-10; the zone coincides roughly with the region of low transmissivity. On the western side of the zone, halite in the Rustler Fm. has been found only in the unnamed lower member; in the eastern portion of the zone, halite has been observed throughout the Rustler Fm. (Figure 3-4). Zone B is an area of dilute, CaSO_4 -rich water (ionic strength <0.1 molal) in the southern part of the area shown in Figure 3-11. This zone coincides with a high-transmissivity region; halite is not found in the Rustler Fm. in this zone. Zone C contains waters of variable composition with low to moderate ionic strength (0.3 to 1.6 molal) in the western part of the WIPP site and the



TRI-6330-78-0

Figure 3-11. Hydrochemical facies of the Culebra Dolomite. Compositions of waters at locations indicated by solid circles are described in Figure 3-12. Compositions of several other wells indicated by open circles were not included in original data set used to define the facies, but their compositions are consistent with the facies boundaries (- * - * - *) (Siegel, Lambert, and Robinson, 1989).

Trilinear Diagram (eq. ratio)
for Culebra Waters



TRI-6330-35-0

Figure 3-12. Trilinear diagram for Culebra ground waters (Siegel, Lambert, and Robinson, 1989).

eastern side of Nash Draw. Mg/Ca molar ratios are <1.2 . This zone coincides with a region of variable transmissivity. In the eastern part of this zone, halite is present in the lower member of the Rustler Fm.; on the western side of the zone, halite is not observed in the formation. The most saline (NaCl-rich) water is found on the eastern edge of the zone, close to core locations where halite is observed in the Tamarisk Member. Zone D is a fourth zone, comprising wells WIPP-27 and WIPP-29, defined based on inferred contamination related to potash refining operations. Waters from these wells have anomalously high salinities (3 to 6 molal) and K/Na weight ratios (0.2) compared with other wells in the region (0.01 to 0.09). At WIPP-29, the composition of the Culebra water has changed over the course of a seven-year monitoring period. The Mg/Ca molar ratio is anomalously high, ranging from 10 to 30 during the monitoring period.

The chemical characteristics of each facies are described by a Piper (trilinear) diagram that summarizes relationships between the major solutes in the Na-K-Mg-Ca-Cl-SO₄-CO₃ system (Figure 3-12). The diagram shows the relative proportions of the ions on the basis of equivalents/liter. Relative proportions of cations and anions are displayed in the triangular plots in the bottom half of the figure; relative proportions of divalent to monovalent cations and chloride to (sulfate + carbonate) are shown in the rhombus in the upper portion of the diagram.

Compositions of Culebra waters from Zone A have nearly identical ionic proportions and plot on the same location in the graph near the Na-Cl corner. They are distinguished from waters in Zone C by their higher Mg/Ca ratio and ionic strengths. Dilute ground waters from Zone B plot near the Ca-SO₄ corner, and water from Zone C covers a wide area. Waters from Zone D have ionic proportions similar to those of Zone A and are distinguished primarily on the basis of salinity and K/Na ratio, parameters that are not shown in Figure 3-12.

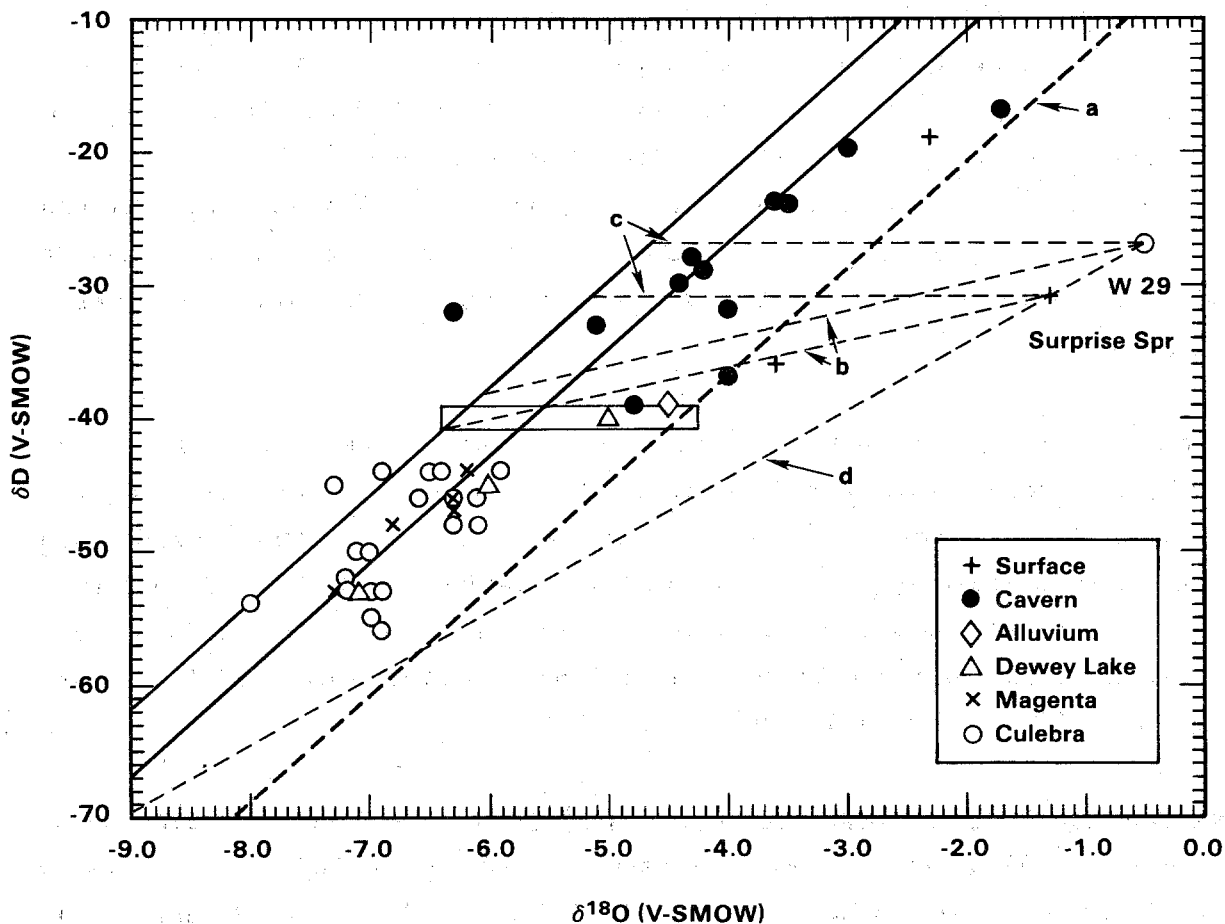
3.3.3.2 Hydraulic Versus Geochemical Confinement. Hydrologic tests with durations of a few months have revealed that on such a time scale the Culebra Dolomite is hydrologically confined at all locations that have been sampled, except WIPP-25, WIPP-27, and WIPP-29, and possibly WIPP-26 and H-7.

Generally, the hydraulic relationships suggest that there is only limited vertical connection between the Culebra and overlying strata. Hydraulic measurements can quantify short-term responses of the hydrologic flow system to transient pressure pulses such as slug- and pump-testing, but geochemical measurements are more related to mass transport and rock/water interactions that take place over longer periods, up to several thousand years. Relevant geochemical observations include studies of stable isotopes and mineral alteration.

Lambert (1989) discussed in detail the isotopic geochemistry of Rustler and related ground waters and summarized the data (oxygen and hydrogen isotopes; carbon isotopes including radiocarbon; tritium; radiochloride; and uranium concentration and $^{234}\text{U}/^{238}\text{U}$ activity ratios) and their interpretations. This discussion is in turn a summary of that work, which is drawn from several sources (Lambert and Mercer, 1978; Lambert and Robinson, 1984; Lambert and Harvey, 1987; Lambert and Carter, 1984, 1987).

Hydrogen and Oxygen Isotopes in Ground Waters. Confined Rustler ground waters near the WIPP and in Nash Draw have isotopic compositions very tightly clustered along the worldwide meteoric field in $\delta\text{D}-\delta^{18}\text{O}$ space (Figure 3-13). Ground waters whose stable-isotope compositions deviate markedly from that of a characteristically meteoric signature occur at the Rustler/Salado contact in the low-permeability portions of that zone in the central and eastern parts of the WIPP site (Lambert, 1989) and near the surface in the Culebra and Tamarisk Members in the southwest portion of Nash Draw, where hydrologic conditions are not as confining. Deviations in waters at the Rustler/Salado contact are attributable to a profound degree of rock/water interaction involving a relatively large rock/water ratio. The isotopic signatures observed in southwestern Nash Draw can arise from partial evaporation from the vadose zone and the capillary fringe above the water table. Confined meteoric Rustler waters are virtually identical in stable-isotope composition to confined meteoric Capitan waters at the basin margin, indicating recharge of both types of confined waters under similar climatic conditions.

By comparison, vadose Capitan waters from the Carlsbad Caverns system, ground water from a water table in alluvium, and near-surface accumulations



TRI-6330-36-0

Figure 3-13. Stable-isotope compositions of ground waters from the Rustler Fm. and other rocks in southeastern New Mexico (Lambert, 1989). Small deviations of ground waters from the meteoric field (up to -10‰), within which nearly all the data lie (line a), are not considered significant (cf. Allison et al., 1985). WIPP-29 Culebra and Surprise Spring can have evolved by evaporation from a shallow water table, with a $\delta D/\delta^{18}O$ trajectory having a slope of 2 (lines b; Allison, 1982), from modern southeastern New Mexico water from the Ogallala aquifer (rectangle; δD range determined by Yapp, unpublished) likely to have been imported for use in nearby potash-refining operations. Alternatively, they can also have evolved from modern-type water by oxygen isotope shift (horizontal dashed lines c). They probably did not originate from partial evaporation of confined Rustler-type water with a trajectory slope of 5 (line d; Craig et al., 1963), a slope representing partial evaporation from a water surface exposed to the atmosphere.

that homogenize seasonal variations in isotopic composition also have meteoric isotopic signatures, but have isotopic compositions more positive in δD - $\delta^{18}O$ space than confined Rustler and Capitan waters (Lambert and Harvey, 1987). The envelope of δ -values for confined Rustler water does not overlap with that of waters from the Carlsbad Caverns system (Figure 3-13). The data of Nativ and Smith (1987) reveal that in Ogallala ground waters underlying the High Plains to the east, climatically similar to the Delaware Basin, the only ground waters containing tritium levels indicative of recent (post-1950) meteoric derivation (>10 TU), all have δD values > -42 ‰, comparable to near-surface unconfined meteoric waters in the Delaware Basin (Figure 3-13). Thus, the isotopic signatures of confined Rustler and Capitan waters are distinct from those of both Ogallala water with discernable modern input and vadose Capitan and alluvial water. It is likely that the isotopic compositions of confined Rustler and Capitan ground waters in the northern Delaware Basin are not characteristic of ground waters receiving modern meteoric recharge under the present climatic conditions. This interpretation is not consistent with the interpretation of Chapman (1986) to the effect that the stable-isotopic character of confined Rustler ground waters is consistent with derivation from modern meteoric precipitation. It is, however, consistent with interpretations of available results of radiocarbon and uranium-disequilibrium studies on Rustler ground waters, discussed below.

Some, but not all, Dewey Lake ground waters may have a component characteristic of climatic conditions fostering modern surficial recharge (Figure 3-13). Some have stable-isotope compositions comparable to the near-surface occurrences, and some are comparable to confined Rustler ground waters. Thus, recharge to the Dewey Lake Red Beds, like recharge to the Ogallala Fm., appears to be variable in both space and time.

Radiocarbon (^{14}C) Ages. Available radiocarbon ages from the Culebra Dolomite are in excess of 12,000 to 16,000 years. Only four (three Culebra, one Dewey Lake) out of 16 well-water occurrences gave internally consistent ages based on the model of Evans et al. (1979) for carbonate rocks (Figure 3-14). Ten of the remaining 16 well-water occurrences were complexly contaminated due to unmitigable well-bore effects. The remaining two are ambiguous, but all 16 probably represent three-component mixing including some

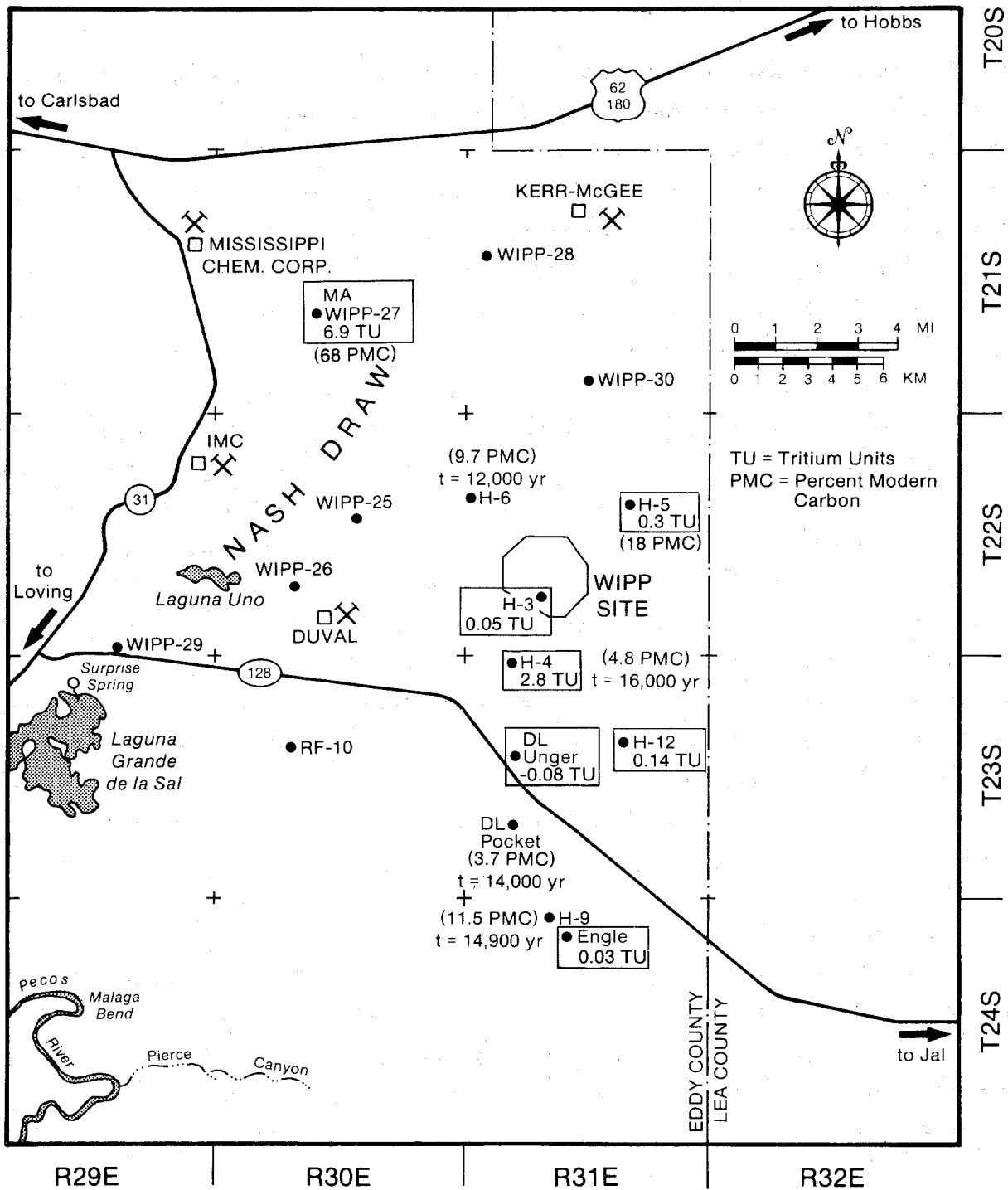


Figure 3-14. Tritium and radiocarbon in Rustler and Dewey Lake ground waters (Lambert, 1989). Unless otherwise specified as Dewey Lake (DL) or Magenta (MA), measurements (all from Lambert, 1987) apply to water from the Culebra Dolomite. Tritium units enclosed in rectangles. These data indicate long residence times or long travel times from recharge areas, but provide no evidence of either modern vertical infiltration or monotonic age gradients indicating north-to-south flow.

contamination. It is not possible to estimate an upper age limit, because of the unavoidable possibility of at least small amounts of unmitigable contamination in these samples.

Three ages for the Culebra Dolomite (at H-6, H-4, and H-9) were determined at localities that effectively "bracket" the WIPP site on the north and south. The lack of a statistically significant difference among these ages, and the lack of a north-south gradient in apparent age suggests either that rates of vertical infiltration at each location have been virtually identical, or that lateral flow times to each location from the surface-recharge area(s) have been virtually identical.

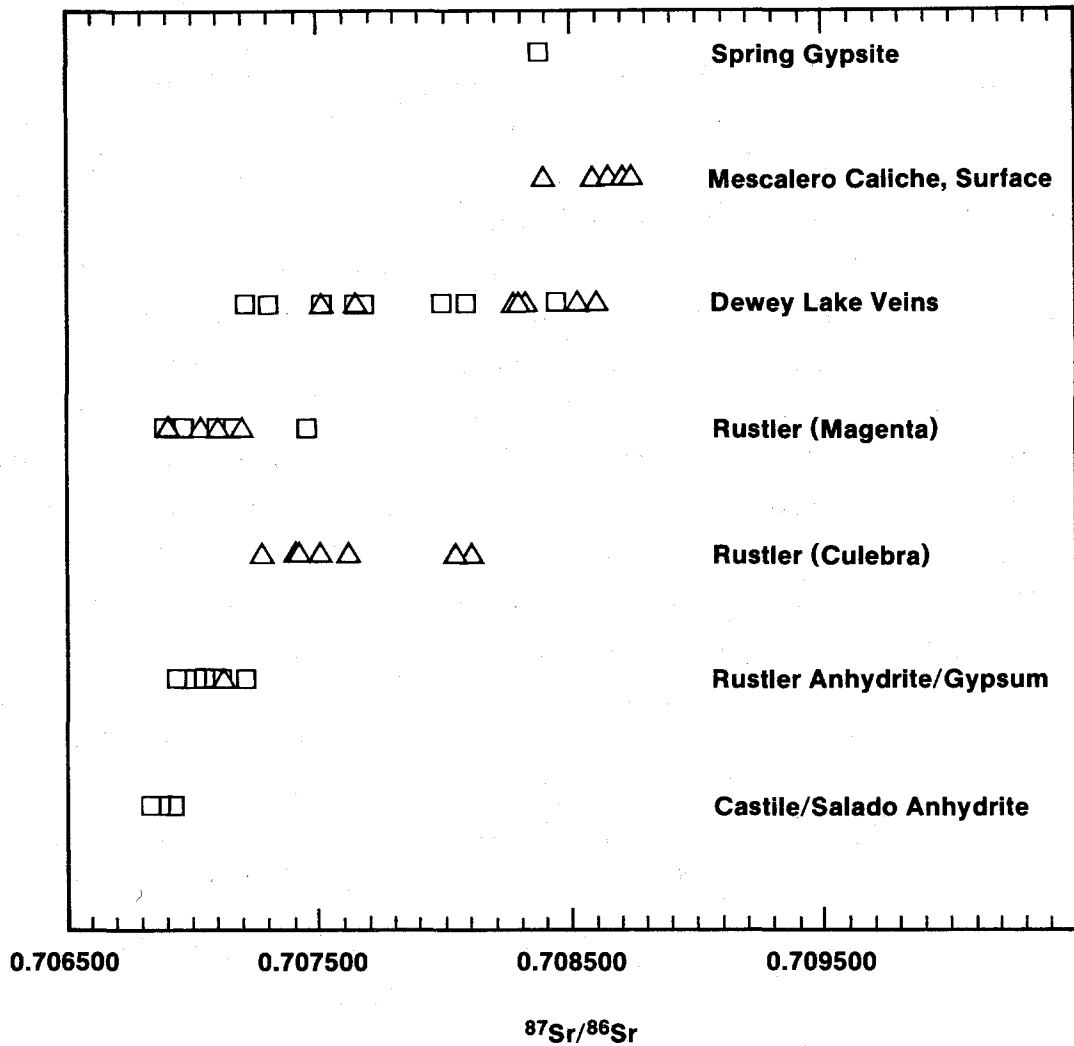
The four dated ground waters (three Culebra and one Dewey Lake [Pocket Well]) all have stable-isotope compositions belonging to the more negative population in δD - $\delta^{18}O$ space (Figure 3-13). Thus, it is inferred that Rustler and Dewey Lake ground waters in this population have a significant component at least 12,000 radiocarbon years old. All the tritium measurements from the WIPP area, which are associated with the more negative (confined Rustler) isotopic compositions, are <3 TU, indicating minimal contribution from the atmosphere since 1950 (cf. Isaacson et al., 1974) (Figure 3-14).

An influx of meteoric water to the Culebra Dolomite no more recently than about 10,000 years ago is consistent with paleoclimatic data. The southeastern New Mexico climate more than 10,000 years ago fostered vegetation now found only at higher elevations, as indicated by packrat-midden studies (Van Devender, 1980). Late Pleistocene climate was probably wetter and more conducive to recharge, as indicated by the concordance between the ages of packrat middens and the relatively less-contaminated radiocarbon in the Rustler and Dewey Lake ground waters described above. Fossil fauna (camels, horses, bison) from extinct spring deposits in Nash Draw near the WIPP site are of similar age and also indicate wetter conditions than at present (Bachman, 1981). The significance of these data to the questions of transience of the hydrologic system is discussed in Section 3.3.3.

Strontium Isotope Chemistry of Sulfates and Carbonates. $^{87}Sr/^{86}Sr$ ratios of sulfate and carbonate mineral veins, generally interpreted as the

depositional record of fluid flow preferentially concentrated in fractures, are indistinguishable from those of their host rocks throughout the Rustler Fm. This indicates a dominantly internal, not external, source for the mass transport represented by the vein fillings (Brookins and Lambert, 1988; Lambert, 1989). Aside from the Magenta and Culebra Dolomites, the $^{87}\text{Sr}/^{86}\text{Sr}$ ratios of the Rustler anhydrites and gypsums (which range from 0.70694 to 0.70714) are similar to but slightly greater than those of unaltered anhydrites interbedded with halite and polyhalite in the Salado Fm. (Figure 3-15), which have never been in contact with large amounts of meteoric water. This similarity shows that mass transport of sulfate and carbonate from surface-weathered outcrops in the recharge zone has made a limited contribution to the soluble cationic constituent of the Rustler Fm. In contrast, veins in the Dewey Lake Red Beds containing selenite and calcite appear to have a continuum of $^{87}\text{Sr}/^{86}\text{Sr}$ ratios (ranging from 0.70722 to 0.70861), representing mixing of materials derived from both Ochoan evaporites typical of the Rustler Fm. and deeper rocks, and near-surface deposits, such as caliche and gypsite spring deposits (Figure 3-15). These relationships show that the spring deposits were not derived solely and directly from Rustler rock dissolved and mobilized westward in the late Pleistocene (cf. Bachman, 1981), but instead require a dominant component similar to the high- ^{87}Sr extreme in Dewey Lake strontium.

The strontium-isotope data suggest that vertical material transport from the surface to layers underlying the Dewey Lake Red Beds has not been extensive. Even at localities of suspected vertical solution or fracture channels (e.g., WIPP-14, WIPP-33, and WIPP-34), the $^{87}\text{Sr}/^{86}\text{Sr}$ ratios in the partially gypsified anhydrites of the Forty-niner and Tamarisk Members indicate minimal admixture of surface-type strontium having a high $^{87}\text{Sr}/^{86}\text{Sr}$ ratio, a moderate amount of such admixture in the Culebra Dolomite, and extensive admixture in the Dewey Lake Red Beds. This stratification of strontium constitutes evidence of minimal mass transport across the Rustler/Dewey Lake contact, while allowing lateral transport of some surface-type strontium through the Culebra Dolomite from its near-surface exposures. This conclusion is supported by the preservation of extensive amounts of anhydrite and a varying water/rock ratio during partial gypsification in the non-dolomitic Rustler units overlying the Culebra Dolomite, which suggest



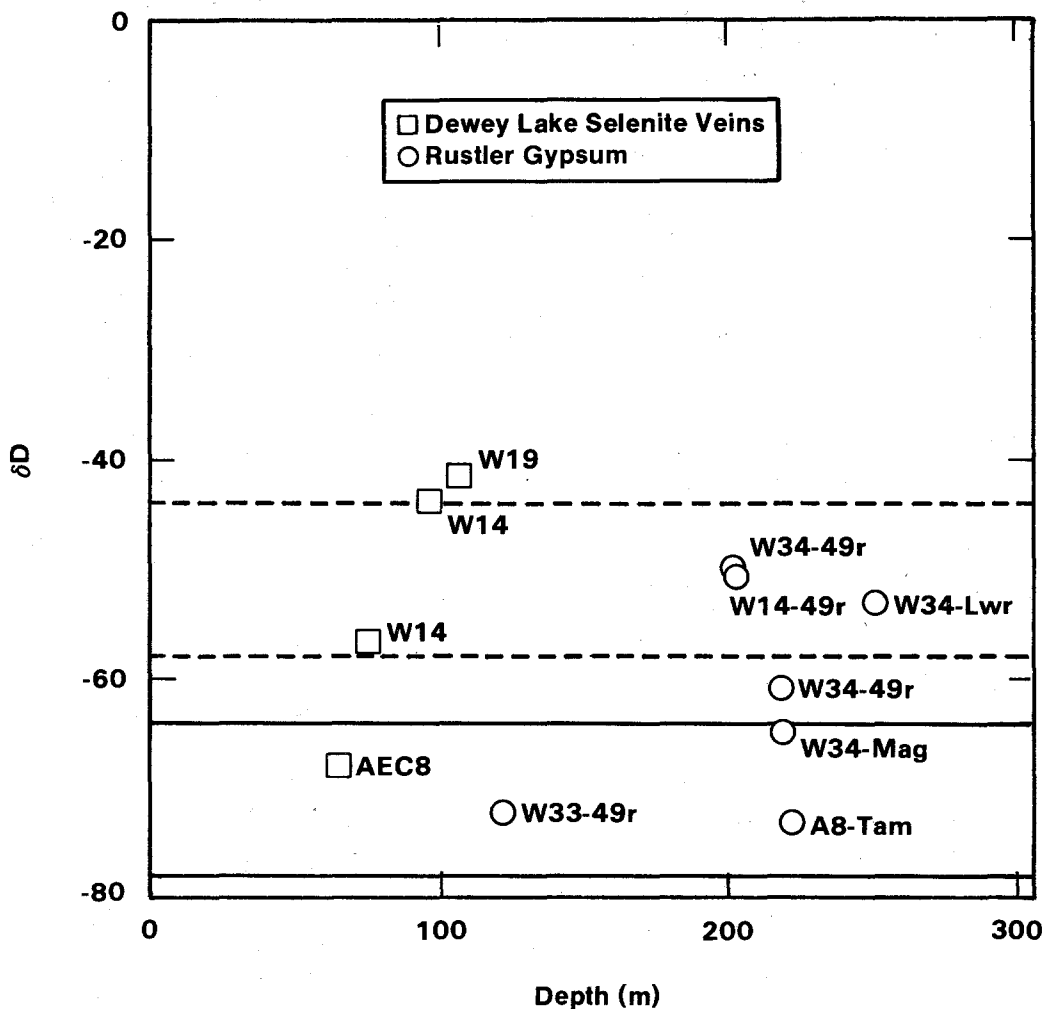
TRI-6330-37-0

Figure 3-15. $^{87}\text{Sr}/^{86}\text{Sr}$ ratios in Ochoan and related rocks (Lambert, 1989). Higher $^{87}\text{Sr}/^{86}\text{Sr}$ ratios progressively higher in the stratigraphic section reflect a greater contribution of surface-derived cations. Sulfates are indicated by squares; carbonates are indicated by triangles.

that large amounts of water have not permeated vertically from the surface to recharge the Culebra.

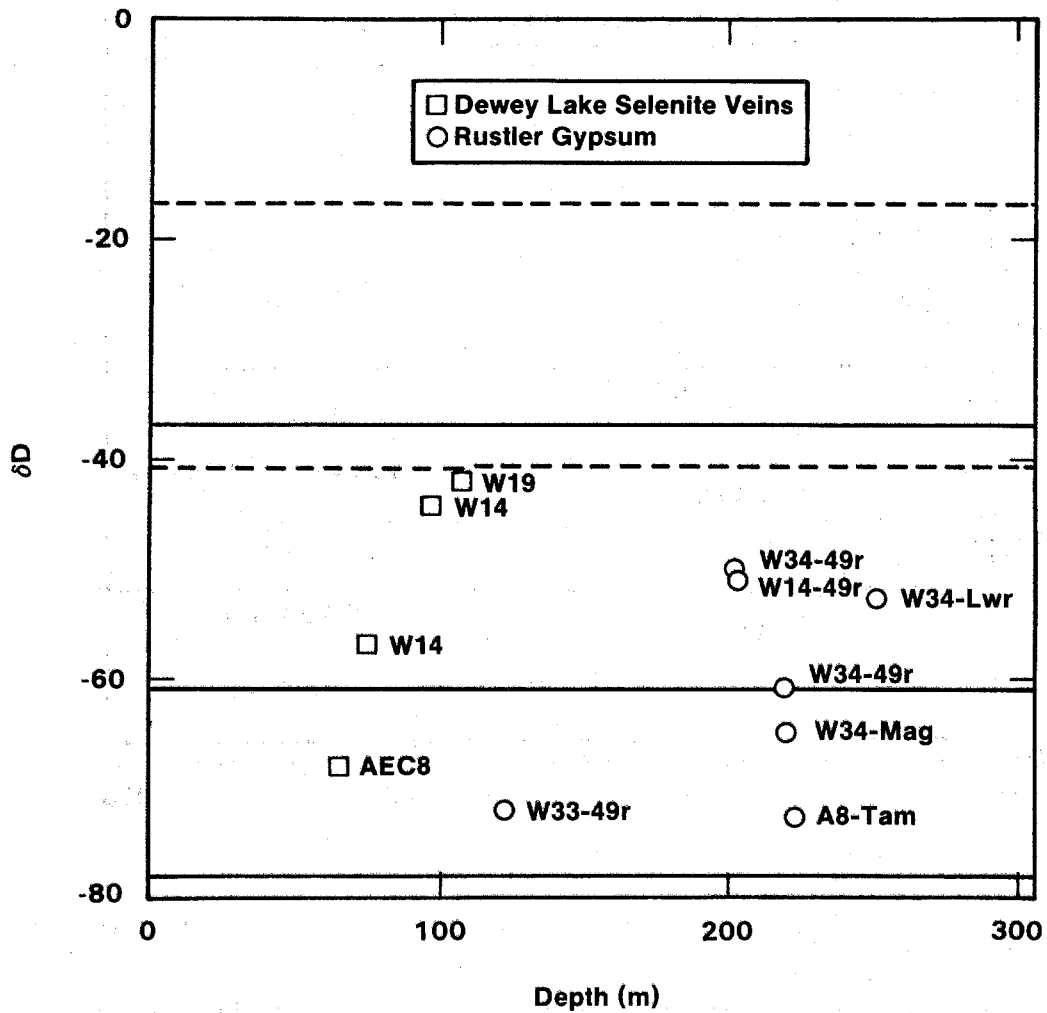
Hydrogen Isotopes in Gypsum and Anhydrite. Vertical variations in D/H ratio; together with the minimal surficial component of Sr described above, suggest that ground-water flow within the Rustler Fm. near the site is largely stratabound, having been recharged where near-surface exposures of water-bearing units can receive infiltration and subsequently having moved laterally. The D/H relationships in gypsums from the Rustler Fm. and Dewey Lake Red Beds are characteristic of gypsification of anhydrite (or recrystallization of pre-existing gypsum) in the presence of meteoric water. No gypsum thus far examined bears an isotopic signature that would be expected for primary marine evaporitic sulfate ($\delta D > 0\text{‰}$). Although all gypsums examined were meteorically influenced ($\delta D \leq -40\text{‰}$), their δD values vary widely (Figure 3-16). All δD values except from WIPP-19 are consistent with isotopic equilibrium between their waters of crystallization and varying amounts of Rustler-type (Pleistocene) meteoric water (Figure 3-16a). Some of the gypsums and selenites could have recrystallized in the presence of surface-type (modern) meteoric water given a high water/rock ratio (Figure 3-16b). Rustler gypsum and Dewey Lake selenite at AEC-8 and gypsum from WIPP-33 Forty-niner and WIPP-34 Magenta have δD values that are not consistent with recrystallization in the presence of any amount of shallow-type (modern) water.

Regionally, δD does not correlate with depth, suggesting a nonuniform vertical permeability throughout the Rustler/Dewey Lake section. In a given borehole core, the water/rock ratio inferred from the gypsum D/H ratio is highest, as might be expected, near the brittle, water-bearing zones in the Rustler Fm. and diminishes with distance from such a zone. In addition, the water/rock ratios in gypsiferous horizons adjacent to the water-bearing dolomites are much lower than in the dolomites themselves, as suggested by the D/H ratios of gypsum and of various ground waters. Such variations in the water/rock ratio are consistent with some water having escaped from the Culebra Dolomite into adjacent beds (perhaps acquiring some solutes from halite dissolution).



TRI-6330-38-0

Figure 3-16a. δD values of the water of crystallization in gypsums as a function of depth (Lambert, 1989). Circles represent Rustler gypsum; squares correspond to samples from Dewey Lake selenite veins. Abbreviations: Lwr = lower member; Tam = Tamarisk; Mag = Magenta; 49r = Forty-niner. Solid lines delineate the range of gypsum compositions expected from recrystallization in the presence of a large amount of Rustler-type meteoric water (extremely high water/rock ratio). Dashed lines bound gypsum δD values expected from small amounts of such water completely scavenged during gypsification of anhydrite, and correspond to the δD field for confined Rustler waters in Figure 3-11.



TRI-6330-126-0

Figure 3-16b. Ranges for gypsum and selenite δD values expected from crystallization or recrystallization in the presence of surface-type (modern ?) meteoric water ($\delta D = -17$ to -41 ‰) given high (solid lines) and low (dashed lines) water/rock ratios (Lambert, 1989). Abbreviations and symbols are the same as those in Figure 3-16a.

The above observations show that recharge has not taken place vertically from the surface. The variations in D/H are not consistent with water migrating downward into the Culebra Dolomite, first passing through a region of low water/rock ratio without having affected the gypsification of overlying anhydrite. If this were a significant mechanism of recharge to the Culebra Dolomite, the stable-isotope composition of Culebra waters would exhibit a measurable shift away from meteoric values as a result of water/rock interaction in a zone of low water/rock ratio.

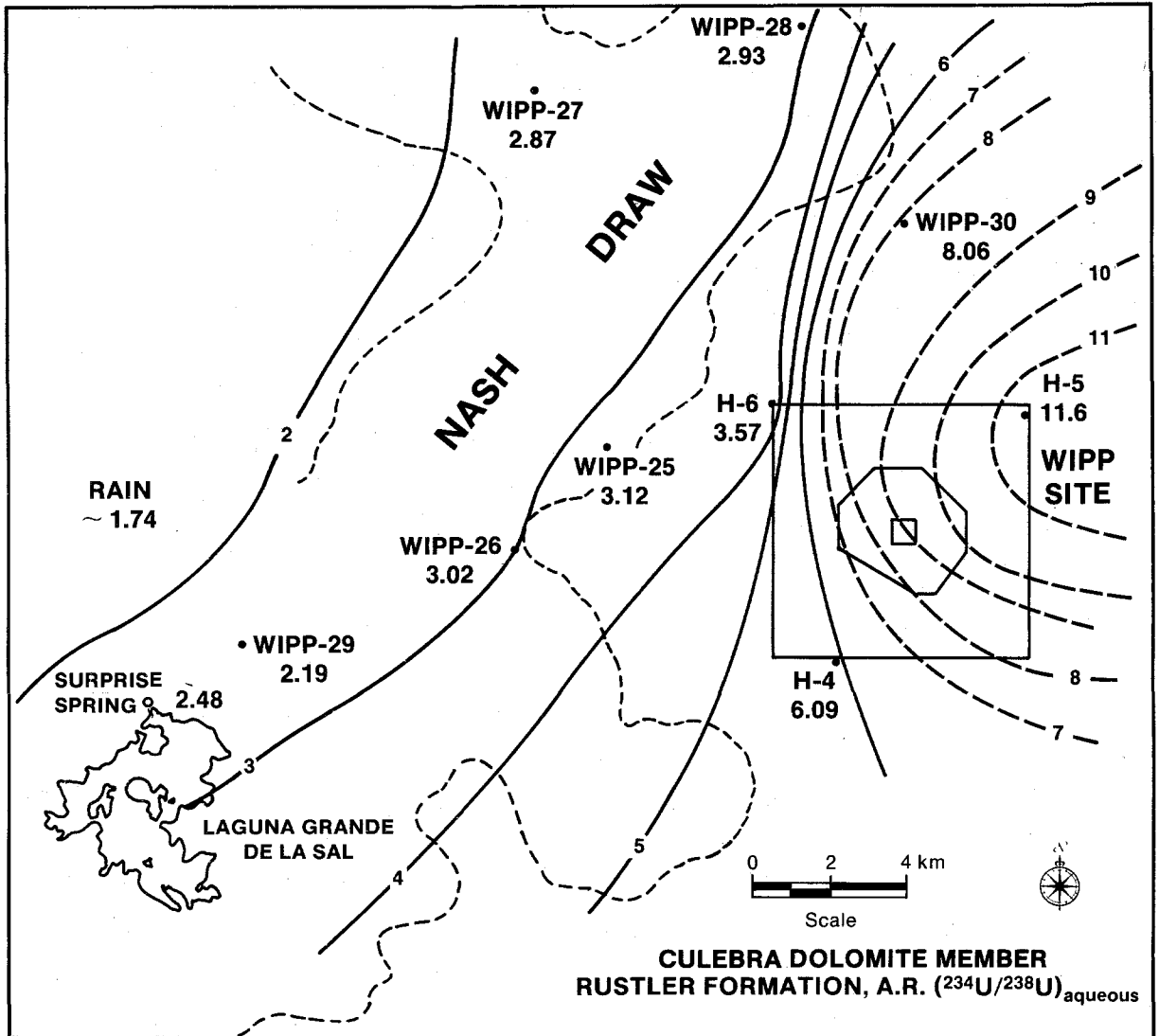
3.3.3.3 Steady-State Versus Transient Flow. Ramey (1985) observed that if the Culebra Dolomite is a confined aquifer at steady state, then present-day regional water-flow directions are not consistent with the salinity distribution at the WIPP site, given the assumption of steady-state, confined flow. He based this observation on a fairly limited number of water samples analyzed as of 1983. The more extensive data sets examined by Siegel, Robinson, and Myers (1989) and Section 3.3.2 confirm this observation. As shown in Figure 3-11, Zone B, a facies with low salinity and element ratios inconsistent with halite dissolution, lies downgradient from more-saline water in Zone C. Flow within Zone C may be consistent with progressive addition of solutes from dissolution of halite in the lower member; however, the current uncertainties in the hydrologic models and geochemical data do not allow for quantitative mass balance modeling along the hydrologic flow paths.

The inconsistencies between the steady-state, confined-flow, hydrologic model and geochemical interpretations might be reconciled by considering the differences in the time scales reflected by the computed hydrologic flow field, isotope ratios, and spatial distributions of solutes and minerals. Specifically, the assumption of steady-state confined flow may be adequate on the 100-year time scale of hydrologic testing and disturbances related to the construction of the WIPP shafts. Measurements of modern head potentials, transmissivities, and fluid densities, however, do not directly indicate time scales on which the system might be transient. In fact, isotopic data suggest that transient phenomena have taken place over the past 10,000 to 20,000 years in response to climatic change.

Uranium-Isotope Disequilibrium Data. Lambert (1989) suggested that the apparent inconsistency between the steady-state hydrologic model and solute-distribution pattern can be explained by a change in flow direction in the past 30,000, perhaps 12,000, years. As discussed above, the hydrologic balance has changed since the Pleistocene Epoch, and ground water currently flows southwesterly. Evidence for a change in flow direction consists partly of the available uranium-isotope disequilibrium data.

Given the assumptions of the model of Osmond and Cowart (1976) for uranium systematics in confined hydrologic flow systems, generalized flow directions in confined Rustler ground waters as inferred from $^{234}\text{U}/^{238}\text{U}$ relationships appear to require recharge from a direction with an eastward-flowing component (Figure 3-17). This is not parallel to modern flow directions inferred from potentiometric heads alone (cf. Figure 3-11). A change in flow direction back toward the west (the modern flow direction indicated for saturated portions of the Magenta Dolomite [Mercer, 1983]) during the past 10,000 to 30,000 years is likely. During the time of wetter Pleistocene conditions, when the Rustler Fm. was being recharged at its outcrops in Nash Draw, the base level there was probably also being lowered by accelerated erosion and dissolution. With the onset of a drier Holocene climate and the cessation of significant recharge, the area whose base level was lowered has probably governed the local hydraulic gradient, resulting in a general southward drainage.

Origin of the Southern Low-Salinity Zone. More-oxidizing conditions in the south than in the north have been interpreted to indicate possible vertical recharge in the south, accounting for dilution of more saline brine apparently flowing from the north (Myers et al., 1989). However, the available radiocarbon-model age in the southern, less saline Zone B (H-9), is no younger than in the northern, more saline Zone C (H-4 and H-6 wells); this argues against dilution by modern vertical recharge in the south. Similarly, model ages are no older in the south, arguing against a monotonic, north-to-south, steady-state flow persisting since the Pleistocene Epoch. The one available radiocarbon age from the Dewey Lake Red Beds overlying the Rustler Fm. (Pocket Well) is consistent with this interpretation. The stable-isotope characteristics of the Dewey Lake Red Beds, however, are consistent with the interpretation that both waters are at least 12,000 to 16,000 years old and



TRI-6330-79-0

Figure 3-17. $^{234}\text{U}/^{238}\text{U}$ activity ratios (ARs) in ground water from the Culebra Dolomite (Lambert and Carter, 1987). AR decreases westward and somewhat southward toward Nash Draw; high AR values typically develop downgradient in hydrologic systems under confined, reducing conditions and are associated with long residence times.

that waters representing modern meteoric recharge in the area may be present in this unit.

Steady-state, north-to-south, confined flow would not have preserved the lower salinity zone downgradient from the saline zone (Figure 3-11). The lower-salinity zone could have arisen if the regional flow direction originally had a significant westerly component, as suggested by the generally eastward-increasing $^{234}\text{U}/^{238}\text{U}$ activity ratios discussed above. Similarities in radiocarbon age in the north and south are consistent with water recharging both north and south parts of the WIPP area simultaneously from a near-surface Pleistocene infiltration zone in the west-northwest (Figure 3-11), with ground water at one time flowing locally subparallel rather than subnormal to the hydrochemical facies boundary between Zones B and C. A likely paleorecharge zone is nearby in surface outcrops of the Rustler Fm. to the west in Nash Draw.

A likely explanation for the less saline waters of Zone B is that at the time of influx of the present generation of Culebra ground water in late Pleistocene time, Rustler halite was absent adjacent to the Culebra Dolomite, thus not providing a source of NaCl. This is consistent with the present-day correlation of halite occurrence in the Rustler Fm. (Figure 3-4) and the hydrochemical facies pattern (Figure 3-11). The halite might never have been deposited in the south, or pre-existing halite may have been removed by earlier dissolution during the development of the southeastern lobe of Nash Draw, which is included in Zone B. This dissolution, however, would have taken place in response to an episode of ground-water flow older than the present regime, which began as early as 16,000 years ago. This older episode of dissolution could have occurred as early as 600,000 years ago, in a time of wetter climate, while Nash Draw was still forming as part of the channel system of the ancestral Pecos River (Bachman, 1980).

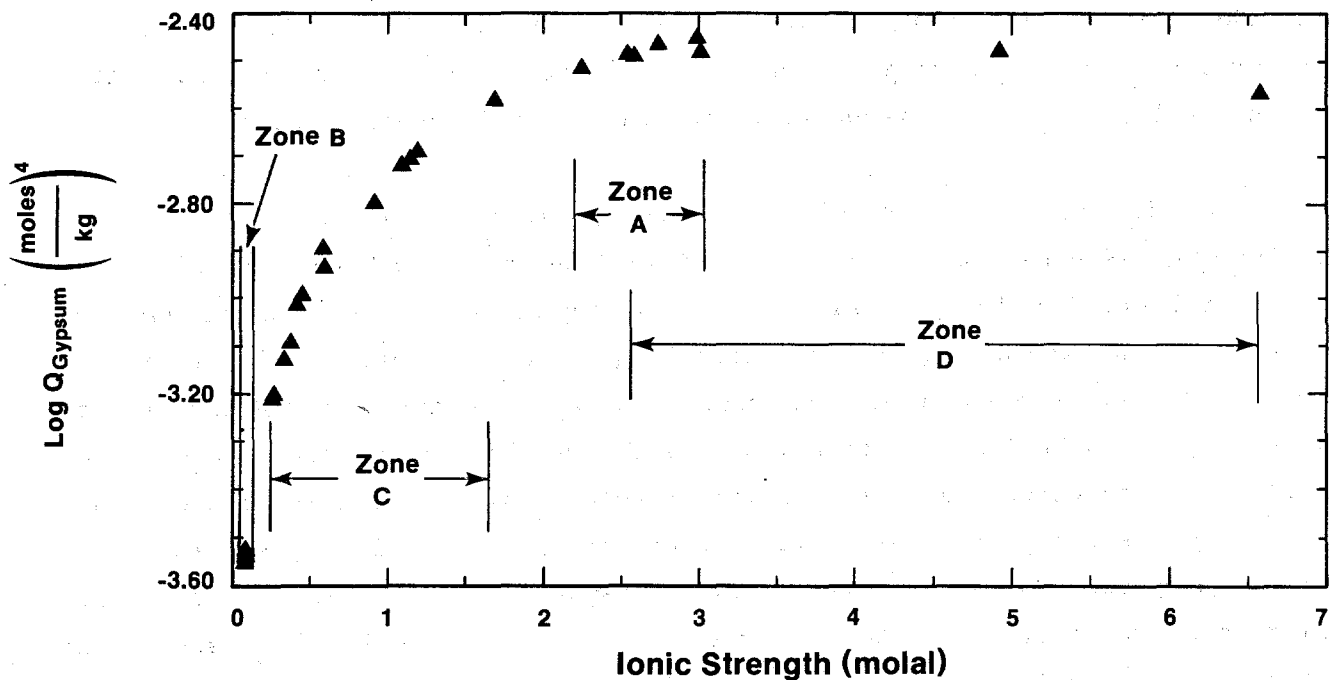
3.3.3.4 Chemical Reaction Model for Composition of Culebra Ground Waters.

Mineral saturation indices illuminate the nature of chemical processes that control solute concentrations in ground waters. Saturation indices in Culebra waters have been calculated for minerals commonly observed in the Ochoan Series. The computer code PHRQPITZ (Plummer et al., 1988), which uses the

Pitzer model for ion-interactions, was used. These calculations show that all waters are undersaturated with respect to halite, and with the exception of WIPP-29 in Zone D, all samples are undersaturated with respect to anhydrite. All water samples are saturated with respect to gypsum; dolomite and calcite saturation indices generally indicate supersaturation with respect to the carbonates. As discussed by Siegel, Robinson, and Myers (1989), the loss of CO₂ gas from the water during sample collection or uncertainties in the pH measurements resulting from the use of an activity scale inappropriate for saline NaCl brines may be responsible for the apparent supersaturation.

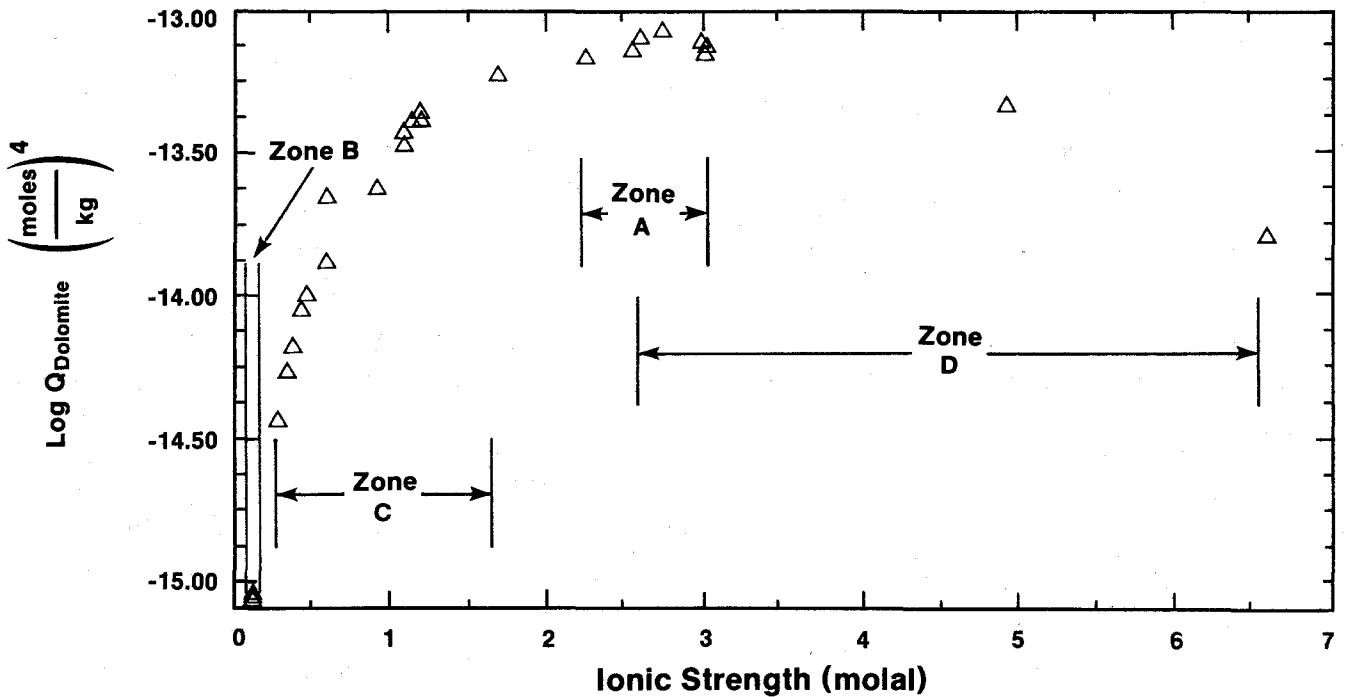
A partial-equilibrium model for the chemical evolution of water in the Culebra Dolomite has been proposed by Siegel, Robinson, and Myers (1989). In a partial-equilibrium system, solution/mineral equilibria shift nearly reversibly in response to an irreversible process (Helgeson, 1968; Plummer, 1984). All Culebra water samples that have been analyzed are undersaturated with respect to halite. Dissolution of salt and the concomitant increase in salinity is an effectively irreversible chemical reaction affecting the water chemistry. Although the saturation indices for gypsum, calcite, and dolomite are near zero, the waters may still be capable of dissolving significant amounts of these phases. The increase in salinity caused by the dissolution of halite changes the apparent solubilities of carbonates and sulfates. Apparent solubilities of gypsum and dolomite increase up to 3 molal ionic strength and then decrease (Figures 3-18 and 3-19). Similar relationships exist between the solubilities of calcite and anhydrite and ionic strength. This means that as waters in the Culebra Dolomite gain solutes by dissolution of halite, they may either dissolve or precipitate carbonates and sulfates depending upon the ionic strength.

Isotopic studies of minerals and waters provide some support for this model. Stable-isotope compositions of carbonates indicate no recrystallization of dolomite in equilibrium with the ground water now found in the Culebra Dolomite, but local precipitation of calcite at the expense of dolomite has apparently occurred in samples from WIPP-33 in the Magenta and possibly the Culebra Dolomites. Dissolution of dolomite still is possible, which would leave neither mineralogical nor isotopic record. Thus, the mineralogical and isotopic records are consistent with widespread dissolution of dolomite and



TRI-6330-81-0

Figure 3-18. Relationship between apparent solubility product (log Q) for gypsum and ionic strength in Culebra water samples (Siegel, Robinson, and Myers, 1989). Log Q is calculated from the thermodynamic solubility constant log K and the activity coefficients of the reactants ($\log Q = \log K^{\circ} - \log \gamma_{\text{Ca}^{2+}} - \log \gamma_{\text{SO}_4^{2-}} - 2 \log a_{\text{H}_2\text{O}}$). The activity coefficients γ_i and activity of water $a_{\text{H}_2\text{O}}$ were calculated from the water composition analyses listed in Table 1 of Siegel, Robinson, and Myers (1989), using the PHRQPITZ code (Plummer et al., 1988). See Section 4.2.2 in Siegel, Robinson, and Myers (1989) for discussion of method of calculation.



TRI-6330-83-0

Figure 3-19. Relationship between apparent solubility product (log Q) for dolomite and ionic strength in Culebra water samples (Siegel, Robinson, and Myers, 1989). Log Q is calculated from the thermodynamic solubility constant and the activity coefficients of Ca^{2+} , Mg^{2+} , and CO_3^{2-} . Activity coefficients were calculated for the water compositions listed in Table 1 in Siegel, Robinson, and Myers (1989). See Section 4.2.2 in Siegel, Robinson, and Myers (1989) for discussion of method of calculation.

local precipitation of calcite, which are indicated to be possible by the thermodynamic calculations.

Although reprecipitated carbonate in the Rustler Fm. under the present hydrologic regime appears to be rare, reprecipitated gypsum appears to be common. $^{87}\text{Sr}/^{86}\text{Sr}$ ratios (Figure 3-15) indicate that the calcium sulfate was not imported by dissolution in a near-surface weathered recharge zone. The variations in D/H ratios in the waters of crystallization of Rustler gypsum attest to recrystallization in the presence of meteoric water. Although most of the dissolved calcium sulfate originated locally within the evaporite section, the solid calcium sulfate hydrated in response to influx of meteoric water (Figure 3-16). The variations in D/H ratio, both laterally and vertically, attest to differing generations of meteoric water of different isotopic compositions hydrating the sulfate, or else differing water/rock ratios with an isotopically uniform reservoir contributing to the crystallographically bound water, or some combination of the two. Thus, there is isotopic as well as thermodynamic indication that gypsum has recrystallized (both dissolved and reprecipitated) in the presence of Rustler ground waters.

3.3.3.5 Conclusion. The geochemical and isotopic data presented in this section suggest that inferences about flow direction and velocity based on hydrologic testing may not be applicable to directions and velocities in the past 10,000 years, or in the next 10,000 years, the interval of interest to regulatory agencies governing radioactive-waste repositories. The present-day regional water-flow directions are not consistent with the salinity distribution at the WIPP site, given the assumption of steady-state, confined flow.

Modern flow within the Culebra Dolomite at and near the WIPP site appears to be largely north-to-south, except in relatively low-transmissivity areas directly affected by either the high-transmissivity zone in the southeastern portion of the site or by Nash Draw west of the site. However, hydrochemical facies Zone B, a facies with low salinity and element ratios inconsistent with halite dissolution, lies downgradient from more saline water in Zone C. One view, based partially on uranium-isotope disequilibrium data, suggests that this apparent anomaly can be explained by a change in flow direction in the

past 30,000, perhaps 12,000, years. Prior to that time, the recharge direction was dominantly from the west-northwest.

The amount of possible vertical flow into and out of the Culebra Dolomite near the center of the WIPP site cannot be determined from the hydrologic data alone. Isotopic and mineralogic data suggest that vertical material transport into the Culebra Dolomite at a few locations in the WIPP area and to the east and south is currently not occurring and has not occurred to a significant degree for several thousand years.

A model for the chemical evolution of water in the Culebra Dolomite suggests that dissolution of salt and the concomitant increase in salinity is an important irreversible process affecting water chemistry. The solubilities of the carbonate and sulfate minerals increase over the range of ionic strengths observed in Zones A, B, and C. Thus, the Culebra waters in these zones are capable of dissolving additional halite and anhydrite and of dissolving or precipitating gypsum, calcite, and dolomite.

3.3.4 Radionuclide Retardation in the Culebra Dolomite

The major conclusions of Section 3.3.4 are listed below.

- If large amounts of organic ligands and brine are mixed into the Culebra Dolomite during human intrusion, radionuclide K_d 's applicable to transport in the Culebra will be lower than the values assumed in the FEIS.
- The usefulness of K_d 's in transport modeling is limited, because their use assumes that the reactions involved are reversible, and because the coefficients do not distinguish among such processes as sorption, precipitation, and coprecipitation.
- K_d 's assumed here are estimated from experimentally measured data by considering the expected ranges in pH, Eh, concentration of organic compounds, ionic strength, and carbonate complexation of brines. The estimated K_d 's are a compromise between empirical data and calculations for simplified systems.

- Assuming that the sorption of actinides onto surface hydrolysis sites of mixed-layer clays is similar to the sorption behavior of U and Pu onto iron hydroxides (goethite), K_d 's may be reduced by several orders of magnitude, but K_d 's of zero are extremely unlikely.

3.3.4.1 Limitations in the Use of Distribution Coefficients (K_d).

Radionuclide distribution coefficients (K_d) are used in transport codes to calculate the partitioning of radioelements between ground water and rock. The K_d is defined as

$$K_d = \frac{\text{amount of radionuclide per gram rock}}{\text{amount of radionuclide per mL solution}}$$

Although convenient for use in transport equations, K_d 's are based on a number of questionable or invalid assumptions. In theory, the notation K_d is used for the thermodynamic distribution coefficient describing reversible sorption or coprecipitation. Most measured K_d values are based solely on measurements of radionuclide concentrations remaining in solution after contact with the rock of interest. Commonly used techniques cannot distinguish among several processes that can lead to loss of the radionuclide from solution, including sorption, precipitation, and irreversible incorporation (coprecipitation) of the radionuclide into a precipitate formed from the constituents of the background electrolyte. The extent of sorption of the radionuclide onto a substrate depends strongly on the nature of several reactions that compete for both the radionuclide and the sorption sites. These include hydrolysis, complexation of the radionuclide with inorganic or organic ligands, and competition with other sorbing species for the sorption sites. Rather than being a constant, in general the K_d for an element depends strongly on a large number of solution and solid properties.

The use of a constant K_d in solute-transport calculations is accurate only when several conditions are met:

1. Reactions such as precipitation, dissolution, and colloid formation do not change the aqueous concentration of the solute along the flow path;

2. The compositions of water and rock along the flow path are the same as those used in the K_d experiment;
3. All aqueous species containing the solute are in chemical equilibrium at all points along the flow path; and
4. The extent of sorption is independent of the concentrations of solute and the amount of solid present, i.e., independent of the rock/water ratio.

Most of these conditions are not met at the WIPP repository and site. Water chemistry varies spatially and temporally along potential radionuclide flow paths (Sections 3.3.2 and 3.3.3; Siegel, Lambert, and Robinson, 1989); therefore, the amount of sorption would be expected to deviate considerably from the amount calculated from any single K_d value. As discussed below, changes in the pH, partial pressure of CO_2 , and concentrations of complexing ligands and competing cations can increase or decrease the K_d by several orders of magnitude.

Table 3-13 compares radionuclide distribution coefficients (K_d 's) used in the radionuclide-transport calculations of the FEIS (DOE, 1980a) to the ranges of values used in this report. The FEIS assumed that the salinity of the ground water in the Culebra Dolomite was 8,000 mg/L at all points along the flow path. It also assumed that radionuclide retardation within the Rustler Fm. could be calculated using the K_d values listed in Table 3-13 in equations for transport within porous media. Recent work, however, has shown that these assumptions are inadequate to accurately represent transport within the Culebra Dolomite. Geochemical and hydrological data presented in Sections 3.3.2 and 3.3.3 suggest that the salinity of water within the Culebra Dolomite is commonly higher than 8,000 mg/L, and that the concentrations of both organic and inorganic constituents will increase during reasonable release scenarios. K_d values are valid only for the conditions under which they were gathered; K_d 's obtained in studies cited by the FEIS will not be applicable for conditions now expected for radionuclide release. In addition, it is likely that much of the radionuclide transport will take place within discrete fractures; the use of the K_d values in transport equations for porous media may not be valid for the Culebra Dolomite. This section discusses the

Table 3-13. Comparison of Radionuclide Distribution Coefficients for Culebra Dolomite Used in the FEIS (DOE, 1980a) and in this report (K_d in mL/g)

<u>Element</u>	<u>FEIS K_d</u>	<u>K_d Range for Matrix in this Report²</u>
Pu	2100	25 to 300
Am	1460	100 to 500
Cm	NC ³	100 to 500
U	10	1 to 10
Np	350	1 to 10
Ra	25	0.05 to 100
Pb	NC ³	0.05 to 100
Th	2190	25 to 300

1. Total dissolved solids (TDS) of Culebra Dolomite assumed to be 8,000 mg/L along flow path.
 2. Actual K_d values used in numerical calculations depend on substrate and solution compositions, as defined by the case assumed for the calculation.
 3. NC = not considered in transport calculations of FEIS.
-

inadequacy of the assumptions used in the FEIS and the procedures used here to represent radionuclide retardation within the Culebra Dolomite.

The choice of "recommended" K_d values for the transport calculations described in Chapter 5.0 and Appendix E of this report required many subjective assumptions that cannot be supported rigorously. The values given in Appendix E are considered to be realistic in light of available data; however, research in progress may invalidate the logic and recommendations presented below. The following sections describe the expected geochemical

conditions in the Culebra Dolomite and provide a conceptual basis for estimating appropriate K_d values for the transport calculations.

3.3.4.2 Geochemical Conditions in the Culebra Dolomite. The geochemistry of the Culebra Dolomite under undisturbed conditions is summarized in Sections 3.3.2 and 3.3.3. Potential changes in the composition of the Culebra waters resulting from a breach of the repository that are important to radionuclide retardation are discussed here. Within the WIPP site, salinities of water in the Culebra Dolomite range from ~10,000 to >200,000 mg/l. The ground water is saturated with respect to gypsum, calcite, and dolomite and undersaturated with respect to halite and anhydrite. The ground water is in a state of partial equilibrium; dissolution of additional halite will be accompanied by dissolution of additional gypsum, calcite, and dolomite (Siegel, Robinson, and Myers, 1989).

In the repository, solution chemistry will be dominated by the composition of Salado brines, leachates from the waste, concrete, and steel drums, and the products of anaerobic microbial degradation. Fluids in contact with the waste will contain high concentrations of salts and unknown amounts of organic sequestering agents and radionuclides. These solutions from the waste panels will be modified by interactions with solids along transport paths through the drifts and shafts. As discussed in Sections 4.5 and 4.6, the uncertainties in the pH, redox conditions, and concentrations of radionuclides and other solutes in these fluids span many orders of magnitude.

The composition of radionuclide-bearing solutions at various locations within the Culebra Dolomite will depend on the composition and volume of the solution from the repository that reaches the aquifer. In Case I, the ratio of the flux of the repository fluid to the flux of Culebra water is assumed to be very small; therefore the major solute composition of the resultant fluid is assumed to be similar to that of the undisturbed Culebra Dolomite. Alternatively, if the mixing ratio (repository fluid/Culebra fluid) is high, then the resultant composition will resemble that of the repository fluid. In Case IIA, the composition of the fluid in the Culebra Dolomite is assumed to be affected by the high salinity of the Salado and Castile brines. In Cases IIB, IIC, and IID, it is also assumed that organic ligands from the waste are

brought to the Culebra Dolomite from the repository by brines from the Castile and Salado Fms., decreasing K_d 's.

The mineralogy of the Culebra Dolomite has been described by Searwards et al. (1989). The dominant mineral in the matrix is a fairly pure dolomite. Clay, gypsum, and calcite are distributed heterogeneously both vertically and horizontally in the matrix. Clay and quartz together comprise about 3% by weight of the matrix on average. Within the fractures, gypsum and corrensite, a mixed-layer chlorite/smectite, are most commonly observed. For the actinides, within the matrix, sorption by clay disseminated within the dolomite may dominate radionuclide retardation; within the fractures, uptake by clay may be the dominant retardation mechanism.

3.3.4.3 Review of Available K_d Data. K_d data relevant to the WIPP are summarized in Tables 3-14 and 3-15. The K_d data that were examined included those obtained for several reference clays in WIPP A and B brines (Table 3-16) in inorganic systems (Nowak, 1980), similar data for WIPP clay and dolomite in WIPP Brines A and B, Solution C and "Culebra H₂O" (Serne et al., 1977; Dosch, 1981; Dosch and Lynch, 1978) and data from experiments carried out using organic leachates from aerobic degradation of WIPP waste in WIPP Brine B with Culebra Dolomite (Paine, 1977; Dosch, 1979). Additional K_d values were obtained from a review of data contained in the International Sorption Information Retrieval System (ISIRS) reported by Tien et al. (1983). Data for saline waters with and without organics are summarized in Table 3-14; data for fresher waters are described in Table 3-15.

Data obtained in Brines A and B with added organic complexants (Paine, 1977; Dosch and Lynch, 1978; Dosch, 1979, 1981) are germane for Cases IIA and IIB. However, the compositions of these brines are not representative of the water in the repository horizon. As discussed above, organic and metal-containing waste, cement, and backfill additives will change the solution pH, dissolved organic carbon speciation, dissolved oxygen content and concentrations of metal ions. Comparison of K_d data obtained in these solutions provides insight into the effects of high concentrations of competing cations and complexing ligands on sorption.

Table 3-14. Sources of K_d Data Used to Estimate Values for Repository (Case I) and Culebra (Case II) Transport (saline water \pm organic ligands). See Table 3-16 for compositions of WIPP Brines A and B.

Reference	Water	Rock	Organics	Reported K_d Range						
				Pu	Am	Cm	U	Np	Eu	
Nowak (1980)	Brine A	Bentonite	None	2.3 x 10 ³ to 3.4 x 10 ³						350
	Brine B	Bentonite	None	2 x 10 ⁴ to 4 x 10 ⁴	4.1 x 10 ³ to 1.4 x 10 ⁴					1.4 x 10 ³ to 1.7 x 10 ³
Dosch and Lynch (1978)	Brine A	Clay	None							> 1 x 10 ³
	Brine B	Clay	None	4 x 10 ⁴ to 7.2 x 10 ⁴	310 to 1100	2.7 x 10 ³ to 1.9 x 10 ⁴				> 1 x 10 ⁴
	Dissoln Brine	Halite (As Clay)	None None	17 to 59 (1 x 10 ⁴ to 2 x 10 ⁴)	11 to 306 (3.8 x 10 ³ to 1.8 x 10 ⁵)	56 to 354 2 x 10 ⁴ to 2.1 x 10 ⁵				
	Brine A	Rustler Dolomite								> 5 x 10 ³
	Brine B	Rustler Dolomite	None	2.1 x 10 ³ to 5.4 x 10 ³	3.2 x 10 ² to 2.6 x 10 ³	1.3 x 10 ³ to 1.2 x 10 ⁴				> 5 x 10 ³
	Brine B	Anhydrite	None	6.7 x 10 ³	2.9 x 10 ²	4.2 x 10 ³				> 1 x 10 ³
Dosch (1981)	Brine A	Culebra Dolomite	None				0 to 2			
	Brine B	Culebra Dolomite					1.5 to 608			
Serne et al. (1977)	Brine A	Rustler Dolomite								29 to 52
	Brine B	Culebra Dolomite	None	50 to 200	340 to 1160	0.0 to 1.2 x 10 ⁴	0 to 7.1	10 to 28		22 to 40

Table 3-14. Sources of K_d Data Used to Estimate Values for Repository (Case I) and Culebra (Case II) Transport (saline water \pm organic ligands). See Table 3-16 for compositions of WIPP Brines A and B.

Reference	Water	Rock	Organics	Reported K_d Range					
				Pu	Am	Cm	U	Np	Eu
Paine (1977) and Dosch (1979)	Brine B	Culebra Dolomite	EDTA, etc.	25 to 6000	100 to 2.8×10^4				
	Brine B	Rustler Dolomite	Waste	560 to 1.8×10^4	5.7×10^4 to 1.7×10^5				70 to 660
	Brine B Brine B	Anhydrite Clay	Waste Waste						400 2.8×10^4
Tien et al. (1983)	Salt Brine (TDS: $> 3 \times 10^4$)	Claystone	None	3×10^2 to 1×10^4 Ra = 3	90 to 1000	3×10^2 to 1×10^4	50		5 to 2000
		Carbonate	None	50 to 6×10^3	3×10^2 to 2×10^4	3×10^2 to 1×10^4	0 to 3		15 to 30
		Salts	None	20 to 1×10^4	3×10^2 to 2×10^5	3.5×10^2 to 2×10^5			

Table 3-15. Sources of Additional K_d Data Used to Estimate Values for Culebra Dolomite in Cases I and II (Inorganic Solutions). See Table 3-16 for compositions of solutions.

Reference	Water	Rock	K_d Range					
			Pu	Am	Cm	U	Np	Eu
Dosch and Lynch (1978)	Solution C	Rustler Dolomite	2.4×10^3 to 7.3×10^3	2.4×10^3 to 2.2×10^4	4.2×10^4 to 1.1×10^5			$> 1 \times 10^4$
	Solution C	Clay	4×10^4 to 1.8×10^5	2.3×10^3 to 3.5×10^3	1.6×10^5 to 4.2×10^5			$> 1 \times 10^4$
	Solution C	Anhydrite	7.7×10^4	2.2×10^3	1.8×10^5			$> 1 \times 10^3$
Dosch (1981)	Solution C	Rustler Dolomite					13 to 175	
	H2(B,C)	Culebra Dolomite					0.6 to 7.4	
Lynch and Dosch (1980)	H2(B,C)	Rustler Dolomite	83 to 1055	119 to 383				
Serne et al. (1977)	Solution C	Culebra Dolomite	42 to 2206	2500 to 3000	1.6×10^3 to 4.3×10^4	0 to 16	5 to 35	
Tien et al. (1983)	Saline H ₂ O	Claystone	300 Ra = 30	200 to 1×10^4	1000	20	1 to 75	
	(TDS: 5×10^3 to 3×10^4)	Carbonate	500 Th = 2.7×10^3 to 1×10^4	3000	3000	3	21	
	fresh H ₂ O	Claystone	30 to 1×10^4 Ra = 300	700 to 1×10^4	700 to 1×10^5	1.270	2 to 400	
	(TDS: < 5×10^3)	Carbonate	100-7000 Th = 1×10^3 to 1×10^5	500 to 1×10^5	6×10^3 to 4×10^4	0 to 15	15 to 30	

Table 3-16. Nominal Compositions of Ground-Water/Brine Simulants Used in Batch K_d Experiments Summarized in Tables 3-14 and 3-15

Species*	Brine A	Brine B	Solution C	H2(B,C) Culebra H2O
Na	42,000	115,000	100	2,850
K	30,000	15	5	105
Mg	35,000	10	200	140
Ca	600	900	600	685
Fe	2	2	1	0.07
Sr	5	15	15	--
Li	20	--	--	--
Rb	20	1	1	--
Cs	1	1	1	--
Mn	--	--	--	0.17
Si	--	--	--	2.6
Cl	190,000	175,000	200	3,750
Br	400	400	--	--
I	10	10	--	--
F	--	--	--	1.8
SO ₄ ²⁻	3,500	3,500	1,750	3,100
B(BO ₃ ³⁻)	1,200	10	--	9.8
HCO ₃ ⁻	700	10	100	59.5
NO ₃ ⁻	--	--	20	0.09
pH	6.5	6.5	7.5	7.5

*All concentrations given in units of mg/liter.

K_d data obtained in the "Culebra H₂O", designated H2(B,C) in Table 3-15 (Dosch and Lynch, 1978; Dosch, 1981), are most relevant for sorption and transport in Case I. This solution (TDS = 10,700 mg/L; pH = 7.5; bicarbonate alkalinity = 59.5 mg/L) represents an average composition between waters

sampled in well H-2B (sampled 2/77) and H-2C (sampled 3/77). Robinson (1989; see also Section 3.3.2), however, noted that it is possible that none of the samples collected from the H-2 pad are representative of Culebra water. Contamination by water from other horizons or from another source is indicated by changing concentrations of Na and Cl and density over a 9-year period. In addition, water from wells near the H-2 well pad are considerably more saline than the "Culebra H₂O."

Solution C described by Dosch and Lynch (1978) and Dosch (1981) was considered to be representative of stock wells south and southwest of the WIPP site. This water is relatively fresh (TDS = 2,993 mg/L) and mildly alkaline (pH = 7.5). In this report, transport within a solution this dilute has not been considered; however, K_d data from this solution provide some insight into the effects of dilution on sorption.

The compositions of the solutions listed in Table 3-16 do not adequately bracket the range in fluid chemistry that is plausible for the release cases considered in this report. However, these solutions can be used in conjunction with the theoretical principles described in the next section as the basis for estimating K_d 's under conditions assumed in the transport calculations.

3.3.4.4 Extrapolation of K_d Values: General Principles. The uncertainties in the composition of the water that will be produced by mixing fluids from the repository and aquifer require consideration of large ranges of pH, Eh, organic content, and carbonate content of the ground waters. These possible variations in solution chemistry could result in order-of-magnitude changes of the K_d 's from the values obtained in the experimental studies listed in Tables 3-14 and 3-15.

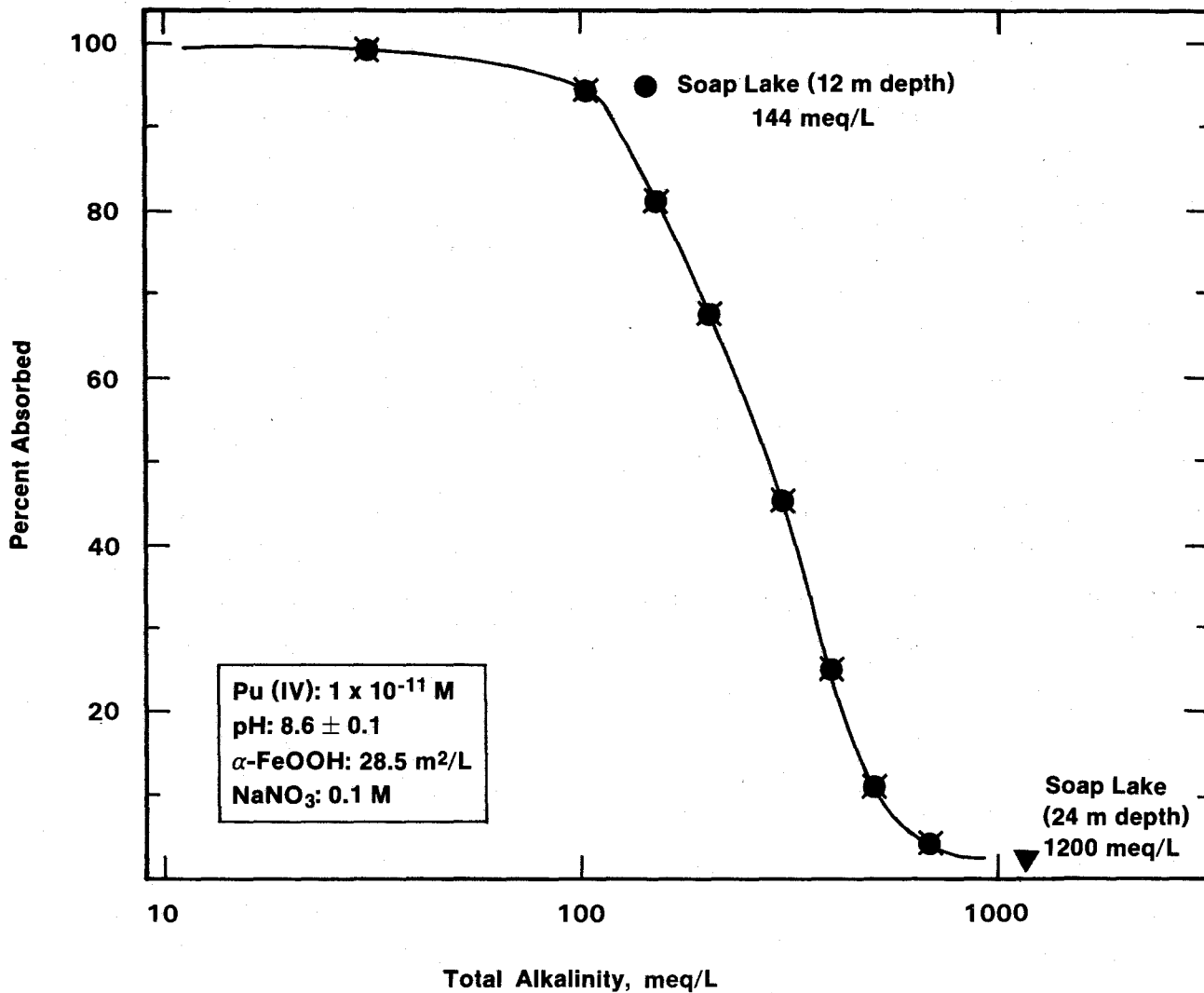
Evaluating the magnitude of the changes in the K_d 's requires several assumptions about the nature of sorption reactions occurring on the substrates. The sorption of trace metals onto salt-like minerals such as gypsum, calcite, and dolomite is poorly understood; the paucity of relevant data precludes extrapolation of sorption behavior to physicochemical conditions that differ from those specifically examined in the experimental

studies (Tables 3-14, 3-15). For the transport calculations in Chapters 6.0 and 7.0 and Appendix E, some qualitative extrapolations were based solely on the predicted aqueous speciation of the radionuclides.

Qualitative predictions about the surface properties of the clays in the Culebra Dolomite over a wide range of physicochemical conditions are possible. Here it is assumed that radionuclides could be adsorbed onto mixed-layer clays in the fractures and matrix by both fixed-charge ion-exchange sites and surface hydroxyl groups (cf. Kent et al., 1988). The charge on the ion-exchange sites is determined by cationic substitutions within the crystal lattice of the clay and is independent of the solution composition. The ratio of protonated and deprotonated surface hydroxyl (-OH) groups determines the charge resulting from surface hydrolysis and is related to the pH of the solution.

The sorption chemistry of hydrous iron oxyhydroxides is dominated by reactions at surface hydrolysis sites. This report assumes that these sites are similar to the surface hydrolysis sites of clays. Data and calculations from studies of simple, well-constrained iron oxyhydroxide systems have been used to evaluate possible variations in the extent of actinide sorption onto these sites as a result of changes in carbonate complexation, ionic strength, competition for sorption sites by other cations, such as Mg^{2+} and Ca^{2+} , and organic complexation.

Figure 3-20 illustrates the effects of carbonate alkalinity on the sorption of Pu(IV) onto goethite (α -FeOOH) in simple electrolyte solutions (0.1 M $NaNO_3$) and surface waters. The amount of plutonium sorbed by the iron oxyhydroxide varied from 100% to <1% over the alkalinity range of 10 meq/L to 1,000 meq/L. For comparison, bicarbonate alkalinity of Culebra waters within the WIPP site boundary ranges from 0.66 meq/L (40 mg/L) to 2.0 meq/L (120 mg/L) (Section 3.3.2). The alkalinity of reference Salado fluids at the repository level before waste emplacement is about 14 meq/L (Section 3.2.2). Degradation of the waste and reaction with backfill additives may change the alkalinity; however, because of uncertainties about the nature of microbial reactions and backfill additives, no estimate of the alkalinity of the repository fluid after repository closure is available.



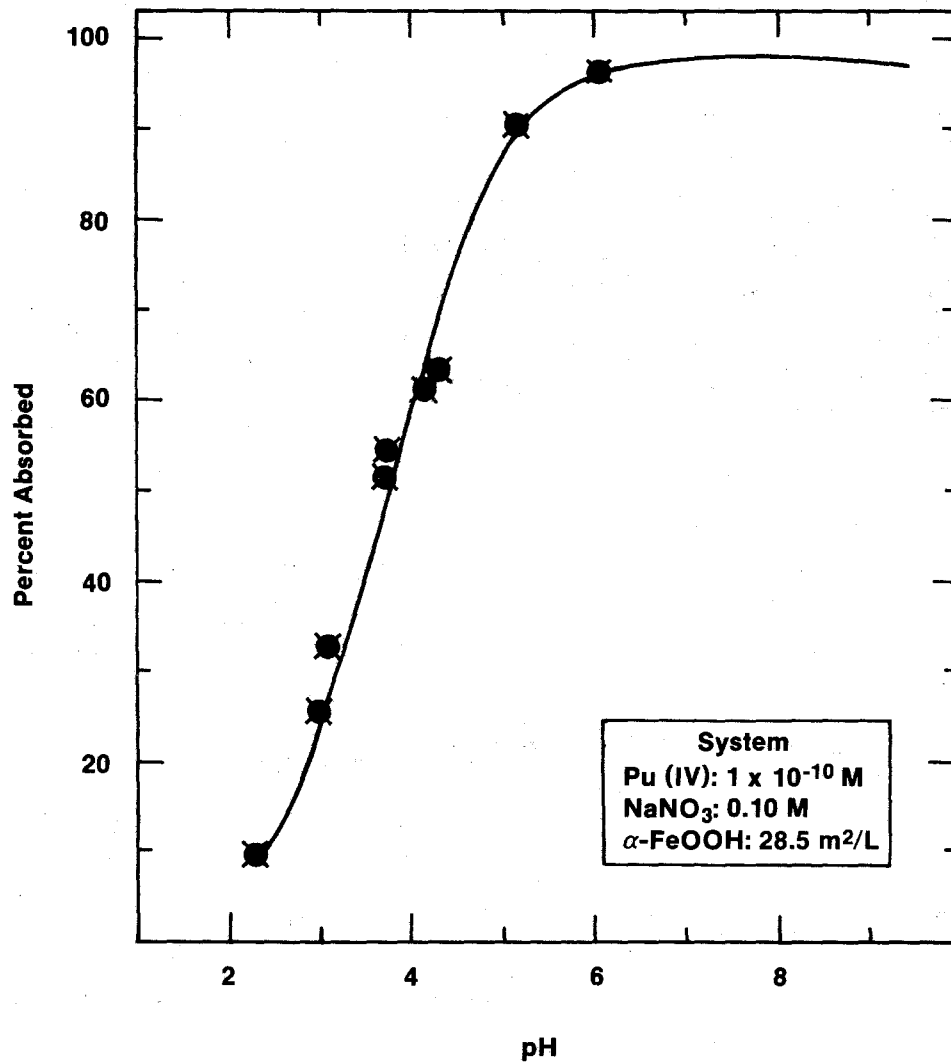
TRI-6330-39-0

Figure 3-20. Effect of variation in carbonate alkalinity on the adsorption of Pu(IV) on goethite in 0.1 M NaNO₃ solution at pH = 8.6 (after Sanchez et al., 1985). Total plutonium concentration is 10⁻¹¹ M; surface area of the goethite suspension is 28.5 m²/L; radionuclide contact time was 96 hours. Adsorption from two waters from Soap Lake, Washington, is also shown.

The effect of pH on Pu(IV) sorption in the simple electrolyte is illustrated by Figure 3-21. Sorption decreases from >95% at pH = 6.0 to <20% at pH = 2.3. A decrease in sorption over a narrow range is commonly observed in studies of cationic sorption on iron oxyhydroxides; it is related to changes in aqueous speciation and surface charge. The fluids in the repository could become acidic as a result of microbial degradation of the waste (Section 4.5); therefore, decreases in the K_d to values much smaller than those listed in Tables 3-14 and 3-15 must be considered in the transport calculations.

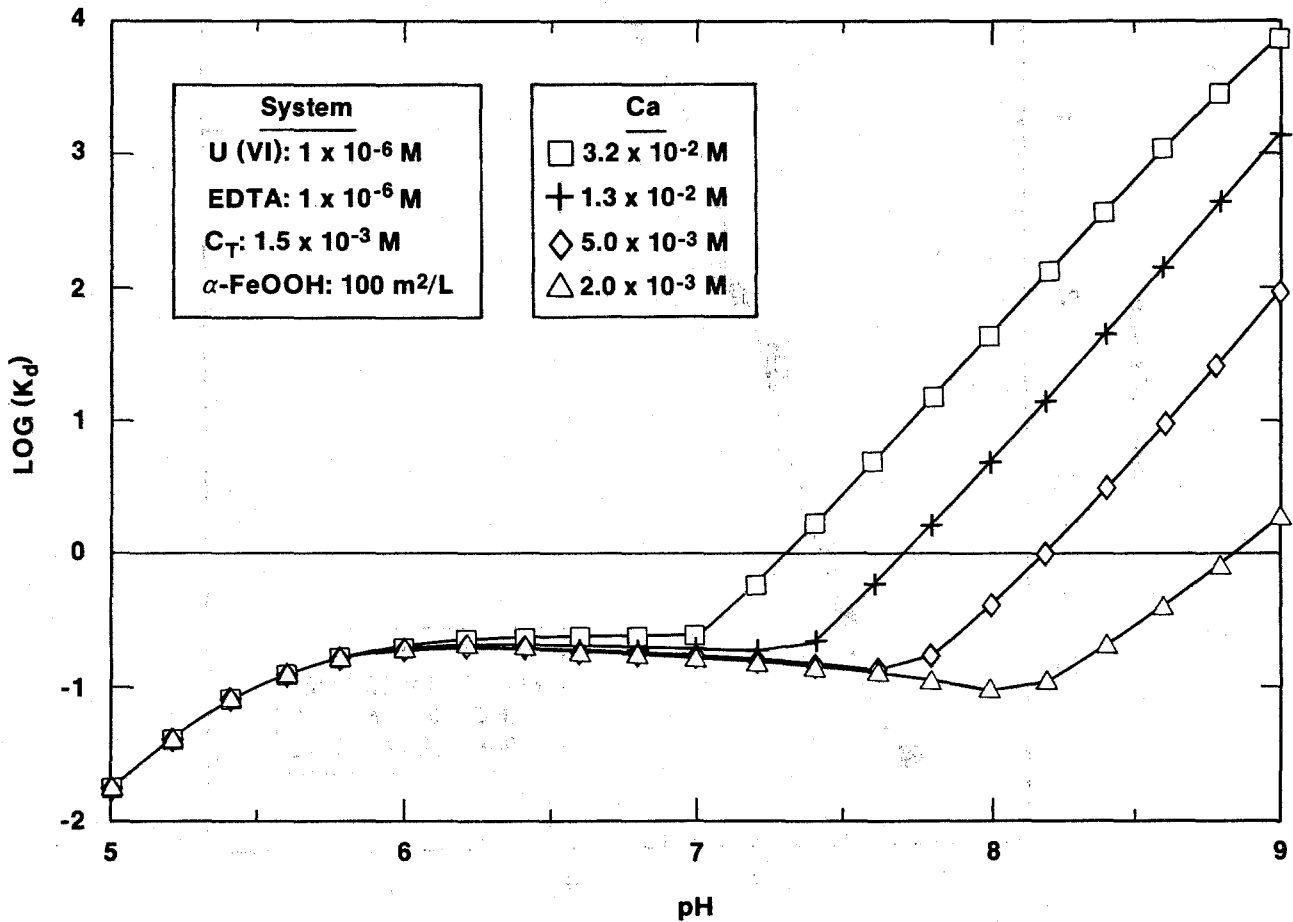
Additional examples of the effects of changes in solution composition on K_d are illustrated in Figures 3-22 and 3-23. In these figures, the K_d 's were calculated from predicted concentrations of sorbed and aqueous species containing uranium in simple electrolytes (0.1 M NaCl). The simulations were carried out with the HYDRAQL computer code (Papelis et al., 1988) using thermodynamic data. The effects of pH and Ca concentration on the sorption of uranium onto goethite are illustrated in Figure 3-22. This figure shows that the extent of sorption (expressed as $\log [K_d \text{ mL/g}]$) can range from -1.0 to +4.0 over a pH range of 5 to 9 and a Ca-concentration range of $2 \times 10^{-3} \text{ M}$ to $3 \times 10^{-2} \text{ M}$. In this example, the sorption of uranium is affected by competition between Ca^{2+} and UO_2^{2+} for EDTA ligands and sorption sites. At the higher Ca^{2+} concentrations, most of the EDTA is bound up by calcium, leaving the UO_2^{2+} ions free to sorb onto the goethite. The solution considered in these simulations is less saline than those observed at the WIPP site, but qualitatively similar deviations in solution composition and sorption behavior could result from mixing solutions from the repository and the Culebra Dolomite.

Other factors, such as the rate of CO_2 consumption and generation, may indirectly affect the amount of sorption onto surface hydrolysis sites. The calculations illustrated in Figure 3-22 assume a fixed total CO_2 content (10^{-6} M). Under these conditions, a limited amount of carbonate is available for carbonate complexation in solution. A large fraction of the total uranium will not be complexed with carbonates and may sorb onto the surface hydrolysis sites, increasing the calculated K_d at alkaline pH values. If the gas-generation rate is high enough within the repository to maintain a constant or



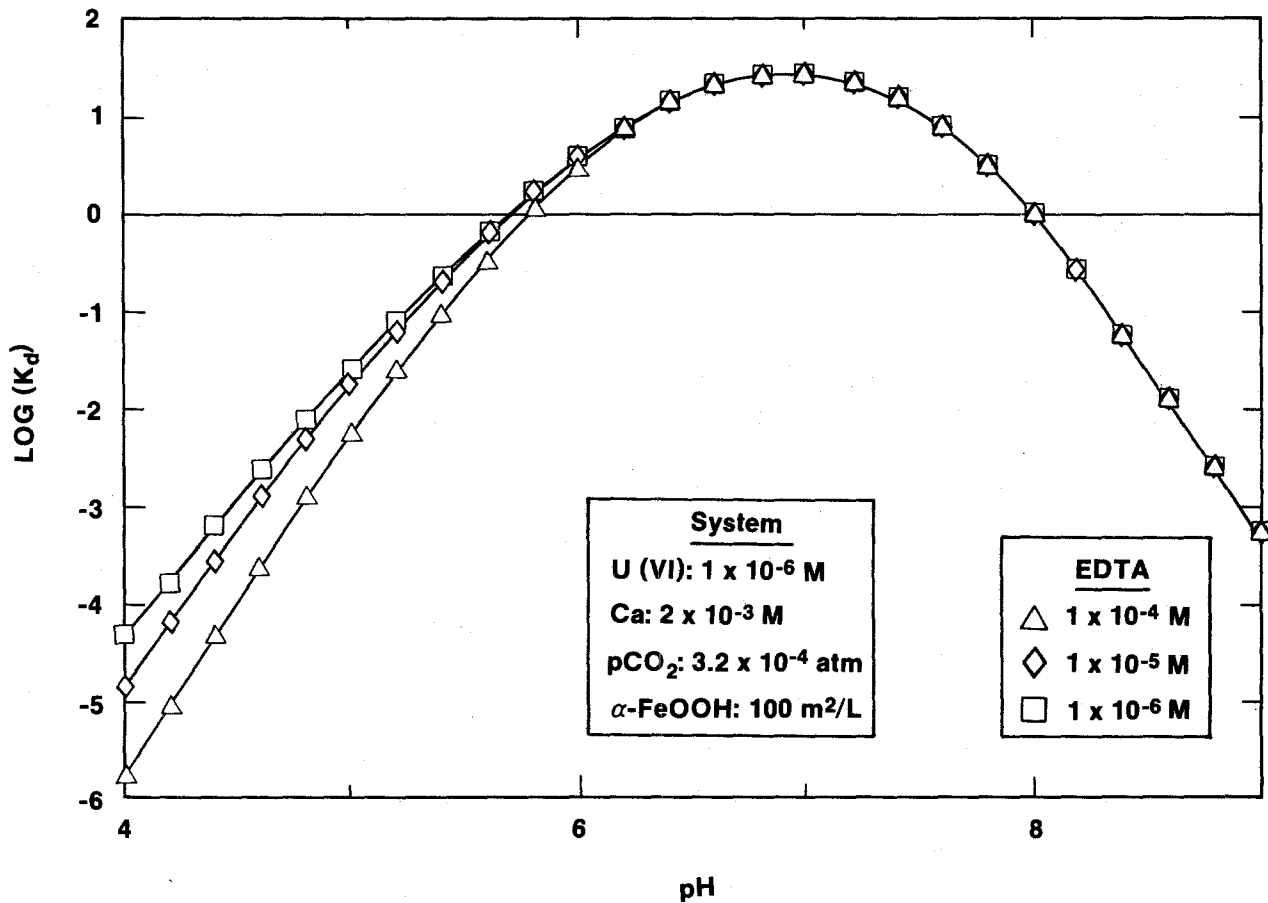
TRI-6330-40-0

Figure 3-21. Effect of variation in pH on adsorption of Pu(IV) onto goethite in 0.1 M NaNO₃ solution (after Sanchez et al., 1985). Total plutonium concentration was 10^{-10} M; surface area of goethite suspension was 28.5 m²/L; contact time was 24 hours.



TRI-6330-41-0

Figure 3-22. Calculated K_d for sorption of U(VI) onto a goethite substrate as a function of pH at fixed total carbon concentration, in the presence of EDTA (after Leckie, 1989). K_d 's are shown for several levels of calcium concentration. Surface area of the substrate (α -FeOOH) was 100 m²/L; total carbon (C_T) was 1.5×10^{-3} M; total uranium concentration was 10^{-6} M.



TRI-6330-42-0

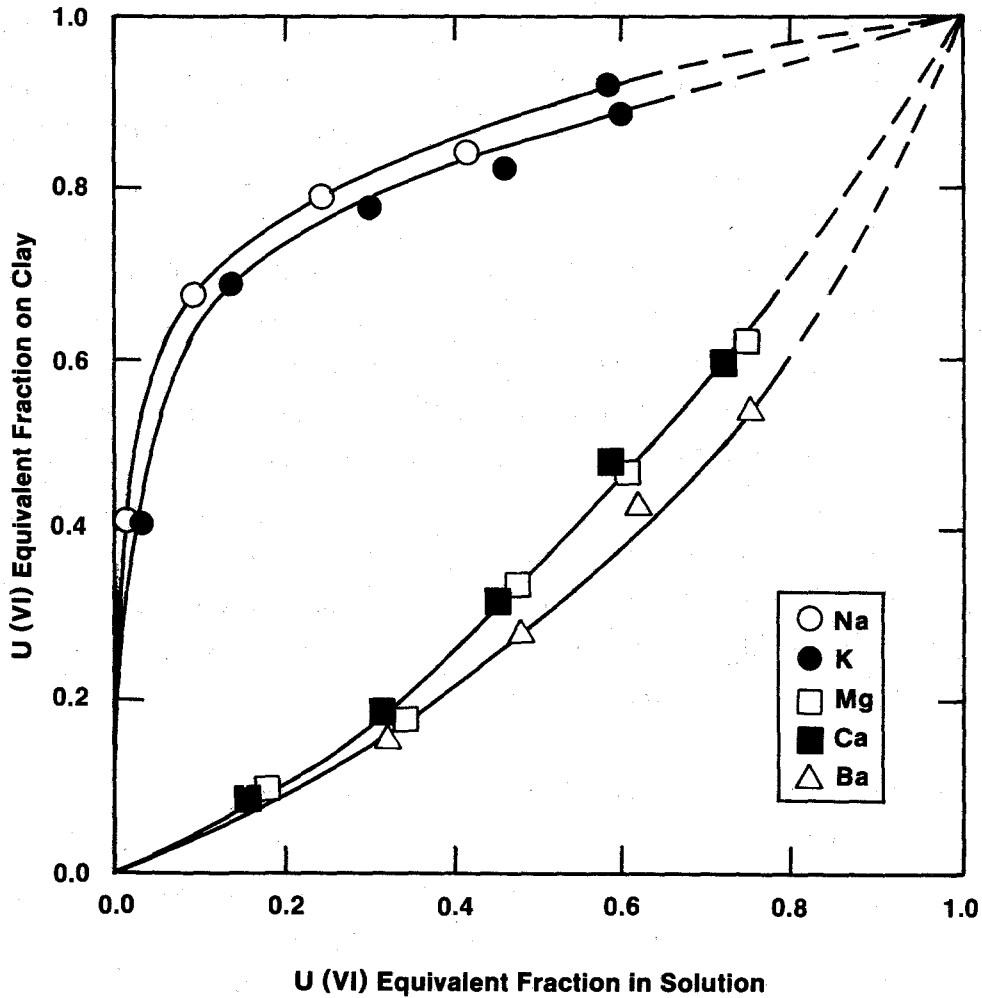
Figure 3-23. Effect of variable EDTA concentration and pH on calculated K_d for sorption of U(VI) onto goethite at a fixed partial pressure of CO_2 and Ca concentration (after Siegel, Phillips, et al., 1989). K_d values are plotted for three EDTA concentrations. Total uranium concentration (U_T) was 10^{-6} M; CO_2 was 3.2×10^{-4} atmospheres; surface area of substrate (α -FeOOH) was 100 m²/L; calcium concentration was 2×10^{-3} M.

increasing $p\text{CO}_2$ upon mixing in the Culebra, a large reservoir of CO_2 will exist to supply carbonate for formation of non-sorbing actinide complexes.

This condition may result in a relationship between the K_d and pH similar to that shown in Figure 3-23. The K_d reaches a maximum at a near-neutral pH and decreases to very low values at moderately alkaline pH.

Uptake of actinides will also occur on the fixed-charge sites in clays and may dominate sorption under acidic conditions. Tsunashima et al. (1981) estimated that under acidic conditions (pH = 4 to 6) the maximum sorption capacity of montmorillonite (a mineral similar to the smectitic component of the Culebra clays) for uranium was equal to the total cation exchange capacity of the clay (82 meq/100 g). Moderate concentrations of carbonate, organic complexing ligands, Mg^{2+} , and Ca^{2+} , however, will prevent all of the fixed-charge sites from being occupied by actinide ions. Figure 3-24 shows the partitioning of uranium between solution and montmorillonite under oxidizing conditions in systems containing other cations that compete for sorption sites on the clay. Uranium will displace Na^+ and K^+ from sorption sites, but Ca^{2+} and Mg^{2+} are preferentially sorbed instead of uranium onto the montmorillonite. Thus, uranium and the other actinides may not sorb strongly onto the fixed-charge sites of Culebra clays if calcium- and magnesium-rich solutions from the repository are mixed into the aquifer.

The redox speciation of radioelements in the repository or the Culebra is not known. As discussed in Section 4.2, microbial degradation of organic material in the waste will probably consume all available oxygen, and anoxic conditions may prevail. Reduction of the radioelements to lower oxidation states is likely under these conditions; however, the rates of the redox reactions are not known, and the speciation at any given time cannot be predicted with the available data. The K_d values in Tables 3-14 and 3-15 were based on review of experimental data obtained under oxic conditions. The sorption behavior of the radioelements under anoxic conditions cannot be extrapolated from these data. Some field studies of radionuclide partitioning between soils, solutions, and organic matter suggest that the K_d 's of radioelements in their lower oxidation states will be lower than those reported for the oxidized forms (Choppin and Allard, 1985).



TRI-6330-43-0

Figure 3-24. Variations in adsorption of U(VI) onto montmorillonite with constant amounts of clay, water, and total ionic strength and variable proportions of uranyl [U(VI)] ion and other cations (Tsunashima et al., 1981). Relative proportions of charged sites on the clay occupied by uranium are shown as equivalent fractions of uranium on clay plotted against equivalent fractions in solution. (Concentration in equivalents equals molarity x charge of ion).

3.3.4.5 Procedure for Choice of Recommended K_d Values for Transport in the Culebra Dolomite. Tables 3-13 and E-10 to E-12 describe the distribution coefficients used in transport calculations in this report. The following procedure was used to obtain the recommended K_d values. First, initial ranges of values were obtained from studies carried out under chemical conditions that were similar in some way to those expected under a variety of mixing ratios in the Culebra Dolomite. Second, K_d values obtained under conditions closest to those expected in the WIPP were extrapolated to reference conditions consistent with the descriptions of Cases I and II. Data from parametric studies or theoretical calculations for simple, well-constrained systems were used to estimate the magnitude of the change in the K_d that might be related to differences between the actual experimental conditions and the range of conditions possible for the cases. Finally, uncertainties in the future physicochemical conditions in the repository and along the flow path in the Culebra Dolomite were considered. Possible deviations of K_d values from those estimated in the previous step were evaluated, and a set of conservative, realistic K_d 's was selected.

The data for simple systems discussed above suggest that the amount of sorption of actinides onto either clays in the fractures or dolomite in the matrix of the Culebra Dolomite could be several orders of magnitude less than that suggested by the K_d data in Tables 3-14 and 3-15. Although it is possible that under some extreme conditions, the K_d 's will be close to zero, there is evidence that some sorption will occur; therefore, the K_d 's were assumed not to be zero. In general, it was assumed that K_d 's in brines (Cases IIA and IIB) would be lower than those in undisturbed Culebra waters (Case I), and that K_d 's for clays would be higher than those for dolomite. The K_d 's for Case IIA were chosen to represent conditions under which the solution chemistry is dominated by the influx of inorganic salts from the Salado and Castile Fms. K_d values in Case IIB include the additional effects of organic ligands, which form complexes that do not sorb. Other explanations for the K_d values chosen for each element are given in Appendix E.2.4.

3.3.4.6 Use of K_d 's in Transport Equations. Simulating the migration of radionuclides within a fractured porous medium requires consideration of transport through discrete fractures and the adjacent porous matrix. Tables

3-14 and 3-15 (experimental values) and Tables 3-13 and E-10 (recommended, extrapolated values) contain K_d values that could be used to calculate radionuclide retardation in the matrix of the Culebra Dolomite when the entire matrix is accessible to the radionuclides over the time period of the simulation. Under these conditions, the retardation factor for the porous matrix is

$$R = 1 + \psi K_d \rho_R (1 - \phi') / \phi'$$

where ρ_R is the grain density (without pores) of the matrix, ϕ' is the matrix porosity, and ψ is a utilization factor equal to 1.0 for ideal porous media. In equivalent porous-medium calculations, the factor R is used directly (Chapter 6.0). It is assumed here that the effective porosity is equal to the total matrix porosity ϕ .

Tables 3-13, 3-14, 3-15, and E-11 (recommended values) contain K_d 's for the clays within the matrix and that line the fractures in the aquifer. No K_d data are available describing the uptake of Ra or Pb onto dolomite. This report assumes that these elements would sorb onto clay particles within the matrix. A utilization factor, ψ , can be used to calculate radionuclide retardation within a porous matrix in which only a fraction of the matrix participates in sorption (Neretnieks, 1980). A utilization factor of 0.01 was assumed for the Culebra matrix based on the 3% average weight fraction of clay and quartz observed in massive Culebra Dolomite blocks. The K_d 's for Ra and Pb in Table E-10 were obtained by multiplying the K_d 's for clays in Table E-11 for these elements by a factor of 0.01.

If the volume of the clay within the fractures is known, then K_d 's in the tables can be used to calculate retardation within the fractures using the following expression

$$R_f = 1 + \rho_c K_{dc} (\delta_c / \delta)$$

where K_{dc} is the distribution coefficient for the clay; ρ_c is the density of the clay (2.5 g/cc); δ_c is the thickness of the clay coating the fracture and δ is the fracture aperture (Neretnieks and Rasmusson, 1984).

Surface-area-based distribution coefficients K_a (mL/m²) for the clay (Table E-12) were calculated from the K_d 's assuming a surface area of 50 m²/g. This is similar to the surface area of 32 m²/g measured by Nowak (1980) on a reference montmorillonite used in europium-sorption studies and within the range of 15 to 88 m²/g measured by Soudek (1984) on montmorillonite used in ion-exchange studies. Surface areas were not measured on the clays used in any of the actinide-sorption studies listed in Tables 3-14 and 3-15. A retardation factor for use in a transport equation for fracture-dominated flow where sorption occurs on the surface of the fracture-fill clay can be calculated as

$$R_a = 1 + aK_a$$

where K_a is sorption ratio in Table E-12 and a is the specific surface of the fracture (fracture surface area per unit volume of fracture) (Neretnieks and Rasmusson, 1984).

3.3.4.7 Conclusion. The extent of sorption of actinides onto fracture surfaces and dolomite matrix in the Culebra Dolomite cannot now be predicted accurately because of uncertainties about the expected chemical environment of the aquifer after mixing of water from the Culebra Dolomite and fluid from the repository and the lack of relevant empirical K_d or thermodynamic data. In Appendix E.2.4, a set of recommended K_d values have been chosen based on a review of available K_d data, obtained in systems that are similar in some way to the reference conditions assumed in this report, and from insights gained from theoretical calculations of radionuclide behavior in simple, well-constrained systems. Many of the available K_d 's are large (>10,000), indicating significant sorption under specific experimental conditions. However, within the range of solution compositions that are possible for the Culebra Dolomite, there are conceivable conditions under which the K_d for any of the elements considered here could drop to very low values (<1). The recommended K_d values represent a compromise between empirical data that show that sorption will occur under some physicochemical conditions relevant to the WIPP and theoretical calculations that suggest that many factors can decrease the extent of sorption significantly under other conditions that are possible in the Culebra Dolomite.

3.3.5 Numerical Ground-Water-Flow and Transport Model of the Culebra Dolomite

The following are the major conclusions of Section 3.3.5.

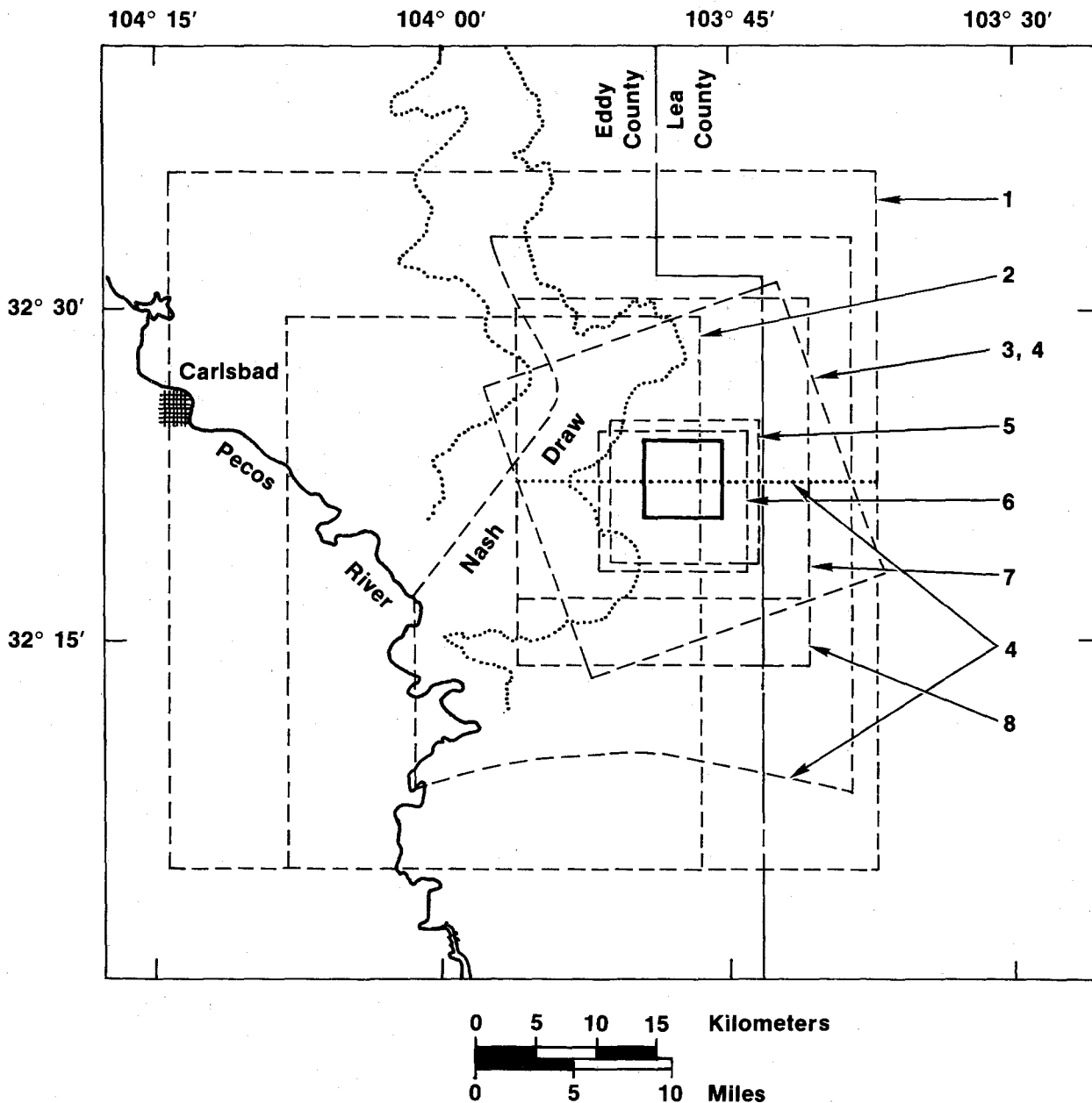
- Fracturing within the Rustler Fm. was recognized at the time of the FEIS (e.g., Mercer and Orr, 1979), but it could not be included in flow and transport modeling.
- Data indicating effects of fracturing on flow and transport are available from hydraulic interference tests at H-3, WIPP-13, and H-11. Conservative-tracer tests indicating the local role of fracturing have been conducted at H-3, H-6, and H-11. Interpretation of the multipad interference test at H-11 remains to be completed, as does interpretation and reporting of conservative-tracer tests at H-11 and H-6.
- Recent estimates of ground-water travel times in the Culebra Dolomite for undisturbed flow from a position directly above the center of the waste-emplacement panels to the southern boundary of the site have ranged from 5,100 to 13,000 years. Both estimates are based on porous-medium flow, i.e., they do not consider fracturing.
- Final interpretation of the recently completed multipad interference test at H-11 is expected to indicate that the zone of relatively high transmissivity between H-11 and DOE-1 extends further to the north, toward H-15 (Figure 1-4). This extension may or may not affect ground-water flow directions near the center of the site. Although Culebra data are essentially complete, the final estimate of the distribution of Culebra transmissivity awaits completion of numerical modeling. This modeling will use an objective adjoint-sensitivity calibration technique.

3.3.5.1 Modeling History. Modeling of the hydrologic system near the WIPP repository has changed dramatically since the original FEIS model was constructed (DOE, 1980a). These changes reflect the development of a more-detailed data base and a more thorough understanding of what has proved to be a complex flow system. Models developed since the FEIS have been designed to address a variety of questions and are based on data sets that have evolved

through time as ongoing field investigations produce additional data. Therefore, these models are based on somewhat different flow-system descriptions and on different numerical implementations of those descriptions. The domains of the various models are presented in Figure 3-25.

The first ground-water-flow model of the WIPP region was developed by INTERA Environmental Consultants (1978) for the FEIS (DOE, 1980a) and for the WIPP Safety Analysis Report (SAR; DOE, 1980b). The model encompassed an area of 58 x 58 km (36 x 36 mi) (Figure 3-25) and simulated the Rustler Fm., Rustler-Salado contact zone, Delaware Mountain Group, and Capitan reef water-bearing units. The objectives of the study were to check the degree of consistency between various sets of hydrologic data, to calculate the extent of vertical hydraulic connection between various hydrologic units, to delineate spatial variations in hydraulic conductivity, to calculate hydraulic-head potentials and hydraulic conductivities in areas where data were lacking, and to calculate boundary conditions for local repository-breach simulations. Simulations were carried out using the three-dimensional, finite-difference code SWIFT (Sandia Waste-Isolation Flow and Transport) (Dillon et al., 1978).

At the time of the FEIS modeling, data on the hydraulic properties of the water-bearing units under consideration were extremely limited. For example, transmissivity data for the Culebra and Magenta Dolomite Members of the Rustler Fm. were available from only four (Table 3-17) and three locations, respectively (Mercer and Orr, 1979; Cooper and Glanzman, 1971). One value of storativity was available for the Culebra, and none for the Magenta. Hydraulic-head data were available from six locations in the Culebra Dolomite and from three locations in the Magenta Dolomite. Despite hydraulic head differences of over 30 m between the Culebra and Magenta, the two dolomites were modeled as a single "Rustler aquifer." The lumped Culebra-Magenta aquifer was assumed to behave hydraulically as an isotropic single-porosity medium, essentially homogeneous over tens of square kilometers, with uniform storativity. Similar generalizations from sparse data were made for the other water-bearing units.



- 1 U.S. Department of Energy (1980a, 1980b); Cole and Bond (1980)
- 2 D'Appolonia Consulting Engineers (1981)
- 3 Barr et al. (1983)
- 4 Davies (1989)
- 5 Niou and Pietz (1987)
- 6 Haug et al. (1987); Reeves et al. (1987)
- 7 LaVenu et al. (1988); Reeves et al. (1989)
- 8 LaVenu et al. (1989)

TRI-6330-99-0

Figure 3-25. Approximate boundaries of ground-water flow and transport models in the WIPP region (Davies, 1989).

Table 3-17. Comparison of Transmissivity Data (m^2/s) for Culebra Modeling

Well	FEIS (1980)	Barr et al. (1983)	Haug et al. (1987)	LaVenue et al. (1988)	LaVenue et al. (1989)
H-1	1.1×10^{-7}	7.5×10^{-8}	7.5×10^{-8}	7.56×10^{-7}	9.36×10^{-7}
H-2	--	4.3×10^{-7}	6.0×10^{-7}	5.61×10^{-7}	6.30×10^{-7}
H-3	--	2.0×10^{-5}	4.0×10^{-6}	2.47×10^{-6}	2.46×10^{-6}
H-4	--	9.7×10^{-7}	1.2×10^{-6}	1.02×10^{-6}	1.01×10^{-6}
H-5	--	2.2×10^{-7}	1.6×10^{-7}	1.52×10^{-7}	9.74×10^{-8}
H-6	--	7.8×10^{-5}	7.9×10^{-5}	7.95×10^{-5}	3.55×10^{-5}
H-7	--	2.5×10^{-3}	1.2×10^{-3}	1.11×10^{-3}	1.54×10^{-3}
H-8	--	NA	NA	NA	8.82×10^{-6}
H-9	--	9.6×10^{-4}	NA	1.73×10^{-4}	1.25×10^{-4}
H-10	--	7.5×10^{-8}	NA	7.56×10^{-8}	7.53×10^{-8}
H-11	--	--	1.1×10^{-5}	2.76×10^{-5}	2.92×10^{-5}
H-12	--	--	4.5×10^{-8}	1.84×10^{-7}	1.94×10^{-7}
H-14	--	--	--	3.29×10^{-7}	3.28×10^{-7}
H-15	--	--	--	1.32×10^{-7}	1.32×10^{-7}
H-16	--	--	--	7.56×10^{-7}	4.90×10^{-7}
H-17	--	--	--	2.16×10^{-7}	2.31×10^{-7}
H-18	--	--	--	--	1.67×10^{-6}
WIPP-12	--	--	--	3.24×10^{-8}	1.08×10^{-7}
WIPP-13	--	--	--	7.45×10^{-5}	7.42×10^{-5}
WIPP-18	--	--	--	3.24×10^{-7}	3.23×10^{-7}
WIPP-19	--	--	--	6.48×10^{-7}	6.45×10^{-7}
WIPP-21	--	--	--	2.70×10^{-7}	2.69×10^{-7}
WIPP-22	--	--	--	4.00×10^{-7}	3.98×10^{-7}
WIPP-25	--	2.8×10^{-4}	2.9×10^{-4}	2.92×10^{-4}	2.88×10^{-4}
WIPP-26	--	1.1×10^{-3}	NA	1.35×10^{-3}	1.22×10^{-3}
WIPP-27	--	2.6×10^{-4}	NA	7.02×10^{-4}	4.27×10^{-4}
WIPP-28	--	2.3×10^{-5}	NA	1.94×10^{-5}	2.07×10^{-5}
WIPP-29	--	NA	NA	1.00×10^{-3}	1.08×10^{-3}
WIPP-30	--	2.0×10^{-5}	NA	3.24×10^{-7}	2.50×10^{-7}
P-14	1.5×10^{-4}	5.1×10^{-4}	2.5×10^{-4}	2.30×10^{-4}	2.77×10^{-4}
P-15	--	7.5×10^{-8}	8.9×10^{-8}	9.26×10^{-8}	9.22×10^{-8}
P-17	--	1.1×10^{-6}	1.8×10^{-6}	1.38×10^{-6}	1.08×10^{-6}
P-18	1.1×10^{-10}	1.1×10^{-9}	2.1×10^{-9}	1.87×10^{-9}	7.53×10^{-11}
AEC-7	--	--	NA	--	2.80×10^{-7}
DOE-1	--	--	3.6×10^{-5}	1.19×10^{-5}	1.18×10^{-5}
DOE-2	--	--	3.9×10^{-5}	9.61×10^{-5}	9.57×10^{-5}
ERDA-9	--	--	--	5.08×10^{-7}	5.05×10^{-7}
D-268	--	--	--	--	2.04×10^{-6}
Cabin Baby-1	--	--	--	3.02×10^{-7}	3.01×10^{-7}
Engle	--	--	NA	4.64×10^{-5}	4.62×10^{-5}
USGS-1	5.0×10^{-4}	5.0×10^{-4}	NA	5.54×10^{-4}	5.52×10^{-4}
	4 Values	19 Values	16 Values	37 Values	41 Values

-- means no data available at time of model

NA means not applicable; well outside model domain

The early INTERA model was reworked by Cole and Bond (1980) using the same conceptual model but a different simulation code, VTT (Variable Thickness Transient), which is a two-dimensional, finite-difference code that simulates multiple aquifers using interaquifer transfer coefficients (Reisenauer, 1979). The study provided a benchmark comparison between SWIFT and VTT. The input data used by Cole and Bond (1980) were similar to those used by INTERA. The model results were, therefore, similar.

D'Appolonia Consulting Engineers (1981) constructed a model of the WIPP region with the primary objective of verifying the calculational procedures used by the early INTERA model for the analysis of liquid breach and transport scenarios. D'Appolonia (1981) modeled the Rustler Fm., lumped as a single unit, in a rectangular 34 x 46 km (21 x 29 mi) area, located with the WIPP site along the eastern model margin (Figure 3-25). In a separate simulation, D'Appolonia modeled the Permian Bell Canyon Fm. (the uppermost formation of the Delaware Mountain Group) over a somewhat larger area. D'Appolonia used a two-dimensional, finite-element code, GEOFLOW. D'Appolonia's results were generally similar to INTERA's. The two studies did, however, draw different conclusions about Rustler flow conditions in southern Nash Draw. INTERA interpreted a trough in the Rustler potentiometric surface in southern Nash Draw as resulting from downward leakage to the Rustler-Salado contact zone. D'Appolonia interpreted the same trough as resulting from a higher Rustler hydraulic conductivity near Nash Draw, caused by extensive fracturing. Perhaps related to this difference in flow-system interpretations, D'Appolonia computed travel times between the WIPP site and the Pecos River that were about half those computed by INTERA.

Using new, more-detailed data on the Rustler Fm., Barr et al. (1983) constructed a model that explicitly simulated the Magenta and Culebra Dolomite as separate units within a 26 x 26 km (16 x 16 mi) area centered on the WIPP site (Figure 3-25). Transmissivity and head data were available from 19 locations in the Culebra Dolomite and ten locations in the Magenta Dolomite, and storativity data were available from 17 locations in the Culebra and seven locations in the Magenta. Table 3-17 shows how the Culebra transmissivity data base has expanded since 1980. Barr et al. (1983) used a porous-medium approximation for their Culebra model, introduced greater heterogeneity in

both transmissivity and storativity than was used in the FEIS model, and also incorporated anisotropy in transmissivity. Their Magenta model was similar to their Culebra model, except that isotropic transmissivity was assumed. Barr et al. (1983) examined transport of an ideally nonsorbing contaminant from the center of the WIPP site. Their simulations indicated that contaminant travel times may be significantly longer than those computed in previous modeling studies, particularly within the Magenta Dolomite. For numerical simulations, the study used ISOQUAD, a two-dimensional, finite-element code that solves flow and transport equations (Pinder, 1974).

Niou and Pietz (1987) performed a modeling study designed to demonstrate how regionalized values of transmissivity and storativity could be determined for the Culebra Dolomite using an inverse analysis of large-scale hydraulic stresses. For this demonstration, they presented an inverse analysis of the H-3 multipad pumping test. The study used a two-dimensional inverse code known as INVERT (Carrera, 1984; Carrera and Neuman, 1986) and covered a 12 x 12 km (7.5 x 7.5 mi) area centered on the H-3 hydropad (Figure 3-25). In addition to generating transmissivity and storativity distributions for the Culebra Dolomite, the study attempted to incorporate parameter uncertainty directly into the simulations.

From 1983 through 1988, many hydrologic data on the Culebra Dolomite were collected, and old data were reinterpreted, leading to a revised conceptual model of flow within the Culebra. Fracturing of the Culebra Dolomite and its contribution to high transmissivities was recognized early in the hydrologic characterization of the WIPP site (Mercer and Orr, 1979). Early models of the Culebra Dolomite and interpretations of test data, however, treated the Culebra as a simple porous medium. Beauheim (1986) demonstrated the double-porosity hydraulic behavior of the Culebra during testing at well DOE-2. Subsequent analyses of pumping tests performed at H-3 (Beauheim, 1987a), WIPP-13 (Beauheim, 1987b), H-11 (Saulnier, 1987), and other wells (Beauheim, 1987c) showed the pervasiveness of double-porosity behavior wherever the Culebra Dolomite has a transmissivity greater than about 10^{-6} m²/s. Kelley and Pickens (1986) demonstrated the controlling influence of fracture flow and matrix diffusion on solute transport in the Culebra Dolomite on a local (30-m [98-ft]) scale.

In 1986, INTERA began a process of model development that will continue through at least 1989. The overall objective of this study is to develop a detailed understanding of flow and transport in the Culebra Dolomite in the immediate vicinity of the WIPP site. The code used in this model study is SWIFT II (Reeves et al., 1986a, 1986b), which is an enhanced version of SWIFT capable of double-porosity flow and transport simulations. The primary objective of the first model in this series (Haug et al., 1987) was to calibrate an undisturbed, steady-state simulation and then use the transient hydraulic stresses created by the excavation of the WIPP shafts and by the H-3 multipad pumping test and other aquifer tests to develop a detailed understanding of the transmissivity distribution in the Culebra Dolomite in the immediate vicinity of the WIPP site. The model domain for this study was a 12.2 x 11.7 km (7.6 x 7.3 mi) area around the site (Figure 3-25). The transmissivity data available at the time of Haug et al.'s (1987) modeling are given in Table 3-17. Haug et al. (1987) investigated how single- and double-porosity conditions affect regional ground-water flow and found no significant differences between the two. They therefore used a porous-medium (single-porosity) approximation for the Culebra Dolomite in their model. During calibration of the steady-state simulation, Haug et al. (1987) found that matching the relatively low hydraulic heads at wells H-11 and DOE-1 required the introduction of a high-transmissivity feature extending southward from these wells.

Conservative-tracer tests have been performed at the H-3, H-4, H-6, and H-11 hydropads. Kelley and Pickens (1986) reported dual-porosity interpretations of the tests at H-3 and H-4. Reeves et al. (1987) investigated the role of various retardation mechanisms in dual-porosity transport, such as matrix diffusion, advective coupling, and sorption on fracture surfaces. Reeves et al. (1987) also used Haug et al.'s (1987) model to examine solute transport in the fractured Culebra Dolomite near the WIPP site under natural hydraulic-gradient conditions. Reeves et al. (1987) showed that matrix diffusion dominates regional solute-transport behavior under natural gradient conditions, allowing the use of a single-porosity approach in simulations, for the range of parameters they examined. The travel time required for the concentration of a conservative solute released from a drop point above the centroid of the waste-storage panels to reach 50% of its

injection concentration at the WIPP-site boundary was computed to be 5,100 years.

The second model in the INTERA series (LaVenue et al., 1988) incorporated more transmissivity and hydraulic-head data (Table 3-17) and the results of another large multipad pumping test centered at WIPP-13 in the northern part of the model area. In order to accommodate these new data, the model boundaries were expanded to encompass a 24 x 25 km (14.9 x 15.5 mi) area (Figure 3-25). In addition to model calibration, this study included a preliminary examination of system sensitivity to transmissivity and storativity properties. As in the Haug et al. (1987) study, calibration of the LaVenue et al. (1988) model produced a high-transmissivity feature south of H-11 and DOE-1. However, the feature is somewhat wider in the east-west direction, and transmissivities within this zone are approximately a factor of four lower than in the earlier study. Particle travel time from a drop point above the centroid of the waste-storage panels to the WIPP-site boundary was computed to be approximately 13,000 years.

LaVenue et al.'s (1988) model was later used to predict the responses of various observation wells to the H-11 multipad pumping test. Drawdowns north of H-11 were underestimated by the model. The zone of relatively high transmissivity extending north from H-11 to DOE-1 in the model will most likely have to be extended farther north toward H-15, east of the storage panels, during the continuing INTERA modeling program. This change in the transmissivity distribution may or may not affect the travel times reported by LaVenue et al. (1988), depending on whether increasing the transmissivity between DOE-1 and H-15 diverts flow passing over the waste-storage panels toward the east, allowing it to enter the high-transmissivity zone sooner than it does following the southerly flow direction presented by LaVenue et al. (1988).

At the same time that the first and second of the INTERA model series were being developed to examine detailed flow-system behavior near the site, a model study of the Rustler Fm. on a regional scale was completed by the USGS (Davies, 1986, 1987, 1989). This study included both a 36 x 46 km (21 x 29 mi), regional-scale model of the Culebra Dolomite and a 30-km (18.6-mi) long,

east-west, cross-sectional model extending from the top of Salado Fm. to the ground surface (Figure 3-25). The simulation codes used in this study were the variable-density, flow and transport code SUTRA (Voss, 1984) for the regional model and a two-dimensional, finite-difference flow code by Trescott et al. (1976) for the cross-sectional model. This study examined fluid-density effects, sensitivity to regional flow boundaries, sensitivity to vertical flux, and the potential for long-term transient influences on the flow system.

The third model in the INTERA series is nearing completion (LaVenué et al., 1989). This modeling study will include a further expanded model domain (to 24 x 31 km [14.9 x 19.3 mi], Figure 3-25) and expanded and revised data (Table 3-17). The study will use an adjoint-sensitivity approach to calibrating the steady-state and transient Culebra flow fields. Major transient hydraulic stresses that will be included in the calibration procedure include WIPP shaft construction, the H-3, WIPP-13, and H-11 multipad pumping tests, and the H-4 tracer test. The adjoint-sensitivity approach quantifies the effects that changes in transmissivity or storativity in each grid block have on the calculated flow field. Thus, the approach can define areas where assumed transmissivities or storativities can be changed to improve the model fit to the observed hydraulic heads, as well as areas where transmissivities or storativities could differ from assumed values without significantly affecting the fit to observed heads. The adjoint-sensitivity approach will allow improvements in model calibration and also permit modeling of different interpretations of the flow system that fit the observed head distribution equally well but may result in different flow paths or travel times from above the waste-storage panels to the site boundary. The technique can be used to optimize the locations of new wells so as to most reduce modeling uncertainty.

A complementary study (Reeves et al., 1989) is examining the transport behavior of the Culebra Dolomite under high hydraulic-gradient (brine-reservoir breach) conditions. Preliminary results indicate that matrix diffusion is much less effective at retarding solute transport under high-gradient conditions than under natural-gradient conditions. Thus, travel times for solutes injected into the Culebra Dolomite over the waste-storage

panels to reach the WIPP-site boundary would be decreased both by higher velocities resulting from increased gradients and by less matrix diffusion.

3.3.5.2 Limitations of Current Data Base. The planned data-collection phase of the Culebra hydrologic characterization program is essentially complete. Some existing data remain to be reinterpreted, notably from wells H-4, H-6, H-7, H-9, and P-14. Minor gaps in the well distribution exist (e.g., in the northeast quarter of the WIPP site, west of H-12 in the assumed high-transmissivity feature, between H-7 and H-9, and east of H-8), but no new wells are currently scheduled to be drilled and tested. Thus, all future modeling will be affected by the limitations of the current data base. The importance of these limitations will not be known until INTERA completes the transient adjoint-sensitivity calibration of their ground-water-flow model.

3.3.5.3 Limitations of Modeling Approach. Within the context of the current INTERA hydrologic model of the Culebra Dolomite, a number of assumptions or idealizations have been made. First, the Culebra Dolomite has been assumed to be vertically homogeneous, with hydraulic conductivity, and hence flow, distributed equally throughout the thickness of the unit. In limited testing performed at five locations, Mercer and Orr (1979) and Beauheim (1987c) have shown hydraulic-conductivity variations ranging from a factor of two to a factor of five between various sections of the Culebra Dolomite one or more meters thick. Testing on a smaller scale might reveal even greater degrees of vertical heterogeneity.

Despite this difference between the actual Culebra Dolomite and the conceptual model, both the flow and transport modeling should be reliable, because the areal flow modeling of the Culebra Dolomite relies on transmissivity, not hydraulic conductivity. Transmissivity of a specific test interval is the property actually measured in the field and is unaffected by vertical heterogeneity within the test interval. The transport modeling of Reeves et al. (1987, 1989) relies on the areal modeling to provide a flux per unit width of the Culebra Dolomite, and then drives that flux through a specified fracture porosity. This treatment tends to magnify the effects of fracturing by assigning all of the measured transmissivity to the fractures

and none to the matrix. Thus, the modeled flux through the fractures is the maximum possible and results in minimum travel times.

A second assumption used in the Culebra flow and transport modeling in this report and by LaVenue et al. (1988), from whose work the transmissivity distribution used in this report was taken, is that the Culebra Dolomite is completely confined, with no vertical flux either in or out. Haug et al. (1987) examined this assumption and determined that spatially varying vertical fluxes from the Tamarisk or unnamed lower member to the Culebra Dolomite could be accommodated while preserving model calibration by varying the transmissivity distribution within reasonable bounds, and that these vertical fluxes might in fact aid in calibrating the fluid-density distribution within the model. Haug et al. (1987) recommended the use of a multi-layered model to investigate further the possibility and implications of vertical fluxes. Davies's (1989) cross-sectional model of the Rustler Fm. also showed vertical flux to be a realistic possibility, but no additional work in this area has been performed. Thus, the uncertainty in the modeling for this report related to lack of consideration of vertical flux cannot be evaluated.

A third assumption of the current generation of Culebra hydrologic models is that the Culebra Dolomite is hydraulically isotropic. Gonzalez (1983) and Saulnier (1987) reported evidence of horizontal anisotropy in the Culebra Dolomite at four locations, with anisotropy ratios ranging from 1.6/1 to 2.7/1. Because of the paucity of anisotropy data, and because no consistent orientation of the transmissivity tensor is evident from the available data, possible anisotropy cannot be rigorously included in the modeling. This deficiency is not considered important, because implementing an anisotropy ratio of 2.7/1 within the model would only require changing the current effective transmissivities by a factor of 1.6 (the square root of 2.7), which is well within the existing calibration uncertainty.

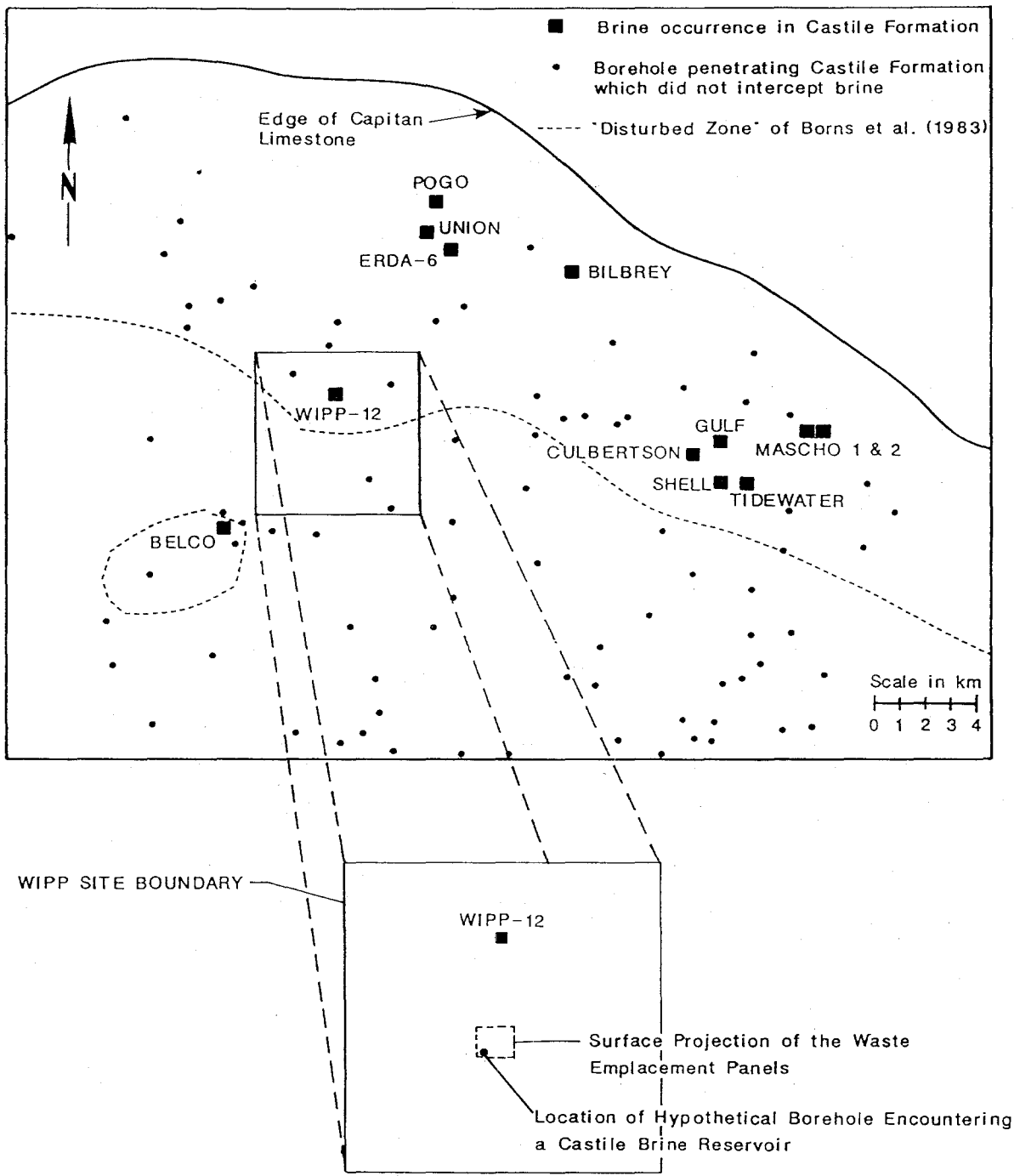
3.4 Castile Formation, Including Brine Reservoirs

The major conclusions of Section 3.4 are listed below.

- Pressurized brine is known to be present at borehole WIPP-12 and at the Bellco-Hudson hydrocarbon borehole southwest of the site. Geophysical studies that are correlated with the known occurrence of brine at WIPP-12 indicate the presence of brine to the south. Based on these studies and on borehole experience, the WIPP-12 reservoir is assumed to extend underneath at least a portion of the waste-emplacement panels.
- The origin of Castile brine reservoirs is not conclusively known. Present interpretations are that their origin is either local, by limited movement of intergranular brines from adjacent Castile halites, or long-range, by the previous existence of a lateral hydraulic connection of the Castile Fm. with the Capitan reef. The assumed presence of a Castile brine reservoir beneath the repository is of concern only in the event of human intrusion.
- Hydraulic testing indicates that the WIPP-12 reservoir is characterized dominantly by fracture flow in a very tight anhydrite matrix and that the reservoir is limited in extent. For purposes of modeling, the reservoir is assumed to be radially symmetric, with a central high-transmissivity zone surrounded by two outer zones, one of slightly increased transmissivity relative to the undisturbed country rock, and one the undisturbed country rock.
- Hydraulic testing at WIPP-12 and monitoring of the long-term pressure buildup indicates the presence of a gas cap in the borehole at long times. Gas evolution during flow would tend to increase flow rates and pressures relative to those estimated here assuming a single brine phase (Section 3.2). This two-phase gas effect cannot be modeled with available techniques. However, it should operate only at late times, when flow rates have decreased.

3.4.1 Castile Formation Hydrology in the FEIS

During the past 50 years, a number of hydrocarbon-exploration boreholes have encountered pressurized brine in the Castile Fm. (Figure 3-26). The pressurized brine most commonly occurs in the uppermost anhydrite of the Castile Fm. Because the anhydrites have very low primary (matrix) porosity,



TRI-6330-112-0

Figure 3-26. Deep boreholes that have encountered pressurized brine within the Castile Fm., northern Delaware Basin.

the brine occurrences are generally associated with secondary (fracture) porosity.

Understanding of the hydrology of the Castile brine occurrences has evolved considerably since the FEIS (DOE, 1980a) was completed. The following sections briefly summarize information on Castile hydrology available at the time of the FEIS, new information that has developed since the FEIS, and brine-reservoir breach analyses that are currently under way.

As discussed in Sections 7.3.5 and 7.4.2 of the FEIS (DOE, 1980a), the data base on Castile hydrology consisted of general reviews of Castile brine occurrences in the Delaware Basin (Griswold, 1977; Powers et al., 1978); seismic reflection data (Powers et al., 1978; Bell and Murphy and Associates, 1979); and borehole information for the Castile Fm. from ERDA-6, ERDA-9, WIPP-11, WIPP-12, and WIPP-13. Pertinent interpretations regarding Castile hydrology are summarized in the following quotations from the FEIS.

The seismic reflection data available ... all confirm the existence of an area in the northern part of the site with significant differences in the seismic character of the Castile and Salado. This area has been called the "disturbed zone." The salient features of this area ... are an anticlinal structure at its southern margin, interruptions and discontinuities in the seismic returns from the lower evaporites, thinning and thickening of evaporite beds, and seismic reflections from the upper Salado that are extremely difficult to interpret. Preliminary examination of cores from boreholes WIPP 11, 12, and 13 confirms thinning and thickening of evaporite beds in the Castile and the lower Salado. (DOE, 1980a, Vol. 1, p. 7-42)

The interception of a brine reservoir in ERDA-6 at a now-abandoned site ... has caused concern over the possible existence of such reservoirs at the present site and the consequences to a repository ... The nearest [Castile brine occurrence] is immediately southwest of the site at the Hudson-Belco well. The next closest is ERDA-6, about 2 miles northeast of the outer site boundary ... All of the brine appears to come from the Castile Formation, and it is associated with the middle, or possibly upper, anhydrite of the Castile. However, the Castile has been penetrated many times without producing brine, and WIPP-11 in particular penetrated through an anticlinal structure in the Castile without detecting any brine or fluids. With this background, the broad anticlinal structure in the Castile at the northern edge of control zone II is the closest area to the site that might be suspected of containing a brine reservoir. ERDA-9 (to the south), WIPP-12 (on the crest of the structure), and WIPP-13 (immediately northwest of the structure) have penetrated into

the upper Castile anhydrite (WIPP-13 to the base of the Castile) without revealing any brine reservoir. (DOE, 1980a, Vol. 1, p. 7-45)

Because of the 700 foot layer of evaporites between the repository level and the Castile Formation, a deep Castile brine pocket would pose no hazard to the repository even if one should be present in the Castile--an unlikely probability for an area of gentle structure. (DOE, 1980a, Vol. 1, p. 7-46)

The release scenarios analyzed in the FEIS did not include a borehole breach penetrating both the repository and a Castile brine occurrence. However, an "informal scenario" discussed in Section 9.7.1.3 of the FEIS examined some of the immediate effects that might follow the penetration of an undetected brine pocket located 60 m (200 ft) beneath the WIPP repository. In this scenario, the breach of a hypothetical brine pocket resulted in the passage of 7,816 m³ (276,000 ft³) of brine through the repository and into the Rustler Fm. Making the assumption that the waste materials are as soluble in brine as pure salt is in distilled water, it was estimated that no more than 1,416 m³ (50,000 ft³) of waste could be transferred to the Rustler Fm. through the postulated breach. The consequences of intercepting the hypothetical brine pocket were not carried beyond this point in the FEIS for two reasons:

First, brine pockets of the size assumed in this example are extremely unlikely near the repository. (DOE, 1980a, Vol. 1, p. 9-134).

Second, the development of a continuous natural connection with a sufficiently high hydraulic conductivity or a large enough area is considered unlikely--particularly if the connection must penetrate to the Castile in order to intercept a brine pocket. A cased wellbore that penetrates a pocket would indeed provide a connection--but one that would result in the release of no waste other than the material intercepted during drilling...(DOE, 1980a, Vol. 1, p. 9-135)

3.4.2 General Information on Castile Hydrology Developed Since the FEIS

As a result of the agreement between the DOE and the State of New Mexico (1981), studies were initiated in 1981 to gather additional information on brine occurrences in the Castile Fm. These studies included reopening and testing of ERDA-6; deepening WIPP-12; and producing a comprehensive topical report on brine reservoirs in the Delaware Basin, including the results of the new field investigations. In November of 1981, during deepening of WIPP-12, pressurized brine was encountered at a depth of about 914 m (3,000) ft in

fractured anhydrite located in the upper portion of the Castile Fm. WIPP-12 was subsequently sampled and tested to provide a detailed geochemical and hydraulic characterization of this brine occurrence. The possible presence of Castile brines within fractured Castile anhydrite beneath the WIPP facility is of no concern except in the event of human intrusion, because the brine, even if present, is separated from the repository horizon by ~250 m of evaporites. The possible effects of a Castile brine reservoir on long-term performance of the WIPP were not specifically addressed in the FEIS (Table 1-1), but preliminary calculations of the effects indicated that they would not be unacceptable (e.g., Channell, 1982).

Popielak et al. (1983) discussed in detail the results of the ERDA-6 and WIPP-12 testing and sampling and the geologic, hydrologic, and geochemical characteristics of Castile brine occurrences. Their conclusions are as follows. Ratios of major and minor element concentrations in the brines indicate that these fluids originated from ancient seawater and that there is no evidence for fluid contribution from present meteoric waters. The gas and brine chemistries of the two reservoirs are distinctly different from each other and from local ground waters. The brines are saturated, or nearly so, with respect to halite and consequently have little or no halite dissolution potential. The ERDA-6 and WIPP-12 brine reservoirs are located in fractured anhydrites above thickened halite and may be modeled as fractured heterogeneous systems. The vast majority of brine is stored in low-permeability microfractures; about five percent of the overall brine volume is stored in large open fractures. The volumes of the ERDA-6 and WIPP-12 brine reservoirs are estimated to be 630,000 and 17,000,000 barrels respectively. The brine reservoirs have maintained hydraulic heads greatly in excess of those in neighboring ground-water systems for at least a million years. Given the evidence for hydrologic isolation and the substantial thickness of intact halite between the WIPP disposal horizon and any possible brine reservoir in the Castile Fm., Popielak et al. (1983, p. 6) concluded that "...pressurized brine reservoirs occurring in the Castile Formation do not affect the suitability of the present WIPP site."

In a later study of brine geochemistry using uranium-disequilibrium methods, Lambert and Carter (1984) reached a different conclusion regarding

the origin of the Castile brine fluids than did Popielak et al. (1983). They concluded that Castile brine occurrences are the result of the isolation of waters transmitted to the Castile Fm. from the adjacent Capitan Reef via an intermittent or episodic hydrologic connection and that the isolation times for the Castile brines at ERDA-6 and WIPP-12 are between 360,000 and 880,000 years.

Geophysical investigations of the possible presence of brine within the Castile Fm. at the WIPP site have continued since 1983, partly in response to recommendations of the New Mexico Environmental Evaluation Group (Neill et al., 1983). Preliminary results played a significant role in the siting of hole DOE-2 (Figure 1-4) (Mercer et al., 1987). This borehole penetrated a basinal structure within the lower Salado Fm. and upper Castile Fm. However, the structure was found to result from deformation rather than evaporite dissolution; i.e., to result from the gravitational settling of dense anhydrite through underlying less-dense halite. No Castile brine was encountered in borehole DOE-2. Although early geophysical studies characterized the extent of the "disturbed zone" in the vicinity of the site (Borns et al., 1983), they were not successful in determining whether Castile brines were present directly beneath the WIPP underground workings. More recently, a geophysical survey using time domain electromagnetic (TDEM) methods was completed over the WIPP-12 brine occurrence and the waste storage panels (The Earth Technology Corp., 1988). The TDEM measurements detected the brine occurrence at WIPP-12 and also indicated that brines are probably present within the Castile Fm. under a portion of the WIPP waste panels.

Based on the new information that has been developed since the FEIS, brine in the Castile Fm. is now assumed to be present under a portion of the WIPP waste panels (Lappin, 1988). Current studies are analyzing a wide range of breach scenarios involving brine reservoirs. A newly revised version of SWIFT II has been developed to model the dynamics of a brine-reservoir breach and the associated flow and transport of contaminants to the ground surface or within the Culebra Dolomite. This code has been used for the Case II analysis described in Section 7.3 and Appendix E.

3.4.3 Updated Interpretation of the Properties of the WIPP-12 Brine Reservoir

WIPP-12 was originally drilled in 1978 to a depth of ~846 m below ground surface (BGS). WIPP-12 was re-entered on November 16, 1981, to map the stratigraphy through the Castile Fm. and to confirm the presence or absence of a Castile brine reservoir at that location. A Castile brine reservoir was encountered in Anhydrite III of the Castile Fm. at WIPP-12 on November 22, 1981, while coring the interval from 846.1 to 919.3 m. Brine production began at a depth of 918.1 m, where downhole pressure was enough to displace the annular fluid column and produce fluid at the surface at significant rates. The borehole was drilled to a total depth of ~1,197 m. The bottom of the borehole was located in the upper part of the Anhydrite I unit of the Castile Fm. (Beauheim, 1987c). Except when the well was shut in, WIPP-12 produced brine-reservoir fluids at the surface from the time the reservoir was encountered until the well was plugged above the Castile Fm. in June, 1983 (D'Appolonia, 1983).

An extensive array of activities was conducted during the deepening of WIPP-12, including a complete geologic, hydrologic, and geochemical reconnaissance (Table 3-18). Table 3-18 lists the duration of each activity and the estimated volume of reservoir fluid produced from the well during periods when it was open, allowing outflow at the surface (flow sequences). The cumulative volume produced during these flow sequences was ~37,300 m³. This cumulative production value should be viewed as an estimate, because total-flow estimates for some activities were based upon indirect methods, and because production values were not reported for some activities (D'Appolonia, 1982, 1983; Popielak et al., 1983).

3.4.3.1 WIPP-12 Testing Program and Factors Limiting Interpretation.

From 1981 to 1983, two sets of drill-stem tests and three flow and recovery tests were performed on the Castile brine reservoir encountered at WIPP-12. The two drill-stem tests are referred to as DST-3020 and DST-2986 and the three flow tests are referred to as Flow Test 1, Flow Test 2, and Flow Test 3 (Popielak et al., 1983). The two drill-stem tests were of short duration, and ports within the drill-stem tool located downhole were too small to allow flow at a rate equal to what the formation could produce. Because these tests only

Table 3-18. Summary of Hydraulic Testing Activities at WIPP-12 from November 10, 1981, to March 7, 1983

<u>Activity</u>	<u>Description</u>	<u>Duration (Days)</u>	<u>Type¹</u>	<u>Volume² Produced (m³)</u>
WIPP-12.01	Well Set-up	5.49	NA	
WIPP-12.02	Coring (846.1 - 919.3 m) ³	7.68	FL	526
WIPP-12.03	Pressure Buildup (open hole TD = 919.3 m)	1.43	BU	0
WIPP-12.04	Coring (919.3 - 928.7 m)	2.41	FL	4305
WIPP-12.05	Geophys. Logging (TD = 928.7 m)	1.90	FL	NR
WIPP-12.06	Pressure Buildup (open hole TD = 928.7 m)	4.17	BU	0
WIPP-12.07	Flow Test 1 (open hole TD = 928.7 m)	0.87	FL	} 5262
WIPP-12.08	DST-3020 (920.5 - 928.7 m)	1.78	FL/BU	
WIPP-12.09	DST-2986 (910.1 - 928.7 m)	0.71	FL/BU	NR
WIPP-12.10	Pressure Buildup (910.1 - 928.7 m)	4.90	BU	0
WIPP-12.11	Coring (928.7 - 947.0 m)	3.82	FL	6050
WIPP-12.12	Pressure Buildup (open hole TD = 947.0 m)	1.45	BU	0
WIPP-12.13	Coring (947.0 - 1092.7 m)	6.04	FL	7468
WIPP-12.14	Pressure Buildup (open hole TD = 1092.7 m)	5.09	BU	0

Table 3-18. Summary of Hydraulic Testing Activities at WIPP-12 from November 10, 1981, to March 7, 1983 (concluded)

<u>Activity</u>	<u>Description</u>	<u>Duration (Days)</u>	<u>Type¹</u>	<u>Volume² Produced (m³)</u>
WIPP-12.15	Coring (1092.7 - 1196.3 m)	3.92	FL	} 9381
WIPP-12.16	Geophys. Logging (open hole TD = 1196.3 m)	1.18	FL	
WIPP-12.17	PIP Installation (947.0 - 1196.3 m)	2.08	FL	
WIPP-12.18	Pressure Buildup (open hole TD = 1196.3 m)	135.0	BU	0
WIPP-12.19	Flow Test 2 (open hole TD = 1196.3 m)	0.23	FL	359
	Pressure Buildup (open hole TD = 1196.3 m)	2.69	BU	0
WIPP-12.20	Flow Test (open hole TD = 1196.3 m)	1.75	FL	} 3943
	Pressure Buildup (open hole TD = 1196.3 m)	1.20	BU	
	Flow Test 3 (open hole TD = 1196.3 m)	7.00	FL	
	Pressure Buildup (open hole TD = 1196.3 m)	278.4	BU	

1. Type refers to the type sequence the particular activity was. BU refers to a buildup period under shut in conditions, and FL refers to a flow period.

2. This refers to the amount of formation fluid produced at the surface during a particular activity. These values were obtained from D'Appolonia (1982, 1983) and Popielak et al. (1983).

3. All depths are measured in meters below ground surface (BGS).

tested small volumes of rock and were adequately interpreted by Popielak et al. (1983), they are not reinterpreted here. For Case II, characterization of the long-term behavior of the reservoir is desired. The analysis of the DST's does not offer much information about the extent of the reservoir and its long-term behavior.

The three flow tests were intended to be constant-pressure, variable-discharge tests. Flow Test 1 was performed primarily to collect brine samples for geochemical analysis. In order to operate the gas-liquid separator, the well was backpressured during the test (Popielak et al., 1983). The corresponding pressures and flow rates were not reported (D'Appolonia, 1982, 1983), and the reservoir hydraulic parameters cannot be interpreted. Of the other two hydraulic tests, Flow Test 2 had a flow period of 0.23 days and a recovery period of 2.69 days. Flow Test 3 had a flow period of 7.0 days and a recovery period of 278.4 days, by which time the reservoir had recovered to within 17 percent of the estimated static formation pressure of 14.7 MPa.

Because of the corrosive nature of the fluids in the brine reservoir and the high pressures encountered, testing the WIPP-12 reservoir was difficult. Factors that contribute to uncertainty in WIPP-12 hydraulic interpretations are briefly discussed below.

During hydraulic flow tests, flow was measured with flow meters. For all other activities, flow and total-volume estimates were based on indirect methods, such as estimates of how many times brine had been hauled away during a given time interval (Popielak et al., 1983). Even when flow meters were used, the meters were subject to flow restriction by salt precipitation and to frequent malfunction as a result of the corrosive fluids and gases (H_2S) present in the reservoir brine. Salt precipitated in surface flow meters and flowlines, restricting flow and causing back pressuring of the formation.

Pressure was measured with downhole transducers, surface transducers, and mechanical pressure gages at the wellhead. Downhole transducers could not be left downhole for long periods, because of the extremely corrosive nature of the brine. For test sequences that recorded pressure at the surface, surface pressures were extrapolated to brine-reservoir pressures based upon an

estimated fluid-column density. This data manipulation adds some uncertainty to the pressure responses used for interpretation. In addition, over long periods of pressure buildup, a gas cap formed at the wellhead in WIPP-12. Over time, this gas cap could be expected to decrease the integrated density of the fluid column and to affect the measured pressure responses. Because the gas cap formed slowly and the amount of gas produced during buildup was small (Popielak et al., 1983), adequate records of gas-cap evolution were not recorded. Consequently, the transient effect on fluid-column density is not known. The evolution of the gas cap can be expected to affect the buildup curves (Popielak et al., 1983); however, these effects have been assumed to be minor and not detrimental to data interpretation.

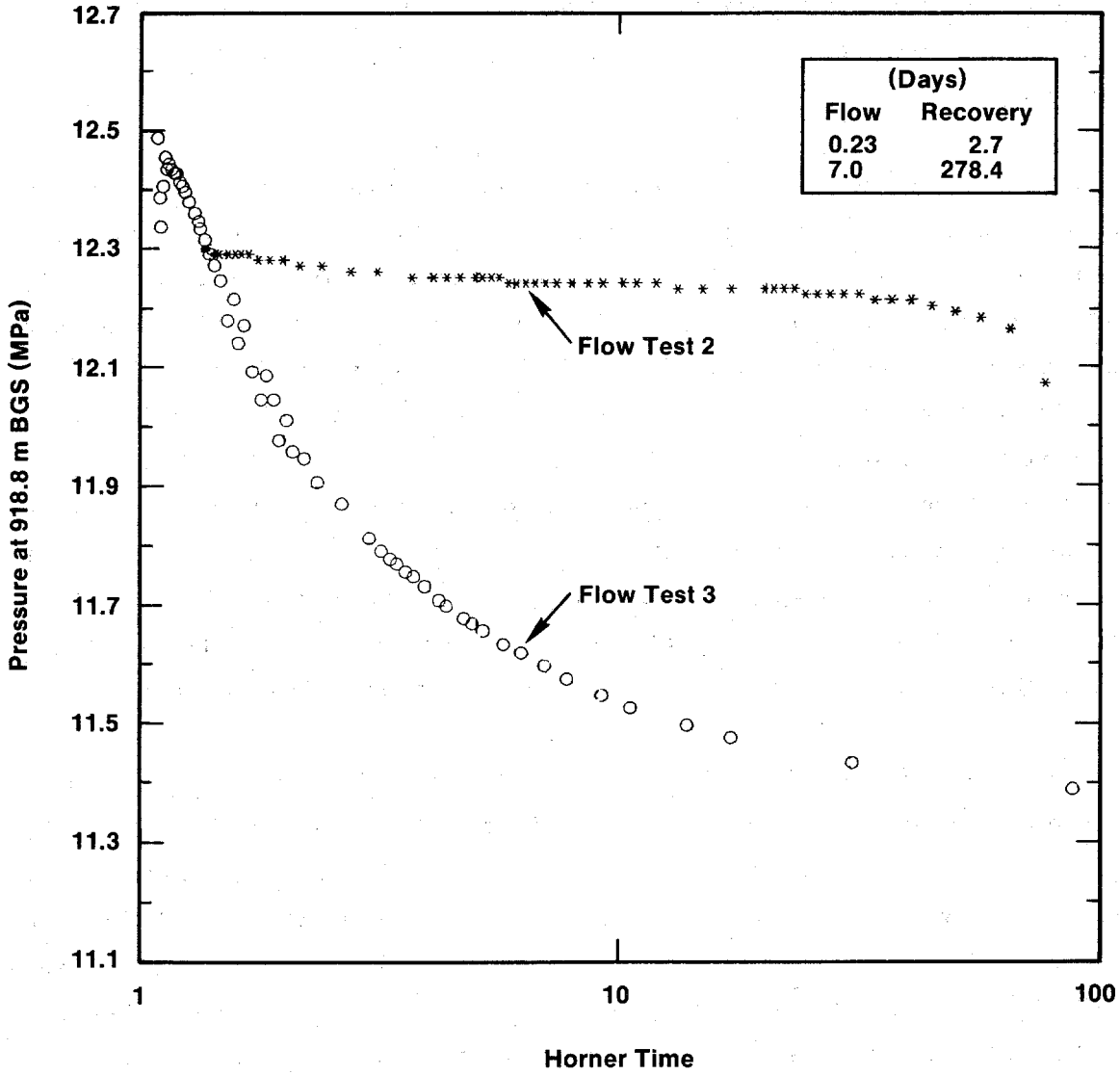
The gas encountered during the WIPP-12 testing program (and in other brine encounters) raises a question about the role gas may play during the long-term, large-scale reservoir depletion simulated in Case II (Section 7.3.1). If enough gas is present, then gas coming out of solution as reservoir pressure drops could play an active role as a flow-driving force. Because gas phase change occurs as the result of reduced pressure, gas effects probably would be most pronounced at intermediate and late times, when relatively large portions of the reservoir have been depressurized. If it were present, the gas drive could produce longer and greater flow than predicted by a single-phase flow model. Because the WIPP-12 tests were relatively short in duration, a single-phase flow model is considered adequate for their interpretation. The possible impact of multi-phase flow on long-term brine-reservoir behavior has not yet been quantified and should be considered a potentially important source of uncertainty in the brine-reservoir breach simulations.

3.4.3.2 Conceptual Model of the WIPP-12 Brine Reservoir. In a relatively impermeable medium with discontinuous fractures, permeability depends on the connectivity of the fractures (Long et al., 1982): as the density of fracture intersections increases per unit volume of rock, so does the permeability increase, assuming all fractures are open. If the fracture network has some uniformity within the tested rock volume, then the volume of rock tested is generally considered homogeneous. Because no truly homogeneous media exist in the subsurface, Long et al. (1982) proposed two criteria that should be met

before a fractured heterogeneous medium is simulated with a homogeneous continuum model. The first criterion is that there is an insignificant change in permeability with an addition or subtraction to the test volume (i.e., a constant representative elementary volume (REV) can be established within the test volume). The second criterion is that a systematic permeability tensor exists that will correctly define flux through the medium if the gradient direction is changed.

In a naturally fractured, heterogeneous medium composed of discontinuous fractures, non-unique medium parameters are commonly derived from hydraulic tests performed over different time and volume scales. The differences will be functions of the variation of the continuity and interconnectivity of the fractures in space. This so-called "scale effect" has recently been discussed in detail with regard to Culebra hydraulic-test results (Beauheim, 1988). When fractures are continuous and the networks they create are uniform, a representative elementary volume can be defined, and the medium will exhibit a uniform effective transmissibility as described above (Streltsova, 1988). If fracture networks lack uniformity and change as a function of the volume of rock considered, then no suitable REV can be defined and hydraulic tests of varying duration will result in different values of medium transmissivity.

Flow into the wellbore from the brine reservoir at WIPP-12 was apparently derived from a fractured portion of Anhydrite III (Section E.2.1). The fractures are very conductive, and the matrix of the anhydrite is very tight. In addition to being a fractured reservoir, the reservoir is of limited extent. The brine reservoir at WIPP-12 exhibits a heterogeneous response. Figure 3-27 is a Horner plot of pressure buildup at WIPP-12 after Flow Tests 2 and 3. The transmissivities determined by Horner's semi-log method for each test differ by nearly three orders of magnitude (Popielak et al., 1983). Flow Test 2 lasted for 0.23 days, followed by a 2.69-day buildup period. This test apparently stressed the well-connected fractures near the wellbore and yielded a higher interpreted transmissivity. Flow Test 3 lasted 7 days followed by a buildup period of 278 days. This test stressed a much larger volume of rock, which has a mean transmissivity much less than that of the fractures near the well. The Horner plot for this buildup exhibits an ever-increasing slope, indicative of a highly heterogeneous fractured medium (Streltsova, 1988).



TRI-6330-125-0

Figure 3-27. Horner-pressure plots for WIPP-12 Flow Tests 2 and 3.

The conceptual model used to interpret hydraulic tests at WIPP-12 assumes that Anhydrite III of the Castile at WIPP-12 is a fractured, heterogeneous medium with discontinuous fractures. The brine reservoir that occurs within this unit is of limited areal extent. A hydraulic test that stresses a limited volume of rock around the wellbore may yield a high effective transmissivity, indicative of a well-connected array of fractures. As the volume of rock stressed increases, the effective formation transmissivity decreases. This effect could be caused by the late-time response of a coupled matrix and fractures, or it could be the result of discontinuous and localized networks of fractures that are poorly connected to the main producing fractures near the wellbore. A few laboratory estimates of permeability and porosity of the Castile anhydrite have been made. The permeability of the anhydrite core is less than $2 \times 10^{-19} \text{ m}^2$ and the porosity values range from 0.8 to 0.2 percent (Popielak et al., 1983). If these low permeabilities are representative of the matrix, the matrix would contribute little to fluid flux within the reservoir over the time scales of the hydraulic tests performed. For that reason, the reservoir is interpreted as a heterogeneous, fractured medium composed of two regions having different transmissivities. When considering long flow periods, as in the simulations for Case II, the matrix will contribute to reservoir response. For this reason, the modeled reservoir for Case II simulations (Chapter 7.0 and Appendix E) has an infinite low-transmissivity medium, representative of the matrix, attached at the peripheral edge of the modeled region by a Carter-Tracy boundary condition.

The translation of the reservoir conceptual model to a spatially discretized numerical model for hydraulic-test interpretation produced a radial system composed of two concentric media with different transmissivities. Consistent with the responses presented in Figure 3-27, the inner region has a higher transmissivity than the outer region. The boundary of the inner high-transmissivity region is located 300 m from the grid center. The location of this inner boundary is not meant to imply that a boundary exists within the reservoir at that location, but rather is a simplified approach to representing heterogeneity. Figure 3-27 suggests that the transmissivity of the reservoir decreases as the volume of rock increases. The model presented here is simple, but greater complexity is not warranted, considering the uncertainties in the data.

3.4.3.3 Interpretative Approach and Results. Two tests have been used to define parameters for the brine reservoir at WIPP-12. These are Flow Tests 2 and 3 and their subsequent buildup periods. The primary goal in interpretation was to produce a single model that would explain the early- and late-time behavior of the brine reservoir. The tests performed at WIPP-12 were constant-drawdown, variable-rate flow tests. In addition to attempting to fit the buildup curves after each flow sequence, fitting the flow-versus-time record during the flow sequence was also considered important. One additional calibration parameter was the total volume of fluid produced from WIPP-12 from reservoir interception to the final buildup considered in this study. In the calibration of the model to the observed hydraulic responses, only transmissivity was allowed to vary. Other parameters were fixed before calibration, and their values were taken as the base-case values discussed in Appendix E.2.

Because of the complex flow histories and numerous flow and buildup sequences that occurred at WIPP-12 during hole deepening and testing of the brine reservoir, and because of the heterogeneous responses observed during testing, analytical-solution or type-curve methods that rely on simplified initial conditions do not lend themselves to use in interpreting the test data. Because long-term pressure depletion and flow history are important to understanding the reservoir, a model was selected that would allow simulation of multiple flow and build-up sequences. The model used for interpretation of the WIPP-12 tests is GTFM. Pickens et al. (1987) described the theoretical basis of the model and its verification.

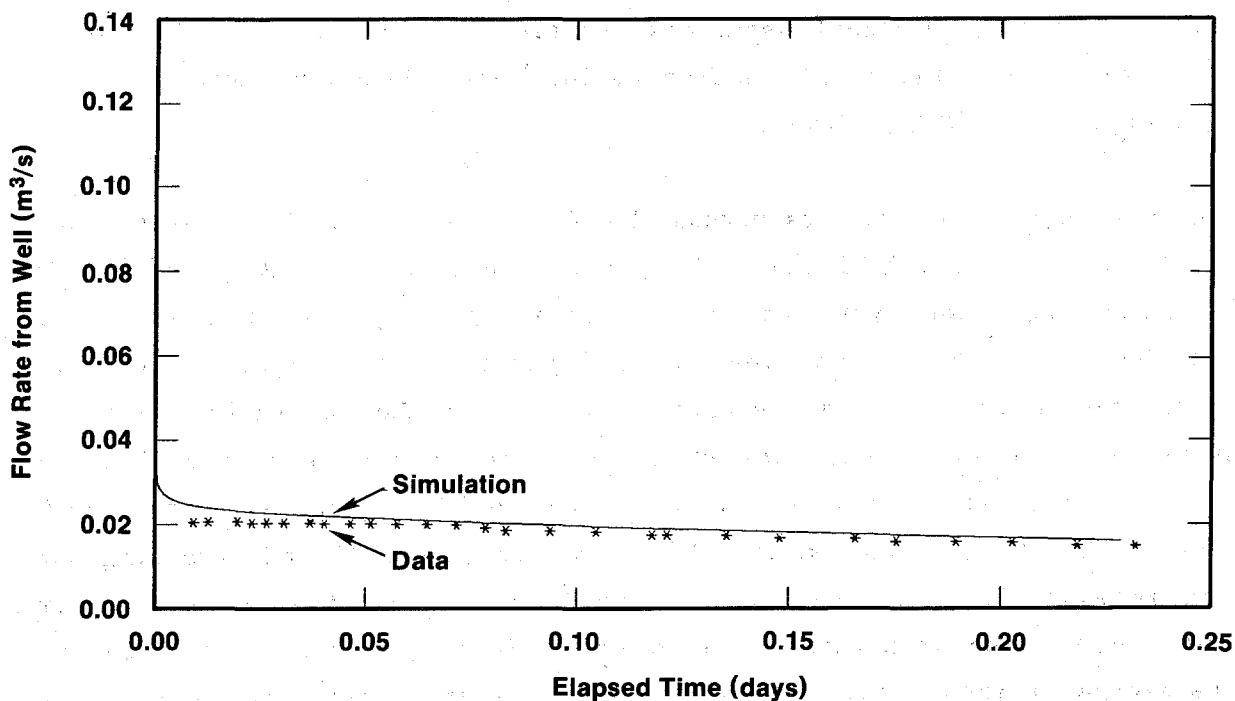
In the GTFM model formulation, each flow and buildup sequence in Table 3-18 is represented. The pressure in the brine reservoir was sufficient to flow at the surface, and, therefore, when the well was open to atmospheric pressure, it flowed. During these periods, the formation would be at a constant pressure equal to the pressure exerted by the fluid column above the formation plus any overpressuring due to flow restriction from surface equipment. In the GTFM simulations, these flow sequences, referred to as history sequences, are modeled as constant-pressure periods. For buildup sequences, the formation is allowed to build up from whatever pressure the reservoir attained at the end of the flow period. The full model simulation

is composed of 24 individual sequences representing 12 flow periods and 12 buildup sequences. The total testing period represented by these flow and buildup sequences is 475.6 days.

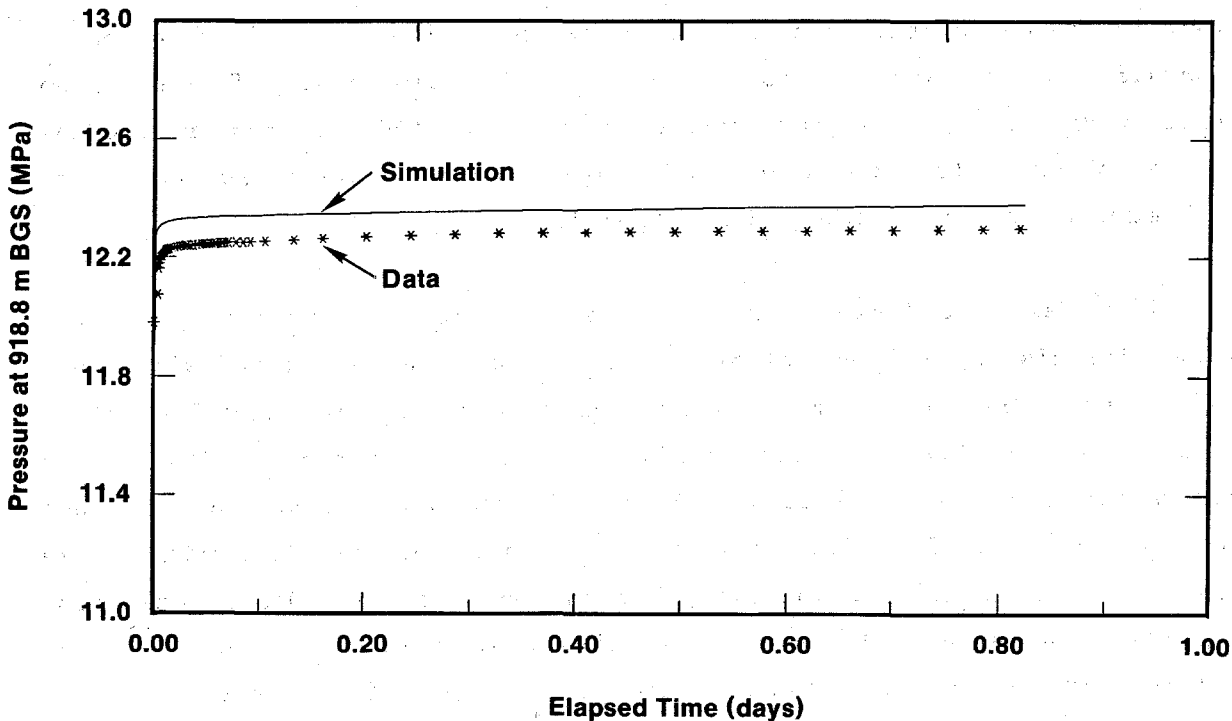
The GTFM simulation results versus the observed data for Flow Tests 2 and 3 are shown in Figures 3-28 and 3-29. As can be seen in these figures, the calibration was based upon not only pressure versus time of the buildup periods but also flow versus time during individual flow tests. Hydraulic characterization of the brine reservoir has led to the conclusion that the reservoir is a heterogeneous, discontinuously fractured reservoir of limited extent. The analysis identifies two regions of differing permeability within the reservoir. The region immediately surrounding the well and extending out approximately 300 m is interpreted to have a mean transmissivity of $7 \times 10^{-4} \text{ m}^2/\text{s}$. The area within the reservoir from this inner region out to the base-case reservoir boundary, at 2,000 m, is interpreted to have a mean transmissivity approximately two orders of magnitude less than the inner region, or $7 \times 10^{-6} \text{ m}^2/\text{s}$. The storage coefficient of the reservoir is held constant in the calibration and was calculated to be 8.5×10^{-5} from the base-case parameters summarized in Table 3-19. The transmissivities of each region and their radii result from the interpretations presented here and are used as base-case values in the reservoir-model simulations that are presented in the Case II simulations of Section 7.3 and Appendix E.

For Flow Test 2 and Flow Test 3, calibration efforts attempted to match both the flow history and the following pressure buildup associated with shut-in conditions. The model simulation matches flow versus time closely (within 5 percent) for Flow Test 2 (Figure 3-28). The pressure match for Flow Test 2 is not as good as the flow-history match. Figure 3-29 shows the flow- and history-match plots for Flow Test 3. The shape of the flow-versus-time simulation is close to that observed, but the model over-predicts total flow during the flow sequence by ~60%. The simulated pressure history for Flow Test 3 is good, better than that predicted by the model for Flow Test 2. The model predicts, within 30%, the total volume produced from WIPP-12 during the deepening and testing activities.

Flow Test 2: Flow-Rate History



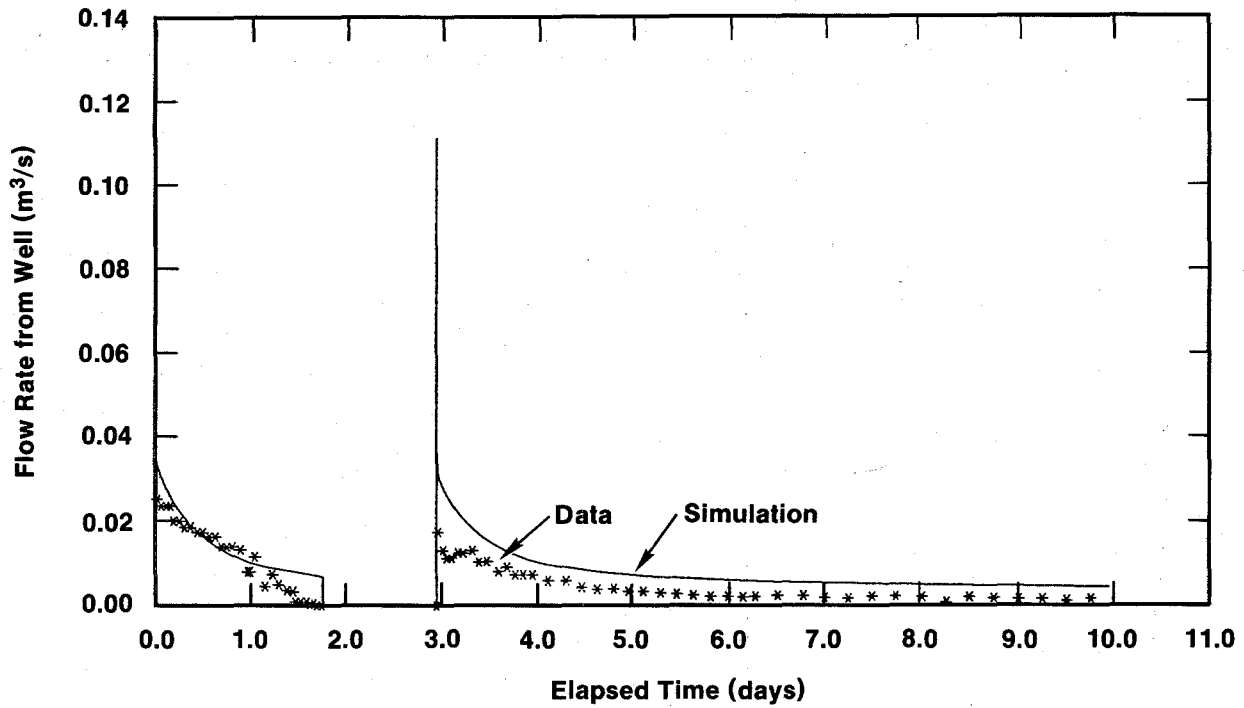
Flow Test 2: Pressure Buildup



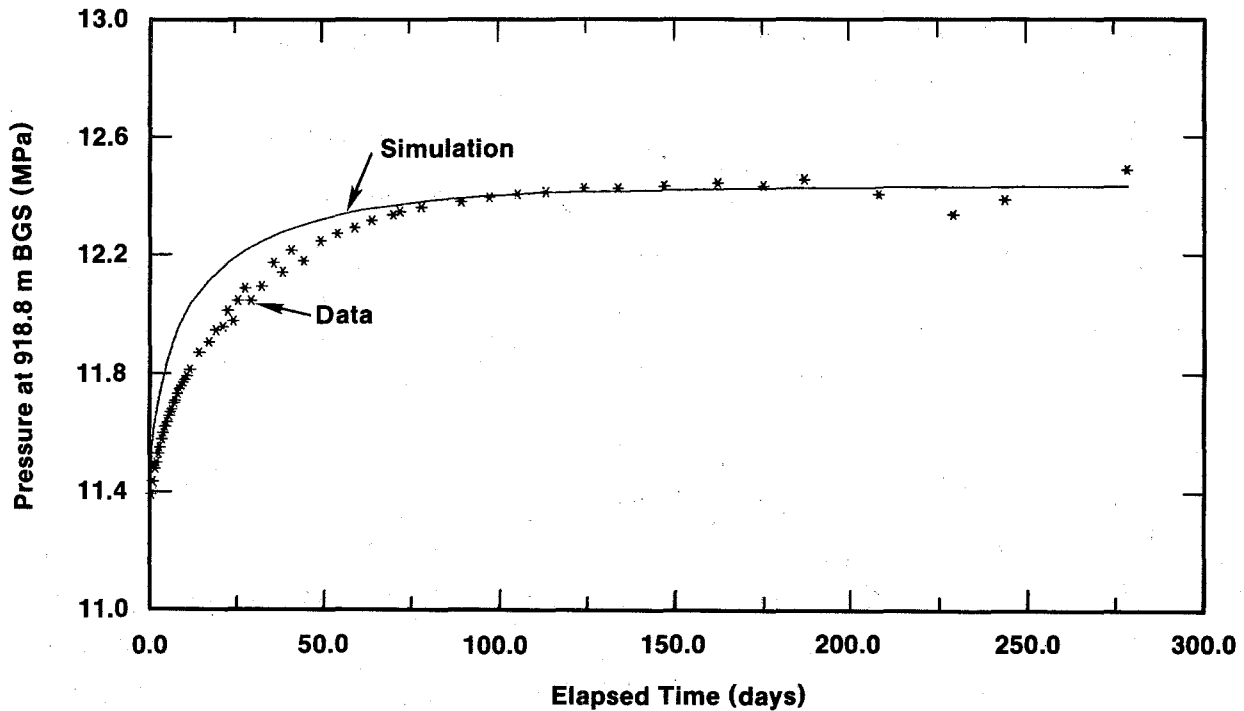
TRI-6330-124-0

Figure 3-28. Simulated and observed flow-rate history and pressure buildup for WIPP-12 Flow Test 2.

Flow Test 3: Flow-Rate History



Flow Test 3: Pressure Buildup



TRI-6330-123-0

Figure 3-29. Simulated and observed flow-rate history and pressure buildup for WIPP-12 Flow Test 3.

Table 3-19. Summary of Interpreted Properties of the WIPP-12 Brine Reservoir and Estimated Ranges of Properties for Similar Reservoirs in the Northern Delaware Basin

<u>Parameter</u>	<u>Symbol</u>	<u>Base Case (based primarily on WIPP-12)</u>	<u>Range</u>	<u>Units</u>
Initial pressure	P_i	12.7	7.0 - 17.4	MPa
Effective thickness	b	7.0	7.0 - 24.0	m
Transmissivity of inner zone	T_i	7×10^{-4}	7×10^{-6} to 7×10^{-2}	m^2/s
Distance to inner/intermediate zone contact	r_2	300	100 - 900	m
Transmissivity of intermediate zone	T_o	7×10^{-6}	7×10^{-8} to 7×10^{-4}	m^2/s
Distance to intermediate/outer zone contact	r_3	2000	30 - 8600	m
Transmissivity of outer zone of intact Castile	T_m	1×10^{-11}	constant	m^2/s
Fluid density	ρ_f	1240	constant	kg/m^3
Porosity	ϕ	0.005	0.001 - 0.01	
Compressibility of medium	α	1×10^{-9}	1×10^{-10} to 1×10^{-8}	1/Pa

Considering the uncertainties in the hydraulic data and the inherent problems in characterizing a heterogeneous medium from single-well tests, the test interpretation has resulted in a consistent set of parameters for the WIPP-12 brine reservoir. The reservoir is a much more complicated medium than is suggested by a simple double-permeability reservoir, although this simplifying conceptual model has reasonably described the transient behavior of the brine reservoir. Because of limitations in the data, more complicated representations are not warranted.

3.5 Bell Canyon Formation and Dewey Lake Red Beds

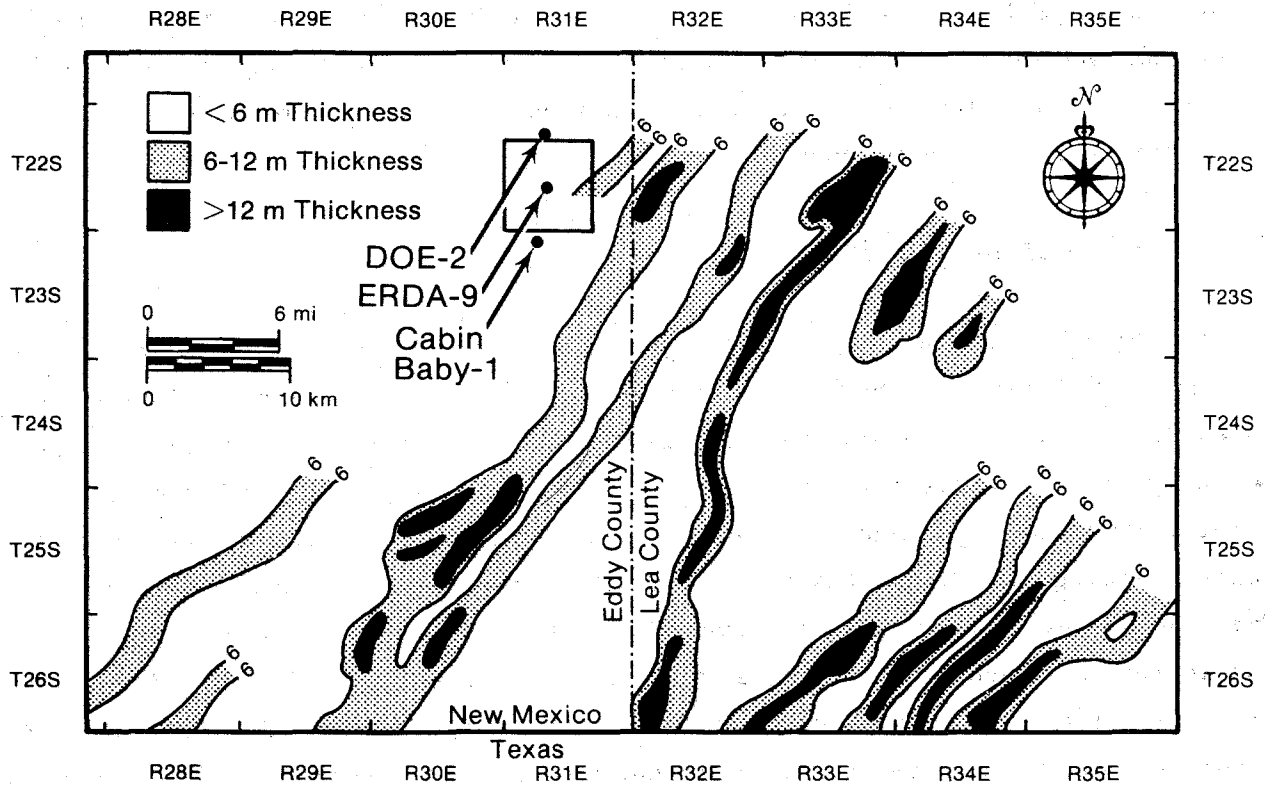
The following is the major conclusion of Section 3.5.

- Testing in holes Cabin Baby-1 and DOE-2 indicates strongly that the final direction of fluid flow in the event of human intrusion connecting the Bell Canyon and Rustler Fms. would be downward, into the Bell Canyon. Although variable, Bell Canyon brines are highly saline and are not suitable for either human or stock consumption.

3.5.1 Bell Canyon Formation

At the time of the FEIS (DOE, 1980a), little hydrologic characterization of the Bell Canyon Fm. had been performed for the WIPP project. Drill-stem tests (DSTs) of portions of the Bell Canyon had been performed at well AEC-8, but only the hydraulic-head data had been interpreted (Mercer and Orr, 1979). After conversion to freshwater density, these heads were higher than Rustler heads, leading to the conclusion that flow between the Bell Canyon and Rustler Fms. would be upward if the two were ever connected. Thus, the FEIS considered a scenario in which a drillhole penetrated the Rustler Fm., the WIPP repository, and the Bell Canyon Fm., and fluid from the Bell Canyon dissolved waste from the repository and was then injected into the Rustler. The hydraulic conductivity of the Bell Canyon in this scenario was assumed to be about 7×10^{-8} m/s.

Williamson (1979) described the Bell Canyon Fm. as consisting of permeable channel sandstones separated by shales and siltstones (Figure 3-30), rather than a continuous, homogeneous sandstone aquifer. Mercer (1983) provided the first comprehensive discussion of the Bell Canyon Fm. at the WIPP site, using completed interpretations of testing performed at AEC-7, AEC-8, and ERDA-10. Mercer (1983) found that the hydraulic conductivities of the Bell Canyon sandstones, siltstones, and shales ranged from 2×10^{-7} to 7×10^{-12} m/s. Mercer (1983) updated Hiss's (1976) potentiometric-surface map for the upper Bell Canyon Fm. and confirmed the interpretation of Hiss that flow in the Bell Canyon is northeastward, toward the Capitan reef. Mercer (1983) also



TRI-6330-73-0

Figure 3-30. Boreholes Cabin Baby-1 and DOE-2 relative to the distribution of known Bell Canyon sands at and near the WIPP site (after Davies, 1983).

concluded that flow would be downward, not upward, if the Rustler and Bell Canyon Fms. were ever interconnected.

Beauheim et al. (1983) and Beauheim (1986) reported on later DSTs of the Bell Canyon Fm. at wells Cabin Baby-1 and DOE-2, respectively (Figure 3-30). Hydraulic conductivities reported for the sandstone/siltstone members of the Bell Canyon Fm. ranged from 1×10^{-8} to 2×10^{-10} m/s at Cabin Baby-1 and from 2×10^{-8} to 7×10^{-10} m/s at DOE-2. From hydraulic heads measured in the Bell Canyon Fm. and Culebra Dolomite at DOE-2, Beauheim (1986) concluded that the direction of flow in a cased borehole open only to the Bell Canyon and Culebra would be upward. In an open borehole, however, dissolution of halite in the intervening Castile and Salado Fms. would increase the specific gravity of the Bell Canyon fluid so that, at the elevation of the Culebra Dolomite, the Culebra head would be higher than the Bell Canyon head, resulting in downward flow. Consequently, the FEIS scenario involving upward flow of Bell Canyon fluid into the Rustler Fm. was unrealistic. Even though the scenario explicitly recognized that halite from the Castile and Salado Fms. would be dissolved as Bell Canyon fluid moved through an open borehole, it failed to realize that the increase in fluid density associated with this dissolution would cause the direction of flow to reverse.

3.5.2 Dewey Lake and Shallower Units

Little new information on the Dewey Lake Red Beds and shallower units has become available since the FEIS was written (DOE, 1980a). The only indications of ground water found in the Dewey Lake during extensive drilling at the WIPP site have been moist drill cuttings from some zones (Mercer, 1983). Testing at H-2c (Mercer, 1983), DOE-2 (Beauheim, 1986), and H-14 (Beauheim, 1987c) showed no evidence of a water table in the Dewey Lake Red Beds. Losses of circulation fluid during drilling (Mercer, 1983; Mercer et al., 1987), however, provide evidence of permeability within the Dewey Lake, even if it is not saturated. A water table, possibly perched, is present within the Dewey Lake Red Beds just south of the WIPP site at the J.C. Mills Ranch. Mercer (1983) speculated that the water may be contained in lenticular sandstone beds recharged through nearby dune fields.

A small quantity of ground water was found in the lower part of the undifferentiated Dockum Group (called the Santa Rosa Sandstone in the FEIS) at well H-5 in the northeast corner of the WIPP site (Mercer, 1983). This occurrence appears to represent the westernmost edge of a water table lying downdip to the east. No evidence of ground water in the Dockum Group was found during drilling of other wells on the WIPP site or at well H-10, southeast of the site. No evidence of ground water was found in shallower units during drilling at the site (Mercer, 1983).

4.0 CONDITION OF THE REPOSITORY IN THE ABSENCE OF HUMAN INTRUSION

4.1 Overview of the Disposal-Room Model

The long-term radionuclide-transport calculations described in later sections of this report assume that the waste-emplacement rooms and panels reach "steady-state" before ground-water transport begins. "Steady-state" is used here only to indicate that processes of compaction and porosity reduction resulting from the creep closure of the repository have greatly slowed from their initial rates. This section describes the logic used in estimating the final or steady-state room parameters, which in turn serve as input parameters to radionuclide-transport calculations.

The model for the final state of waste in the WIPP disposal rooms is frequently referred to as the "source term," because one of its components defines the masses of radionuclides that are taken up by ground water in contact with the waste and hence become available for transport. "Source term" is used here in a broad sense that includes estimates of in-situ porosities and permeabilities as well as total inventory and inventory in ground water in the repository. In the absence of detailed information about the distribution of the radionuclide inventory, each disposal room is assumed to contain a homogeneous waste mixture that has the average composition of the entire radionuclide inventory. Rooms will be backfilled to the extent practicable with a mixture of 70% crushed salt and 30% bentonite, by weight.

A major part of the disposal-room model defines the generation rates and total volumes of gases produced by bacterial decomposition, radiolysis, and chemical corrosion (Section 4.2). Because brine is the principal vehicle for transporting radionuclides out of the repository, the amount of brine that can flow into the repository must also be specified (Section 4.3), in addition to the total inventory of radionuclides (Section 4.4) and their solubilities (Section 4.5). Given the amount of brine present, the amounts of dissolved radionuclides can be estimated for hydraulic-flow analyses (Chapters 6.0 and 7.0). The potential for sorption of radionuclides by the surroundings is discussed in this report (Section 4.6), but radionuclide sorption within the

waste panel has not been included in the calculations. The structural behavior of the Salado Fm. adjacent to the repository (Section 4.7) also strongly affects the long-term state and properties of the waste and backfill (Section 4.8) and the panel and shaft seal systems (Section 4.9).

Gas evolution is coupled to brine inflow, because in some reactions the gas generated depends on the amount of water present. This coupling makes estimating the amount of brine in the room particularly important and difficult. Gas has an internal source, unlike brine, which enters the WIPP from an external source. Gas can enhance connectivity between void spaces in the process of escaping from the waste, although this possibility is not evaluated numerically in this report. In addition, gas generation within the repository could retard brine inflow. The total volumes of gas generated, the potential response of the WIPP repository, and the interaction of gas and brine are considered here, however (Section 4.10).

The final void volumes and the hydraulic conductivities of the compacted waste are also required for the disposal-room model, assuming backfill permeabilities are negligible. At saturation, the waste void volume determines the amount of brine in contact with the waste at any one time and the permeability of the waste, which is assumed to control the rate of brine flow through it and the rate of brine mixing within it. Even though various categories of waste will compact differently, the final void volume and permeability, like the radionuclide masses, are based on average waste compositions. The permeability of the waste is given in terms of hydraulic conductivity for consistency with the rest of the report. Average properties are used, because waste categories will be mixed during emplacement. Uncertainties about composition of the waste and its inherent variability will probably decrease as additional information becomes available.

A quantitative description of the near-final condition of the disposal room was developed after the important components of the model were apparent. Table 4-5 (p. 4-48) summarizes some of the major assumptions and parameter values of the model.

4.2 Gas-Production Rates, Potentials, and Periods

The major conclusions of Section 4.2 are listed below.

- Anoxic corrosion of drums and metallic wastes will be the dominant gas-producing process within the repository if sufficient Mg-rich brine is present. Anoxic corrosion has an estimated gas-generation potential of 894 moles/drum.
- Microbial activity will produce gas, even if supported only by the initial water content of waste and sludges or by water vapor, by consuming cellulosic materials and possibly plastics and rubbers. The estimated total potential for gas generation by microbial activity is 606 moles/drum-equivalent.
- At different times and oxidation potentials, gases that could be produced by microbial activity include CO₂, CH₄, H₂S, and N₂. In the absence of an engineering modification that removes organic compounds, the conditions governing microbial activity may vary with time and location within the repository. Therefore, it is not possible at present to define the expected gas compositions quantitatively; it may vary within the repository.
- The total estimated average rate of gas generation by microbial activity, 0.85 mole/drum per year, is qualitatively the same as that estimated in the WIPP FEIS (DOE, 1980a). Although waste geometry and water availability may affect both the generation rate and total generation potential, these effects cannot be quantified without additional experiments. The current estimate of gas potential, 1,500 moles/drum-equivalent, is less than the FEIS estimate of 2,000 moles/drum-equivalent.
- Both the total amounts and total volumes of gas that will be generated within the WIPP repository are uncertain. Some microbial gas will be generated by the present waste form even in the complete absence of inflowing brine, because of the water originally present in the waste and the long-term buffering of room humidity near 70% by intergranular brines

in the surrounding Salado Fm. Even without microbial activity, the presence of Mg-rich Salado brine in the repository would result in anoxic corrosion of drums and metallic wastes. Gas-production rates are also uncertain, because gas production will retard brine inflow.

- The net effect of microbial activity on the room water budget is not known. Some microbial reactions consume water, some produce it. The net effect is assumed here to be zero.

4.2.1 Processes that Produce Gas

The gas and water (H₂O) contents of WIPP disposal rooms will affect the long-term performance of the repository, especially in the event of human intrusion. Because chemical reactions can produce or consume large amounts of gas and H₂O, repository chemistry must be quantified to predict repository gas and H₂O budgets. During the last year, the WIPP Performance Assessment (PA) Source-Term Group (STG) has performed several tasks. They reviewed relevant investigations carried out by the WIPP Project and for other applications; identified and assigned priorities to additional laboratory studies required to quantify repository gas and H₂O budgets; and developed a conceptual design for the studies. Appendices A.1 through A.3 describe these activities in detail. Data from the laboratory investigations recommended by the STG will not be available for several months.

Several processes could affect repository gas and H₂O budgets. The air trapped in disposal rooms at the time they are filled and sealed will comprise mostly nitrogen (N₂) and oxygen (O₂). The Salado Fm. will release brine and will initially release gas, mostly N₂. Eventually, the Salado Fm. will serve as a sink for all gases, except perhaps N₂. Microbial activity, either aerobic or anaerobic, halophilic or nonhalophilic, will consume cellulosic and perhaps other materials in the waste and will produce carbon dioxide (CO₂) in potentially large amounts, as well as other gases under certain conditions. These other gases could include hydrogen sulfide (H₂S), methane (CH₄), and N₂. The net effect of microbial activity on the H₂O budget of the repository, however, is unclear. Corrosion, either oxic or anoxic, of drums, metal boxes, and metallic constituents of the waste (hereafter called "metals"), will

consume large quantities of H₂O, and (in the case of anoxic corrosion) produce large amounts of hydrogen (H₂). Microbial consumption of H₂ during sulfate (SO₄²⁻) reduction might remove one of these gases. The reaction of H₂S with metals or their corrosion products to form pyrite (FeS₂) will probably remove another. The formation of FeS₂, however, will release the H₂ consumed during SO₄²⁻ reduction and perhaps produce additional H₂ and release any H₂O consumed during oxic or anoxic corrosion. Radiolysis of brines, cellulosic materials, plastics, and rubbers will consume H₂O and produce carbon monoxide (CO), CO₂, H₂, and O₂. Appendices A.1 through A.3 describe these reactions in detail.

4.2.2 Microbial Gas Production

The laboratory investigations recommended by the STG will provide detailed information on several of the processes described above. In lieu of these results, the best available data are those reviewed by Molecke (1979). Based on an extensive literature review and experimental program, Molecke (1979) concluded that the "most probable overall average" gas-production rate for TRU waste in disposal rooms will be 0.3 to 1.4 moles/drum per year, with 0.0005 moles as the lower limit and 2.8 moles as the upper limit. This estimate considered four processes--microbial degradation (the most important), chemical corrosion, radiolysis, and thermal degradation--and was based on estimated properties of the TRU waste existing at the Idaho National Engineering Laboratory (INEL) at that time.

Sandia Laboratories (1979) also estimated a "worst case" gas-production rate of 5 moles/drum per year for 400 years. The results given in Sandia Laboratories (1979) were calculated by Martin A. Molecke of Sandia, but that report did not describe in detail the calculations and assumptions used. Molecke has, however, described those assumptions and calculations to the authors of this report, and his description is briefly summarized here. To calculate the "worst case" gas-production rate and gas-production period, Molecke estimated that the theoretical, maximum total gas-production potential of a typical TRU waste drum under aerobic conditions is 5,600 moles, but that the actual gas-production potential under the conditions expected for the WIPP is 2,000 moles/drum.

The "best estimate" of the gas-production rate, i.e., the expected or most realistic value, is 0.85 moles/drum per year. This rate is the arithmetic mean of 0.3 and 1.4 moles/drum per year, the range estimated by Molecke (1979). This gas-production rate does not include the H₂ produced by anoxic corrosion of metals (see below). The calculations in this report, however, do not use the gas-production potential of 2,000 moles/drum estimated by Sandia Laboratories (1979); instead, they use a total gas-production potential of 1,500 moles/drum.

The new gas-production potential of 1,500 moles/drum has been calculated using the same assumptions used for the estimate of 2,000 moles/drum proposed by Sandia Laboratories (1979), but using new estimates of the quantities of some of the nonradioactive constituents of the WIPP inventory (Appendix A.9) and using an estimate of the H₂-production potential from anoxic corrosion of metals. The gas-production potential of 1,500 moles/drum does not include radiolysis, which is probably a minor component of the total gas-production potential for most of the nonradioactive constituents of TRU waste.

To calculate a gas-production potential of 2,000 moles/drum for Sandia Laboratories (1979), Molecke assumed that 100% of the cellulosic materials and 50% of the Neoprene and Hypalon (two types of rubber) in the waste will be converted to gas by microbial degradation. Furthermore, Molecke assumed that the theoretical, maximum yields for the conversion of these materials by aerobic degradation will be 37.1 moles of carbon oxides (CO_x) and 30.9 moles of H₂ per kg of cellulosic materials; 4.16 moles of chlorine gas (Cl₂), 28.8 moles of CO_x, 24.9 moles of H₂, and 4.81 moles of sulfur oxides (SO_x) per kg of Hypalon; and 8.05 moles of Cl₂, 45.2 moles of CO_x, and 28.3 moles of H₂ per kg of Neoprene.

Appendix A.9 estimates that there will be 253,000 kg of cloth, 66,600 kg of treated lumber, 56,700 kg of untreated lumber, 3,280,000 kg of paper, and 93,400 kg of plywood in the TRU waste that will be emplaced in the WIPP. Furthermore, Appendix A.9 estimates that 4,500 of the 6,000 "old" boxes that contain TRU waste (see below) are made of plywood. For these boxes, the average mass of plywood per box (excluding any plywood in the waste) is 158 kg. Because neither the "new," metal, standard TRU-waste boxes nor the drums

contain plywood (excluding any plywood in the waste), the total quantity of plywood in containers will be 711,000 kg. Based on the estimates in Appendix A.9, the total quantity of cellulosic materials in the WIPP will be 4,461,000 kg.

Appendix A.9 also estimates that there will be 118,000 kg of Hypalon, 135,000 kg of Neoprene, 591,000 kg of surgical gloves, and 80,000 kg of miscellaneous rubbers in the WIPP inventory. Prorating the 671,000 kg of surgical gloves and miscellaneous rubbers between Hypalon and Neoprene, the waste is estimated to contain 431,000 kg of Hypalon and 493,000 kg of Neoprene.

Appendix A.9 estimates that the WIPP inventory will consist of 385,000 drums of TRU waste, 6,000 "old" boxes of TRU waste, each equivalent to 15 drums, and 13,500 "new" boxes of TRU waste, each equivalent to 6 drums. Thus, the equivalent of 556,000 drums of TRU waste will be emplaced in the WIPP.

Dividing the estimates of the total quantities of cellulosic materials, Hypalon, and Neoprene given above by 556,000 drums gives 8.02 kg of cellulosic materials, 0.775 kg of Hypalon, and 0.887 kg of Neoprene per equivalent drum. The same microbial conversion factors and yields assumed by Molecke for Sandia Laboratories (1979) were used to calculate gas-production potentials for these quantities of materials: 545 moles/drum for cellulosic materials, 24.3 moles/drum for Hypalon, and 36.2 moles/drum for Neoprene. The total gas-production potential is 606 moles/drum for these materials. Molecke's (1979) gas-production rate of 0.85 moles/drum per year and the gas-production potential of 606 moles/drum imply a gas-production period of 713 years, assuming brine saturation. These estimates do not include the H₂ that will be produced by anoxic corrosion of metals (see below).

4.2.3 Anoxic Corrosion

Although Molecke (1979) considered chemical corrosion for his estimate of the "most probable overall average" gas-production rate, he assumed that corrosion of metals will only occur prior to filling and sealing of WIPP disposal rooms. Such corrosion will consume O₂ from the mine air. After

sealing, depletion of this O_2 and any O_2 produced by radiolysis, and resaturation of the repository by magnesium (Mg^{2+})-bearing brine, anoxic corrosion of metals will consume H_2O and produce H_2 . An estimate of the potential H_2 -production rate must therefore be added to the value of 0.85 moles/drum per year for those cases in which resaturation of WIPP disposal rooms is assumed.

Data reviewed by Molecke (1979) provide the highest estimate of the H_2 -production rate. These data, which were obtained from a laboratory study of the corrosion of 1018 mild steel (the same alloy used for the drums) in sodium-chloride-saturated brine at $25^\circ C$, imply that anoxic corrosion will produce 2 moles of H_2 per drum per year for 336 years, when all of the drums will be consumed. In addition, Appendix A.1 extrapolates data reported by Haberman and Frydrych (1988) from a laboratory study of the corrosion of A216 Grade WCA mild steel in Permian Basin brines at 90, 150, and $200^\circ C$ to expected WIPP temperatures of about $30^\circ C$ and the lower Mg^{2+} concentrations of intergranular Salado brines. Based on these extrapolations, anoxic corrosion will consume all of the drums in 500 to 2,000 years. The lowest estimate of the H_2 -production rate, based on the corrosion period of 2,000 years, is 0.262 moles/drum per year. The arithmetic mean of the lowest and the highest rates, 1.13 moles/drum per year, is the "best estimate" of the H_2 -production rate. Molecke (1979) calculated an H_2 -production potential of 672 moles/drum, but Appendix A.1 calculates an H_2 -production potential of 524 moles/drum. The mean of these two values is 598 moles/drum. These mean values lead to an estimate of anoxic drum corrosion of 1.13 moles of H_2 /drum per year for 529 years. These estimates do not include the H_2 that will be produced by anoxic corrosion of metal boxes and metallic constituents of the waste, discussed below, nor do they account for retardation of brine inflow by gas generation.

Because much of the waste will be emplaced in metal boxes, the estimates of the H_2 -production potential and the H_2 -production period given above must be corrected to account for the difference between the quantities of steel per equivalent drum of waste in the metal boxes and the mass of steel per 55-gallon drum used in Appendix A.1, 29.3 kg. (Because no corrosion data are available for the metal boxes, H_2 -production rates for metal boxes are assumed to be identical to the rate for drums. The steel alloy used in boxes is

similar to that used in drums.) Appendix A.9 estimates that 1,500 of the 6,000 "old" boxes and all of the 13,500 "new" boxes will be made of steel. Each "old" metal box contains 236 kg of steel and that each "new" box contains 341 kg of steel. Because each "old" box contains the equivalent of 15 drums of waste and each "new" box contains the equivalent of 6 drums of waste, there are 15.8 kg of steel per equivalent drum of waste in the "old" boxes and 56.8 kg of steel per equivalent drum of waste in the "new" boxes. The weighted average for the mass of steel per equivalent drum of waste in the WIPP inventory, M_A , is

$$\begin{aligned}
 M_A = & \left[385,000 \text{ drums} \left(\frac{29.3 \text{ kg}}{55\text{-gal drum}} \right) \right. \\
 & + 22,500 \text{ equivalent drums in "old" boxes} \left(\frac{15.8 \text{ kg}}{\text{equivalent drum in "old" box}} \right) \\
 & + 81,000 \text{ equivalent drums in "new" boxes} \left(\frac{56.8 \text{ kg}}{\text{equivalent drum in "new" box}} \right) \left. \right] \\
 & + 556,000 \text{ equivalent drums} \\
 & = 29.2 \text{ kg/equivalent drum}
 \end{aligned}$$

The weighted average, 29.2 kg of steel per equivalent drum, is virtually identical to 29.3 kg per 55-gallon drum, the value used in Appendix A.1. Nevertheless, the estimate of the H₂-production potential has been reduced from 598 moles/drum per year to 596 moles per equivalent drum, and the estimate of the H₂-production period from 529 years to 527 years.

In addition to the H₂ produced by anoxic corrosion of drums and metal boxes, anoxic corrosion of various iron (Fe) and steel alloys in the waste will also produce H₂. These alloys are assumed to corrode at the same rate as mild steel. Appendix A.9 estimates that there are 5,110,000 kg of stainless steel alloys and 3,000,000 kg of miscellaneous Fe-based alloys in the WIPP inventory. Based on these estimates, there are 14.6 kg of Fe and steel per equivalent drum of waste. Because each equivalent drum of waste contains 14.6 kg of Fe or steel in addition to the 29.2 kg of steel used to fabricate the

drum or metal box, the H₂-production potential is increased by 50% from 596 moles/drum to 894 moles/drum. If sufficient brine were present (see below), anoxic corrosion of drums, metal boxes, and Fe-bearing constituents of the waste would occur simultaneously; therefore the H₂-production rate will increase by 50% from 1.13 moles/drum per year to 1.70 moles/drum per year, but this rate will still be applicable for 527 years. Because no information is available to evaluate the possibility of H₂-production by anoxic corrosion of other metals in the waste, the estimate described above cannot be corrected for these metals. About 64% of metallic constituents of the waste, however, comprises Fe-based alloys. Other metallic constituents are lead, 7%; tantalum, 4%; and others (mainly aluminum and copper), 25%.

Appendix A.1 calculates that 102 m³ of brine will be consumed by anoxic corrosion of all of the drums in a WIPP disposal room, but this value was based on the assumptions that there will be 6,750 drums/room and that the mass of steel per drum is 29.3 kg. Assuming 7,000 drums/room and 29.2 kg of steel per equivalent drum, 105 m³ of brine would be required. At 6,800 drums/rooms (Section 4.8), 102 m³ would be required, assuming the same amount of steel per equivalent drum. Furthermore, this value must be increased by an additional 50%, to 158 m³, to account for Fe-bearing constituents of the waste. If all of the brine that enters the rooms were consumed by absorption by bentonite or crushed salt in the backfill, or by other processes such as microbial hydrolysis of cellulosic materials or radiolysis, anoxic corrosion of metals might not occur, and H₂ might not be produced by this process. It is possible that anoxic corrosion could proceed using H₂O vapor present in disposal rooms after they are sealed and O₂ is depleted, or using H₂O previously absorbed by bentonite in contact with metals, but there is no evidence yet that anoxic corrosion will actually occur in the absence of condensed H₂O. If sufficient brine were present for anoxic corrosion to occur, the total gas-production rate would be the sum of 0.85 and 1.70 moles/drum per year, or 2.55 moles/drum per year. This estimate assumes that microbial degradation and anoxic corrosion occur simultaneously. The total gas-production potential would be the sum of 606 and 894 moles/drum, or 1,500 moles/drum.

Although the chemical reactions discussed above will also affect the H₂O budget of the repository, whether they will consume or produce H₂O is not

known. In lieu of results from the laboratory investigations proposed by the STG, these reactions are assumed to have no net effect on the repository H₂O budget.

4.2.4 Discussion

The estimates of the gas-production rates and the gas-production potentials discussed above raise concerns about the long-term performance of the WIPP (Section 4.10). These estimates must be justified, especially with respect to the possible choice of lower values for these parameters.

Paul Drez of IT Corporation, Albuquerque, NM, has calculated gas-consumption and -production rates based on the results of analyses by Clements and Kudera (1985) of head-space gases from drums of Rocky Flats TRU waste stored at INEL. Drez concluded that both rates decrease to low values after a few years. This conclusion might be applicable to waste in WIPP disposal rooms prior to filling and sealing, but is probably inapplicable thereafter, for two reasons. First, the low relative humidity during near-surface storage at INEL probably prevented significant microbial degradation of the waste at that time, but microbial activity will occur after the rooms are sealed, the drums are crushed, and the repository resaturates. Even without resaturation, the relative humidity in WIPP disposal rooms after sealing will be higher than it is during near-surface storage at INEL, and it could be high enough to promote microbial activity, albeit at slow rates. Second, in the event of brine saturation of the repository, anoxic corrosion of metals will produce copious quantities of H₂. Even without resaturation, anoxic corrosion might proceed using H₂O vapor, if Mg²⁺ is available.

Recently, critics of the laboratory studies reviewed by Molecke (1979) have stated that these experiments yielded microbial gas-production rates greater than those expected for actual repository conditions, because they were carried out under conditions optimized for microbial activity. Molecke (1979) pointed out, however, that experiments conducted under saline or asaline conditions, brine-saturated or moist conditions, and with glucose or less bioavailable waste simulants as the substrate all yielded similar gas-production rates. Critics have also suggested that Molecke's (1979) "most probable overall average" gas-production rate of 0.85 moles/drum per year is

actually a "worst case" estimate because his experiments were short relative to the period of interest to the WIPP PA, and that the microbial gas-production rate will probably decrease greatly with time. This rate could indeed decrease with time as microorganisms turn to less efficient metabolic pathways upon depletion of electron acceptors (oxidants) that yield more free energy per mole of organic carbon consumed (cf. Appendix A.1). Molecke (1979), however, reviewed the results of both aerobic and anaerobic microbiological experiments and concluded that the gas-production rates were similar. The proposed rate of 0.85 moles/drum per year thus probably already reflects the expected decrease in microbial gas-production rates with time. It is still possible, of course, that additional laboratory or underground studies will yield microbial gas-production rates lower than those reviewed by Molecke (1979). Whether these studies will yield gas-production rates low enough to preclude significant pressurization of the repository, however, is unclear. In any case, it would be difficult at this time to justify any rate lower than 0.85 moles/drum per year for microbial and radiolytic gas production.

The use of a gas-production potential less than the current estimate of 1,500 moles/drum is also appealing. Appendix A.1 for example, calculates a microbial gas-production potential of 690 moles/drum based on the assumption that the only substrate used by microorganisms would be cellulosic materials, a previous estimate of 6.90 kg of cellulosic materials per drum from Drez, and the assumptions that microorganisms would consume all of the cellulose by using SO_4^{2-} as the electron acceptor and that none of the CO_2 or H_2S produced would dissolve in any brine present or react with metals or their corrosion products. The estimate of 690 moles/drum from Appendix A.1 must now be revised for several reasons. First, the previous estimate of 6.90 kg of cellulosic materials per drum did not include the plywood boxes in which much of the waste will be emplaced. Plywood boxes have been included in the current estimate of the gas-production potential. Second, microorganisms could well consume waste constituents in addition to cellulosic materials. The most important potential additions are plastics, which are not included in the current estimate, and rubbers, of which 50% are assumed to be converted to gas in the current estimate. Although microorganisms will almost certainly consume cellulosic materials in preference to plastics, they could turn to

plastics after depletion of the cellulosic materials. Furthermore, radiolysis of plastics could transform them into more bioavailable materials. Third, the stoichiometry of the microbial reactions proposed in Appendix A.1 must be revised to include factors such as the hydrolysis of cellulose and the synthesis of cellular material (biomass) by microorganisms. Fourth, the microbial gas-production potential will also depend on estimates of the quantities of waste constituents in addition to cellulosic materials, such as NO_3^- (a potential electron acceptor) and plastics. Fifth, the estimate of 690 moles/drum did not include the H_2 -production potential from anoxic corrosion of metals. Anoxic corrosion has been included in the current estimate of the total gas-production potential, 1,500 moles/drum. Based on these considerations, the current estimate of the gas-production potential will be revised in the next few months.

4.3 Expected Brine Inflow to Waste Rooms and Panels

Based on a Darcy-Flow Model

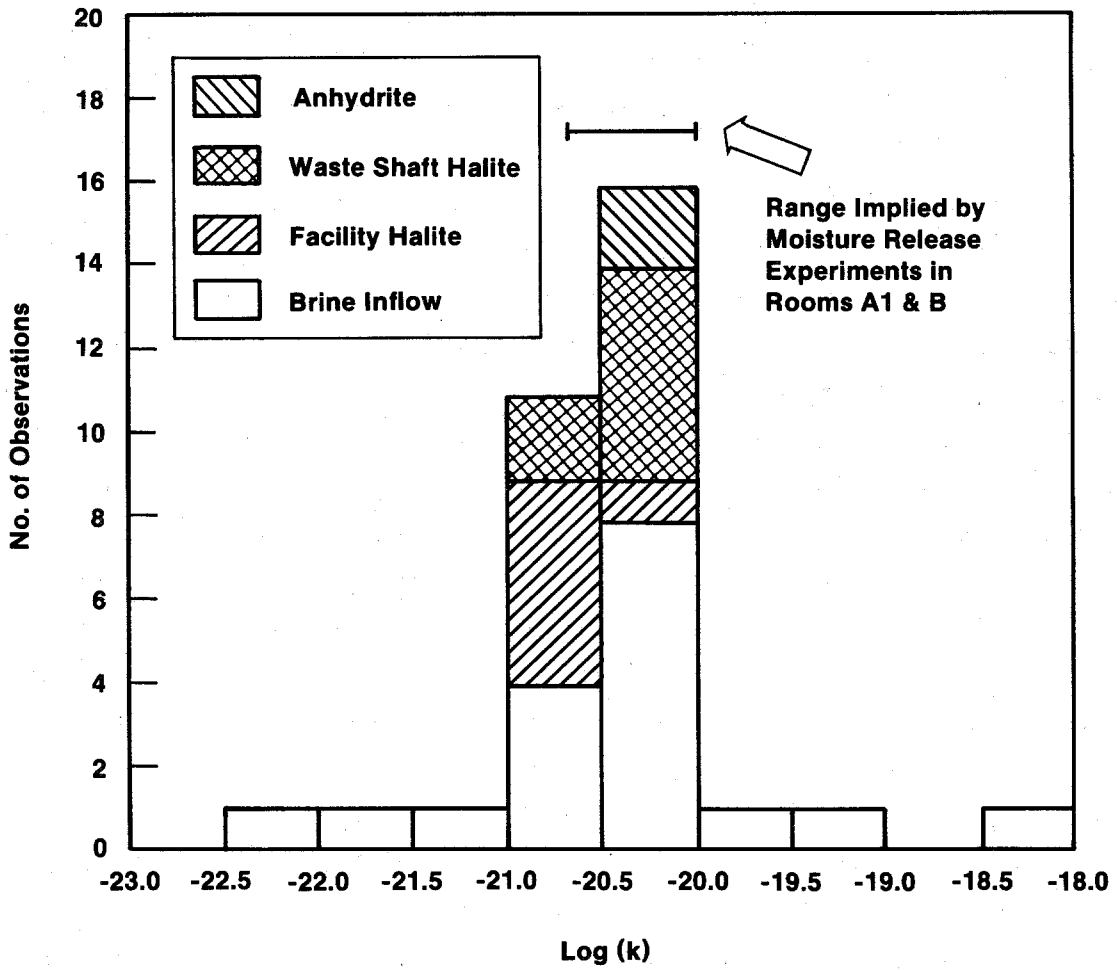
The following are the major conclusions of Section 4.3.

- Under expected conditions, no free brine will be present within the repository until well after structural closure, at which time room porosity will be too small to allow slurry formation.
- Calculated brine-inflow volumes over 30 years, the approximate time of interest for evaluating the formation of a brine slurry during repository closure (Section 4.10.1), range from ~3.5 to 24 m^3 for permeabilities of 10^{-21} to 10^{-20} m^2 , without and with a disturbed rock zone assumed to have a limiting porosity of 0.04. These volumes are approximately one and one-half orders of magnitude below the estimated 900 m^3 required for saturation of waste and backfill 30 years after decommissioning (Section 4.10.1). At 30 years, brine-inflow rates appear independent of gas generation, because gas pressures are still expected to be very low.

- Similarly calculated volumes at 60 years range from ~6 to 38 m³, less than the expected sorption capacity of bentonite assumed to be present in the design-basis salt/bentonite backfill (Table 4-7).
- Major uncertainties in the present model (Section 3.2.1) include stratigraphic effects, uncertainty in the storativity parameter, and the possibility of two-phase flow.
- The calculated long-term inflow rate of 1.3 m³/year to a full waste-disposal panel, based on the assumption of Darcy flow and a far-field permeability of 10⁻²⁰ m², is probably an overestimate. Therefore, a lower rate of 0.1 m³/year per room has been used in Case IID.

4.3.1 Brine-Inflow Volumes for Early-Time, Undisturbed Conditions

The current working model for simulating brine inflow is that of Nowak et al. (1988). A qualitative description of the flow mechanisms, assumptions, and uncertainties associated with this brine-inflow model, which assumes Darcy flow, is contained in Section 3.2.1. Nowak et al.'s (1988) model can be used to estimate the brine-inflow volume to a room or panel prior to termination of the inflow by back pressure from waste-generated gas (Section 4.10) or consolidation of the room contents (Section 4.8). Brine inflow during this early period is transient, and the primary controlling parameters are driving pressure and the permeability and storativity of the Salado Fm. The driving pressure is the difference between pre-excavation pore pressure in the salt and atmospheric pressure within the repository. Nowak et al. (1988) examined two initial pore pressures, hydrostatic and lithostatic (Section 3.2.1). Use of a lithostatic initial pressure provides an upper bound on pore-pressure changes resulting from volumetric strain near the excavation and is the preferred pore pressure for calculations. Nowak et al. (1988) reviewed the in-situ experimental data and concluded that the far-field permeability of the Salado Fm. lies between 1 x 10⁻²⁰ to 1 x 10⁻²¹ m² (Figure 4-1). The storage parameter in Nowak et al.'s (1988) model is based on the elastic properties of the salt, producing an equivalent specific pressure storativity of 6 x 10⁻¹² Pa⁻¹. In addition to examining brine inflow assuming a homogeneous salt mass, Nowak et al. (1988) carried out simulations in which a



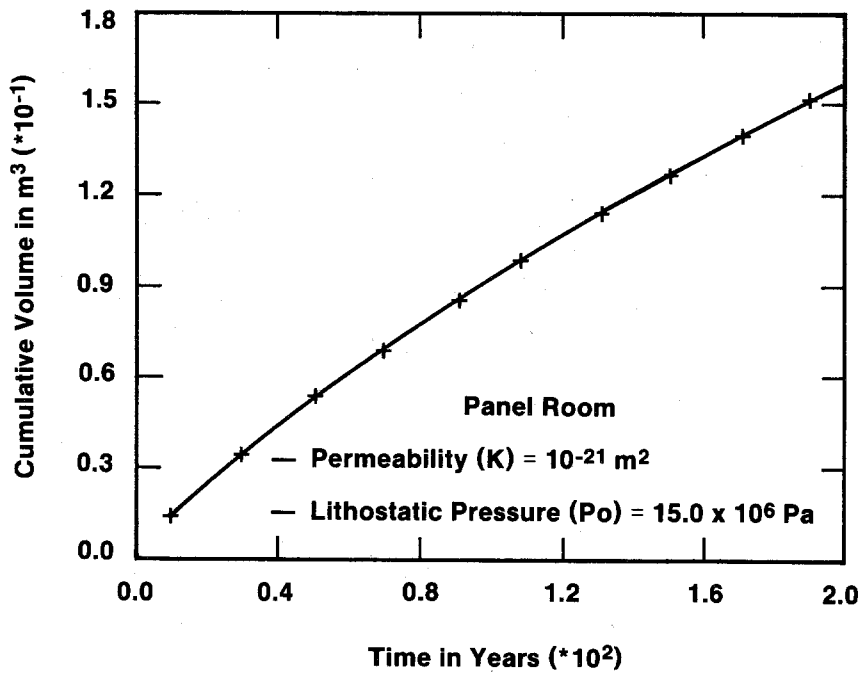
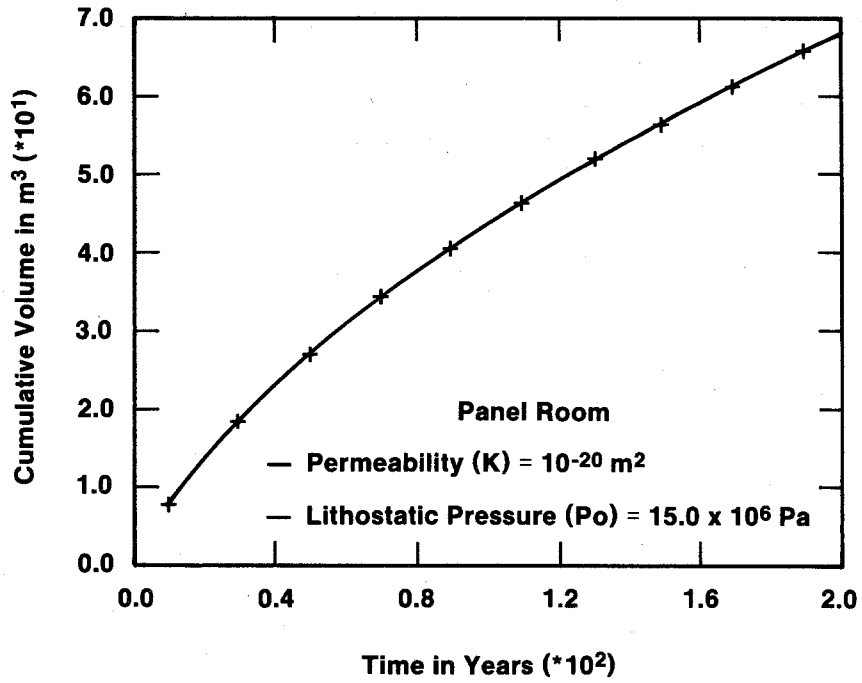
TRI-6330-86-0

Figure 4-1. Salado Fm. permeabilities derived from in-situ experiments (Nowak et al., 1988).

disturbed rock zone (Section 4.7) was assumed to be present and to have infinite permeability. For these simulations, the atmospheric-pressure boundary condition was moved 5 to 10 m into the host rock, and brine inflow was calculated at that boundary. An alternative approach to examining the impact of a disturbed rock zone used an idealized radial model with permeabilities in the disturbed rock zone decreasing from 1×10^{-18} to $1 \times 10^{-21} \text{ m}^2$ within the first ten meters from the excavation (Appendix A.8).

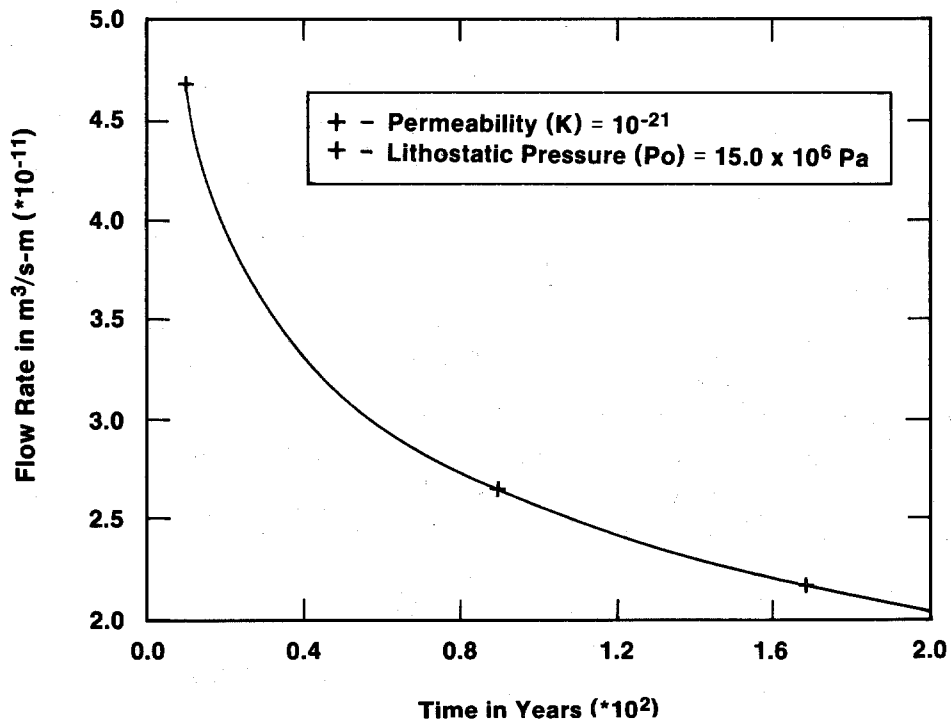
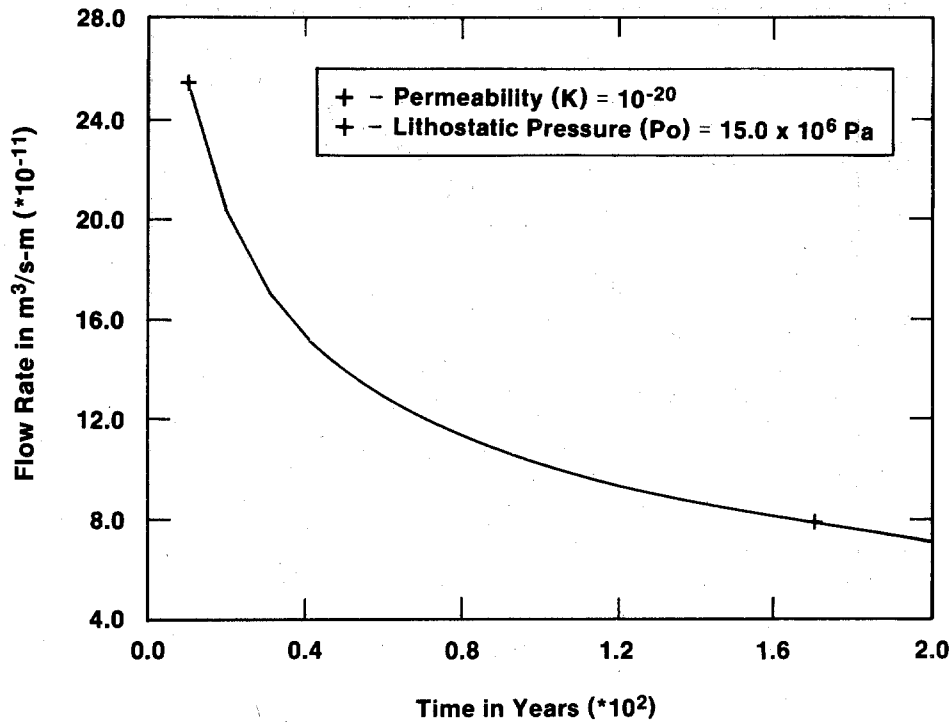
The simulations of Nowak et al. (1988) examined a 200-year time period using lithostatic and hydrostatic initial and far-field pore pressure and salt permeabilities of 1×10^{-20} and $1 \times 10^{-21} \text{ m}^2$. Cumulative brine-inflow volumes and time-dependent brine-inflow rates for a representative waste-emplacement room are presented in Figures 4-2 and 4-3, respectively. Cumulative brine volumes for the 30- and 60-year time periods (see below) pertinent to potential slurry formation (Section 4.10.1) and to mechanical consolidation (Section 4.7) are summarized in Table 4-1. Table 4-1 also includes simulation results for a salt permeability of $1 \times 10^{-19} \text{ m}^2$. Although a far-field permeability of $1 \times 10^{-19} \text{ m}^2$ is highly unlikely given the distribution of permeability values in Figure 4-1 (Nowak et al., 1988), the simulation using this value provides useful information about the brine-inflow volume that would result from this extreme permeability value.

For lithostatic pore pressures and the expected permeability range of 1×10^{-21} to $1 \times 10^{-20} \text{ m}^2$, cumulative brine-inflow volumes for a representative waste-emplacement room range from 3.5 to 19 m^3 in 30 years and from 6.2 to 31 m^3 in 60 years. As discussed in Section 4.10.1, 30 years is the estimated time required for repository porosity to be reduced to 0.4, the minimum porosity at which a slurry can form. As discussed in Section 4.8, 60 years is the time assumed to be required for repository porosity to be reduced to 0.18, the "final" porosity considered in this report. Simulations that incorporate the disturbed rock zone indicate that enhanced permeability near the excavations will increase brine-inflow rates by a factor ranging from 1.2 to 2.0. Nowak et al. (1988) did not vary storativity. As discussed in Section 3.2.1, inelastic volumetric deformation in the salt or the presence of a gas phase may affect transient brine-inflow behavior. Increased volumetric strain caused by inelastic deformation may increase early- or intermediate-



TRI-6330-44-0

Figure 4-2. Cumulative brine-inflow volumes for a representative waste-emplacement room at permeabilities of 10^{-20} and 10^{-21} m^2 , assuming lithostatic far-field pore pressure (Nowak et al., 1988).



TRI-6330-45-0

Figure 4-3. Time-dependent brine-inflow rates per meter of tunnel at permeabilities of 10^{-20} and $10^{-21} m^2$, assuming lithostatic far-field pore pressure (Appendix A.5).

Table 4-1. Variations in Cumulative Brine Inflow (in m³) to a Waste-Disposal Room as a Function of Variations in Far-Field Permeability, Far-Field Fluid Pressure, Time, and Presence or Absence of a Disturbed Rock Zone

Far-Field Pressure and Model Configuration Variation	Permeability and Time Variation					
	<u>k = 10⁻¹⁹ m²</u>		<u>k = 10⁻²⁰ m²</u>		<u>k = 10⁻²¹ m²</u>	
	30 Yr	60 Yr	30 Yr	60 Yr	30 Yr	60 Yr
Room in panel:						
Hydrostatic Po (6 MPa)	26	41	7	12	1.3	2.5
Lithostatic Po (15 MPa)	65	93	19	31	3.5	6.2
Enlarged room to simulate DRZ:						
Lithostatic Po (15 MPa)	--	--	24	38	7	12
Idealized radial room with DRZ k = 10 ⁻²¹ → 10 ⁻¹⁸ over 10 m						
Lithostatic Po (15 MPa)	--	--	--	--	5	10

Note: Some values are approximate and are interpolated from cumulative volume-versus-time plots (Nowak et al., 1988; Appendix A.5; Appendix A.8).

time brine-inflow rates. The presence of a gas phase may increase intermediate or late brine-inflow rates by decreasing the rate of pressure decrease in response to flow. The magnitude of the impact of these flow-mechanism uncertainties has not yet been assessed.

4.3.2 Brine-Inflow Rates for Long-Term Breach Conditions

In Case II, a hydrocarbon-exploration borehole is assumed to breach the repository and penetrate a Castile brine reservoir (Section 7.1). Following the degradation of the plugged borehole to a rubble-filled hole, brine from two sources flows up the borehole and is released to the Culebra Dolomite. One source of brine is the Castile brine reservoir. The other, much smaller source of brine, is the Salado Fm. An estimate of the long term brine-inflow rate from the Salado Fm. based on the Darcy model of Nowak et al. (1988) is described below.

After the borehole plugs fail and the flow resistance in the borehole is that of a rubble-filled hole, it is assumed that the breached waste panel becomes fully resaturated and that pore pressure throughout the panel stabilizes at hydrostatic pressure with respect to the Culebra Dolomite (assuming a fluid column of brine), producing long-term, steady-state brine-inflow from the Salado Fm. to the boundary of the waste panel. The resulting driving pressure differential is the difference between the pore pressure in the borehole at the altitude of the repository (i.e., $[1200 \text{ kg/m}^3] \cdot [9.8 \text{ m/s}^2] \cdot [537 \text{ m}] = 6.3 \text{ MPa}$) and the pore pressure in the host rock (14 MPa, see Tables 4-6 [p. 4-55] and 4-9 [p. 4-91] and Section 3.2.1), creating a net driving force of 7.7 MPa. This pressure differential is assumed to be present throughout an entire waste panel. It is further assumed that all brine entering the waste panel is accessible to the borehole. This assumption is conservative, because pore-pressures within the waste panel will increase with increasing distance from the borehole, producing a driving pressure differential at the panel boundaries that is less than 7.7 MPa. This assumption is especially conservative under the conditions assumed to be present as the result of waste compaction and grouting. These modifications are expected to reduce the hydraulic conductivity of the waste from 1×10^{-6} to $1 \times 10^{-11} \text{ m/s}$ (Section 4.11). With such low hydraulic conductivities,

hydrostatic pressure present at the breach borehole is not expected to propagate very far into the waste mass. Therefore, while brine inflow for Cases IIA, IIB, and IIC has been scaled to an entire panel, brine inflow after waste compaction and grouting has been scaled to a single room for Case IID.

To compute the brine-inflow rate, Nowak et al.'s (1988) brine-inflow model with a permeability of $1 \times 10^{-20} \text{ m}^2$ was used. Because steady-state brine-inflow rates scale linearly with driving pressure, the brine-inflow rate for one driving pressure can be directly scaled to brine-inflow rates for a different driving pressure (assuming long-term, steady-state conditions). At 200 years (the end of Nowak et al.'s [1988] simulations) the flow rate is approaching, but has not yet reached, steady state (Figure 4-3). Using the brine-inflow rate at 200 years ($7 \times 10^{-11} \text{ m}^3/\text{s-m}$) as a first approximation of the long-term, steady brine-inflow rate, q , this rate scales to a panel as follows:

$$q = q' \Delta p L C$$

$$\begin{aligned} q &= (7 \times 10^{-11} \text{ m}^3/\text{s-m}) \cdot (7.7 \text{ MPa}/15.0 \text{ MPa}) \cdot (1128 \text{ m}) \cdot (3.156 \times 10^7 \text{ s/yr}) \\ &= 1.3 \text{ m}^3/\text{yr} \end{aligned}$$

where

q' = flow rate per unit length of tunnel,

Δp = scaling of driving pressure,

L = length of tunnel in 7 rooms and 2 access drifts, and

C = conversion factor, seconds to years.

Therefore, a first approximation of the long-term, steady brine-flow rate of Salado brine into the borehole is $1.3 \text{ m}^3/\text{yr}$ for Cases IIA, IIB, and IIC. An inflow rate of $0.1 \text{ m}^3/\text{year}$ to the borehole is assumed in Case IID. The varying assumptions about the mixing of brine from the Salado Fm. with brine from the Castile Fm. in the Case II simulations is described in Section 7.3.1.

An important limitation on the estimation of brine-inflow rates for long-term, breach conditions is that large-scale hydraulic behavior of the design-

basis panels (Cases IIA, IIB, and IIC) and of the assumed engineered modifications (Case IID) has not been rigorously analyzed for borehole-breach conditions. The assumption that the hydrostatic pressure at the borehole is present throughout the waste panel may be overly conservative, especially in Case IIB, in which the waste is assumed to be precompacted. An important, nonconservative assumption about potential flow-driving mechanisms within the waste panel is that any excess waste-generated gas vents passively up the borehole. Because Case II simulates a single borehole penetrating an entire panel, it is possible that the system behaves more heterogeneously. For example, gas might be produced in a distant part of the panel, providing an additional driving force for moving fluid toward and eventually up the borehole.

4.4 Initial Inventory and Decay Chains

The major conclusions of Section 4.4 are listed below.

- Only the CH-TRU radionuclide inventory is considered here, both because of the uncertainty in the RH-TRU inventory and because of the relatively small loading of RH-TRU. For calculations, it is assumed that the four dominant radionuclides in the initial CH-TRU inventory are ^{238}Pu , ^{241}Am , ^{239}Pu , and ^{240}Pu .
- The inventory and decay chains used in transport analyses are slightly simplified by eliminating very short-lived radionuclides and some of the daughters late in the chains.
- The only volatile radionuclide expected to be present in the CH-TRU inventory is radon-222, a decay product of radium-226. The maximum expected inventory of radon-222 is 10^{-3} Ci at 10,000 years, which is negligible. Therefore, gaseous transport of volatile radionuclides is not considered in this report.

Table 4-2. CH Waste Inventory

a. Initial Inventory

<u>Radionuclide</u>	<u>t_{1/2}(yr)</u>	<u>Curies</u>
Th-232	1.41 x 10 ¹⁰	2.74 x 10 ⁻¹
U-233	1.59 x 10 ⁵	7.72 x 10 ³
U-235	7.04 x 10 ⁸	3.70 x 10 ⁻¹
U-238	4.47 x 10 ⁹	1.47
Np-237	2.14 x 10 ⁶	8.02
Pu-238	8.77 x 10 ¹	3.90 x 10 ⁶
Pu-239	2.41 x 10 ⁴	4.25 x 10 ⁵
Pu-240	6.54 x 10 ³	1.05 x 10 ⁵
Pu-241	1.44 x 10 ¹	4.08 x 10 ⁶
Pu-242	3.76 x 10 ⁵	1.80 x 10 ¹
Am-241	4.32 x 10 ²	6.37 x 10 ⁵
Cm-244	1.81 x 10 ¹	1.27 x 10 ⁴
Cf-252	2.64	2.03 x 10 ⁴

4.4.1 Radionuclides in the CH Inventory

Only the CH inventory is considered in this analysis. Table 4-2a lists the initial CH-waste inventory. Because some radionuclides decay into a series of other radionuclides, it is important not only to consider those radionuclides in the original inventory but also daughters in the chain that are of significant radiological consequence.

The following four chains represent the decay of all the major radionuclides contained in the inventory:

- $244\text{Cm} \rightarrow 240\text{Pu} \rightarrow 236\text{U} \rightarrow 232\text{Th} \rightarrow 228\text{Ra}$
 \uparrow
 $252\text{Cf} \rightarrow 248\text{Cm} \rightarrow 244\text{Pu}$
- $241\text{Pu} \rightarrow 241\text{Am} \rightarrow 237\text{Np} \rightarrow 233\text{U} \rightarrow 229\text{Th}$
- $242\text{Pu} \rightarrow 238\text{U} \rightarrow 234\text{U} \rightarrow 230\text{Th} \rightarrow 226\text{Ra} \rightarrow 210\text{Pb}$
 \uparrow
 238Pu
- $239\text{Pu} \rightarrow 235\text{U} \rightarrow 231\text{Pa}$

In deriving these chains, all radionuclides with half-lives less than a few hours have been eliminated. Another intermediate radionuclide (Th-234, half-life 24 days) was eliminated because of its low radiological toxicity and relatively short half-life.

4.4.2 Radionuclides Included in Transport Calculations

The four decay chains were further reduced and simplified by eliminating those short-lived radionuclides in the inventory that decay into long-lived daughters (Tables 4-3 and E-5). This decay mode produces daughters of low activities. For example, Cm-244 ($t_{1/2} = 18.1$ years) decays into Pu-240 ($t_{1/2} = 6540$ years). The original inventory of Cm-244 is 1.27×10^4 curies, but after 100 years, most of the Cm-244 becomes Pu-240, reducing the activity to 35 curies, which is a small fraction of the activity of 1.05×10^5 curies associated with the original inventory of Pu-240.

Cf-252 has been eliminated for a similar reason, and its daughters Cm-248 and Pu-244 are also eliminated because of their low activities. Plutonium-241 was eliminated from the second chain because of its short half-life; however, the decay of Pu-241 to Am-241 results in a significant amount of activity associated with Am-241. This activity was added to the activity of the original inventory of Am-241. In the third chain, Pu-242 and U-238 were

Table 4-2. CH Waste Inventory

b. Modified Inventory Used in Calculations

<u>Radionuclide</u>	<u>t_{1/2} (yr)</u>	<u>Curies</u>	<u>Grams</u>
Pu-238	8.77 x 10 ¹	3.90 x 10 ⁶	2.28 x 10 ⁵
Pu-239	2.41 x 10 ⁴	4.25 x 10 ⁵	6.84 x 10 ⁶
Pu-240	6.54 x 10 ³	1.05 x 10 ⁵	4.61 x 10 ⁵
U-233	1.59 x 10 ⁵	7.72 x 10 ³	8.15 x 10 ⁵
U-234	2.44 x 10 ⁵	0	0
U-235	7.04 x 10 ⁸	3.7 x 10 ⁻¹	1.71 x 10 ⁵
U-236	2.34 x 10 ⁷	0	0
Am-241	4.32 x 10 ²	7.75 x 10 ⁵	2.26 x 10 ⁵
Np-237	2.14 x 10 ⁶	8.02	1.14 x 10 ⁴
Th-229	7.43 x 10 ³	0	0
Th-230	7.70 x 10 ⁴	0	0
Ra-226	1.60 x 10 ³	0	0
Pb-210	2.23 x 10 ¹	0	0

Table 4-3. Simplified Radionuclide Chains Used in the Calculations

-
- (1) $^{240}\text{Pu} \rightarrow ^{236}\text{U}$
 - (2) $^{241}\text{Am} \rightarrow ^{237}\text{Np} \rightarrow ^{233}\text{U} \rightarrow ^{229}\text{Th}$
 - (3) $^{238}\text{Pu} \rightarrow ^{234}\text{U} \rightarrow ^{230}\text{Th} \rightarrow ^{226}\text{Ra} \rightarrow ^{210}\text{Pb}$
 - (4) ^{239}Pu

Note: The inventory to be used for the above four chains is listed in Table 4-2b.

eliminated because of their very small activities (18 curies and 1.47 curies, respectively).

Finally, for transport analyses that only consider times less than 10^4 years, some of the daughters late in the chains can be eliminated.

The only radioactive gas expected in the WIPP repository is radon-222, the daughter of radium-226 ($^{226}\text{Ra} \rightarrow ^{222}\text{Rn}$). The inventory of radium-226 increases with time. The inventory of ^{226}Ra is 2×10^{-4} Ci at 5,000 years and 1.1×10^{-3} Ci at 10,000 years. Because the half-life of ^{222}Rn is only 3.8 days, and the half-life of ^{226}Ra is 1,600 years, radon will always be in secular equilibrium with its parent ^{226}Ra . Therefore the inventory of radon is 2×10^{-4} Ci at 5,000 years and 1×10^{-3} Ci at 10,000 years. This small quantity of radon is neglected in the calculations.

4.4.3 RH-TRU Inventory

The WIPP inventory comprising RH-TRU waste is not considered in the transport and dose calculations presented here for three reasons: low loading, inaccessibility, and low probability of interception during human intrusion. In addition, the RH-TRU inventory available at this time is not considered to be an accurate-enough source of information on individual radionuclides to support meaningful transport and dose calculations.

According to the WIPP Final Safety Analysis Report, the repository will contain 4,000 to 5,000 RH canisters with an average radionuclide content of 37 curies per canister (DOE, 1988, p. 3.1-11 and Table 3.1-5). Thus the maximum RH loading is expected to be 185,000 Ci, 2% of the initial CH loading shown in Table 4-2a. Half of the RH radionuclides are short-lived, with half lives <30 years. Only the uranium and plutonium isotopes and ^{241}Am are important to the transport and dose calculations, either because they are long-lived or because they have important daughters. Of the U, Pu, and ^{241}Am , the U isotopes have very low activities per canister ($<10^{-3}$ Ci/canister). The Pu and ^{241}Am isotopes also exist in the CH inventory, and with the exception of ^{240}Pu , the RH contribution is <10% of the total for each isotope. The ^{240}Pu chain is not an important contributor to total consequence calculated here.

RH-TRU waste will be emplaced in individually drilled and sealed boreholes in the pillers, not in the waste panels proper. Preliminary calculations suggest that these boreholes will creep closed in about 10 years, making wastes inaccessible to brine intrusion and degradation. Each canister will have an outer shell of 0.64-cm-thick (1/4-in.) steel. Thus it is unlikely that RH waste will be accessible from the waste rooms, or vice versa.

Finally, RH-TRU waste is less likely to be intercepted during human intrusion than CH waste (Hunter, 1989). The total area of excavated, waste-filled panels for CH TRU is expected to be $1.21 \times 10^5 \text{ m}^2$. The area occupied by a single RH canister is 2.04 m^2 , or $1.02 \times 10^4 \text{ m}^2$, 8% of the CH-waste area.

4.5 Radionuclide Concentrations in Brines

The following are the major conclusions of Section 4.5.

- There is currently a wide range of uncertainty in actinide solubilities within the WIPP repository, from $\sim 10^{-9}$ to 10^{-3} molar. In addition, it is not clear whether this range includes the effects of colloid formation within the brine or possible sorption of radionuclides onto these and other particles (Section 4.6). It is assumed that the estimated range in effective radionuclide concentrations includes potential effects of both particle transport and sorption.
- The uncertainty about radionuclide solubility is a result of several factors, including the high ionic strength of Salado and Castile brines, uncertainties about the local Eh and pH values within the repository as a function of time, and the amount of carbonate complexing that can be expected. In addition, the identities, amounts, and effects of organic complexing agents within the waste are unknown.
- Because of the variability of the present waste form, the geochemical environment within the repository may vary as a function of time and location in the heterogeneous mix of waste and backfill.

4.5.1 Sources of Uncertainty

The WIPP PA STG recently attempted to estimate the solubilities of some of the actinide elements in likely WIPP brines under the conditions expected for WIPP disposal rooms. The STG attempted these estimates to provide input for the calculations for the upcoming forecast of the comparison to 40 CFR 191 and methodology demonstration (Bertram-Howery et al., 1989). A detailed description of this exercise appears in Appendix A.2.

Appendix A.2 defines two standard brines, an average, intergranular brine from the Salado Fm., now referred to as PAB 1, and a representative fluid from a brine reservoir in the Castile Fm. Appendix A.2 assumes that three possible quantities of brine could eventually resaturate the disposal rooms and uses these quantities, along with estimates by Paul Drez of IT Corp. of the total quantities of four organic ligands in the WIPP inventory, to estimate the possible concentrations of these ligands in the brines. Gregory Choppin of Florida State University then attempted to calculate the speciation and solubilities of Am, Np, Pu, U, and Th in both the Salado and Castile brines with the estimated concentrations of four organic ligands.

Choppin concluded that there are no thermodynamic data (solubility products for solid phases, or stability constants for dissolved organic or inorganic complexes) for these elements in solutions with ionic strengths (I) equal to those of the standard Salado and Castile brines defined in Appendix A.2 (I = 7.66 and 6.14 M respectively). Most existing data apply to solutions with I of 1 M or less, and only a few pertain to values of I as high as 2 or 3 M. Furthermore, most of the data are for 1:1 (metal:ligand) or 1:2 complexes; very few data exist for 1:3 or 1:4 complexes, which could be important species in these brines. Choppin therefore attempted to estimate thermodynamic data for the actinides listed above by (1) extrapolating existing data to the ionic strengths of likely WIPP brines; (2) in those cases in which data at lower values of I are so few that extrapolation is impossible, using these data directly for the WIPP brines or arbitrarily adding one log unit to them; and (3) in those cases in which there are no data at all for the appropriate complex, extrapolating data for chemically analogous organoactinide or organolanthanide complexes.

These procedures result in order-of-magnitude uncertainties in any estimates of thermodynamic data for WIPP brines. Furthermore, it is not yet possible to predict how processes such as microbial activity, anoxic corrosion of metals, or radiolysis will affect the Eh of the repository or to what extent these processes will influence the oxidation states of Np, Pu, and U. Finally, the values of pH reported for the Salado and Castile brines could differ greatly from the actual values because of the difficulty of measuring pH in concentrated brines. Even if the reported values are accurate, the dissolution of microbially produced CO₂ or reactions between the brines and nonradioactive constituents of the waste such as cements could change the pH. Eh and pH affect the speciation and solubilities of the actinides, increasing the uncertainties associated with estimating thermodynamic data at high ionic strengths.

Preliminary results from an ongoing sensitivity study suggest that, in addition to the solubilities of radionuclide-bearing solids, the sorption of radionuclides by bentonite or by Fe oxides formed by anoxic corrosion of metals will also affect the source term. There are virtually no data on the sorption of radionuclides by bentonite and Fe oxides under the wide-ranging conditions expected for WIPP disposal rooms.

4.5.2 Radionuclide Concentrations Used in Transport Calculations

Laboratory experiments may eventually provide data on the solubilities and sorption of radionuclides under expected repository conditions. In lieu of such data, a "best estimate" of 10⁻⁶ M is proposed for the concentration of Pu and Am, the important actinide elements in TRU waste, in any brine that resaturates WIPP disposal rooms. This is the intermediate value (on a logarithmic scale) of the range of dissolved radionuclide concentrations (10⁻³ to 10⁻⁹ M) that have been and are being used for sensitivity studies of the source term. Neither the intermediate value nor the range can be justified on the basis of experimental data or modeling studies. The STG thinks, however, that the concentrations of radionuclides dissolved in likely WIPP brines are unlikely to exceed this intermediate value significantly. The effects of two orders of magnitude increase in effective solubility are examined here in Case IB (Chapter 6.0) and Cases IIB, IIC, and IID (Chapter 7.0).

4.6 Radionuclide Sorption in the Waste Panels

The major conclusions of Section 4.6 are listed below.

- Although the sorption capacities of iron oxides and bentonite are high in dilute solutions, the possible concentrations of carbonate, organic complexing agents, and competing ions such as Mg^{2+} and Ca^{2+} will greatly reduce these sorption potentials within the repository.
- Estimated sorption capacities within the repository are assumed to be as low as 1 meq per 100 g of solid for relatively strong sorbers such as Am, Th, and Pu and 0.1 meq/100 g of solid for relatively weak sorbers such as U and Np.
- More accurate estimation of the sorption capacity within the WIPP is not possible at this time because of the large uncertainties in brine composition, carbonate alkalinity, pH, and Eh after brine interacts with waste and backfill.
- The qualitative effects of sorption within the waste-emplacement areas of the WIPP depend on the character of flow under undisturbed conditions and in response to human intrusion. If particulate materials are not transported by flow of fluids, then sorption within the waste-emplacement areas is beneficial. If, however, particulate material is transported by fluid flow, then sorption of radionuclides on the particulate materials would be detrimental. It is not possible to include the effects of particulate flow in numerical modeling at this time.
- Because of the current level of uncertainty, it is assumed in this report that the estimated range of radionuclide concentration (Section 4.5) brackets the potential effects of sorption.

4.6.1 Effects of Solution and Backfill Chemistry on Sorption

In waste panels, solution chemistry will be dominated by the composition of Salado brines, leachates from the waste, concrete and steel drums, and the

products of microbial degradation. This analysis assumes that the important substrates for sorption will be iron oxide corrosion products and bentonite backfill. The effect of sorption within the waste panel on radionuclide release will depend on the magnitude of particulate transport from the waste panels. If transport of iron corrosion products and clay backfill is substantial, then sorption onto these substrates may enhance radionuclide release. If particulate transport is minor, then sorption onto iron oxides and clays will reduce radionuclide release. In this report, radionuclide transport within the waste panel has not been considered; the amount of radionuclide sorbed onto solid phases has been included in the total radionuclide concentrations described in Section 4.5.

The amount of radionuclides sorbed to solids will be related to the solution composition and to the total number of sorption sites of the substrate. The properties of the substrates have been used to estimate the maximum possible sorption capacity independent of the effects of solution composition. For an oxide or oxyhydroxide, the total sorption capacity is related to the number of surface hydroxyl groups. For a clay, such as bentonite, the sorption capacity will be determined both by the number of exchangeable (fixed-charge) sites and by the number of surface hydroxyl groups (Kent et al., 1988; cf. Section 3.3.4).

The total sorption capacities of iron oxyhydroxide and bentonite were estimated from experimental data obtained under conditions very different from those assumed for the waste panel. Under conditions of low total dissolved solids, low concentrations of cations like Mg^{2+} and Ca^{2+} , and low organic concentrations, sorption capacities of bentonite could range from 10 to 100 milliequivalents/100 grams (Drever, 1982; Tsunashima et al., 1981). Under similar conditions, the sorption capacity of iron oxyhydroxides could range from 60 to 300 meq/100 grams (cf. Hayes et al., 1988, Table 1). The actual sorption capacities will depend on the crystallinity and stoichiometry of the clays and iron oxides present in the repository.

Moderate concentrations of carbonate, organic sequestering agents, Mg^{2+} , and Ca^{2+} , however, will prevent all of the sorption sites from being occupied by actinide ions. For example, Figure 3-21 shows that Pu (IV) is

quantitatively removed from solution by sorption onto goethite at pH values above 6 but that sorption decreases markedly at pH values below 5. At pH values of 3, less than 25% of solution Pu (IV) is removed from solutions containing 0.1 M NaNO₃ and 10⁻¹⁰ M total Pu. The effects of pH and Ca concentration on sorption are illustrated in Figure 3-22. This figure shows that the extent of sorption of uranium onto goethite (α -FeOOH) (expressed as K_d) can range from 0.02 mL/g to 10,000 mL/g over a pH range of 5 to 9 and a Ca concentration of 2×10^{-3} M to 3×10^{-2} M. The effects of the solution composition on sorption are discussed in more detail in Section 3.3.4.

The extent of sorption of actinides onto particulates in the repository cannot yet be calculated because of uncertainties in the expected chemical environment of the rooms and the lack of relevant empirical K_d or thermodynamic data. For example, the range of uncertainty in the pH of the brines in the repository is many pH units (acidic to extremely basic). Pressure-induced carbonation of the brine caused by microbial degradation of the organic waste could lower the pH; dissolution of backfill components could raise the pH (cf. Section 4.5).

Data for the simple systems discussed above suggest that the amount of sorption of actinides onto either clays or iron oxides present in the repository could be several orders of magnitude less than the maximum sorption capacity estimated from the properties of the solid substrates alone. For this reason, the calculations in this report assume that the sorption capacities of both clays and iron oxides for relatively strong sorbers such as Am, Th, and Pu have been decreased from the maximum values listed in Table 4-4 to 1 meq/100 g solid. The sorption capacity of the solids for weak sorbers such as U and Np is assumed to be 0.1 meq actinide/100 g solid (Table 4-4).

4.7 Structural Interaction of the Salado Formation and Repository

The major conclusions of Section 4.7 follow.

- Measured in-situ wall-closure rates are at least three times those estimated prior to underground experience in the WIPP. Current numerical

Table 4-4. Estimated Sorption Capacities of Bentonite Backfill and Iron Oxides

<u>Substrate</u>	<u>Maximum Sorption Capacity (meq/100g)</u>	<u>Reduction by Solution Chemistry</u>	<u>Reference Value for This Report (meq/100g)</u>
Iron Oxide	60 - 300 ^a	10 ⁻³ to 10 ^{-4b}	Th, Am, Cm, Pu = 1 Pb, Ra, U, Np = 0.1
Bentonite	10 - 100 ^c	10 ⁻² to 10 ^{-3d}	Th, Am, Cm, Pu = 1 Pb, Ra, U, Np = 0.1

a. Range estimated from surface areas (SA) and site densities (Ns) of goethite and amorphous hydrous ferric oxide from Hayes et al. (1988):

$$\text{meq cation/100 g solid} = \frac{\text{SA (m}^2/\text{g)} \times \text{Ns (sites/nm}^2\text{)} \times 10^{23}}{6.02 \times 10^{23} \text{ sites/eq.}}$$

- b. Reduction primarily due to carbonate and organic complexation.
- c. Estimated from Langmuir isotherm plot (Tsunashima et al., 1981).
- d. Reduction due to competition of Mg²⁺ and Ca²⁺ for fixed-charge sites and by carbonate and organic complexation of actinides.

modeling has achieved greatly improved agreement by reevaluating the stress generalization, constitutive model, and material properties from WIPP-specific samples. The current numerical-modeling approach does not incorporate a disturbed-rock zone around the underground workings.

- On the basis of borehole observations, geophysical studies, and gas-flow tests, a disturbed-rock zone (DRZ) is known to be present adjacent to the WIPP underground workings at the repository horizon. The DRZ extends outward from 1 to 5 m (0.3 to 1.5 ft), depending on the age and span of a given excavation. It is assumed here that, with the exception of fractures in Marker Bed 139, the DRZ returns to its initial porosity during the final stages of closure.

- Processes active within the DRZ include desaturation as a result of dilation and mine ventilation, microfracturing (probably in response to the rapid relief of initial in-situ fluid pressures), and macrofracturing (especially the opening of fractures within Marker Bed 139).
- Structural impacts of the DRZ may extend the time required to reach final mechanical closure of the repository (Section 4.8).
- Hydrologic impacts of the DRZ include generation of a region of relatively high permeability near the repository horizon and development of an interconnected flow path (Marker Bed 139) immediately beneath the repository horizon. Sealing of Marker Bed 139 is a design-basis assumption (Section 4.9).
- Although the presence of a DRZ complicates numerical modeling of the long-term behavior of the WIPP, it may have beneficial impacts as well. For example, the DRZ may serve as an effective sink for at least part of the brine expected to flow into the repository (Section 4.3) and at least part of the gas generated by the waste and containers (Sections 4.2 and 4.10.2).

4.7.1 Understanding and Assumptions Prior to Mining

The development of a disturbed rock zone around the WIPP workings was not considered in the FEIS, although the possible formation of a dilatant zone was recognized (Table 1-1; DOE, 1980a). It was assumed at that time that salt would behave as an isotropic, homogeneous material and that underground excavation could be accomplished with only a minimum of ground control to mitigate fracturing. Prior to mining the underground WIPP workings, structural studies concentrated on the creep properties of salt through laboratory determination of material properties and the development of constitutive and numerical models of the creep behavior of salt. These efforts attempted to develop the means to predict short- and long-term deformation of the underground workings.

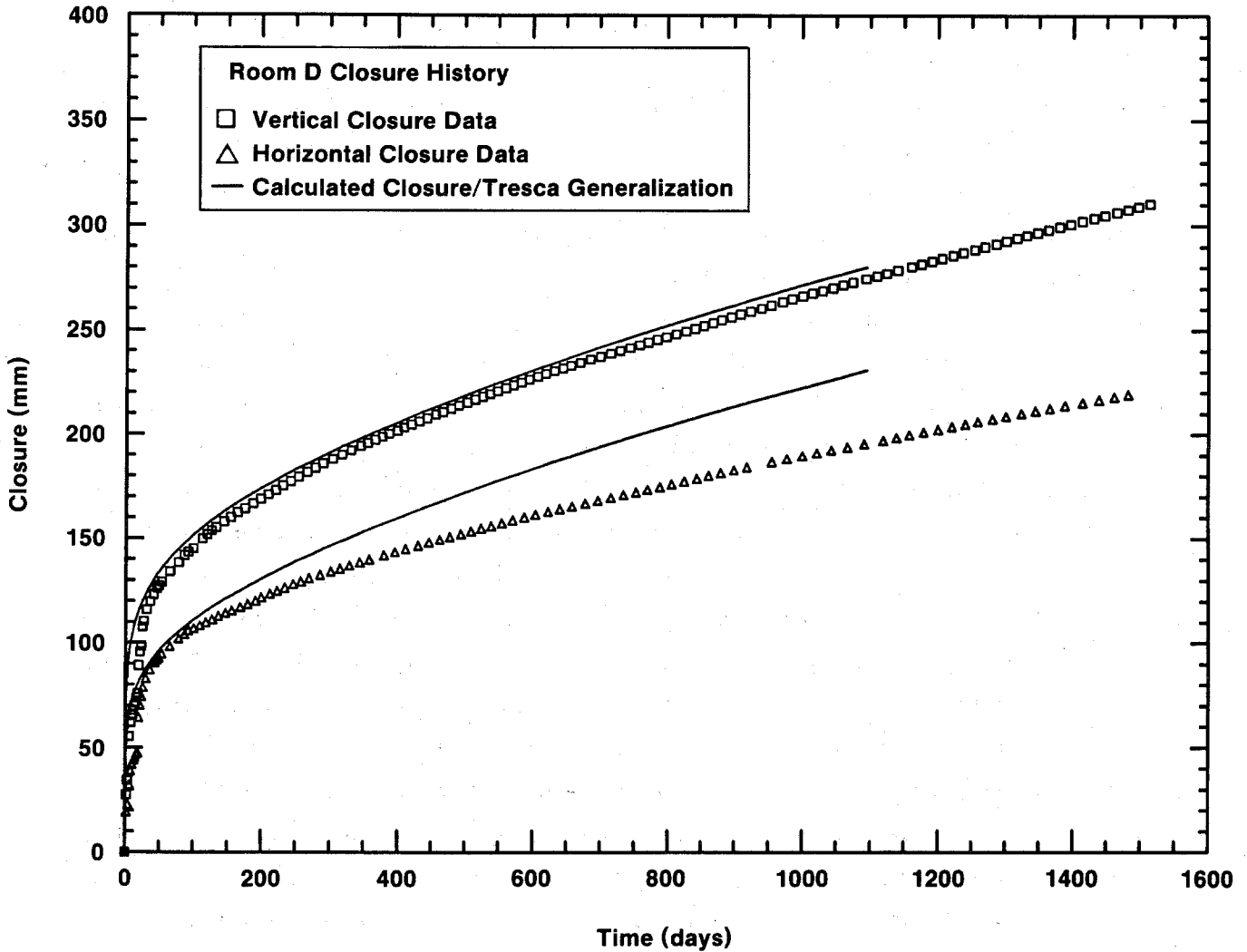
4.7.2 Experience Gained Underground

After the excavation of the underground workings began in 1982, in-situ experiments on structural and thermal interactions were initiated to partially validate the constitutive models and numerical codes that had been developed. Rock specimens from the repository horizon were obtained for laboratory determination of properties, and a detailed reference stratigraphy was mapped for use in the numerical codes.

Morgan et al. (1986) showed that the rate of closure measured in situ was at least three times greater than that predicted by numerical models. The fit between calculations and measurements has improved steadily (Figure 4-4) (e.g., Munson and Fossom, 1986; Munson et al., 1989). This improvement stems from the re-evaluation of the stress generalization or flow potential, the constitutive model, and the material properties specifically for the WIPP. The match for horizontal and vertical closure and the match between the in-situ data and the calculated closure remain to be reconciled. In addition, the current numerical modeling does not take account of dilation during the formation of a disturbed-rock zone, which is not amenable to available numerical-modeling techniques. However, numerous holes drilled from the underground workings in the course of stratigraphic studies, experiments, and construction have revealed a zone of fractures around the excavations. These fractures are part of what is now known as the disturbed rock zone (DRZ). As the DRZ became evident, Bechtel National (1986) drilled numerous holes specifically to investigate the DRZ. Direct observations of the DRZ indicate that fractures with apertures greater than 2 mm (0.08 in) are common in the wall rock of the underground workings. The importance of the DRZ to the conceptual modeling of repository systems has been reported by Borns and Stormont (1988, 1989).

4.7.3 Generation and Character of the DRZ

Following mining, an excavation influences a zone of rock extending outward 5 to 6 times the radius of the opening (Brady and Brown, 1985). Within this zone of influence, a disturbed rock zone forms in the wall rock and is defined as the zone of rock in which mechanical properties (e.g.,



TRI-6330-87-0

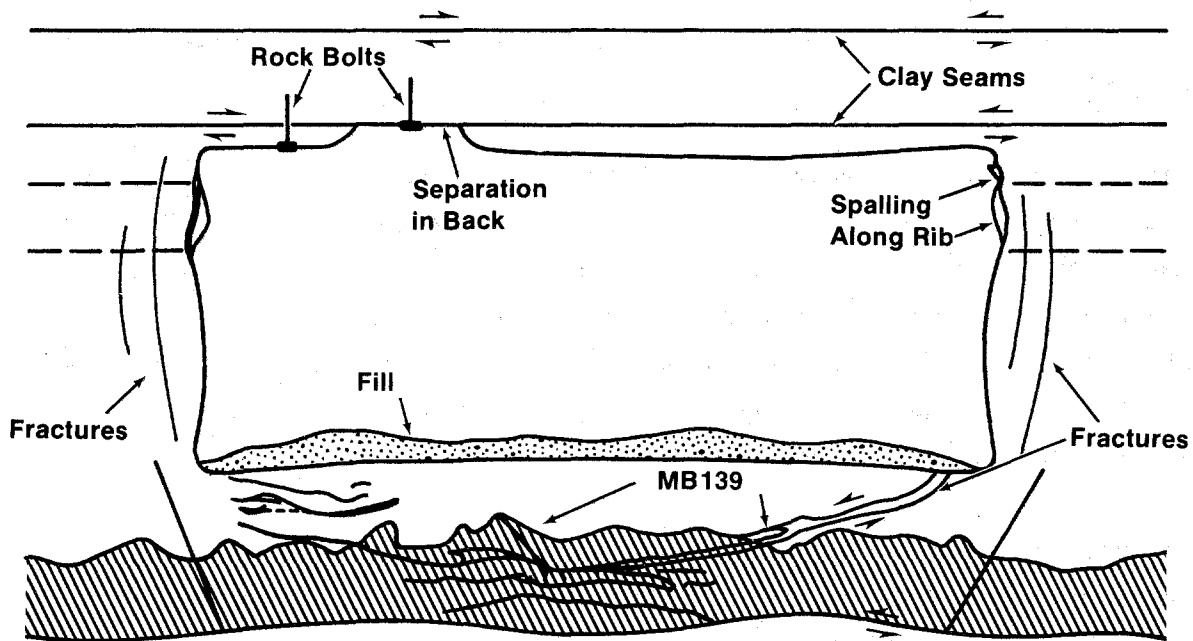
Figure 4-4. Comparison of calculated and measured Room D closures (Munson et al., 1989).

elastic modulus) and hydrologic properties (e.g., permeability and perhaps degree of saturation) have changed in response to excavation. The development of a DRZ is common in underground engineering (e.g., Baar, 1977; Brady and Brown, 1985). At the WIPP, the existence of a DRZ has been confirmed by borehole observations, geophysical surveys, and gas-flow tests. All three approaches show that the DRZ extends laterally throughout the excavation and varies in depth from 1 to 5 m (0.3 to 1.5 ft), according to the size and age of the opening. Some loss of intergranular brines (desaturation) and microfracturing has occurred within the zone. The dilation that results from the microfracturing in the DRZ provides a component of the observed closure that cannot be accounted for in existing creep models for closure in salt repositories.

The fractures that develop in the DRZ, especially in the anhydrites of Marker Bed 139, will provide an interconnected flow path. These flow paths may close at a slower rate than the backfilled repository. Hence, these fractures may provide sinks and conduits for fluids originating in the formation and the waste. Special attention to the design of underground seals is required to account for the continued deformation of the marker bed after the initial emplacement of the composite seals.

Observations also suggest the development of an ellipsoidal pattern of fractures around an excavation. Several features are shown in an idealized cross section of a WIPP room (Figure 4-5). An arcuate fracture system, concave toward the opening, develops in the floor and the roof, crosscutting the stratigraphy. Separations may develop along stratigraphic markers, such as clay seams. Shear displacements are observed along some fractures and separations. Vertical fractures and spalling are observed within the ribs.

Existing boreholes (DOE, 1988b, Section 3.3) showed that the extent of observed fracturing in borehole arrays increased from 48% of the array locations in 1986 to 73% in 1987. The locations without fractures are largely restricted to drifts with narrow spans (4 x 4 m). In the oldest 10 x 4 m test rooms (Rooms 1 through 4), 100% of the locations exhibited fractures 2 mm or greater.

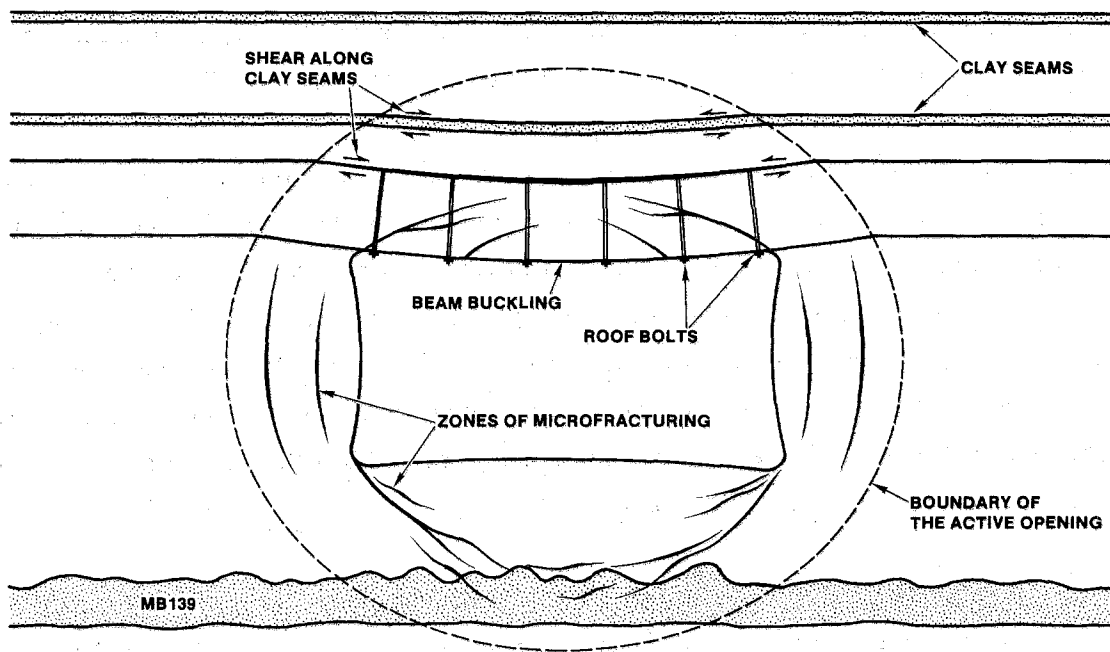


TRI-6330-80-0

Figure 4-5. Schematic distribution of the DRZ around a representative waste room (Borns and Stormont, 1988).

The origin of the DRZ is complex, with several processes competing or acting in concert. Mine ventilation, aided by the enhanced interconnectivity created by microfractures, dehydrates the pore space adjacent to opening. The local stress field and resultant DRZ reflect any preexisting features, such as fractures, bedding, clay and anhydrite interbeds, as well as the effects of mining (Coates, 1981). Several processes may play a significant role in the development of the DRZ at the WIPP (Figure 4-6):

1. Strain-rate dependent brittle failure results in an ellipsoidal zone in the host rock immediately around the opening, in which the brittle failure envelope based on a strain-rate criterion is exceeded by the accelerated strain-rate adjacent to the opening (Dussealt et al., 1987).
2. Microfracturing develops in response to the release of in-situ fluid pressure. If an appreciable pore pressure exists and salt obeys an effective stress law, then the redistribution of stresses in response to excavation combined with the low permeability and low tensile strength of salt will produce tensile failure. Very small volume increases (dilatancy) will relieve the pore pressure and halt fracturing. Such failure may tend to create grain boundary microfractures, which may heal after cessation of tensile failure.
3. A volume of disturbed rock develops, bounded by the excavation face and the elliptical surface of the "active opening" (Mraz, 1980). This volume of rock can separate from the host rock along a shear zone that follows the elliptical surface of the "active opening."
4. Shear displacements along planes of weakness such as clay seams are induced by the excavation (Brady and Brown, 1985).
5. Beam buckling and flexural slip folding develop within the "active opening." The horizontal component of radial creep causes stress-relieved salt beds within the "active opening" to buckle, as observed immediately above and below excavations (Baar, 1977). These layers continue to deform with time in response to horizontal and vertical loading by creep of the adjacent intact salt mass.



TRI-6330-90-0

Figure 4-6. Schematic representation of processes acting in the DRZ (Borns and Stormont, 1989).

6. A pressure arch develops symmetrically above and below the opening, redistributing stresses and concentrating stress around the opening (Coates, 1981). Within the pressure arch, zones that are in tension develop within the host rock.

4.7.4 Impact of the DRZ

4.7.4.1 Structural Effects. The DRZ affects early (<5 yr) deformation around the underground opening. Such deformation affects mining operations. The studies described above and the work of Francke (1987) showed that a DRZ will develop around all of the underground workings, given sufficient time. The DRZ already has affected the maintenance of openings in several underground areas. A primary concern of mining operations is to maintain a safe roof (ceiling) and rooms from which the retrieval of waste will not be impeded during the first 5 to 10 years by failure of the roof. An additional consideration will be the maintenance of room and tramway tolerances over the extended periods of operations (15 to 25 years). Maintenance may require trimming the floor into the fractured anhydrite of MB 139 in order to maintain the required thickness of salt in the roof for stability. The fractured anhydrite in the floor may require further maintenance.

The dilatant component of deformation within the DRZ influences the interpretation of in-situ tests. Dilatancy refers to the volumetric strain that results from the opening of microfractures (Brace et al., 1966). Dilatancy around the WIPP excavations is observed or inferred from in-situ studies. Measurements of gas flow, apparent resistivity, and seismic velocity indicate that the porosity of the host rock increases within the DRZ. The 10^4 increase in gas-flow rates within the DRZ indicates that the changes in hydrologic and geophysical properties result both from desaturation and from an increase in fracture porosity. The change in porosity (primarily dilatant volume increase) is accommodated by displacement of the excavation surface inward and contributes to the observed closure. Appendix A.4 calculates the magnitude of this component of closure, using the increase (0.001 to 0.010) in gas porosity inferred from the gas-flow testing program (Stormont et al., 1987) and the increase (0.02 to 0.04) in porosity inferred by analysis of seismic velocities (Skokan et al., 1988). The calculation assumes a thickness for the zone of dilatancy (1 or 2 m) and a cylindrical and isotropic room

configuration. Dilatancy within the DRZ causes measurable closure within the adjacent opening. For both an experimental room (4-m radius) and an SPDV room (5-m radius), the apparent closure is ~4.5 cm for a zone of dilatancy 2 m thick and ~2.0 cm for a dilatant zone 1 m thick. These components are of same magnitude as the early closure (Munson et al., 1989, Figure 1). The fractures that are observed around the openings could contribute approximately an additional 2 cm of vertical closure and 1 cm of horizontal closure.

Deformation around the WIPP excavations is controlled by creep outside the DRZ. This process drives the repository, including the DRZ, toward reconsolidation approaching the virgin state. The DRZ retards the attainment of final closure. Factors that affect reconsolidation are the effective enlargement of the excavation by the growth of the DRZ, the fracture-propping potential of fluids and stiffer material such as anhydrite in Marker Bed 139, and the interaction of large metallic components of the waste with blocks of salt or anhydrite that form during failure of the DRZ after a room is decommissioned. Predicting room behavior with constitutive and numerical models requires multiple mechanisms of deformation to be accounted for, including the discontinuous behavior within the DRZ.

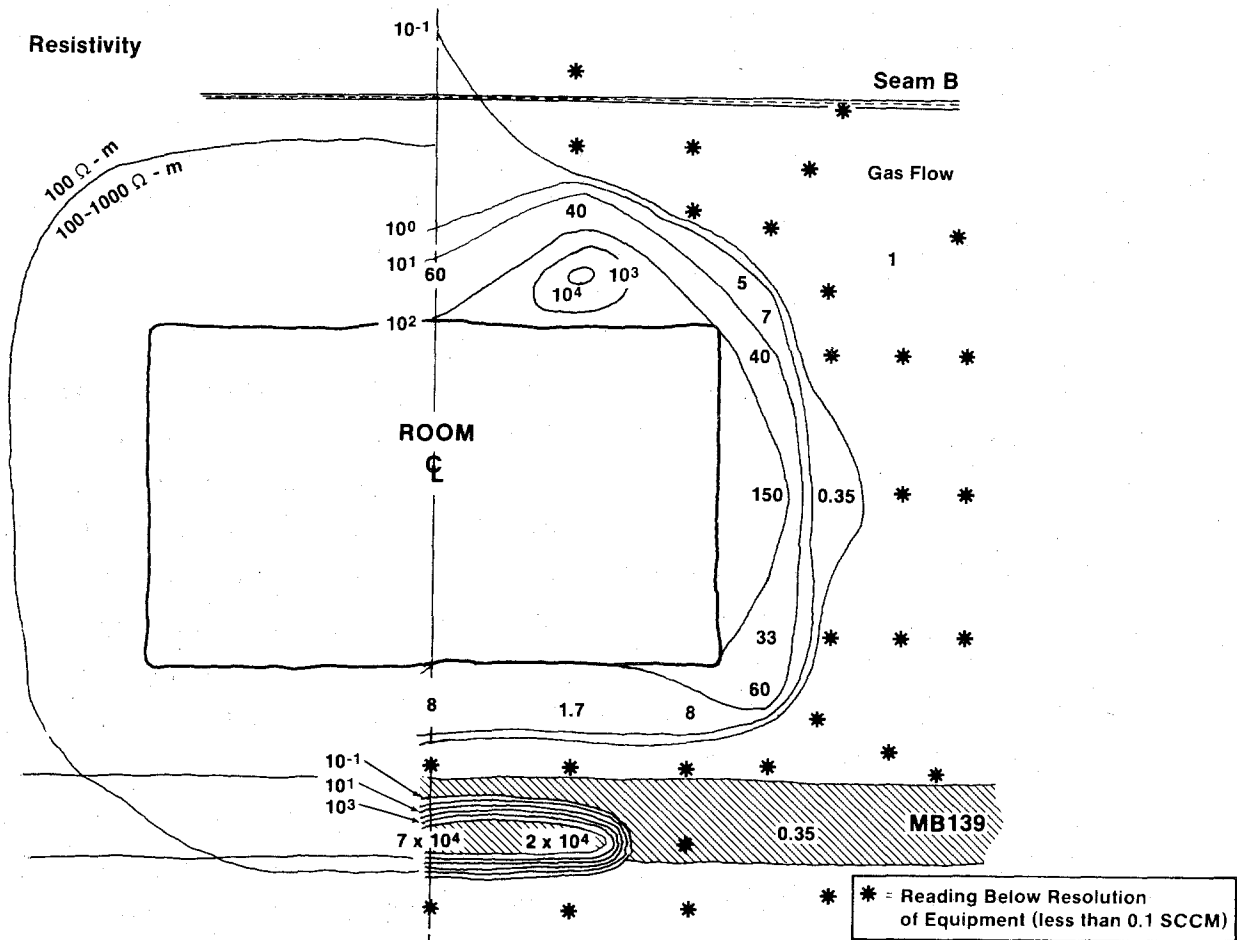
4.7.4.2 Hydrologic Effects. Studies are underway to determine the effect of fracture-induced porosity increase within the DRZ on the hydrologic properties of the zone. Tracer-gas studies were conducted from the N1420 drift in 1986 (Stormont et al., 1987) and the N1100 drift in 1987 (Peterson et al., 1987b). The tests injected a diluted tracer gas into a packed-off region of the test borehole and sampled the surrounding boreholes for its arrival. The purpose of the N1420 testing was to estimate fracture continuity and apertures in MB 139. The tracer arrivals indicate that the flow-path width in MB 139 increases as the span of the drift increases from an estimated 0.002 cm in a 6.6-m-wide drift to 0.04 cm at the intersection of two 11-m-wide drifts. These tests also revealed that tracer gas was being transmitted from MB 139 to the drift through the ~1-m-thick layer of salt between MB 139 and the floor of the drifts. Consistent with the inferences about MB 139, apparent vertical flow paths in the salt were found to increase with drift dimension from 0.002

cm in a 6.6-m-wide drift to 0.02 cm at the intersection of two 11-m-wide drifts.

In the 6.6-m-wide N1100 drift, tracer-gas studies were conducted in three boreholes: one vertically up, one vertically down, and one horizontal. All test intervals were in the salt within 1 m of the drift face. The tests in the vertically up and vertically down boreholes both indicate larger flow paths in the vertical direction (between the test interval and the drift). The test in the horizontal borehole indicated flow paths parallel to the drift face appreciably larger than those between the test interval and the drift. The inferred aperture of the flow path in all tests was small, about 1×10^{-6} m (Figure 4-7).

The development of the DRZ will affect the hydrologic environment around seals. The major considerations in rock-mass sealing are the seal/rock interface and the DRZ near the seals. A substantial DRZ that persists in time could provide a path through which fluid could bypass the seals. If a DRZ is not healed with time, it could connect the waste-disposal panels with other portions of the repository. Delineation of the DRZ is required to determine what, if any, remedial action is necessary to establish effective seals. Stress buildup in the vicinity of a relatively stiff inclusion (e.g., concrete or consolidated-salt seals) may reverse the disturbance by forcing the rock back together, thereby decreasing its permeability. Preliminary studies by Arguello and Torres (1988) suggest that stresses within the host rock around a seal build up toward lithostatic. Qualitatively, the stress buildup should initiate healing, but the rates and amount of permeability reduction are not well known. The behavior of anhydrite is important, because a major fracture system develops within MB 139, and fractures in anhydrite will heal at a different rate than fractures in halite. Lateral displacement (shear) across the fractures in the DRZ prevents asperities on opposite walls of the fracture from matching. This mismatch will retard healing of the fracture. If the DRZ does not heal fast enough, excavation of the excessively transmissive portion of the DRZ at strategic locations is an option.

Salado rock salt near and surrounding all seal systems (except in the DRZ) is assumed here to have a permeability of 3×10^{-21} m² ($10^{-20.5}$ m², or 3



TRI-6330-82-0

Figure 4-7. Schematic distribution of fluid-flow behavior around a waste room. Contours to the right of the room centerline show gas-flow rates in standard cubic centimeters per minute (SCCM). The contour to the left of the centerline shows a qualitative decrease in resistivity away from the room.

nanodarcy), the log mean of the expected range of 10^{-21} to 10^{-20} m² (1 to 10 nanodarcy), or less, and an effective porosity of 0.001. These are estimated values for intact WIPP rock salt outside the DRZ (in the far-field) (Nowak et al., 1988). Rock in the DRZ, while estimated to have much higher permeability during closure, is assumed to heal eventually to a final state that is equivalent to undisturbed WIPP rock salt, except for Marker Bed 139. The reasons for this conclusion, which is assumed to apply after fluid pressures have decreased well below lithostatic, follow.

The self-healing behavior of salt by creep-resealing of fractures under pressure has been observed. The results of laboratory permeability testing of ERDA-9 deep borehole core specimens indicated the effect of pressure on the elimination of fractures (Sutherland and Cave, 1978). Sutherland and Cave found that mechanical damage to the core caused high permeability, but permeability decreased below the sensitivity of the measurement system during application of a large confining pressure. These results indicate that the fractures in halite due to mechanical damage were eliminated by healing under pressure. The application of 13.8 MPa (slightly smaller than the 14.8-MPa lithostatic load in the WIPP underground workings) led to an order-of-magnitude decrease in permeability within 200 hours. An applied pressure of 34.5 MPa produced the same healing effect within 6 hours. This result indicates that healing will proceed under a wide range of applied pressures.

Theoretically, the effective-pressure component of the general stress field is the one that leads to the closure and healing of fractures. Later experiments (Costin and Wawersik, 1980) on the healing of fractures that were generated in the laboratory directly demonstrated fracture healing in WIPP rock salt under an effective confining pressure (at temperatures $>100^{\circ}\text{C}$ and pressures >15 MPa).

4.7.4.3 Gas and Brine Storage. A sink for gas and brine is provided by a network of fractures and zones of higher permeability that develop in the DRZ. This sink can accept fluids introduced during construction and after decommissioning. The fracture porosity of the DRZ has been studied primarily for its effects on brine influx. However, the DRZ may also provide a sink or reservoir for gas or brine in the repository, because it may be the last

component of the system to approach its original porosity. Gradients for gas and brine flow would cause gas or brine to collect in the DRZ and retard closure of the fractures. Fracture porosities within the zone of rock from the excavation wall to a depth of 2 m may be greater than 0.15. Borns and Stormont (1988, 1989) have demonstrated that the pore space within the DRZ has become unsaturated in response to microfracturing and mine ventilation and thus enhances the ability of the DRZ to accept available fluids. If brine is forced out of the DRZ and into the waste room during the final stages of closure, the potential exists for a temporary rise in gas-generation rate.

4.7.5 Closure Mechanisms

A major reason for locating the WIPP in a deep, natural, geologic deposit of salt was the long-term potential of salt to encapsulate waste and heal accidental fractures (Tyler et al., 1988). Encapsulation occurs because excavated mine openings deep underground will gradually reduce in volume as the surrounding salt deforms, or creeps, to reduce the void created within it. Waste present in the room will be surrounded and compacted by the salt, as the void volume decreases, until it becomes a dense and relatively impermeable mass of material.

Several important factors determine the final state of the waste and how long will be required to achieve it. First, because any solids within the room will occupy volume that would otherwise have to be eliminated by creep closure, the greater the initial solid volume of the room contents, the sooner the waste will be compacted to a terminal state (Section 4.8). Some space not filled by the waste itself will be filled with crushed-salt or salt and bentonite backfill, to minimize the initial void volume within the room.

Compressive stress is applied to the waste as the surrounding salt comes in contact with it, densifying the waste until it is stiff enough to prevent further closure. This state represents the near-term terminal state of the repository as achieved by purely mechanical means (Section 4.8). A long-term terminal state of the repository will occur when biological decomposition and chemical corrosion alter the chemical and structural nature of the waste, permitting it to achieve a denser state after elimination of any gases

generated by decomposition and corrosion. This report assumes the near-term, mechanically compacted state of the waste as the terminal state of the repository (Table 4-5), and, except for Section 4.10, does not quantitatively consider possible later changes in structural state.

Three factors might operate to alter the assumed normal in-situ compaction of the waste. First, if enough brine can enter the room before complete mechanical reduction of the void volume, the waste will saturate. Brine pore pressure within the waste will increase until it is great enough to halt closure, and the terminal state of the waste will be less dense and more permeable than if compacted mechanically. Estimates show that premature termination of room closure by brine inflow is not likely for the cases in this report (Section 4.10). In the absence of gas generation, and assuming interconnected porosity in the Salado Fm., the pores will eventually fill with brine over long periods of time, after mechanical compaction is complete. In fact, small volumes of brine aid in compaction and reconsolidation of crushed salt (Holcomb and Shields, 1987).

Gas produced by bacterial action and chemical corrosion is a second factor that may disturb normal in-situ compaction of the waste. Gas may be produced more rapidly than it can diffuse out of the disposal area. The gas pressure within the disposal room might increase as the void volume that it occupies is reduced by room closure and as additional gas is generated, until the pressure is high enough to prevent additional closure (cf. Section 4.10). As in the case of excessive brine inflow, the terminal state of the waste in response to gas generation would be less dense and more permeable than if the waste compacted mechanically. Estimates suggest that insufficient gas is generated to prematurely terminate closure before near-term mechanical compaction is achieved (Section 4.10). However, the total gas generation potentials described in Section 4.2 suggest that sufficient gas will eventually be produced to exceed the available storage volume estimated solely on the basis of mechanical closure.

A final factor influencing closure of the disposal room, as discussed above, is the disturbed rock zone (Borns and Stormont, 1988). The DRZ is important to disposal-room closure because it can act either as a reservoir or

Table 4-5. Solid and Void Volumes in Waste (Oak Ridge National Laboratory, 1988; Clements and Kudera, 1985; Butcher, 1989)

	Waste Form				Total
	Combustible	Sludge	Metal/Glass	Other	
<u>Emplaced</u>					
Percent of Total Volume					
By Weight in Storage	30	17	33	20	100
Initial Volume In Disposal Room	429	243	472	286	1430 m ³
Percent of Solids Per Drum	24.8	66.5	21.9	--	
<u>Final</u>					
Solids Volume (m ³)	106	162	103	93	464 m ³
Void Volume (m ³)	12	18	68	25	123 m ³
Waste Volume					587 m ³

as a channel for inflowing brine, and gases can expand into it, at least during closure. No allowance for gas-pressure reduction because of void volume in the disturbed rock zone is assumed for the numerical cases examined here, although this possibility is evaluated in Section 4.10.

4.8 Terminal Waste State

The major conclusions of Section 4.8 are listed below.

- Lithostatic load will be insufficient to remove all porosity from the waste and backfill. The expected "final" porosity of emplaced design-basis waste is 0.18, with a range from 0.15 to 0.21. The estimated permeability of the "final"-state waste, attained within 60 to 200 years, is $\sim 10^{-13}$ m².
- It is expected that closure to 70 to 95% of the "final" state will occur as if the waste were not present, because the waste and backfill will not

exert any appreciable backpressure until this degree of closure is reached.

- The structural effect of the backpressure from waste and backfill and of the presence of a DRZ is assumed to be simple retardation of the final stages of closure, not alteration of the estimated final state.
- It is assumed that mechanical closure to "final" state occurs within 60 years, independent of gas generation and brine inflow. It is further assumed, for purposes of estimating gas-storage volumes within the repository (Section 4.10.1), that the final room porosity remains unchanged in response to brine inflow and gas generation.
- The estimated permeability of the final state does not enter directly into transport calculations. Rather, it is assumed that a permeability of 10^{-13} m² is sufficient to allow complete mixing of brines from a Castile brine reservoir and waste within the repository. In contrast, a waste/backfill permeability of $\sim 10^{-18}$ m² is assumed to eliminate this mixing.
- The "final" porosity enters into calculations in two ways: by affecting the potential for gas storage within waste-emplacement rooms at final state (Section 4.10), and by affecting the initial concentration of radionuclides for which the initial inventory is not sufficient to saturate the available porosity (Section 7.3.4).

4.8.1 Void Volume (Porosity)

If it is assumed, for purposes of calculation, that structural changes do not take place after mechanical compaction, the void volume remaining within a room after waste compaction determines the maximum amount of brine that may eventually enter the room. This value is difficult to estimate, however, because the mechanical and physical properties of the waste are highly variable and poorly characterized.

The compressive stress exerted by the surrounding salt is not sufficient to eliminate all voids in the waste. As the waste is compacted, its resistance to additional densification increases, and it becomes stiff enough to prevent further void reduction. A near-term limiting void volume within the repository, associated with purely mechanical densification and estimated to be attained in ~60 years, is used for this analysis and is assumed to represent "steady-state."

Even after 60 years, the state of the repository will continue to change, as biological decomposition and chemical corrosion alter the chemical and structural nature of the waste. This longer-term evolution of the physical state of the repository is expected to be complex, to occur over a long period of time, and to include interaction between compaction processes and possible repository expansion as a result of gas generation (Section 4.10). Its quantitative characterization may never be possible. At least for metal wastes, densification may continue beyond that produced by early room closure, and consequently the near-term limiting void volume is considered the greatest void volume that will exist within the waste. The final room porosity enters the calculations in this report in three ways. First, the porosity is used to estimate the final permeability of the repository. Permeability is used indirectly in the calculations to determine whether Castile brine-reservoir fluids effectively mix with the waste in the repository (Table 1-2). Second, the final porosity estimate is used in Section 4.10 to estimate the volumes available within the repository for gas storage or saturation with brine. Finally, the porosity estimate is used to determine the volume of brine available to dissolve radionuclides. Dissolution is limited either by the mass required to reach the solubility limit of individual radionuclides or by the total mass of the radionuclides present, whichever is less.

The final void volume used here is based on the distribution of waste types in storage (Table 4-5) (Oak Ridge National Laboratory, 1988). A total of 6,804 drums are assumed to be stored in seven-pack configurations within a disposal room, each with an initial internal volume of 0.21 m³. In assigning final porosities to each component, combustible waste (low-strength plastics, paper, and rags) is assumed to have such low strength that the near-term interconnected void porosity will be 0.1 or less after compaction to

lithostatic pressure (approximately 15 MPa). Because combustible waste will collapse to a dense, interlocking structure, its hydraulic response is considered to be similar to silt, with a hydraulic conductivity of 10^{-8} m/s (10^{-15} m² permeability). (The porosity is $n = V_v/V$, where V is the compacted volume, and V_v is the void volume. $V = V_v + V_s$, where V_s is the solid volume that the waste would occupy if no voids were present. Later, the void ratio, e , will be used, which is defined as $e = V_v/V_s$, or $e = n/(1-n)$.)

The mechanical properties of cemented sludge are not well-defined, but this category of waste represents only 17% of the total waste inventory. Cemented sludge is much more difficult to compact than combustible waste, and therefore its total void content after compaction is likely to be greater. An interconnected porosity of 0.1 is assumed for it in the compacted state, however, because many sludges may have a high cement content and are expected to form hydration products that decrease void interconnectivity. In the absence of any data about the hydraulic conductivity of cemented sludge, a value two orders of magnitude greater than for grout has been assumed. The hydraulic conductivity of grout is 1×10^{-11} m/s (10^{-18} m² permeability) (Coons et al., 1987), implying a final-state conductivity of 1×10^{-9} m/s (10^{-16} m² permeability) for sludges.

The strengths of metallic and glass wastes make them much less compactible than combustible and sludge wastes. About 33% of the waste is metallic in content. The final porosity assumed for metal and glass waste is 0.4, based upon powder metallurgy literature (Hausner and Kumar Mal, 1982) and on data on supercompaction, which suggest that compaction of metal waste to much greater than 0.6 of theoretical solid density is not likely. A lower final porosity for the metal waste can be expected, however, if the crushed-salt and bentonite backfill intrudes into the open spaces between the pieces of metal, a process that could reduce porosity by as much as 50%. Thus, a lower bound to metal-waste porosity is taken to be 0.20.

The properties of the waste category referred to as "other" remain undefined. In the absence of further information about the composition of this waste, its compacted porosity is assumed to be the average porosity of the combined combustible, cemented-sludge, and metal and glass waste

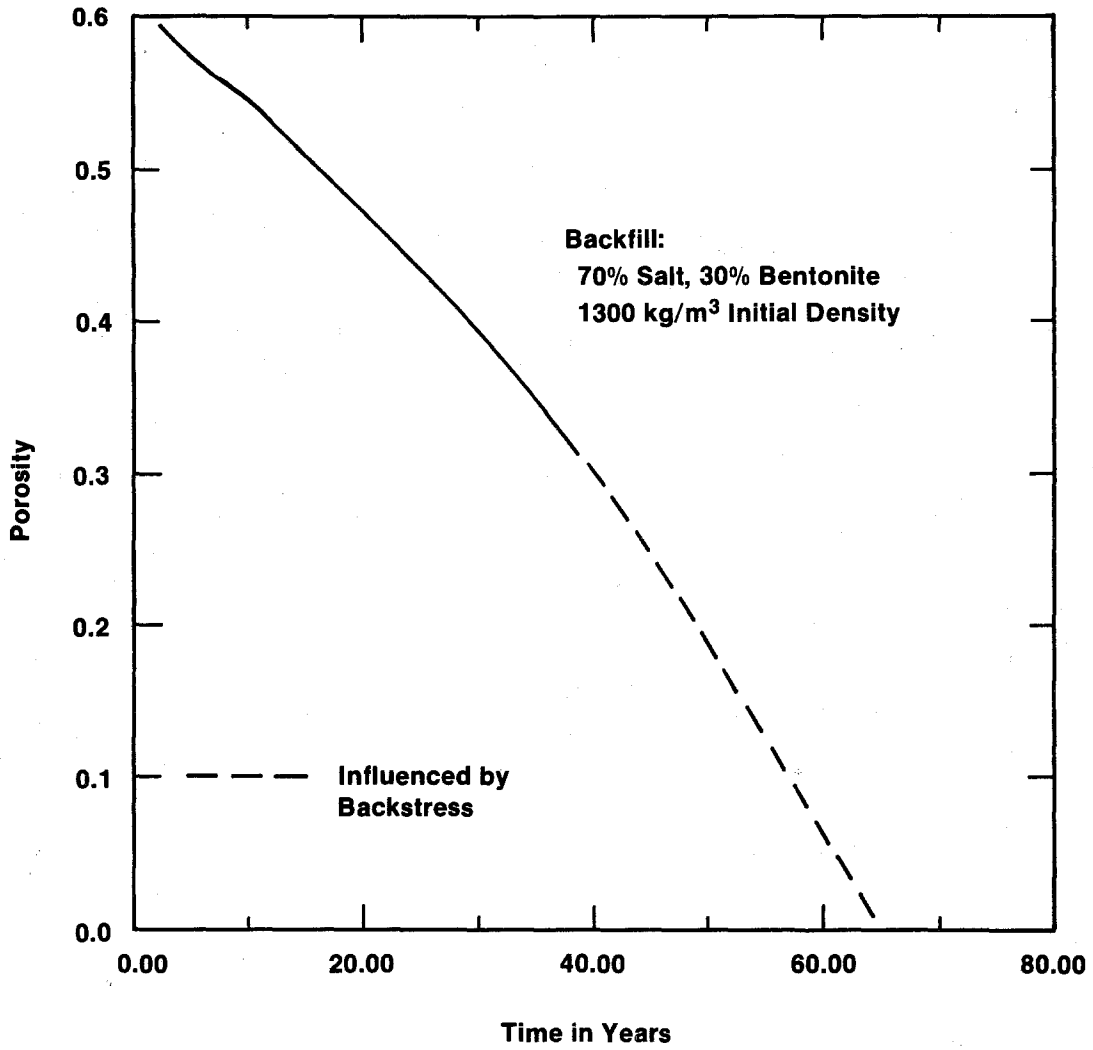
categories, weighted according to the portion of the inventory that each represents.

Final void volumes for combustible, cemented-sludge, and metal and glass waste categories are given in Table 4-5. The volume of solid waste per drum is computed using the average initial void fraction of each waste category (Clements and Kudera, 1985; Butcher, 1989). Adding in the void volume of the unspecified "other" category of waste (20% of the inventory), the total void volume per room is 123 m^3 , corresponding to a solids volume of 464 m^3 . This yields a porosity of 0.212, of the final total waste volume of 587 m^3 . If the void volume of the metal waste is assumed to be reduced 50% by salt intrusion, the waste void volume per room is approximately $123 \text{ m}^3 - 34 \text{ m}^3 = 89 \text{ m}^3$, but the total solid volume enclosed by the waste increases by 34 m^3 , from 464 to 498 m^3 . This corresponds to a final waste porosity of 0.152. The "expected" final void volume for the consolidated waste is the average of the estimated void volumes, or 106 m^3 per room, corresponding to an interconnected void porosity of 0.182.

The estimates above apply only to the waste and do not include any final-state porosity of backfill in the room, because the compacted salt/bentonite backfill is expected to be relatively impermeable. The void-volume calculations take no credit for the fact that the metal and glass waste may contain minor amounts of easily compacted materials such as combustibles or sorbents. The only study that has quantitatively inventoried the contents of TRU waste in detail (Clements and Kudera, 1985) showed that metals represent only about 80% by weight of the INEL metal waste (Butcher, 1989). The remainder of the metal category contents is combustible material (12%) and cement (5%), which would reduce its compacted porosity. A major uncertainty in this analysis is introduced by the absence of any information about the compactibility of the various waste types, although tests to determine compactibility are in progress.

An estimate was made of how rapidly the limiting void volume within a disposal room is approached (Figure 4-8). The calculated rate of closure of an empty disposal room (Munson et al., 1989) was used to determine the void volume at a given time. The void volume was obtained by subtracting the

**Void Reduction During Room Closure
(assuming no resistance to closure)**



TRI-6330-46-0

Figure 4-8. Expected total room porosity as a function of time.

volumes of the solids in the waste and backfill and the volume of brine flowing into the room as a function of time (Nowak et al., 1988) from the time-dependent room volume. Figure 4-8 is not completely consistent with values listed in Table 4-5, because, in the absence of experimental results, equal rates of consolidation of waste and backfill were assumed.

An assumption in using closure data for an empty room for this estimate is that any backstress by the room contents is insufficient to retard void reduction. This appears to be warranted for waste porosity greater than ~0.3: finite-element calculations show that backstress is significant only during the latest stages of closure. The no-backstress assumption is also consistent with the current model for compaction of the waste, which assumes that the final void volume depends only on the stress applied to the waste, and not on the stress history; that is, the only effect of backstress is to prolong the time required to achieve the final compacted state. This assumption, however, is another source of uncertainty. Estimates using these assumptions show that the limiting void volume could be achieved in 40 to 60 years; 60 years is assumed in Section 4.3. The total volume of brine flowing into the room during the 60 years is estimated to be between 6 and 38 m³ (Table 4-1), a factor of at least three less than would be required to uniformly saturate the 123 m³ of void volume at final state. In fact, all this brine can be sorbed by the bentonite in the backfill (Table 4-6). In addition, the pressure of decomposition gases within the room, even assuming none leak out, would not reach lithostatic pressure in 60 years (Section 4.10.2).

Brine sorption may be an important backfill function. Although recent estimates suggest that the expected amount of brine is small (Nowak et al., 1988), positive steps to control brine are being explored. Additives to crushed salt backfill, in particular bentonite, are being examined for their ability to adsorb water. A mixture of 70% crushed salt and 30% bentonite, by weight, has been selected as the design-basis backfill material in the waste panels. The current estimate is that between 40 and 80 m³ of brine per room can be sorbed by the salt-bentonite mixture without degrading its strength or imperviousness in the compacted state. The calculations take no credit for this sorption, but it would retard gas buildup by making brine unavailable for corrosion during the early stages of closure. Other sorbents may also be

Table 4-6. Disposal-Room Parameters for Cases IIA and IIC

	<u>Base Case</u>
Initial Room Volume:	3640 m ³
Initial Panel Volume:	45,700 m ³
Lithostatic Pressure:*	14.8 MPa
Final Room Void Volume:**	106 m ³ average: with a range from 89 to 123 m ³ (0.18: 0.15 to 0.21 porosity or 0.03: 0.024 to 0.034 of the initial room volume)
Final Room Hydraulic Conductivity:	<10 ⁻⁶ m/s
Volume of Brine Sorbed by Salt/Bentonite Backfill:	40 to 80 m ³

*The best estimate of lithostatic pressure is 14.8 MPa (Section 3.2.1). When the simulations for Case II began, this value had not been selected as the best estimate, and 14.0 MPa was used in the Case II calculations.

**Case II simulations assume an accessible final-state pore volume of 228 m³, based on information available as of January 20, 1989.

considered, as will engineering modifications, such as layers of bentonite around the waste to act as a barrier to brine penetration. Sorption of brine by backfill may simply postpone the effect of brine inflow on the waste. Assuming that the Darcy-flow model is correct for low-permeability media, enough brine will eventually (in hundreds of years) flow into the repository to use up the sorption capacity of the backfill and cause complete saturation. From then on, backfill will act like any other inert material within the repository: flow through it will depend on its permeability. Bentonite around the waste could form a relatively impermeable barrier to brine flow.

4.8.2 Permeability

The estimated permeability of the room contents at terminal state is influenced by the large difference in estimated permeabilities of the three waste categories. Computation of an average permeability depends on whether the flow paths are parallel or in series: the estimated average cemented-sludge hydraulic conductivity of 4×10^{-9} m/s (4×10^{-16} m² permeability) dominates the series path, and the estimated average metal waste hydraulic conductivity of 4×10^{-6} m/s (4×10^{-13} m² permeability) dominates the parallel path. Flow in parallel is conservatively implied by assigning an average hydraulic conductivity of the order of 10^{-6} m/s (10^{-13} m² permeability) to the room contents. A source of uncertainty in the analysis is the lack of data on the permeability of the compacted waste. In Case IIB, grout is assumed to control the permeability of the room contents. The hydraulic conductivity of grout is 1×10^{-11} m/s (10^{-18} m² permeability) (Coons et al., 1987) (Section 4.11.1).

The method of analysis used for closure-time estimates was also used to estimate the final void volume, and hence permeability, of the backfill for comparison with the permeability of the waste. The rate of closure of an empty room is used for estimates of backfill consolidation, because results from finite-element calculations suggest that crushed-salt backfill (as opposed to backfilled waste) has no effect on drift closure until the backfill becomes 90 to 95% dense (5 to 10% porosity) (Sjaardema and Krieg, 1987). The bentonite in the backfill is assumed to be so plastic that it fills the voids without offering any resistance to void reduction. The bentonite will continue to sorb brine during backfill compaction (Pusch, 1980) and to swell until space between the solid salt particles is filled. The final density of the mixture depends on how much water is available. Although no measured hydraulic conductivities have been published for high-density mixtures of salt and bentonite, values can be estimated from data for mixtures of sand and bentonite. These results suggest that terminal hydraulic conductivities of 10^{-13} to 10^{-14} m/s (10^{-20} to 10^{-21} m² permeability) are likely (Coons et al., 1987), which are comparable to the far-field permeability of the salt. In defining room-model parameters, therefore, any brine flow through the backfill is assumed to be insignificant in comparison with flow through the waste,

because the conductivity of the backfill is so small. The assignment of an effective room conductivity of 10^{-6} m/s (10^{-13} m² permeability) also assumes, therefore, that the compacted backfill does not form a continuous phase within the waste-emplacement room: the controlling permeability is assumed to be that of metallic waste.

4.9 Expected State of the Design-Basis Drift and Shaft Seal and Backfill Systems

The major conclusions of Section 4.9 are listed below.

- Major long-term reliance is placed on structural compaction of crushed salt and a crushed salt/bentonite mixture. Laboratory experiments indicate that permeability of crushed salt reduces to $\sim 10^{-20}$ m² at a porosity of 5%. Possible permeability effects of bentonite, which may be added to control brine, are not considered.
- Composite seals will be emplaced at three locations in each shaft, although effective sealing of only ~ 200 m of salt above the repository horizon is assumed here.
- Multicomponent seals, the major component of which will be preconsolidated salt, will be emplaced at the entryway to each waste-emplacement panel and at two locations in the main access tunnels. The main function of preconsolidation is to minimize the time required for reconsolidation of the crushed salt sufficiently to reach a permeability comparable to that of host rock. Relatively rapid reconsolidation will preclude the possibility that inflowing brine inhibits reconsolidation and will assure continuous, effective sealing after the longevity of concrete or composite seal components can no longer be assured.
- Gas generation at up to lithostatic pressure in the waste-disposal area is not expected to affect the performance of the shaft seal systems at any time. At early times, before the crushed-salt seal components and the crushed-salt drift backfill have reconsolidated to states of low

permeability, gas-pressure drops resulting from gas flow will be approximately equal across each of the temporary composite (or cementitious) seal components of the seal systems in both shafts and drifts. Each seal will be designed to withstand upstream pressures up to the local confining lithostatic pressure (e.g., by means of keyways). As a result of pressure attenuation across each component, only the component nearest the waste-disposal area will experience an upstream pressure equal to the local lithostatic confining pressure. In particular, the upstream gas pressures at the temporary composite shaft-seal components will in all cases remain below the local lithostatic confining pressure. At later times, after the crushed salt-seal components and drift backfill materials have reconsolidated, the gas pressure gradient caused by gas flow will be sufficiently small throughout the sealed and backfilled region to present no threat to seal-system integrity. If any gas escapes, it will do so predominantly by flow through disturbed rock zones and fractures in the salt.

4.9.1 Room, Panel, and Drift Backfill

The current WIPP conceptual design assumes that all access-ways, drifts, and waste-filled rooms will be backfilled with materials tailored to improve the entombment process (Tyler et al., 1988). Backfilling was considered in the original FEIS (DOE, 1980a), but only as it might affect subsidence (Table 1-1). Backfill materials being considered are pure crushed salt, with an emplacement density of ~1300 to 1400 kg/m³, and a mixture of ~70% pure crushed salt and 30% bentonite, by weight, with an emplacement density of ~1300 kg/m³. The main functions of the bentonite would be sorption of free brine and retardation of radionuclides in certain failure scenarios. Crushed salt is likely to be used in the access-ways, and either crushed salt or the salt-bentonite mixture will be used in the disposal rooms. Emplacement densities are loose-filled densities, because compaction of backfill to denser states before emplacement appears to be costly (requiring manual labor in limited surroundings), without much additional benefit. Other additives, e.g., gas getters, may also be mixed with the backfill (Section 4.11.2).

Model calculations have shown that reconsolidating crushed salt offers little resistance to creep closure until it has reconsolidated to 95% of the density of intact WIPP salt (relative density = 0.95) (Sjaardema and Krieg, 1987). Therefore, assuming no retardation of room closure, crushed-salt backfill in the underground drifts is expected to reconsolidate in ~100 years to 0.95 relative density. Laboratory tests have shown that the permeability of reconsolidating crushed salt decreases monotonically with increasing relative density and reaches a permeability of $1 \times 10^{-20} \text{ m}^2$ at 0.94 relative density (Holcomb and Shields, 1987). Reconsolidation may continue to somewhat higher relative densities and lower permeabilities, but probably the resistance to creep closure will rise rapidly as reconsolidation progresses past 0.95 relative density, and little further reconsolidation will occur. Therefore, the measured value of $1 \times 10^{-20} \text{ m}^2$ (10 nanodarcy) was chosen as the expected value.

Because reconsolidating crushed salt approaches a state with permeabilities comparable to intact salt (Holcomb and Shields, 1987; Nowak et al., 1988), a reasonable uncertainty range is the range for intact WIPP salt, namely an order of magnitude (Nowak et al., 1988). Therefore, the expected range for permeabilities of the reconsolidated-salt components of the repository seal systems is 3×10^{-21} to $3 \times 10^{-20} \text{ m}^2$ (3 to 30 nanodarcy); 10^{-20} m^2 is used in the calculations (Chapter 6.0).

After a room is filled with waste to the point that backfilling can begin, crushed salt from concurrent mining operations or from above-ground storage will be screened to remove oversized pieces, mechanically mixed with any additives, transported either pneumatically or by conveyor belt to the emplacement location, and emplaced by gravity feed. Backfilling will proceed sequentially in both directions from the midpoint of a room, retaining a 0.61-m (2-ft) ventilation space above the backfill. When a waste storage panel is completely backfilled, panel seals will be constructed to isolate the panel from the rest of the repository.

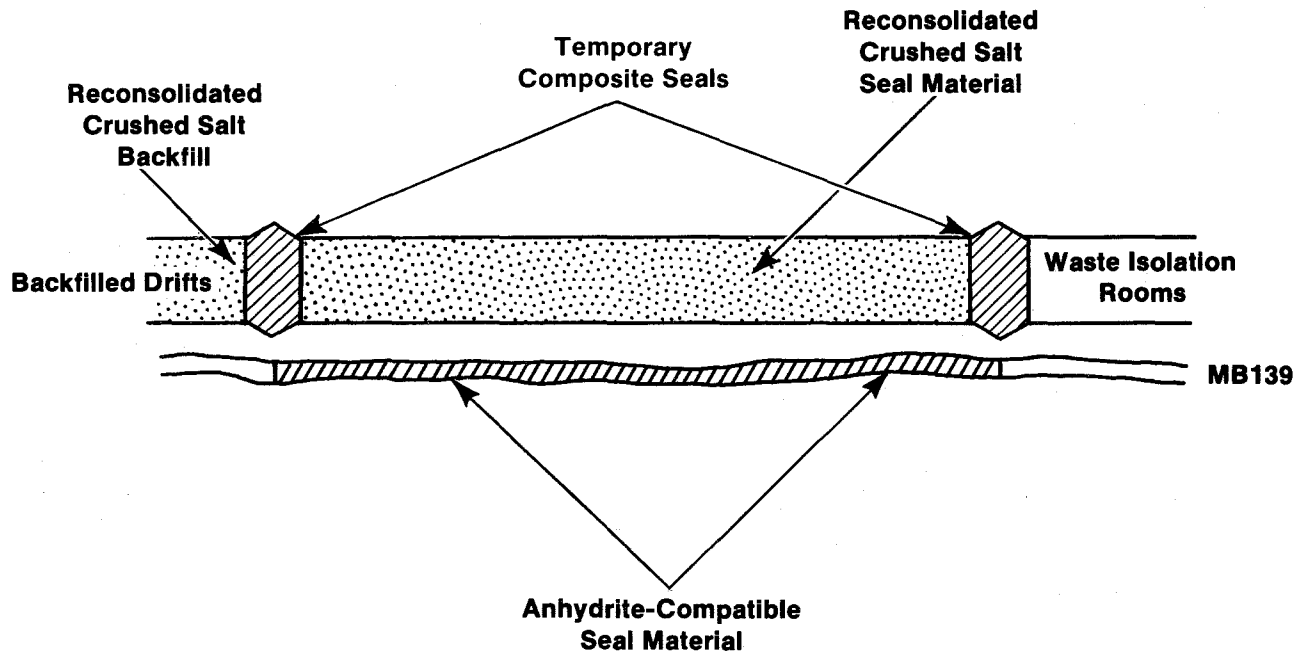
4.9.2 Drift and Panel Seal Systems

A seal consisting of several components will be emplaced in each entrance drift to a panel of waste-disposal rooms, in each main access drift approximately midway among the panels, and in each main access drift just outside the panels to the north (Figure 4-11, p.73). The latter emplacements will be the final seal-system barriers between the waste and the WIPP shafts, because it is planned to put waste in the portions of the main access drifts that lie between the panels.

Each seal will be configured as shown schematically in Figure 4-9. The portion of the drift that is at the seal location will be filled with preconsolidated crushed salt, possibly in the form of blocks. Creep closure of the drift surrounding the seal will continue to consolidate this crushed salt until it reaches at least 0.95 relative density (95% of the density of intact WIPP salt). At that density, the expected permeability of the reconsolidated salt is $1 \times 10^{-20} \text{ m}^2$, with an expected range of 3×10^{-21} to $3 \times 10^{-20} \text{ m}^2$. The expected porosity is 0.05 (Section 4.9.1). The crushed salt in the seal systems is distinguished from the backfill in the drifts by its higher initial density and resulting shorter reconsolidation time.

The crushed salt may be temporarily retained at the ends by rigid, temporary composite seals as shown in Figure 4-9; they will have no long-term sealing function. However, they will serve as effective short-term seal components for controlling brine flow and for attenuating pressure from possible gas flow from the waste-disposal area. Model calculations have shown that, for a geometry that represents repository seals, creep closure of a portion of a drift between stiff end bounds is practically unaffected by the stiff bounds (Arguello, 1988). Therefore, the stiff temporary seals will not inhibit the reconsolidation of the crushed salt that is contained between them.

Drift seals will be emplaced after each panel of rooms or interval of access drifts behind the specified location has been filled with waste and backfill. Drifts outside and north of the final seal-system barriers will be backfilled with crushed salt until the entire repository (except for the



TRI-6330-47-0

Figure 4-9. Schematic design of a WIPP panel seal.

shafts) has been backfilled. Crushed-salt backfill in the northern drifts will be reconsolidated by creep closure of the drifts to at least 95% of theoretical density, but the time to reach that state will be longer than for the reconsolidated crushed salt in the seal system, as a result of the lower initial density of the drift backfill. Seal systems will then be emplaced in the shafts. Stormont (1988) evaluated a preliminary seal-system design for the WIPP.

4.9.2.1 Sealing Marker Bed 139. Four years after room excavation, Marker Bed 139 is fractured at all tested borehole locations in all 4 x 10 m WIPP rooms and in 80% of smaller rooms (DOE, 1988b) (Section 4.7). Fracturing increases with the passage of time. Geophysical studies (Pfeiffer, 1987; Borns and Stormont, 1988; Skoken et al., 1988) demonstrated the continuity of the fracturing in MB 139 over a distance of ~1000 m. Both seismic and electromagnetic methods were used. Because electromagnetic methods measure interconnected porosity, the interconnected nature of the fractures in MB 139 is suggested by these measurements. Tracer-gas studies (Stormont et al., 1987) provided further evidence for the connectivity of fractures in MB 139 over several tens of feet.

Marker Bed 139 is taken to have a hydraulic conductivity equivalent to that of a single 0.1-m-thick continuous fracture throughout the disturbed region under the WIPP drifts between the waste-panel area and the shafts. This value represents the unhealed fractures in the marker bed after backfill in the overlying drifts has reconsolidated and lithostatic load has been applied to the marker bed. The corresponding porosity is 0.1.

Fractures in MB 139 are not expected to heal completely. Shear displacements that cause abutment of asperities (gross roughness) have been observed. The abutments are expected to prop open the fractures and prevent healing.

At critical seal locations, fractures in MB 139 could be filled with an anhydrite-compatible, deformable seal material, such as a crushed-salt-based grout. This seal material will be designed to deform and flow into any new fractures that may form in MB 139 as displacements occur and forces are

applied by creep closure. Alternatively, a reservoir of this seal material may be provided in the drift above, or the drift could be excavated to eliminate the marker bed in critical areas. The conceptual seal of MB 139 is assumed to have an effective permeability of $4 \times 10^{-19} \text{ m}^2$ (~400 nanodarcy) and a porosity of 0.03. Both the drift and MB 139 will be sealed at each drift-seal location.

The seal material in MB 139 is expected to be compatible with WIPP host rock over very long times, as evidenced by observed, long-term, geologic stability of the material, e.g., crushed-salt-based grout or bitumen. It is expected to have an effective permeability that is as low or lower than the measured values from existing WIPP small-scale-seal in-situ test emplacements of cementitious material. The only applicable in-situ measurements are from the WIPP Small Scale Seal Performance Tests A and B (Peterson et al., 1987b), which yielded an average effective permeability of $4 \times 10^{-19} \text{ m}^2$ and a porosity of 0.03. The uncertainty range in the effective permeability of Marker Bed 139 seal components is taken to be 1×10^{-19} to $7 \times 10^{-19} \text{ m}^2$ (100 to 700 nanodarcy), the same range as was calculated from the WIPP Small Scale Seal Performance Tests A and B (Peterson et al., 1987b).

4.9.3 Shaft Seal Systems

Two multi-component shaft seal systems will be emplaced in each shaft, an upper seal system in the Rustler Fm. and a lower seal system in the Salado Fm. The seal system in the Rustler Fm. has one primary function: to limit the quantity of brine that enters the crushed salt of the lower seal system to ensure effective reconsolidation of the crushed-salt seal material. This is a relatively short-term function, and no long-term performance is required of the upper seal system. The lower seal system in the Salado Fm. is required to perform as an effective long-term barrier.

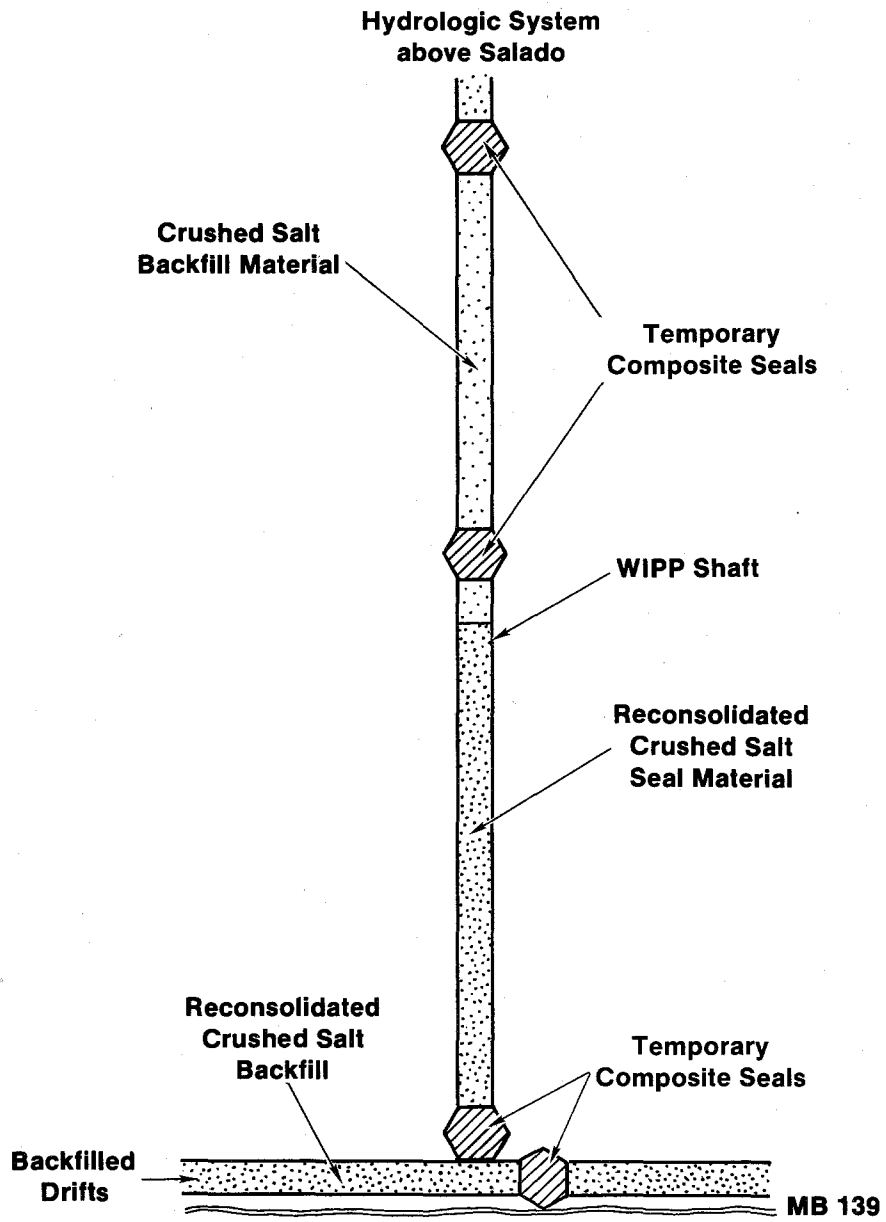
4.9.3.1 Lower Shaft Seal System. The primary components of the lower shaft seal system in the Salado Fm. will be configured as shown in the simplified schematic diagram in Figure 4-10. The primary long-term seal component is the reconsolidated crushed salt in the lower part of the shaft. Preconsolidated crushed salt will be emplaced there, possibly in the form of

poured and tamped material or blocks. Creep closure of the lower part of the shaft will continue to consolidate this crushed salt until it reaches at least 95% of the density of intact WIPP salt.

An analysis of crushed-salt reconsolidation in a WIPP shaft showed that 95% of intact salt density will be reached in the lower parts of the shaft seals (Nowak and Stormont, 1987). This analysis took into account the potential retardation of reconsolidation by inflowing brine and the effect of permeability of the reconsolidated salt is $1 \times 10^{-20} \text{ m}^2$, with an expected range of 3×10^{-21} to $3 \times 10^{-20} \text{ m}^2$. The expected porosity is 0.05 (Section 4.9.1).

Other temporary, composite seals, shown in Figure 4-10, will be emplaced in each shaft near the bottom and in the underlying drift adjacent to the bottom of each shaft to protect the primary shaft seal material from brine that may flow from the repository. These composite seals may also resist gas flow from the waste-disposal area. Each seal component will be designed to withstand the maximum expected fluid-pressure difference at the depth of the component. Therefore, sudden failure of a seal component is not expected.

Gas generation in the waste-disposal area (Sections 4.2 and 4.10) is not expected to affect the performance of shaft seal systems during the required seal-system life. At late times, after crushed salt in seal components and drifts has reconsolidated, the pressure gradient caused by gas flow will be sufficiently small to present no threat to seal integrity. The reconsolidated salt is expected to respond to gas flow nearly the same as the host rock. At earlier times, before the crushed salt has reconsolidated to states of low expected shaft-closure rates. At that relative density, the expected permeability, pressure drops caused by gas flow would appear primarily across the temporary composite (or cementitious) seals in the shafts and drifts. These seal components are expected to be similar in shape and in the resistance that each of them and the surrounding disturbed rock zone offers to gas flow. Gas pressures will therefore be attenuated equally at each composite seal. The upstream gas pressure at any seal at early times is expected to be considerably less than the local lithostatic pressure on that



TRI-6330-48-0

Figure 4-10. Schematic design of a WIPP lower shaft seal system.

seal. Each of these seals will, however, be designed to withstand upstream pressures up to the local lithostatic pressure.

Before the crushed salt in the seals and drifts reconsolidates, gas generated at up to lithostatic pressure (14 to 15 MPa) in the waste-disposal area will encounter resistance at composite seal emplacements as it flows through drifts and shafts to the Culebra Dolomite. The Culebra Dolomite serves as a sink for the gas at a nearly constant pressure of ~1 MPa, the approximate Culebra head at the shaft locations. The 13 to 14 MPa pressure drop is divided approximately equally across each of the intervening composite seals.

At least six, hydraulically equivalent, temporary composite seals per shaft will attenuate gas pressure if gas flows from the disposal rooms and the southern and northern equivalent panels of Figure 4-11, through unconsolidated waste-free drifts to the bottom of shafts, and then up the shafts to the top of the Salado Fm. Two components are located in the drift seal system just north of the disposal area (temporary composite seals in Figure 4-9); one is located in the drift adjacent to the bottom of the shaft (Figure 4-10); and one is located in the bottom portion of the shaft (Figure 4-10). There will be two more composite seal components in the Salado Fm. above the drifts, i.e., the two temporary composite seals shown in Figure 4-10 above the reconsolidated crushed-salt seal material.

A gas pressure of no more than 5 to 5.5 MPa can exist at any time anywhere within the portion of the shaft between the lowest and middle composite shaft seals in the Salado Fm. That pressure range is calculated by subtracting four-sixths of the total pressure drop of 13 to 14 MPa up to the Culebra Dolomite from the 14 to 15 MPa lithostatic pressure at the first seal north of the waste-emplacment zone. The lithostatic pressure exerted on the middle composite seal in the shaft (the lower seal shown in Figure 4-10) will be at least half of the lithostatic pressure at the waste-disposal horizon, i.e., at least 7 to 7.5 MPa. Therefore, the pressure of flowing gas is not expected to dislodge or damage the middle shaft seal. An analogous argument can be made for the composite seal at the top of the Salado Fm., where the greatest

expected gas pressure is ~3.2 to 2.2 MPa (14 to 15 MPa minus 5/6 of the total pressure drop of 13 to 14 MPa).

An analogous argument, however, indicates that if gas pressures within the repository approach lithostatic, effective isolation of individual emplacement panels may not be possible until after the gas-generation phase.

4.9.3.2 Seal and Backfill Material in Upper Shafts. The composite seals above the reconsolidated crushed salt in the shafts, i.e., above the lower composite seal shown in Figure 4-10, are expected to reach a final state of severe degradation. This degraded state is likely to be hydraulically equivalent to silty sand with a permeability of 10^{-12} m² (Stormont and Arguello, 1988). Because no flow-barrier function is expected from the crushed-salt backfill above the lower shaft seal, the same permeability of 10^{-12} m² (1 Darcy) is arbitrarily assigned to this backfill. All of these materials are assigned a porosity of 0.2, the baseline case porosity for as-emplaced crushed salt in the shaft (Nowak and Stormont, 1987).

4.10 Possible Repository Response to Gas Generation and Total Volumes Generated

The major conclusions of Section 4.10 follow.

- The formation of a brine slurry or "sludge" during mechanical closure is extremely unlikely. The estimated porosity limit, below which no slurry can form, is 40%, obtained ~30 years after decommissioning. The estimated total void space per room at 30 years is 900 m³, ~35 times the largest reasonable brine inflow per room at 30 years, 24 m³.
- In undisturbed performance, assuming successful seal performance, there are four major locations or mechanisms of gas storage or pressure release: (1) reexpansion of waste-emplacement rooms and panels by expansion of contained waste and backfill; (2) development of a new zone of alteration (DRZ) at the repository horizon (or retention of a portion of the present DRZ by elevated gas pressures prior to complete closure); (3) use of

existing or newly created fractures in Marker Bed 139 and stratigraphic contacts near the repository horizon; and (4) storage in the shafts and adjacent DRZ.

- Regardless of mechanism, the porosity increase required to store reasonable quantities of gas, even assuming the gas-production rates estimated in Section 4.2, would occur approximately an order of magnitude more slowly than porosity reduction during the first 60 years of closure. There is no reason to expect any dramatic process to take place during gas storage or release.
- Given the estimated total gas volumes, the total storage volumes within (a) rooms and panels in the disposal area; (b) a DRZ similar in properties and extent to that now present; (c) Marker Bed 139; and (d) five stratigraphic contacts near the repository horizon would be approximately adequate at lithostatic pressure. However, unless gas-generation rates are high, the DRZ might be eliminated before lithostatic gas pressures are reached. In this case, new porosity would have to be generated.
- The WIPP is eventually expected to saturate with brine. Partial or complete saturation in response to either final or interim reductions in gas pressure will be driven largely by buoyancy as gas migrates upward and is replaced from below by brine. The low far-field permeabilities of the Salado Fm. suggest that this process would be extremely slow and might require thousands of years.

4.10.1 Slurry Formation within the Disposal Rooms

An idea about WIPP of recent concern is that sufficient brine will enter the waste rooms and mix with the waste and backfill to form a slurry. A slurry is a watery mixture of insoluble matter, with little or no resistance to shear, that is easily transported by flowing water or brine. Slurried waste might escape from the repository in the same way that ground-up matter from home garbage disposals is transported through sewer systems. Such venting might occur during human intrusion, when the slurry is envisioned to flow out of the room and rapidly escape to Earth's surface. In fact, however,

the formation of waste mixtures with such fluidity seems to be impossible, because the waste will reach a sufficiently low porosity in the compacted state to be solid-like in response before it becomes saturated with brine.

Information from soil mechanics and technology relating to hydraulic transportation of solids (for example, coal- or sand-slurry pipelines) can be used to define the conditions under which particulate matter such as waste would exhibit fluidity. Hydraulic transport of solids in pipes is not possible unless the volumetric concentration of loosely packed solids in a unit volume is ~ 0.5 or less, and the dry porosity of the solids is 0.5 or greater (Eyler and Lombardo, 1982). (If the mixture is drained, the concentration of loosely packed solids in a unit volume corresponds to the dry porosity. The dry porosity is a useful parameter because it defines the void volume within the mixture, and hence how much water is required for complete saturation.) Similarly, in soil mechanics the plastic limit of soils (no confining pressure) is used to define the limit of semisolid response. The plastic limit is the point at which, after adding more and more water, soils begin to rapidly lose their rigidity. It is defined as the ratio of the weight of water divided by the weight of solids in a given volume. For bentonite, the plastic limit corresponds to a dry porosity of ~ 0.65 (Lambe and Whitman, 1979), but for some silts and clays the plastic limit is considerably less, corresponding to equivalent dry porosities of ~ 0.2 to 0.3 (Lambe and Whitman, 1979). For fine-grained sands, the critical void ratio, or dry porosity at which the material loses its strength, is ~ 0.2 to 0.3 when completely unconfined and 0.5 for a confining stress of 1 MPa (Lambe and Whitman, 1979). The values for the critical void ratio for sand show that even slight confinement greatly increases the resistance of granular materials to shear.

The various conditions that cause granular solids to lose their resistance to shear suggest that the porosity of most of the waste must be on the order of 0.5 or greater for a slurry to form. In contrast, metal waste is estimated to compact to less than 0.4 porosity and sludges and combustibles to less than 0.1 porosity before resaturation occurs. Although metal waste is initially quite porous, it reinforces the compacted waste and gives it strength. Much later in time, much of the metal waste may corrode to rust, which also resists

shear. Cemented sludges are granular in nature, being composed in part of cement and earth materials, and glass would remain granular.

Defining the final state of combustible waste is more difficult. Although initially compactible to a dense and impermeable state, the plastic component of combustible waste may eventually break down, because of radiolysis and decomposition, to a gelatinous form that is insoluble in brine. Cellulose would also decompose, leaving weak residues. If these products had more water in them, they might be akin to silts and clays in their plasticity, but because they compact to a dense state (0.1 porosity or less), they are expected to be highly viscous, and not a slurry. Upon resaturation, migration of combustible decomposition products from their original location would probably be an extrusion process, as opposed to flow, and might even beneficially fill voids in less-dense waste.

Slurry formation within the repository is not considered possible, because of the high state of compaction of the waste. Nevertheless, the volume of brine required to cause slurry-like behavior is of interest. This analysis assumes that a large amount of brine is available and can enter the room before mechanical reduction of the void volume is complete. As brine flows into the room, the waste will become saturated with brine, and the pore pressure will increase to the point that void reduction ceases.

In estimating the volume of brine required for slurry-like states, it was first determined that the dry porosity of the waste would have to be ≥ 0.4 . The porosity value was computed by weighting the loss-of-strength porosities of the various components of waste according to their prevalence in the total waste inventory. Loss-of-shear-resistance porosity values of 0.5 were assigned to cemented sludge, metal, and glass waste, and combustible waste was conservatively assumed to be silt-like and to become plastic at dry porosities of 0.2 to 0.3. In addition, the porosity of the backfill would have to be ≥ 0.5 but, for simplicity, its critical porosity value was also taken to be ≥ 0.4 .

Next, the calculational method used for room-closure estimates (Sections 4.7 and 4.8) was used to estimate that compaction of the room contents to a

porosity of 0.4 would take ~30 years. Rates of compaction of the waste and backfill were assumed to be identical. Thirty years after emplacement, the volume of a typical disposal room is estimated to be ~2240 m³; at 0.4 porosity, the volume of the pores would be ~900 m³. To achieve slurry conditions, all of this pore volume would have to fill with brine. If the pore volume did not fill with brine, compaction to denser states would continue.

Estimates of the amount of brine actually flowing into a disposal room in 30 years are at most 19 to 24 m³ (Table 4-1). Brine flow into the disposal room would have to increase by at least a factor of 35 to approach conditions that might lead to the formation of slurries. This enormous increase in the amount of brine coming into the room has not been observed in controlled experiments underground. The conclusion of this analysis is that the formation of waste mixtures with slurry-like fluidity is impossible, because insufficient brine is available within the disposal room.

4.10.2 Potential Gas-Storage Volumes and Pressures Within and Surrounding the Repository

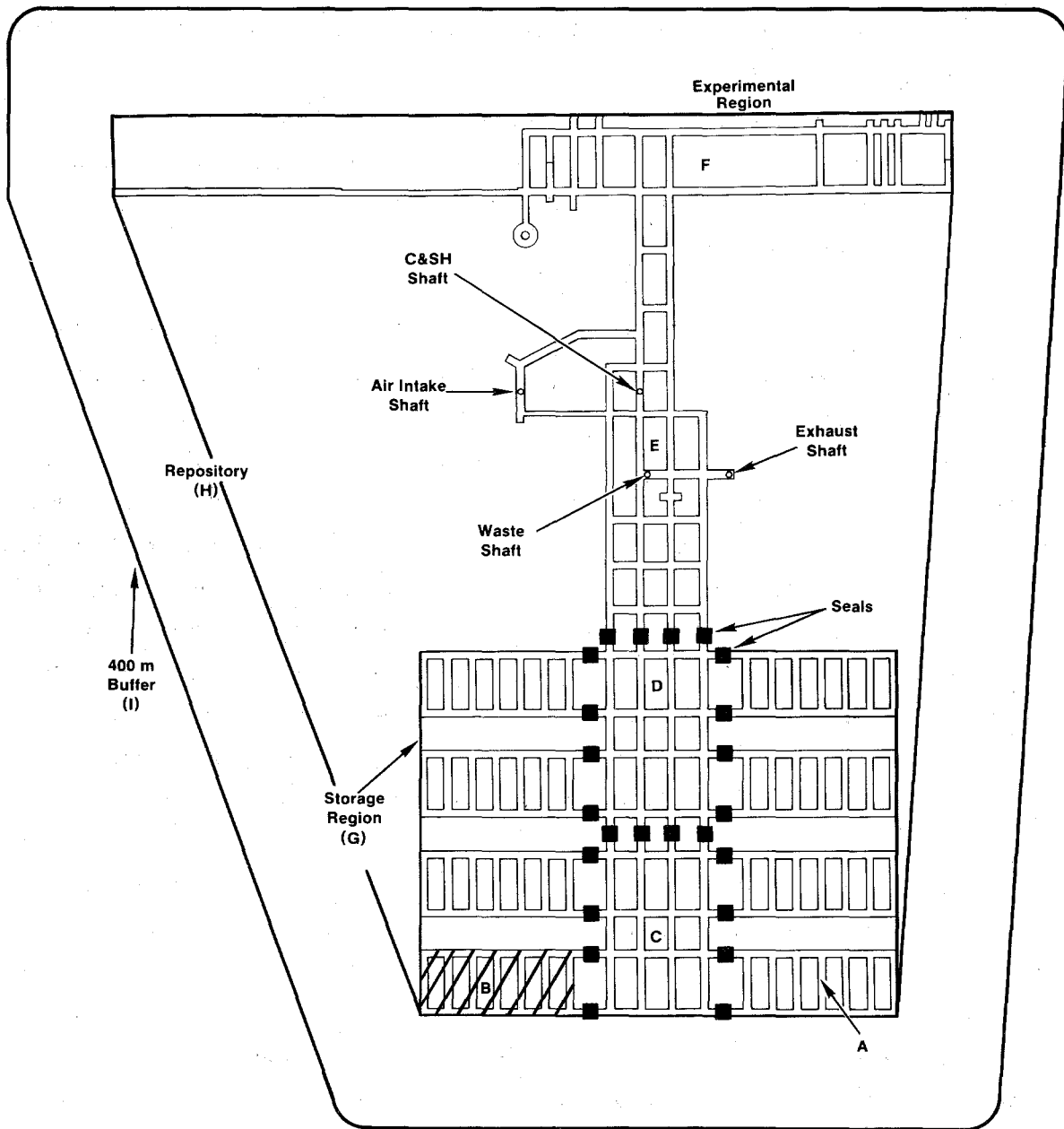
4.10.2.1 Excavated and Enclosed Volumes. Four general regions within the WIPP repository can store gas generated by anoxic corrosion of the steel containers and metallic waste and microbial decay of organic matter in the waste. In order of increasing distance from the position of emplacement, these include (1) excavated regions; (2) the disturbed rock zone (DRZ) around the underground openings at the repository horizon; (3) bedding planes above, within, and below the repository horizon, such as Marker Bed 139; and (4) the shafts and any adjacent DRZ. Detailed storage mechanisms differ in each of the storage volumes considered. In excavated regions, gas may be stored either within existing porosity after mechanical closure to "steady state" (Section 4.8) or, if gas pressures locally exceed lithostatic loads, within newly generated porosity resulting from gas-driven expansion of waste and backfill. Gas might also be stored within an altered zone of increased porosity around the underground workings. Such a disturbed-rock zone is known to be present around the underground workings at this time (e.g., Borns and Stormont, 1988) (Section 4.7), but is expected to be eliminated in the final

stages of closure, unless gas or brine pressures have reached lithostatic by that time (Section 4.8). Within Marker Bed 139, gas might be stored within the fractures known to open under the floor of the WIPP excavation with time and in fractures newly opened as a result of gas pressures locally exceeding the lithostatic load (or least principal stress) (Section 4.7). Finally, gas might be stored within the porous material emplaced in the WIPP shafts or in any adjacent existing or newly created DRZ. Work to date, however, has not identified a DRZ of significant size adjacent to the WIPP Waste-Handling Shaft (Section 3.2.1).

Figure 4-11 shows the planned excavated and "enclosed" regions in the WIPP repository (DOE, 1986b). ("Enclosed" regions include both excavated and intact zones within a given boundary.) Nine general regions (A through I) are shown. Region A is a single room; region B is one panel; region C is the southern equivalent panel, and region D is the northern equivalent panel. Together regions A through D comprise the region where waste is stored, storage region G. Two other major excavated regions are the access drifts outside the waste-emplacment region (E) and the experimental region (F). For the purposes of the following discussion, the access drift region (E) extends from the northern seals of the storage region to the first major east-west drift in the experimental region (F). Two other regions, the DRZ and WIPP site, are omitted because they are too small and too large for Figure 4-11.

The convex polygon that encloses regions A through F (all the underground workings) is the repository region (H), as defined in the WIPP Project's compliance strategy (DOE, 1989). Region I is a 400-m buffer zone surrounding the repository. Four hundred meters was chosen because it approximates the distance between the repository and the Salado/Rustler interface (Figure 6-1, p. 6-2) and thus defines a salt "cube" around the repository. This "buffer zone" currently has no statutory significance. Region J is the WIPP site (Figure 1-4), less the total areas included in areas H and I.

In cross section, the rooms (A) are 4 x 10 m (13 x 33 ft). The heights of the drifts and experimental rooms vary, but in general the experimental rooms are 5.5 x 5.5 m (18 x 18 ft), and the drifts vary from 4 x 7.6 m (13 x 25 ft) and 2.4 x 4.3 m (8 x 14 ft).



TRI-6330-85-0

Figure 4-11. Excavated and enclosed areas in the WIPP repository.

The areas and initial volumes for excavated and enclosed regions (Table 4-7) are shown in Figure 4-11. The total excavated and enclosed areas for the storage area (G) are about $1.1 \times 10^5 \text{ m}^2$ and $4.9 \times 10^5 \text{ m}^2$, respectively, which implies an average extraction ratio of 22%. The volumes in Table 4-7 are used below to calculate hypothetical gas pressures. In evaluating final storage volumes, an average void ratio (final void volume to initial excavation volume) of 0.03 was assumed for the storage region (G) and for all other excavated areas (H) (Table 4-7).

The second storage volume considered is the DRZ. Although potentially large in volume and gas-storage capacity (Section 4.7), the DRZ has not yet been well characterized. For the purposes of this discussion, a zone 1.5 m (5 ft) thick is assumed to surround the excavation, with a porosity of 0.14. These values approximate the current extent and character of the DRZ. However, it is generally assumed in this report that void volume within the DRZ, barring gas pressurization, is eliminated during the final stages of closure. If not, then the "final" porosity and permeability of the repository would be increased. Because repository permeability does not enter directly into these calculations, this should not affect the calculated results. If the DRZ is initially eliminated during closure, then its participation in later gas storage would require formation of a new zone of alteration.

Besides the excavated regions of Figure 4-11, an anhydrite layer, Marker Bed 139, 1.5 m below the repository horizon; a clay seam 2.1 m directly above the repository horizon; and four salt bedding planes at the repository horizon potentially can store gas (Figure 4-12). Potential gas-storage volumes within these bedding planes at assumed fracture apertures are also used below in calculating hypothetical pressures within the repository. Although formation of the DRZ (Section 4.7) includes local interconnection of MB 139 with the excavations, the availability of these storage areas is not uniform over the areal extent of the repository.

For MB 139, the volume initially available is located directly under the excavations, where stress release has caused MB 139 to open existing fractures and develop new ones (Section 4.7). This fracture porosity is absent under unexcavated portions of the underground workings (Stormont et al., 1987). The

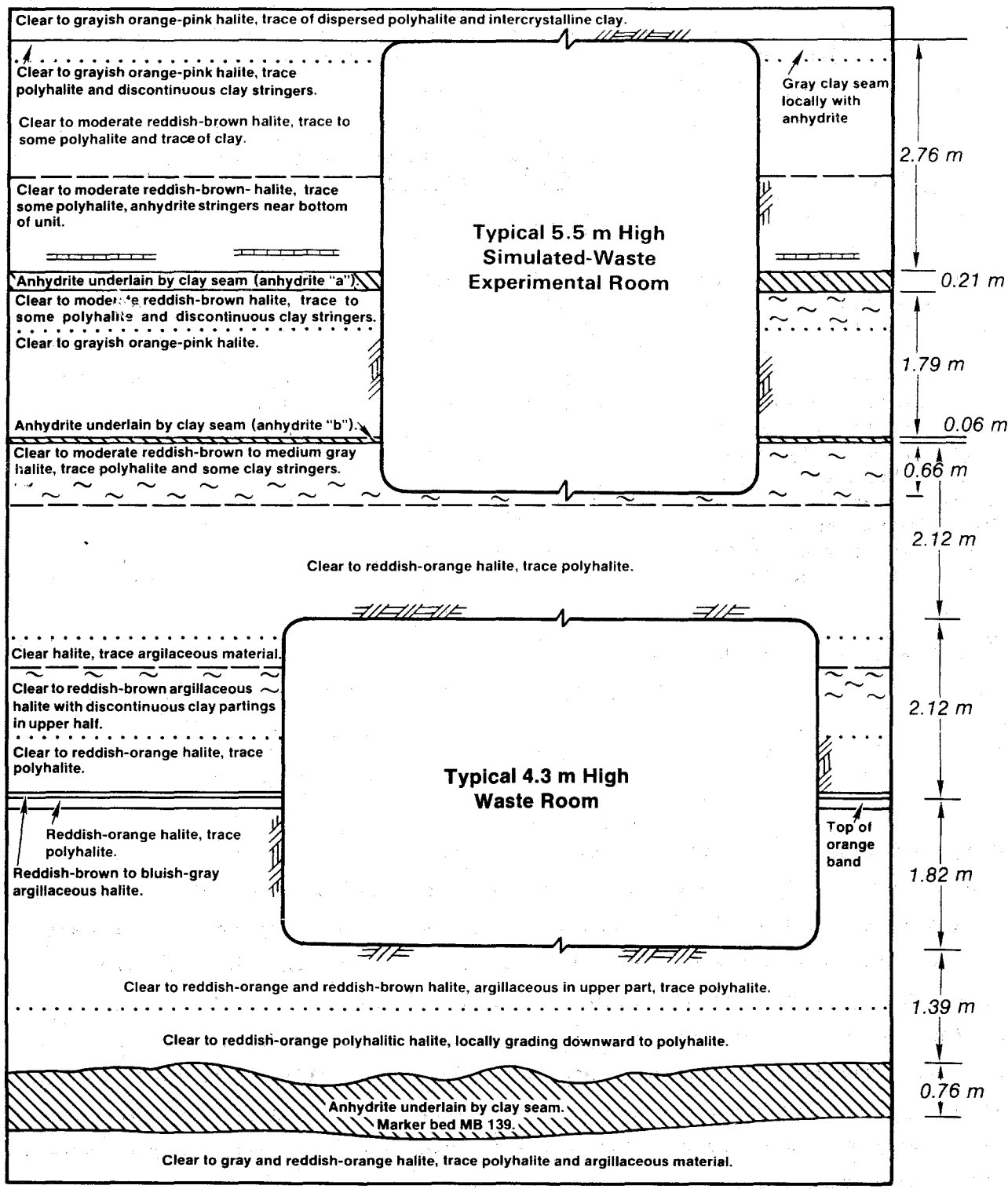
Table 4-7. Summary of Excavated and Enclosed Areas and Initial Volumes Within the WIPP Repository and Site, Not Considering Closure

<u>Region*</u>	Areas		Volume	
	Excavated (10 ⁴ m ²)	Enclosed (10 ⁴ m ²)	Excavated (10 ⁴ m ³)	Enclosed (10 ⁴ m ³)
Room (A)	0.092	0.092	0.36	0.36
One panel (B)	1.2	2.8	4.6	11.0
Southern equivalent panel (C)	0.84	3.5	3.3	14.0
Northern equivalent panel (D)	0.87	3.6	3.4	14.0
Access drifts (E)	2.2	28.0	7.8	100.0
Experimental area (F)	2.2	30.0	7.2	110.0
Total storage area (G)	11.0	49.0	43.0	190.0
Total repository (H)	15.0	170.0	58.0	690.0
Buffer zone (only) (I)	0.0	270.0	0.0	
Land-withdrawal zone (less H and I)	0.0	3700.0	0.0	
Four shafts (only) to base of Rustler Fm.	0.009	0.009	3.5	3.5
DRZ in storage region	0.0		0.0	57.0

*Regions shown in Figure 4-11.

same phenomenon, fracture dilation, is assumed to occur in the clay seam above the repository. In calculating available gas storage, an equivalent void height of 0.1 m for MB 139 (Section 4.9.2) and 0.01 m for the clay seam and each of the salt bedding planes in the repository horizon was assumed where appropriate. The large apertures assumed probably overestimate the gas-storage potential at stratigraphic contacts near the repository horizon. Although fracture openings are known to be present within MB 139 and the clay seam above the repository horizon, gas storage in the bedding planes in the repository horizon would require their being opened against approximately lithostatic pressure.

Potential gas-storage volumes within the WIPP shafts have not been examined in detail. Assuming an average volume reduction of 0.5 due to



TRI-6330-84-0

Figure 4-12. Geologic cross section at the repository horizon (after Bechtel, 1985).

closure and an average final porosity of 0.05 for backfill in the shafts, however, the storage volume within the shafts themselves would only be $9 \times 10^2 \text{ m}^3$.

4.10.2.2 Hypothetical Gas Pressures. The following pressure calculations answer a simplified question: assuming no decrease in gas pressure as a result of leakage through seals and plugs or of gas flow into the Salado Fm., will enough gas be generated to exceed lithostatic pressure (14.8 MPa) in voids remaining after complete creep closure? As described below, calculated gas pressures for available storage volumes within the waste-emplacement area exceed lithostatic using the currently assumed potentials described in Section 4.2 and the assumptions listed above. This response for a bounding calculation does not necessarily imply failure of the repository, but it does require that the issue of net gas generation and gas-generation rates within the WIPP repository be aggressively pursued. Experimental plans to address this issue have been summarized by Bertram-Howery and Hunter (1989).

From available storage volumes, potential pressures were calculated using the Redlich-Kwong equation of state and appropriate mixture constants (Prausnitz, 1969):

$$P = \frac{n_t RT}{V} \left(\frac{V}{V - n_t b_{\text{mix}}} - \frac{n_t a_{\text{mix}}}{RT^{3/2} (V + n_t b_{\text{mix}})} \right) \quad (4-1)$$

where

- a_{mix} = mixture constant,
- b_{mix} = mixture constant,
- n_t = total number of moles,
- P = total pressure,
- R = universal gas constant,
- T = temperature, and
- V = volume.

The ideal gas equation of state and appropriate compressibility factor for the various component gases provided similar results:

$$P = Z_{\text{mix}} n_t \frac{RT}{V} \quad (4-2)$$

where

$Z_{\text{mix}} = f(P_c, T_c)$ = generalized compressibility factor for gas mixture,

$P_c = \sum y_i P_i$ = pseudocritical pressure,

$T_c = \sum y_i T_i$ = pseudocritical pressure,

y_i = mole fraction of gas component i ,

P_i = critical pressure of gas component i , and

T_i = critical temperature of gas component i .

Although various gases may be generated (Section 4.2), for these simple calculations only three gases were considered: hydrogen (H_2) from the anoxic corrosion of iron (Fe) alloys in Mg^{2+} brines, assuming a total generation potential of 4.3×10^8 moles (~894 moles/drum-equivalent) (67% from the steel containers and 33% from metals in the waste) and methane (CH_4) and carbon dioxide (CO_2) from anoxic microbial decay, assuming a total generation potential of 3.3×10^8 moles (~589 moles/drum-equivalent). (The current best estimate of microbial gas-generation potential is 606 moles/drum. The value of 589 moles/drum was used here before the best estimate was selected.) Other gases that might be generated, such as N_2 , H_2S , and volatile organic compounds, are not considered here (Section 4.2, Appendix A.1, A.2, A.3). The potentials considered here were calculated from existing waste inventories (33% of the expected total) and projections of waste from nuclear-weapons activities for the next 25 years (Section 4.2).

For purposes of calculation, the mix of gases from microbial decay was assumed to be 65% methane and 35% carbon dioxide, a representative mixture found in anaerobic digesters for municipal waste (Clark et al., 1977). (Replacing CH_4 with N_2 has little effect below lithostatic pressures.) Although a higher percentage of CO_2 might be present (Section 4.2), the resulting total pressures would then be less than those estimated here, because CO_2 is more compressible ($Z < 1$) than methane or nitrogen at the

pressures and temperatures expected in the repository. Furthermore, above a CO₂ partial pressure of 7.4 MPa, CO₂ would condense, provided the repository temperature remained below 31°C. The calculations in this section assume a 2°C temperature rise above ambient (27°C), caused by RH-TRU waste.

Several combinations of available volumes (listed in order of increasing storage capacity) were used in calculating the pressures reported in Table 4-8. The final two available volumes in Table 4-8 are hypothetical, but they put gas-generation volumes in perspective. Although many more combinations are possible (e.g., those including the buffer region), only available volumes in or near the waste-storage region are considered in Table 4-8.

Several observations can be made from Table 4-8. First, hydrogen gas resulting from metal corrosion is the major contributor (partial pressure) to the total pressure (about a factor of 2.5 greater than carbon dioxide and methane at low pressures). Although the gas-generation potential for hydrogen is greater than the gas-generation potential for microbial action by only a factor of ~1.5 (Section 4.2), the compressibility factor (Z) of more than one for H₂ (and less than one for the assumed mix of microbial gases) increases the impact of H₂ at low pressures. At high pressures, the partial pressures no longer sum linearly, as demonstrated in Table 4-8. At very high pressures the Redlich-Kwong equation of state is no longer applicable.

Second, all the gas would easily fit into the initially excavated but waste-filled volume of the storage region if no creep closure occurred; the maximum calculated pressure is 6.7 MPa, approximately the hydrostatic pressure for saturated brine with respect to the Culebra Dolomite (6.3 MPa). This puts the volume of gas produced in perspective, in that it demonstrates that the very properties of salt generally thought to make it attractive for radionuclide containment, creep closure and low permeability, result in potential difficulties in isolating gas-generating waste.

Finally, using this simple bounding model, and assuming that gas generation by both microbial activity and corrosion is compatible, calculated potential pressures exceed lithostatic for most of the potential storage areas defined in Table 4-7.

Results 1 through 6 in Table 4-8 indicate, given the simplifying assumptions made here, that gases estimated to be generated within the WIPP repository by the combination of microbial activity and metal corrosion cannot be stored within the expected final volumes available in the WIPP workings themselves, including the entire excavated area, Marker Bed 139 under the excavated areas, and the first clay seam above the repository horizon. Generation of a DRZ after closure or maintenance of the volumes estimated within the present DRZ in the waste-emplacement area (results 7 through 9) might provide the accessible volumes required. However, the time required to eliminate the DRZ, even in the absence of gas generation, is not well known at present (Section 4.7).

Two additional ways to describe the volumetric increase required for gas storage in the absence of a stable DRZ are to estimate (1) the necessary total fracture aperture in MB 139 to the boundary of the repository, buffer zone, or site; and (2) the necessary porosity within a hemisphere above the storage region, resulting from formation of a secondary altered zone after closure.

A fracture system with a total average vertical aperture of 0.06 m everywhere out to the repository boundary (Figure 4-11), including under pillar areas within the excavation area, or an average aperture of 0.025 m out to the 400-m buffer zone is sufficient to maintain pressures below lithostatic. The currently assumed total vertical aperture in Marker Bed 139 directly under repository excavations is 0.1 m. Both these calculations assume that the excavated area of the repository region (H) also stores gas. However, these calculations assume blunt ends to fracture systems. It is also possible that a more narrow fracture zone (i.e., less fracture aperture) would extend beyond the current estimates.

Alternatively, it is possible that a secondary alteration zone of increased porosity might form after the current DRZ is removed by closure. A uniform porosity of only 0.002, twice the estimated effective porosity of undisturbed halite in the Salado Fm., within a hemisphere with a base area circumscribed by the minimum dimension of the storage region (radius of 315 m) would be sufficient to maintain pressures below lithostatic. (The distance to the Salado/Rustler interface above the repository is about 400 m.) This

Table 4-8. Gas-Storage Volumes and Calculated Pressures in Storage Area from Maximum Gas Potentials, (Assuming that Salt Does Not Creep Open After Initially Closing and Has Zero Permeability)

Void Space	Final Void Volume $\times 10^4 \text{ m}^3$	Pressure		
		Total MPa	Microbial MPa	H ₂ MPa
1. Excavated storage (G) (final)	1.3	*	70.0	170.0
2. Total repository excavation (excluding shaft) (H)	1.8	*	52.0	98.0
3. MB 139 and clay seam above excavations (G)	1.2	*	270.0	200.0
4. MB 139 under, clay seam above plus excavated storage (G)	2.5	190.0	24.0	58.0
5. MB 139 under, and clay seam above total excavated repository area (H)	1.7	*	59.0	105.0
6. MB 139 under, clay seam above plus total repository excavation (H) (excluding shaft)	3.4	84.0	16.0	38.0
7. DRZ in excavated storage area	8.0	25.0	8.1	15.0
8. DRZ in storage area plus final excavated storage (G)	9.3	21.0	7.2	12.0
9. DRZ, MB 139, clay seam, plus excavated storage (G)	10.5	18.0	6.5	11.0
10. Excavated storage (G) (<u>initial</u> , empty)	43.0	4.4	1.8	2.5
11. Excavated storage (G) (<u>initial</u> , filled)	28.0	6.7	2.7	4.0

*Beyond applicable range of Redlich-Kwong equation of state, as a result of excessive pressures.

latter way of viewing the volumetric increase required for gas storage more favorably presents the problem, but neglects the difficulty of moving gas under either a concentration or pressure gradient in the low-porosity salt; the porosity increase within a secondary zone of alteration, and hence its dimensions, would of necessity be nonuniform.

Because calculated gas pressures can exceed lithostatic pressure using a simple bounding model and assuming design-basis waste and backfill, a more-

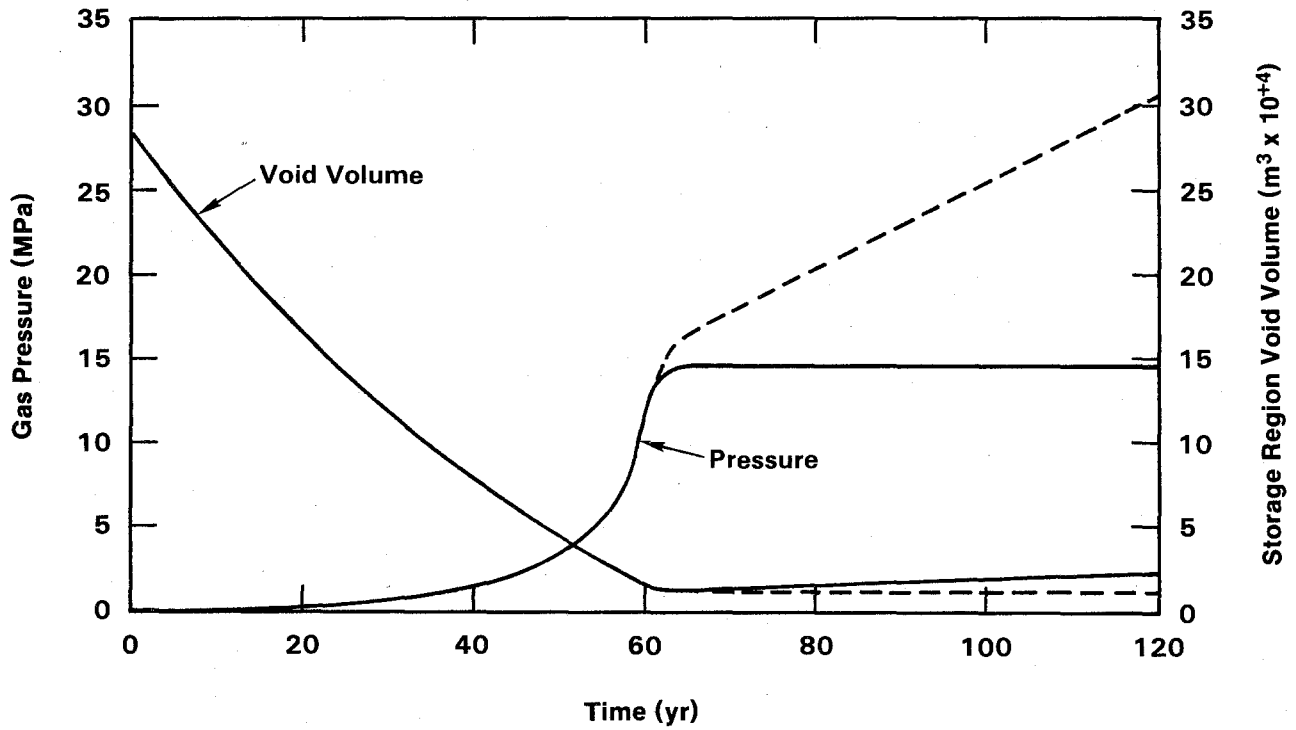
detailed model of the repository that includes the escape of gas (diffusion and leakage), the rate at which gas is generated (not just the gas potential), and volumetric responses of the storage region probably must be considered in the performance assessment unless engineering modifications are included in the design (Section 4.11). For example, although the hydrogen gas is a major component, several options are available for its removal. Because 67% of the H₂ gas potential derives from the waste containers, and of these, ~67% do not yet exist, using containers constructed out of something other than iron alloys may be an option for reducing the H₂-generation potential. Purposeful corrosion of Fe-alloy drums using copper sulfate, which prevents H₂ formation, is another potential approach (Section 4.11).

The combined effect of void-space reduction and the gas-generation rate is explored briefly in the next section, assuming design-basis waste.

4.10.2.3 Storage-Region Pressures from Combined Gas Generation and Creep Closure. Figure 4-13 presents the calculated pressure increase and void-space reduction in the entire waste-storage area (G) from the combined effects of creep closure and gas generation. It conservatively assumes that creep closure and microbial and corrosive gas generation begin immediately after sealing off the storage area (G of Table 4-7), implying that no creep closure of the rooms has occurred prior to sealing; that sufficient free water exists immediately for bacteria to degrade organic matter, and that all iron alloys are immediately bathed in brine. Furthermore, this bounding estimate assumes that no gas escapes from the storage area and ignores the presence of a DRZ during closure.

The closure rate in the storage region is estimated here using an empirical fit to results from a finite-element closure analysis of an empty room (Morgan, 1987). Back pressure from backfill, waste, and gas is neglected (cf. Figure 4-6). Assuming a negligible effect from backfill, waste, and gas is valid until the back pressure is a significant portion of lithostatic pressure. The empirical fit to the finite-element results is

$$\frac{V}{V_0} = e^{-0.0156t} \quad (4-3)$$



TRI-6330-70-0

Figure 4-13. Pressure history to initial closure of storage area, assuming no leakage.

where

- V = available volume,
- V₀ = initial volume, and
- t = time in years.

The solid volume from backfill, waste, and drums within a room was assumed to be 1,300 m³, which must be subtracted from the available volume (V) (cf. Table 4-6). This solid volume assumes that the volume of solids in the waste is 570 m³ per room and that the volume of solids in a 70% salt, 30% bentonite backfill mixture is 730 m³ per room (Section 4.8).

Although Equation 4-3 was developed for one room, it is assumed to adequately model the creep closure of the storage region as a whole; hence, Equation 4-1 was increased by the ratio of total excavated storage area to room volume (μ) (44/0.36, Table 4-8). Hence, the equation for creep closure of the entire storage region (G) is

$$V = \mu (V_0 e^{-0.0156t} - 1300) \quad (4-4)$$

The hydrogen and microbial gas-generation rates used in Figure 4-13 are 1.70 mole/drum-equivalent/yr (9.5×10^5 mole/yr) for 527 years for hydrogen, resulting in a total potential of 896 moles/drum equivalent; and 0.85 mole/drum-equivalent/yr (4.7×10^5 mole/yr) for 693 years for microbial gas, resulting in a potential of 589 moles/drum.

As described in Section 4.2, hydrogen is produced by anoxic corrosion of iron alloys. The H₂-generation rate of 1.7 mole/drum-equivalent/yr assumes that all Fe is 1.52 mm thick (less than 1/16 in.) (the thickness of drums is 1.52 mm and comprises about 47% of Fe waste) and that the iron is bathed in brine (Section 4.2). The microbial gases are assumed to arise from the degradation of cellulosic materials and rubbers in waste. The 0.85 mole/drum-equivalent/yr used is a composite of only carbon-dioxide generation over 3 months in laboratory experiments from various cellulose matrices (e.g., paper, cloth, and plywood) (Molecke, 1979). Limited availability of water over long times probably would reduce this rate (Section 4.2).

Even with these conservative assumptions, the pressure increase is modest until the storage region is nearly compacted (about 50 years) (Figure 4-13). Furthermore, although the dashed lines in Figure 4-13 show some potential effect on final consolidation, i.e., calculated gas pressures approach lithostatic shortly after 60 years, minor decreases in gas-generation rates or delays in the time that gas generation begins would indicate that salt would likely encapsulate the waste at near "final" porosity before impacts of continued gas generation were felt. At the assumed rates, however, encapsulation could be incomplete, and complete healing of the DRZ could be forestalled.

Two separate lines are shown in Figure 4-13 for pressure and volume after 60 years. The dashed lines assume constant excavation size after closure. As demonstrated in Table 4-8, the pressures eventually become excessive. The solid lines indicate the volume increase necessary to maintain constant lithostatic (14.8 MPa) pressures for 120 years. The necessary rate of volume (porosity) increase is more than an order of magnitude slower than the initial closure ($1.5 \times 10^4 \text{ m}^3$ expansion in ~60 years versus $27 \times 10^4 \text{ m}^3$ closure over approximately the same time interval). Although not shown, the gas would have to increase the void volume to $1.3 \times 10^5 \text{ m}^3$ at the end of the gas-generation phase, from a void volume after closure of $1.3 \times 10^4 \text{ m}^3$. The final volume is about 45% of the initial excavated (but filled) volume of $2.8 \times 10^5 \text{ m}^3$ (Table 4-7). This corresponds to a porosity increase within the excavated storage area alone (G) from 0.18 at "final" state, not including gas generation, to a final porosity of 0.26, within which gas would be at lithostatic pressure.

Two major points can be drawn from Figure 4-13. First, at the assumed gas-generation rates, at least some gas may be stored within the DRZ, retarding its elimination by structural closure. Second, the rate of porosity increase resulting from gas generation is an order of magnitude slower than early closure.

4.10.3 Possible Paths and Mechanisms for Relief of Elevated Gas Pressures

As mentioned at the beginning of Section 4.10.2, there are (in the absence of human intrusion) four possible paths and mechanisms for relief of elevated

gas pressures in the WIPP repository: (1) gradual increase in porosity of the salt encasing the waste within the waste-emplacement excavation (Figure 4-13); (2) gas movement into a remnant or regenerated DRZ in the host salt; (3) gas movement into consolidated but unsaturated drifts and either preexisting or newly generated fracture apertures in Marker Bed 139 and along stratigraphic contacts near the repository horizon; and (4) storage within the WIPP shafts and any adjacent DRZ. Gas would only have to expand the final room porosity after 60 years (0.18) to less than half of the initial porosity (0.28 vs. 0.63), and this expansion would occur much more slowly than the initial closure.

However, if gas pressure within the WIPP waste-disposal area does approach the local lithostatic pressure, fractures are expected to form at the surfaces of the excavations and propagate into the surrounding host rock, either by generation of tensile zones around an expanding excavation or by release into a remnant DRZ, within which the effective stress is less than lithostatic. Results from fracturing experiments by Wawersik and Stone (1986) indicated that there was no preferential direction outside the DRZ for fracture propagation, at least on the small scale of their tests. There is no sound basis for assigning preferential gas-driven fracture-growth directions over long distances from WIPP excavations. Therefore, it is possible that a volumetric zone of dilation (DRZ) will be either maintained or generated by gas pressurization around the repository at long times.

Gas is expected to escape from the rooms gradually, rather than catastrophically. Although fluctuations in the room gas pressure are expected as gas production is balanced against brine inflow over a period of at least hundreds of years, each time the pressure reaches a certain level, new paths will open. With new opportunities for release, some gas will diffuse out of the disposal room and excess pressure will be relieved. The possibility that gas-driven fractures in salt can propagate at high velocities, releasing large volumes of gas, was discounted in an analysis of gas-driven fracture propagation (Sandia Laboratories, 1979, p. 3-58). One conclusion from this study was that

Due to the steep stress gradients present around the drifts, fractures propagating from the drifts would most likely be arrested

within a short distance--approximately 7-10 m for drift gas pressures below crack clamping stress. However for drift gas pressure above crack clamping stress, crack propagation would be expected to progress until enough new void volume was created to drop the drift gas pressure below lithostatic pressure.

An added factor in preventing the rapid extension of fractures is the fact that the tips of the cracks are always surrounded by a compressive stress field, as opposed to a tensile stress field, which assures stable, rather than unstable, crack propagation.

The conceptual model of gas escape, therefore, is that after emplacement of the panel seals, pressure will gradually build up within the disposal rooms. As noted above (Sections 4.2 and 4.10.2), the time required for this process could range from hundreds to thousands of years. At some time, however, the pressure inside the rooms may become sufficiently large to initiate gas flow to a region at lower pressure outside the rooms.

The paths for such gas flow cannot be defined quantitatively at this time, but it is likely to be through a combination of preexisting discontinuities, such as Marker Bed 139, and cracks within new or remnant zones immediately around the repository (the DRZ). Estimates contained in Section 4.10.2 (Table 4-8) indicate that, assuming a uniform DRZ and the presence of storage space in MB 139 and along stratigraphic contacts near the repository horizon, it might be possible to store the volumes of gas produced within and immediately adjacent to the repository.

Quite likely, however, gas release will be along very tortuous routes, connecting a number of weak links within these features. For example, a path could begin at a preexisting crack in a repository wall that intersects a clay seam, extend along the clay seam and enter reconsolidated salt in a shaft that intersects the clay seam, continue up the shaft to an interface between it and a seal, and eventually reach the Culebra Dolomite. Gas may also diffuse into the rock adjacent to fractures and dissolve in brine. Data to evaluate the extent of these processes do not exist, however. Therefore, while gas storage within excavated rooms and MB 139 will occur, the available volumes are not adequate, and the estimated distances required for gas transport to relieve gas pressures cannot be specified.

A special case of early-time gas flow and release of elevated gas pressures could occur. Gas may flow through temporary seals or the disturbed rock surrounding these seals before the crushed-salt seals and backfill have reconsolidated to states of low permeability. In that case, the disposal-area gas pressure would be attenuated at each temporary seal as the gas flows toward and up the shafts to the Culebra Dolomite. The seal systems would remain undisturbed and effective for long-term waste isolation. This case of gas flow is treated in some detail in Section 4.9.3.

4.10.4 Possible Resaturation Mechanisms

The cases considered in this report assume that any void space remaining within the disposal room after most of the gas has escaped gradually fills with brine. This is assumed because upward migration of gas or gas bubbles in brine will cease only when the gas becomes trapped below an impermeable barrier. Further upward migration will not occur, unless additional gas is added to enable or force circumvention of the barrier. Gas migration would also resume if the permeability of the barrier is degraded enough to reestablish flow through it.

Significant gas retention within the waste is not likely once gas generation ceases, because the waste is still relatively porous and permeable in its compacted state (Section 4.8). Brine will replace the gas as it migrates upward within the disposal room. Small bubbles of gas will remain intact, but most of the gas will collect at the upper boundary between the waste and the backfill, where upward mobility is much more difficult. Pore space at the top of the disposal room will be filled with a gradually diminishing amount of gas, and pore space at the bottom of the room will be saturated with brine. Because the roof of the repository is not likely to be completely impervious, the interface between brine-saturated and gas-filled pores will gradually move upward with time, as brine displaces gas from the room. Eventually, the repository will be saturated, the terminal condition of the disposal room assumed for Case I analyses (Chapter 6.0). If gas does remain trapped within the disposal room, brine will not be able to reach the portion of the waste within the gas bubble, and both gas generation as a result of corrosion and migration of soluble radionuclides will be reduced.

The time required for saturation of the WIPP repository is not known. Case I calculations assume that saturation is instantaneous at the end of a 2000-year gas-generation phase. This estimate is almost certainly too short and may be needlessly conservative.

4.11 Possible Engineered Modifications of Waste and Backfill

- Waste compaction is assumed in Case IIB (Chapter 7.0). As a result, Case IIB takes credit for elimination of free Castile-brine mixing within the repository (cf. Case IIA). In Case IID, credit is taken for reduction of Salado brine inflow by either grouting or compaction, and a Salado inflow of $0.1 \text{ m}^3/\text{year}$ to the borehole is assumed.
- Long-term brine elimination appears to be difficult with design-basis metallic waste. Mechanical compaction of metallic waste alone would require pressures approximately an order of magnitude greater than lithostatic pressure ($\sim 150 \text{ MPa}$ or $2.2 \times 10^4 \text{ psi}$) for significant porosity reduction. These pressures are not routinely available for large containers. Use of bitumen or grout within drums to control permeability would be labor intensive and might prove unreliable. The estimated gas potential from organic materials in the waste might make reduction of permeability of combustible waste to extremely low values impossible because of internal gas generation.
- With the design-basis waste, processes by which gas might be eliminated within the repository are also poorly defined. Backfill additives might remove CO_2 , which is expected to be the dominant gas under many conditions (Section 4.2). Reduction of the H_2 produced by anoxic corrosion also appears feasible by emplacing amounts of CuSO_4 chemically equivalent to the amount of Fe and possible other corrodible metals in waste and drums. No getters have been proposed for CH_4 , N_2 , and H_2 , however. In addition, the volumes of materials required to control CO_2 and H_2 from anoxic corrosion are expected to degrade the fluid-flow and mechanical properties of the backfill relative to either crushed salt or salt and bentonite.

- It would be possible to remove the potential gas-source term due to microbial activity by incinerating organic compounds in the waste, but this approach alone does not appear adequate to eliminate the gas, because incineration leaves the majority of metals unaltered. Therefore, the dominant potential gas source, production of hydrogen by anoxic corrosion in Mg-rich brines, would remain.

4.11.1 Disposal-Room Assumptions for Cases IIB and IID

This section describes the conditions of the disposal room assumed for the Case IIB and Case IID analyses (Table 4-9). For the Case I analyses, waste with an average initial porosity of ~0.685 was assumed to compact by room closure alone to a steady-state porosity of ~0.18. These porosities are typical of waste that was placed in drums and boxes without any precompaction. Future precompaction of waste is being considered, however, because of limited storage space at the generating sites. Cases IIB and IID reflect this trend by investigating the consequences of the precompaction process that Rocky Flats may adopt.

Other considerations for defining the state of the disposal room for Cases IIB and IID were related to human intrusion. Precompaction is a relatively simple modification that can increase the mechanical strength of the waste sufficiently to eliminate any erosion of the walls of a borehole drilled through the repository, in addition to eliminating further compaction beyond emplacement density by addition of lithostatic load.

Precompaction is assumed to decrease the permeability of the waste and eliminate mixing of brine from the brine reservoir with brine within the repository. In spite of this reduction in permeability, the waste is still expected to be permeable enough to allow gas to escape. The source of soluble radionuclides for the brines injected through the intrusion borehole would be limited, therefore, to brine flowing from the Salado Fm. through the disposal room to the borehole at a rate of 1.3 m³/yr for Case IIB. Because grout barriers around the waste would further retard this flow (Case IID), entrainment of particulates would be unlikely. Thus, the radionuclide source term in cases here that include compaction consider only addition of

Table 4-9. Disposal-Room Parameters for Cases IIB and IID

Initial Room Volume:	3640 m ³
Initial Panel Volume:	45,700 m ³
Lithostatic Pressure:*	14.8 MPa
Gas Generation:	
Gas	606 moles per drum over ~700 years from combustible waste. Gas production from corrosion processes is extremely small because of brine unavailability.
Water	The net effect of water produced or used up in the chemical reactions is zero.
Final Room Void Volume:**	0.18 porosity, with grout barriers to fluid flow
Final Room Hydraulic Conductivity:	<10 ⁻¹¹ m/s

*The best estimate of lithostatic pressure is 14.8 MPa (Section 3.2.1). When the simulations for Case II began, this value had not been selected as the best estimate, and 14.0 MPa was used in the Case II calculations.

**Case II simulations assume an accessible final-state pore volume of 228 m³, based on information available as of January 20, 1989.

contaminated Salado brine to the Castile brines. Cases that do include this modification inject variable flux into the Culebra Dolomite, but, in the absence of panel depletion, this flow has a constant radionuclide concentration, because of mixing or equilibration of brine within the repository.

Hard waste in 35-gallon drums will be compacted by the proposed Rocky Flats Compaction Facility to an average volume reduction of 2.6:1, with an average net container weight of 110 lbs (Barthel, 1989). Assuming a solid density of 1,500 kg/m³, which appears to be representative of metal waste (Butcher, 1989), the porosity corresponding to this state of compaction is 0.35. When a value of 0.35 is used to estimate the average total waste

porosity as described in Section 4.8, an average void volume of 107 m³ is calculated for the room, which corresponds to a porosity of 0.18. This value is approximately equal to the average porosity defined for the naturally compacted room contents. Some intrusion of the salt during room closure was assumed in defining the value for waste with no precompaction, because the metal waste is so porous. In contrast, the precompacted waste is dense enough that no salt intrusion is assumed.

Another, more pronounced difference exists between normal waste and waste compacted by the Rocky Flats process. During precompaction, the load applied to the waste exceeds the lithostatic stress at the repository level. After emplacement, the void volume of the precompacted waste is not likely to change, and grouting can be used to retard brine flow to the borehole. Grouting is effective because the combined compressive strength of the grout and waste is more than sufficient to support the roof of the disposal room and terminate closure. When the backfill consolidates, room closure ceases. In contrast, during compaction by closure alone, the void volume of the waste continuously decreases. Under these circumstances, grouting of the waste during emplacement is assumed here (Case IIB) to be of little benefit, because the grout between the waste drums, while rigid, is not strong enough by itself to support the roof. As entombment proceeds, the grout fails and becomes permeable, allowing brine to reach the waste.

Cases IIB and IID assume that groups of tens of drums of precompacted waste are emplaced within the rooms. Instead of stacking drums three deep within the room, there would be just one layer of precompacted waste drums, thus maintaining approximately the same areal density of radioactive material. Grout would be placed between the drums, and the groups of drums would be surrounded by barriers of grout, about half a meter in thickness. The rest of the room would be backfilled normally. Cases IIB and IID do not consider any change in room dimensions, although the height of the ceiling could be reduced. Numerically in Case IIB (Appendix E), precompaction is considered to be only partially effective in reducing hydraulic conductivity, i.e., it is assumed that it eliminates free mixing of Castile brines within the repository, but does not reduce access of the Salado brine inflow from an entire panel (1.3 m³/year) to the borehole. In Case IID, the grout is assumed

to control the permeability of the room, with a hydraulic conductivity of 1×10^{-11} m/s (Coons et al., 1987). Numerically in Case IID, precompaction and grouting are assumed to reduce Salado brine inflow to $0.1 \text{ m}^3/\text{yr}$ (Section 4.3.2).

Grout stability does not affect this entombment concept, because the long-term function of the grout is to be a dense filler or barrier around the waste. No large shear stresses will act upon it at any time to break it up, because it is surrounded by a plastic material, salt. Although its permeability may increase with time because of brine leaching, this effect will be countered by the decreasing permeability of its surroundings. In summary, the principal function of the grout is to act as a barrier to brine during the early stages of room closure, after which it becomes a dense filler material.

4.11.2 Other Engineered Modifications

Various engineered modifications are frequently suggested for reducing the consequences of adverse conditions on the WIPP repository. Most methods for improving performance are related either to minimizing interactions between brine and the waste or to controlling gases produced by bacterial decomposition, radiolysis, and chemical corrosion. Other engineered modifications of lesser importance are also being considered to facilitate waste handling and storage.

Brine flow through the waste must be minimized, because its flow provides a means for the migration of soluble radionuclides, or, in the instance of very rapid flow, the erosion of solid particles and colloids. Gas control is necessary for several reasons. First, because gas is produced internally within the waste, its escape may promote connectivity of voids and increase the permeability of the waste, making it more accessible to brine permeation. This effect, however, requires low initial waste/backfill permeability. Second, large-scale permeability enhancement must be avoided, as gas collects and escapes from the repository. The escape of repository gas (Section 4.10) is not of concern here, because the gas contains so little radioactive material (Section 4.4); however, it may provide new paths for brine inflow.

Finally, if the repository is perfectly sealed, gas pressure will become great enough to retard or locally reverse closure. Section 4.10 discusses gas generation.

The objectives of brine and gas control are contradictory. Ideally, the waste, backfill, and surroundings would be porous enough to let gas out or store it internally, but not permeable enough to let brine in. Engineered modifications that have as their objective complete isolation of the waste from brine are not realistic, however: even if no brine could get into the waste, gas would be generated, because moisture already exists within the waste, and gas-generating reactions might produce water as a by-product (Section 4.2).

4.11.2.1 Brine Control. Other engineered modifications intended to control brine focus on reducing the permeabilities of the waste. Because the permeability of the waste is directly related to its porosity, porosity must either be eliminated or filled with material that is insoluble in brine. The advantages and disadvantages of various engineered methods depend, therefore, on their ability to produce a compact mass that is significantly denser than the average porosity of 0.18 (cf. Section 4.8.1). Unfortunately, eliminating voids may have little effect upon the amount of gas generated. Brine permeation of the waste may be retarded in a denser waste, and therefore the duration of gas reactions that require water for completion may be prolonged. These factors are secondary, however, in comparison with the potential for generating large amounts of gas, which is qualitatively unchanged by compaction.

To be worth considering, methods for void-volume reduction must consolidate the waste to a much denser state than achieved by closure alone (0.18 porosity). There may be other good reasons for less drastic volume reduction of the waste before emplacement, but there is no substitute for compaction to as dense a state as possible when reduction in permeability is the objective. The average density of waste is dominated by the metal waste and cemented sludges, which are difficult to densify because of their strength. These materials are stiff and resist additional densification by the time natural closure ceases (at ~15 MPa). In view of such stiffness, the

pressure exerted during precompaction would probably have to be increased at least an order of magnitude above lithostatic pressure to reduce waste porosity much below 0.18.

The need for large compaction pressures is illustrated by porosity estimates using the Kozeny-Carman equation, a theoretical relationship commonly used in soil mechanics. This relationship states that the Darcy coefficient of permeability k is proportional to n^3 for low porosities, where n is the porosity. Thus, the Kozeny-Carman equation implies that a 50% reduction in the porosity of the waste, from 0.18 to 0.09, would be required to decrease the permeability of the waste by about a factor of 10. This is a large change in porosity at such low porosities.

To estimate what conditions might be required to achieve a porosity of 0.09, the extreme assumption is made that all metal waste is mild steel, with a nominal yield strength of 165 MPa. To collapse most of the voids in a 55-gallon drum of this material would require a force of over 10^7 lbs, or a press of 5,000 tons (4,500 tons metric) capacity. This exceeds the capacities of most presses for the compaction of low-level wastes, which are generally limited to 2,200 tons (metric). For hard waste the average compaction ratio is about 2.6:1, which corresponds roughly to a final porosity of 0.35 in metal waste (Section 4.11.1). Compaction of the waste to a product typical of the proposed Rocky Flats Compaction Facility was assumed for the Case IIB analysis of this report, not because it represents an acceptable state of compaction, but because it represents a process that waste generators are likely to use in the future to reduce initial waste volume, circumventing the need for additional on-site storage.

Although the above estimates are crude, they reinforce the conclusion that the waste must be consolidated to a much denser state than achieved by closure alone (0.18 porosity) for precompaction to be effective by itself. For this reason, pretreatment processes, such as shredding, that make smaller pieces out of larger pieces of waste, are effective in reducing the initial volume of waste, but have lesser effect upon its final state. However, components of metal waste, such as pipes, motors, and tools, that resist compaction are

usually culled before shredding to avoid damage to the equipment. Because these hard elements must be disposed of regardless, waste behavior would remain inhomogeneous.

Other processes to reduce void volume, such as grouting or bituminizing the waste, would be effective only to the extent that penetration of most voids was achieved. For grouting penetration to occur, the waste would have to be thoroughly perforated to destroy previously sealed components such as bagged material and bottles. The cost and labor-intensive nature of these preparations, which essentially amount to repackaging and additional processing of the waste, suggest that their usefulness is questionable. Bituminization adds material with the potential for generating gas, both by decomposition and radiolysis, compounding a potentially serious gas-control problem.

4.11.2.2 Gas Control. Engineered modifications to control gas within the repository are also being examined. The simplest solution is to include additives within the backfill and between drums and boxes to chemically scavenge gases. The effectiveness of this approach remains to be demonstrated, however, and getters for hydrogen, nitrogen, and methane are not available. Furthermore, unless estimates of the potential for producing gas are reduced, large volumes of getter material would be required.

Chemical Controls. The backfill additives proposed in Appendix A.1 might remove much of the microbially produced gas from WIPP disposal rooms. Backfill additives such as calcium carbonate (CaCO_3), calcium oxide (CaO), potassium hydroxide (KOH), and sodium hydroxide (NaOH) could remove most of the CO_2 , probably the most abundant microbial gas under most conditions. CaCO_3 would remove CO_2 only if brine were present. CaO , KOH , and NaOH might remove CO_2 in the absence of brine, but if brine subsequently entered the rooms its pH would increase significantly after the dissolution of these backfill additives or their CO_2 -bearing reaction products. Appendix A.1 calculates that about 87,000 kg of KOH or 62,000 kg of NaOH per room would be required to remove all of the microbially produced CO_2 . It does not calculate the required quantities of CaCO_3 or CaO , because the stoichiometry of CO_2 uptake by these compounds has not yet been defined for expected WIPP

conditions. The required quantity of any backfill additive for the removal of CO₂ depends critically on how much of the microbially produced gas is in fact CO₂, which is unknown. Furthermore, CO₂ will likely condense at partial pressures above 7.4 MPa, provided temperatures remain below 31°C. The quantities of KOH and NaOH calculated in Appendix A.1 must be revised during the next several months as data from additional laboratory studies of microbial gas production become available. Although removal of CO₂ appears to be reliable by addition of getters, getters for H₂, CH₄, and N₂, which might also be produced (Section 4.2), are not known.

It might, however, be possible to reduce the microbial gas-production rate and potential by storing cemented sludges containing nitrate (NO₃⁻) separately from waste with cellulosic materials. This might prevent denitrification, i.e., microbial N₂ production resulting from the use of NO₃⁻ as an electron acceptor (Appendices A.1 and A.3). Storage of sludges in separate rooms, however, might not preclude denitrification; NO₃⁻ is very soluble, diffuses rapidly in aqueous solutions, and could well diffuse from room to room through brine-saturated fractures in Marker Bed 139 during the 10,000-year period of interest.

Addition of manganese dioxide (MnO₂) to the backfill might prevent SO₄²⁻ reduction, the concomitant production of H₂S, the reaction of H₂S with metals or their corrosion products to form FeS₂, and the concomitant production of H₂. The use of MnO₂ as a backfill additive, however, has two potential problems. First, it must be demonstrated that there are halophilic or halotolerant bacteria that can use MnO₂ as an electron acceptor under expected WIPP conditions and that they would survive in the repository until conditions conducive to MnO₂ reduction occur or throughout the period during which MnO₂ reduction would be required. Second, MnO₂ is extremely insoluble and thus might not migrate fast enough through any brine present to prevent significant SO₄²⁻ reduction in isolated locations within the rooms. Even if it could be demonstrated that MnO₂ were effective, it would be impossible to calculate the quantity required to prevent SO₄²⁻ reduction in the absence of an estimate of the quantity of NO₃⁻ in the inventory. Microorganisms would use all available NO₃⁻ as an electron acceptor before turning to MnO₂, thus reducing the quantity of MnO₂ required to prevent SO₄²⁻ reduction.

Finally, the proposed backfill additive copper sulfate (CuSO_4), an oxidant, might corrode drums, metal boxes, and Fe-bearing constituents of the waste under anoxic conditions without producing H_2 . CuSO_4 will only be effective if brine is present; but anoxic corrosion might not occur in the absence of brine anyway. Assuming that 1 mole of CuSO_4 would be required to corrode 1 mole of Fe in metals without producing H_2 , the total quantity of CuSO_4 required per room would equal the quantity of Fe per room. Appendix A.1 calculates that there will be 3,540,000 moles of Fe per room, but this value was based on the assumption that there will be 6,750 drums/room and did not include the metal boxes or the Fe-bearing constituents of the waste. Assuming 7,000 drums/room and an Fe content of 29.2 kg per equivalent drum (see Section 4.2), there will be 3,660,000 moles of Fe per room. Furthermore, this value should be increased by an additional 50% to 5,490,000 moles of Fe per room to account for the Fe in the waste. Assuming that 5,490,000 moles/room of CuSO_4 will be required and a molecular weight of 160 g for CuSO_4 , 878,000 kg/room of CuSO_4 would be required. Finally, assuming a particle density of 3.60 g per cm^3 and a bulk density that is 60% of the particle density, the total volume of CuSO_4 required would be 244 m^3 per room, roughly 10% of the initial room porosity.

The effectiveness of the getters discussed above has yet to be determined, and, based on present gas-production estimates, their volume might represent a major portion of the backfill. For example, the volume of CuSO_4 required to scavenge the maximum potential H_2 per drum is ~40% of the initial drum volume. Substitution of CuSO_4 for backfill replaces material with the potential for becoming highly impermeable (salt) with material that is highly permeable (CuSO_4). In addition, the mechanical properties of particulate CuSO_4 and its reaction products would be more like quartz sand than crushed salt, and thus would represent a conduit for brine flow within the repository. For this reason, no credit was taken for any getter gas sorption in this report.

Physical Controls. Incineration of combustible waste could mitigate gas generation by eliminating organic decomposition. Processes such as used in the PREPP facility at Idaho National Engineering Laboratory, which shred the waste and then incinerate it, are examples of this type of approach. Incineration may be of limited effectiveness, however, because organic-

decomposition gas is less than half of the total estimated gas potential (Sections 4.2, 4.10.2). Much of the waste is metallic and will remain essentially unchanged by incineration, as will the gas potential from metal corrosion.

Engineered modifications to reduce brine flow into the waste and retard water-dependent gas reactions are also being considered, with the objective of compacting the waste to decrease its permeability. For example, the surface area available for corrosion reactions will be much less in metal waste reduced to a semi-solid billet than in loosely compacted material. Alternative schemes for isolation provide clay barriers to sorb brine before it reaches the waste. Bentonite within the backfill serves a similar function.

As discussed above, modifications that reduce brine flow are assumed effective only in the short term. With time, brine will saturate barriers, even those constructed from concrete or grout, and will eventually diffuse through them into the waste. Gas generation may be retarded by these types of modifications, but the total potential for gas generation will remain unchanged. Brine-flow retardation was the principal reason for including grout barriers in the room configuration specified for the Case IIB analyses, but stabilization of the waste within a non-leaching inert material is the only solution that would be fully effective.

Gas might be controlled by mining out additional volume within the repository to act as a gas-storage chamber. The effectiveness of this type of engineered modification is questionable, however, because the storage volumes required may be large (Section 4.10.2). If these storage areas are not leak-proof over the years, the gas will escape, and collapse of the chamber might enhance subsidence.

Another engineered modification might be the controlled filtering and release of any excess gas to the surface, in a manner similar to commercial gas production. Above-ground maintenance of the venting system would be required for times that might exceed institutional control of the site. On the other hand, it might be better to have a gas leak that can be monitored

and controlled than to have undefined leakage paths. Vents might be difficult to keep open, and they could provide paths for brine inflow. Because the vents represent paths of easy escape for the gas, they will remain open as long as gas pressure is elevated within the repository. Furthermore, the gas might dewater small regions of non-salt rocks adjacent to the vents, particularly in the Culebra Dolomite, in the same way that ventilation removes moisture from the repository.

In summary, no engineered modification represents an ideal solution to brine control, short of encapsulating the waste in an impermeable material like glass. Encapsulation by vitrification would be expensive. Getters for removing gas would not be fully satisfactory, because their large volumes and high porosity would promote brine flow within the room in the event of human intrusion. Incineration would not be fully effective, because even though it would eliminate waste decomposition as a source of gas, it does not stop corrosion reactions. Long-term ventilation would elicit strong institutional concerns. Conversely, gas produced within a sealed repository, even if leading to pressures approaching lithostatic, would not lead to a failure to isolate radionuclides from the accessible environment. No radioactive gases are produced by CH-TRU waste, except for negligibly small quantities of radon. Gas slowly disseminated outside the repository would carry no radioactive particles. Indeed, gas pressures that keep the repository "dry" for long periods of time, i.e., thousands of years, would prove beneficial to long-term containment.

5.0 EVALUATION OF PATHWAYS TO MAN

The major conclusions of Chapter 5.0 are listed below.

- Exposure and health effects from several sources are estimated in this report, including short-term effects at the well head and at a hypothetical, nearby farm, and long-term effects resulting from ground-water transport of radionuclides through the Culebra Dolomite. Effects of ground-water transport to the stock well are evaluated for ~10,000 years after decommissioning.
- Exposure at the wellhead is estimated for the most-exposed member of the drilling crew, assumed to be the geologist examining cuttings. It is assumed that coherent core is not taken through the repository horizon, because this is not normal exploratory practice.
- Erosion of the borehole during drilling is considered. Flow through the borehole, both in any free-flow phase and during continued drilling to deeper exploration targets, is estimated to erode ≤ 10 cm (3.9 in) into the waste. The direct total release of cuttings and particulate material to contaminated drilling mud is estimated to be three drum equivalents of waste. At present, this estimate is independent of waste form.
- Calculations indicate that the Culebra Dolomite is capable of accepting the estimated brine volumes from the Castile reservoir without head increases reaching the surface (Chapter 7.0). Therefore, no long-term release directly to the surface after degradation of the borehole plug is considered here.
- The dose estimates take no credit for decay of the radionuclide source term prior to human intrusion and direct release to the surface.
- Potential doses to a hypothetical farm family living 500 m (1,640 ft) downwind of the intrusion borehole result from evaporation of drilling fluid, resuspension by wind, and transport to the farm location. Doses

from several pathways are estimated, including inhalation of contaminated air and consumption of home-grown meat, milk, and above- and below-surface crops.

- A hypothetical stock-well location is chosen that is in the Culebra flowpath from the site center toward the south, ~5 km (3.1 mi) south of the waste-emplacment panels. Stock are assumed to tolerate water as saline as 10,000 mg/L TDS.
- The salinity in the stock well will increase as a result of flow of Culebra ground water toward the south, which will make a pond at the hypothetical location non-potable for stock, independent of waste emplacement in the WIPP. The modeling takes no credit for the expected increase in the salinity at the well. In addition, no credit is taken for the fact that brine injected into the Rustler as a result of human intrusion of the WIPP will likely be saturated with halite; transport of this brine to the stock may make the water non-potable for stock, independent of possible radionuclide contamination.
- In evaluating potential doses from the hypothetical stock well, it is assumed that the only potential use of Culebra brine is as a stock well. It is further assumed that a rancher eats 86 g/d (7 oz) of beef that has been contaminated by drinking only water from the contaminated stock well.

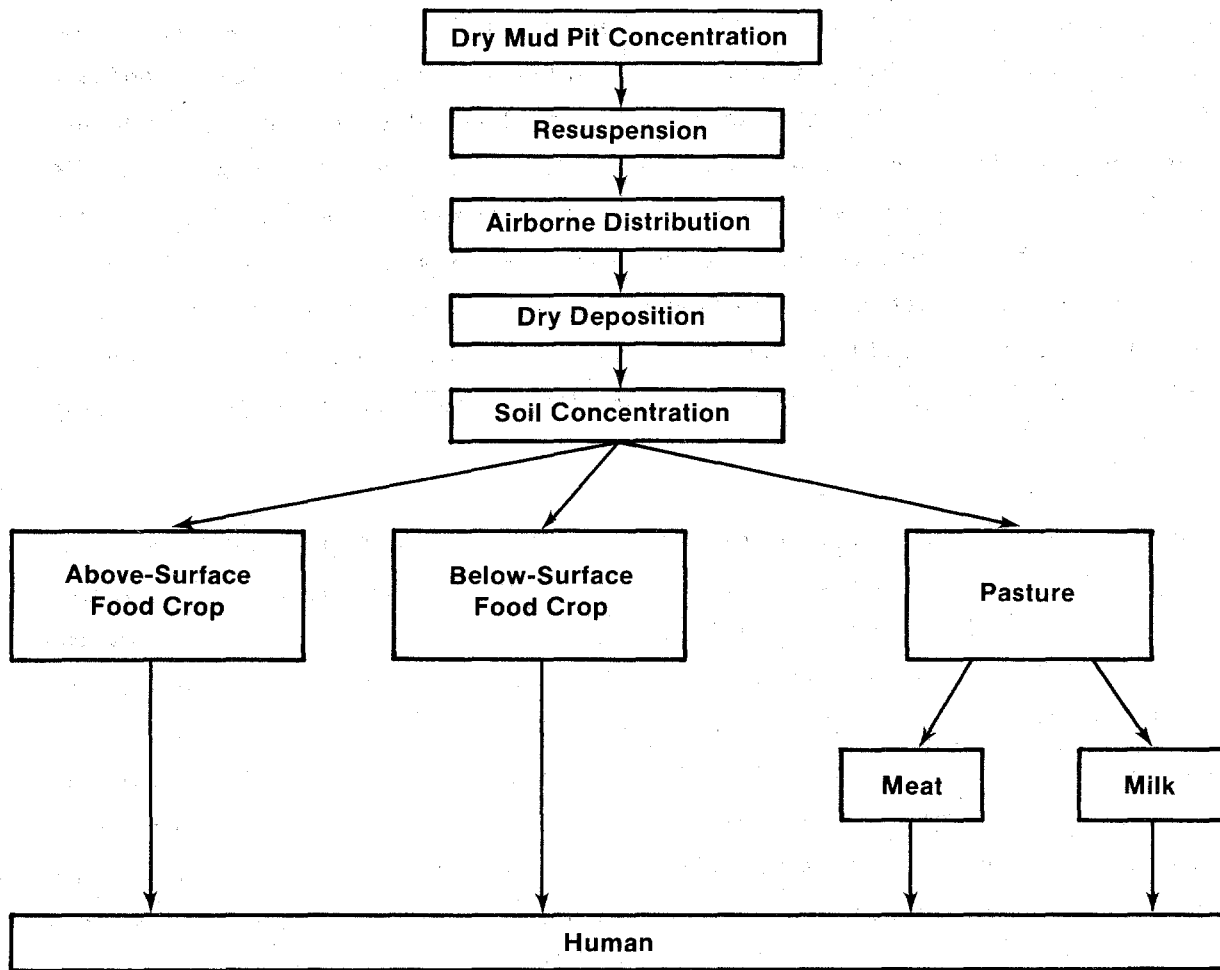
5.1 Overview

The FEIS (DOE, 1980a) analyzed the effects of release of radioactivity from WIPP by estimating the consequences of five scenarios that might transport radionuclides to the biosphere. The analyses of these scenarios examined radionuclide movement through the geosphere, discharge into the Pecos River at Malaga Bend, transport through the biosphere, and radiation doses to people. Direct releases to the surface from an intruding borehole were also considered. The human dose estimates were based on the "Report of ICRP Committee II on Permissible Dose for Internal Radiation, International Commission on Radiological Protection" (ICRP 2) (ICRP, 1959).

This report analyzes the effects of release of radioactivity from the WIPP by estimating the consequences of two hypothetical cases, described in Chapters 6.0 and 7.0. The pathways considered are shown in Figures 5-1, 6-1, and 7-1. The human dose estimates are based on the new ICRP philosophy described in ICRP 26 and 30 (ICRP, 1977, 1979). The differences in philosophy between ICRP 2 and ICRP 26 and 30 are discussed below. Past analyses with the new ICRP philosophy for internal dose assessment indicate that it is less restrictive for about 25% of the radionuclides considered, more restrictive for about 25%, and about the same for the remaining 50% (Vennart, 1981). Otherwise, this report repeats the FEIS pathways calculations with a minimum of change whenever possible. In this way, differences in dose estimates between the FEIS scenarios and the cases considered here will reflect changes in repository design and improved understanding of local geohydrology, rather than changes in biological pathway parameters.

ICRP 26 recommended a system of dose limitations that is based on three principles. The first is that no practice shall be adopted unless it produces a net positive benefit. The second is that all exposures shall be kept as low as reasonably achievable (ALARA); and the third is that the dose equivalent to an individual shall not exceed the ICRP recommended limits. The ICRP also introduced two other methods of controlling exposure. They recommend controlling exposure on an annual basis with an annual dose equivalent limit and also with a "committed dose equivalent." Committed dose equivalent is the dose equivalent received from internally deposited material integrated over a 50-year working life. It is used for calculating internal dose.

These new ICRP recommendations for internal dose are based on the principle that the risk should be equal whether the whole body is irradiated uniformly or nonuniformly. Under this system, a series of weighting factors for the most important organs has been introduced. These weighting factors are based on an evaluation of the tissues at risk and are the ratio of the risk of producing a cancer (or some other fatal result) in certain organs or tissues if they were irradiated nonuniformly compared with the risk associated with uniform irradiation of the whole body. This weighting factor is multiplied by the dose to a particular organ. The values for these organs are



TRI-6330-50-0

Figure 5-1. Generalized pathways for possible radionuclide dose and health effects.

summed and compared with the annual dose equivalent limit. If the annual dose equivalent limit has not been exceeded, then the exposure is within acceptable limits. The effective dose equivalent limit set by the DOE is 100 mrem/yr for prolonged periods of exposure.

The radionuclide chains discussed in Section 4.4 for hydrologic transport are used in the biological-pathway and dosimetric calculations.

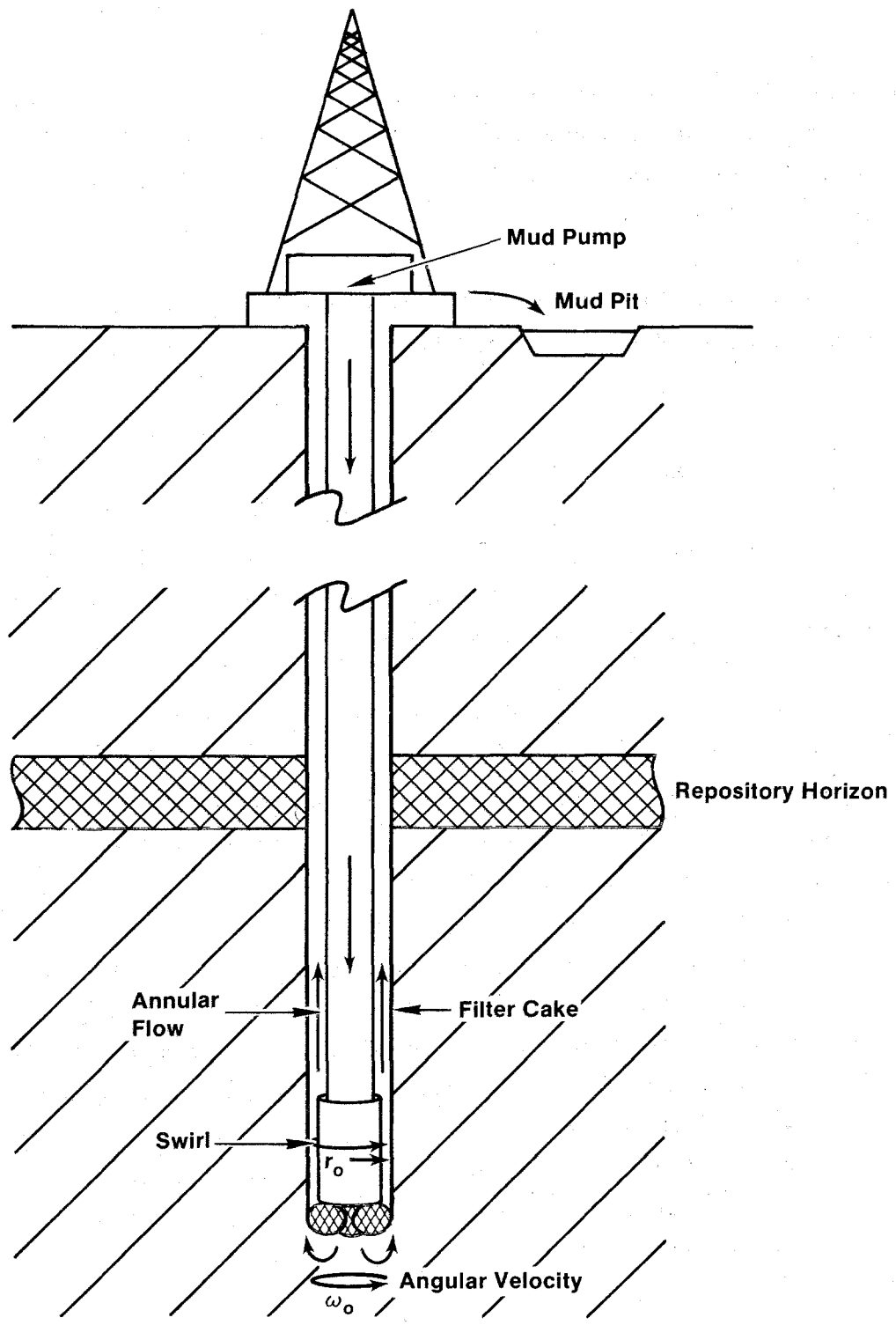
5.2 Approach to Calculating Releases (Case II)

The exposure pathways for all cases considered begin with release to the surface at the head of the intrusion well or at a stock well in the Culebra Dolomite located down gradient from the repository.

5.2.1 Removal of Cuttings to the Head of the Breaching Well

An estimate of the volume of cuttings removed from a waste panel both by the intersection of waste by the drill bit and by erosion of the borehole wall by circulating drilling mud is required to characterize the source for the exposure pathway at the surface. It is assumed here that a rotary-drilling method is used. The borehole is drilled by rotating a bit while cuttings are removed by continuously circulating drilling fluid. Drilling fluid is pumped down through the drill pipe and exits through ports in the bit. The fluid consists of suspended cuttings and a drilling mud that flows upward through the annular space between the pipe and borehole wall. Particles are eroded by the swirl of drilling fluid around the bit and collar (Figure 5-2). At the surface, the fluid circulates through a mud pit, where cuttings settle out before the mud recirculates down the borehole.

Drilling fluids are custom mixed to efficiently seal and stabilize boreholes to reduce fluid loss and prevent caving; they are composed of a liquid phase, a suspended particle or colloidal phase, and, as drilling continues, entrained cuttings. Possible additives are clays, polymers, flocculants, weighting materials, corrosion inhibitors, lubricants, bactericides, lost circulation materials, etc. It is assumed that bentonite



TRI-6330-51-0

Figure 5-2. Schematic diagram of drill string for purposes of pathway evaluation.

clay is mixed with water to form the drilling fluid. Bentonite base increases the gel strength of the drilling fluid, causing it to develop non-newtonian fluid properties with a well-defined yield point. The borehole is held open by the drilling fluid. If sloughing occurs or if formation pressure increases beyond the weight of the drilling fluid, additives are mixed with the drilling fluid to increase its weight. Normally, water in the drilling fluid is lost to the surrounding formation at the contact between the drilling fluid and the borehole wall. As water is lost to the formation, a film of particle gel is formed. This film is called filter cake. Water loss to the formation is inversely proportional to filter-cake thickness. The filter cake also reduces the erosion of the borehole wall by the upward flow of the drilling fluid.

Assumptions made in this report about the nature of the drilling operation are discussed in Appendix C. Here the following additional assumptions are made. The drilling bit diameter is 334 mm (13.15 in), the average of the diameters of oil and gas boreholes (Table C-1). The drilling mud is a 1,200 kg/m³ (10 lb/gal) bentonite mud with viscosity of 45 cP (Driscoll, 1986, p. 354). The drill stem passes through the panel with an angular velocity of 25 rpm. Swirl velocity on the rotating cylinder, $r\omega$, is about 30 cm/s (11.8 in/s). The mud pit is assumed to contain about three times the volume of the borehole itself, ~76 m³ (20,000 gal) for a borehole that is 1,200 m (4,000 ft) deep. Following the recommendations of Driscoll (1986, p. 363), the mud pit is assumed to have two parts, a settling pit and a suction pit. The settling pit contains 170 m³ (44,000 gal) with a surface area of 46 m² (500 ft²). The heavy bentonite drilling fluid is assumed to be circulated at a relatively slow rate when the bit passes through the repository horizon, so the annular velocity is also about 30 cm/s (11.8 in/s) or less.

The condition of the final consolidated state of the panel contents is discussed in Sections 4.8 and 4.11.1. The panel is gas filled when penetrated; no brine is present. The initial void fraction of the waste has decreased from 0.68 to a most probable value of 0.18, with a possible range of 0.15 to 0.21. The initial height of waste in the room has decreased to a most probable value of 107 cm (3.52 ft) with a range of 103 to 111 cm (3.39 to 3.65 ft). An intact disposal drum of 0.21 m³ (55 gal) contains 0.14 m³ (37.4 gal) of void space and 0.07 m³ (17.6 gal) of waste. If the waste is

incompressible, in the most probable case the consolidated drum still contains 0.07 m^3 (17.6 gal) of waste and has a void fraction of 0.18. A crushed drum then represents a volume of 0.081 m^3 (21.5 gal) in the panel. The range of final void fraction of 0.15 to 0.21 gives a range of 0.078 to 0.084 m^3 (20.7 to 22.3 gal) for consolidated drum volumes.

The total number of drums and boxes in the repository is assumed here to be 3.69×10^5 and 2.28×10^4 respectively. Assuming that a box is equivalent to 15 drums, the total number of equivalent waste containers in the repository is estimated in this section to be 7.11×10^5 drums. The total inventory in Table 4-3 is defined on a per-drum basis in Table 5-1. This inventory, initially contained in an average drum, is contained in a volume of 0.081 m^3 (21.5 gal) after room consolidation. The volume of cuttings, including material eroded from the borehole wall, is divided by 21.5 to estimate the number of consolidated drums removed by drilling. The inventory per drum (Table 5-1) is used to obtain the total amount of radionuclides that are removed to the surface.

Flow of a newtonian fluid between rotating concentric cylinders is a well-known problem with an analytical solution (White, 1974). If the inner and outer cylinders are defined by radii and angular velocities of (r_0, ω_0) and (r_1, ω_1) respectively and the outer cylinder does not rotate ($\omega_1 = 0$), then the solution is a superposition of a solid body rotation and a potential vortex. Further, if $(r_1 - r_0)$ is much less than r_0 , then

$$\frac{u_{\theta}}{r_0 \omega_0} = 1 - \frac{r-r_0}{r_1-r_0}$$

This equation represents linear Couette flow between parallel plates. If the ratio r_1/r_0 is less than 2, linear flow is a good approximation.

Flow over a bed can erode material by either of two mechanisms. Bulk failure may occur when the applied stress exceeds the bulk shear strength of the bed. Then the bed can fail to the depth where the applied stress equals the shear strength. Cohesive material may erode particle by particle or aggregate by aggregate. One method, similar to a viscometer, of measuring

Table 5-1. Initial CH-TRU Waste Inventory, Defined on the Basis of Drum Equivalents.

<u>Radionuclide</u>	<u>g/drum equivalent</u>	<u>Ci/drum equivalent</u> (1)
Pu-238	0.325	5.5
Pu-239	9.7	0.6
Pu-240	0.67	0.15
U-233	1.15	0.01
U-235	0.24	0.5×10^{-6}
Am-241	0.32	1.1
Np-237	0.02	1.13×10^{-5}

(1) The estimate made here is based on 7.11×10^5 drum equivalents in the repository. In Section 4.2, it is estimated that there will be 5.56×10^5 drum equivalents in the repository, based on recently available data. Assuming constant radionuclide inventory, the Ci/drum-equivalent values in this column would be increased by 28% using the smaller number of drum equivalents.

critical shear stresses for erosion uses a cylinder rotating about an inner soil core sample (Sarganum et al., 1973). The annular space is filled with the eroding fluid. Critical shear stresses for montmorillonite clay soils with various salt concentrations of interstitial fluid vary from 10 to 50 dynes/cm² (1.5×10^{-4} to 7.25×10^{-4} lb/in²). If the annular flow for this drilling operation for small $r_1 - r_0$ is linear Couette flow, an analogy to flow over a bed seems appropriate. In this case the frictional velocity u^* and viscous sublayer thickness are characterized by

$$u^* = \sqrt{\tau/\rho}$$

and

$$z_v = 12\nu/u^*$$

where τ is the shear stress, ρ is the density, and ν is the kinematic viscosity (Wimbush, 1976).

As a lower bound, if 10 dynes/cm² (1.5×10^{-4} lb/in²) for the critical shear stress for erosion is chosen, then u^* is about 3 cm/s (1.2 in/s) for a

critical velocity. This threshold velocity is low, based on previous experience for a variety of seabed clays that have threshold velocities greater than 20 cm/s (7.9 in/s) (McCave, 1983). In this case the viscous sublayer would be about 2 cm (0.79 in) thick. The consolidated panel contents are assumed to have properties characteristic of silty sands. Silty sands have a permeability of 0.1 darcy (Freeze and Cherry, 1979, p. 29). Such materials may have greater shear strength than these clays.

A finite-element simulation of brine flowing through a borehole in a panel was performed to describe the velocity profile with depth into the borehole wall (analogous to the above flow over a bed). Using a 0.1 darcy permeability for the panel contents, assuming a newtonian fluid, and scaling the overlying flow to 30 cm/s indicated that a flow of 3 cm/s could penetrate 10 cm into the bed. At this depth the applied stress equals the critical shear stress for erosion, and the bed would erode to this depth as defined above. This approach to estimating the volume of eroded material ignores the formation of the filter cake and the non-newtonian advantages of the drilling mud. It is assumed here that this depth of erosion would be independent of additional drilling.

The total volume removed using the most probable estimates is a cylinder with diameter of 53.4 cm (21.0 in), height of 107 cm (42.1 in), and volume of 0.24 m³ (63 gal) (2.9 consolidated drums). Using parameter ranges for the more-consolidated material also results in 2.9 consolidated drums being removed. The end of the ranges for the least-consolidated case also gives 2.9 consolidated drums. Therefore, an estimate of three drums removed by cuttings and erosion seems appropriate and conservative. The amount of radionuclides transported to the surface is calculated by multiplying the inventory per drum equivalent (Table 5-1) by three.

5.2.2 Radionuclide Release at the Head of the Breaching Well (Case II).

Releases at the head of the intrusion well comprise two possible parts. First, the borehole penetrates a repository panel, removing cuttings and particles eroded from the consolidated wastes by the swirl of the drilling fluid (Section 5.2.1). At this time, the panel contents are gas filled and no

brine is present. Second, assuming that the repository is not detected and the borehole abandoned, drilling continues for an assumed period of 15 hours prior to encountering brine in the Castile Fm. (Section 7.1). During this period, erosion of particles from the room contents could continue as a result of continued circulation of drilling fluid. Upon penetration of a Castile brine occurrence, pressurized brine may mix with drilling fluid and flow back through the borehole to the surface. It is assumed that about 1,000 barrels of brine-pocket fluid could mix with drilling fluid in this way and recirculate through the panel to the surface. This recirculating flow is assumed to continue for 80 hours, at which time the brine pocket and the panels are sealed. As discussed above, the filter cake protects the borehole wall from erosion and fluid loss. After the filter cake forms, very little erosion occurs. It is assumed here that continued drilling does not result in further erosion. Drillers would notice the addition of 1,000 barrels of fluid to their drill pits, but the addition of 3.79 m³ (1,000 gal) of Castile brine is small compared with the total volume of drilling fluid and would go unnoticed; this volume is also assumed to have no erosional effect.

In Section 5.2.1, it is estimated that three drums of consolidated wastes could be removed in the form of cuttings. After the drilling operation ceases and the borehole is plugged and capped, fluid flows slowly upward as a result of the pressure gradient between the brine pocket and the Culebra Dolomite. Flow and transport through the Culebra Dolomite is discussed in Section 7.3. Brine might also continue to seep directly to the surface at the head of the intrusion well, but the pressure gradient assumed in Section 7.3 would not sustain such seepage to the surface. Long-term release at the well head is not considered further in this exposure pathway. All contaminated brine is assumed to discharge into the Culebra Dolomite. Cuttings and eroded material are considered to comprise the total release to the surface at the intrusion borehole. Credit for radioactive decay is not taken here, because the time interval between closure and intrusion is uncertain, and most of the radionuclides considered are long-lived. The latter assumption produces higher-than-realistic human exposures from these hypothetical pathways.

All cuttings and particles eroded from the room contents by drilling fluid are immediately deposited into a settling pond at the well head. An external

radiation exposure may be received by the drilling crew. Only the member of the crew who receives the maximum exposure is considered. A geologist who examines cutting chips for one hour at a distance of one meter is assumed to be that individual (DOE, 1980a, p. 9-144). The geologist's dose is assessed and reported here. It was also reported in the FEIS. After drilling operations cease, radioactive material remains in the settling pond and is available for transport through airborne or surface-water pathways. Doses to a hypothetical farm family living 500 m (1,600 ft) downwind from the settling pond were assessed in the FEIS.

The pathways to a hypothetical farm family are not believed to be plausible, because it is very doubtful that a farm would ever exist at the repository location, for two reasons. First, the region is too arid for farming to rely on precipitation, and second, soils in the area are unsuitable for farming. Irrigation water is currently unavailable and likely to remain so (cf. Hunter, 1985); with enough effort and expense, water might be imported for irrigation, but it is very unlikely. Two soil types are predominant in the coverage of the WIPP site. The Berino series and the Kermit series each account for ~50% of the coverage. Both series are composed of noncalcareous sands that are especially vulnerable to wind erosion. The Kermit series is noted for a very high permeability. According to the Soil Conservation Service (1971), the Berino series is rated as a poor topsoil that would have moderate seepage for farm ponds and rapid infiltration if irrigated. The Kermit series also is rated as a poor topsoil and is considered unsuitable for farm ponds and irrigation. The Mescalero caliche underlies the soils throughout most of the site. This material is 0.9 to 1.5 m (3 to 5 ft) thick and is composed of sandy calcium carbonate. Because the calcium carbonate is the result of reprecipitation, the caliche is massive, dense, and generally impermeable to infiltration. Based on the poor quality of the soils at the WIPP site and their high permeability and vulnerability to wind erosion, the area is not suitable for farming. In the event that the soils are stripped away, either by human or natural activity, the presence of a relatively thick caliche layer also would prevent farming.

The pathways that result in doses to the hypothetical farm family begin with particle transport from the mud pit by wind or surface-water erosion.

Surface-water transport was not included in either the FEIS or current calculations, because no integrated surface-water drainage from the WIPP site exists (DOE, 1980a, p. 9-145; Hunter, 1985). The pathways considered here are the same as those that were used in the FEIS. They include inhalation of contaminated air and ingestion of foods (meat, milk, and above- and below-surface food crops) produced on the hypothetical farm (Figure 5-1).

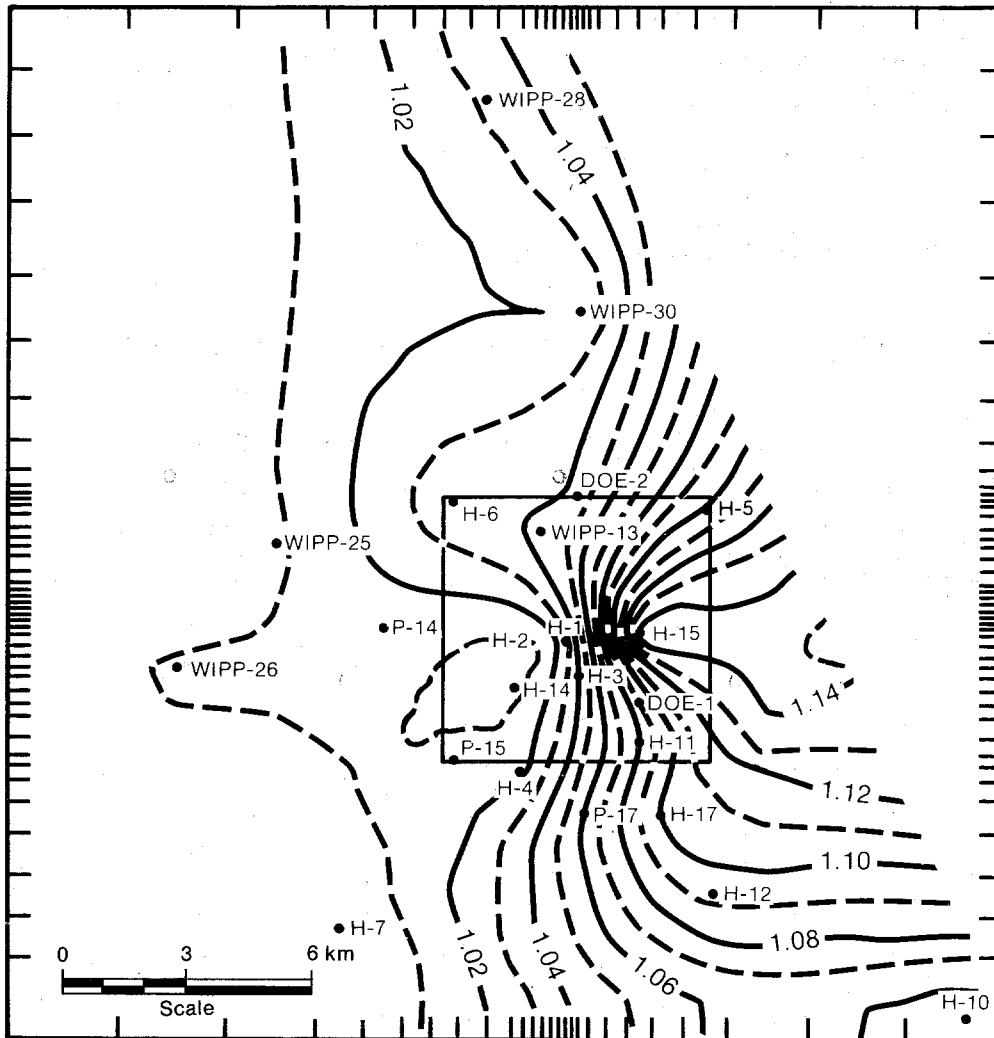
5.2.3 Radionuclide Release at a Stock Pond

Radioactive material is assumed to be carried by brine-reservoir fluids from the waste panel and to enter the Culebra Dolomite. Section 7.3 describes the sequence of events and processes that transport radionuclides to the hypothetical stock well (Section 5.3). The biological pathway begins at the head of the stock well, where beef cattle drink contaminated water. All doses to humans result from ingestion of contaminated beef. A simple food chain (stock pond to beef cattle to man) is the only pathway considered. Other ingestion pathways could exist, as discussed above, but the location selected for the stock well is arid. It is assumed that the land will only be used for range, and the contaminated-beef pathway is the only one considered.

5.3 Hypothetical Culebra Stock-Well Location

For the calculations in this report, the specified release point to the biosphere from the Culebra Dolomite is a hypothetical stock well. The location of this well is constrained by two factors. First, the well must lie on one of the principal (i.e., fastest) flow paths leaving the WIPP site. Second, the well must be located in an area where the water is sufficiently fresh (i.e., TDS < 10,000 mg/L) to support stock.

Water quality in the Culebra Dolomite along the potential flow paths leaving the site improves south of the site (Figure 5-3), although water quality is poor at P-17 (~90,000 mg/L), H-17 (~154,000 mg/L), and H-12 (~140,000 mg/L) (Table 3-12). Approximately 9 kilometers further south, water quality at H-9 (~3,000 mg/L) and Engle (~3,200 mg/L) (Table 3-12) is



TRI-6330-74-0

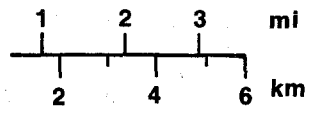
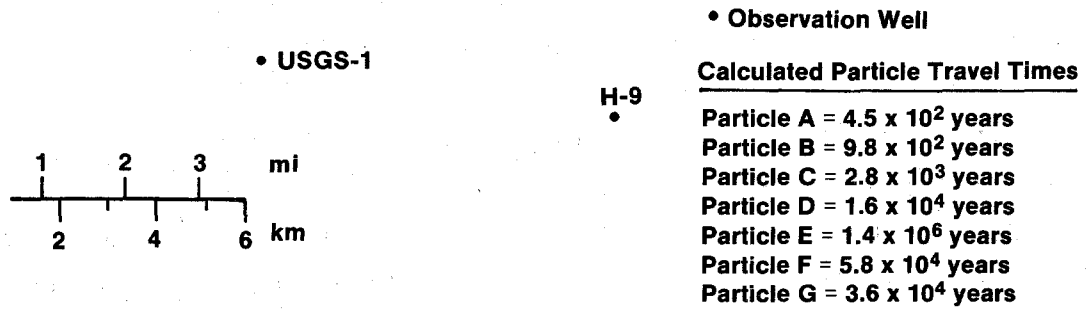
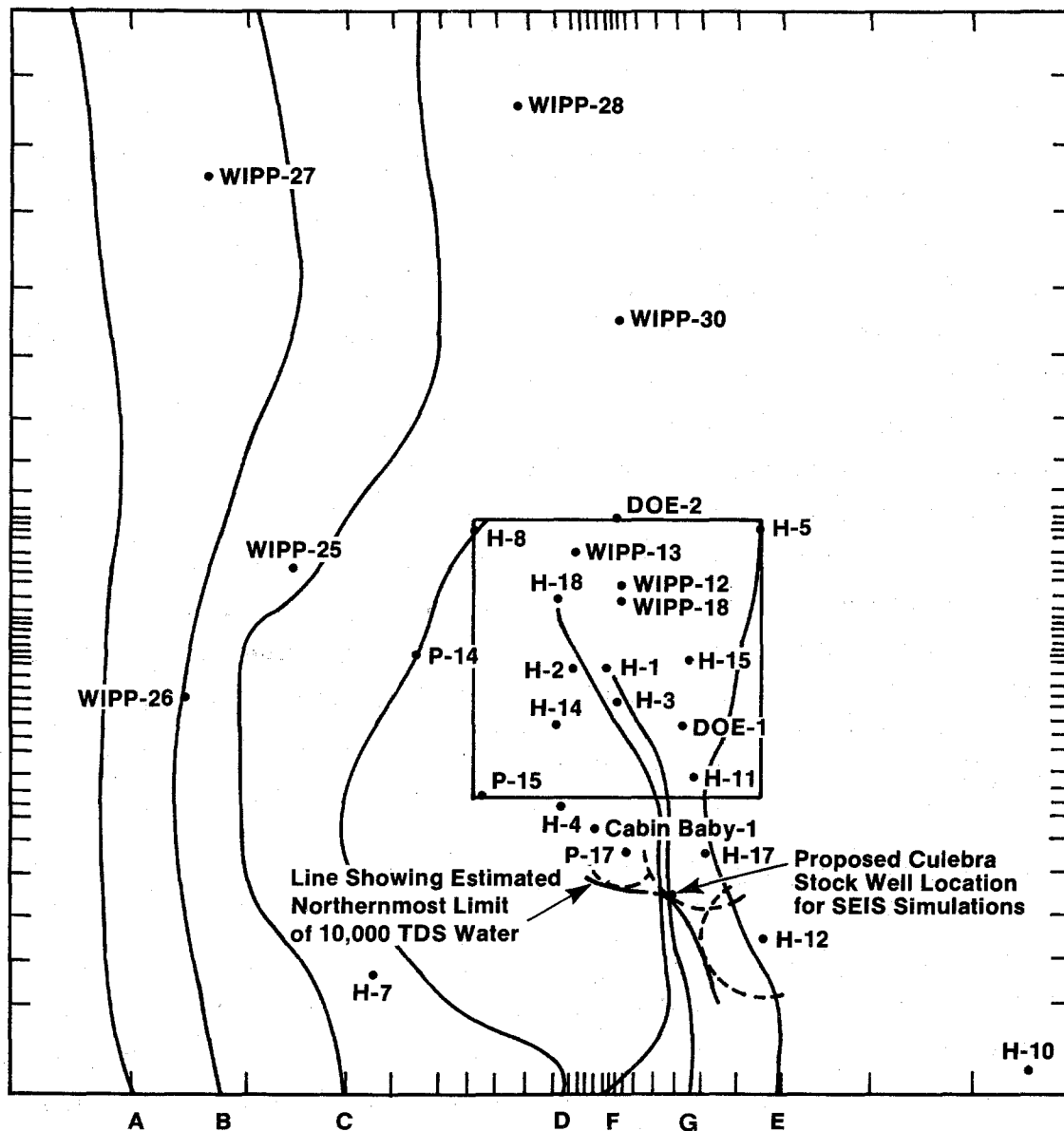
Figure 5-3. Distribution of estimated brine densities within the Culebra Dolomite (LaVenue et al., 1988).

sufficiently fresh for stock use. No data are available within the 9-kilometer stretch between P-17, H-17, and H-12 to the north and H-9 and Engle to the south. Therefore, where the actual transition to 10,000-mg/L water occurs cannot be determined directly. Because this transition must occur south of P-17, H-17, and H-12 and must occur gradually over some distance, the following procedure has been used to estimate the northernmost location at which 10,000-mg/L water could occur. The steepest water-quality gradient observed near the site, where data are sufficient to reliably determine gradients, is between H-15 (230,000 mg/L) and H-1 (30,000 mg/L) (Table 3-12). This gradient has been used to estimate the shortest distance to 10,000-TDS water from wells P-17, H-17, and H-12. The curve resulting from this extrapolation (Figure 5-4) represents the current best estimate of the northernmost possible occurrence of stock water. The intersection of this curve with the principal flow path leaving the site provides the location of the hypothetical stock well for Culebra discharge for the calculations. Determination of the principal flow path for the calculations is part of the simulation analysis discussed in Section 7.3 and Appendix E.

5.3.1 Uncertainties in Stock-Well Location

The selected stock-well location is consistent with the concept that the Culebra Dolomite contains the highest-transmissivity pathways leaving the site and with the present-day flow paths in the Culebra. This location represents a best-estimate discharge point. Uncertainties associated with selecting the discharge-well location are related to long-term TDS changes, long-term flow-path changes, and locations having marginal water quality or yield.

The solute distribution in the Culebra Dolomite is not static. Solutes will redistribute slowly as the result of ground-water flow. Because velocities in the current flow system are relatively low, solute redistribution will take place slowly. By simulating long-term transient flow and transport, Davies (1989) showed that over 1,000 years, fluid-density changes very little near the WIPP site. No information is available for a 10,000-year period. Given the presence of relatively dense, high-TDS water north of the selected stock well, the long-term water quality at this location is expected to increase slowly in TDS. This suggests that the length of the



TRI-6330-52-0

Figure 5-4. Particle travel paths and the location of the hypothetical Culebra stock well (after LaVenue et al., 1988).

travel path required to reach potable water to the south will increase with time, making the hypothetical stock-well location selected conservative with respect to long-term salinity changes.

In the Culebra Dolomite, H-2 now contains water with total dissolved solids of slightly more than 10,000 mg/L (Table 3-12), which is almost stock potable. Although this well does not lie on flow paths that currently pass over the waste panels, it is close to the waste panels. A large shift in flow directions would be necessary for H-2 to lie on a flow path that passes over the waste panels. Because the highly variable transmissivity distribution exerts a strong control on flow directions, a shift of this magnitude is unlikely under natural flow conditions. Under some extreme brine-reservoir breach conditions, however, flow paths leaving the site could be temporarily shifted to pass over H-2. If this were to occur, the H-2 location might lie on one of the near-radial flow paths emanating from the breach hole during the early high-flow period. This condition would only last until the early, high pressures in the brine reservoir were depleted. Under these conditions, most likely the H-2 location would experience an increase in total dissolved solids, making it a less likely source of stock water.

Another potential stock-well location worth considering is the H-3 well in the Magenta Dolomite, which has total dissolved solids of ~8,500 mg/L (Table 3-12). H-3 lies just south of the waste panels and, therefore, represents a very short travel path. Although H-3 could theoretically represent a stock-well location for Case II, two factors make this unlikely. First, the Magenta transmissivity at this location is only 0.1 ft²/day (Mercer, 1983), which would most likely yield only a marginal quantity of water to a well. Second, the current water quality is near the upper end of the usable range, and the Case II brine-reservoir breach would likely increase the total dissolved solids at this location dramatically.

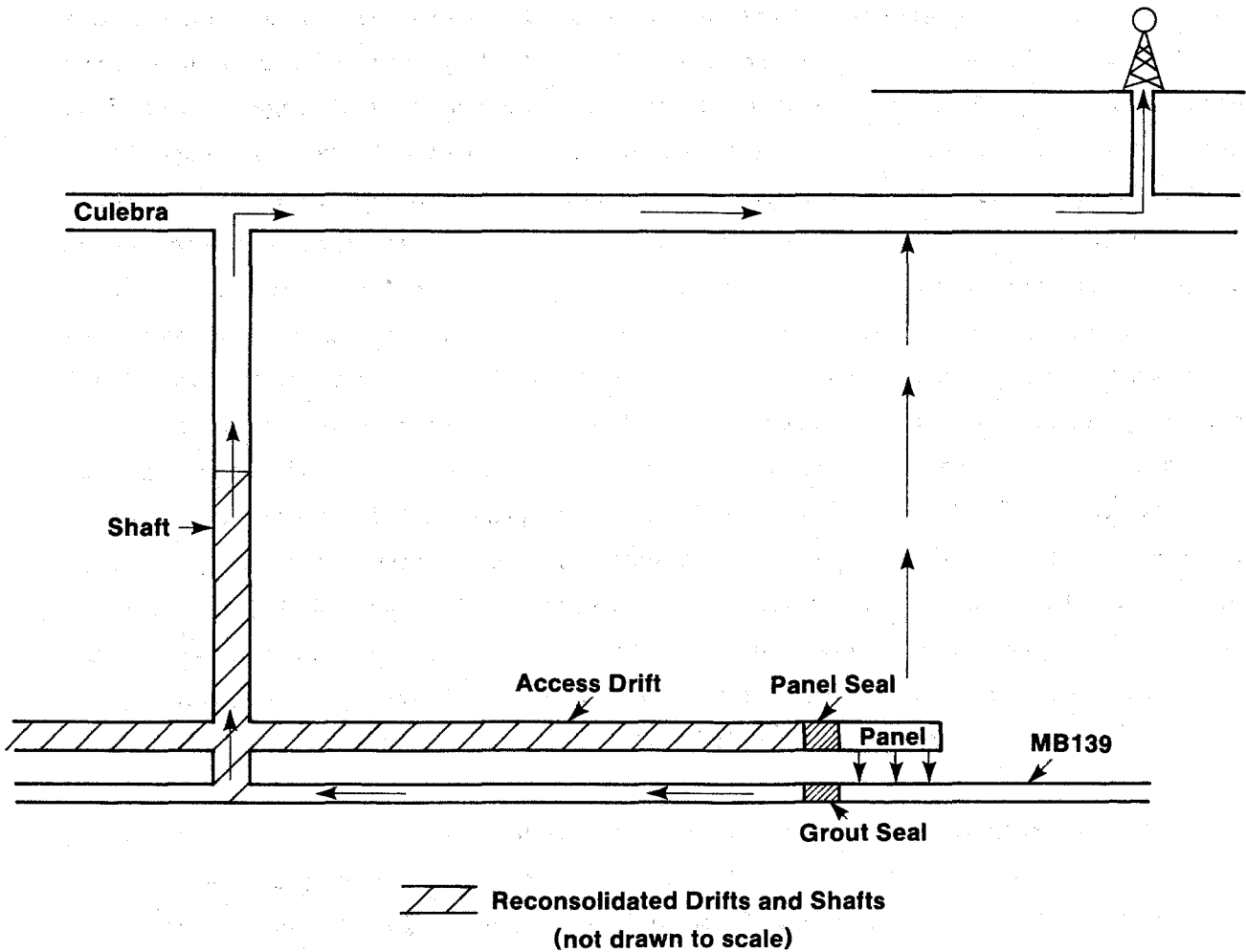
Finally, the Dewey Lake Red Beds currently provide stock water at the James (Mills) Ranch, which is closer to the site than the well in the Culebra Dolomite selected for the calculations. The Dewey Lake is a heterogeneous formation consisting of siltstone and mudstone, with lenticular interbeds of fine-grained sandstone. The Dewey Lake does not normally yield water to

wells, and the James Ranch wells are thought to be completed in one of the lenticular sandstone beds receiving their recharge from an area of thick sand dunes to the east (Mercer, 1983; Beauheim, 1986, 1988). The low permeability of the siltstones and mudstones and the discontinuous nature of the lenticular sandstones suggest that potential travel paths in the Dewey Lake would have travel times that are slower than those in the Culebra Dolomite for Case II. No sandstone lens is known to be present over the waste panels.

6.0 RADIONUCLIDE TRANSPORT IN THE ABSENCE OF HUMAN INTRUSION (CASE I)

Case I examines the performance of the repository under undisturbed conditions by analyzing the potential migration of radionuclides from the repository through engineered sealing systems (Section 4.9) and geologic media to the biosphere. For a period of 10,000 years after repository decommissioning, there are no radiation doses to humans who ingest meat from cattle that use a stock well located ~4,800 m (~15,700 ft) from the repository in the Culebra Dolomite (Section 5.3), because no radionuclides are released to the stock well. The analyzed system comprises the wastes, the engineered barriers, and the surrounding geologic media, including Marker Bed 139 (Figure 6-1). Case I is divided into two parts. Case IA simulates expected performance using representative values for all input parameters, which are generally discussed in Chapter 4.0. This simulation represents the most realistic evaluation of expected long-term repository behavior without modifications of the existing designs of engineered barriers or wastes, assuming that the repository has reached steady state after a period of relatively high gas-generation rates (Sections 4.2 and 4.10). Case IB simulates degraded performance using parameter values that assume less than expected performance. This provides a measure of performance under unfavorable and less probable conditions.

These analyses define a conceptual model of the system and use a generalized network model to calculate ground-water flow and radionuclide transport. The conceptual model forming the framework for the calculations is described in Chapters 3.0 and 4.0. The simulation of Case I is described here. The computer code used is called NEFTRAN (NETwork Flow and TRANsport; Longsine et al., 1987). This computer code simulates radionuclide transport through complex but steady-state ground-water flow fields by subdividing the flow field into a lattice of legs along which one-dimensional flow and transport are calculated. NEFTRAN is briefly described in the following section. The code, setup for simulating the system conceptual model, calculations, and input data tables are described in Appendix D.



TRI-6330-53-G

Figure 6-1.. Schematic diagram of Cases IA and IB, showing the travel paths (arrows) from the repository to the accessible environment modeled in Figure D-1.

6.1 Narrative Description of Cases IA and IB

This section describes Cases IA and IB as they are assumed to occur. At the time of repository decommissioning, the system conceptual model consists of panels filled with waste and backfill with no free water present (Sections 4.8 and 4.10). New fractures have been formed in MB 139, as a result of earlier excavation of the drifts and panels, and in response to later salt creep into these excavations prior to closure. These new fractures in MB 139 only occur directly under excavations, including the experimental area to the north of the access shafts (Figure 4-6). Seals have been emplaced in MB 139 only directly under panel and drift seals. All access drifts and the experimental area have been backfilled. Shaft seals have been emplaced. However, the system is not at steady state.

Gas generation by microbial degradation of organic material in waste containers begins prior to final repository closure and continues after closure, because it does not require free brine (Section 4.2). As rooms and drifts creep closed, waste containers rupture. Gas from microbial activity and corrosion fills the rooms and migrates through the fractured rock to MB 139 and fills the fractures under all previous excavations, regardless of other possible storage mechanisms (Section 4.10.2). Gas pressure rises to lithostatic pressure at some time later than 60 years after decommissioning, slowing brine inflow and helping to maintain open fractures in MB 139. Gas generation is assumed to continue for ~2000 years, although this time period is uncertain. As gas generation slows and gas pressures decrease below that required to prevent brine inflow, brine begins to saturate both the repository and MB 139 (Section 4.10). The interaction of closure, gas generation and dispersion, and saturation with host-rock brines is complex and depends strongly on room chemistry and waste types (Chapter 4.0).

NEFTRAN assumes that one-phase Darcy flow occurs in each leg of the network. Therefore, transport calculations for Cases IA and IB assume complete resaturation of all media along the flow paths. In the conceptual model of the system to be analyzed by NEFTRAN, the repository and MB 139 are gas filled for 2,000 years and then are instantaneously resaturated with brine. Radionuclides from the entire repository are assumed to be available

for dissolution in the brine according to the solubility limits. Transport calculations are started at 2,000 years after waste emplacement, and credit is taken for 2,000 years of radioactive decay. Because the time required for repository saturation may exceed 2,000 years (Section 4.10.4), Cases IA and IB may be very conservative.

Figures 6-1 and D-1 (p. D-3) illustrate the idealized repository system to be simulated. Based on the data in Chapter 4.0, the preferred transport path is assumed to be from the waste panels into MB 139, through the MB 139 seal, and along fractures in MB 139 to the base of the shafts. Transport continues through the lower and upper seal systems of the shaft toward the Culebra Dolomite. As discussed in Section 4.9, the lower seal system is assumed to be well consolidated, while the upper seal system is less consolidated. Flow is driven by a pressure gradient between the panels and Culebra Dolomite and eventually follows a path within the Culebra Dolomite to the stock well (Section 5.3).

Although the pathway described above is a more likely path because each leg has a higher permeability than the host rock, a flow path from the repository through the host rock directly to the Culebra Dolomite also must be considered because of the large cross-sectional area of the repository. Darcy flow may not occur in the Salado Fm. (Section 3.2.1), but such flow must be assumed in the NEFTRAN network model.

Thus the transport calculations for Cases IA and IB, using NEFTRAN, made the following assumptions.

1. The presence of pressurized gas in the rooms is ignored.
2. Before transport of radionuclides begins at 2,000 years, the repository and the transport paths are saturated with brine.
3. Brine flow along each leg is one-dimensional, steady state, and described by Darcy's Law.

4. The fracture spacing in MB 139 is sufficiently dense that the fractured medium is hydraulically similar to granular porous media, therefore the flow can be described by Darcy's Law. No diffusion into the matrix is allowed.
5. The transport path in the conceptual model is from the waste panels into MB 139, through the MB 139 seal, along fractures in MB 139, and then upward through the shaft system toward the Culebra Dolomite. The flow is driven by the hydraulic gradient between the panels and Culebra. The brine pressure is constant and lithostatic (14.8 MPa) in the panels and hydrostatic (1 MPa) in the Culebra Dolomite.
6. The volumetric flow rate is conserved throughout the flow path;
7. The travel time of a radionuclide K through n legs is given by

$$\sum_{j=1}^n \frac{L_j R_{k,j}}{v_j}$$

where $R_{k,j}$ is the retardation factor of the radionuclide k in leg j of length L_j , and $v_j = q_j/\phi_j$ is the interstitial or particle brine velocity in leg j, with q_j and ϕ_j being the Darcy velocity and porosity respectively of leg j. Dispersion and diffusion effects are neglected.

8. Sorption processes are adequately represented by the distribution-coefficient approach in deriving the retardation factors of radionuclides. No sorption is used in the MB 139 seal, and surface sorption values (K_a) are used in the MB 139 fractures (Table D-5). The use and numerical form of retardation factors is briefly discussed in Section 3.3.4.
9. The entire CH-waste inventory is available to be dissolved in the brine. Solubility (10^{-6} M for Case IA and 10^{-4} M for Case IB) controls the

release of all radionuclides. Leach rates and diffusion rates within the waste and backfill are ignored.

10. In Case IA, all the seal systems are in their expected conditions, but Case IB represents degraded performance of the MB 139 seal and the lower seal system. A two-order-of-magnitude increase of the permeabilities of the MB 139 and lower seals from expected conditions is used in Case IB.

6.2 Results of NEFTRAN Calculations

Case IA calculations using representative conditions and properties (Table D-2) estimate first arrival times (defined as the time when the discharge rate of a radionuclide reaches 10^{-18} Ci/day) for the least retarded radionuclides (U, Np, Pb, and Ra; Table D-4) at the top of the Culebra Dolomite in the shaft (Node 6, Figure D-1) to be 2,800,000 years, at the middle of the shaft at the top of the reconsolidated salt (Node 5) to be 900,000 years, and at the bottom of the shaft (Node 4) to be 500,000 years. Because this system's model is linear, the least retarded radionuclide is estimated to have travelled less than ten meters beyond the seal in MB 139 (Node 3) in 10,000 years. Case IB calculations using degraded conditions in the MB 139 seal and lower shaft-seal system (between Nodes 4 and 5) (Table D-3) estimate arrival times for the same least-retarded radionuclide at the top of the shaft in the Culebra Dolomite to be 25,000 years and at the middle of the shaft at the top of the reconsolidated salt to be 8,000 years. The least retarded radionuclide is estimated to have travelled less than 20 m (65.6 ft) above the top of the lower shaft seal (Node 5) in 10,000 years. Thus, assuming that drift and shaft permeabilities after repository saturation are within two orders of magnitude of design-basis values, there should be no release to the Culebra Dolomite or above the top of the Salado Fm. within 10,000 years.

Calculations for transport, applicable to both Case IA and Case IB, were also performed for the path through the host rock (along Leg 7, Figure D-1), assuming a cross-sectional area of 8030 m² for this leg (Table D-2). The arrival time for the least retarded radionuclide at the Culebra Dolomite (Node

7) is estimated to be 400,000 years. The least retarded radionuclide traveled about 10 m (32.9 ft) from the repository in 10,000 years. The travel time through the host rock is much shorter than that calculated for Case IA as a direct result of Darcy's Law and the extremely low effective porosity (0.001) of the Salado Fm. The validity of using Darcy's Law in such a low-permeability medium is questionable (Section 3.2.1).

In summary, based on these calculations for representative conditions and degraded conditions, there are no releases of radionuclides to the Culebra Dolomite in Case I, and therefore, no releases to either the surface or the hypothetical stock well in 10,000 years. Because radionuclides are not available for transport through exposure pathways to humans, dose calculations are not warranted in either Case IA or IB. Specific assumptions made in these calculations are summarized in Section 6.1; the calculational approach and input data are summarized in Appendix D.

7.0 RADIONUCLIDE TRANSPORT AFTER HUMAN INTRUSION INVOLVING A CASTILE BRINE RESERVOIR (CASE II)

7.1 Narrative Description of Case II

Case II examines a potentially high-impact, human-intrusion breach of the WIPP repository (Figure 7-1). In Case II, a hydrocarbon-exploration borehole penetrates both the repository and an underlying occurrence of pressurized brine in the Castile Fm. During the initial breach, contaminants are carried to the ground surface in the form of cuttings and contaminated drilling mud (Section 7.2). The borehole is assumed to be plugged, either after drilling or when abandoned. Following plug degradation, pressurized brine in the Castile Fm. provides the primary driving force for moving contaminated fluids up the borehole and into the Culebra Dolomite, where the contamination is carried by the regional ground-water-flow system to a stock well (Section 7.3). Release to the biosphere occurs as the result of the consumption of contaminated water by stock animals. A simulation time of 10,000 years (following the beginning of degradation of the borehole-plug permeability 75 years after emplacement) has been examined for each radionuclide decay chain and for stable lead.

Four versions of Case II have been examined (Table 1-2). Case IIA incorporates representative flow and transport properties for geosphere transport coupled with the design-basis waste form and backfill. Case IIB incorporates degraded geosphere-transport properties, increased radionuclide solubility, and compaction of the waste prior to emplacement that eliminates Castile brine flow through the repository. Case IIC is similar to Case IIB, except that Case IIC assumes that waste is not precompacted and that Castile brine therefore flows through the repository. Case IID incorporates degraded geosphere-transport properties, representative values for radionuclide solubility (same as Case IIA values), and generic engineered modifications of the waste and backfill that eliminate Castile brine flow through the repository and reduce Salado brine-inflow rates to the penetrating borehole.

Detailed background information and parameter values pertinent to Case II are contained in the following sections: Section 3.4 and Appendix E, Castile

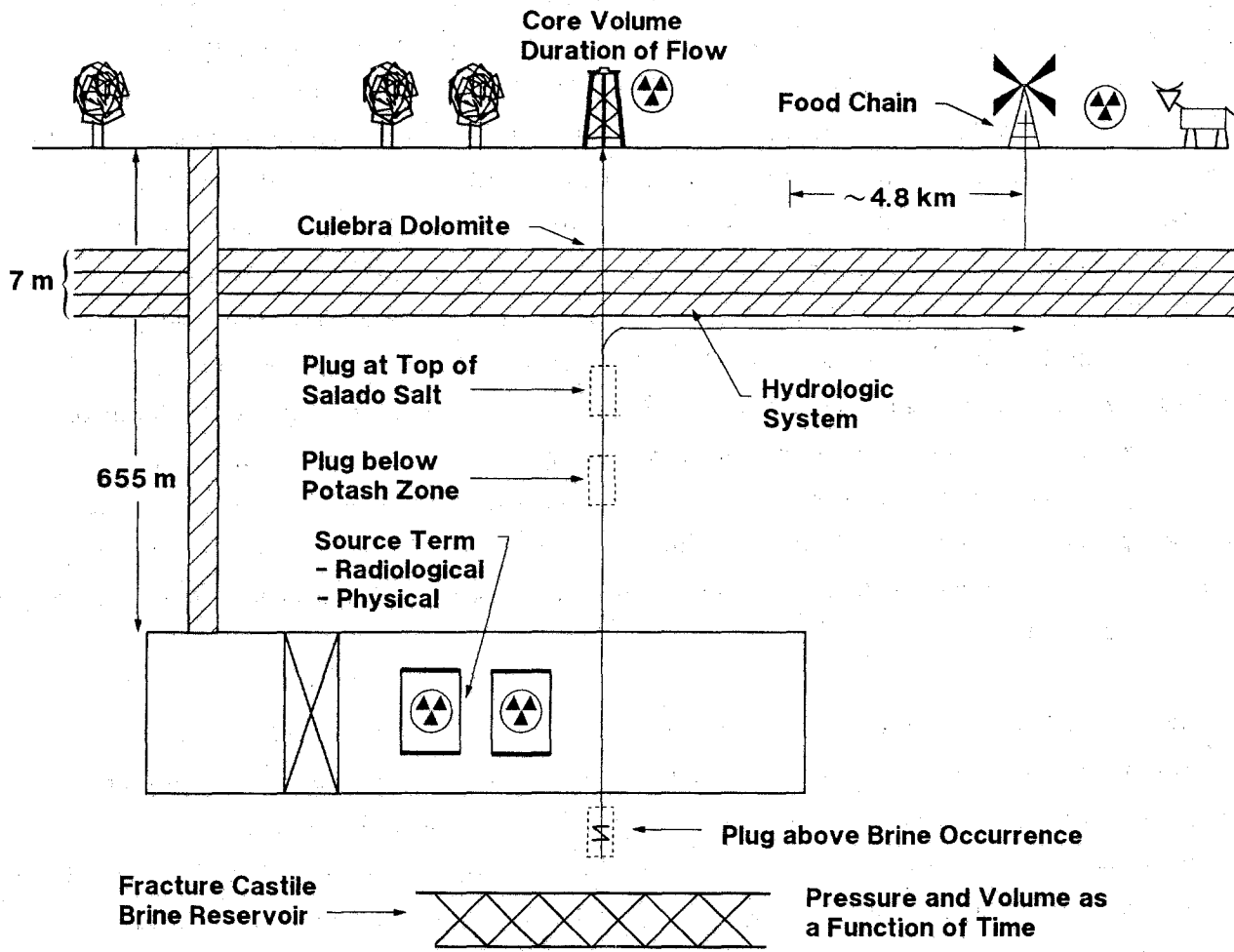


Figure 7-1. Schematic diagram illustrating the principal components of Case II.

brine-reservoir characteristics; Chapter 4.0, repository state at the time of breach; Appendix C, hydrocarbon borehole characteristics; Section 3.3 and Appendix E, Culebra flow and transport system; and Section 5.3, stock-well location. The sequence of events assumed for Case II is summarized below.

A hydrocarbon-exploration well penetrates the repository. At the time of penetration, the repository is unsaturated, with most of the available pore space filled with gas at lithostatic pressure. Because pressurized pockets of brine or gas are occasionally encountered in the Delaware Basin, the driller is assumed to control any pressure increase by increasing mud weight and to continue drilling.

Approximately 15 hours are spent drilling from the level of the repository to the top of the Castile Fm. During this time, some waste is incorporated into the circulating drilling mud and carried to the surface. In the upper Castile Fm., pressurized brine is encountered. As in the earlier encounter with the repository, the driller is expected to control any pressure increase associated with the brine by effective use of a blowout preventer (BOP) or by further increasing mud weight and then to continue drilling. The brine occurrence might be "squeeze grouted" to facilitate continued drilling.

Approximately 80 hours are spent drilling from the upper Castile Fm. to the Bell Canyon Fm. During this time, up to 1000 barrels of Castile brine are also released to the hole by slow leakage. If the hole encounters no hydrocarbon (i.e., a "dry hole") upon reaching the Bell Canyon Fm. or deeper units, it is assumed to be plugged following standard industry practices for the Delaware Basin (Appendix C). This plugging would consist of 60-m cement plugs located at and directly above the Castile brine occurrence; below the McNutt Potash zone (Salado Fm.), and at the top of salt in the Salado Fm. If the hole does encounter hydrocarbons, then a string of production casing would be placed in the hole. Case II further assumes that the production casing in the hole would be removed at the end of production, after which the procedure would be the same as that assumed for a dry hole.

After 75 years, the plugs begin to deteriorate, and the borehole reaches a fully degraded, rubble-filled state at 150 years (Appendix C). As the plugs

deteriorate, pressurized brine flows up the borehole. Because the borehole is also connected to the Bell Canyon Fm., which has hydraulic heads that are low relative to the pressurized Castile brine occurrence, some Castile brine will also flow down the borehole. The Bell Canyon has a limited capacity to accept fluids, however (Section 3.5), and the quantity of downward flow will be small. The calculations in this report assume that downward flow into the Bell Canyon is negligible.

Case II examines four possible releases of contaminants to the Culebra Dolomite (Table 1-2). All variants of Case II are conservative, in that they assume the repository is brine-saturated when the borehole plug begins to degrade. The following four paragraphs contain narrative descriptions of these variations.

In Case IIA, all Castile brine is assumed to mix within the breached waste panel, dissolving waste up to a solubility limit of 1×10^{-6} molar for radionuclide constituents and 116 mg/L for stable lead. Brine seepage from the Salado Fm. provides a second, smaller source of waste-dissolving fluid. All contaminated fluid flows up the borehole, discharging into the Culebra Dolomite.

In Case IIB, precompaction of waste is assumed to eliminate circulation of Castile brine through the waste. Therefore, the only source of waste-dissolving fluid is brine from the Salado Fm., which dissolves waste up to the specified solubility limits or until all mass for a given waste constituent is dissolved. The specified solubility limits for Case IIB are 1×10^{-4} molar (mass fraction of $\sim 2.4 \times 10^{-5}$ kg/kg) for radionuclide constituents and 116 mg/L (1.16×10^{-4} kg/kg) for stable lead. The sole role of Castile brine in Case IIB is to dilute contaminated brine from the Salado Fm. and transport it up the borehole to the Culebra Dolomite.

In Case IIC, all Castile brine is assumed to mix in the breached waste panel, dissolving waste up to the specified solubility limits or until all mass for a given waste constituent is dissolved. The specified solubility limits for Case IIC are 1×10^{-4} molar for radionuclide constituents and 116 mg/L for stable lead. As in Case IIA, brine inflow from the Salado Fm.

provides a smaller source of waste-dissolving fluid than does flow from the brine reservoir. Contaminated fluid flows up the borehole, discharging into the Culebra Dolomite.

Case IID incorporates generic engineered modifications that are assumed to eliminate mixing of Castile brine in the waste (similar to Case IIB) and to reduce Salado brine-inflow rates to the intrusion borehole by approximately one order of magnitude, from 1.3 m³/year to 0.1 m³/year (Section 4.3). The specified solubility limits for Case IID are the same as the values specified for Case IIA, 1 x 10⁻⁶ molar for radionuclides and 116 mg/L for stable lead. As in the previous cases, contaminated fluid flows up the borehole, discharging into the Culebra Dolomite.

Contaminants released to the Culebra Dolomite are carried southward by the regional ground-water-flow system. In Case IIA, representative values (Section 1.1 and Tables E-6 and E-10 through E-12) for Culebra transport properties have been used. In Cases IIB, IIC, and IID, degraded values for Culebra transport properties have been used, resulting in shorter transport times (Section 7.3). If contaminants reach the stock well within 10,000 years, water consumption by stock animals releases them to the biosphere.

7.2 Releases From the Head of an Intrusion Well (Case II)

These simplified calculations were made primarily with NRC transfer-factor data (Till and Meyer, 1983), DOE committed-dose-equivalent data (DOE, 1988a), data used in the FEIS, Appendix K, and some new data from other sources when required.

7.2.1 Release to the Surface in the Form of Cuttings and Drilling Mud

It has been estimated that the contents of three waste drums could be removed to the surface during drilling. The total inventory discharged to the surface is obtained by multiplying the waste inventory per drum-equivalent (Table 5-1, Section 5.2.1) by three (Table 7-1).

Table 7-1. Inventory Discharged to the Settling Pit (Cases IIA and IIB)

<u>Nuclide</u>	<u>g/3 drums</u>	<u>Ci/3 drums</u>
Pu-238	0.975	16.5
Pu-239	29.1	1.8
Pu-240	2.0	0.45
U-233	3.45	0.03
U-235	0.72	1.5×10^{-6}
Am-241	0.96	3.3
Np-237	0.06	3.39×10^{-5}

7.2.2 External Dose Received by Drill-Crew Member

The approach used in the FEIS (DOE, 1980a, p. 9-144) was used to calculate the highest individual external dose received by a drill-crew member. This maximum-dosage individual is assumed to be a geologist who examines chip samples from a distance of one meter for one hour. As in the FEIS, the chip samples are treated as point sources with no self-shielding effects.

This calculation approximates the exposure rate from any gamma-ray point source. Data are taken from the Radiological Health Handbook (U.S. Public Health Service, 1970). The exposure rate per mCi at a one-meter distance from the source, Ex, is given by

$$Ex = (0.5)(n)(E)(C)$$

where

- E = gamma-ray energy (MeV),
- n = gamma-quanta/disintegration, and
- C = mCi/chip.

Ex has units of mR/hr. The geologist is assumed to examine chips for one hour. The assumed drill-bit diameter is 334 mm (Section 5.2.1), and the

estimated depth of eroded material from the borehole wall is 10 cm. The maximum-radius spherical chip that could be removed from the waste and transported by annular flow to the surface is assumed to be 5 cm, with a volume of 524 cm³. The probable values of the parameter ranges for consolidated room conditions imply that a single consolidated drum occupies a volume of 0.081 m³ with a range of 0.078 to 0.084 m³ (Section 5.2.1). Dividing 0.081 m³ by the volume of a chip results in 155 chips/drum, and the radioactivity in a single chip is obtained by dividing the inventory per drum by 155. The geologist receives a dose from the chips of 0.08 mR/hour per chip (Table 7-2).

The exposure rate from natural background radiation is 0.01 mR/hr (100 mrem/yr). The exposure rate from the chips to the geologist is eight times the background exposure rate, but the exposure only lasts for one hour. Therefore, the incremental dose is only 0.08 mR/yr. One mR/hr is approximately 1 mrem/hr if the quality factor is 1 for gamma rays.

7.2.3 Doses Received by a Hypothetical Farm Family Through Indirect Pathways

The inventory in three drums of consolidated waste is estimated to circulate to the surface during drilling. The settling pit is assumed to be 4.3 m wide, 11 m long, and 3.7 m deep, containing 170 m³ and having a surface area of 46 m² (Driscoll, 1988). A second pit, the suction pit, is downstream of the settling pit. The combined volume of these two pits is about three times the volume of the borehole (Section 5.2.1). All waste materials are assumed to settle out in the settling pit. The surface area of the settling pit is assumed to be the same after evaporation and during later wind erosion. Half the volume in the settling pit is assumed to be water, which evaporates. The inventory is assumed to be mixed in 83 m³ of remaining solid material. The drilling-fluid density is 1.2 g/cm³, or 1.4 g/cm³ dry. Concentrations of radionuclides in the dry mud are given in Table 7-3.

A procedure for a squared Gaussian plume model (DOE, 1980a, Appendix K, p. K-25) has been used to calculate the downwind surface air concentration 500 m from the mud pit (the hypothetical farm site) and the dry-deposition flux (Table 7-4).

Table 7-2. Maximum Dose Received by a Member of the Drilling Crew (Case II)

<u>Nuclide</u>	<u>mCi/chip</u>	<u>E (MeV)</u>	<u>n (gam-q/dis)</u>	<u>Ex (mR/hr-chip)</u>
Pu-238	35.0	0.099	8.0×10^{-5}	1.4×10^{-4}
Pu-239	4.0	0.0		
Pu-240	1.0	0.65	2.0×10^{-7}	6.5×10^{-8}
U-233	0.06	0.029	1.7×10^{-4}	1.5×10^{-7}
U-235	3.2×10^{-6}	0.143	0.11	
		0.185	0.54	
		0.204	0.05	3.0×10^{-7}
Am-241	7.1	0.06	0.36	0.077
Np-237	7.3×10^{-5}	0.0		
	Total			0.08 mR/hr-chip

Table 7-3. Radionuclide Concentrations in the Dry Mud Pit (Case II)

<u>Nuclide</u>	<u>Ci / g</u>
Am-241	2.83×10^{-8}
Np-237	2.91×10^{-13}
Pu-238	1.42×10^{-7}
Pu-239	1.54×10^{-8}
Pu-240	3.86×10^{-9}
U-233	2.57×10^{-10}
U-235	1.29×10^{-14}

The calculation assumes a resuspension rate of 1.0×10^{-13} times $U^3/U_0^3/s$, where $U_0 = 1.0$ m/s, and $U = 3.7$ m/s (7.6 mi/hr); density of dry drilling mud of 1.4 g/cm³; mud pit surface area of 46 m²; depth available for resuspension of 1.0 cm; deposition velocity of 0.01 m/s; and particle size of 1.0 micron. An area source is approximated by choosing a vertical standard deviation and lateral width of the assumed Gaussian distribution and identifying a virtual point source 20.6 meters upwind of the leeward side of the pit, i.e., a

downwind transport distance of 521 m. Reproducing the table on p. K-26 of the FEIS for downwind surface level concentration in the air at 500 m gives

$$X_i = (0.91 \times 10^{-10}) \Omega_i$$

where the Ω_i are the above concentrations of radionuclides in the dry mud pit (Table 7-3) and the X_i (Table 7-4) have units of Ci/m³.

Following the assumptions used in the FEIS (BDM Corporation, 1978), the plow depth at the hypothetical farm is 20 cm, density of soil is 1.4 g/cm³, and the transfer coefficient to the underlying soil sink is 1.1 x 10⁻⁴ d⁻¹. Let P(t) be the concentration (Ci/kg-soil) of radionuclides in a well-mixed (by the plow) soil layer, 20 cm thick. Then the time rate of change of P is equal to the dry deposition flux onto the soil surface minus the infiltration flux through the bottom of the 20-cm layer. Calculating the steady-state concentrations at 100 years gives values (within 2% of steady state) listed in Table 7-5.

Table 7-4. Air Concentration (Ci/m³) and Deposition Flux Values (Case II)

<u>Nuclide</u>	<u>Ci/m³</u>	<u>Ci/m²-s</u>	<u>Ci/m²-yr</u>
Am-241	3.07 x 10 ⁻¹⁸	3.07 x 10 ⁻²⁰	9.70 x 10 ⁻¹³
Np-237	3.16 x 10 ⁻²³	3.16 x 10 ⁻²⁵	9.96 x 10 ⁻¹⁸
Pu-238	1.54 x 10 ⁻¹⁷	1.54 x 10 ⁻¹⁹	4.85 x 10 ⁻¹²
Pu-239	1.68 x 10 ⁻¹⁸	1.68 x 10 ⁻²⁰	5.29 x 10 ⁻¹³
Pu-240	4.19 x 10 ⁻¹⁹	4.19 x 10 ⁻²¹	1.32 x 10 ⁻¹³
U-233	2.79 x 10 ⁻²⁰	2.79 x 10 ⁻²²	8.82 x 10 ⁻¹⁵
U-235	1.40 x 10 ⁻²⁴	1.40 x 10 ⁻²⁶	4.41 x 10 ⁻¹⁹

Table 7-5. Soil Radionuclide Concentrations (Case II)

<u>Nuclide</u>	<u>Ci/kg-soil</u>
Am-241	9.48 x 10 ⁻¹⁸
Np-237	9.74 x 10 ⁻²³
Pu-238	4.74 x 10 ⁻¹⁷
Pu-239	5.17 x 10 ⁻¹⁸
Pu-240	1.29 x 10 ⁻¹⁸
U-233	8.62 x 10 ⁻²⁰
U-235	4.31 x 10 ⁻²⁴

Transfer factors used in the dose calculations are given in Table 7-6. Data on human food consumption per capita are required for the four pathways. Consumptions in the United States (Till and Meyer, 1983, Table 6.8) are 508 g/d for milk, 86 g/d (National Council on Radiation Protection and Measurements [NCRP], 1984) for beef products, 103 g/d for below-surface crops, and 202 g/d for above-surface crops. Cattle consume 15 kg of fresh, local forage per day per head (Till and Meyer, 1983, p. 585).

Past studies have used various computer codes to tabulate the committed dose equivalent for various body organs per unit activity inhaled or ingested. The organs included in these tabulations are explicitly considered by the ICRP to be at risk. The committed dose equivalent represents the total dose equivalent that an organ or tissue of the body is expected to receive over the 50-year period following exposure. Tabulations in these previous studies have been used to calculate doses in this study.

For most applications, a more rigorous evaluation would require information on the time variation in the dose equivalent rates for the various tissues at risk. With such information, the time dependence of environmental conditions and, therefore, of the intake (rather than simply the total intake), could be assessed by considering the years of remaining life, as derived from the age distribution of the exposed population. However, such

Table 7-6. Soil-to-Plant and Forage-to-Food Product Transfer Factors
(Case II) (Till and Meyer, 1983, Tables 5.16, 5.18, 5.36, 5.37)

<u>Nuclide</u>	<u>Soil-to-Plant</u> (kg-soil/kg-plant)	<u>Forage-to-Food Product</u> (d/kg-food or d/kg-milk)
Beef:		
Am-241	4.2×10^{-2}	3.6×10^{-6}
Np-237	9.2×10^{-2}	5.0×10^{-6}
Pu-238	1.4×10^{-2}	1.0×10^{-6}
Pu-239	1.4×10^{-2}	1.0×10^{-6}
Pu-240	1.4×10^{-2}	1.0×10^{-6}
U-233	1.7×10^{-2}	3.4×10^{-4}
U-235	1.7×10^{-2}	3.4×10^{-4}
Milk:		
Am-241	4.2×10^{-2}	2.0×10^{-5}
Np-237	9.2×10^{-2}	5.0×10^{-6}
Pu-238	1.4×10^{-2}	2.7×10^{-9}
Pu-239	1.4×10^{-2}	2.7×10^{-9}
Pu-240	1.4×10^{-2}	2.7×10^{-9}
U-233	1.7×10^{-2}	6.1×10^{-4}
U-235	1.7×10^{-2}	6.1×10^{-4}
Dried edible below surface crops (1,3)		
Am-241	6.4×10^{-5}	
Np-237	---	
Pu-238	1.4×10^{-3}	
Pu-239	1.4×10^{-3}	
Pu-240	1.4×10^{-3}	
U-233	9.0×10^{-4}	
U-235	9.0×10^{-4}	
Dried edible above surface crops (2,3)		
Am-241	2.8×10^{-5}	
Np-237	1.5×10^{-2}	
Pu-238	1.7×10^{-4}	
Pu-239	1.7×10^{-4}	
Pu-240	1.7×10^{-4}	
U-233	1.0×10^{-3}	
U-235	1.0×10^{-3}	

Notes: 1. These data are divided by 10 for a dry-to-wet conversion, Table 5.16.

2. These data are divided by 4.5 for a dry-to-wet conversion, Table 5.16.

3. Transfer factors were selected assuming that vegetables would be washed before eaten.

information is not now available for many radionuclides. Overestimates of the risk by factors of two to three may result from failure to consider the time-dependent nature of the organ dose equivalent rates and the years of life remaining.

In these calculations, doses to other tissues in the body are at least one order of magnitude lower than the doses to the bone from radiation taken up through ingestion or inhalation (Table 7-7). The sum of 0.77 mrem calculated for a person living on the hypothetical farm is the 50-year committed dose equivalent (Table 7-8). The estimated dose from ingestion of contaminated food products is only 4.9×10^{-10} mrem.

7.3 Post-Plugging Release to Culebra Dolomite and Resulting Doses

7.3.1 Fluid Release to the Culebra Dolomite for Cases IIA, IIB, IIC, and IID

Figure 7-2 presents the contrast in flow rates to the Culebra Dolomite for Cases IIA, IIB, IIC, and IID. In Cases IIB and IIC, the flow rates into the Culebra Dolomite are the same, because the borehole permeabilities and Salado brine-inflow rate, $1.3 \text{ m}^3/\text{yr}$, are the same. In Case IID, the flow rate into the Culebra Dolomite is slightly lower, because the Salado brine-inflow rate is smaller, $0.1 \text{ m}^3/\text{yr}$. These flow rates are strongly influenced by the permeability of the degraded borehole plug. The borehole plugs are assumed to hold their initial low permeabilities for 75 years and then to degrade continuously over the next 75 years to a permeability appropriate for a rubble-filled borehole (Appendix C and Table E-2). The flow rate during the first 75 years is more than five orders of magnitude less than that for times greater than 150 years ($t = 75$ years, Table E-1), justifying the assumption of insignificant flow during the first 75 years. Because fluid release during the undegraded lifetime of the plugs is insignificant ($\sim 3 \text{ L}$), calculations using SWIFT II begin at a time corresponding to 75 years after plug emplacement, i.e., to the beginning of plug degradation. The time axis in all plots is labeled with $t = 0$ for the simulation time, corresponding to 75 years after plug emplacement.

Table 7-7. 50-Year Committed Dose Equivalent Factors (Case II) (DOE, 1988a)

<u>Nuclide</u>	<u>Ingestion CEDE (rem/μCi)¹</u>	<u>Inhalation CDE (rem/μCi)²</u>
Am-241	4.5	10000
Np-237	3.9	9600
Pu-238	0.054	3300
Pu-239	0.058	3800
Pu-240	0.058	3800
U-233	0.025	1100
U-235	0.025	1000

Notes: 1. CEDE's are for whole body.

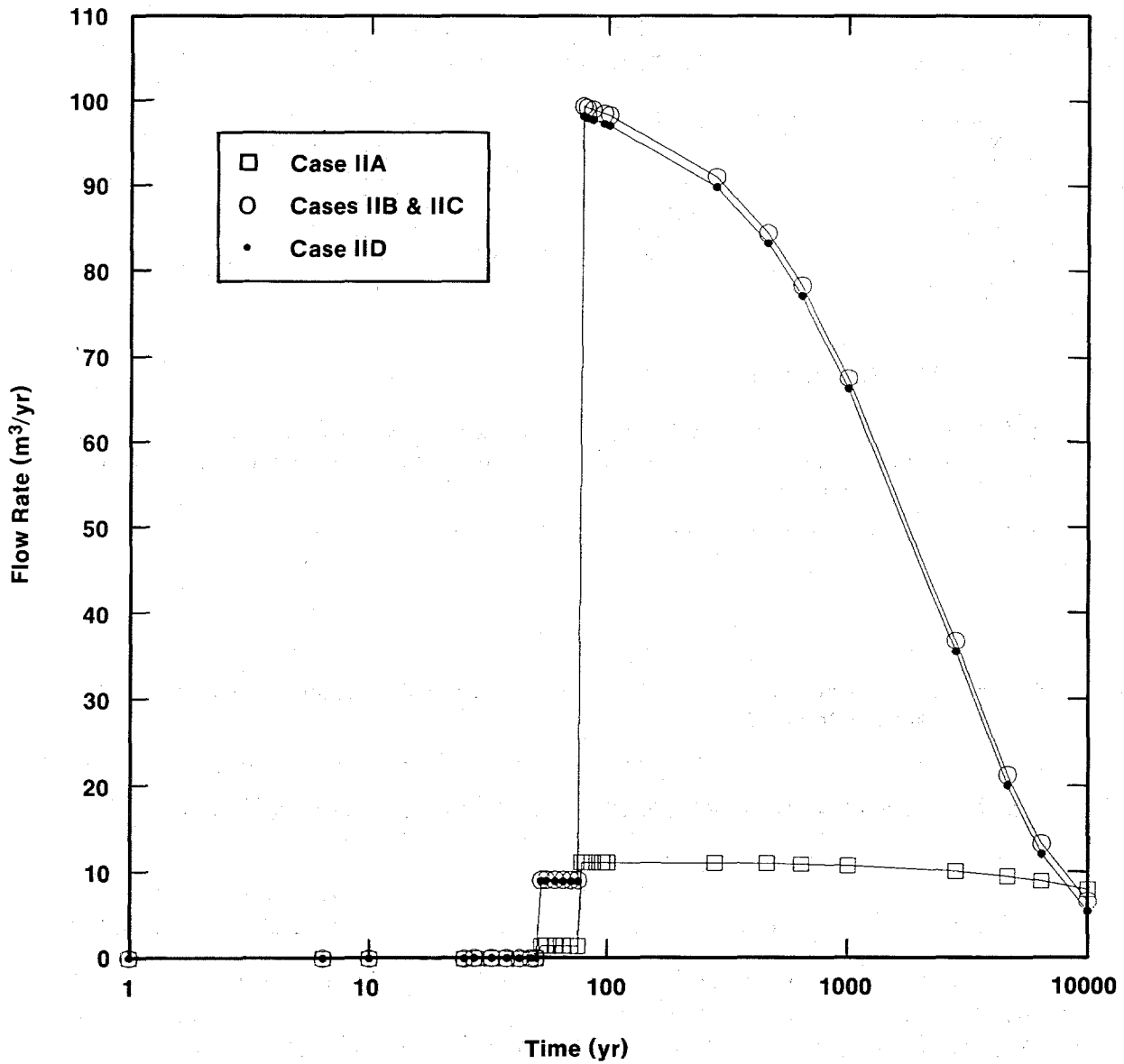
2. CDE's are for critical organs. Lungs are the critical organ for uranium inhalation. Bone is the critical organ in all other inhalation cases.

Table 7-8. Maximum Doses Received by a Hypothetical Farmer Through Indirect Pathways (Case II)

Committed Dose Equivalent After 1-Year Exposure (mrem/50 yr)

<u>Nuclide</u>	<u>Beef</u>	<u>Milk</u>	<u>Above-Surface Crops</u>	<u>Below-Surface Crops</u>	<u>Inhalation</u>
Am-241	3.04×10^{-12}	9.97×10^{-11}	8.81×10^{-11}	1.03×10^{-10}	2.62×10^{-1}
Np-237	8.23×10^{-17}	4.86×10^{-16}	4.20×10^{-13}	---	2.58×10^{-6}
Pu-238	1.69×10^{-14}	2.69×10^{-16}	3.30×10^{-11}	1.35×10^{-10}	4.37×10^{-1}
Pu-239	1.98×10^{-15}	3.15×10^{-17}	3.87×10^{-12}	1.58×10^{-11}	5.40×10^{-2}
Pu-240	4.94×10^{-16}	7.89×10^{-18}	9.68×10^{-13}	3.95×10^{-12}	1.35×10^{-2}
U-233	5.87×10^{-15}	6.22×10^{-14}	1.59×10^{-13}	7.29×10^{-14}	2.62×10^{-4}
U-235	2.93×10^{-19}	3.11×10^{-18}	7.95×10^{-18}	3.65×10^{-18}	1.19×10^{-8}
Total Ingested Dose:			4.87×10^{-10}		
Total Inhaled Dose:					7.66×10^{-1}

Note: Includes breathing rate of 2.7×10^{-4} m³/s.



TRI-6330-54-0

Figure 7-2. Flow rates to the Culebra Dolomite from the breach borehole for Cases IIA, IIB, IIC, and IID.

Borehole degradation dominates the behavior of flow rates between 75 and 150 years (0 to 75 years in Figure 7-2). During this time the stair-step effect results from coarse temporal gridding of borehole permeability changes. Flow rate increases and reaches a maximum at about the same time that the borehole permeability reaches its maximum value. This maximum permeability characterizes the final rubble-filled state of the borehole. The maximum borehole permeability for Cases IIB, IIC, and IID bears a 10:1 ratio to the Case IIA permeability, and the Case IIB/IIC maximum flow rate for Cases IIB, IIC, and IIB bears a similar (~9:1) ratio to the Case IIA flow rate. No decrease in borehole permeability is assumed over the 10,000-year period, although salt creep and precipitation are likely to decrease this permeability with time.

Brine-reservoir depressurization dominates the period beginning 150 years after plug emplacement (after 75 years in Figure 7-2). For Case IIA, depressurization is minimal, and at 10,000 years, the total brine-inspection rate into the Culebra Dolomite is equal to 71% of the maximum value. For Cases IIB, IIC, and IID however, depressurization effects are more substantial, and at 10,000 years, the flow rate is equal to only 6.7% of the maximum value for Cases IIB and IIC and 5.5% of the maximum value for Case IID (Table E-3).

The numerical implementation of the coupling of the brine reservoir and the Culebra Dolomite (Appendix E.1.3) assumes that all flow enters the Culebra and no fluid is released to the ground surface. The maximum pressure build-up values simulated at the borehole location in the Culebra Dolomite are <18 kPa (261 psi) for all four cases. This pressure increase, which is small relative to the 2.4-MPa (348-psi) pressure that would be required to drive brine to the surface, confirm that there would be no flow to ground surface for the selected brine-reservoir, Culebra, and borehole properties used in the Case II simulations.

The total fluid discharge from the breach borehole to the Culebra Dolomite is the sum of the flow rate from the brine reservoir, Q , and the flow rate from Salado brine inflow, q , to the borehole (Table E-3). In Cases IIA, IIB, and IIC, the flow-rate q from the Salado Fm. is constant at $1.3 \text{ m}^3/\text{yr}$

(Section 4.3). In Case IID, the flow-rate q from the Salado Fm. is constant at $0.1 \text{ m}^3/\text{yr}$.

The rate of flow from the Castile Fm., Q , decreases slightly with time in Case IIA, ranging from a high of $9.7 \text{ m}^3/\text{yr}$ at 75 years (150 years after plug emplacement) to a low of $6.7 \text{ m}^3/\text{yr}$ at 10,000 years (Table E-3). In Case IIA, all brine from the Castile Fm. is assumed to mix within the waste panel, bringing the concentration of dissolved radionuclides up to the solubility limit, 1×10^{-6} molar. Therefore, brine flows up the borehole and into the Culebra Dolomite in Case IIA at a rate of $Q + q$. This brine contains a constant concentration of dissolved radionuclides equal to the specified solubility limit. Lead is less soluble in Culebra ground waters than in concentrated brines (Table E-1). Therefore input concentrations to the stream tube are controlled by the solubility of lead in Culebra ground waters. Another factor keeping source concentrations constant in Case IIA is the lack of inventory depletion; i.e., no radionuclide is depleted from the panel inventory after 10,000 years of flow.

Case IIB is more complex. The rate of flow from the Castile Fm., Q , is initially much higher ($98.1 \text{ m}^3/\text{yr}$ at 75 years) than in Case IIA, as a result of the factor-of-ten increase in borehole permeability (Tables E-3 and E-2). However, the flow rate Q decreases approximately exponentially over time, because pressure is depleted in the brine reservoir, reaching a low of $5.3 \text{ m}^3/\text{yr}$ at 10,000 years (Figure 7-2, Table E-3). In contrast to Case IIA, waste compaction is assumed to prevent brine from the Castile Fm. from mixing within the waste panel in Case IIB. In this case, uncontaminated brine from the Castile Fm. flows up the borehole and mixes with brine from the Salado Fm. that has traveled through the waste panel and that contains dissolved waste. Therefore, the Castile brine dilutes the contaminated Salado brine by a factor equal to $(Q+q)/q$ prior to the fluid's entry into the Culebra Dolomite. Because the Castile brine-flow rate decreases with time, this source-dilution factor also decreases with time, ranging from 76 at 75 years to 5.1 at 10,000 years (Table E-3). For waste constituents having sufficient mass to saturate the total fluid volume contained in one panel, the initial concentration of dissolved waste in the Salado brine is the specified solubility limit, 1×10^{-4} molar for radionuclides and 116 mg/L for stable lead (Table E-1). For waste constituents not having sufficient mass to reach saturation, the

initial concentration of dissolved waste is equal to the available waste mass divided by the fluid volume contained in one panel. Subsequent concentrations in the waste panel are reduced both by mass discharge to the borehole and by radioactive decay.

Case IIC assumes the same increased borehole permeability that was assumed by Case IIB, resulting in the same Castile brine-flow rates, Q , (from 98.1 to 5.3 m^3/yr at 75 and 10,000 years, respectively). Unlike Case IIB, in which Castile brine is assumed to be prevented from circulating through the waste panel by waste compaction, Case IIC assumes that Castile brines penetrate into and mix within the waste panel. For waste constituents having sufficient mass to saturate the total fluid volume contained in one panel, the initial concentration of dissolved waste in the Salado brine is the specified degraded solubility limit, 1×10^{-4} molar for radionuclides and 116 mg/L for stable lead. For waste constituents not having sufficient mass to reach saturation, the initial concentration of dissolved waste is the available waste mass divided by the fluid volume contained in one panel. Subsequent concentrations in the waste panel are reduced by mass discharge to the borehole and by radioactive decay.

Case IID assumes the same increased borehole permeability that was assumed in Cases IIB and IIC, resulting in the same Castile brine-flow rate Q (from 98.1 m^3/yr at 75 years to 5.3 m^3/yr at 10,000 years). Case IID assumes that engineered modifications prevent brine from the Castile Fm. from mixing with the waste (similar to Case IIB) and reduce the Salado brine-inflow rate to the borehole (q) to 0.1 m^3/yr from the 1.3 m^3/yr used in Cases IIA, IIB, and IIC (Section 4.3). Brine from the Salado Fm. in Case IID is assumed to pass through the waste and dissolve radionuclides up to the same 1×10^{-6} molar solubility limit that was used in Case IIA. At the borehole, this contaminated Salado brine is diluted by uncontaminated brine from the Castile Fm. The dilution factor is $(Q+q)/q$, which for Case IID yields a range from 980 at 75 years to 55 at 10,000 years (Table E-3). These values are approximately one order of magnitude larger than the dilution factors in Case IIB, because the Salado brine-inflow rate in Case IID is approximately one order of magnitude lower. The quantity of waste accessible to circulating

brine in Case IID is assumed to be restricted to one room. However, because no inventory depletion occurs within 10,000 years, this restriction was not a limiting factor in the Case IID simulation.

The end result of the flow-rate complexities described above can be summarized as follows. In Case IIA, contaminated brine enters the Culebra Dolomite at a rate $Q + q$ that varies slightly over the 10,000-year simulation time (from 11.2 to 8.0 m³/yr), and the concentration of radionuclides remains constant for 10,000 years at the "expected" solubility limit, 1×10^{-6} molar. In Case IIB, contaminated brine enters the Culebra Dolomite at a rate $Q + q$ that varies greatly over time (from 99.4 to 6.7 m³/yr). Unlike Case IIA, the concentration of the contaminants entering the Culebra Dolomite in Case IIB varies widely over time because of variation in the source-dilution factor $(Q+q)/q$, inventory depletion of some radionuclides, and radioactive decay. In Case IIC, brine from the breach borehole enters the Culebra Dolomite at the same rates as in IIB; however, Case IIC contaminant concentrations are higher, because the Castile brine reservoir fluids are assumed to mix within the repository and dissolve waste. In Case IIC, the concentration of contaminants entering the Culebra Dolomite varies widely with time as a function of greater source depletion and radioactive decay. In Case IID, brine from the breach borehole enters the Culebra Dolomite at rates (98.2 to 5.4 m³/yr) that are slightly less than in Cases IIB and IIC, because of the decreased Salado brine flow. Like Case IIB, Castile brine reduces contaminant concentrations in the Salado brine by the $(Q+q)/q$ dilution factor. Because there is no inventory depletion in Case IID, the concentration of contaminants entering the Culebra varies only as a function of variation in the dilution factor.

7.3.2 Contaminant Transport for Case IIA

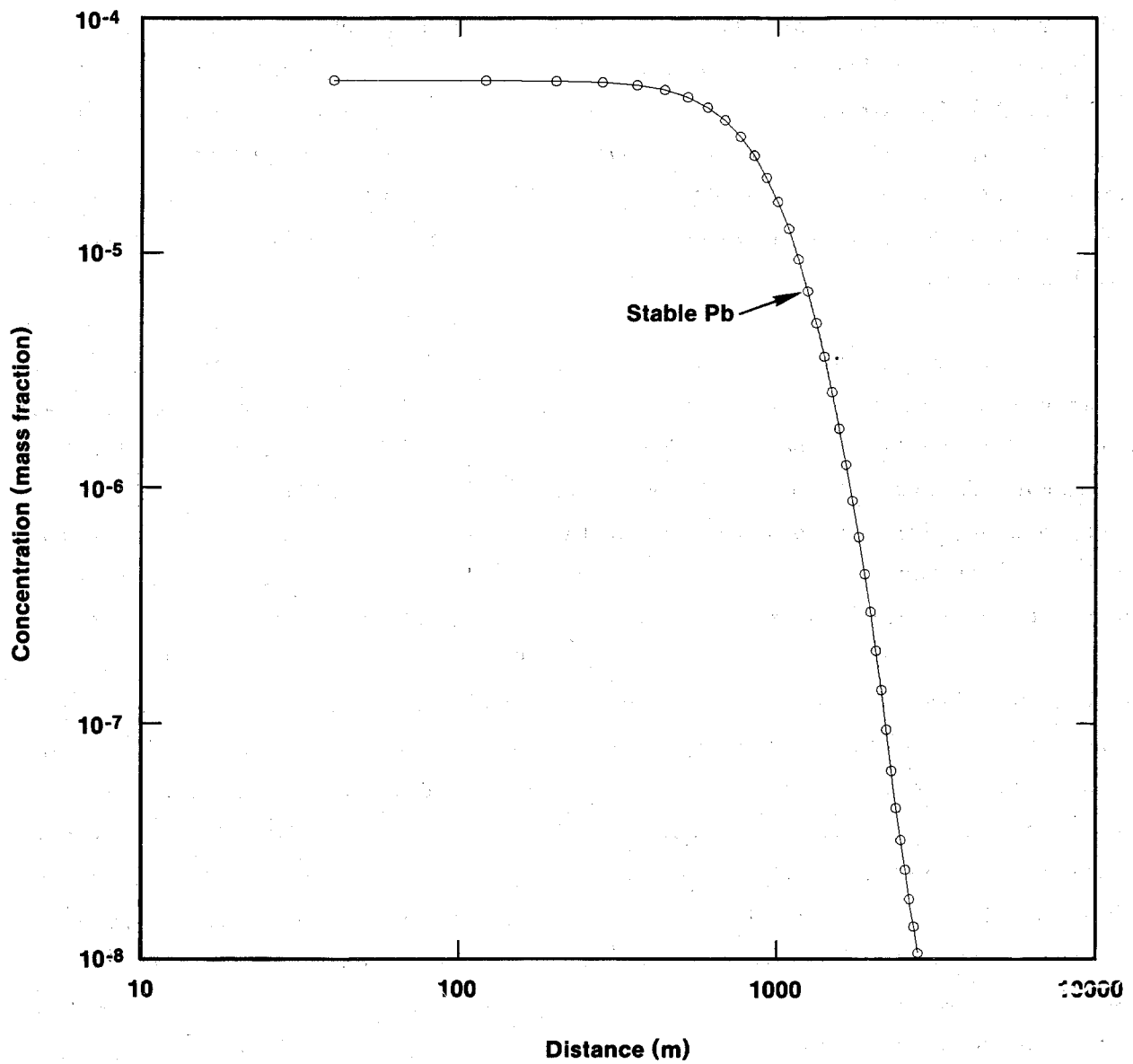
For all species considered, Case IIA yields negligible breakthrough at the stock well, with maximum concentrations lying one order of magnitude or more below drinking water standards. Drinking-water quality is regulated by the National Primary Drinking Water Standard, 40 CFR 141. The maximum contaminant level for lead is 0.05 mg/L (40 CFR 141). Maximum contaminant levels for radioactive contaminants are given in 40 CFR 141.15 and 141.16. Paragraph 15 sets maximum contaminant levels for ²²⁶Ra, ²²⁸Ra, and gross alpha particles.

The maximum level for combined ^{226}Ra and ^{228}Ra is 5 pCi/L. The maximum contaminant level for gross alpha particle activity, including ^{226}Ra but excluding radon and uranium, is 15 pCi/L. Paragraph 16 limits maximum contaminant levels for beta particles and photon radioactivity from man-made radionuclides in community water systems to a concentration that produces an annual dose equivalent to the total body or to any individual organ no greater than 4 mrem/yr based on consumption of 2 L/day of drinking water. New Mexico Water Quality Control Commission Regulations Section 1-103 sets a standard of 5 mg/L for uranium.

Selected profiles in this report show the spatial extent of the contaminated region at 10,000 years. Figures 7-3 and 7-4 provide spatial profiles for stable Pb and the ^{238}Pu chain for Case IIA. Spatial profiles are not shown for members of the ^{240}Pu chain, the ^{241}Am chain, or ^{239}Pu . For these species, calculated migration distances are smaller than those shown for stable Pb and for ^{226}Ra (Figures 7-3 and 7-4), with the most mobile species (Np and U) migrating distances similar to those shown for ^{234}U (Figure 7-4).

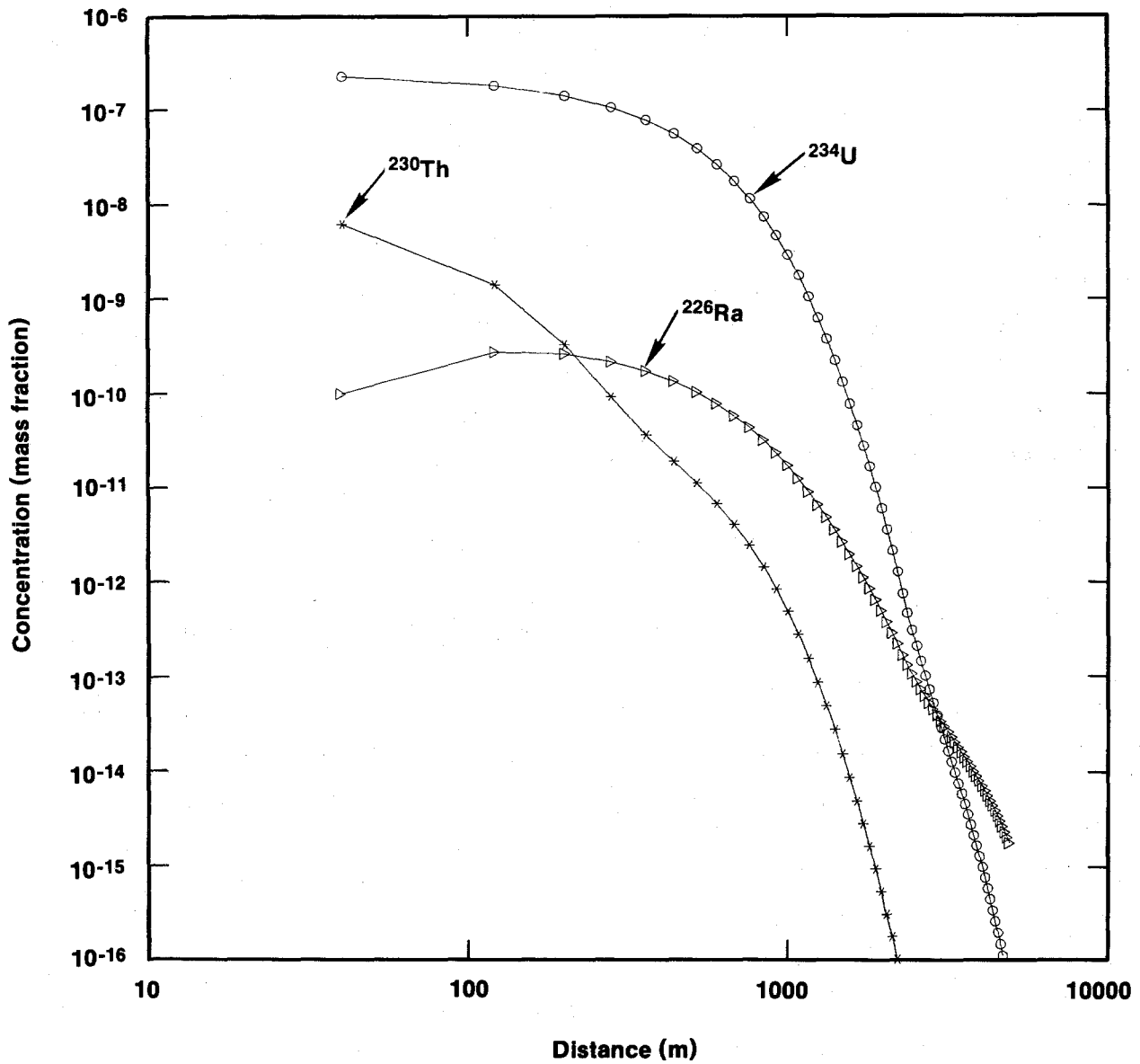
Figures 7-3 and 7-4 show concentrations along the plume centerline connecting the point of release (the borehole) with the stock well. The concentration profile plots (Figures 7-3 and 7-4) do not include concentration reduction caused by lateral dispersion (Section E.1.5.2, Table E-3). Because of the smaller relative magnitudes of their matrix distribution coefficients, ^{226}Ra and Pb ($K_d = 0.1$ mL/g) migrated the greatest distances, with ^{234}U ($K_d = 1$ mL/g) and ^{230}Th ($K_d = 50$ mL/g) migrating correspondingly smaller distances (Figure 7-4). However, ^{234}U maintains a higher relative concentration profile along the flow path than either ^{230}Th or ^{226}Ra , as a result of its higher concentration at the release point in the Culebra Dolomite and its longer half life. The migration of ^{230}Th mimics that of its parent, ^{234}U , thereby moving to greater distances than its relatively large K_d would otherwise permit.

Near the point of release ($x = 0$), the profiles of both ^{234}U and stable Pb display concentrations at $t = 10,000$ years equal to their solubility limits (2.4×10^{-7} kg/kg for ^{234}U and 5.4×10^{-5} kg/kg for Pb). The initial inventory contains a sufficiently large mass of Pb (1.33×10^6 kg) (Table E-5)



TRI-6330-55-0

Figure 7-3. Concentration profile along the stream-tube centerline for stable Pb at 10,000 Years, Case IIA.



TRI-6330-56-0

Figure 7-4. Concentration profiles along the stream-tube centerline for the ^{238}Pu decay chain at 10,000 Years, Case IIA.

to maintain its concentration at the solubility limit throughout the 10,000-year simulation period. Although the initial inventory contains no ^{234}U , decay of ^{238}Pu (231 kg) produces an inventory sufficient to maintain the concentration at the solubility limit for ^{234}U throughout the simulation period.

The calculations do not explicitly consider two members of the ^{238}Pu chain. The parent, ^{238}Pu , has a large K_d (50 mL/g). Consequently, if it were present for the full 10,000 years, its migration distance would be restricted to less than two percent of that for ^{234}U . In addition, ^{238}Pu has a very short half life (87.7 years). It quickly decays to ^{234}U , with only minor amounts remaining at 10,000 years. For simplicity, the ^{238}Pu inventory was converted and added to the initial inventory of ^{234}U , using the relation

$$\text{mass}(^{234}\text{U}) = (234/238) \times \text{mass}(^{238}\text{Pu}). \quad (7-1)$$

The simulations using SWIFT II did not include the transport of ^{238}Pu .

In addition, the calculations did not include the transport of ^{210}Pb , because, assuming that Pb and Ra have equal K_d 's, its concentration is a simple multiple of the concentration of ^{226}Ra . Because of its relatively short half life (22.3 years), ^{210}Pb travels in secular equilibrium with its parent ^{226}Ra , which has a half life of 1,600 years. Consequently, the simple relation

$$\text{concentration}(^{210}\text{Pb}) = (22.3/1,600) \text{ concentration}(^{226}\text{Ra}) \quad (7-2)$$

yields the concentration of ^{210}Pb at all distances along the plume centerline.

Because the plume-centerline concentrations simulated in Case IIA are at least one order of magnitude below existing drinking-water standards, breakthrough curves are not presented. At 10,000 years at the stock well, the concentration-reduction factor that accounts for the effects of lateral dispersion (Section E.1.5.2) has a value of ~37 (Table E-3). Thus, the concentrations at a distance of 4,840 m in Figure 7-4, i.e., at the hypothetical stock well, would be reduced by a factor of at least 37 to

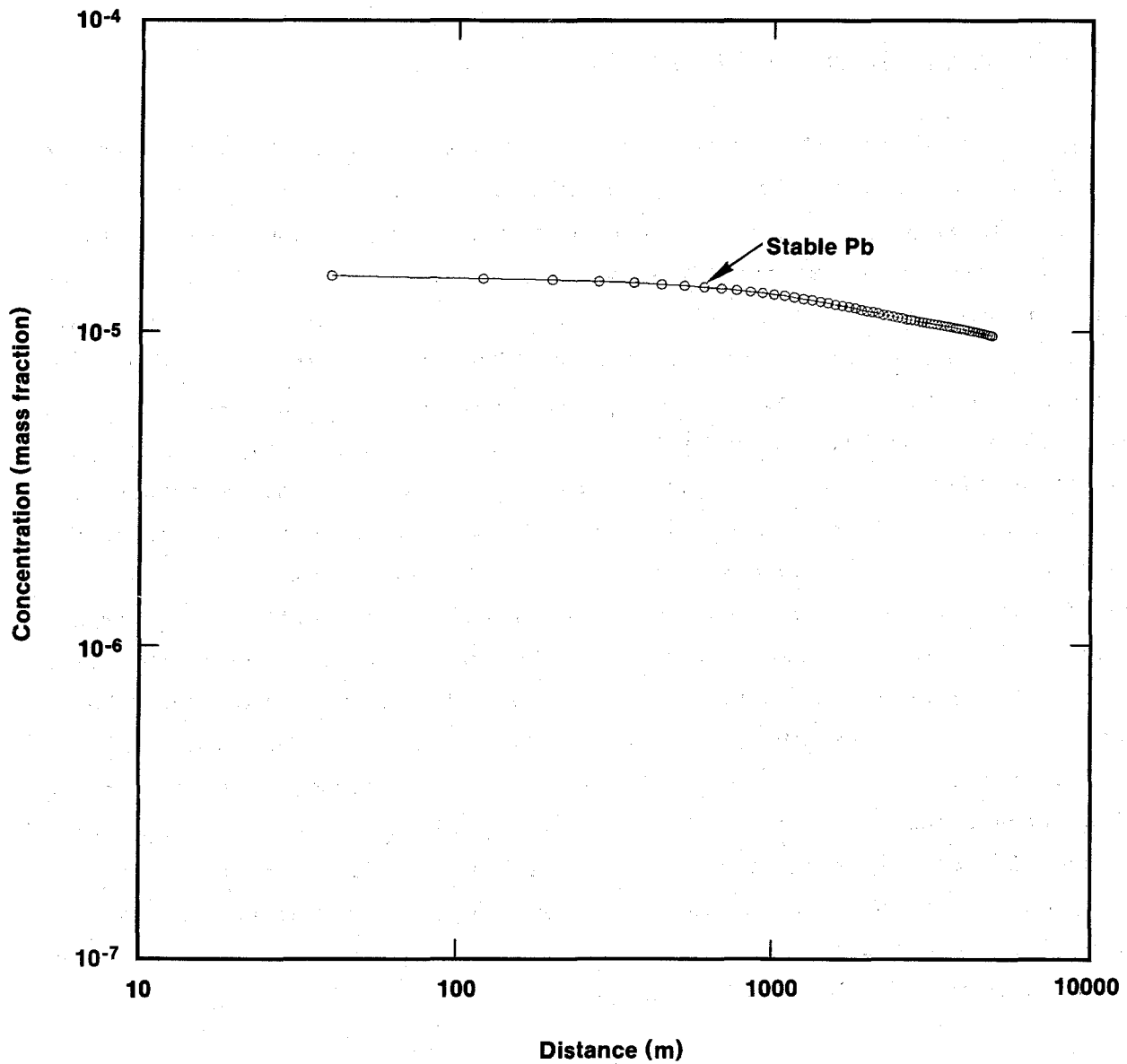
include lateral dispersion. This reduction factor has been used in calculating health effects.

7.3.3 Contaminant Transport for Case IIB

Figures 7-5 through 7-14 display the results for Case IIB. In contrast to Case IIA, Case IIB yields breakthrough of several species at the stock well prior to 10,000 years. This difference results from changes in transport parameters relating to matrix porosity, matrix diffusion and matrix sorption and to changes in repository-release assumptions (Tables E-1 and E-6). All changes in transport parameters enhanced the fracture component of transport, increasing migration distances, and, for many species, causing breakthrough at the stock well within 10,000 years. Changes in the repository-release assumptions lead to a mixed response. For ^{239}Pu and ^{233}U , assumed increases in repository solubility limits (10^{-6} to 10^{-4} molar) increase concentrations at early times at the release point to the Culebra Dolomite in spite of assumed waste compaction, which eliminates direct contact between brine-reservoir fluid and the waste. For stable Pb, the repository solubility limit (1.16×10^{-4} kg/kg) was controlling for Case IIB, rather than the Culebra solubility limit (5.4×10^{-5} kg/kg), which was controlling for Case IIA. In Case IIB, for stable Pb, ^{240}Pu , ^{234}U , and ^{237}Np , the assumed waste compaction yields concentration inputs within the Culebra Dolomite that were lower than for Case IIA (cf. Figures 7-5 and 7-3). For Case IIB, all breakthrough-curve concentrations at the stock well can be reduced by a factor of at least 4.2 to account for the effects of lateral dispersion (Section E.1.5.2) and have been so reduced in health-effect calculations.

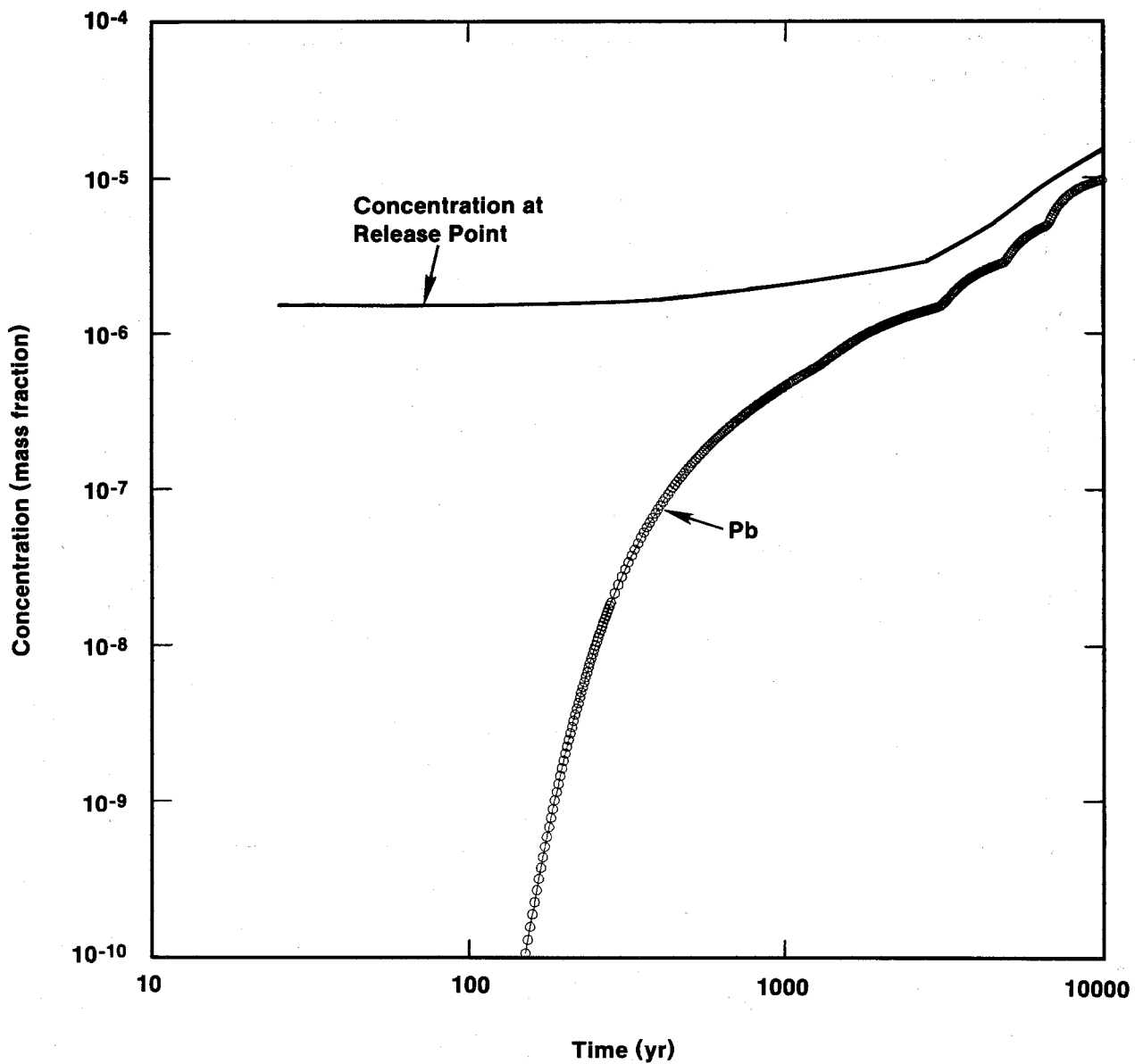
7.3.3.1 Stable Lead. Figures 7-3, 7-5, and 7-6 illustrate some of the contrasts between Cases IIA and IIB for stable Pb. They show spatial profiles at 10,000 years for Cases IIA and IIB and a breakthrough curve at the stock well for Case IIB. Instead of stopping short of the 4,840-m distance to the stock well, as in Case IIA (Figure 7-3), the spatial profile now extends to the stock well (Figure 7-6).

Table E-6 presents the changes in Culebra transport parameters between Cases IIA and IIB. For Case IIB, matrix porosity ϕ' is reduced from 16 to 7%,



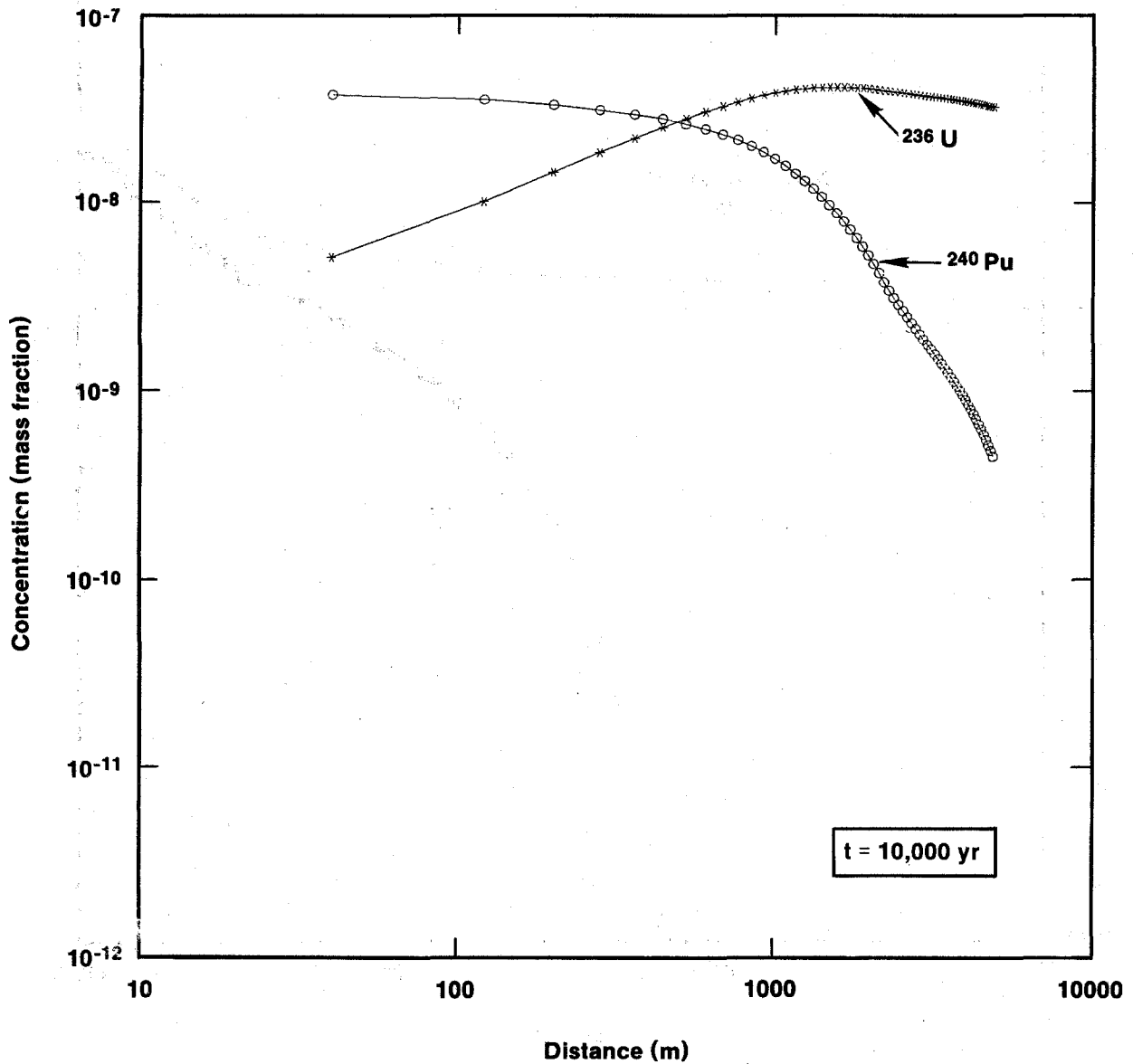
TRI-6330-57-0

Figure 7-5. Concentration profile along the stream-tube centerline for stable Pb at 10,000 Years; Case IIB.



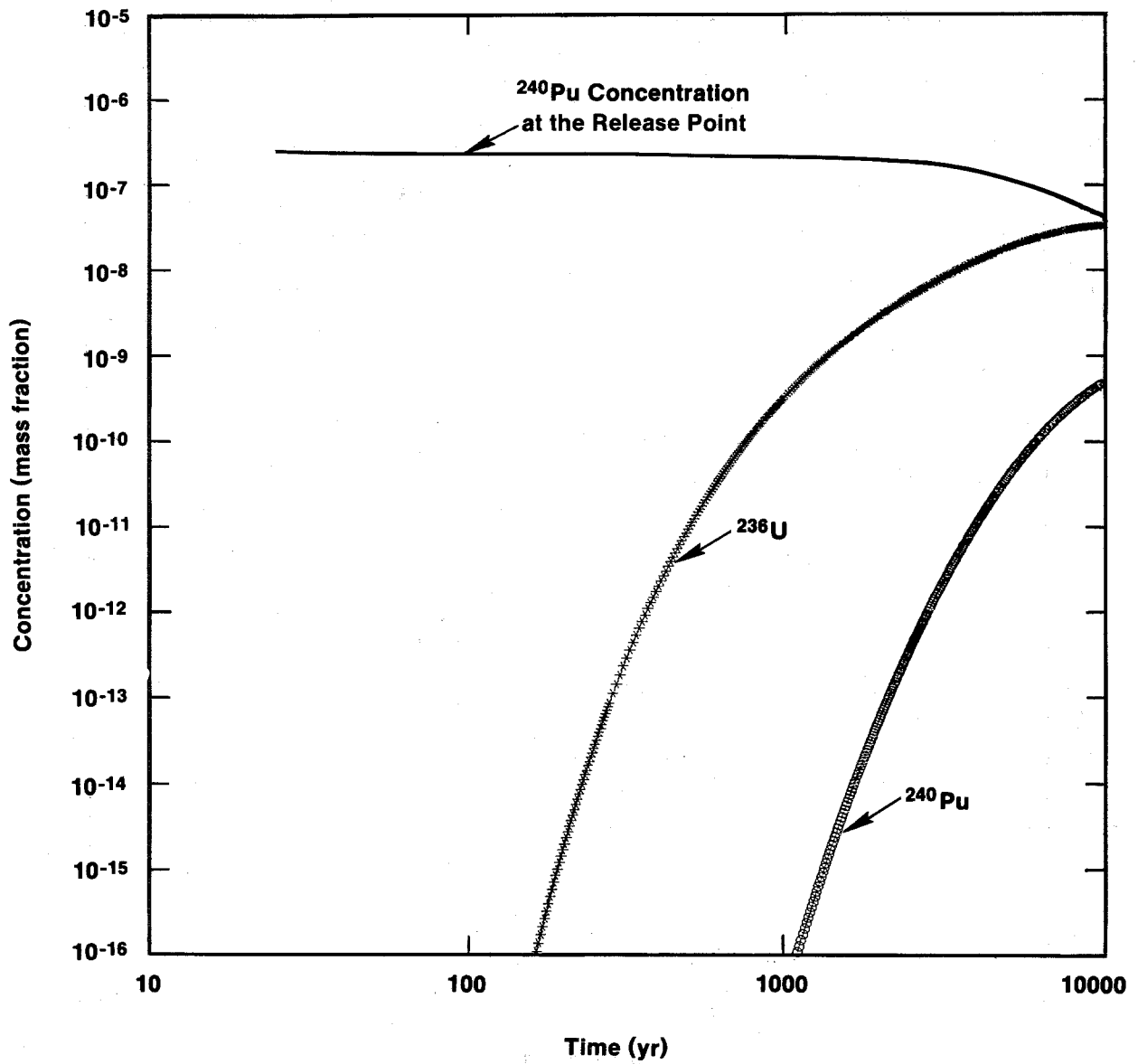
TRI-6330-58-0

Figure 7-6. Breakthrough and boundary concentrations for stable Pb as a function of time, Case IIB.



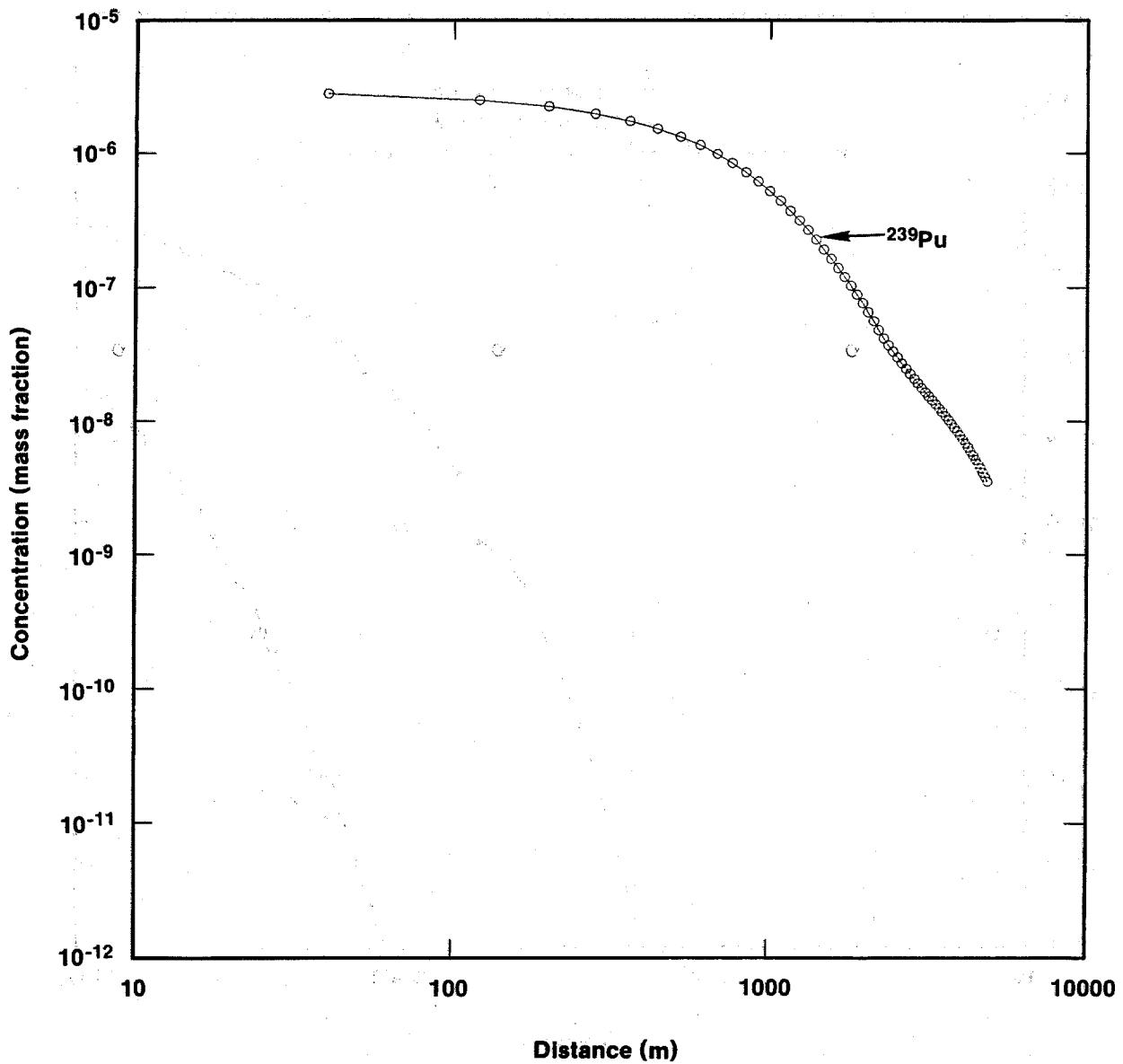
TRI-6330-59-0

Figure 7-7. Concentration profiles along the stream-tube centerline for the ^{240}Pu decay chain at 10,000 Years, Case IIB.



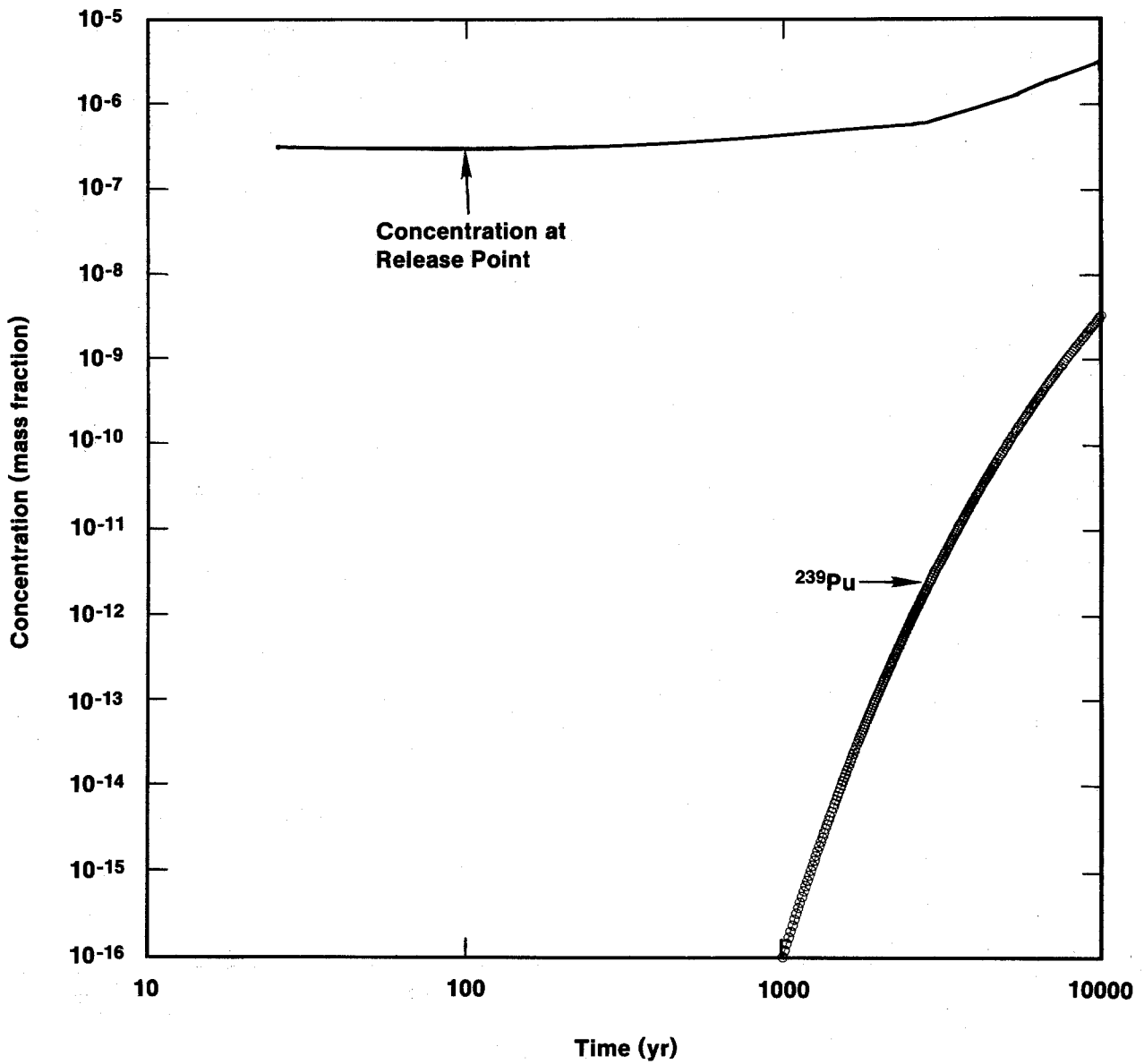
TRI-6330-60-0

Figure 7-8. Breakthrough and boundary concentrations for the ^{240}Pu decay chain, Case IIB.



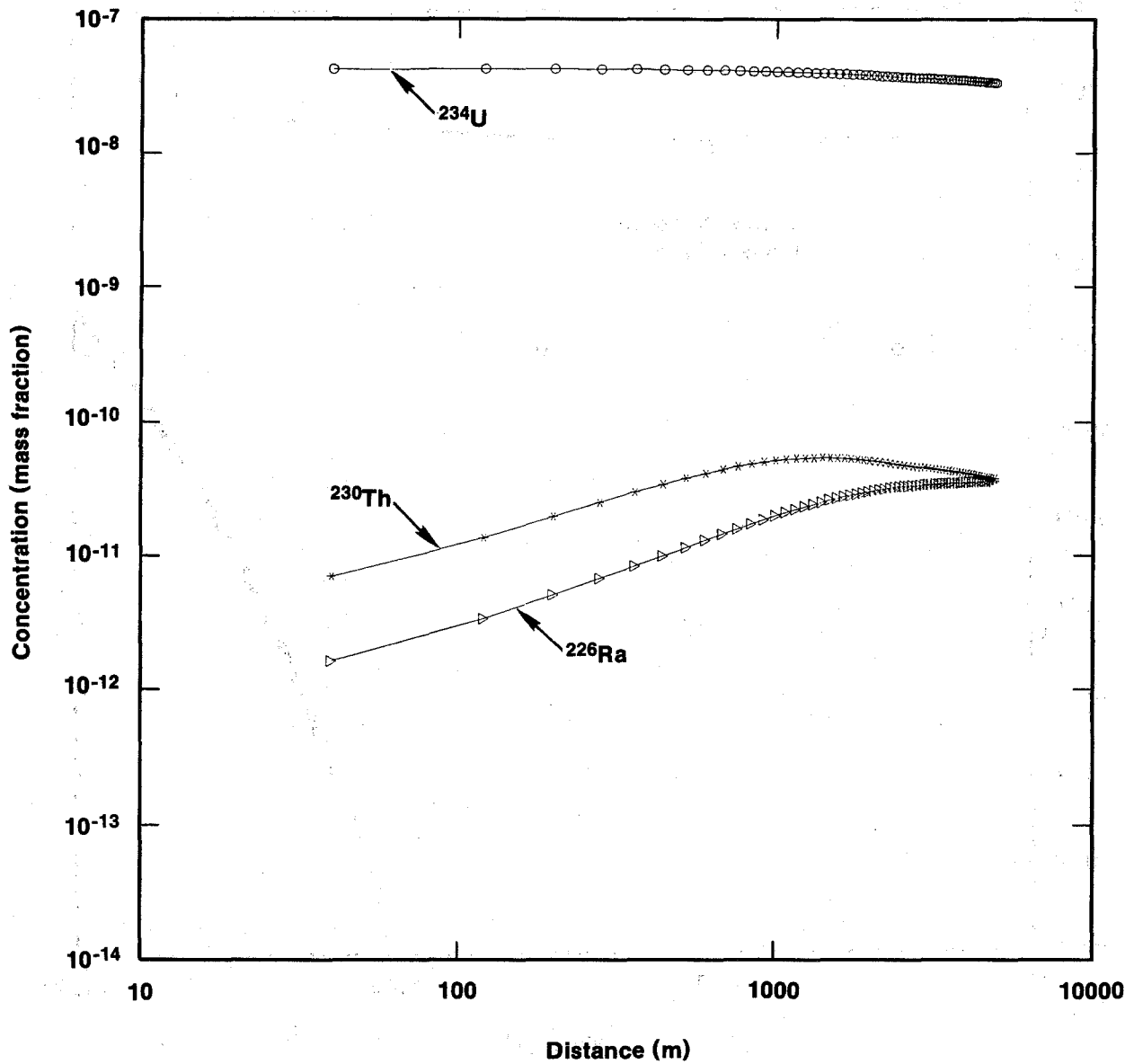
TRI-6330-61-0

Figure 7-9. Concentration profiles along the stream-tube centerline for the ²³⁹Pu decay chain at 10,000 Years, Case IIB.



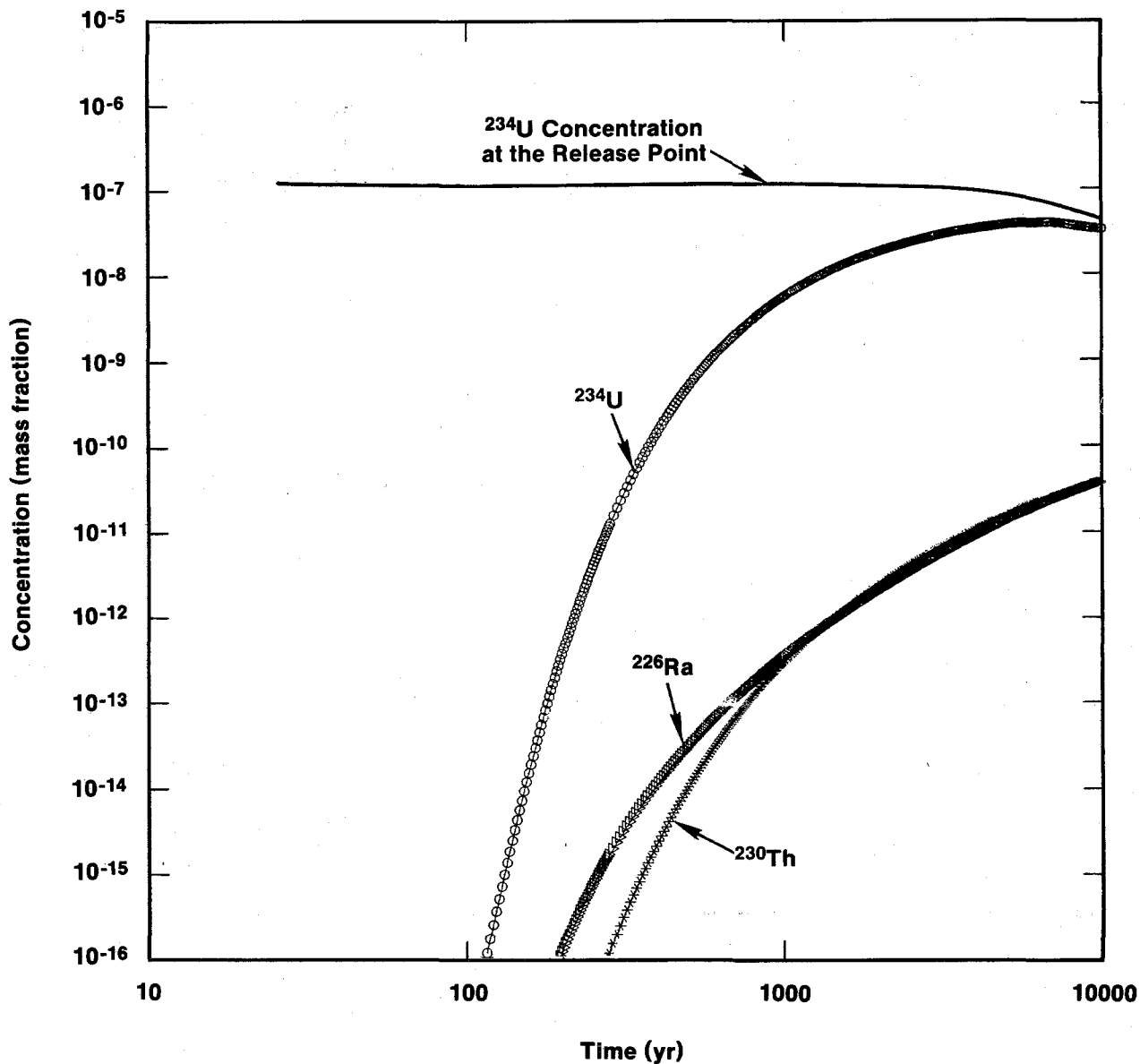
TRI-6330-62-0

Figure 7-10. Breakthrough and boundary concentrations for the ^{239}Pu decay chain, Case IIB.



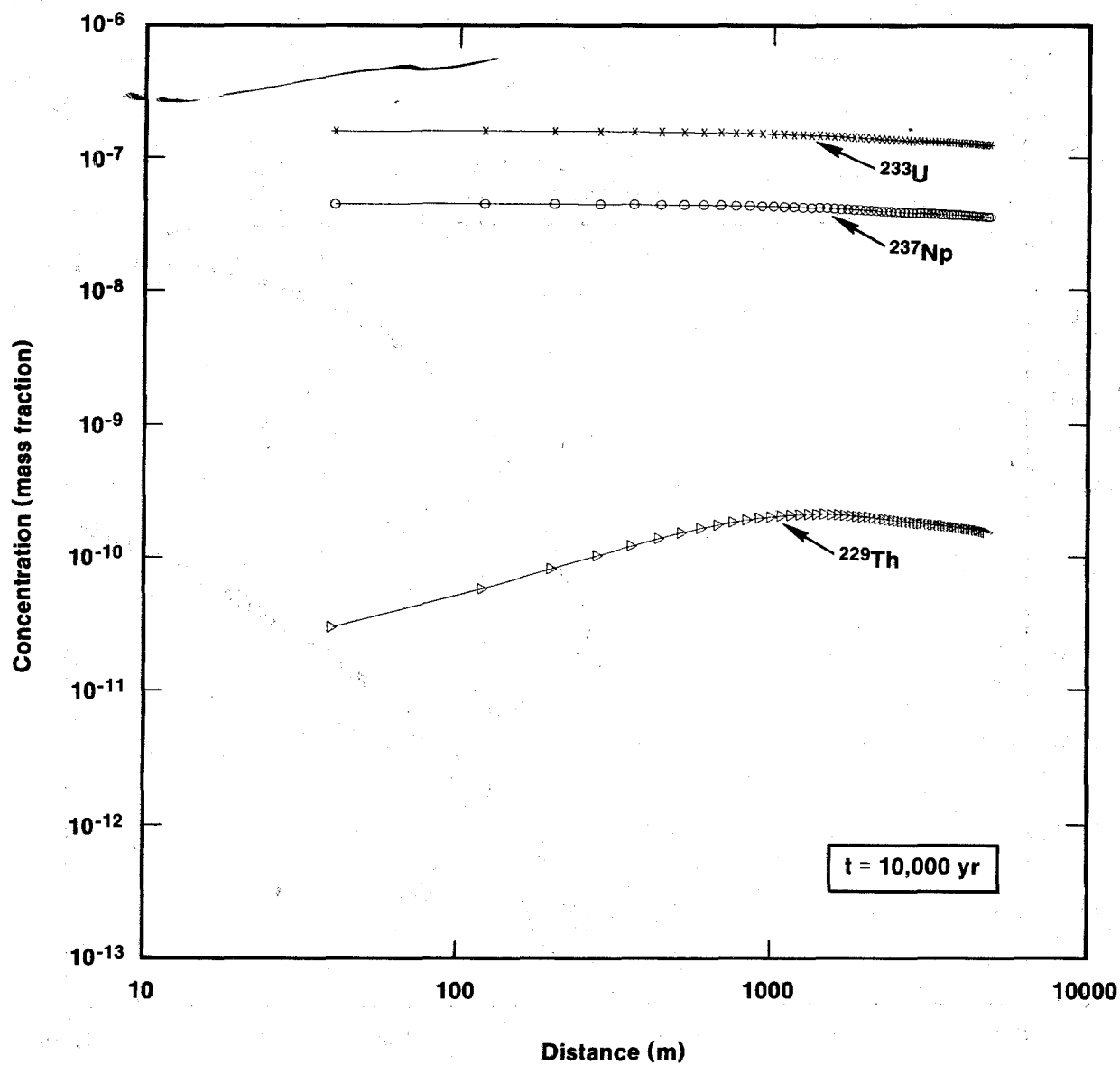
TRI-6330-83-0

Figure 7-11. Concentration profiles along the stream-tube centerline for the ^{238}Pu decay chain at 10,000 Years, Case IIB.



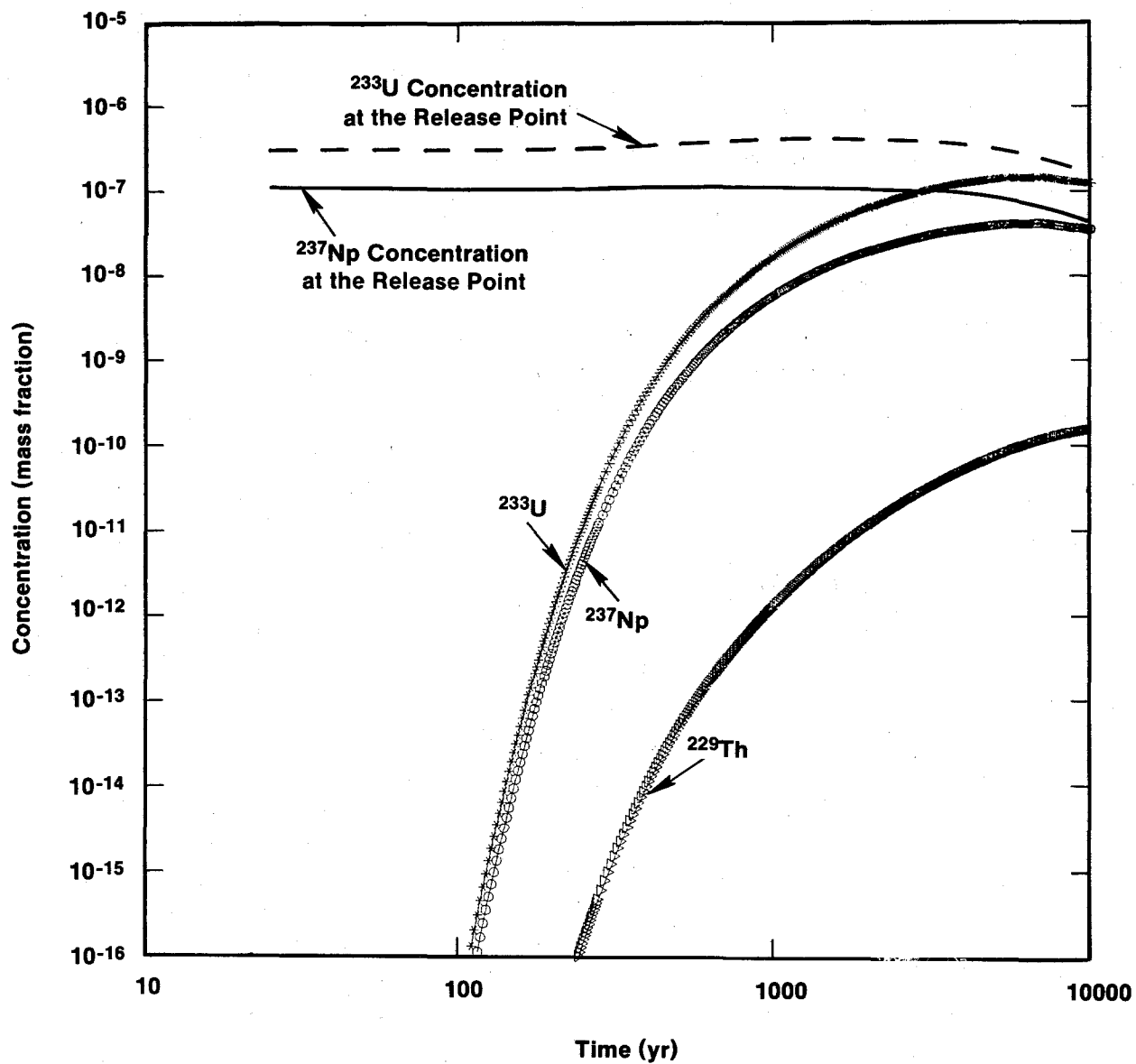
TRI-6330-64-0

Figure 7-12. Breakthrough and boundary concentrations for the ^{238}Pu decay chain, Case IIB.



TRI-6330-65-0

Figure 7-13. Concentration profiles along the stream-tube centerline for the ^{241}Am decay chain at 10,000 Years, Case IIB.



TRI-6330-66

Figure 7-14. Breakthrough and boundary concentrations for the ^{241}Am decay chain, Case IIB.

and the Pb matrix distribution coefficient (K_d) is reduced from 0.1 to 0.05 mL/g. In addition, free-water diffusivity (D') is reduced from 4×10^{-6} to 2×10^{-6} cm²/s for stable Pb, tortuosity (θ') is reduced from 0.15 to 0.03, and fracture separation ($2L'$) is increased from 2 to 7 m. All of these changes reduce the retention capacity of the matrix and increase fracture transport beyond that of Case IIA.

A few observations indicate the significance of these changes. For example, increasing the fracture separation decreases matrix surface exposure to fluid within the fractures by a factor of 3.5 and reduces matrix diffusion. Decreasing free-water diffusivity and tortuosity reduces the characteristic diffusion distance $(\theta'D'T)^{1/2}$ by a factor of $(10)^{1/2}$ for the time period $T = 10,000$ years. For Case IIA, this distance, 4.3 m, is greater than half the fracture spacing, 1 m, indicating relatively full solute saturation of the rock matrix. For Case IIB, this distance, 1.4 m, is less than half the fracture spacing, 3.5 m, indicating partial solute saturation of the rock matrix and an increase in the fracture component of the transport. The rock matrix is important, because without any diffusion into the rock matrix, the calculated particle travel time in the fractures between the release point and the stock well is only 144 years.

Figure 7-6 shows the effects of repository-release assumptions for stable Pb. It shows the concentration released to the Culebra Dolomite as a function of time. Concentrations within the repository panel are solubility limited at $C_{SR} = 116$ mg/L (Table E-5). Case IIA assumes that precipitation occurs immediately following entry into the Culebra Dolomite, and the input concentration became the Culebra solubility limit, $C_{SC} = 54$ mg/L. Case IIB assumes that brine inflow from the Salado Fm. (at a rate of $q = 1.3$ m³/yr) dissolves stable lead to the 116 mg/L solubility limit and transports it to the borehole. There, mixing with fluids of rate Q from the brine reservoir dilutes the dissolved lead to the value $C_{SR}/[(Q+q)/q]$. The quantity $(Q+q)/q$ is the source-dilution factor (Section 7.3.1). When flow rate Q begins to decrease markedly at 150 years, the concentration of dissolved lead released to the Culebra Dolomite begins to increase, reaching a maximum at 10,000 years (Figure 7-6). This increase in dissolved lead concentration does not reach

the Culebra solubility limit for stable lead (5.4×10^{-5} kg/kg) within the 10,000-year simulation period.

Figure 7-6 also indicates travel times from release point to stock well. A given concentration at the stock well lags a concentration of equal magnitude at the point of release by only ~2,000 years. A comparison of this value with that for Case IIA (Figure 7-3), in which the time lag between equal concentrations at the stock well and injection point exceeds 10,000 years, indicates the extent to which the modified Culebra parameters of Case IIB have degraded geologic containment.

7.3.3.2 Radionuclides. Figure 7-7 provides a spatial profile within the Culebra Dolomite for the radionuclide chain $^{240}\text{Pu} \rightarrow ^{236}\text{U}$ at 10,000 years. Figure 7-8 provides concentrations as a function of time at the point of release and at the stock well. In response to the decay of ^{240}Pu (half life $t_{1/2} = 6,540$ years), ^{236}U concentrations increase as a function of distance for ~2000 m. Figure 7-7 indicates a difference of about two orders of magnitude between ^{240}Pu concentrations at the point of release and at the stock well. In spite of a distribution coefficient of 25 mL/g (Table E-6), which is sufficiently large to yield a calculated single-porosity travel time of 6.3×10^6 years, ^{240}Pu still breaks through at the stock well. Thus, the concentration reduction of two orders of magnitude at the stock well at 10,000 years is small, emphasizing the extent to which the modified parameters for matrix diffusion and porosity, particularly the former, have degraded geologic containment relative both to dual-porosity behavior assuming representative properties (Case IIA) and to porous-medium behavior.

The discussion for fluid release to the Culebra Dolomite (Section 7.3.1) and for stable Pb (Section 7.3.3) introduces the source-dilution factor $(Q+q)/q$, which varies from a maximum of 76 at 75 years to a minimum of 5.1 at 10,000 years. For most radionuclides, however, two additional factors contribute to the source model in Case IIB: an increase in the assumed solubility within the repository, and radioactive decay. The increased solubility limit for radionuclides for Case IIB is almost offset at early times by the dilution of contaminated Salado-inflow fluids with brine-reservoir fluids. Most radionuclides have concentrations less than in Case

IIA, with the exception of ^{239}Pu and early-time concentrations of ^{233}U . Case IIB radionuclide input concentrations are smaller at the release point than in Case IIA because of mass depletion. Stable lead does not increase enough in solubility to offset the factor of 77 to 5.1 dilution factor applied in Case IIB. Therefore the Case IIB stable-lead input concentration at 150 years is less than that of Case IIA by a factor of 35. The large increase in lead concentrations seen at the stock well in Case IIB results from degradation of Culebra transport properties, not from input-concentration increases.

For ^{240}Pu , more than the full waste-panel inventory of 59.5 kg can be converted to the solution phase. Here, setting $\rho CV_r = 59.5$ kg gives an initial concentration in the repository of $C = 1.88 \times 10^{-5}$ kg/kg, where ρ is the fluid density, and V_r is the void volume of the repository panel. Thereafter, the ^{240}Pu inventory decreases in accordance with the mixing-cell factor, $\exp[-(\lambda+q/V_r)t]$, where $\lambda = (\ln 2)/t_{1/2}$ is the decay constant, and $t_{1/2}$ is the half life. ^{237}Np and ^{234}U also have an insufficient initial inventory to reach the solubility limit.

Figure 7-8 shows ^{240}Pu concentration at the release point as a function of time. Although this concentration decreases continuously for the entire 10,000-year period, it varies almost imperceptibly for the first 1,000 years, indicating that concentration decrease resulting from inventory depletion almost matches the concentration rise in response to depressurization of the brine reservoir. The composite dilution factor $[(Q+q)/q] \exp[-(\lambda+q/V_r)t]$ combines the two effects. The first bracketed term expresses the dilution due to mixing with brine-reservoir fluids, and the second expresses the source depletion in response to radioactive decay and mixing with Salado inflow fluids. Over the first 1,000 years, the composite dilution factor increases from 80 to 87, remaining reasonably constant. It increases to a value of 890 at 10,000 years. For times greater than 1,000 years, inventory depletion noticeably dominates the concentration at the release point.

Figure 7-9 provides a spatial profile for ^{239}Pu within the Culebra Dolomite, and Figure 7-10 provides ^{239}Pu concentrations as a function of time at the point of release and at the stock well. With one notable difference, the curves are similar to those of ^{240}Pu discussed above. The difference in

half lives, 6,540 years for ^{240}Pu versus 24,100 years for ^{239}Pu , apparently causes only minor differences in computed concentrations. The major difference arises from the source term. The initial panel inventory of ^{239}Pu (866 kg) is large enough and the half life is long enough to prevent inventory depletion in 10,000 years. Initial concentrations differ only slightly, with the release-point concentration of ^{239}Pu exceeding that of ^{240}Pu by a factor of 1.3. However, the ^{240}Pu concentrations decrease monotonically with increasing time, and the ^{239}Pu concentrations increase monotonically. For ^{239}Pu , repository concentrations are maintained at their solubility limit ($\sim 2.4 \times 10^{-5}$ kg/kg), and release-point concentrations vary inversely as the dilution factor $(Q+q)/q$. The factor decreases from a maximum of 76 at 150 years to a minimum of 5.1 at 10,000 years.

Figures 7-11 and 7-12, for the ^{238}Pu chain for Case IIB, provide an interesting contrast with Figure 7-4 for Case IIA. Both cases consider the radionuclide chain $^{238}\text{Pu} \rightarrow ^{234}\text{U} \rightarrow ^{230}\text{Th} \rightarrow ^{226}\text{Ra} \rightarrow ^{210}\text{Pb}$, and both calculate concentrations only for the U, Th, and Ra members. Because its half life is short (87.7 years), the inventory of ^{238}Pu rapidly decays. The simulations assume instantaneous decay by adding the ^{238}Pu inventory to that of ^{234}U , using the appropriate conversion. Because of the short half life (23.3 years) of ^{210}Pb , ^{210}Pb concentrations maintain secular equilibrium with ^{226}Ra , with concentrations given as a simple multiple of those of ^{226}Ra (Section 7.3.2).

For ^{234}U , the Case IIB release-point concentration ($\sim 1.2 \times 10^{-7}$ kg/kg) is slightly smaller than for Case IIA ($\sim 2.0 \times 10^{-7}$ kg/kg). The concentration in Case IIB is limited by the inventory (see discussion for ^{240}Pu), and potential concentration increases because of enhanced solubility are insufficient to offset concentration decreases resulting from dilution with brine-reservoir fluids. Enhanced advection within the fractures does not permit buildup of ^{234}U daughter products near the release point to the same extent as in Case IIA (Figures 7-4 and 7-11). However, the enhanced fracture component of the transport also yields significant breakthroughs at the stock well in 10,000 years. During transport within the fractures, a K_d of 0 is assumed for all radionuclides. Thus, the differences in the shapes of the Th and Ra curves for Case IIA (Figure 7-4), caused by significantly different values of K_d

within the matrix, are barely evident in Figure 7-11, because of the increased importance of fracture flow.

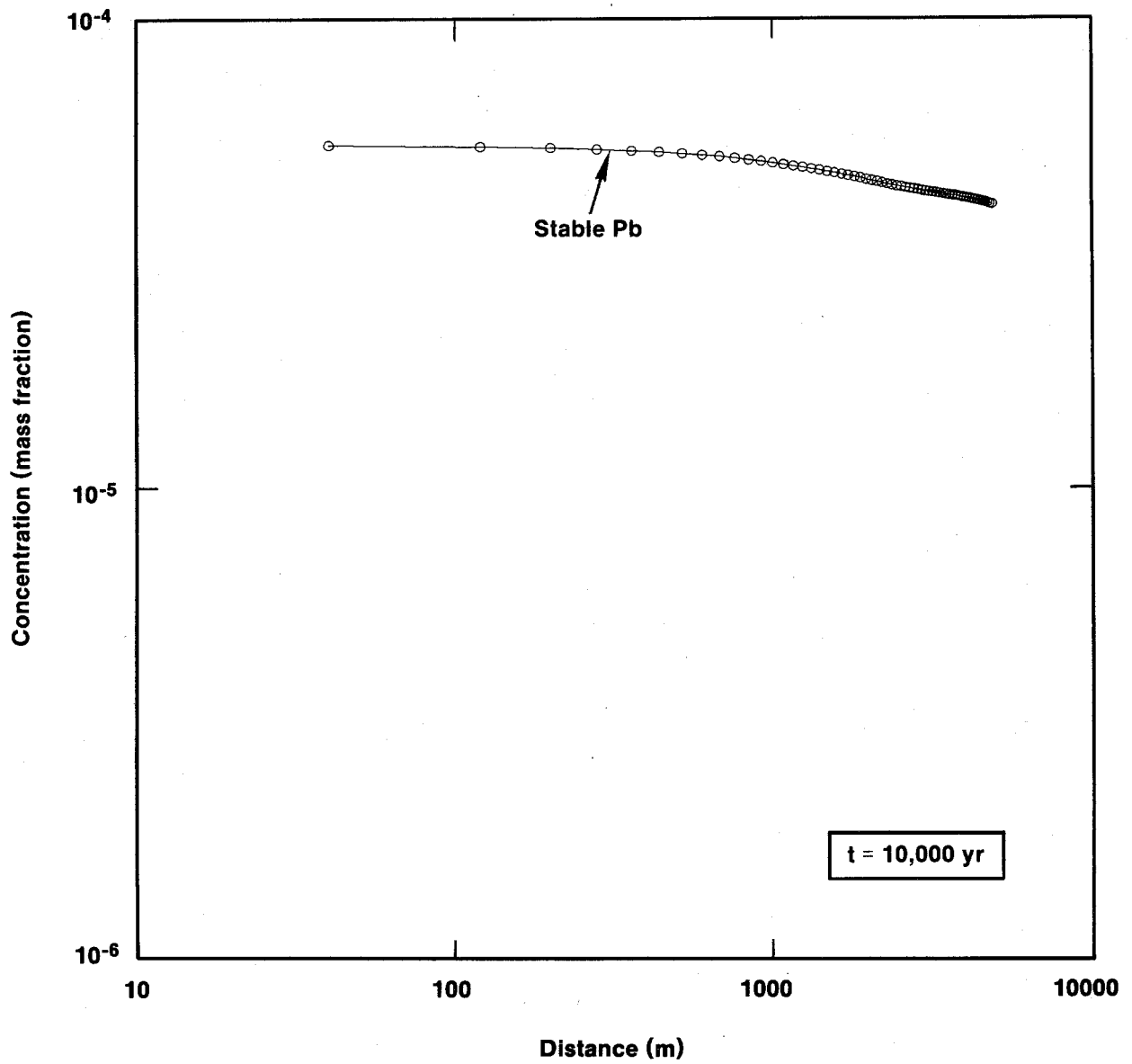
Figures 7-13 and 7-14 display spatial and temporal distributions for the radionuclide chain $^{241}\text{Am} \rightarrow ^{237}\text{Np} \rightarrow ^{233}\text{U} \rightarrow ^{229}\text{Th}$. Because of its relatively short half life (432 years), the inventory of ^{241}Am was combined with that of ^{237}Np . Other comments presented above, regarding the repository-release assumptions, source depletion (in this case at 817 years for ^{233}U), and the enhanced fracture component of transport (relative to Case IIA), apply equally well to the ^{241}Am chain. The validity of the approximation to convert the ^{241}Am inventory to ^{237}Np for the simulations is discussed below.

7.3.4 Contaminant Transport for Case IIC

Case IIC differs from Case IIB only with respect to its repository-release assumptions. Case IIB assumes that Salado-inflow fluids, having come into direct contact with the waste present in a single panel, are subsequently mixed with uncontaminated brine-reservoir fluids during transit from the repository to the Culebra Dolomite. Prior to inventory depletion, the concentration of a given species first reaches the solubility limit within the repository and then is reduced by mixing with brine-reservoir fluids within the borehole. For the stable or long-lived species, with negligible radioactive losses in 10,000 years, the expression $\rho q C_s$ characterizes the inventory depletion rate. Here ρq and C_s represent Salado fluid-mass inflow rate and solubility, respectively.

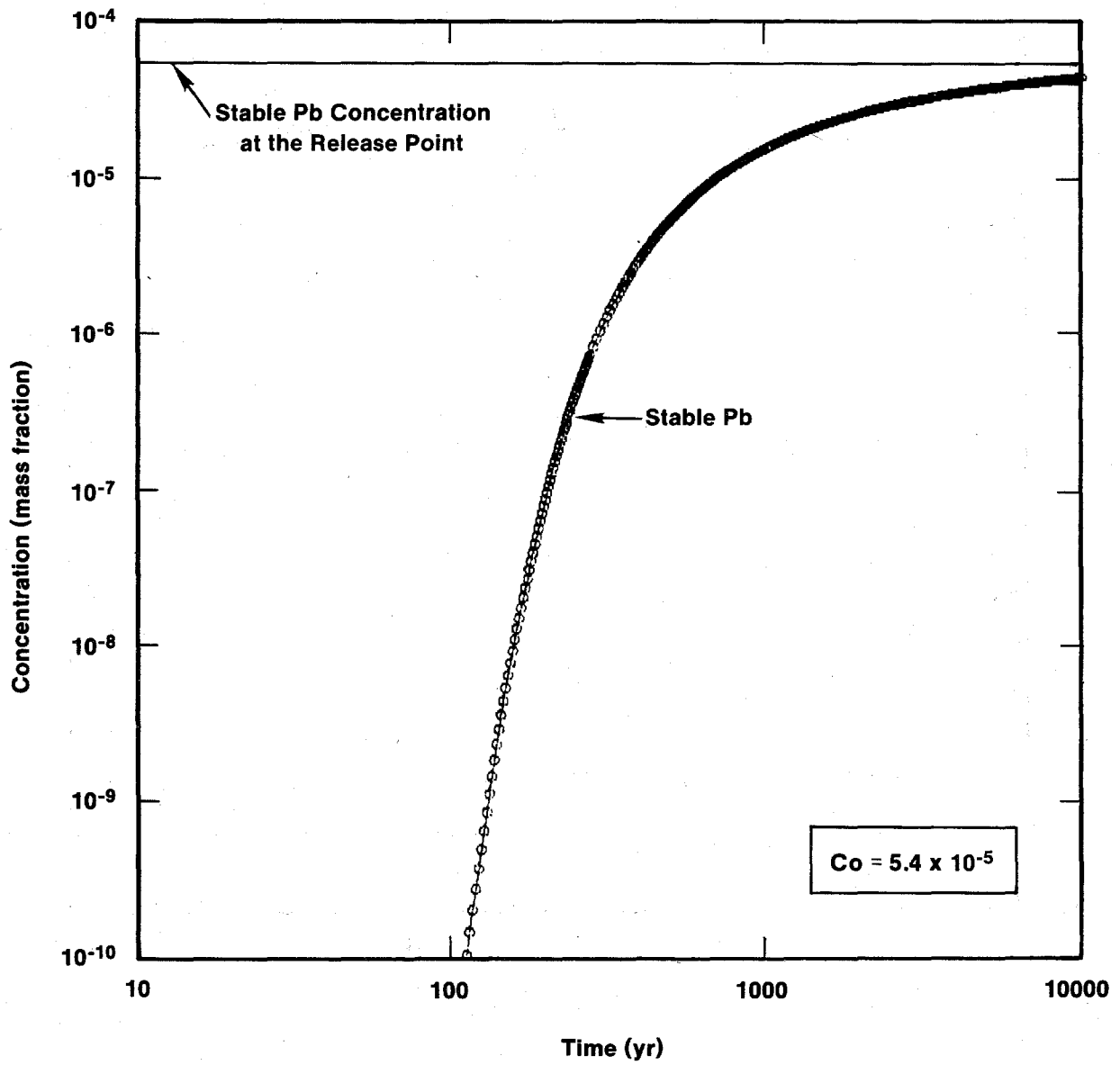
Case IIC assumes that both Salado-inflow and brine-reservoir fluids come into direct contact with the waste present in a single panel. Here, the expression for the inventory depletion rate is $\rho(Q+q)C_s$ for long-lived or stable species. Thus, the inventory depletion rate for Case IIC is enhanced by a factor $(Q+q)/q$ relative to Case IIB. Depending on the brine-reservoir release rate Q , this factor ranges from a maximum of 76 at 150 years to a minimum of 5.1 at 10,000 years.

The change in repository-release assumptions leads to two general effects within the Culebra Dolomite, namely earlier inventory depletions and elevated concentrations. Figures 7-15 through 7-24 display the results for Case IIC.



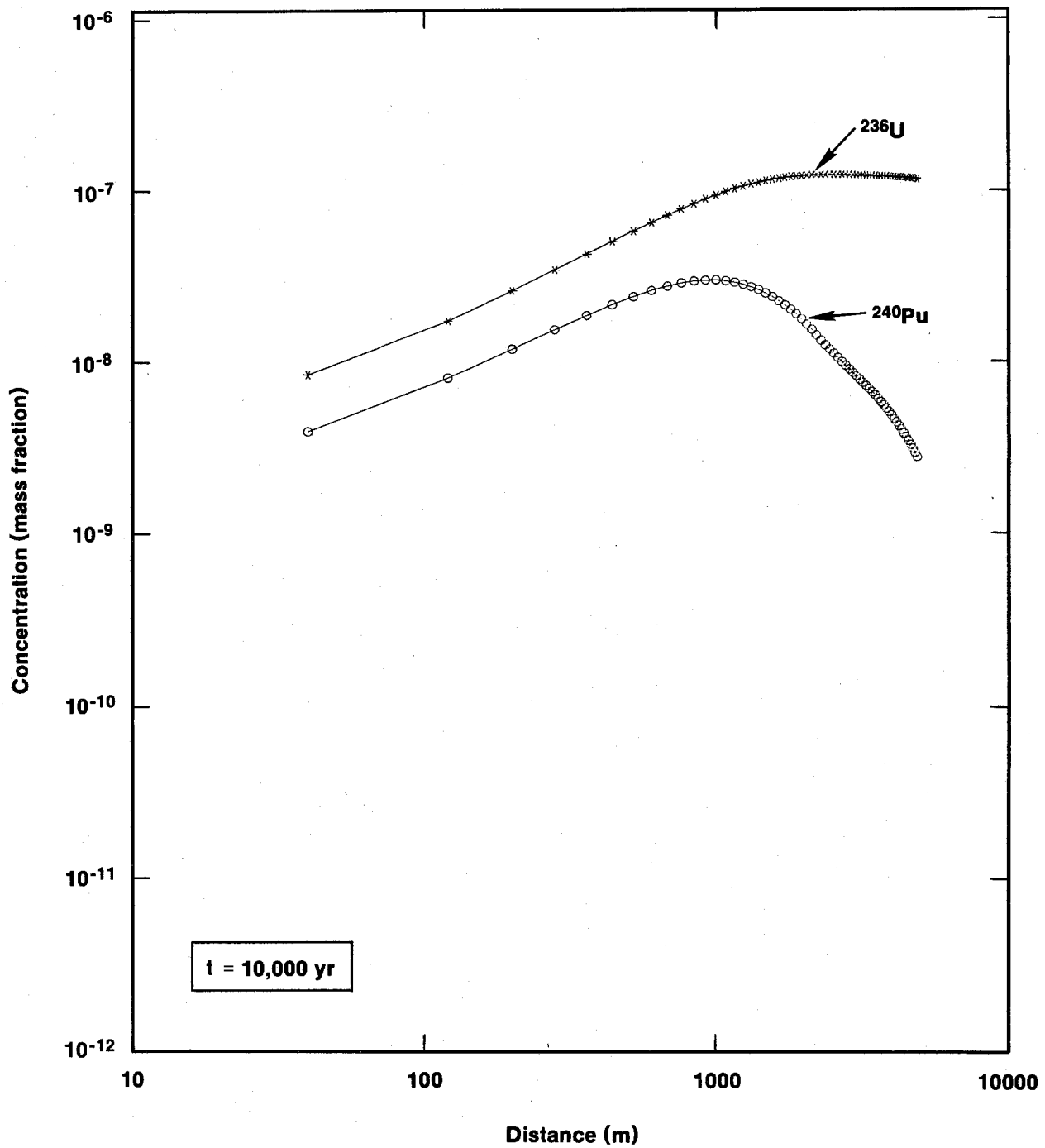
TRI-6330-100-0

Figure 7-15. Concentration profile along the stream-tube centerline for stable Pb at 10,000 years, Case IIC.



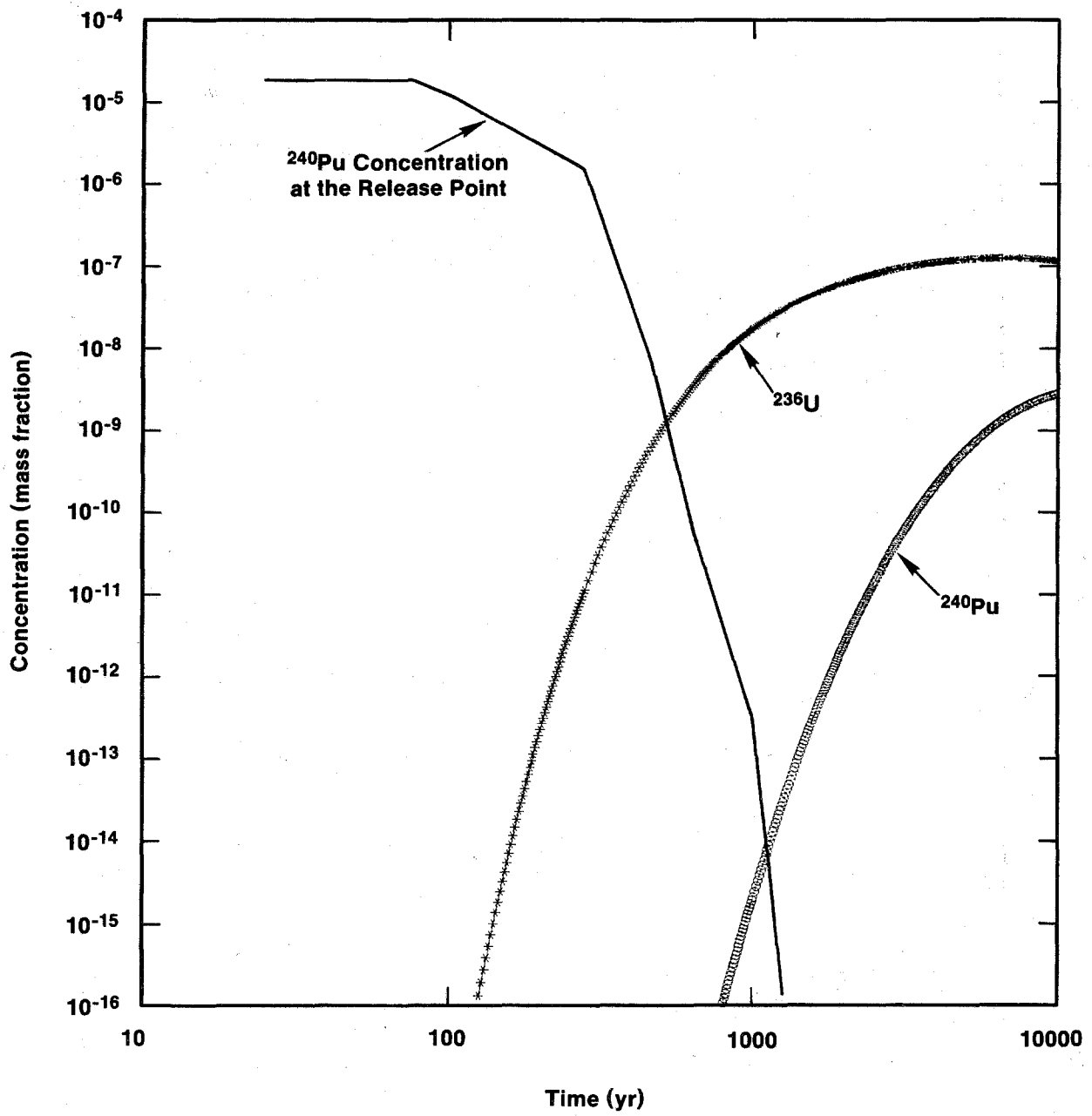
TRI-6330-101-0

Figure 7-16. Breakthrough and boundary concentrations for stable Pb as a function of time, Case IIC.



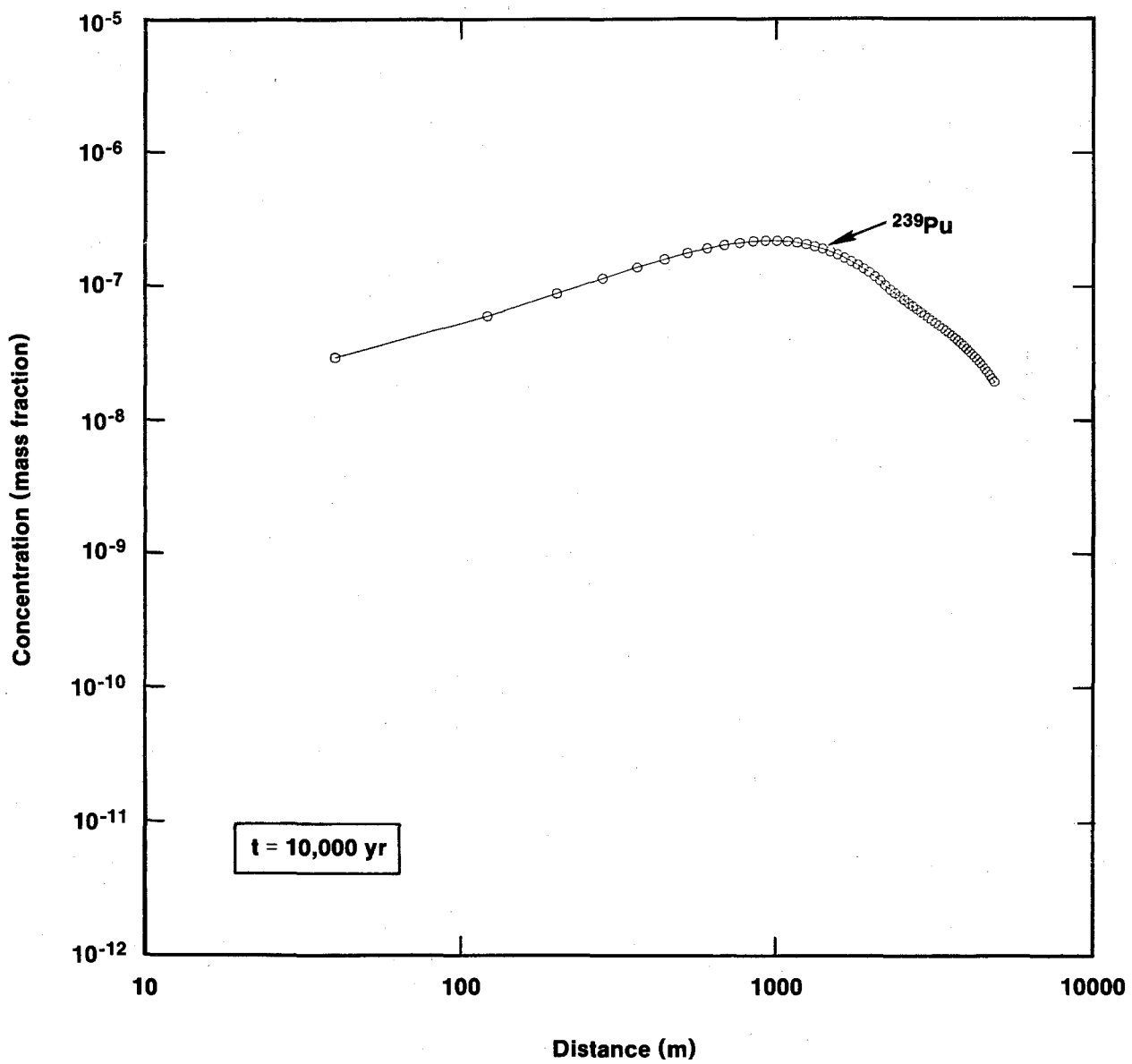
TRI-6330-102-0

Figure 7-17. Concentration profiles along the stream-tube centerline for the ^{240}Pu decay chain at 10,000 years, Case IIC.



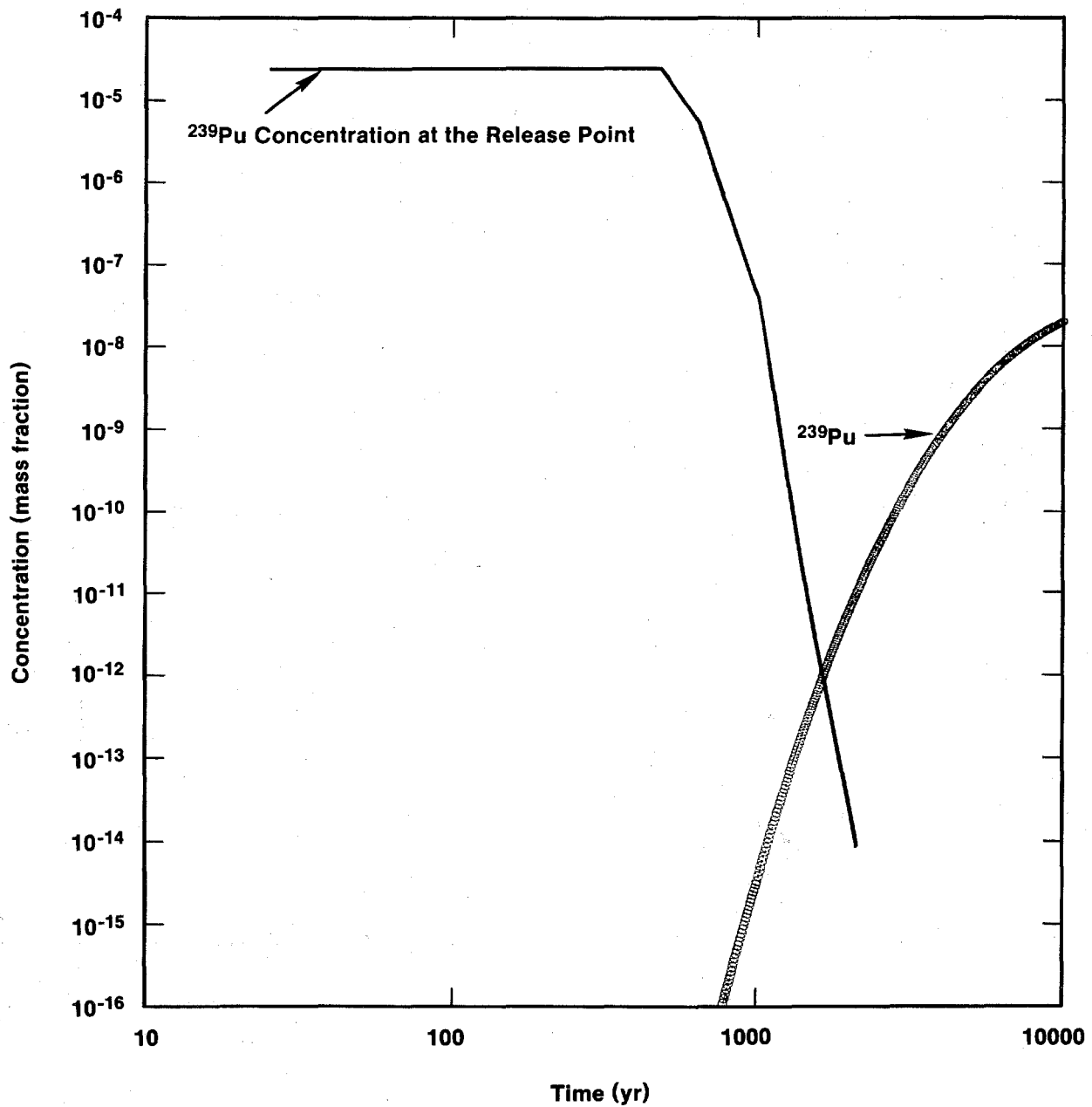
TRI-6330-103-0

Figure 7-18. Breakthrough and boundary concentrations for the ^{240}Pu decay chain, Case IIC.



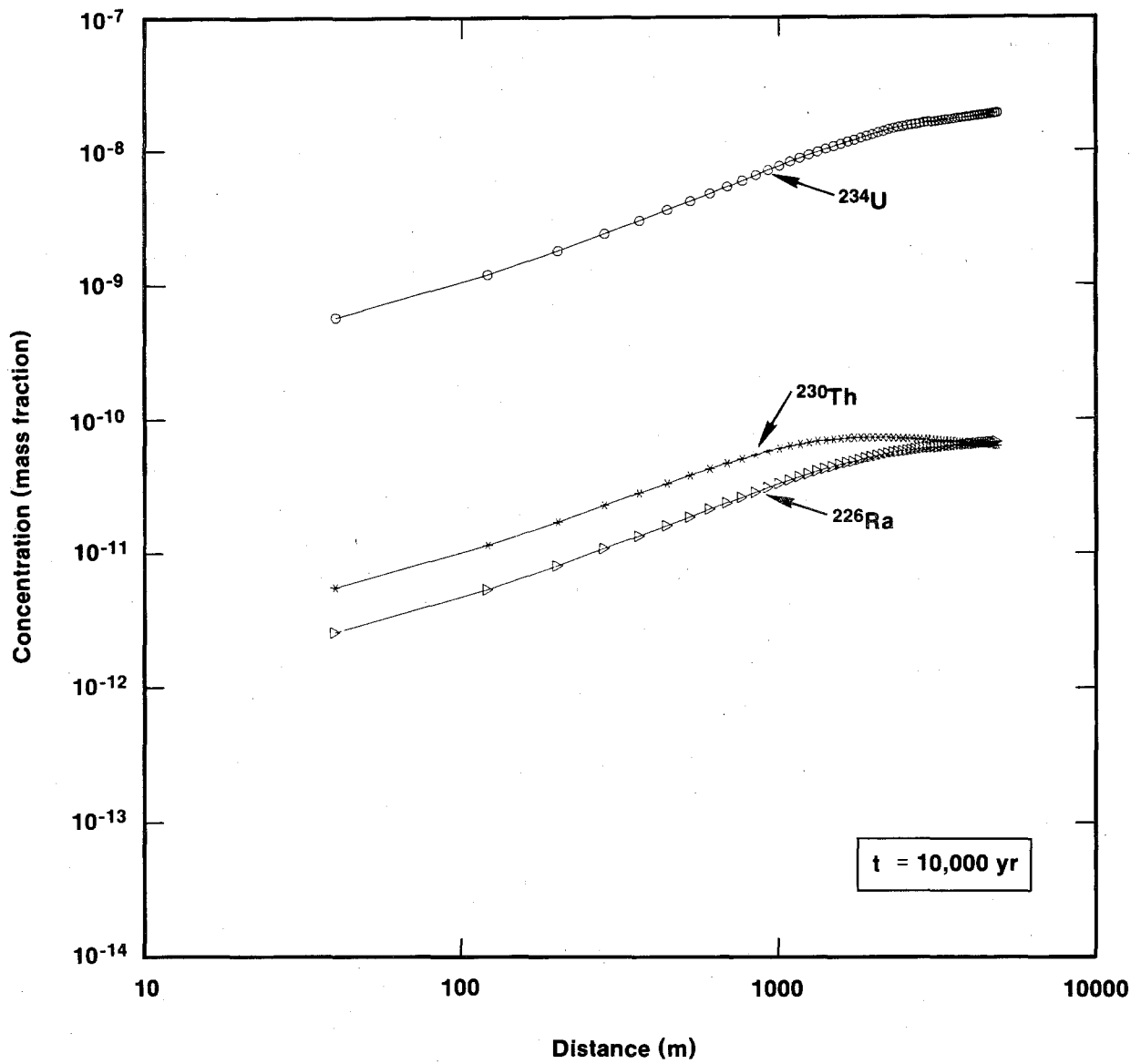
TRI-6330-104-0

Figure 7-19. Concentration profiles along the stream-tube centerline for the ^{239}Pu decay chain at 10,000 years, Case IIC.



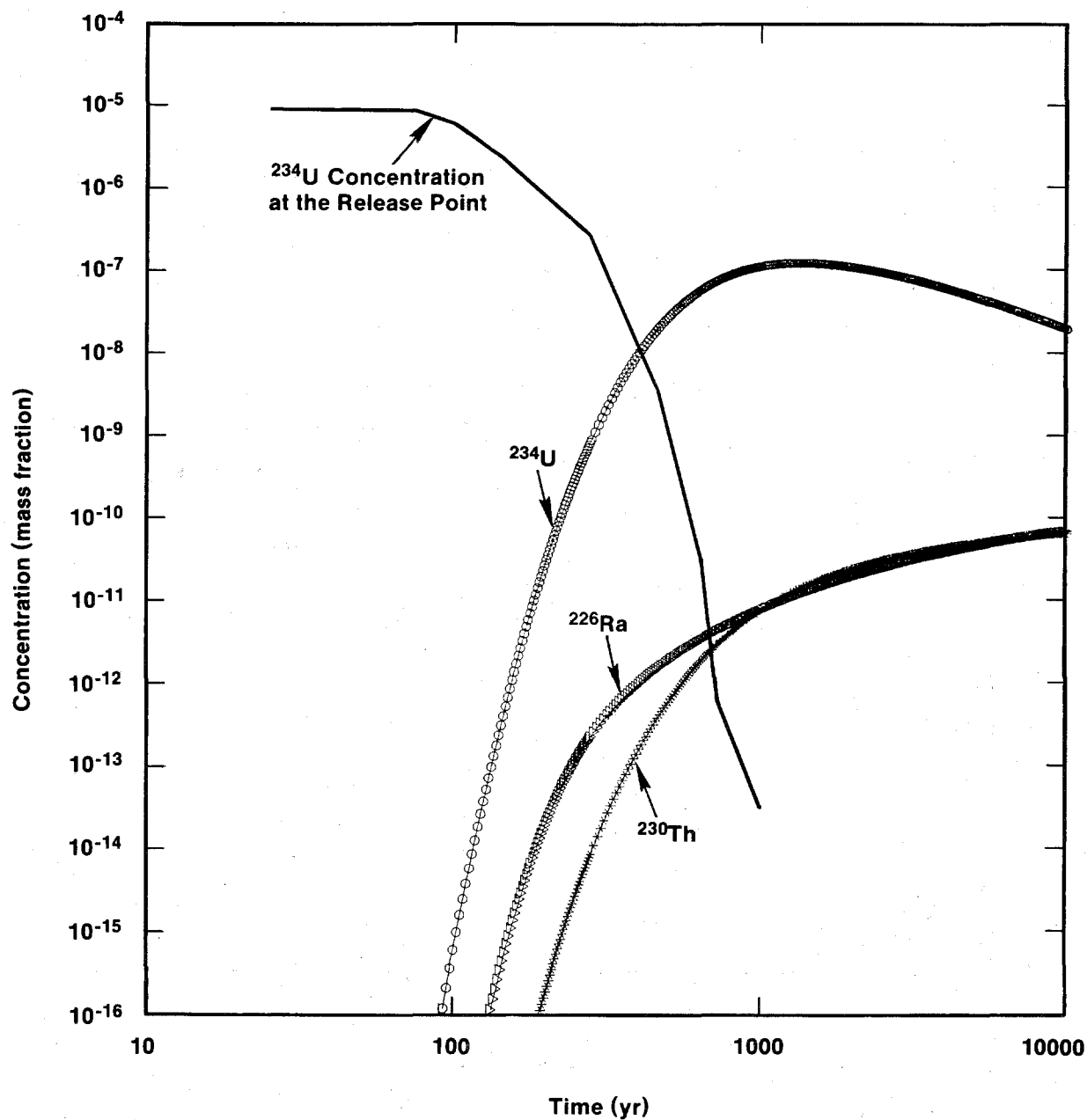
TRI-6330-105-0

Figure 7-20. Breakthrough and boundary concentrations for the ^{239}Pu decay chain, Case IIC.



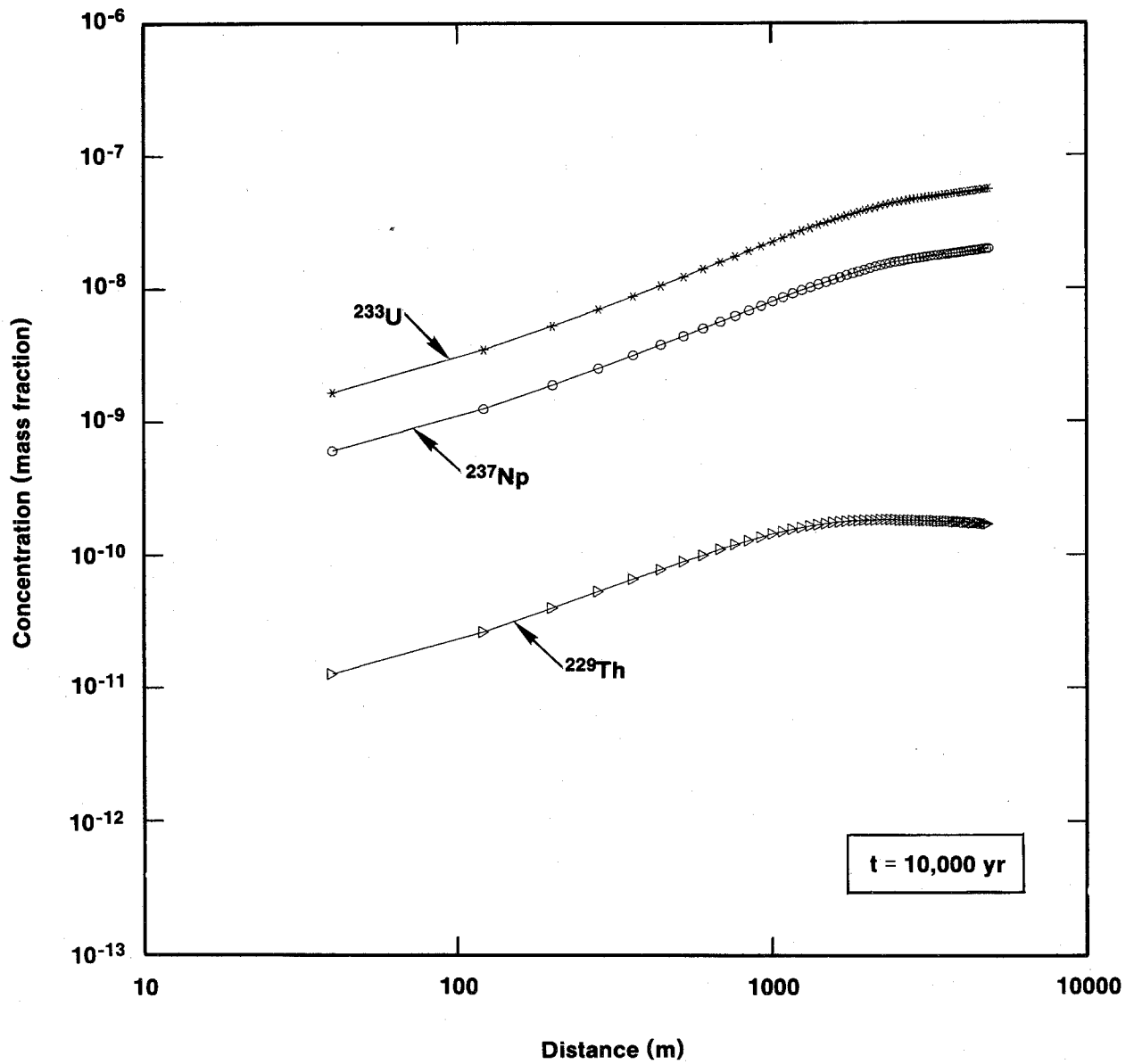
TRI-6330-106-0

Figure 7-21. Concentration profiles along the stream-tube centerline for the ^{238}Pu decay chain at 10,000 years, Case IIC.



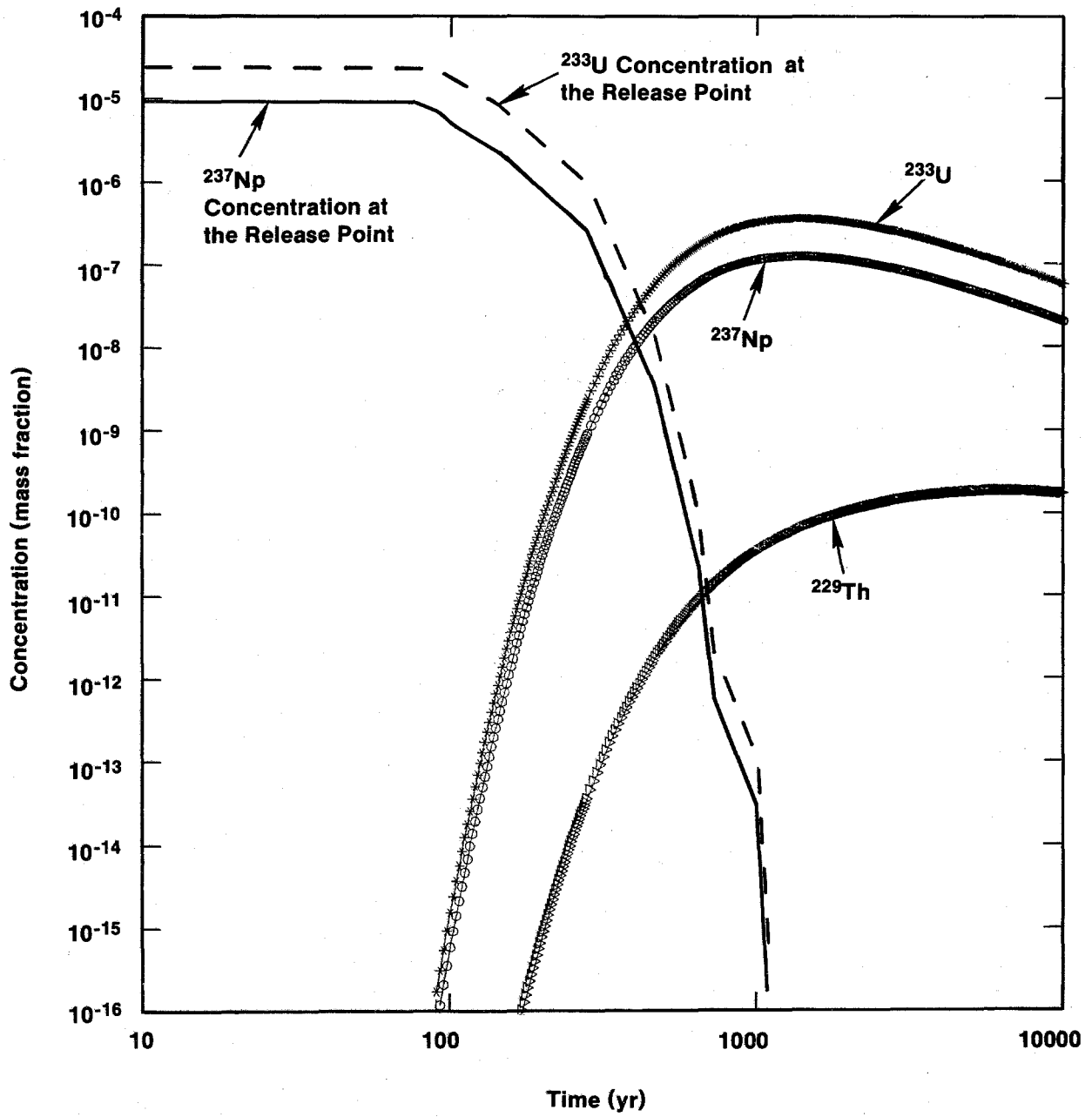
TRI-6330-107-0

Figure 7-22. Breakthrough and boundary concentrations for the ^{238}Pu decay chain, Case IIC.



TRI-6330-108-0

Figure 7-23. Concentration profiles along the stream-tube centerline for the ^{241}Am decay chain at 10,000 years, Case IIC.



TRI-6330-109-0

Figure 7-24. Breakthrough and boundary concentrations for the ^{241}Am decay chain, Case IIC.

The profiles show concentrations at 10,000 years as a function of distance along the plume centerline, and the breakthrough curves show concentrations as a function of time both at the point of release and at the stock well. These figures may be compared with Figures 7-5 through 7-14, which display similar results for Case IIB.

For ^{240}Pu , ^{234}U , and ^{237}Np , initial inventories are insufficient to reach the solubility limits. The same situation arises in Case IIB, but a major difference appears in the release-point concentrations. As a function of time, the concentrations in Case IIC show a much more rapid rate of decrease at the release point than in Case IIB. This results from the more rapid flushing action associated with the combined flow rate for the Salado and Castile Fms. ($q + Q$) as it passes through the repository. For ^{239}Pu , inventory depletion (below solubility limit) occurs in 482 years (Figure 7-20); it does not occur in 10,000 years for Case IIB (Figure 7-10). For ^{233}U , inventory depletion occurs in 88 years (Figure 7-22), compared with 817 years for Case IIB (Figure 7-12). Following depletion, the release-point concentration of ^{233}U drops much more rapidly for Case IIC, as noted above for ^{239}Pu .

A comparison of maximum concentration levels at the stock well yields the expected results: both concentrations and time-integrated concentrations are larger for Case IIC than for Case IIB. For some species, however, the increase is not as great as would be expected. Without mitigating circumstances, one would expect that, for the inventory constituents listed in Table E-4, the Case IIC concentrations would exceed those for Case IIB by a factor ranging from 5.1 to 76 (Table E-1). This factor, the source-dilution factor, characterizes the contaminant-release-rate enhancement of Case IIC relative to Case IIB.

Although its breakthrough curves (Figures 7-16 and 7-6) increase by a factor of only 4.1 at 10,000 years, stable Pb does show an increase in concentration at the stock well. The relatively short travel time required for concentration at the stock well to be similar to that at the release point, ~2,000 years, indicates that the concentration enhancement at 10,000 years should be much closer to the late-time value of 5.1 than to the early-

time value of 76. Furthermore, the controlling solubility levels, 116 mg/L (within the repository) for Case IIB and 54 mg/L (within the Culebra Dolomite) for Case IIC, indicate that the factor 4.1 should be normalized upward to $4.1 \times (116/54) = 8.8$, to put the concentration enhancement on the same basis as the dilution factor.

Increases in peak concentration of ^{237}Np and ^{233}U at the stock well (relative to Case IIB) are also less than one might expect, with factors of 3.0 and 2.5, respectively. The breakthrough curves (Figure 7-24) indicate that maximum concentrations at the release point have had adequate time to appear at the stock well, because concentrations at the stock well at 10,000 years are below their peak values. Furthermore, at the release point, maximum concentrations for Case IIC exceed those of Case IIB by factors of 82 for ^{237}Np and 57 for ^{233}U (cf. Figures 7-24 and 7-14). Nevertheless, in contrast to the case of stable Pb, such factors do not survive the transport from release point to stock well, because inventory dilution introduces peaks in the spatial profiles, the trailing edges of which are still evident at 10,000 years (Figure 7-23). These peaks, in turn, because of their relatively large concentration gradients, cause longitudinal dispersion. Dispersion, then, disperses mass longitudinally during transport, degrading the concentration-increase factors to 3.0 and 2.5, as noted above.

A comparison of time-integrated concentration levels for Cases IIC and IIB indicates uniformly higher peak concentrations for Case IIC. Enhanced flow within the repository yields correspondingly higher time-integrated concentrations at the stock well. Without examining the details, one would expect the factor of increase to lie in the range 5.1 and 76. Inventory depletion, however, can affect this factor. There are two different perspectives from which to view the effects of depletion.

On the one hand, depletion means that, in an attempt to achieve the expected increase in time-integrated concentrations, the repository has run out of inventory, thereby defeating the hydrologic system in its attempt to maintain enhanced concentration levels. On the other hand, depletion means that the full inventory of a given constituent, having been released earlier for Case IIC than for Case IIB, has more time to travel to the stock well.

This is particularly pertinent for the earlier depletions (817 years or less). Although this effect has not yet been quantified, a comparison of the figures shows that, for each species, the total mass reaching the stock well for Case IIC is significantly greater than for Case IIB.

For Cases IIA, IIB, IIC, and IID, the analysis assumes that the rapid decay of ^{241}Am prevents any significant transport to the stock well. The ^{241}Am inventory is converted to an equivalent inventory of its first daughter, ^{237}Np , and ^{241}Am is not explicitly treated. For Case IIA, this approximation is justified by the large number of half lives required to reach the boundary. For Cases IIB, IIC, and IID, travel times are much shorter as a consequence of the increased fracture component of the transport, and the effect of the ^{241}Am approximation requires comment.

The ^{241}Am assumption does affect the concentrations of ^{237}Np and its daughters (Figure 7-24). A peak concentration of $\sim 1.3 \times 10^{-7}$ occurs for ^{237}Np at $\sim 1,350$ years based on the composite inventory of the initial mass of ^{237}Np plus the mass from conversion of ^{241}Am . However, ^{241}Am is responsible for most of the composite inventory, and at that time only 80% of the ^{241}Am has actually converted to ^{237}Np . Thus, the concentrations given in Figure 7-24 are all conservatively high, and the concentration peak for ^{237}Np is overestimated by $>20\%$.

For ^{241}Am transport, the approximation is justified because there is no significant transport to the stock well. To demonstrate this aspect requires a detailed comparison of the properties of ^{241}Am and ^{237}Np . Transport properties of ^{241}Am differ greatly from those of ^{237}Np in two major respects. First, the half life of ^{241}Am , 432 years, is short compared with 10,000 years, and the half life of ^{237}Np , 2.14×10^6 years, is long. Second, for Cases IIB, IIC, and IID, the matrix distribution coefficient of ^{241}Am is 100 mL/g, much larger than that of ^{237}Np , 1 mL/g. These two differences in their properties cause substantial differences in the breakthrough of these two species. Figure 7-24 shows the breakthrough of ^{237}Np at the stock well. This curve can be transformed into a breakthrough curve for ^{241}Am by a simple approximation. The first step of the transformation shifts the time axis by a factor of 100 to account for the difference in K_d values. This shifts the concentrations

$>10^{-6}$ kg/kg, which in Figure 7-24 lie in the time regime $90 \leq t \leq 10,000$ years, to the time regime $9,000 \leq t \leq 10^6$ years. This step alone establishes an ^{241}Am concentration of 6×10^{-16} kg/kg as the upper bound for times $<10,000$ years. The second step of the transformation reduces concentrations to much lower values by correcting for radioactive decay. At 10,000 years, concentration reduction from decay amounts to a factor of 10^7 . Thus, these two transformations reduce the upper-bound ^{241}Am concentration over the 10,000-year period to 6×10^{-23} kg/kg.

7.3.5 Contaminant Transport for Case IID

The following points place the analysis of this section in perspective. Case IIA illustrates matrix-dominated transport in the Culebra Dolomite, assuming representative or base-case flow and transport behavior of both borehole and Culebra. The effect of matrix diffusion within the Culebra Dolomite proves to be so dominant that only minor waste concentrations reach the stock well. Thus, for Case IIA, variations of the uncertain repository parameters will not significantly influence the release. In contrast to Case IIA, Cases IIB, IIC, and IID all assume significant fracture transport within the Culebra Dolomite, by selecting Culebra parameter values that enhance transport in the fractures. In addition, long-term borehole permeability is assumed to be an order of magnitude greater than in Case IIA, with the result that early-time flow rates to the Culebra Dolomite are similarly increased (Figure 7-2). As a result, significant waste concentrations reach the stock well in less than 10,000 years in Cases IIB and IIC. Comparisons of the results of Cases IIB and IIC indicate that the uncertain repository parameters strongly influence the release to the stock well for degraded flow and transport properties outside the repository.

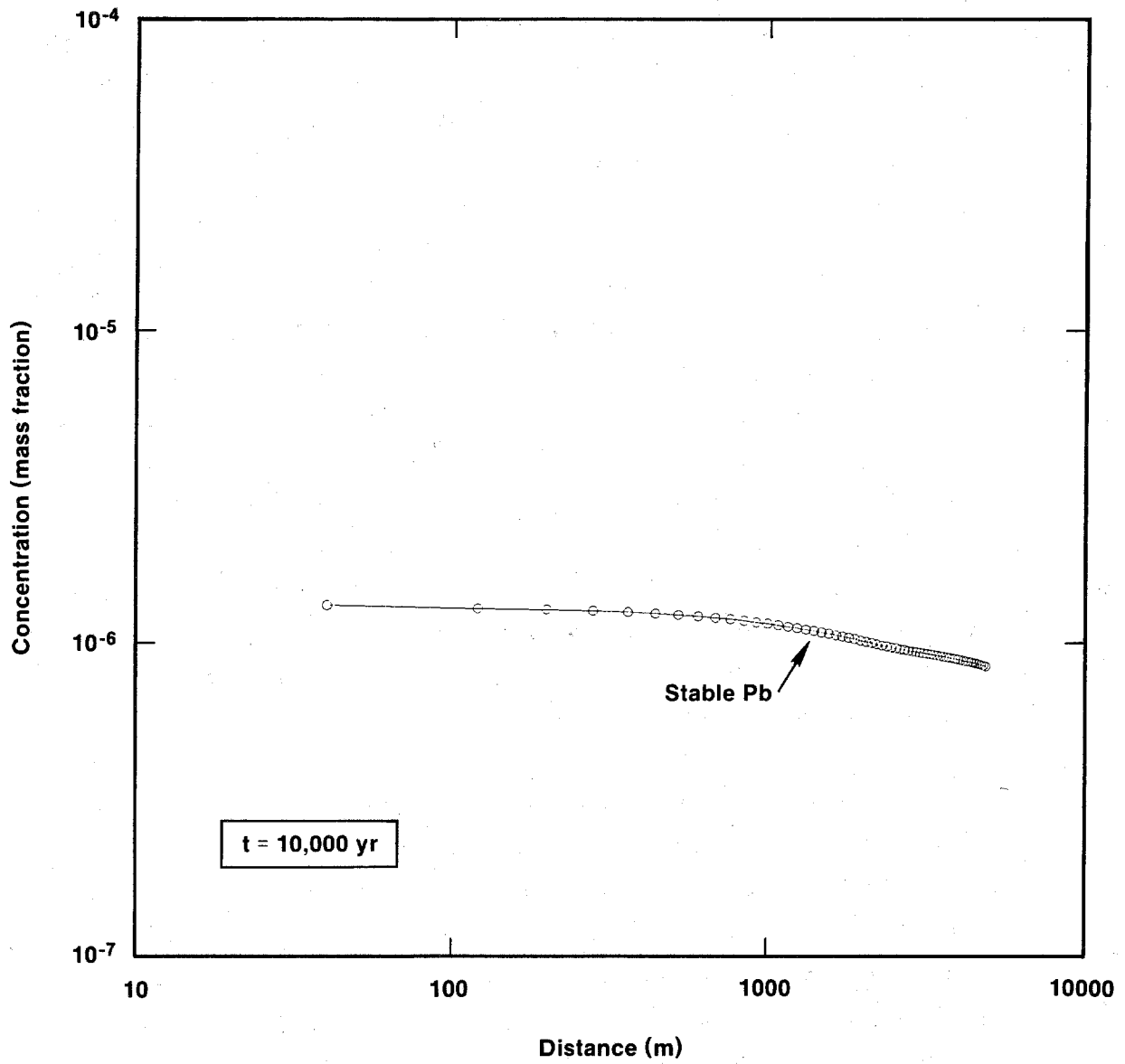
For both radioactive and stable species, the analysis considers two repository parameters. They are the extent of the repository region exposed to circulating fluids, panel or room, and the rate of flow of these fluids to and through the borehole, q or $q + Q$, where q is the Salado inflow and Q is the brine-reservoir discharge. For the radioactive species only, the analysis also considers variation in the solubility (10^{-4} or 10^{-6} molar).

Of the cases with fracture-enhanced transport, Case IIC has the highest concentrations at the stock well. It assumes both the largest reasonable repository region, a panel, and the largest rate of flow within the repository, $q + Q$. Consequently, Case IIC yields the largest time-integrated concentrations at the stock well, and, in spite of relatively large effects of dispersion, the largest peak concentrations.

Case IID, while assuming the same degraded flow and transport properties outside the repository as were assumed for Cases IIB and IIC, assumes a generic engineering modification of waste and backfill that maintains radionuclide solubility at 10^{-6} molar (similar to Case IIA) and reduces permeability sufficiently to eliminate mixing of Castile brines within the waste and limit Salado brine inflow to that estimated for a room, $0.1 \text{ m}^3/\text{yr}$. In a sense, Case IID is the "best" of the fracture-enhanced cases with respect to concentration levels at the stock well. It cannot match the small stock-well concentrations of Case IIA, but, among the cases with fracture-enhanced transport, Case IID provides both the smallest concentration and the smallest time-integrated concentration at the stock well. As in Case IIA, the inventory is not depleted for any waste species.

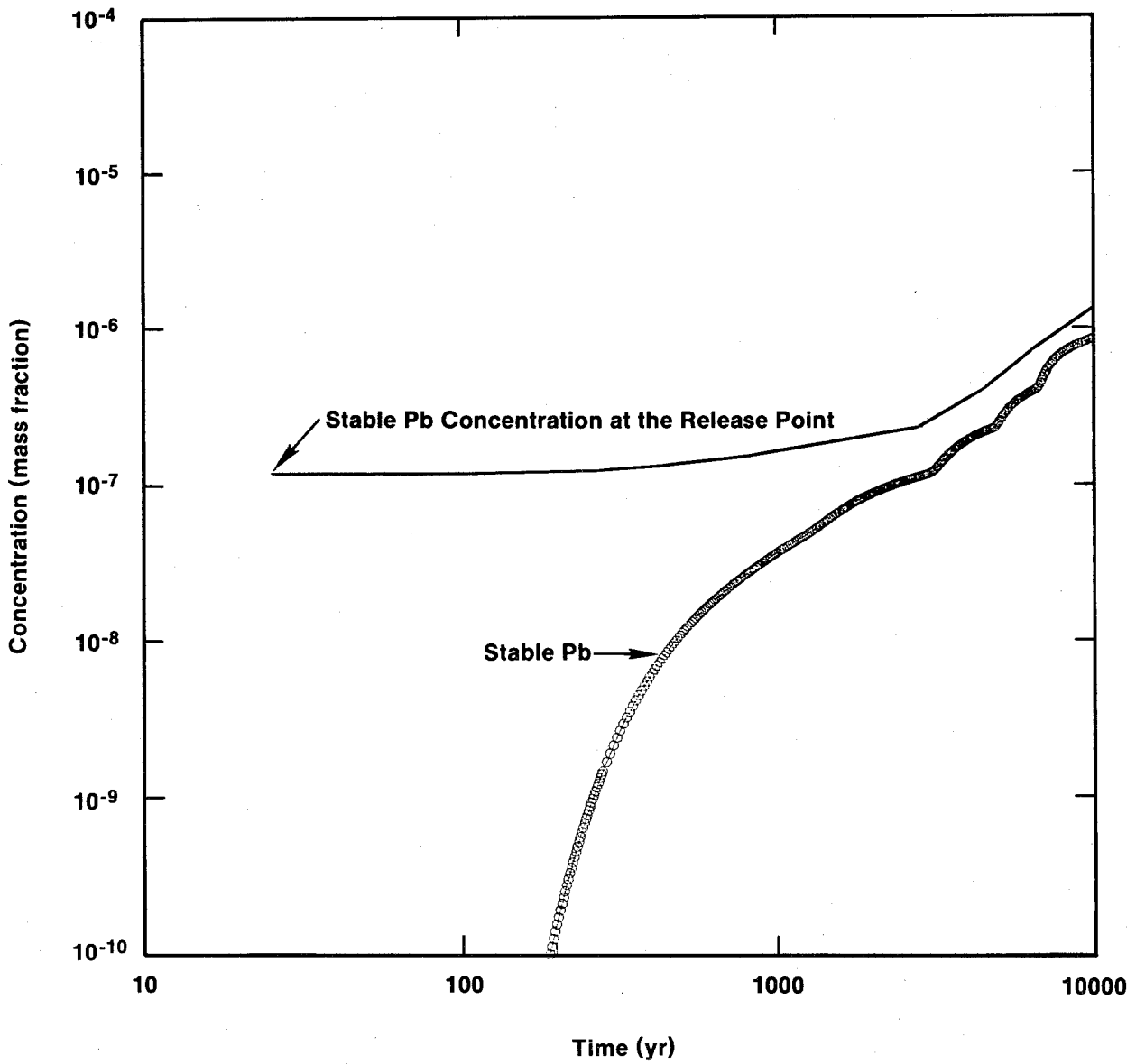
Figures 7-25 through 7-34 show the results for Case IID. When compared with the results of Case IIB, the calculated concentrations of the radionuclides for Case IID evidence some of the effects of the factor-of-100 reduction in solubility and the factor-of-13 reduction in Salado-inflow rate to the borehole. This is particularly true for release-point concentrations, because, of the calculated concentrations, these are altered least by radioactive transformations and transport mechanisms. For radioactive species with insufficient inventories to reach the solubility limits in Case IIB, the full factor-of-1,300 reduction could not be achieved in Case IID, even for the release-point concentrations. The stable Pb concentrations at the release point show only the factor-of-13 reduction, because Pb solubility is the same in Cases IIB and IID (cf. Figures 7-26 and 7-6).

A comparison of results for Case IID with those of IIC is straightforward for stable Pb (Figures 7-15, 7-16, 7-25, and 7-26). Concentrations of stable Pb in Case IID are reduced by a net factor of $(54/116) \times (Q+q)/q$. The first



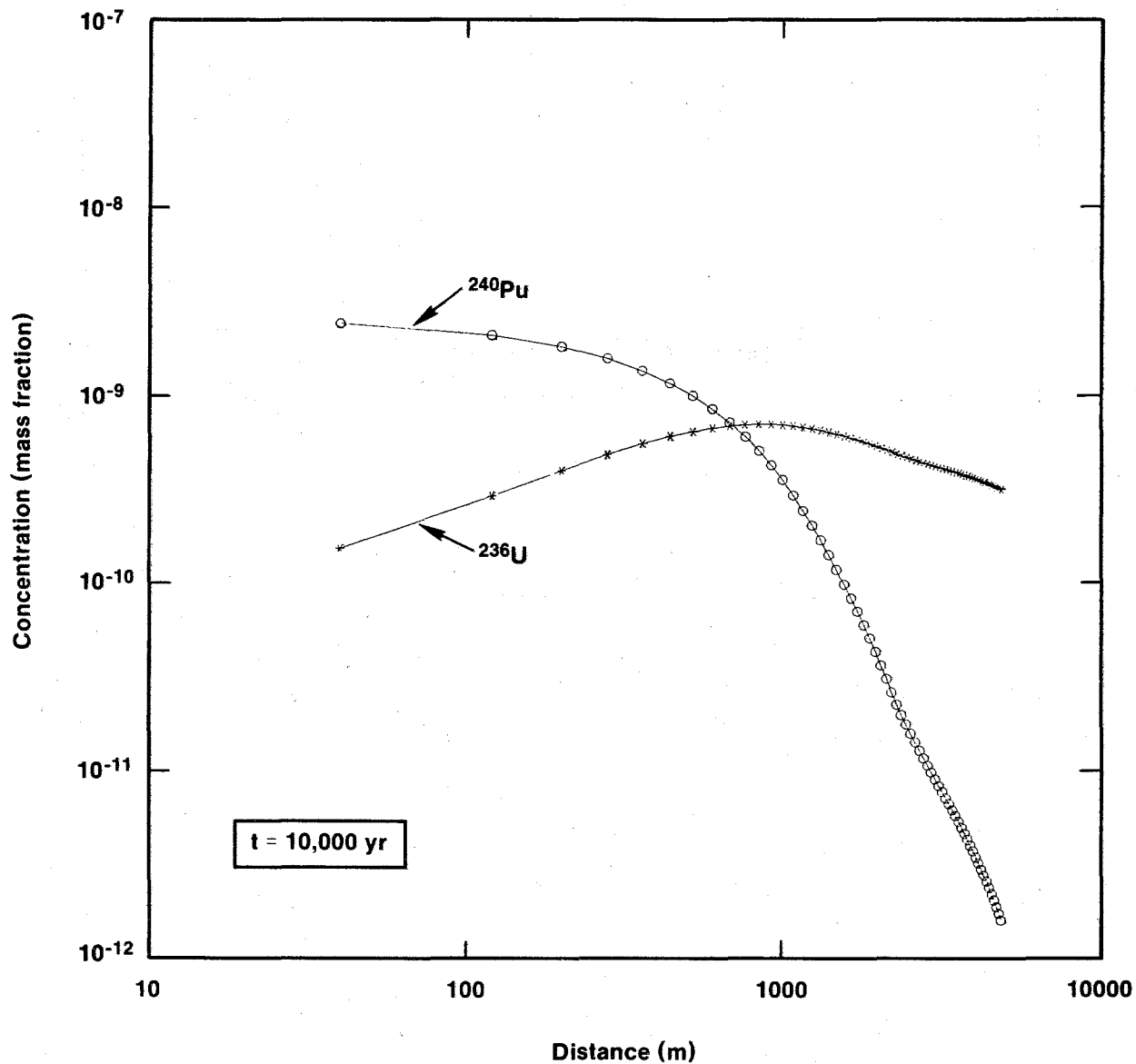
TRI-6330-113-0

Figure 7-25. Concentration profile along the stream-tube centerline for stable Pb at 10,000 years, Case IID.



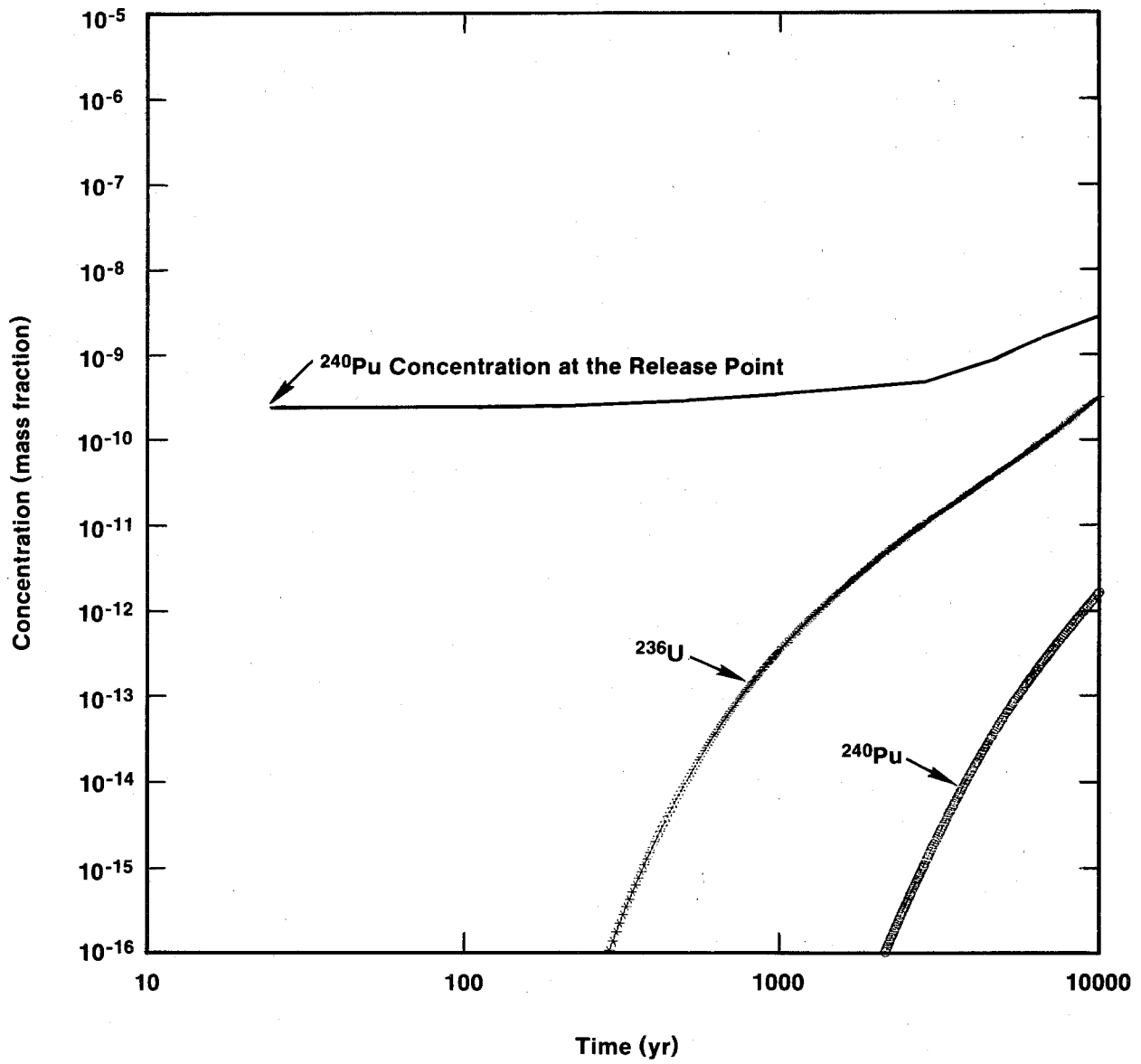
TRI-6330-114-0

Figure 7-26. Breakthrough and boundary concentrations for stable Pb as a function of time, Case IID.



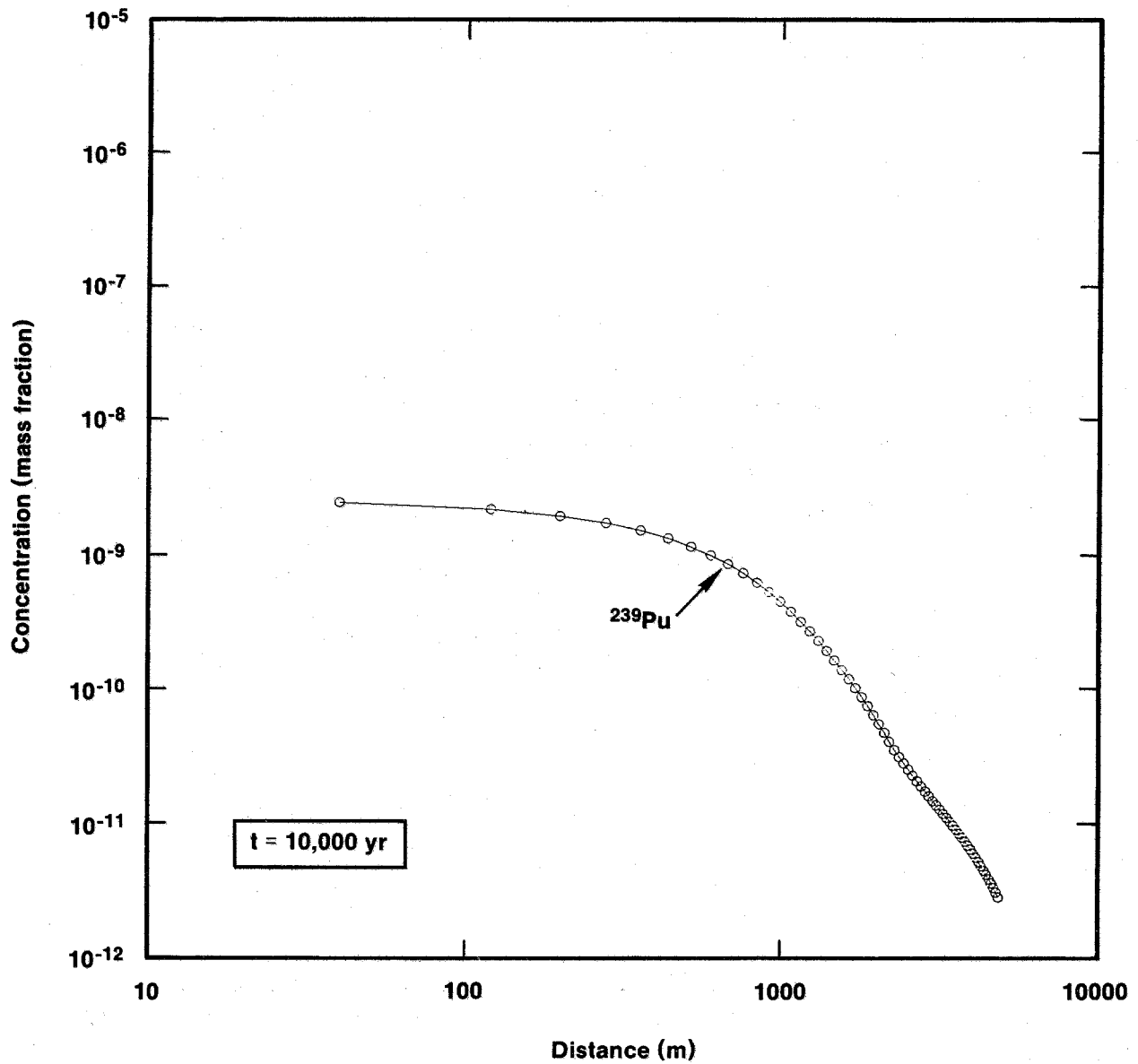
TRI-6330-115-0

Figure 7-27. Concentration profiles along the stream-tube centerline for the ^{240}Pu decay chain at 10,000 years, Case IID.



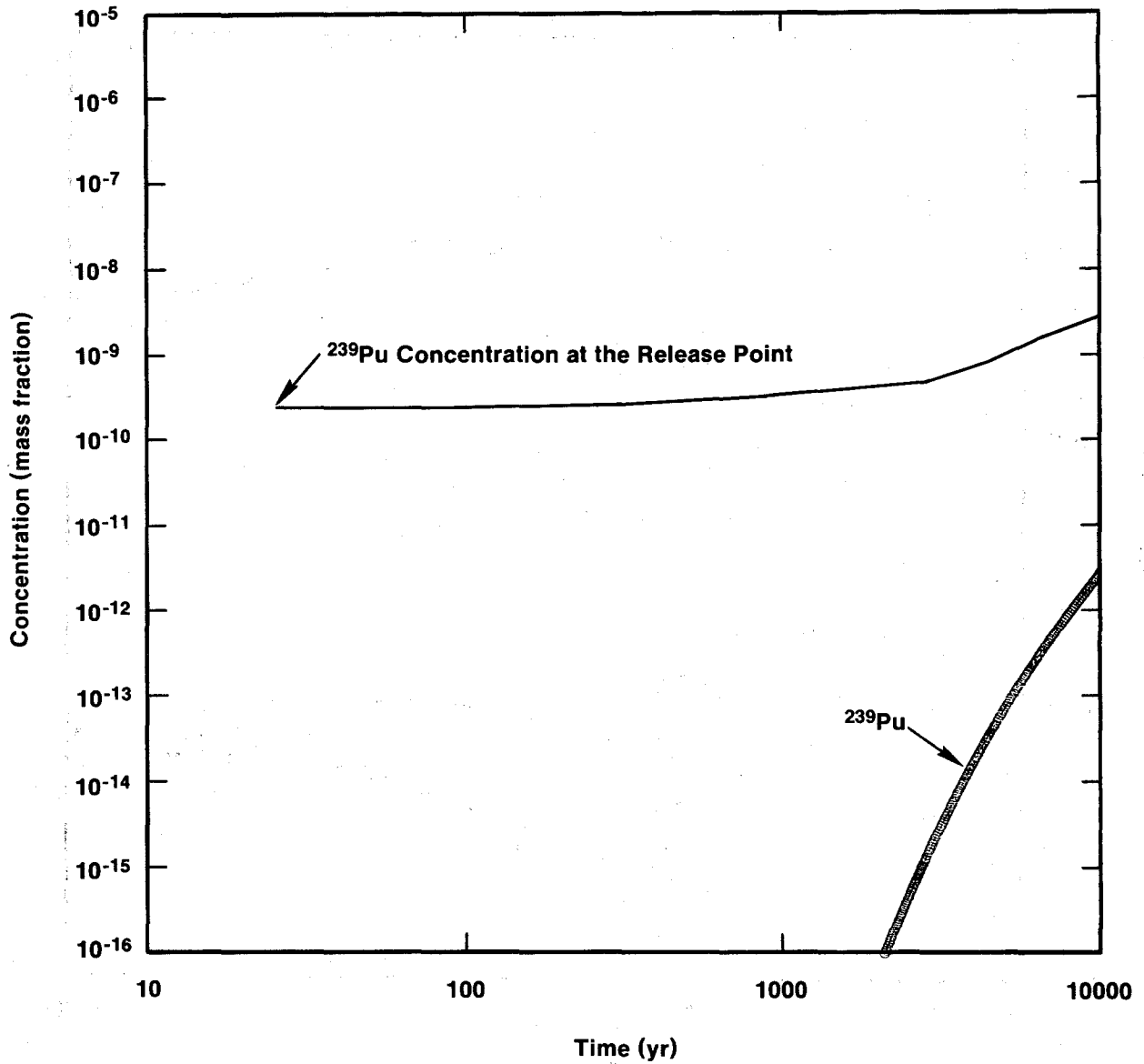
TRI-6330-116-0

Figure 7-28. Breakthrough and boundary concentrations for the ^{240}Pu decay chain, Case IID.



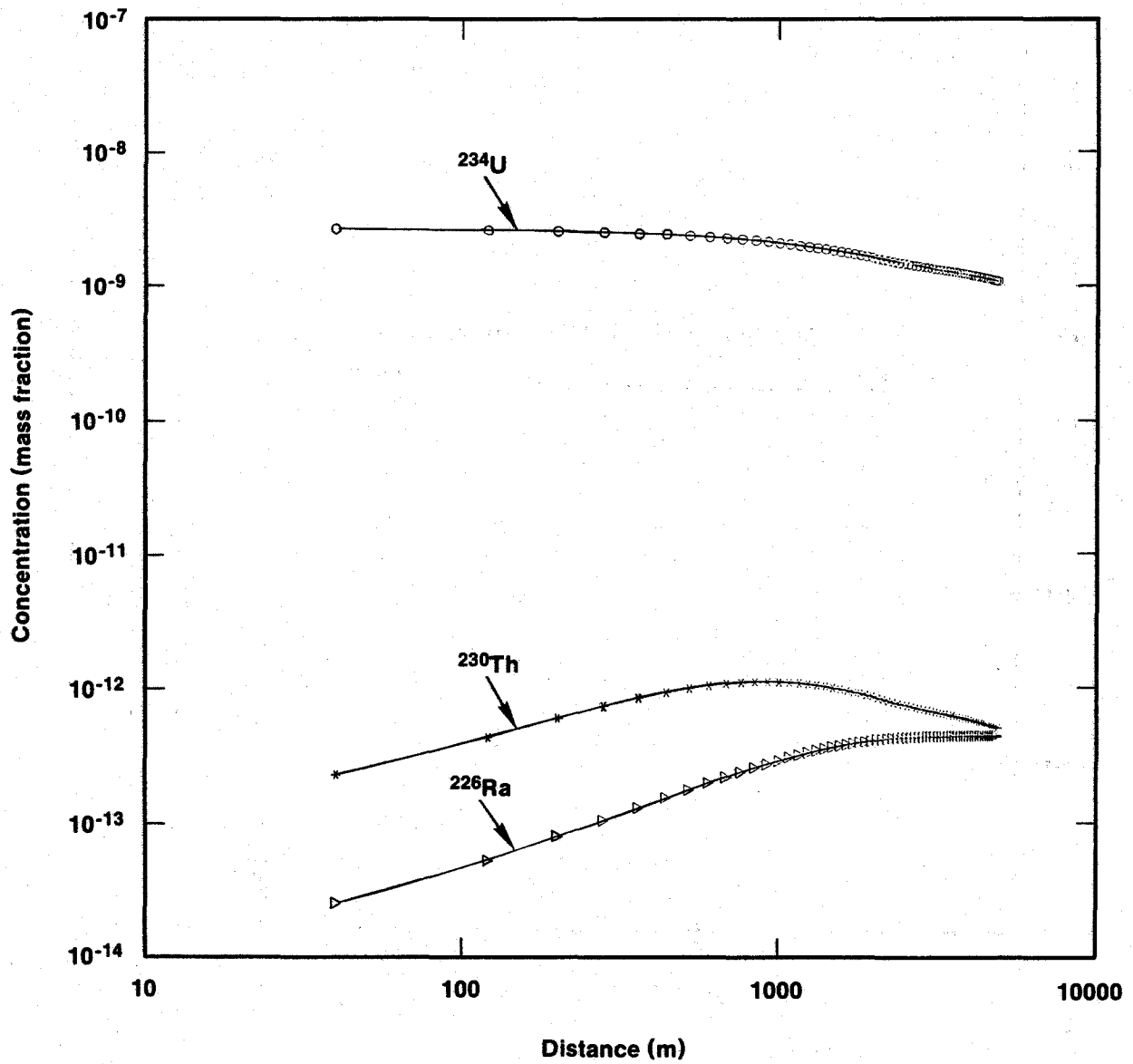
TRI-6330-117-0

Figure 7-29. Concentration profiles along the stream-tube centerline for the ^{239}Pu decay chain at 10,000 years, Case IID.



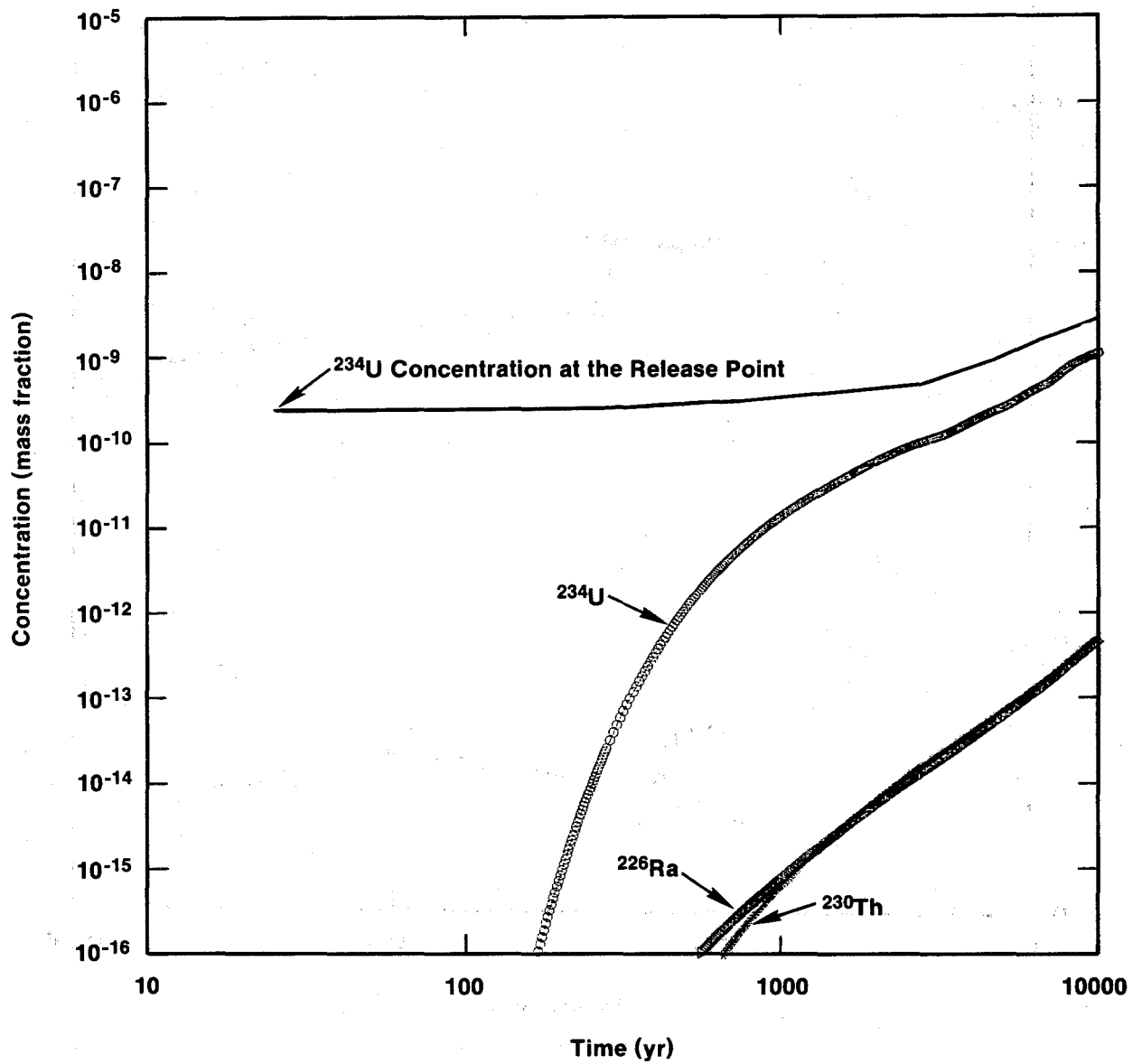
TRI-6330-118-0

Figure 7-30. Breakthrough and boundary concentrations for the ^{239}Pu decay chain, Case IID.



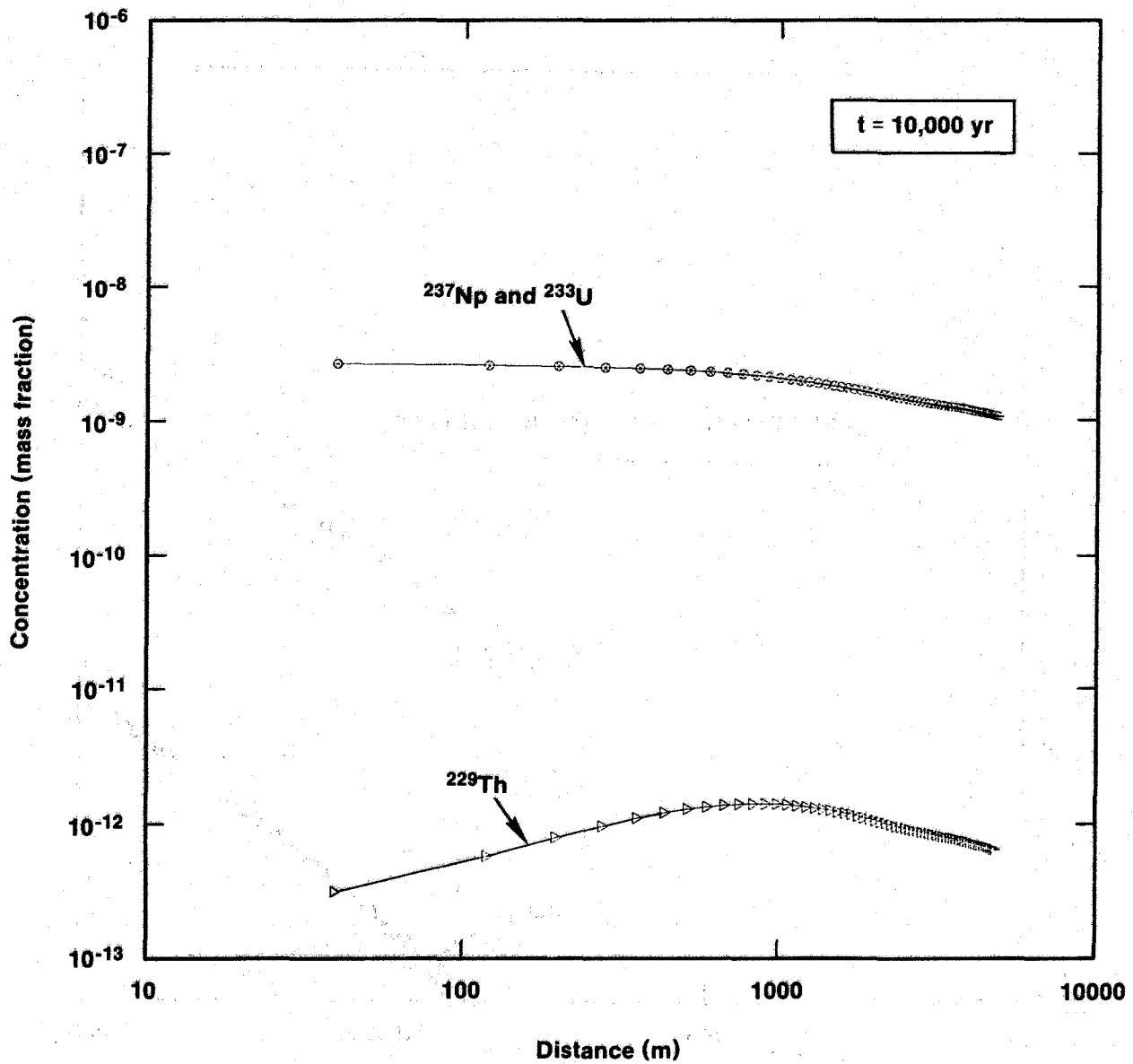
TRI-6330-119-0

Figure 7-31. Concentration profiles along the stream-tube centerline for the ^{238}Pu decay chain at 10,000 years, Case IID.



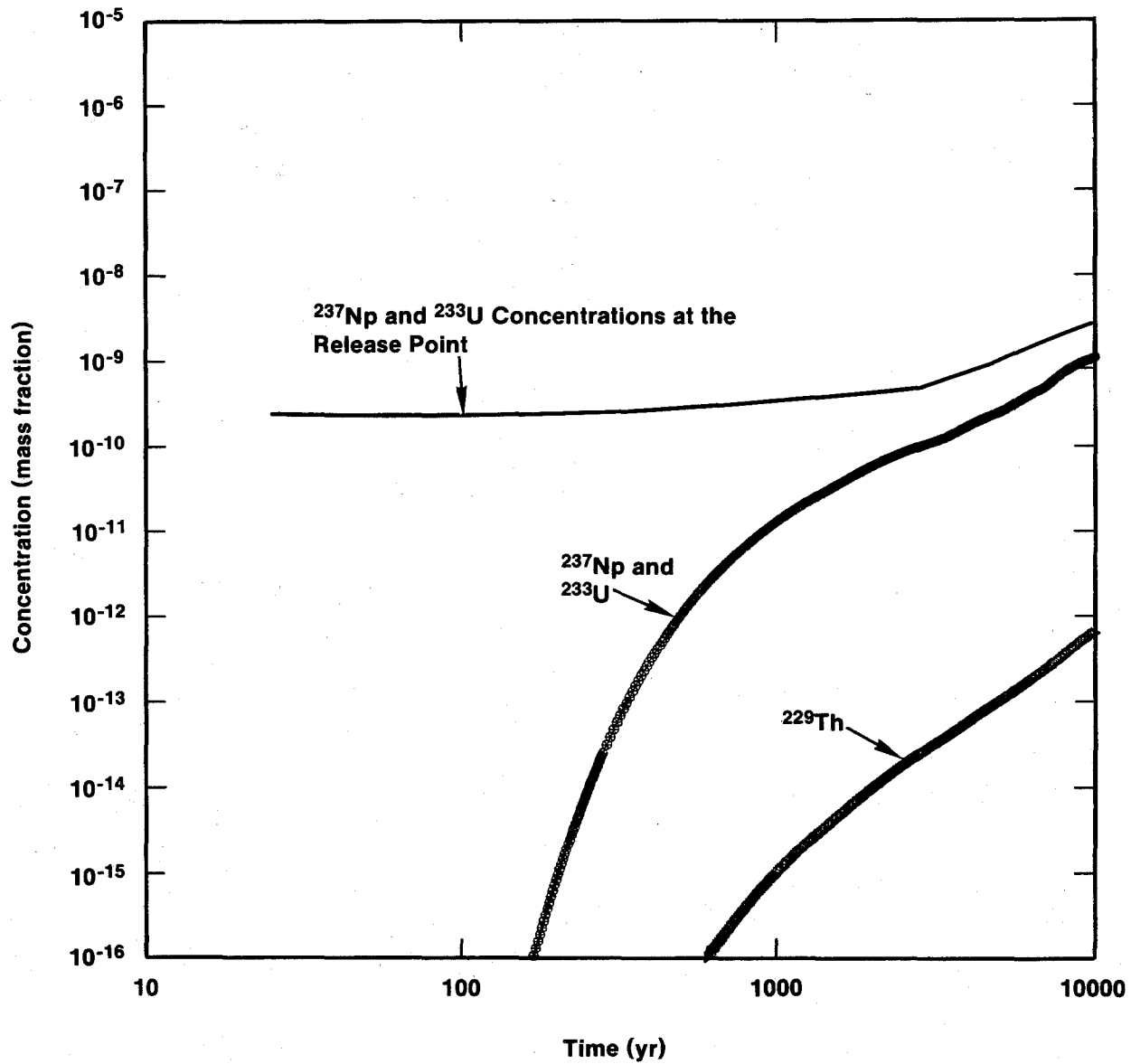
TRI-6330-120-0

Figure 7-32. Breakthrough and boundary concentrations for the ^{238}Pu decay chain, Case IID.



TRI-6330-121-0

Figure 7-33. Concentration profiles along the stream-tube centerline for the ^{241}Am decay chain at 10,000 years, Case IID.



TRI-6330-122-0

Figure 7-34. Breakthrough and boundary concentrations for the ²⁴¹Am decay chain, Case IID.

factor accounts for the difference in the controlling solubilities between the two cases (Culebra Dolomite in IIC, repository in IID), and the second factor accounts for the much greater dilution by brine-reservoir fluids in Case IID. The latter varies from a maximum of 980 at 150 years to a minimum of 55 at 10,000 years (Table E-1). For the radioactive species, Case-IID solubilities are reduced by a factor of 100 relative to Cases IIB and IIC, and the accessible volume of waste is reduced from a panel to a room. Concentrations input to the Culebra Dolomite are further diluted by a factor of $(Q+q)/q$ (Table E-1). The effects of early inventory depletion and dispersion in Case IIC make quantitative comparison difficult. Qualitatively, however, comparison of Figures 7-17 through 7-24 with Figures 7-27 through 7-34 shows that calculated concentrations for Case IID are substantially lower than those of Cases IIB and IIC.

7.3.6 Releases From a Stock Pond (Case II)

The radionuclides released to the hypothetical stock pond ultimately give rise to radiation doses to human beings who consume contaminated beef. The selection of the stock-well location is described in Section 5.3. Sections 7.3.2 through 7.3.6 discuss the concentrations of the radionuclides at this location with time. The concentrations at 10,000 years and at all peak arrival times were used for dose calculations. At the end of the 10,000-year record for Cases IIA and IID, each concentration is increasing with time; the last entry (the highest value) was used for dose calculations. The time of intrusion is uncertain, but the resulting concentrations at the stock well 10,000 years after intrusion could not be higher than these 10,000-year values, because later intrusion would result in a lower source term. For Cases IIB and IIC, some radionuclides have peak arrival times less than 10,000 years, while other radionuclides are still increasing at 10,000 years. Therefore, several human-exposure calculations were performed. One used the 10,000-year entries and the others used the peak-arrival time entries. For Cases IIA, IIB, IIC, and IID, these concentrations are given in Table 7-9.

In the region around the well location, one head of cattle requires about 100,000 m² of range for grazing; eight head of cattle can graze on a single section. This calculation assumes that there is one section with eight head

Table 7-9. Radionuclide Concentrations in Culebra Brine at the Hypothetical Stock Well Location. (Concentrations calculated here are at depth in the Culebra Dolomite, not in the stock pond).

Radio-nuclide	kg-nuc./kg-brine	Spec. Act.(Ci/g)	Ci-nuc./liter	
<u>Case IIA</u> (at 10,000 years)				
Ra-226	2.02×10^{-15}	9.89×10^{-1}	6.91×10^{-14}	$\rho = 1.1$
Pb-210	2.82×10^{-17}	7.63×10^1	7.45×10^{-14}	
<u>Case IIB</u> (at 10,000 years)				
Np-237	3.52×10^{-8}	7.05×10^{-4}	7.56×10^{-9}	$\rho = 1.1$
Pb-210	5.05×10^{-13}	7.63×10^1	1.17×10^{-8}	
Pu-239	3.51×10^{-09}	6.22×10^{-2}	6.65×10^{-8}	
Pu-240	4.51×10^{-10}	2.28×10^{-1}	3.13×10^{-8}	
Ra-226	3.62×10^{-11}	9.89×10^{-1}	1.09×10^{-8}	
Th-229	1.53×10^{-10}	2.13×10^{-1}	9.92×10^{-9}	
Th-230	3.78×10^{-11}	2.02×10^{-2}	2.33×10^{-10}	
U-233	1.23×10^{-7}	9.68×10^{-3}	3.63×10^{-7}	
U-234	3.34×10^{-8}	6.25×10^{-3}	6.36×10^{-8}	
U-236	3.24×10^{-8}	6.47×10^{-5}	6.39×10^{-10}	
<u>Case IIC</u> (at 1,345 years)				
Np-237	1.26×10^{-7}	7.05×10^{-4}	2.71×10^{-8}	$\rho = 1.1$
Pb-210	1.64×10^{-13}	7.63×10^1	3.81×10^{-9}	
Pu-239	1.11×10^{-13}	6.22×10^{-2}	2.10×10^{-12}	
Pu-240	6.18×10^{-14}	2.28×10^{-1}	4.29×10^{-12}	
Ra-226	1.18×10^{-11}	9.89×10^{-1}	3.55×10^{-9}	
Th-229	6.17×10^{-11}	2.13×10^{-1}	4.00×10^{-9}	
Th-230	1.39×10^{-11}	2.02×10^{-2}	8.55×10^{-11}	
U-233	3.61×10^{-7}	9.68×10^{-3}	1.06×10^{-6}	
U-234	1.21×10^{-7}	6.25×10^{-3}	2.30×10^{-7}	
U-236	3.42×10^{-8}	6.47×10^{-5}	6.74×10^{-10}	
<u>Case IID</u> (at 10,000 years)				
Np-237	1.08×10^{-9}	7.05×10^{-4}	2.32×10^{-10}	$\rho = 1.1$
Pb-210	6.14×10^{-15}	7.63×10^1	1.43×10^{-10}	
Pu-239	2.76×10^{-12}	6.22×10^{-2}	5.23×10^{-11}	
Pu-240	1.61×10^{-12}	2.28×10^{-1}	1.12×10^{-10}	
Ra-226	4.40×10^{-13}	9.89×10^{-1}	1.33×10^{-10}	
Th-229	6.37×10^{-13}	2.13×10^{-1}	4.13×10^{-11}	
Th-230	5.04×10^{-13}	2.02×10^{-2}	3.10×10^{-12}	
U-233	1.07×10^{-9}	9.68×10^{-3}	3.16×10^{-9}	
U-234	1.07×10^{-9}	6.25×10^{-3}	2.04×10^{-9}	
U-236	3.11×10^{-10}	6.47×10^{-5}	6.13×10^{-12}	

and one stock pond providing water for all eight. Each head requires about $0.049 \text{ m}^3/\text{d}$, or $0.394 \text{ m}^3/\text{d}$ for all eight. Stock ponds are typically 0.3 m deep and are large enough to store ten days' worth of water, 3.94 m^3 . If the pond is 0.3 m deep, the surface area is about 12.9 m^2 . Evaporation in this area is about 2 m/yr, and rainfall is about 0.2 m/yr, for a net loss of $23.6 \text{ m}^3/\text{yr}$. The cattle consume $143 \text{ m}^3/\text{yr}$. The total loss of water from the pond is $167 \text{ m}^3/\text{yr}$, which is the volume of water that must be pumped. On a daily basis, $0.072 \text{ m}^3/\text{d}$ evaporate, $0.394 \text{ m}^3/\text{d}$ are consumed by the cattle, $0.007 \text{ m}^3/\text{d}$ enter by rainfall, and $0.458 \text{ m}^3/\text{d}$ must be pumped from the Culebra Dolomite.

When the pump is running, ground water flows radially through the Culebra Dolomite toward the pipe. If pumping occurs twice in the 10-day storage period, 2.29 m^3 must be pumped each time. All ground water is assumed to be pumped from the Culebra Dolomite. The volume pumped during a year would drain a cylindrical disk in the Culebra Dolomite with a radius that is very small compared with the spatial increment used in the transport calculation. Therefore, it is assumed that pumping the stock well does not disturb the upstream flow field. Furthermore, the well is located in the contaminated plume, so that ground water is pumped directly to the stock pond without dilution by uncontaminated ground water from outside the plume. The contaminated water is pumped at an average rate of $0.458 \text{ m}^3/\text{d}$. Radionuclides are lost by consumption and infiltration, but the concentration in the pond increases to a steady value by evaporation. The steady-state concentration is the input concentration from the pipe multiplied by 1.16.

Using pond concentrations calculated from data in Table 7-9 and the data in Tables 7-10 and 7-11, the estimated exposure to an individual consuming 86 g/d of contaminated beef has been calculated for Cases IIA, IIB, IIC, and IID using the procedure outlined in Table 7-12. Estimated doses are shown in Table 7-13 as committed effective dose equivalents. The 50-year committed effective dose equivalents (CEDE's) are 2.1×10^{-4} mrem for Case IIA at 10,000 years, 72 mrem for Case IIB at 10,000 years, 130 mrem for Case IIC at 1,345 years, and 0.91 mrem for Case IID at 10,000 years.

Data applicable to dose calculations were gathered from several readily available sources. Table 7-14 indicates that the variation in estimated dose

Table 7-10. Water-to-Food-Product Transfer Factors

<u>Nuclide</u>	<u>d/kg-beef¹</u>	<u>d/kg-beef³</u>
Np-237	$5.0 \times 10^{-6}{}^2$	5.5×10^{-5}
Pb-210	4.0×10^{-4}	3.0×10^{-4}
Pu-239	1.0×10^{-6}	5.0×10^{-7}
Pu-240	1.0×10^{-6}	5.0×10^{-7}
Ra-226	5.1×10^{-4}	2.5×10^{-4}
Th-229	2.0×10^{-4}	6.0×10^{-6}
Th-230	2.0×10^{-4}	6.0×10^{-6}
U-233	3.4×10^{-4}	2.0×10^{-4}
U-234	3.4×10^{-4}	2.0×10^{-4}
U-236	3.4×10^{-4}	2.0×10^{-4}

NOTES: 1. Data are from Table 5.37, Till and Meyer (1983). These forage-to-food-produce data were used as water-to-food-produce data as recommended by NRC (1976). Cattle consumption per head is 50 (NRC, 1976)

2. Value for milk was used (Till and Meyer, 1983, Table 5.36).

3. Data are from Baes et al., 1984.

Table 7-11. 50-Year Committed Dose Equivalent Factors

Ingestion (1)

<u>Nuclide</u>	<u>CDE (Sv/Bq)</u>	<u>CEDE (REM/μCI)²</u>
Np-237	1.7×10^{-7}	3.90
Pb-210	1.7×10^{-6}	5.10
Pu-239	2.3×10^{-7}	4.30
Pu-240	2.3×10^{-7}	4.30
Ra-226	6.8×10^{-7}	1.10
Th-229	2.1×10^{-6}	3.50
Th-230	3.2×10^{-7}	0.53
U-233	4.9×10^{-8}	0.27
U-234	4.9×10^{-8}	0.26
U-236	4.6×10^{-8}	0.25

Note: 1. All data are from U.S. DOE (1985).

2. All data are from U.S. DOE (1988a).

Table 7-12. Sample Calculation for Np-237, Case IIC, 1345 Years

Multiplication Factors	Values
Culebra Brine Concentration (kg/kg)	1.26 x 10 ⁻⁷
	x
Brine Density (g/L)	1.1 x 10 ³
	x
Specific Activity (Ci/g)	7.05 x 10 ⁻⁴
	x
Lateral Dispersion Factor (One)	1/4.2
	x
Equilibrium Pond Concentration Factor (One)	1.164
	x
Cattle Brine Ingestion Rate (L/d)	50
	x
Transfer Factor (d/kg)	5.5 x 10 ⁻⁵
	x
Human Beef Ingestion Rate (kg/d)	0.086
	x
1-Year Ingestion Period (d)	3.65 x 10 ²
	x
Unit Conversion (μ C/Ci)	1.0 x 10 ⁶
	x
Committed Effective Dose Equivalent Factor (Sv/Bq)	3.9
	x
Unit Conversion (mrem/Rem)	1000
	=
50-Year Committed Effective Dose Equivalent (mrem)	9.11

using a wide range of assumptions is less than an order of magnitude. For Case IIC at 1,345 years, estimated doses were calculated using CEDE's for both soluble and insoluble chemical forms of the radionuclides; insoluble CDE's for bone; transfer factors (Baes et al., 1984; Till and Meyer, 1983); and ingestion rates for meat consumption of 86 g/d (NCRP, 1984) and 206 g/d (Till and Meyer, 1983).

The assessments considered to be the most realistic are those yielding 50-year committed dose equivalents of 380 and 220 mrem, slightly higher than the dose of 130 mrem calculated using the DOE CEDE's (Table 7-13). Because bone is the target tissue for the radionuclides considered in this assessment and the chemical forms of those radionuclides will likely be insoluble, bone

Table 7-13. Maximum Doses Received by a Person Through the Contaminated Beef Pathway, 86 g/d Beef Ingestion¹

<u>Committed Effective Dose Equivalent After 1-Year Exposure (mrem/50 yr)</u>			
	<u>Nuclide</u>	<u>mrem</u>	<u>Sum²</u>
<u>Case IIA</u>	Ra-226	3.0×10^{-5}	
	Pb-210	1.8×10^{-4}	2.1×10^{-4}
<u>Case IIB</u>	Np-237	2.5	
	Pb-210	2.8×10^1	
	Pu-239	2.2×10^{-1}	
	Pu-240	1.1×10^{-1}	
	Ra-226	4.7	
	Th-229	3.3×10^{-1}	
	Th-230	1.2×10^{-3}	
	U-233	3.1×10^1	
	U-234	5.2	
	U-236	5.0×10^{-2}	7.2×10^1
<u>Case IIC³</u> <u>1.345 years</u>	Np-237	9.1	
	Pb-210	9.2	
	Pu-239	7.1×10^{-6}	
	Pu-240	1.4×10^{-5}	
	Ra-226	1.5	
	Th-229	1.3×10^{-1}	
	Th-230	4.3×10^{-4}	
	U-233	9.0×10^1	
	U-234	1.9×10^1	
	U-236	5.3×10^{-2}	1.3×10^2
<u>Case IID</u>	Np-237	7.8×10^{-2}	
	Pb-210	3.4×10^{-1}	
	Pu-239	1.8×10^{-4}	
	Pu-240	3.8×10^{-4}	
	Ra-226	5.7×10^{-2}	
	Th-229	1.4×10^{-3}	
	Th-230	1.5×10^{-5}	
	U-233	2.7×10^{-1}	
	U-234	1.7×10^{-1}	
	U-236	4.8×10^{-4}	9.1×10^{-1}

1. Values are based on CEDE's for soluble or insoluble forms of radionuclides, depending on availability of data.
2. 206 g/d beef ingestion: IIA, 5.0×10^{-4} mrem/50 yr; IIB, 1.7×10^2 mrem/50 yr; IIC, 3.1×10^2 mrem/50 yr; IID, 2.2 mrem/50 yr.
3. Am-241 was not included in the transport calculations.
See Section 7.3.4

Table 7-14. Comparison of Estimated 50-Year CEDE's Using Data from Various Sources,
Case IIC at 1,345 Years

DOE, 1985 Bone CDE's	DOE, 1988 CEDE's	Baes et al., 1984 Transfer Factors	Till and Meyer, 1983 Transfer Factors	Beef Consumption		50-Year Commitment (mrem)
				86 g/d	206 g/d	
	soluble	x		x		130
x			x	x		160
x		x		x		90
	insoluble	x		x		30
x			x		x	380
x		x			x	220
	insoluble				x	70

CDE's for insoluble forms (DOE, 1988a) were used. A beef consumption rate of 206 g/d was found in several references (e.g., Till and Meyer, 1983; NRC, 1976). A beef-consumption rate of 86 g/d assumes that other meats are eaten as well. The NCRP (1984) gave consumption rates for poultry and pork along with beef in order to determine total daily meat consumption. The total meat consumption given by the NCRP is over 200 g/d. Only beef consumption is considered in this assessment, and beef might be substituted for poultry and pork by ranchers in this area. Table 7-13 also gives estimated maximum doses for beef consumption of 206 g/d. There is no obvious reason for preferentially selecting transfer factors from either Till and Meyer (1983) or from Baes et al. (1984).

7.3.7 Interpreting Predictions of Radiation Doses

The average background radiation exposure in the United States is about 100 mrem/yr. Background radiation results from radioactive materials in the earth and cosmic radiation coming through the atmosphere. Man-made radionuclides add to the natural background exposure to humans. Fallout from atmospheric nuclear-weapons testing is one source of radionuclides to which everyone is exposed. Whicker (1980) reported that worldwide Pu-239 fallout levels are 0.1 disintegrations per minute (dpm)/g-soil ($0.002 \mu\text{Ci}/\text{m}^2$ or $2000 \text{ pCi}/\text{m}^2$). The dry deposition flux at the hypothetical farm shown is $5 \text{ pCi}/\text{m}^2$ for plutonium (Table 7-4).

Whicker (1980) reported that five-year studies at areas contaminated with Pu-239 showed that readings in the principal study areas ranged from 100 to over 20,000 dpm per gram in the upper 3 cm (2 to $400 \mu\text{Ci}/\text{m}^2$ or 2.0×10^6 to $4.0 \times 10^8 \text{ pCi}/\text{m}^2$). Although minor differences in certain biological attributes between study areas were observed, none could be related to Pu levels. Effects on animals could have been masked by immigration of unaffected individuals from uncontaminated areas outside the study area, however.

Using United Nations (1972) data, Whicker (1980) calculated that the upper 3 cm of soil in the United States averages roughly $0.3 \mu\text{Ci}$ ($3.0 \times 10^5 \text{ pCi}$) of natural alpha activity per square meter. A similar calculation applied to

atypically high-natural-radiation-background areas yielded alpha activities of $7.0 \mu\text{Ci}/\text{m}^2$ ($7.0 \times 10^6 \text{ pCi}/\text{m}^2$) in the upper 3 cm near Central City, Colorado (Mericle and Mericle, 1965), $50 \mu\text{Ci}/\text{m}^2$ ($5.0 \times 10^7 \text{ pCi}/\text{m}^2$) in local areas in Brazil (Eisenbud et al., 1964), and $200 \mu\text{Ci}/\text{m}^2$ ($2.0 \times 10^8 \text{ pCi}/\text{m}^2$) in the Soviet Union (Maslov et al., 1967). Even though some biological effects were described, Whicker (1980) was not convinced from these studies that naturally occurring alpha emitters, even in unusually high-natural-background regions of the world, cause demonstrable ecological consequences.

Healy (1974) calculated the levels of Pu in soil that might be considered "guideline" levels for humans residing on and deriving sustenance from such soils. These calculations suggested that $4.0 \times 10^{-4} \mu\text{Ci Pu-239}$ ($400.0 \text{ pCi}/\text{g}$) or $25 \mu\text{Ci Pu-239}/\text{m}^2$ ($2.5 \times 10^7 \text{ pCi}/\text{m}^2$) in the top 3 cm of soil was probably conservative. Using a similar approach and site-specific data from the Nevada Test Site, Martin and Bloom (1976) calculated that $3 \text{ nCi Pu-239}/\text{g}$ of soil ($3.0 \times 10^3 \text{ pCi}/\text{g}$) or $170.0 \mu\text{Ci}/\text{m}^2$ ($1.7 \times 10^8 \text{ pCi}/\text{m}^2$) could result in the nonoccupational maximum permissible dose to the lung (1.5 rem/yr) of a person living over and obtaining food from the soil in question.

Whicker (1980) reported that early results from studies at Battelle Northwest Laboratories on biological effects of transuranic elements in the environment indicated radiation toxicity from Pu-238 and Pu-239 to some strains of soil actinomycetes and fungi at levels of $0.7 \mu\text{Ci}/\text{g-soil}$ ($7.0 \times 10^5 \text{ pCi}/\text{g}$) or about $2.5 \times 10^4 \mu\text{Ci}/\text{m}^2$ (about $2.5 \times 10^{10} \text{ pCi}/\text{m}^2$). This toxicity was expressed as a decline in microbial numbers. Because microbes perform functions in soil that are important to plant growth, indirect effects to higher plants and animals could occur through microbial perturbations from Pu in soil.

Whicker (1980) calculated that about $5.4 \times 10^6 \mu\text{Ci}/\text{m}^2$ ($5.0 \times 10^{12} \text{ pCi}/\text{m}^2$) of Pu-239 are required to show measurable changes in species diversity in plant communities. He also calculated that about $630 \mu\text{Ci}/\text{m}^2$ ($6.3 \times 10^8 \text{ pCi}/\text{m}^2$) of Pu-239 is required to produce subacute deaths in animals exposed by inhalation of contaminated soil particles. Large amounts of transuranic radionuclides appear to be required in the field to cause obvious ecological effects.

7.3.8 Risk Associated with Environmental Radiation Standards

Lifetime risks associated with various environmental standards and guidances range from 3×10^{-2} (guidance on radon in homes) to 5×10^{-8} (containment requirements for high-level waste disposal). Average risks to the American population from all natural sources (4×10^{-3}) are at least an order of magnitude greater than risks associated with all radiation standards, except for uranium mill tailings standards (1×10^{-2}).

Total risk per unit dose equivalent from uniform whole-body irradiation as recommended in ICRP 26 (ICRP, 1977) is $2 \times 10^{-2} \text{ Sv}^{-1}$ ($2 \times 10^{-4} \text{ rem}^{-1}$). The estimate of lifetime risk associated with an annual dose equivalent to the whole body of 25 mrem, as in 40 CFR 191, is 4×10^{-4} .

8.0 SUMMARY AND CONCLUSIONS

This chapter briefly summarizes the main conclusions of this report. Sections 8.1 through 8.13 address the conceptual models and data that were used in the detailed calculations of long-term performance. These sections are arranged here in the same sequence in which more-detailed discussions of the same topics occur in Chapters 3.0, 4.0, and 5.0. The main conclusions reached within each section of the report are listed here in abbreviated form, without additional discussion. Section 8.14 summarizes the results of calculations of undisturbed performance and some of the specific assumptions that went into these calculations. Section 8.15 summarizes calculations examining the WIPP response to human intrusion involving a Castile brine reservoir.

8.1 Hydrology and Geochemistry of the Salado Formation

The interpreted far-field permeability of the Salado Fm. is 10^{-20} to 10^{-21} m², based on brine-inflow measurements and testing. The effective far-field permeability in the absence of significant pressure gradients may be much lower, however, and Darcy-flow assumptions may not be appropriate.

Experimental results have been modeled successfully with a one-phase (brine only), poroelastic, Darcy-flow model. Uncertainties include stratigraphic effects, variations in storativity, effects of borehole deformation on permeability and pore-pressure measurements, far-field pore pressures, and the possibility of two-phase flow. With the possible exception of two-phase flow, however, Darcy-flow calculations should overestimate brine flow as a function of time.

Testing of the Salado Fm. in holes drilled from the surface is unreliable for several reasons. Therefore, test results from the surface are not included in estimates of far-field Salado permeability. Similarly, high permeabilities interpreted from the results of gas-flow testing in the disturbed rock zone (DRZ) surrounding the underground workings are not considered in evaluating the estimated far-field permeability.

The reference Salado brine, present along grain boundaries and defined for purposes of performance assessment, is relatively high in Mg. It appears to be in equilibrium with anhydrite, gypsum, and halite.

8.2 Hydrology and Geochemistry of the Rustler Formation

8.2.1 Physical Hydrology

Five water-bearing zones within the Rustler Fm. are now recognized, rather than the three recognized at the time of the FEIS. In ascending order, these zones are the siltstone of the lower unnamed member and the Rustler/Salado contact; the Culebra Dolomite; the Tamarisk claystone; the Magenta Dolomite; and the Forty-niner claystone.

The transmissivity of the lower claystone is generally $<6 \times 10^{-10} \text{ m}^2/\text{s}$, except where dissolution of the upper Salado Fm. has occurred. Flow in this interval appears to be generally westward, except within Nash Draw, where it is southwesterly.

The transmissivity of the Culebra Dolomite at the WIPP site and in Nash Draw ranges from $<10^{-7}$ to $>10^{-3} \text{ m}^2/\text{s}$, a direct result of fracturing. Except in Nash Draw, the Culebra Dolomite appears to be effectively confined. Modern flow within the Culebra Dolomite is southerly near the site and southwesterly in Nash Draw. South of the site, flow is apparently to the west, although there is considerable uncertainty in actual flow directions, because of very gentle gradients and variable brine density. The Culebra Dolomite dominates the hydrology of the Rustler Fm. at the WIPP site.

Culebra tests indicating transmissivities between 10^{-6} and $10^{-4} \text{ m}^2/\text{s}$ show evidence of fracture flow. Perhaps because of very closely spaced fractures, tests indicating higher transmissivities do not show hydraulic effects of fracturing.

Except in Nash Draw, the Tamarisk claystone is separated from the Magenta and Culebra Dolomites by intervening anhydrite and gypsum. The Tamarisk

Member has been tested at only four locations; at all four the transmissivity was too low to interpret. No hydraulic-head data are available from the Tamarisk Member.

The transmissivity of the Magenta Dolomite is generally at least an order of magnitude below that of the Culebra Dolomite. Modern flow within the Magenta Dolomite is to the west near the site and to the southwest in Nash Draw.

The Forty-niner claystone, bounded above and below by relatively impermeable anhydrite, has been tested at only three locations, where its transmissivity is estimated to be 10^{-8} to 10^{-9} m^2/s . Forty-niner heads estimated at H-3d, H-14, H-16, and DOE-2 are below those of the underlying Magenta Dolomite.

East of the center of the WIPP site, where there has been little evaporite dissolution, relative heads within the Rustler Fm. indicate vertical flow into the Culebra Dolomite from below and above, i.e., the Culebra is locally draining the Rustler system. The persistent difference between hydraulic head potentials in the different units indicates that this drainage is very slow. At the site, the relative head potentials between the Magenta and Forty-niner Members indicate that there is no modern vertical recharge from the Dewey Lake Red Beds into any portion of the Rustler Fm. below the Forty-niner Member. West of the site, the decreasing difference between Magenta and Culebra heads may indicate a combination of westward and downward drainage of the Magenta Dolomite.

Modern flow within the Rustler Fm. is toward the west and then parallel to the axis of Nash Draw. The exception is the Culebra Dolomite, in which flow near the site is to the south. With the exception of the Culebra, the flow directions would generally be interpreted to indicate recharge from the north and east. The units to the north and east are deeper and are separated by thicker confining beds than at the site. These results, combined with the geochemical and isotopic variability of Culebra ground waters, indicate that modern flow directions within the Rustler Fm., specifically including the

Culebra Dolomite, do not reflect flow from a modern recharge area to a modern discharge area, but rather reflect a transient discharge cycle.

8.2.2 Geochemistry

The estimated TDS contents of Rustler ground waters in the WIPP region range from <3,000 to >300,000 mg/L. Near the site, TDS concentrations in Culebra waters range from ~10,000 mg/L to >200,000 mg/L. No Culebra ground waters near the site are generally suitable for stock, let alone human consumption. Magenta waters are less saline than those in the underlying Culebra Dolomite, with TDS concentrations ranging from ~4,000 to 25,000 mg/L within the site boundary. Waters from the Rustler/Salado contact zone are quite saline; TDS concentrations are ~300,000 to 400,000 mg/L within the site boundary.

Because of the variability of ground-water compositions, four hydrochemical facies are defined for the Culebra Dolomite. Dilute CaSO₄ waters south of the site (Facies B) lie directly downstream along modern flow directions from more saline and variable brines (Facies C). This is inconsistent with steady-state confined flow. Available isotopic results indicate that any vertical fluid flow must be limited within the Rustler Fm. Confined Rustler and Capitan ground waters have a stable-isotope character distinct from that of waters interpreted to represent modern precipitation in the northern Delaware Basin. These results indicate that the Rustler ground waters were recharged in a different climatic setting than that of the present time. Four radiocarbon ages calculated on samples from the WIPP area indicate that these waters (three from the Culebra Dolomite and one from the Dewey Lake Red Beds) were isolated from the atmosphere at least 12,000 to 16,000 years ago. The calculated radiocarbon ages represent minimal values, because some undetected contamination may still be present. The locations of the successful radiocarbon measurements effectively bracket the WIPP site, but do not imply any single flow direction. All ground waters for which the radiocarbon measurements are interpretable have stable-isotopic character consistent with those of other confined Rustler waters. The radiocarbon measurements are all consistent with lack of significant vertical influx to the Culebra Dolomite near the WIPP site for $\geq 10,000$ years and isolation of

confined Rustler waters from the atmosphere (and vertical recharge) for $\geq 10,000$ years. Both stable-isotope variations and radiocarbon results are consistent with the presence of both "modern" waters and older waters within the Dewey Lake Red Beds. Uranium-disequilibrium studies, specifically an eastward increase in $^{234}\text{U}/^{238}\text{U}$ activity ratios, imply that ground-water flow at the time of Rustler recharge had an easterly component, in contrast to the modern southerly flow within the Culebra Dolomite.

$^{87}\text{Sr}/^{86}\text{Sr}$ ratios of host rocks and veins within the Rustler Fm. are indistinguishable, implying an internal source for the solutes. Ratios within the Culebra and Magenta Dolomites are distinct from those of the surrounding parts of the Rustler Fm. and from ratios characteristic of surficial input. Ratios within the Dewey Lake Red Beds imply mixing of Rustler-type waters and surface waters. Flow from the surface to layers beneath the Dewey Lake is minimal, implying that the isotopic distinction of the Culebra and Magenta Dolomites is the result of lateral flow.

The isotopic character of waters of hydration from vein gypsums analyzed from the Rustler Fm. and Dewey Lake Red Beds is consistent with crystallization in the presence of Rustler-type ground water, as distinct from the interpreted isotopic character of modern precipitation. Several of the analyzed gypsums could not have precipitated in equilibrium with any amount of modern water.

The geochemical and isotopic data are consistent with four interpretations: (1) confined Rustler waters at and near the WIPP site were isolated both from the atmosphere and from any significant vertical recharge $\geq 12,000$ to 16,000 years ago; (2) Rustler ground-water flow at the time of recharge had an easterly component; (3) neither flow directions nor fluid compositions within the Culebra Dolomite are at steady-state; and (4) the time scale of change in flow directions is $\geq 10,000$ years.

8.2.3 Radionuclide Retardation in the Matrix of the Culebra Dolomite

If large amounts of organic ligands and brine are mixed into the Culebra Dolomite during human intrusion, radionuclide K_d 's applicable to transport in the Culebra will be lower than the values assumed in the FEIS.

The usefulness of K_d 's in transport modeling is limited, because their use assumes that reactions are reversible, and because the coefficients do not distinguish among such processes as sorption, precipitation, and coprecipitation. In addition, a single K_d is used for each element in each calculation presented here; effects of compositional variation along flow paths are not included.

K_d 's assumed here are estimated from experimentally measured data by considering the expected ranges in pH, Eh, concentration of organic compounds, ionic strength, and carbonate complexation of brines. K_d 's may be reduced by several orders of magnitude, but K_d 's of zero are extremely unlikely. The estimated K_d 's are a compromise between empirical data and calculations for simplified systems.

8.2.4 Numerical Ground-Water-Flow and Transport Model of the Culebra Dolomite

Data indicating effects of fracturing on ground-water flow in the Culebra Dolomite are available from hydraulic interference tests at H-3, WIPP-13, and H-11. Conservative-tracer tests indicating the local role of fracturing have been conducted at H-3, H-6, and H-11. Interpretation of the multipad interference test at H-11 remains to be completed, as does final interpretation and reporting of conservative-tracer tests at H-11 and H-6.

Recent estimates of ground-water travel times in the Culebra Dolomite for undisturbed flow from a position directly above the center of the waste-emplacement panels to the southern boundary of the site have ranged from 5,100 to 13,000 years. Both estimates are based on porous-medium flow.

Final interpretation of the recent multipad interference test at H-11 is expected to indicate that the zone of relatively high transmissivity between H-11 and DOE-1 extends further to the north than previously expected, toward H-15. This extension may or may not affect ground-water flow directions near the center of the site.

8.3 Castile Formation and Shallower Units

Pressurized brine is known to be present at borehole WIPP-12 and at the Bellco-Hudson hydrocarbon borehole southwest of the site. Geophysical studies indicate the presence of brine to the south. Based on these studies and on borehole experience, the WIPP-12 reservoir is assumed to extend underneath a portion of the waste-emplacement panels.

Hydraulic testing indicates that the WIPP-12 reservoir is characterized dominantly by fracture flow in a very tight anhydrite matrix and that the reservoir is limited in extent. The reservoir is modeled with radial symmetry, with a central high-transmissivity zone surrounded by two outer zones, one of slightly increased transmissivity relative to undisturbed country rock, and one of undisturbed country rock.

Hydraulic testing at WIPP-12 and monitoring of the long-term pressure buildup indicates the presence of a gas cap in the borehole at long times. Gas evolution during flow would tend to increase flow rates and pressures relative to those estimated here assuming a single brine phase. This two-phase gas effect cannot be modeled with available techniques, but should operate only at late times, when pressures have decreased.

Testing in holes Cabin Baby-1 and DOE-2 indicates that the final direction of fluid flow in the event of human intrusion connecting the Bell Canyon and Rustler Fms. would be downward, into the Bell Canyon. Bell Canyon brines are highly saline and are not suitable for either human or stock consumption. Flow rates in the Bell Canyon Fm. are very slow because of the small transmissivity.

8.4 Gas-Production Rates, Potentials, and Periods

Anoxic corrosion of drums and metallic wastes will be the dominant gas-producing process within the repository if sufficient Mg-rich brine is present. Anoxic corrosion has an estimated H₂-gas-generation potential of 894 moles/drum. Microbial activity will produce gas by consuming cellulosic materials and possibly plastics and rubbers, even if supported only by the initial water content of waste and cemented sludges or by water vapor. The estimated total potential for gas generation by microbial activity is 606 moles/drum-equivalent. The net effect of microbial activity on the room water budget is not known; it is assumed here to be zero. The current estimate of gas potential, 1,500 moles/drum-equivalent, is less than the FEIS estimate of 2,000 moles/drum-equivalent.

At different times and oxidation potentials, gases that could be potentially produced by microbial activity may include CO₂, CH₄, H₂S, and N₂. In the absence of an engineering modification that removes organic compounds, the conditions governing microbial activity may vary with time and location within the repository.

Both the total amounts and total volumes of gas that will be generated within the WIPP repository are uncertain. Some microbial gas will be generated by the present waste form even in the complete absence of inflowing brine. Even without microbial activity, the presence of Mg-rich Salado brine in the repository will result in anoxic corrosion of drums and metallic wastes. The time over which gas may be generated may exceed 2,000 years.

8.5 Expected Brine Inflow to Waste Rooms and Panels

Based on a Darcy-Flow Model

Under expected conditions, no free brine will be present within the repository until well after structural closure, at which time room porosity will be too small to allow slurry formation.

Calculated brine-inflow volumes over 30 years, the approximate time of interest for evaluating the formation of a brine slurry during repository closure, range from 3.5 to 24 m³ for permeabilities of 10⁻²¹ to 10⁻²⁰ m². These volumes are approximately one and one-half orders of magnitude below the estimated 900 m³ required for saturation of waste and backfill 30 years after decommissioning. At 30 years, brine-inflow rates appear independent of gas generation, because gas pressures are still expected to be very low. Similarly calculated volumes at 60 years range from 6 to 38 m³, less than the expected sorption capacity of bentonite present in the design-basis salt/bentonite backfill.

The calculated long-term Salado brine-inflow rate of 1.3 m³/year per panel, based on the assumption of Darcy flow and a far-field permeability of 10⁻²⁰ m², is probably an overestimate. Uncertainties in the present model include stratigraphic effects, uncertainty in the storativity parameter, and the possibility of two-phase flow.

8.6 Initial Inventory and Decay Chains

Only the CH-TRU radionuclide inventory is considered here, both because of the relatively small loading of RH-TRU and because of the lower probability of interaction of RH-TRU with a human-intrusion event. For calculations, it is assumed that the four dominant radionuclides in the initial CH-TRU inventory are ²³⁸Pu, ²⁴¹Am, ²³⁹Pu, and ²⁴⁰Pu. The inventory and decay chains used in transport analyses are slightly simplified by eliminating very short-lived radionuclides and some of the daughters late in the chains.

The only volatile radionuclide expected to be present in the CH-TRU inventory is radon-222, a decay product of radium-226. The maximum expected inventory of radon-222 is 10⁻³ Ci at 10,000 years, which is negligible. Therefore, gaseous transport of volatile radionuclides is not considered in this report.

8.7 Radionuclide Concentrations in Brines and Sorption in the Repository

There is currently a wide range of uncertainty in actinide solubilities within the WIPP repository, from $\sim 10^{-9}$ to 10^{-3} molar. It is assumed that the estimated range in effective radionuclide concentrations includes potential effects of both particle transport and sorption. The uncertainty about radionuclide solubility is a result of several factors, including the high ionic strength of Salado and Castile brines, uncertainties about the local Eh and pH values within the repository as a function of time and location, and the amount of carbonate complexing that can be expected. In addition, the identities, amounts, and effects of organic complexing agents within the waste are unknown.

Although the sorption capacities of iron oxides and bentonite are high in dilute solutions, the possible concentrations of carbonate, organic complexing agents, and competing ions such as Mg^{2+} and Ca^{2+} will greatly reduce these sorption potentials within the repository. Estimated sorption capacities within the repository are assumed to be as low as 1 meq per 100 g of solid for relatively strong sorbers such as Am, Th, and Pu and 0.1 meq/100 g of solid for relatively weak sorbers such as U and Np.

The qualitative effects of sorption within the waste-emplacement areas of the WIPP depend on the character of flow under undisturbed conditions and in response to human intrusion. If particulate materials are not transported by flow of fluids, then sorption within the waste-emplacement areas is beneficial. If, however, particulate material is transported by fluid flow, then sorption of radionuclides on the particulate materials would be detrimental.

8.8 Structural Interaction of the Salado Formation and Repository

Measured in-situ wall-closure rates are about three times those estimated prior to underground experience in the WIPP. Current numerical modeling has achieved greatly improved agreement by reevaluating the stress generalization, constitutive model, and material properties from WIPP-specific samples. The

current numerical modeling does not incorporate a disturbed-rock zone around the underground workings.

On the basis of borehole observations, geophysical studies, and gas-flow tests, a disturbed-rock zone (DRZ) is known to be present adjacent to the WIPP underground workings at the repository horizon. The DRZ extends outward from 1 to 5 m, depending on the age and span of a given excavation. It is assumed here that, with the exception of fractures in Marker Bed 139, the DRZ returns to its initial porosity during the final stages of closure. Processes active within the DRZ include desaturation, microfracturing, and macrofracturing (especially the opening of fractures within Marker Bed 139).

Structural impacts of the DRZ may extend the time required to reach final mechanical closure of the repository. Hydrologic impacts of the DRZ include generation, prior to closure, of a region of relatively high permeability near the repository horizon and development of an interconnected flow path (Marker Bed 139) immediately beneath the repository horizon.

Although the presence of a DRZ complicates numerical modeling of the near-field structural and hydrologic behavior of the WIPP, it may also have beneficial impacts. For example, the DRZ may serve as a sink for brine expected to flow into the repository and for some of the gas generated by waste and container degradation.

8.9 Terminal Waste State

Lithostatic load will be insufficient to remove all porosity from the waste and backfill in any reasonable length of time. The expected "final" porosity of emplaced design-basis waste is 0.18, with a range from 0.15 to 0.21. The estimated permeability of the "final"-state waste, attained within 60 to 200 years, is $\sim 10^{-13}$ m². It is expected that closure to 70 to 95% of the "final" state will occur as if the waste were not present, because the waste and backfill will not exert any appreciable backpressure until this degree of closure is reached. The structural effect of the backpressure and

any DRZ is assumed to be simple retardation of the final stages of closure, not alteration of the estimated final state.

It is assumed that mechanical closure to "final" state occurs within 60 years, independent of gas generation and brine inflow. It is further assumed, for purposes of estimating gas-storage volumes within the repository, that the final room porosity remains unchanged in response to brine inflow and gas generation.

8.10 Shaft Seal and Backfill Systems

Major long-term reliance is placed on structural compaction of crushed salt or a crushed salt/bentonite mixture. Laboratory experiments indicate that permeability of crushed salt reduces to $\sim 10^{-20}$ m² at a porosity of 5%.

Composite seals will be emplaced at three locations in each shaft, although effective long-term sealing of only ~ 200 m of salt above the repository horizon is assumed.

Multicomponent seals, the major component of which will be preconsolidated salt, will be emplaced at the entryway to each waste-emplacment panel and at two locations in the main access tunnels. The main function of preconsolidation is to minimize the time required for the overall seal system to become effective. The use of cementitious grout at each end of multicomponent seals should minimize the time required for effective sealing. At early times, before effective compaction of backfill between seal locations, the maximum gas-pressure gradient across the cementitious part of any composite seal will be ~ 3 to 4 MPa, and the upstream pressure at all locations will be well below lithostatic load, except at the first seal north of the waste-emplacment area. This seal may be specially engineered to use the pressure effects in aiding sealing tendencies. The gas-generation phase is not expected to affect the primary components of the sealing system from the edge of the waste-emplacment area to the base of the shaft seals. However, if gas pressures within the repository approach lithostatic,

isolation of individual panels may not be effective until after fluid pressures decrease.

8.11 Possible Repository Response to Gas-Generation and Total Volumes Generated

The formation of a brine slurry during mechanical closure of the WIPP repository is extremely unlikely. The estimated porosity limit, below which no slurry can form, is 40%, obtained ~30 years after decommissioning. The estimated total void space at 30 years is 900 m³, ~35 times the largest estimated brine inflow per room at 30 years, 24 m³.

In undisturbed performance, assuming successful seal performance, there are four locations or mechanisms of gas storage or pressure release: (1) reexpansion of waste-emplacement rooms and panels; (2) development of a new zone of alteration (DRZ) at the repository horizon (or retention of a portion of an existing DRZ prior to complete closure); (3) use of existing or newly created fractures in Marker Bed 139 and stratigraphic contacts near the repository horizon; and (4) storage in the shafts and any adjacent DRZ. Regardless of mechanism, the porosity increase required to store reasonable quantities of gas would appear approximately an order of magnitude more slowly than porosity reduction during the first 60 years of closure. There is no reason to expect any dramatic process to take place during gas storage or release.

Given the estimated total gas volumes, the total storage volumes within (a) rooms and panels in the disposal area; (b) a DRZ similar in properties and extent to that now present; (c) Marker Bed 139; and (d) five stratigraphic contacts near the repository horizon would be approximately adequate at lithostatic pressure. However, unless gas-generation rates are high, the DRZ might be eliminated before lithostatic gas pressures are reached.

The WIPP is eventually expected to saturate with brine. Partial or complete saturation in response to either final or interim reductions in gas pressure will be driven largely by buoyancy as gas migrates upward and is

replaced from below by brine. The low far-field permeabilities of the Salado Fm. suggest that this process would be extremely slow and might require thousands of years.

8.12 Possible Engineered Modifications of Waste and Backfill

Elimination of waste porosity to effect long-term brine control appears to be difficult with design-basis metallic waste. Mechanical compaction of metallic waste alone would require pressures approximately an order of magnitude greater than lithostatic pressure (~150 MPa or 2.2×10^4 psi) for significant porosity reduction beyond that eventually obtained by lithostatic load. Use of bitumen or grout within drums to control permeability would be labor intensive and might prove unreliable. The estimated gas potential from organic materials in the waste might make reduction of permeability of combustible waste to extremely low values impossible because of internal gas generation.

With the design-basis waste, processes by which gas could reliably be eliminated within the repository are not yet well defined. Backfill additives might remove CO₂, which is expected to be the dominant gas under many conditions. Reduction of the quantity of H₂ produced by anoxic corrosion also appears feasible by emplacing amounts of CuSO₄ chemically equivalent to the amount of Fe and possible other corrodible metals in waste and drums. No getters have yet been proposed for CH₄, N₂, and H₂, however. The volumes of materials required to control CO₂ and H₂ are expected to degrade the fluid-flow and mechanical properties of the backfill relative to either crushed salt or salt and bentonite. It would be possible to remove the potential gas-source term due to microbial activity by incinerating organic compounds in the waste, but this approach alone does not appear adequate, because incineration leaves the majority of metals unaltered. Therefore, the dominant potential gas source, production of hydrogen by anoxic corrosion in Mg-rich brines, would remain.

Engineered modifications may not be required. Better estimates of net gas-production rates are a major objective of the WIPP demonstration phase.

In addition, numerical results presented here indicate that unless gas generation significantly affects the sealing system, the net effect of gas might be positive, because it would make radionuclides essentially unavailable for ground-water transport.

8.13 Evaluation of Pathways to Man

Exposure and health effects arise from several sources, including effects at the well head and at a hypothetical, nearby farm, and effects resulting from ground-water transport of radionuclides through the Culebra Dolomite to a hypothetical stock well. Effects of ground-water transport to the stock well are evaluated for ~10,000 years after decommissioning.

Exposure at the wellhead is estimated for the most-exposed member of the drilling crew, assumed to be the geologist. Brine flow through the borehole, both in any free-flow phase and during continued drilling to deeper exploration targets, is estimated to erode ≤ 10 cm into the waste. The direct total release of cuttings and particulate material to contaminated drilling mud is estimated to be three drum equivalents of waste, independent of waste form.

Calculations indicate that the Culebra Dolomite is capable of accepting the estimated brine volumes from the Castile reservoir without head increases reaching the surface. Therefore, no long-term release directly to the surface after degradation of the borehole plug is considered here. A hypothetical stock-well location is chosen that is in the modern Culebra flowpath from the site center toward the south, ~5 km south of the waste-emplacment panels. Stock are assumed to tolerate water as saline as 10,000 mg/L TDS. The salinity in the stock well will slowly increase as a result of flow of Culebra ground water toward the south, which will make water at the hypothetical pond non-potable for stock. The modeling takes no credit for the expected increase in the salinity at the well. In addition, no credit is taken for the fact that brine injected into the Rustler as a result of human intrusion of the WIPP will likely be saturated with halite; transport of this brine to the

stock may make the water non-potable for stock, independent of possible radionuclide contamination.

Potential doses to a hypothetical farm family living 500 m downwind of the intrusion borehole result from evaporation of drilling fluid, resuspension by wind, and transport to the farm location. Doses from several pathways are estimated, including inhalation of contaminated air and consumption of home-grown meat, milk, and above- and below-surface crops.

8.14 Undisturbed Performance of the WIPP

Chapter 6.0 of this report summarizes calculations describing the expected long-term performance of the undisturbed WIPP repository, in the absence of human intrusion and assuming steady-state conditions. Calculations assuming expected properties and behavior (Case IA) indicate that first arrival of the least-sorbed materials (U, Ra, Pb) to the Culebra Dolomite occurs 2,800,000 years after the beginning of the calculations; that first arrival of the same materials to the top of the reconsolidated salt, ~200 m above the repository horizon, is 900,000 years; and that first arrival to the bottom of the shafts is 500,000 years. Directly analogous calculations assuming two orders of magnitude increase in both radionuclide solubility and permeability within the repository and shafts indicate travel times for least-sorbed constituents of 25,000 years to the Culebra Dolomite and 8,000 years to the top of consolidated salt within the shaft.

These calculations indicate that there is effectively no potential for release of radionuclides from the WIPP to the Culebra Dolomite within 10,000 years, let alone to the surface, in the absence of human intrusion. This conclusion is similar to conclusions reached in the WIPP FEIS, in spite of the significant development in conceptual and numerical models over the past 10 years.

Both conservative and non-conservative assumptions have been made in calculations of undisturbed performance, however. A major conservative assumption is that the repository instantly saturates with brine 2,000 years

after decommissioning, so that brines are at both effective radionuclide saturation and lithostatic pressure at this time. It is possible (Section 4.2) that in-situ gas production will dominate the repository system for much longer than 2,000 years. If so, radionuclides will not be available for ground-water transport for much longer than 2,000 years, and the radionuclide inventory available at the time of saturation will be smaller than that assumed here. Because of the very low content of volatile radionuclides in CH-TRU waste, gas-phase transport of radionuclides is not of concern.

The major non-conservative assumption in these calculations is that, whatever the behavior of the WIPP might be during the time in which gas production dominates, gas generation and migration does not degrade (increase) the effective permeability of the WIPP seals, shafts, or surrounding rock mass by more than two orders of magnitude above the design values at the time of brine saturation and consequent ground-water migration.

Sealing against gas pressures that approach lithostatic can probably be successful, but it is not required. All that is required is that the effective permeability of the drifts, seals, shafts, and surrounding rock mass at the time of repository saturation be within approximately two orders of magnitude of design values. This appears to be realistic, even if the seals are initially bypassed, because the same decrease in fluid pressure below lithostatic that is required for brine inflow to saturate the repository would allow creep closure and elimination of any remaining disturbed rock zone around drifts and seals.

8.15 Long-Term Performance of the WIPP in Response to Human Intrusion

Four sets of calculations presented in Chapter 7.0 (Cases IIA through IID) examine the 10,000-year response of the WIPP to a human intrusion that penetrates the repository and an underlying reservoir of pressurized brine within the Castile Fm. with an exploratory borehole. Both direct release to the surface and doses to a hypothetical farm family living 500 m downwind from the intrusion hole are calculated to be very low for Case II. The estimated dose to the maximally exposed member of the drilling crew, the rig geologist,

is estimated to be 0.08 mrem. This exposure occurs during an assumed one-hour examination of cuttings from the repository horizon. The indirect pathway considered for the farm family includes evaporation of contaminated drilling mud, resuspension and air-borne transport, and radionuclide deposition onto soils at the farm site. A person living at the hypothetical farm is calculated to receive a 50-year committed dose equivalent of 4.9×10^{-10} mrem after one year of ingestion of home-grown beef, milk and crops, and 0.8 mrem from inhalation of contaminated air.

Post-plugging ground-water transport calculations for Case IIA assume "expected" or "representative" characteristics for the repository, the plugged breaching well, and the Culebra Dolomite. Critical variables include radionuclide solubility, waste permeability, borehole-plug permeability, and transport properties within the Culebra Dolomite (matrix porosity, fracture spacing, matrix tortuosity, free-water diffusivity of radionuclides, and radionuclide distribution coefficient, K_d). The environmental pathway considered is consumption of beef contaminated by drinking water from a hypothetical Culebra stock well ~4.8 km from the intrusion well along the major Culebra flowpath. The waste permeability enters into these calculations only to the extent that the assigned permeability for Cases IIA and IIC (10^{-13} m²) is assumed to allow mixing of Castile brine near the borehole sufficient for these brines to reach the same radionuclide concentration as already exists within the repository. Thus, the radionuclide source term to the Culebra Dolomite for Cases IIA and IIC results from contamination of the combined Castile-brine and Salado-brine volumes by a full complement of radionuclides.

For Case IIA, radium-226 and lead-210 are the only radionuclides reaching the stock well in any significant quantity in 10,000 years. At 10,000 years, the calculated 50-year dose commitment to the whole body after one year of eating contaminated beef is 2.1×10^{-4} mrem for Case IIA (Table 7-13). Fracturing within the Culebra Dolomite plays an important role in radionuclide transport toward the Culebra stock well, even assuming the expected Culebra flow and transport properties.

Case IIB assumes that waste emplaced at WIPP is compacted prior to emplacement and that waste compaction reduces permeability enough to prevent mixing of Castile brine within the repository. Thus, the only radionuclide source term into the Culebra Dolomite in Case IIB results from the flow of contaminated Salado brine into the borehole. The Castile brine merely acts as a carrier. If "expected" transport properties were assumed for waste, drillhole, and Culebra Dolomite in Case IIB, the resulting doses at 10,000 years would be reduced from the already low values calculated in Case IIA. This is because brine circulation is assumed to be restricted within the repository as a result of waste precompaction.

Therefore, Case IIB assumes that, other than the elimination of brine circulation within the repository, flow and transport properties in the repository and geosphere are degraded. Radionuclide solubility is increased by two orders of magnitude, and borehole-plug permeability is increased by one order of magnitude. Analogous changes in the Culebra Dolomite decrease the effectiveness of radionuclide retardation and increase the importance of fracture flow. Matrix porosity, matrix tortuosity, free-water diffusivity, and distribution coefficients (K_{ds}) are all decreased, and fracture spacing is increased.

The combination of changes results in increased radionuclide release from the repository to the borehole, increased flow and transport within the Culebra Dolomite, and increased release at the hypothetical Culebra stock well in less than 10,000 years. First arrival of uranium at the stock well is calculated to occur in slightly more than 100 years. The whole-body 50-year dose commitment from one year of ingesting 86 g/d of beef contaminated by drinking nothing but 1.1-density water from the hypothetical stock well is estimated to be 72 mrem in Case IIB, occurring 10,000 years after repository decommissioning. If 206 g/d of beef is ingested, the corresponding dose commitment is 170 mrem.

Because of the mix of assumptions used in Case IIB, the benefits of waste precompaction cannot be isolated. Therefore, Case IIC assumes the same flow and transport behavior outside the repository as in Case IIB, but also assumes sufficient waste permeability to allow thorough and complete brine mixing

within the repository. Thus, both radionuclide solubilities and flow and transport behavior outside the repository have been degraded in Case IIC, relative to Case IIA. First arrival at the stock well is decreased only slightly in Case IIC, relative to IIB, as a result of the higher radionuclide input into the Culebra Dolomite. However, peak dose commitments at the hypothetical stock well occur much earlier, at ~1,350 years in Case IIC, versus >10,000 years for Case IIB. The maximum whole-body 50-year dose commitment from one year of beef ingestion is estimated to be 130 mrem in Case IIC, occurring ~1,350 years after repository decommissioning.

Because of the conservative assumptions about both radionuclide solubilities and flow and transport behavior in Case IIC, inventories of several radionuclides are partially depleted well before 10,000 years. Inventory depletion is limited in Case IIB. However, the limited mixing of brine within the repository assumed in Case IIB results in a whole-body 50-year dose commitment at 10,000 years that is ~45% lower than the peak whole-body 50-year dose commitment calculated for Case IIC (72 mrem versus 130 mrem). Thus, waste precompaction decreases and delays peak dose commitment.

There is some flexibility in estimating dose commitment from ingestion of contaminated beef. For example, if 206 g of beef consumption per day is assumed in Case IIC, rather than 86 g/d, the corresponding dose commitment is 310 mrem. In addition, the results discussed thus far are equivalent whole-body dose commitments, rather than dose commitments to bone, which may be more appropriate for the radionuclides considered here. Assumption of increased beef consumption and use of committed dose equivalents to the bone result in estimated 50-year dose commitments of 20 mrem and 380 mrem for Case IIC, compared with the 130 mrem reported above. The calculated dose commitments to the bone (Table 7-14) are, however, much less than an order of magnitude higher than calculated whole-body dose commitments (Table 7-13).

The ranges used in this report for radionuclide solubilities and flow and transport properties both within and outside the repository are based on incomplete data. The primary focus of research during the demonstration phase of the WIPP Project is to decrease the uncertainties in parameters important

to long-term performance, but the results of this research cannot be prejudged. Therefore, Case IID examines the potential benefits that might be gained from a generic engineering modification of the WIPP waste or backfill. This case assumes the same radionuclide solubilities as for Case IIA, but also assumes that permeability within the repository is reduced sufficiently to eliminate mixing of Castile brines within the repository and to limit brine inflow from the Salado Fm. to the borehole in such a way that the effective inflow to the penetrating borehole is from a single room, rather than from an entire waste-emplacement panel. Flow and transport properties outside the repository are degraded in Case IID to the same values used in Cases IIB and IIC. Thus, Case IID assumes that parameters that cannot be engineered are degraded relative to expected values and then examines whether engineering modification of waste and backfill can compensate.

The results of Case IID indicate that, because of the assumed flow and transport properties outside the repository, first arrival of radionuclides at the hypothetical stock well is only slightly later than in Case IIB, i.e., between 100 and 200 years. However, because of decreased brine flow from the Salado Fm. to the penetrating borehole, peak concentrations and hence peak doses for Case IID are reduced by two to three orders of magnitude. The maximum whole-body 50-year dose commitment from one year of beef ingestion is estimated to be 0.9 mrem in Case IID, occurring 10,000 years after repository decommissioning.

Several conclusions can be drawn from the calculations presented here:

1. Undisturbed performance of the WIPP will not release radionuclides either to the Culebra Dolomite or to the surface in well over 10,000 years, even assuming increased radionuclide solubilities and degraded flow and transport properties in the WIPP drifts and shafts.
2. If the expected properties of waste, backfill, borehole plugs, and the Culebra Dolomite are supported by results obtained during the WIPP demonstration phase, the WIPP performance assessment will be able to demonstrate compliance with applicable regulatory guidelines with a high degree of confidence.

3. If the final estimates of the flow and transport properties of waste, backfill, borehole plugs, and the Culebra Dolomite are significantly worse than those expected here, and if no significant modification is made to waste or backfill, large releases to the hypothetical stock well could result.

4. Even if the final estimates of the flow and transport properties of borehole plugs and the Culebra Dolomite are worse than those expected here, it should be possible to gain a high degree of confidence in long-term repository performance by modifying the waste or backfill. At this time, it is not known whether such modifications will be required.

APPENDIX A. UNPUBLISHED REFERENCE MEMOS

A.1 Drum (Metal) Corrosion, Microbial Decomposition of Cellulose, Reactions
Between Drum-Corrosion Products and Microbially Generated Gases, Reactions
Between Possible Backfill Constituents and Gases and Water Chemical Reactions

by L. H. Brush and D. R. Anderson

Sandia National Laboratories

Albuquerque, New Mexico 87185

date: March 28, 1988

to: Distribution

L. H. Brush for D. R. Anderson

from: L. H. Brush and D. R. Anderson, 6334

subject: Potential Effects of Chemical Reactions on WIPP Gas and Water Budgets

INTRODUCTION

The gas and water contents of TRU storage rooms could have a profound impact on the long-term performance of WIPP, especially with respect to human intrusion scenarios. Several studies have been carried out recently to quantify the effects of brine influx and its subsequent absorption by backfill on the water content of WIPP storage rooms (Beraum, 1988; Butcher, 1988; Deal and Case, 1987; McTigue, 1987a, 1987b, 1988a, 1988b; Nowak, 1988). In addition, the Scientists' Review Panel on WIPP (1988) has raised concerns about the effects of gases on the performance of WIPP.

There are, however, other processes that could affect the long-term consumption and production of gas and water in WIPP storage rooms. These potential processes include: (1) corrosion of drums; (2) microbial decomposition of organic constituents of the waste, especially cellulosic materials; (3) reactions between drum corrosion products and microbially generated gases; (4) reactions between possible backfill constituents and gases and water. The objectives of this memo are to determine the sensitivity of the WIPP gas and water budgets to these processes; outline the extent of our current knowledge of them, and discuss some possible approaches to increase our understanding of these processes.

CORROSION OF DRUMS

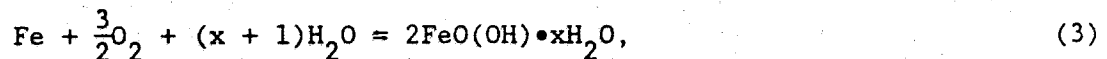
The 55-gallon drums currently being used for the WIPP Simulated Contact Handled (CH) Transuranic (TRU) Waste Tests are identical to the drums used for CH TRU waste storage at Rocky Flats and were, in fact, manufactured* to their specifications and purchased from them (Molecke, 1986). These drums, which consist of 1018 mild steel, are corroding very slowly under oxic overtest conditions (M. A. Molecke, personal communication). It is unclear whether or not they will corrode after

the O₂ initially present in air trapped in WIPP storage rooms is consumed by oxic corrosion of drums and/or microbial decomposition of organic materials. Because radiolysis of H₂O will produce O₂, corrosion could continue after the consumption of the O₂ initially present. If, however, radiolytically produced O₂ is preferentially consumed by microbial activity, anoxic corrosion of drums is also possible.

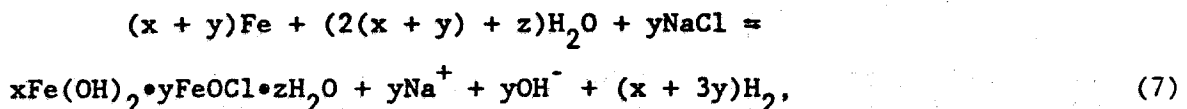
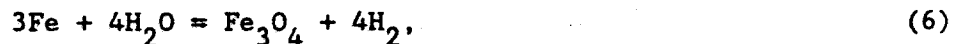
Haberman and Frydrych (in press) studied the anoxic corrosion of A216 Grade WCA mild steel in Permian Basin brines at temperatures of 90, 150, and 200°C. Their results imply that anoxic corrosion of mild steel can be significant in brines that contain appreciable Mg²⁺. Extrapolation of their data to the temperatures and Mg²⁺ concentrations expected for WIPP (see below) suggests that anoxic corrosion of drums is possible.

The drum corrosion products from the WIPP Simulated CH TRU Waste Tests have not been characterized yet. Several possible corrosion products are therefore listed in Table 1. Clearly, not all of these phases are likely to form in the WIPP. FeO, for example, would probably not be stable under low-temperature conditions. We considered a variety of corrosion products, however, to demonstrate the dependence of gas and water consumption and production on the composition of these phases.

Equations 1 through 5 describe the oxic corrosion of drums:



Equations 6 through 9 describe the possible anoxic corrosion of drums:



In these and subsequent equations, only one reaction is written for all of the possible polymorphs, and possible solid solutions are neglected. Table 2 shows the effects of these reactions on the consumption and production of gases and water.

The quantity of mild steel that could be oxidized by the O_2 initially present in air trapped in WIPP storage rooms is small. The ideal gas law implies that:

$$n = 20.9\% \left(\frac{PV}{RT} \right), \quad (10)$$

where n is the number of moles of O_2 ; 20.9% is the O_2 content of air; P is the pressure in atmospheres; V is the void volume of a room in liters; R is the gas constant ($0.0821 \text{ liters} \times \text{atm} \times \text{moles}^{-1} \times \text{K}^{-1}$); T is the temperatures in $^{\circ}\text{K}$. We assumed a pressure of 1 atm and a temperature of 300°K (27°C) at the time the rooms are sealed, and evaluated Equation 10 with the initial room void volumes given in Table 3 (B. M. Butcher, personal communication). Table 3 lists the calculated quantities of O_2 .

If we assume that each drum weighs 64.5 lbs (Molecke, 1986) and that there are 6,750 drums per room, the total quantity of Fe per room is:

$$\begin{aligned} & (64.5 \text{ lbs/drum}) \times (6,750 \text{ drums/room}) \times (454 \text{ g/lb}) + \\ & (55.8 \text{ g/mole of Fe}) = 3.54 \times 10^6 \text{ moles of Fe/room.} \end{aligned} \quad (11)$$

The formation of Fe_3O_4 , a likely corrosion product under oxic conditions (N. R. Sorensen, personal communication), would not consume any H_2O but would consume $2/3$ of a mole of O_2 per mole of Fe oxidized (see Table 2). The quantity of O_2 that would be required to convert all of the drums to Fe_3O_4 by oxic corrosion is:

$$\begin{aligned} & (2/3 \text{ mole of } O_2/\text{mole of Fe}) \times (3.54 \times 10^6 \text{ moles of} \\ & \text{Fe/room}) = 2.36 \times 10^6 \text{ moles of } O_2/\text{room.} \end{aligned} \quad (12)$$

Division of the quantities of O_2 listed in Table 3 by the value obtained from Equation 12 implies that the O_2 initially present in air trapped in WIPP storage rooms would only be sufficient to oxidize about 0.4 to 1.1% of the drums, depending on the initial void volume assumed.

Haberman and Frydrych (in press) reported that the anoxic corrosion of mild steel produced magnetite or magnesioferrite when the Mg^{2+} concentration of their brines was 1,000, 5,000, or 10,000 ppm; and amakinite when the Mg^{2+} concentration was 20,000 or 30,000 ppm. The mean concentration of Mg^{2+} in brines from the Salado Formation at or near the stratigraphic horizon of the WIPP is between 20,000 and 25,000 ppm (D. E. Deal, personal communication; Stein and Krumhansl, 1986; in press); this suggests that anoxic corrosion of drums in the WIPP could form amakinite.

We extrapolated the anoxic corrosion rates for mild steel in Permian Basin brines as follows. First, we assumed that the remote-handled (RH) waste will raise the temperature in WIPP storage rooms from the in situ temperature of 26 or 27°C to 30 or 40°C. (J. G. Arguello is carrying out heat transfer calculations for the current reference RH waste canister configuration.) We then used the Arrhenius plot (log of corrosion rate versus $1,000/\text{temperature in } ^\circ\text{K}$) for 1-month experiments in the Mg^{2+} -rich brine PBB3 (see Haberman and Frydrych, in press, Figure 7) to obtain corrosion rates of -0.2 mil/year ($5 \times 10^{-3} \text{ mm/year}$) at 40°C and -0.08 mil/year ($2 \times 10^{-3} \text{ mm/year}$) at 30°C. Finally, the plot of anoxic corrosion rate versus the Mg^{2+} concentration of Permian Basin brines (see Haberman and Frydrych, in press, Figure 6) implies that the data for the Mg^{2+} -rich brine PBB3 (48,000 ppm) should be multiplied by a factor of 1/3 or 1/2 when applied to brines from the Salado Formation (mean Mg^{2+} concentration = 20,000 to 25,000 ppm). We thus obtained a range of -0.03 mil/year ($8 \times 10^{-4} \text{ mm/year}$) to -0.1 mil/year ($3 \times 10^{-3} \text{ mm/year}$) for Salado brines at 30 or 40°C.

We must emphasize that (1) the data reported by Haberman and Frydrych were obtained with A216 Grade WCA mild steel, not 1018 mild steel; (2) there are other chemical differences between Permian Basin brines and Salado brines in addition to the Mg^{2+} concentration; (3) the corrosion rates that we extrapolated were obtained from experiments carried out with brine but without any solid phases, and are thus probably higher than those that would have been obtained had crushed salt been present (R. E. Westerman, personal communication); (4) the corrosion rates that we extrapolated were from 1-month experiments, and were higher than comparable data from longer experiments (longer experiments were not, however, carried out at all three temperatures); (5) we assumed that the corrosion mechanism of mild steel would be the same at 30 and 40°C as at 90, 150, and 200°C. Nevertheless, our extrapolated corrosion rates of 8×10^{-4} to $3 \times 10^{-3} \text{ mm/year}$ and a nominal drum thickness of 1.52 mm (Molecke, 1986) imply that anoxic corrosion could convert the drums to amakinite in 500 to 2,000 years.

The anoxic corrosion of drums could consume a large quantity of H_2O and produce a large quantity of H_2 . Equation 9 implies that the oxidation of each mole of Fe would consume 2 moles of H_2O and produce 1 mole of H_2 . Because there are 3.54×10^6 moles of Fe per room (see Equation 11), the total quantities of H_2O consumed and H_2 produced by the anoxic corrosion of drums are:

$$(2 \text{ moles of } \text{H}_2\text{O}/\text{mole of Fe}) \times (3.54 \times 10^6 \text{ moles of Fe/room}) = 7.08 \times 10^6 \text{ moles of } \text{H}_2\text{O}/\text{room}; \quad (13a)$$

$$(1 \text{ mole of } \text{H}_2/\text{mole of Fe}) \times (3.54 \times 10^6 \text{ moles of Fe/room}) = 3.54 \times 10^6 \text{ moles of } \text{H}_2/\text{room}. \quad (13b)$$

If we assume a brine density of $1.23 \times 10^3 \text{ kg/m}^3$ (D. E. Deal, personal communication) and a value of 56.2 moles of $\text{H}_2\text{O}/\text{kg}$ of brine (calculated using the EQ3NR solubility and speciation code and chemical data for Salado brines from Deal), the quantity of H_2O in a cubic meter of brine is given by:

$$(56.2 \text{ moles/kg}) \times (1.23 \times 10^3 \text{ kg/m}^3) = 6.91 \times 10^4 \text{ moles/m}^3. \quad (14)$$

The total volume of brine consumed is then given by:

$$(7.08 \times 10^6 \text{ moles}) + (6.91 \times 10^4 \text{ moles/m}^3) = 102 \text{ m}^3. \quad (15)$$

Clearly, the quantity of H_2O that could be consumed by anoxic corrosion of drums is similar to predictions of brine influx from the Salado formation (Beraum, 1988; McTigue, 1987a; 1987b; 1988a 1988b).

The H_2 produced by the anoxic corrosion of one drum is:

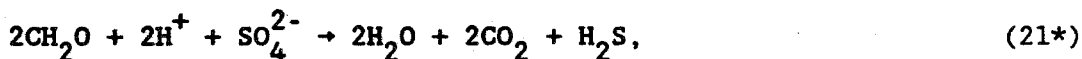
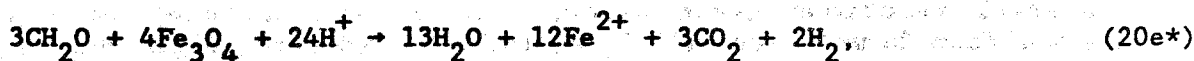
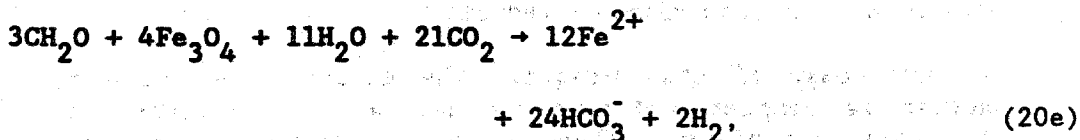
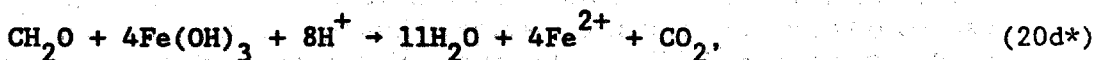
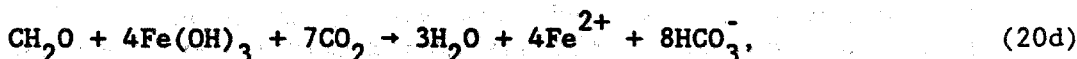
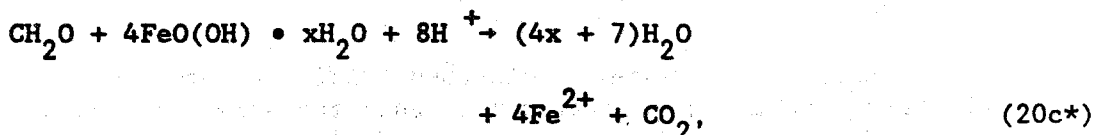
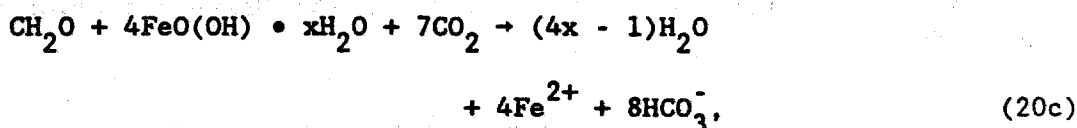
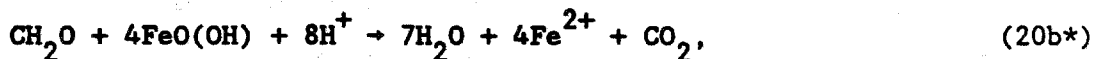
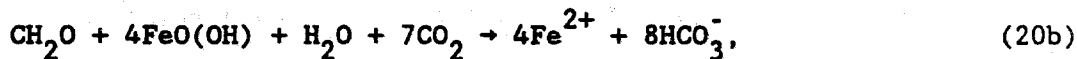
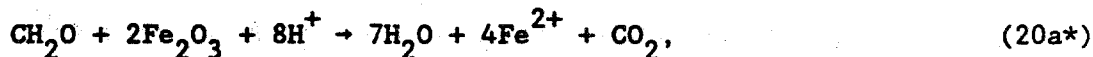
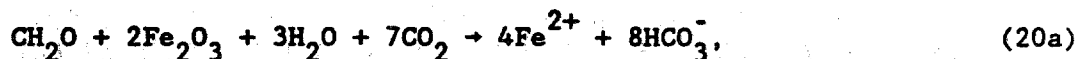
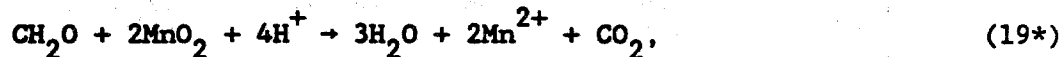
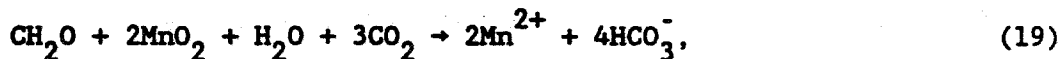
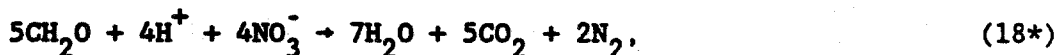
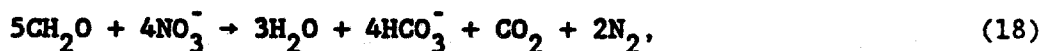
$$(3.54 \times 10^6 \text{ moles of H}_2/\text{room}) + (6,750 \text{ drums/room}) \\ = 524 \text{ moles of H}_2/\text{drum}. \quad (16)$$

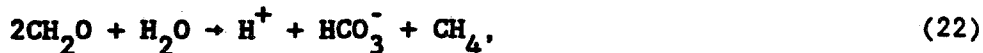
This value is similar to the value of 430 moles per drum estimated by the National Research Council Panel on the Waste Isolation Pilot Plant (1984).

MICROBIAL DECOMPOSITION OF CELLULOSE

In the natural environment, microbes oxidize organic matter by using the electron acceptor that yields the most free energy per mole of organic C consumed. After this oxidant is depleted, the next most efficient electron acceptor is used, and so on, until all degradable organic matter is consumed or all electron acceptors are depleted. Table 4 shows the sequence in which electron acceptors are used during microbial decomposition of organic matter, and lists the sources of potential oxidants in the WIPP. (In natural systems, the reduction of Mn(IV) oxides may precede nitrate reduction.)

At any stage of this process, the microbial decomposition of organic matter is complex and involves several intermediate steps mediated by different organisms. These steps can, however, be represented by the overall reactions given below. In these reactions, we used the simplified formula for cellulose, CH_2O , to represent degradable organic matter rather than a more realistic formula such as the Redfield ratio, $(\text{CH}_2\text{O})_{106} \cdot (\text{NH}_3)_{16} \cdot (\text{H}_3\text{PO}_4)$. We also assumed that microbes will not decompose plastics or rubber. The simplified overall reactions are:





Equations 17*, 18, 19, 20d, 21, and 22* are from Berner (1980); we postulated Equations 20a, 20b, 20c, and 20e based on other possible drum corrosion products; finally, we wrote Equations 17, 18*, 19*, 20a*, 20b*, 20c*, 20d*, 20e*, 21*, and 22 to illustrate the sensitivity of the gas and water budgets to the solubility of CO_2 in any brine present in WIPP storage rooms.

Table 5 shows the effects of these microbial decomposition reactions on the consumption and production of gases and water. Note that the coefficients listed in Table 5 depend critically on how these equations are written. Clearly, the differences between any two equations that describe the same microbial decomposition reaction result from different assumptions as to the solubility of CO_2 produced. In Equations 17, 18, 19, 20a, 20b, 20c, 20d, 21, and 22, all or most of this CO_2 dissolves in the aqueous phase, whereas, in Equations 17*, 18*, 19*, 20a*, 20b*, 20c*, 20d*, 21*, and 22*, all of the CO_2 produced remains in the vapor phase. In the WIPP, the partitioning of CO_2 between any brine and the vapor phase will depend upon factors such as the partial pressure of CO_2 and the composition of the brine, especially its pH. Because of the complex nature of multicomponent chemical systems such as that expected for WIPP, calculations such as this are best carried out using a reaction-path code such as EQ6. Until then, one should not attempt to draw too many quantitative conclusions from Table 5. One can conclude, however, that the use of different electron acceptors and the chemical conditions in WIPP storage rooms could have a profound effect on the types and quantities of gases and water consumed and produced by the microbial decomposition of organic materials.

Although we have not yet modeled the possible effects of microbial decomposition of cellulosic materials on WIPP gas and water budgets with EQ6, we have made a preliminary estimate of the gas and water generation potential of these reactions. For this exercise, P. E. Drez (personal communication) calculated that the total quantity of cellulose in the WIPP CH TRU inventory is 6.07×10^6 lb. Drez obtained this value by scaling up the quantity of cellulose reported by Clements and Kudera (1985) for waste classified under both combustible and noncombustible content codes to the entire WIPP inventory as tabulated by Oak Ridge National Laboratory (1987). Drez neglected plywood boxes in this preliminary calculation. We assumed that microbes would not decompose the plastics and rubber in the waste. We then converted the total quantity of cellulosic materials calculated by Drez to moles of CH_2O , and divided by the total number of drums to be emplaced in the WIPP to obtain the moles of CH_2O per drum:

$$\begin{aligned} & (6.07 \times 10^6 \text{ lbs}) + (4 \times 10^5 \text{ drums/WIPP}) \times (454 \text{ g/lb}) \\ & + (30.0 \text{ g/mole of CH}_2\text{O}) = 230 \text{ moles of CH}_2\text{O/drum.} \end{aligned} \quad (23)$$

The quantity of CH_2O that could be oxidized by the O_2 initially present in WIPP storage rooms is small. The total quantity of CH_2O in a room is:

$$\begin{aligned} & (230 \text{ moles of } \text{CH}_2\text{O}/\text{drum}) \times (6,750 \text{ drums}/\text{room}) \\ & - 1.55 \times 10^6 \text{ moles of } \text{CH}_2\text{O}/\text{room}. \end{aligned} \quad (24)$$

Equations 17 and 17* imply that 1 mole of O_2 is required for the microbial decomposition of each mole of CH_2O . The quantity of O_2 that would be required to oxidize all of the CH_2O in a room is:

$$\begin{aligned} & (1 \text{ mole of } \text{O}_2/\text{mole of } \text{CH}_2\text{O}) \times (1.55 \times 10^6 \text{ moles of } \\ & \text{CH}_2\text{O}/\text{room}) - 1.55 \times 10^6 \text{ moles of } \text{O}_2/\text{room}. \end{aligned} \quad (25)$$

Division of the quantities of O_2 listed in Table 3 by the value obtained from Equation 25 implies that the O_2 initially present would only be sufficient to oxidize about 1.1 to 1.7% of the cellulosic materials in a room. Microbial decomposition of cellulose could, of course, continue using radiolytically produced O_2 or other electron acceptors present in WIPP (see Table 4).

Inspection of Table 5 reveals that the maximum net gas generation potential that would result from Reactions 17 through 22 as written would be about 3 moles of gas per mole of CH_2O (see Reaction 21*). Furthermore, most of these reactions would produce 1 mole or less of gas per mole of CH_2O and, if one assumes that most of the CO_2 produced would dissolve in the aqueous phase and form HCO_3^- , some reactions would even consume gas. (We did not consider Reactions 20c and 20c* because we don't know the hydration number for limonite.) We therefore tentatively conclude that the maximum microbial gas generation potential is due to SO_4^{2-} reduction combined with low CO_2 solubility, and is about:

$$\begin{aligned} & (3 \text{ moles of gas}/\text{mole of } \text{CH}_2\text{O}) \times (230 \text{ moles of } \text{CH}_2\text{O}/\text{drum}) \\ & - 690 \text{ moles of gas}/\text{drum}. \end{aligned} \quad (26)$$

For many of the other reactions, however, the gas generation potential would be 230 moles of gas per drum, or less. The maximum microbial gas generation potential for a WIPP storage room is then:

$$\begin{aligned} & (690 \text{ moles of gas}/\text{drum}) \times (6,750 \text{ drums}/\text{room}) \\ & - 4.66 \times 10^6 \text{ moles of gas}/\text{room}. \end{aligned} \quad (27)$$

Our estimate of 690 moles per drum is significantly less than the value of 2,000 moles per drum estimated by the National Research Council Panel on the Waste Isolation Pilot Plant (1984). The Panel assumed that each drum contains 60 kg of organic waste (20.5 kg of polyethylene and 39.5 kg of other plastics and cellulose). They also assumed that, through

some combination of processes, all of this organic material could be converted to 5,600 moles of gas. The Panel then recognized that conversion would be incomplete, arbitrarily scaled down its estimate to 2,000 moles per drum, and assumed that this would occur at a rate of 5 moles per year for 400 years.

There are at least three possible reasons why our estimate of the mean microbial gas generation potential is lower than the previous estimate: (1) we assumed that microbes would not decompose plastics and rubber in the waste (the Panel, however, might have assumed this too by scaling down their estimate from 5,600 to 2,000 moles per drum); (2) our estimate of the quantity of cellulosic materials could be lower than assumed previously (the Panel did not specify how much of the 60 kg of organic waste is cellulose); (3) the Panel might have included radiolysis in their estimate.

We believe that the maximum microbial water generation potential for cellulosic materials is given by Reaction 20e* with the assumption that none of the CO₂ produced dissolves in the aqueous phase. We chose Fe₃O₄ as the electron acceptor rather than any of the Fe(III) oxide or hydroxide phases because magnetite is the most likely drum corrosion product under oxic conditions (N. R. Sorensen, personal communication). Amakinite, the most likely anoxic drum corrosion product, cannot be used as an oxidant because it is an Fe(II) hydroxide. The maximum H₂O generation potential is then:

$$(4.33 \text{ moles of H}_2\text{O/mole of CH}_2\text{O}) \times (230 \text{ moles of CH}_2\text{O/drum}) = 997 \text{ moles of H}_2\text{O/drum.} \quad (28)$$

One drum would not, however, produce enough Fe₃O₄ to oxidize all of the CH₂O in that drum. The quantity of Fe₃O₄ that can be produced by oxic corrosion of a drum is:

$$\begin{aligned} &1/3 \times (64.5 \text{ lbs/drum}) \times (454 \text{ g/lb}) + (55.8 \text{ g/mole of Fe}) \\ &= 175 \text{ moles of Fe}_3\text{O}_4/\text{drum.} \end{aligned} \quad (29)$$

Equation 20e* implies that 4/3 of a mole of Fe₃O₄ is required to oxidize 1 mole of CH₂O, or that 307 moles of Fe₃O₄ are required to oxidize all of the CH₂O in a drum. Comparison of this value with the value obtained from Equation 29 implies that Fe₃O₄ could only oxidize 57% of the CH₂O. The maximum H₂O generation potential is then:

$$0.57 \times (997 \text{ moles of H}_2\text{O/drum}) = 568 \text{ moles of H}_2\text{O/drum.} \quad (30)$$

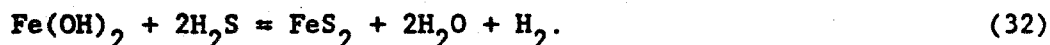
Combining the results of Equations 14 and 30 gives the maximum microbial H₂O generation potential for all of the cellulosic materials in a room:

$$\begin{aligned} &(568 \text{ moles of H}_2\text{O/drum}) \times (6,750 \text{ drums/room}) + (6.91 \\ &\times 10^4 \text{ moles of H}_2\text{O/m}^3 \text{ of brine}) = 55.5 \text{ m}^3/\text{room.} \end{aligned} \quad (31)$$

As in the case of the H₂O consumed by anoxic corrosion of drums (see Equation 15), the quantity of H₂O that could be produced by the microbial decomposition of CH₂O is similar to predictions of brine influx from the Salado formation (Beraum, 1988; McTigue, 1987a; 1987b; 1988a; 1988b).

REACTIONS BETWEEN DRUM CORROSION PRODUCTS AND MICROBIALLY GENERATED GASES

We believe that anoxic corrosion of drums could occur after the O₂ initially present in air trapped in WIPP storage rooms is consumed by oxic corrosion of drums and/or microbial decomposition of organic materials. Any anoxic corrosion would, of course, be confined to regions in which no radiolytically produced O₂ is present. Anoxic corrosion could produce amakinite as microbial activity lowers the oxidation potential (Eh) of the system through values characterized by NO₃⁻ reduction, the reduction of Mn(IV) oxides and hydroxides, and the reduction of Fe(III) oxides and hydroxides (see Table 4). If and when SO₄²⁻-reducing bacteria become active, however, amakinite would become unstable with respect to FeS₂ (pyrite). The amakinite formed at intermediate values of Eh would then react to form FeS₂ and would release significant quantities of H₂O. One possible reaction is:



Similar reactions would, of course, also produce FeS₂ from anoxic drum corrosion products other than amakinite.

After the onset of SO₄²⁻ reduction, any additional drum corrosion could also produce FeS₂ directly:



Table 6 shows the effects of these reactions on the consumption and production of gases and water. Note that although they consume H₂S produced by microbial reduction of SO₄²⁻, these reactions also produce H₂. It is also worth noting that Reaction 32 could release all of the H₂O removed from the system by Reaction 9.

The consumption of the H₂S produced by microbial reduction of SO₄²⁻ would not be limited by the quantity of Fe, Fe(OH)₂, or other drum corrosion products present in a WIPP storage room. Equations 21 and 21* imply that 1/2 mole of H₂S is produced per mole of CH₂O. If we assume that all of the cellulosic materials in a room are decomposed by

SO_4^{2-} -reducing bacteria, the maximum H_2S generation potential is:

$$(230 \text{ moles of } \text{CH}_2\text{O}/\text{drum}) \times (6,750 \text{ drums}/\text{room}) \times (1/2 \text{ mole of } \text{H}_2\text{S}/\text{mole of } \text{CH}_2\text{O}) = 7.76 \times 10^5 \text{ moles of } \text{H}_2\text{S} \text{ room.} \quad (34)$$

Equations 32 and 33 imply that each mole of Fe, $\text{Fe}(\text{OH})_2$, or other drum corrosion products would consume 2 moles of H_2S by forming FeS_2 . Equation 11 implies that there are 3.54×10^6 moles of Fe or Fe corrosion products in a room. This would be more than sufficient to consume all of the H_2S produced. A large quantity of H_2 would be produced by the formation of FeS_2 . If we assume that all of the cellulosic materials in a room are decomposed by SO_4^{2-} -reducing bacteria, that either 1 or 2 moles of H_2 are produced per mole of $\text{Fe}(\text{OH})_2$ or Fe converted to FeS_2 (see Table 6), and that there are 3.54×10^6 moles of Fe in a room (see Equation 11), the total quantity of H_2 produced per room by the formation of FeS_2 is:

$$(1 \text{ mole of } \text{H}_2/\text{mole of } \text{Fe}(\text{OH})_2) \times (3.54 \times 10^6 \text{ moles of } \text{Fe}(\text{OH})_2/\text{room}) = 3.54 \times 10^6 \text{ moles of } \text{H}_2/\text{room}; \quad (35)$$

$$(2 \text{ moles of } \text{H}_2/\text{mole of } \text{Fe}) \times (3.54 \times 10^6 \text{ moles of } \text{Fe}/\text{room}) = 7.08 \times 10^6 \text{ moles of } \text{H}_2/\text{room.} \quad (36)$$

In the case of Reaction 35, the 3.54×10^6 moles of H_2 per room produced by the conversion of $\text{Fe}(\text{OH})_2$ to FeS_2 must be added to the 3.54×10^6 moles produced by conversion of Fe to $\text{Fe}(\text{OH})_2$ (see Equation 13b).

The addition of enough NaNO_3 (or any other nitrate salt), or Mn(IV) oxides or hydroxides to the backfill to oxidize all of the cellulosic materials in the CH TRU waste prior to the onset of SO_4^{2-} -reduction would (1) prevent the conversion of $\text{Fe}(\text{OH})_2$ to FeS_2 and the concomitant release of any of the H_2O removed from WIPP storage rooms by anoxic corrosion of drums; (2) prevent the conversion of $\text{Fe}(\text{OH})_2$ and Fe to FeS_2 and the formation of H_2 .

We calculated the quantity of NaNO_3 or MnO_2 that would be required to prevent SO_4^{2-} -reduction. Equations 18, 18*, 19, and 19* imply that 0.8 moles of NO_3^- and 2 moles of MnO_2 are required to oxidize each mole of CH_2O . The quantity of NaNO_3 or MnO_2 required per room is:

$$(230 \text{ moles of } \text{CH}_2\text{O}/\text{drum}) \times (6,750 \text{ drums}/\text{room}) \times (0.8 \text{ moles of } \text{NaNO}_3/\text{mole of } \text{CH}_2\text{O}) = 1.24 \times 10^6 \text{ moles of } \text{NaNO}_3/\text{room}; \quad (37)$$

$$(230 \text{ moles of CH}_2\text{O/drum}) \times (6,750 \text{ drums/room}) \times (2 \text{ moles of MnO}_2\text{/mole of CH}_2\text{O}) = 3.10 \times 10^6 \text{ moles of MnO}_2\text{/room.} \quad (38)$$

These are equivalent to:

$$(1.24 \times 10^6 \text{ moles of NaNO}_3\text{/room}) \times (85.0 \times 10^{-3} \text{ kg/mole of NaNO}_3) = 105 \times 10^3 \text{ kg of NaNO}_3\text{/room} \quad (39)$$

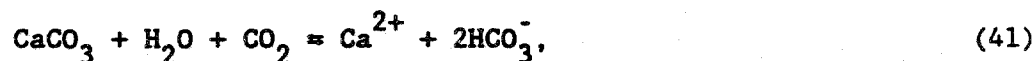
$$(3.10 \times 10^6 \text{ moles of MnO}_2\text{/room}) \times (86.9 \times 10^{-3} \text{ kg/mole of MnO}_2) = 270 \times 10^3 \text{ kg of MnO}_2\text{/room.} \quad (40)$$

The quantity of NaNO₃ obtained from Equation 39 could, of course, be reduced to the extent that nitrate salts are present in the CH TRU waste inventory.

These additives could be dispersed throughout the backfill. MnO₂ would be a better additive than NaNO₃ because the former produces CO₂ which could be consumed by other backfill additives (see below), whereas NaNO₃ produces N₂ for which there is no known scavenger.

REACTIONS BETWEEN POSSIBLE BACKFILL CONSTITUENTS AND GASES AND WATER

At least three solid phases could be added to the backfill to consume CO₂ produced by microbial decomposition of organic materials: CaCO₃, KOH, and NaOH. The reactions between these constituents and CO₂ are:



Reaction 41 would only occur if brine were present; Reactions 42 and 43 would occur in the absence of brine, but if brine subsequently entered the room its pH would increase significantly after dissolution of the KOH, KHCO₃, NaOH, and NaHCO₃ present in the backfill. Table 7 shows the effects of these reactions on the consumption and production of gases and water.

We calculated the quantity of KOH or NaOH that would be required to consume all of the microbially generated CO₂. Equations 17*, 18*, 20a*, 20b*, 20c*, 20d*, 20e*, and 21* imply that 1 mole of CO₂ is produced per

mole of CO₂. If we assume that all of the cellulosic materials in a room are decomposed by these reactions and that none of the CO₂ produced dissolves in the aqueous phase, the maximum CO₂ generation potential is:

$$\begin{aligned} & (230 \text{ moles of CH}_2\text{O/drum}) \times (6,750 \text{ drums/room}) \times \\ & (1 \text{ mole of CO}_2\text{/mole of CH}_2\text{O} = 1.55 \times 10^6 \text{ moles} \\ & \text{of CO}_2\text{/room.} \end{aligned} \tag{44}$$

Equations 42 and 43 imply that 1 mole of CO₂ is consumed per mole of KOH or NaOH added to the backfill. The quantity of KOH or NaOH required is:

$$\begin{aligned} & (1 \text{ mole of KOH or NaOH/mole of CO}_2) \times (1.55 \times 10^6 \\ & \text{moles of CO}_2\text{/room}) = 1.55 \times 10^6 \text{ moles of KOH} \\ & \text{or NaOH/room.} \end{aligned} \tag{45}$$

This is equivalent to:

$$\begin{aligned} & (1.55 \times 10^6 \text{ moles of KOH/room}) \times (56.1 \times 10^{-3} \text{ kg/} \\ & \text{mole of KOH}) = 87.0 \times 10^3 \text{ kg of KOH/room} \end{aligned} \tag{46}$$

$$\begin{aligned} & (1.55 \times 10^6 \text{ moles of NaOH/room}) \times (40.0 \times 10^{-3} \text{ kg/} \\ & \text{mole of NaOH}) = 62.0 \times 10^3 \text{ kg of NaOH/room.} \end{aligned} \tag{47}$$

Because KOH and NaOH are salts of a strong base, mixing these constituents with other constituents of the backfill could prove hazardous to workers. Furthermore, exposure of KOH and NaOH to air during preparation and emplacement of the backfill could result in degradation of these constituents by reaction with atmospheric CO₂. These problems could be solved, however, by placing KOH or NaOH in drums or other containers and interspersing them among the CH TRU drums.

It is tempting to use similar reasoning to calculate that 155×10^3 kg of CaCO₃ would be required to remove all of the microbially generated CO₂ from a WIPP storage room. Reaction 41, however, would not necessarily remove all of the CO₂ even if excess CaCO₃ were present. There are at least three possible reasons why Reaction 41 might not go all the way to completion: (1) not all of the CO₂ would dissolve in the aqueous phase, even at high partial pressures of CO₂; (2) not all of the dissolved CO₂ would react with H₂O to form H₂CO₃ (carbonic acid); (3) the solubility of CO₂ is low in acidic and neutral solutions. Because of the complex, multicomponent nature of this system, the effect of Reaction 41 on the CO₂ budget of a WIPP storage room will have to be carried out with the reaction-path code EQ6.

CONCLUSIONS AND RECOMMENDATIONS

Several chemical reactions could affect the gas and water budgets of WIPP storage rooms. In particular, three of these reactions could consume or produce quantities of water similar to predictions of brine influx from the Salado formation.

The anoxic corrosion of drums could consume significant quantities of water and produce significant quantities of hydrogen. Experiments should be carried out to determine if appreciable anoxic corrosion of 1018 mild steel occurs in Salado brines at 30 or 40°C. The corrosion products of these and ongoing oxic corrosion experiments should be characterized.

Microbial decomposition of organic matter, especially cellulosic materials, could consume or produce significant quantities of water, depending on which electron acceptors are used to oxidize organic matter and the solubility of carbon dioxide in any brine present in WIPP storage rooms. We are surveying the waste generators to improve our knowledge of the nonradioactive waste inventory, especially those constituents that could affect or be affected by microbial activity. Furthermore, we will carry out reaction-path modeling to determine the fate of microbially produced carbon dioxide. Finally, we are reviewing previous studies to determine if additional experiments are required to define the role of microbial activity in the WIPP.

The conversion of drum corrosion products and unaltered drums to pyrite would consume hydrogen sulfide produced by microbial reduction of sulfate, but would produce additional hydrogen and release water consumed during anoxic drum corrosion. The addition of manganese oxides or nitrate salts to the backfill, however, would prevent the formation of hydrogen sulfide, the conversion of drum corrosion products and unaltered drums to pyrite, the formation of additional hydrogen, and the release of water.

Constituents such as calcium carbonate, potassium hydroxide, or sodium hydroxide could be added to the backfill to remove microbially generated carbon dioxide. We will carry out reaction-path modeling to better define the effects of these potential backfill additives. In addition, laboratory and underground experiments should be conducted to validate the results of modeling studies.

REFERENCES

- Beraum, R. (1988). Brine Flow Numerical Modeling for the WIPP Disposal Rooms. Memo to distribution dated 1/22/88, Sandia National Laboratories, Albuquerque, NM.
- Berner, R. A. (1980). Early Diagenesis: A Theoretical Approach. Princeton University Press, Princeton, NJ.
- Butcher, B. M. (1988). Bentonite Water Sorption. Memo of record dated 1/6/88, Sandia National Laboratories, Albuquerque, NM.
- Clements, T. L., Jr., and D. E. Kudera (1985). TRU Waste Sampling Program, Vol. I - Waste Characterization. EGG-WM-6503, Idaho National Engineering Laboratory, Idaho Falls, ID.
- Deal, D. E., and J. B. Case (1987). Brine Sampling and Evaluation Program - Phase I Report. DOE-WIPP-87-008, International Technology Corporation, Albuquerque, NM.
- Haberman, J. H., and D. J. Frydrych. Corrosion Studies of A216 Grade WCA Steel in Hydrothermal Magnesium - Containing Brines. In M. J. Apted and R. E. Westerman, Eds., Scientific Basis for Nuclear Waste Management XI, Materials Research Society, Pittsburgh, PA, in press.
- McTigue, D. F. (1987a). Scaling Relations for Brine Flow. Memo to E. J. Nowak dated 10/6/87, Sandia National Laboratories, Albuquerque, NM.
- McTigue, D. F. (1987b). Brine Flow to a Mined Room. Memo to distribution dated 10/21/87, Sandia National Laboratories, Albuquerque, NM.
- McTigue, D. F. (1988a). Darcy Models for Brine Inflow to the WIPP; Evaluation of Data from the IT Brine Sampling Program. Memo to distribution dated 1/8/88, Sandia National Laboratories, Albuquerque, NM.
- McTigue, D. F. (1988b). Comments on the IT Coupled Brine Transport Model. Memo to distribution dated 2/4/88, Sandia National Laboratories, Albuquerque, NM.
- Molecke, M. A. (1986). TEST PLAN: WIPP Simulated CH and RH TRU Waste Tests: Technology Experiments. Sandia National Laboratories, Albuquerque, NM.
- National Research Council Panel on the Waste Isolation Pilot Plant (1984). Review of the Scientific and Technical Criteria for the Waste Isolation Pilot Plant (WIPP). DOE/DP/48015-1, National Academy Press, Washington, DC.

Nowak, E. J. (1988). Water Absorption by WIPP Disposal Room Backfills. Memo to distribution dated 1/12/88, Sandia National Laboratories, Albuquerque, NM.

Oak Ridge National Laboratory (1987). Integrated Data Base for 1987: Spent Fuel and Radioactive Waste Inventories, Projections, and Characteristics. DOE/RW-0006, Rev. 3, U.S. Department of Energy, Washington, DC.

Scientists Review Panel on WIPP (1988). Evaluation of the Waste Isolation Pilot Plant (WIPP) as a Water-Saturated Nuclear Waste Repository. Unpublished manuscript, Albuquerque, NM.

Stein, C. L., and J. L. Krumhansl (1986). Chemistry of Brines in Salt from the Waste Isolation Pilot Plant (WIPP), Southeastern New Mexico: A Preliminary Investigation. SAND85-0897, Sandia National Laboratories, Albuquerque, NM.

Stein, C. L., and J. L. Krumhansl, An Interpretational Model for the Evolution of Brines in Salt from the Lower Salado Formation, Southeastern New Mexico. Geochimica et Cosmochimica Acta, Vol. 52, in press.

TABLE 1. POSSIBLE DRUM CORROSION PRODUCTS

Formula	Mineral
$\alpha\text{-Fe}_2\text{O}_3$	Hematite
$\gamma\text{-Fe}_2\text{O}_3$	Maghemite
$\alpha\text{-FeO(OH)}$	Goethite
$\beta\text{-FeO(OH)}$	Akaganeite
$\gamma\text{-FeO(OH)}$	Lepidocrocite
$\delta\text{-FeO(OH)}$	Feroxyhyte
$\epsilon\text{-FeO(OH)}$	Synthetic polymorph
$\text{FeO(OH)} \cdot x\text{H}_2\text{O}$	Limonite
Fe(OH)_3	Ferric hydroxide
Fe_3O_4	Magnetite
Fe_2MgO_4	Magnesioferrite
$x\text{Fe(OH)}_2 \cdot y\text{FeOCl} \cdot z\text{H}_2\text{O}$	Green rust
FeO	Wustite
$(\text{Fe, Mg, Mn})(\text{OH})_2$	Amakinite

TABLE 2. CONSUMPTION/PRODUCTION OF GASES
AND WATER BY CORROSION OF DRUMS

Reaction	Moles/Mole of Fe Consumed		
	H ₂	H ₂ O	O ₂
1	0	0	- $\frac{3}{4}$
2	0	- $\frac{1}{2}$	- $\frac{3}{4}$
3	0	$\frac{x + 1}{2}$	- $\frac{3}{4}$
4	0	- $\frac{3}{2}$	- $\frac{3}{4}$
5	0	0	- $\frac{2}{3}$
6	+ $\frac{4}{3}$	- $\frac{4}{3}$	0
7	+ $\frac{x + 3y}{x + y}$	- $\frac{2(x + y) + z}{x + y}$	0
8	+1	-1	0
9	+1	-2	0

TABLE 3. CALCULATION OF THE INITIAL O₂
CONTENT OF A WIPP STORAGE ROOM

Initial Room Void Volume			O ₂ , Moles
Percent	Meters ³	Liters	
84	3,054	3.05 x 10 ⁶	2.59 x 10 ⁴
67	2,436	2.44 x 10 ⁶	2.07 x 10 ⁴
63	2,291	2.29 x 10 ⁶	1.94 x 10 ⁴
60	2,182	2.18 x 10 ⁶	1.85 x 10 ⁴
58	2,109	2.11 x 10 ⁶	1.79 x 10 ⁴

TABLE 4. SEQUENTIAL USE OF ELECTRON ACCEPTORS DURING
MICROBIAL OXIDATION OF ORGANIC MATTER

O_2 (initially present in air, produced by radiolysis)

NO_3^- (present in nonradioactive inventory)

MnO_2 (probably insignificant in WIPP)

Fe_2O_3 , $FeO(OH)$, $Fe(OH)_3$, Fe_3O_4 (possible barrel corrosion products)

SO_4^{2-} (present in brine)

TABLE 5. CONSUMPTION/PRODUCTION OF GASES AND WATER BY MICROBIAL DECOMPOSITION OF CELLULOSE

Reaction	Moles/Mole of CH ₂ O Consumed						
	CH ₄	CO ₂	H ₂	H ₂ O	H ₂ S	N ₂	O ₂
17	0	0	0	0	0	0	-1
17*	0	+1	0	+1	0	0	-1
18	0	+ $\frac{1}{5}$	0	+ $\frac{3}{5}$	0	+ $\frac{2}{5}$	0
18*	0	+ 1	0	+ $\frac{7}{5}$	0	+ $\frac{2}{5}$	0
19	0	-3	0	-1	0	0	0
19*	0	+1	0	+3	0	0	0
20a	0	-7	0	-3	0	0	0
20a*	0	+1	0	+7	0	0	0
20b	0	-7	0	-1	0	0	0
20b*	0	+1	0	+7	0	0	0
20c	0	-7	0	4x-1	0	0	0
20c*	0	+1	0	4x+7	0	0	0
20d	0	-7	0	+3	0	0	0
20d*	0	+1	0	+11	0	0	0
20e	0	-7	+ $\frac{2}{3}$	- $\frac{11}{3}$	0	0	0
20e*	0	+1	+ $\frac{2}{3}$	+ $\frac{13}{3}$	0	0	0
21	0	0	0	0	+ $\frac{1}{2}$	0	0
21*	0	+1	0	+2	+ $\frac{1}{2}$	0	0

TABLE 5. CONSUMPTION/PRODUCTION OF GASES AND WATER
BY MICROBIAL DECOMPOSITION OF CELLULOSE
(Continued)

Reaction	Moles/Mole of CH ₂ O Consumed						
	CH ₄	CO ₂	H ₂	H ₂ O	H ₂ S	N ₂	O ₂
22	+ $\frac{1}{2}$	0	0	- $\frac{1}{2}$	0	0	0
22*	+ $\frac{1}{2}$	+ $\frac{1}{2}$	0	0	0	0	0

TABLE 6. CONSUMPTION/PRODUCTION OF GASES AND WATER BY DRUM CORROSION PRODUCTS

Reaction	Moles/Mole of Fe Consumed		
	H ₂	H ₂ O	H ₂ S
32	+1	+2	-2
33	+2	0	-2

TABLE 7. CONSUMPTION OF GASES AND WATER BY
POSSIBLE BACKFILL CONSTITUENTS

Reaction	Moles/Mole of Backfill Constit- uent Consumed	
	CO ₂	H ₂ O
41	-1	-1
42	-1	0
43	-1	0

Distribution:

1511	D. F. McTigue
6233	J. L. Krumhansl
6233-	C. L. Stein
6300	R. W. Lynch
6330	W. D. Weart
6331	A. R. Lappin
6331	R. L. Beauheim
6331	D. J. Borns
6331	S. J. Lambert
6331	M. D. Siegel
6332	L. D. Tyler
6332	J. G. Arguello
6332	R. Beraum
6332	R. V. Matalucci
6332	M. A. Molecke
6332	E. J. Nowak
6332	J. C. Stormont
6332	T. M. Torres
6333	T. M. Schultheis
6334	D. R. Anderson
6334	S. G. Bertram-Howery
6334	K. Brinster
6334	L. H. Brush
6334	M. S. Y. Chu
6334	L. S. Gomez
6334	R. L. Hunter
6334	M. G. Marietta
6334	A. K. Rutledge

Supplement to Appendix A.1

Brush and Anderson (March 28, 1988) incorrectly concluded on page 8 that, "Inspection of Table 5 reveals that the maximum gas-generation potential that would result from Reactions 17 through 22 as written would be about 3 moles of gas per mole of CH_2O (see Reaction 21*)." Actually, Reaction 21* would produce $3/2$ moles of gas per mole of CH_2O , and the maximum gas-generation potential would result from Reaction 20e*, Fe_3O_4 reduction combined with low CO_2 solubility. Reaction 20e* implies that $1\ 2/3$ moles of gas will be generated per mole of CH_2O . This value in turn implies a gas-generation potential of 383 moles of gas per drum (see Equation 26). This value is significantly less than the value of 690 moles of gas per drum calculated by Brush and Anderson (March 28, 1988) and the value of 1,500 moles per drum calculated in Section 4.2.1.

A.2 Effects of Microbial Activity on Repository Chemistry, Radionuclide
Speciation, and Solubilities in WIPP Brines

by L. H. Brush and D. R. Anderson

Sandia National Laboratories

date: October 26, 1988

Albuquerque, New Mexico 87185

to: Distribution

L. H. Brush D. R. Anderson

from: L. H. Brush and D. R. Anderson, 6334

subject: First Meeting of the WIPP PA Source Term Group

On June 23 and 24, 1988, the Waste Isolation Pilot Plant (WIPP) Performance Assessment (PA) Source Term Group met at the Amfac Hotel in Albuquerque, NM. The objectives of this meeting were to: (1) introduce new members of the group to the WIPP Project; (2) consider the effects of microbial activity on repository chemistry; (3) discuss preliminary estimates of radionuclide speciation and solubilities in selected WIPP brines. The names, addresses, and telephone numbers of the participants appear at the end of this memo.

INTRODUCTION TO THE WIPP PROJECT

W. D. Weart presented an overview of the WIPP Project. D. R. Anderson briefly described the WIPP PA methodology (this will be a major topic of discussion at the next meeting). Next, L. H. Brush presented estimates of the radioactive waste inventory. P. E. Drez then described the nonradioactive constituents of the waste in detail, emphasizing what we know now and how we are finding out more. This presentation included a video tape of the contents of representative drums of transuranic (TRU) waste characterized by Clements and Kudera (1985a), as well as a discussion of the questionnaire sent to the waste generators. Drez also described the differences between the results of laboratory studies of microbial activity carried out with simulated TRU waste (Molecke, 1979; Sandia National Laboratories, 1979; Barnhart et al., 1980; Caldwell et al., 1988), and his calculated gas consumption and production rates based on analyses by Clements and Kudera (1985b) of head-space gases in drums of Rocky Flats TRU waste stored at the Idaho National Engineering Laboratory. (The laboratory studies imply relatively high microbial gas production rates; the field study implies that gas consumption and production decrease to very low rates after several months or a few years of storage under near-surface conditions.) Finally, J. Myers discussed the latest plan for gas monitoring in the First Panel, and how this might resolve the differences between the previous laboratory and field studies.

EFFECTS OF MICROBIAL ACTIVITY ON REPOSITORY CHEMISTRY

Microbial activity could affect the long-term performance of the WIPP significantly (see Brush and Anderson, 1988). Microbial decomposition of nonradioactive constituents of TRU waste, especially cellulosic materials, could influence: (1) the gas and water contents of WIPP storage rooms; (2) the oxidation potential (Eh) and the negative logarithm of the hydrogen ion (H^+) activity (pH) of any brines present; (3) the concentrations of ligands that increase the solubilities of radionuclides by forming complexes with them; (4) the temperature of the repository. Prior to rupture of the drums and resaturation of the repository with brine, nonhalophilic bacteria would dominate; afterward, halophilic and/or halotolerant bacteria could be important. The results of gas analyses by Clements and Kudera (1985b) imply that microbial activity occurs in drums stored at or near the surface; studies carried out by the WIPP Project imply that halotolerant and/or halophilic bacteria degrade nonradioactive waste constituents under optimized laboratory conditions (see Molecke, 1979; Sandia National Laboratories, 1979; Barnhart et al., 1980; Caldwell et al., 1988). We therefore asked the participants at this meeting whether or not microbial activity will occur in the WIPP and, if so, what effects it would have on the repository.

The microbiologists agreed that microbial activity is likely in WIPP storage rooms, and could well affect the long-term performance of the repository. Prior to drum rupture and repository resaturation, the near-surface bacterial activity inferred from the gas analyses of Clements and Kudera (1985b) is likely to continue in the WIPP (see the discussion below of humidity). Afterward, halophilic and/or halotolerant bacteria are likely to influence the repository. Barnhart et al. (1980) did not find any halophilic or other bacteria in the Salado Fm. It is nevertheless possible that extreme halophiles (bacteria that cannot survive in nonsaline environments) from nearby salt lakes have entered the WIPP on dust transported by the wind and the mine ventilation system. Even if extreme halophiles were not present, halotolerant bacteria would probably be important. Because halotolerant bacteria are ubiquitous, it is safe to assume that they are present in the soil at the WIPP site and in TRU waste, and that they will eventually be present in the WIPP itself.

The microbiologists also agreed that the conditions expected for the repository would not preclude microbial activity. Although the humidity of air from the mine ventilation system is only 30 to 35% and fungi and bacteria generally require a humidity of 60 to 70% and 75%, respectively, the humidity of the gases trapped in void spaces in the drums could be significantly higher than that of the mine air. Furthermore, the halophilic and halotolerant bacteria have adapted or can adapt to the low water activities of saline solutions. Although various reactions between brines and nonradioactive constituents of the waste could change the pH of these brines from neutral or nearly neutral values to acidic or basic values, these changes are also

unlikely to inhibit microbial activity. J. K. Lanyi, for example, has cultured a halobacterium from an alkaline lake with a pH of 10.5. The pressures expected for WIPP storage rooms as closure proceeds (up to about 150 atm) could slow, but would not eliminate microbial activity. Elevated salt concentrations, especially magnesium (Mg) and sodium, would increase the barotolerance of bacteria. Finally, sterilization of the waste would probably not be feasible. In conclusion, the only way to prevent microbial activity would be incineration of the waste to remove cellulosic and other materials that could serve as a substrate prior to emplacement. (Construction of such a reprocessing facility would, however, be very expensive and time-consuming.)

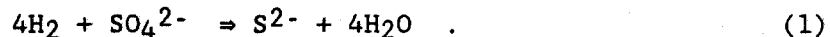
The extent to which microbial activity will degrade cellulosic and other bioavailable materials is unclear. This issue is important because the degradation of all of the cellulosic materials in the waste could produce quantities of water (H₂O) similar to predictions of brine influx from the Salado Fm (see Mctigue, 1987; Beraun, 1988; Brush and Anderson, 1988), as well as significant quantities of carbon dioxide (CO₂) and other gases. B. King believes that a substantial portion of the cellulose will be converted to biomass and hence not to CO₂ and H₂O. D. Grbic-Galic, however, believes that microbial activity could eventually convert most of the cellulose to CO₂ and H₂O, especially under anaerobic conditions. (Anaerobic bacteria would convert a higher proportion of the cellulose to CO₂ and H₂O than aerobic bacteria because the former are less efficient and must therefore consume more of their substrate to obtain an equivalent amount of energy.)

The microbiologists agreed that in the absence of radiolysis, microbes would certainly catabolize cellulosic materials before plastics and rubbers. Aerobic bacteria can degrade plastics and rubbers, albeit much more slowly than cellulose. It is not known if anaerobic bacteria can degrade plastics and rubbers. Radiolysis of plastics and rubbers could, however, increase the bioavailability of these materials. Brush and Anderson (1988) did not include plastics and rubbers in their calculations of potential microbial gas and water generation.

It is unclear whether or not the availability of nutrients will limit microbial activity in the WIPP. The nutritional requirements of halophilic and nonhalophilic bacteria are similar, but our knowledge of the nonradioactive waste inventory is poor. Preliminary estimates, however, suggest that phosphate is the only nutrient that could limit microbial activity. Grbic-Galic suggested that we tabulate all of the organic and inorganic compounds that contain phosphorous (P), and use the Redfield ratio, (CH₂O)₁₀₆·(NH₃)₁₆·(PO₄), to determine if there is enough P relative to cellulosic materials to allow complete microbial degradation of the cellulose. We are already assigning high priority to P in our quantification of the nonradioactive waste inventory. Grbic-Galic also suggested that we also attempt to quantify essential trace elements such as cobalt, copper, molybdenum, and zinc.

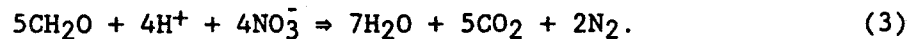
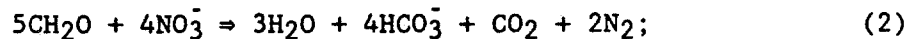
The rates of microbial activity in the WIPP are even more difficult to predict. The rates (but not the extent) of microbial activity will depend critically on the number of microorganisms initially present in the waste, which presumably could be determined. Other factors, however, will also influence the rates of microbial activity. Aerobic bacteria are generally faster than anaerobic bacteria; nonhalophilic bacteria are faster than halophilic bacteria. Increasing pressure and the buildup of metabolites could slow microbial activity somewhat. It is thus likely that the rate of microbial activity in the repository will decrease as time proceeds. Previously measured microbial reaction rates are probably inapplicable, however, to the conditions expected for the WIPP.

The participants felt that the only microbially generated gas that might adversely affect the WIPP is nitrogen (N₂). Backfill additives such as calcium carbonate, calcium oxide, potassium hydroxide, and sodium hydroxide would probably remove CO₂ and H₂O effectively (experiments will soon be underway to confirm this). If hydrogen (H₂) were produced in significant quantities by anoxic drum corrosion (see Brush and Anderson, 1988) or radiolysis, it would be consumed during the microbial reduction of sulfate (SO₄²⁻) to sulfide (S²⁻). The overall reaction would be:



The SO₄²⁻ reducing bacteria might already be present in TRU waste; if not, inoculation of the waste would probably ensure the removal of H₂. Any hydrogen sulfide (H₂S) produced during SO₄²⁻ reduction would probably react with the mild steel drums and/or drum corrosion products to form pyrite (FeS₂). Brush and Anderson (1988) suggested the addition of manganese dioxide (MnO₂), an electron acceptor absent from WIPP brines and TRU waste, to prevent SO₄²⁻ reduction, formation of H₂S, reaction of H₂S with drums and/or drum corrosion products to form FeS₂, and the concomitant release of H₂ and, in the case of drum corrosion products, H₂O. Grbic-Galic thought that MnO₂ might prevent SO₄²⁻ reduction, but cautioned that it is still unclear whether MnO₂ is actually an electron acceptor, or is reduced as an indirect consequence of microbial activity. Eventually, the availability of large quantities of the electron acceptors oxygen (O₂), nitrate (NO₃⁻) and SO₄²⁻ will probably prevent the production of significant quantities of methane. (O₂ is present in mine air and will be produced by radiolysis; NO₃⁻ is present in sludges; SO₄²⁻ is present in WIPP brines.) These electron acceptors will probably prevent significant methanogenesis after the repository resaturates and the drums rupture. (see Brush and Anderson, 1988, for a discussion of the order of usage of electron acceptors by microbes). Methanogenesis could, however, occur in the drums prior to resaturation and rupture.

Because there are large quantities of cellulosic materials and NO_3^- in TRU waste, denitrification (microbial use of NO_3^- as an electron acceptor and the concomitant formation of N_2) appears likely. Two possible reactions (see Brush and Anderson, 1988) are:



In these equations, the simplified formula CH_2O represents cellulose. We do not know how to prevent denitrification except by incineration of the waste or removal of NO_3^- (the latter would not preclude microbial activity using other electron acceptors). The N_2 production rate and the transport rate of N_2 out of the repository thus appear to be critical parameters for the WIPP Performance Assessment. Unfortunately, the intergranular Salado brines appear to be saturated or nearly saturated with N_2 . This will inhibit its diffusion out of the repository.

The participants raised two issues relevant to the Operational Demonstration Period of the WIPP. Grbic-Galic asked whether or not chlorinated solvents such as carbon tetrachloride, chlorinated ethane, or chlorinated ethylene are present in TRU waste. If so, anaerobic bacteria could probably use these compounds as electron acceptors and would produce byproducts which include the toxin chloroform and the carcinogen vinyl chloride. Drez stated that the waste generators purchase large quantities of these solvents. It is unclear, however, how much of them are disposed of as TRU (most if not all of these solvents could evaporate prior to disposal, or be disposed of as low-level waste).

Drez, King and Myers expressed concern that acetic acid (CH_3COOH) from the silicone-based sealant that will be used to grout the roof bolts in the First Panel could exsolve after waste emplacement and stimulate microbial activity by providing additional substrate. If so, this would make the rate of microbial activity to be measured by gas monitoring appear higher than it would be in the absence of the sealant. The microbiologists agreed that CH_3COOH would stimulate microbial activity, but subsequent calculations have shown that its concentration in the sealant is far too low to be of concern (see Brush and Schultheis, 1988).

Finally, the participants discussed possible studies of the effects of microbial activity on repository chemistry. Conceptually, these studies would comprise monitoring the chemistry of microcosms containing: (1) actual nonradioactive constituents of TRU waste; (2) various combinations of backfill constituents; (3) mild steel and/or its corrosion products; (4) various quantities of nonsaline solutions or brines representative of the possible range of water contents expected in WIPP storage rooms (the former would be used to

simulate conditions in the drums prior to rupture); (5) halophilic or nonhalophilic bacteria; (6) the various electron acceptors expected in the WIPP. It is important that these experiments, whether carried out in the laboratory or underground, simulate expected conditions as realistically as possible instead of optimized, "overtest" conditions. Most of the microcosms would thus contain the actual waste constituents rather than more bioavailable substrates such as sugars, as well as the microbes associated with the waste during generation and temporary storage. These microbes could be obtained by producing some waste with procedures used by the generators, except without radionuclides. A few microcosms could be inoculated; still others would have to be sterilized to serve as controls. Experiments with and without alpha radiation would reveal whether or not radiolysis converts plastics and rubbers into usable substrates. Routine chemical analyses at various intervals would define the effects of microbial activity on repository chemistry, especially gas production and consumption rates. Monitoring the Eh would be more difficult, and would probably require analytical techniques similar to those used to study diagenetic oxidation-reduction (redox) reactions in natural environments such as lacustrine, estuarine, and marine sediments. (Eh electrodes are generally considered unreliable.)

Because the rate of microbial activity in WIPP storage rooms will probably decrease with time (see above), it is imperative that any experiments be carried out for periods long enough to provide realistic instead of maximum rates. An alternative approach might be to carry out several experiments, each with one of the electron acceptors expected in the WIPP; this might provide realistic data for various stages of microbial activity without resorting to long-term experiments.

We could probably carry out the experiments outlined above equally well in the laboratory or in the WIPP. It would probably be useful to scale up these experiments eventually to a mesocosm or room-scale test.

PRELIMINARY ESTIMATES OF RADIONUCLIDE SPECIATION AND
SOLUBILITIES IN SELECTED WIPP BRINES

The upcoming forecast of the comparison to the Environmental Protection Agency standard and methodology demonstration by Bertram-Howery et al. (in prep.) will require radionuclide solubilities as input for transport calculations. Various participants at this meeting therefore discussed their estimates of: (1) the composition and quantities of brines likely to enter WIPP storage rooms; (2) the concentrations of organic ligands in these brines; (3) the speciation and solubilities of americium (Am), neptunium (Np), plutonium (Pu), uranium (U), and thorium (Th), given the estimated concentrations of the organic ligands listed above.

It is difficult to quantify the uncertainties in our estimates of the composition and quantities of likely WIPP brines, and the concentrations of organic ligands in these brines. The uncertainties in our actinide speciation and solubility estimates, however, are probably much greater, and are so large that it will be impossible to specify unique values for their solubilities for the upcoming methodology demonstration. Instead, it will be necessary to vary these estimates by several orders of magnitude.

Brush defined two brines for these estimates of radionuclide speciation and solubilities (see Table 1). The Salado brine represents the average composition of intergranular fluids sampled at or near the stratigraphic horizon of the WIPP by Stein and Krumhansl (1986, 1988), Deal and Case (1987), and Deal et al. (1988). These brines are currently seeping into the WIPP through the ribs and, to a lesser extent, the back and floor, but rarely accumulate because of evaporation caused by ventilation of the mine. After the repository is sealed, however, the air trapped in voids will become saturated and these brines could accumulate. Brush included chemical analyses of 29 brine weeps from Stein and Krumhansl (1986, 1988). These brine weeps came from five shallow floor holes in Room J, as well as 24 short (up to 10 in) horizontal holes in the northern part of the WIPP. Brush also included data from ten long (up to 50 ft) downholes, one short floor hole, and one short horizontal hole sampled by Deal and Case (1987) and Deal et al. (1988); Drez and Myers (1988) reported analyses of these brines. Brush excluded data for fluid inclusions from Stein and Krumhansl (1986, 1988) because these brines will not migrate in the absence of a significant thermal gradient. He also excluded data from all of the BTP holes and upholes sampled by Deal and Case (1987) and Deal et al. (1988) because the former are contaminated with fluids from the Rustler Formation spread in the mine to control dust and/or from grouts, and the latter changed composition due to evaporation during accumulation. For those holes which yielded sufficient brine for replicate analyses, Brush averaged the results for each element and used one value per hole to define the Salado brine shown in Table 1. He also averaged results obtained at different times from the same hole.

The other type of brine considered for the radionuclide speciation and solubility estimates occurs in isolated but occasionally large pockets in the underlying Castile Fm. These brines could enter the repository if an exploratory drillhole penetrates both a storage room and a brine reservoir, and the hole is sealed above the repository. For the Castile brine (see Table 1), Brush used the average concentrations reported by Popielak et al. (1983). He selected WIPP 12 because, of all the drillholes studied by Popielak et al. (1983), it is the closest to the WIPP Site. The brines from WIPP 12, however, are not necessarily representative of any Castile brines that might occur beneath the WIPP.

Fluids from overlying formations could seep down the shafts, along the drifts, and around or through plugs and seals to WIPP storage rooms. We did not consider such fluids for these radionuclide speciation and solubility estimates, but will consider them in subsequent studies of repository and radionuclide chemistry.

Next, we estimated how much of the Salado and Castile brines discussed above could enter WIPP storage rooms. Prior to this meeting, D. J. Borns and B. M. Butcher suggested we assume that the residual porosity in each room will be 2, 5, or 10% of the initial volume of a 13-by-33-by-300 ft room ($42,900 \text{ ft}^3$ or $3,640 \text{ m}^3$), and that brine could eventually resaturate these volumes. We thus assumed that there could eventually be 72.8, 182, or 364 m^3 of brine per room.

Drez then estimated the quantities of the following organic ligands in the WIPP inventory: citric acid, dihexyl N,N-diethyl carbamoylmethylenephosphonate, (CMPO), ethylenediaminetetraacetic acid (EDTA), 8-hydroxyquinoline, 1-thenoyl-3,3,3-trifluoroacetone (TTA), tributyl phosphate, (TBP), and tri-N-octylphosphine oxide (TOPO). Drez based his estimates on the annual rates at which these compounds are used at the Rocky Flats Plant, and multiplied the annual rates by 44 years to obtain the total quantity of each organic ligand in the WIPP inventory. (The WIPP will accept waste produced from the beginning of 1970 through the end of 2013.) He thus estimated that there will be 1,950 moles of citric acid, 431 moles of CMPO, 683 moles of 8-hydroxyquinoline, 167 moles of TTA, 612 moles of TBP, and 200 moles of TOPO, in the entire WIPP inventory. Drez did not, however, estimate the quantity of EDTA because Rocky Flats stopped using it in the early 1970s and he could not determine the rate at which it was used.

Although there is probably very little EDTA in the WIPP inventory, Brush estimated the total quantity as follows. First, he assumed that Rocky Flats used EDTA through the end of 1974. Next, G. R. Choppin estimated that they used EDTA at one third the annual rate of TTA. Brush then multiplied the annual rate for TTA by one third and five years to obtain the total quantity of EDTA in the WIPP inventory, 6.35 moles. Because Choppin believes that Rocky Flats substituted TTA for EDTA, Brush reduced the total quantity of TTA from 167 to 148 moles to take account of the 5 years during which they used EDTA.

Choppin recommended that we omit CMPO, TBP, and TOPO from further consideration; these organic ligands would not dissolve in aqueous solutions such as WIPP brines and thus would not affect the speciation and solubilities of radionuclides in these brines.

Finally, Brush used the estimates discussed above to calculate the maximum, intermediate, and minimum concentrations of citric acid, EDTA, 8-hydroxyquinoline, and TTA in Salado or Castile brines in WIPP storage rooms. Drez suggested that these organic ligands will probably occur only in sludges, which will not be stored in boxes. Brush therefore divided the total quantity of each of these organic ligands by 399,000 (the total number of drums to be emplaced in the WIPP), but did not include the 24,100 boxes in the denominator. This yielded the quantity of each organic ligand per drum. Brush then multiplied these values by 7,180 drums per room to obtain the quantities of these organic ligands per WIPP storage room. He divided these quantities by 72.9, 182, and 364 m³ to obtain the maximum, intermediate, and minimum concentrations of each organic ligand. The results of these calculations appear in Table 2.

Choppin attempted to estimate the speciation and solubilities of Am, Np, Pu, U, and Th in both the Salado and Castile brines, given the concentrations of organic ligands discussed above. Unfortunately, there are no thermodynamic data (solubility products for solid phases, or stability constants, β_i , for dissolved organic or inorganic complexes) for these elements in solutions with ionic strengths (I) equal to those of the Salado and Castile brines (I = 7.66 and 6.14 M, respectively). Most existing data apply to solutions with I \leq 1 M, and only a few pertain to values of I as high as 2 or 3 M. Furthermore, most of the data are for 1:1 (metal:ligand) or 1:2 complexes; very few data exist for the 1:3 or 1:4 complexes that will probably be important species in these brines. Finally, data reported by different groups using different experimental techniques are often contradictory; this necessitates subjective judgment for data selection.

Choppin used the extended Davies Equation to extrapolate the stability constants for the 1:1 and 1:2 complexes to high ionic strengths. He then plotted the results on graphs of $\log \beta$ versus I, and assumed that the curves for the 1:3 and 1:4 complexes for which limited data are available would be parallel to the curves for the 1:1 and 1:2 complexes. In some cases, the availability of stability constants for organo-actinide complexes was so limited that Choppin could not use the extended Davies Equation. In these cases, he either used the values for low ionic strengths directly for the Salado and Castile brines, or arbitrarily added one log unit to them. In those cases where no data exist, Choppin used stability constants for chemically analogous organo-actinide or organo-lanthanide complexes.

These extrapolations of thermodynamic data to high ionic strengths result in order-of-magnitude uncertainties. Furthermore, it is not yet possible to predict how processes such as microbial activity, drum corrosion, and radiolysis will affect the Eh of the repository, and to what extent these processes will influence the oxidation states of Np, Pu, and U. Finally, the values of pH reported for the Salado and Castile brines (see Table 1) could differ significantly from the actual values because of problems associated with pH measurements in concentrated brines (J. L. Krumhansl, personal communication). Even if the reported values are accurate, the dissolution of microbially generated CO₂ or reactions between the brines and nonradioactive constituents of the waste such as cements could change the pH significantly. Despite all of these uncertainties, Choppin tentatively concluded that the dominant species of Am, Np, Pu, U, and Th in the brines discussed above would be hydroxy complexes in the case of the III, IV, and VI oxidation states or chloride complexes in the case of the V oxidation state. Choppin does not believe that complexation by organic ligands would be important. This is because the concentrations of organic ligands in any brines would probably be quite low (see Table 2), and because Mg²⁺, which is present in both brines at relatively high concentrations, competes very effectively with the actinides for the binding sites on these organic ligands. Clearly, it will be necessary to confirm these predictions with laboratory experiments.

Choppin also attempted to estimate the solubilities of Am, Np, Pu, U, and Th in the Salado and Castile brines shown in Table 1. Even in the absence of significant complexing by the organic ligands discussed above, the uncertainties in extrapolating thermodynamic data to high ionic strengths and predictions of Eh and pH make this impossible. It will thus be necessary to vary the solubilities of these elements over several orders of magnitude for radionuclide transport calculations, at least until we can carry out laboratory experiments under expected repository conditions.

REFERENCES

- Barnhart, B. J., E. W. Campbell, E. Martinez, D. E. Caldwell, and R. Hallett (1980). Potential Microbial Impact on Transuranic Wastes Under Conditions Expected in the Waste Isolation Pilot Plant (WIPP). Annual Report, October 1, 1978 - September 30, 1979. LA-8297-PR, Los Alamos Scientific Laboratory, Los Alamos, NM.
- Beraun, R. (1988). Brine Flow Numerical Modeling for the WIPP Disposal Rooms. Memo to distribution dated 1/22/88, Sandia National Laboratories, Albuquerque, NM.
- Bertram-Howery, S. G., M. G. Marietta, R. L. Hunter, M. S. Y. Chu, L. H. Brush, R. P. Rechar, and K. F. Brinster. Forecast of the Comparison to 40 CFR Part 191, Subpart B, and Methodology Demonstration for the Waste Isolation Pilot Plant. SAND88-1452, Sandia National Laboratories, Albuquerque, NM, in preparation.
- Brush, L. H., and D. R. Anderson (1988). Potential Effects of Chemical Reactions on WIPP Gas and Water Budgets. Memo to distribution dated 3/28/88, Sandia National Laboratories, Albuquerque, NM.
- Brush, L. H., and T. M. Schultheis (1988). Use of Permatex Clear RTV Sealant for Grouting Around Roof Bolts and Bulkheads in the First Panel. Memo to J. Gilbert dated 7/12/88, Sandia National Laboratories, Albuquerque, NM.
- Caldwell, D. E., R. C. Hallett, M. A. Molecke, E. Martinez, and B. J. Barnhart (1988). Rates of CO₂ Production from the Microbial Degradation of Transuranic Wastes Under Simulated Geologic Isolation Conditions. SAND87-7170, Sandia National Laboratories, Albuquerque, NM.
- Clements, T. L., Jr., and D. E. Kudera (1985a). TRU Waste Sampling Program: Vol. I - Waste Characterization. EGG-WM-6503, Idaho National Engineering Laboratory, Idaho Falls, ID.
- Clements, T. L., Jr., and D. E. Kudera (1985b). TRU Waste Sampling Program: Volume II - Gas Generation Studies. EGG-WM-6503, Idaho National Engineering Laboratory, Idaho Falls, ID.
- Deal, D. E., and J. B. Case (1987). Brine Sampling and Evaluation Program Phase I Report. DOE-WIPP 87-008, US Department of Energy, Waste Isolation Pilot Plant, Carlsbad, NM.

- Deal, D. E., J. B. Case, R. M. Deshler, P. E. Drez, J. Myers, and J. R. Tyburski (1988). Brine Sampling and Evaluation Program Phase II Report, DOE-WIPP-87-010, US Department of Energy Waste Isolation Pilot Plant, Carlsbad, NM.
- Drez, P. E., and J. Myers (1988). Transmittal of Brine Analyses from the Brine Sample and Evaluation Program. Letter to L. Brush dated 3/9/88, International Technology Corporation, Albuquerque, NM.
- McTigue, D. E. (1987). Brine Flow to a Mined Room. Memo to distribution dated 10/21/87, Sandia National Laboratories, Albuquerque, NM.
- Molecke, M. A. (1979). Gas Generation from Transuranic Waste Degradation: Data Summary and Interpretation. SAND79-1245, Sandia National Laboratories, Albuquerque, NM.
- Popielak, R. S., R. L. Beauheim, S. R. Black, W. E. Coons, C. T. Ellingson, and R. L. Olsen (1983). Brine Reservoirs in the Castile Formation, Southeastern New Mexico, TME 3153, US Department of Energy, Waste Isolation Pilot Plant, Carlsbad, NM.
- Sandia National Laboratories (1979). Summary of Research and Development Activities in Support of Waste Acceptance Criteria for WIPP. SAND79-1305, Sandia National Laboratories, Albuquerque, NM.
- Stein, C. L., and J. L. Krumhansl (1986). Chemistry of Brines in Salt from the Waste Isolation Pilot Plant (WIPP), Southeastern New Mexico: A Preliminary Investigation. SAND85-0897, Sandia National Laboratories, Albuquerque, NM.
- Stein, C. L., and J. L. Krumhansl (1988). A Model for the Evaluation of Brines in Salt from the Lower Salado Formation, Southeastern New Mexico, Geochimica et Cosmochimica Acta, Vol. 52, pp. 1037-1046.

TABLE 1. COMPOSITION OF BRINES USED FOR ESTIMATES OF RADIONUCLIDE SPECIATION AND SOLUBILITIES

Element	Intergranular Salado Brines Sampled at or Near the Stratigraphic Horizon of the WIPP	Castile Brines from WIPP-12
B	152 mM ¹	92 mM ²
Br ⁻	13 mM ³	6.4 mM ⁴
Ca ²⁺	10 mM ⁵	8.7 mM ⁶
Cl ⁻	6.04 M ⁷	5.02 M ⁸
K ⁺	500 mM ⁹	74 mM ¹⁰
Mg ²⁺	1.0 M ¹¹	66 mM ¹²
Na ⁺	3.9 M ¹³	6.00 M ¹⁴
SO ₄ ²⁻	160 mM ¹⁵	190 mM ¹⁶
TIC ¹⁷	370 μM ¹⁸	5.6 mM ¹⁹
pH	6.0 ²⁰	7.06 ²¹

¹Mean of ten downholes, one floor hole, and one horizontal hole from Drez and Myers (1988).

²Mean of 13 analyses from Popielak et al. (1983).

³Mean of five floor holes and 23 horizontal holes from Stein and Krumhansl (1986, 1988), and ten downholes, one floor hole, and one horizontal hole from Drez and Myer (1988).

⁴Mean of 13 analyses from Popielak et al. (1983).

⁵Mean of five floor holes and 24 horizontal holes from Stein and Krumhansl (1986, 1988), and ten downholes, one floor hole, and one horizontal hole from Drez and Myers (1988).

TABLE 1. COMPOSITION OF BRINES USED FOR ESTIMATES OF
RADIONUCLIDE SPECIATION AND SOLUBILITIES (Cont.)

-
- ⁶Mean of 13 analyses from Popielak et al. (1983).
- ⁷Mean of five floor holes and 24 horizontal holes from Stein and Krumhansl (1986, 1988), and ten downholes, one floor hole, and one horizontal hole from Drez and Myers (1988).
- ⁸Mean of 13 analyses from Popielak et al. (1983).
- ⁹Mean of five floor holes and 24 horizontal holes from Stein and Krumhansl (1986, 1988), and ten downholes, one floor hole, and one horizontal hole from Drez and Myers (1988).
- ¹⁰Mean of 13 analyses from Popielak et al. (1983).
- ¹¹Mean of five floor holes and 24 horizontal holes from Stein and Krumhansl (1986, 1988), and ten downholes, one floor hole, and one horizontal hole from Drez and Myers (1988).
- ¹²Mean of 13 analyses from Popielak et al. (1983).
- ¹³Mean of five floor holes and 24 horizontal holes from Stein and Krumhansl (1986, 1988), and ten downholes, one floor hole, and one horizontal hole from Drez and Myers (1988).
- ¹⁴Mean of 13 analyses from Popielak et al. (1983).
- ¹⁵Mean of five floor holes and 22 horizontal holes from Stein and Krumhansl (1986, 1988), and ten downholes, one floor hole, and one horizontal hole from Drez and Myers (1988).
- ¹⁶Mean of 13 analyses from Popielak et al. (1983).
- ¹⁷Total inorganic carbon as HCO_3 .
- ¹⁸Mean of ten downholes, one floor hole, and one horizontal hole from Drez and Myers (1988).
- ¹⁹From Popielak et al. (1983); number of analyses not reported.
- ²⁰Mean of ten downholes, one floor hole, and one horizontal hole from Drez and Myers (1988).
- ²¹Mean of 59 field analyses from Popielak et al. (1983).
-

TABLE 2. ESTIMATES OF THE CONCENTRATIONS OF ORGANIC LIGANDS FROM TRU WASTE IN SALADO AND CASTILE BRINES AFTER RESATURATION OF WIPP STORAGE ROOMS

Ligand	Total Quantity of Ligand in WIPP Inventory (moles)	Concentration of Ligand in Salado or Castile Brine (μM)		
		Maximum ¹	Intermediate ²	Minimum ³
Citric acid	1,952	481	193	96.4
EDTA	6.53	1.56	0.626	0.313
8-hydroxy- quinoline	683	169	67.6	33.8
TTA	148	36.5	14.6	7.31

¹Based on 72.9 m³ of brine (2% of initial room volume resaturated).

²Based on 182 m³ of brine (5% of initial room volume resaturated).

³Based on 364 m³ of brine (10% of initial room volume resaturated).

PARTICIPANTS

Rip Anderson
Division 6334
Sandia National Laboratories
Albuquerque, NM 87185
(505) 844-6553

Nisa Brown
Division 6322
Sandia National Laboratories
Albuquerque, NM 87185
(505) 846-6551

Larry Brush
Division 6334
Sandia National Laboratories
Albuquerque, NM 87185
(505) 844-9998 or 846-2799

Jim Butler
Division of Applied Sciences
Harvard University
Cambridge, MA 02138
(617) 495-2845

Greg Choppin
Department of Chemistry
Florida State University
Tallahassee, FL 32310
(904) 644-3875

Paul Drez
IT Corporation
2340 Alamos, SE
Albuquerque, NM 87106
(505) 842-0835

A. J. Francis
Department of Applied Science
Brookhaven National Laboratory
Upton, NY 11973
(516) 282-4534

Dunja Grbic-Galic
Environmental Engineering and Science
Department of Civil Engineering
Stanford University
Stanford, CA 94305
(415) 723-3668

Barry King
IT Corporation
2340 Alamo SE
Albuquerque, NM 87106
(505) 842-0835

Janos Lanyi
Department of Physiology and Biophysics
University of California at Irvine
Irvine, CA 92717
(714) 856-7150

Jon Myers
IT Corporation
2340 Alamo SE
Albuquerque, NM 87106
(505) 842-0835

Wendell Weart
Department 6330
Sandia National Laboratories
Albuquerque, NM 87185
(505) 844-4855

Distribution:

J. N. Butler, Harvard University
G. R. Choppin, Florida State University
P. E. Drez, IT Corporation
A. J. Francis, Brookhaven National Laboratory
D. Grbic-Galic, Stanford University
B. King, IT Corporation
J. K. Lanyi, UC Irvine
J. Myers, IT Corporation
1511 D. F. McTigue
6233 J. L. Krumhansl
6233 C. L. Stein
6300 R. W. Lynch
6322 N. N. Brown
6322 M. M. Warrant
6330 W. D. Weart
6331 A. R. Lappin
6331 R. L. Beauheim
6331 D. J. Borns
6331 P. B. Davies
6331 S. J. Lambert
6331 K. L. Robinson
6331 M. D. Siegel
6332 L. D. Tyler
6332 R. Beraun
6332 B. M. Butcher
6332 R. V. Matalucci
6332 M. A. Molecke
6332 D. E. Munson
6332 E. J. Nowak
6332 T. M. Torres
6333 T. M. Schultheis
6334 D. R. Anderson
6334 S. G. Bertram-Howery
6334 K. F. Brinster
6334 L. H. Brush
6334 M. S. Y. Chu
6334 L. S. Gomez
6334 R. L. Hunter
6334 M. G. Marietta
6334 R. P. Rechard
6334 A. K. Rutledge

A.3 Lab-Scale Microbial Experiments

by L. H. Brush and D. R. Anderson

Sandia National Laboratories

Albuquerque, New Mexico 87185

date: December 9, 1988

to: Distribution

Larry Brush D. R. Anderson

from: L. H. Brush and D. R. Anderson, 6334

subject: Second Meeting of the WIPP PA Source-Term Group

On October 6 and 7, 1988, the Waste Isolation Pilot Plant (WIPP) Performance-Assessment (PA) Source-Term Group (STG) met at the WIPP Site and the Motel Stevens in Carlsbad, NM. The objectives of this meeting were to: (1) take new members of the STG on a tour of the WIPP Site; (2) orient new members to the WIPP PA methodology; (3) develop a conceptual design for the microbiological experiments required for the quantification of repository and radionuclide chemistry. The names, addresses, and telephone numbers of the participants appear at the end of this memo.

INTRODUCTION TO THE WIPP PROJECT

W. White of Westinghouse conducted a tour of the Waste Handling Building; W. D. Weart led the underground tour. Next, D. Powers described halobacteria cultured from nearby salt lakes and the salt tailings pile, and took the participants to some of the lakes in Nash Draw. D. R. Anderson then presented the WIPP PA methodology in detail. (Anderson had presented an overview of PA at the First Meeting of the STG in June.)

MICROBIOLOGICAL EXPERIMENTS

Brush and Anderson (1988a) calculated that chemical reactions such as microbial decomposition of cellulosic materials could significantly affect the gas and water contents of WIPP storage rooms. Although the microbiologists who attended the First Meeting of the STG agreed that microbial activity is likely in WIPP storage rooms (see Brush and Anderson, 1988b), the rate or rates at which microbial activity would occur are unclear. Laboratory studies of microbial activity (see Molecke, 1979) suggest significantly higher rates of microbial gas production than those calculated by P. Drez (personal communication) from analyses by Clements and Kudera (1985) of head-space gases in drums of Rocky Flats TRU waste stored at the Idaho National Engineering Laboratory.

At the First Meeting of the STG, the participants felt that the only microbially generated gas that might adversely affect the WIPP is nitrogen (N_2). This conclusion was based on the assumptions that: (1) backfill additives such as calcium carbonate, calcium oxide, potassium hydroxide, and sodium hydroxide would remove carbon dioxide (CO_2) effectively (laboratory experiments will soon be underway to confirm this); (2) hydrogen (H_2) would be removed during the microbial reduction of sulfate (SO_4^{2-}) to sulfide (see Brush and Anderson, 1988b, for this reaction); (3) any hydrogen sulfide produced during SO_4^{2-} reduction would react with the mild-steel drums and/or drum-corrosion products to form pyrite; (4) methanogenesis would be limited to the period prior to drum rupture and resaturation of the repository with brine.

At this, the Second Meeting of the STG, the participants considered how to demonstrate that SO_4^{2-} -reducing bacteria would remove H_2 . Because it is unlikely that TRU waste already contains SO_4^{2-} -reducing bacteria, it would be necessary to inoculate the waste or the backfill. Halobacteria capable of reducing SO_4^{2-} apparently exist in muds in salt lakes near the WIPP Site. After demonstrating that these bacteria consume H_2 , they could serve as the inoculum. The microbiologists felt, however, that it would be difficult to guarantee that this inoculum would survive until conditions conducive to SO_4^{2-} reduction occur, or throughout the period during which SO_4^{2-} reduction would be required. (Data reviewed by Molecke, 1979, imply that anoxic corrosion of 1018-mild-steel drums will produce significant quantities of H_2 for a period of about 300 years after brine contacts the drums. Furthermore, Brush and Anderson, 1988a, extrapolated corrosion data from Haberman and Frydrych, 1988, for A216 Grade WCA mild steel in Permian Basin brines at 90, 150, and 200°C to expected WIPP temperatures of about 30°C and the lower magnesium concentrations of intergranular Salado-Fm. brines. Based on these extrapolations, they concluded that anoxic corrosion could produce significant quantities of H_2 for 500 to 2000 years.) The STG thus concluded that the WIPP Project cannot assume that H_2 would be removed during the microbial reduction of SO_4^{2-} as stated earlier.

In view of this conclusion, it is necessary to determine if there is an oxidant that could be added to the backfill to corrode the drums without producing H_2 . (Subsequent to this meeting, M. J. Davis, 1830, and N. R. Sorensen, 1831, suggested the use of copper(II) carbonate or copper(II) sulfate as an oxidant for the mild-steel drums.)

The participants also discussed possible laboratory experiments to ascertain whether or not denitrification (microbial N_2 production resulting from the use of nitrate, NO_3^- , as an electron acceptor) would be significant in the WIPP. (These experiments are necessary because there is no known backfill additive that would remove N_2 at a reasonable cost, and its rate of diffusion into the surrounding Salado Fm. would probably be very slow.) The microbiologists outlined a program to: (1) determine whether or not denitrification occurs under expected repository conditions; (2) determine its N_2 yield; (3) measure its rate or rates.

To determine whether or not denitrification is possible, known denitrifiers or halophiles would be placed in likely WIPP brines along with NO_3^- ; detection of N_2 after either type of experiment would suggest that denitrification could occur in the WIPP. These studies would be carried out using glucose as a substrate instead of cellulosic materials to ensure that any microbial activity occurs in experiments of reasonable duration.

To determine the N_2 yield, experiments similar to the first set would be carried out with bacterial cultures obtained from environments similar to those in which TRU waste is generated. Bench, skin, and shoe swipes, for example, would sample a variety of bacteria similar to that in TRU waste. These experiments would indicate how much of the NO_3^- might be converted to N_2 by denitrifiers, and how much might be converted to nitrite and ammonia by nitrate reducers. (The latter two compounds would reside mainly in the brine and would hence not affect the repository gas budget.) These experiments would also indicate how much nitrogen the denitrifiers would incorporate into their biomass, and how much they would release as N_2 . Brush and Anderson (1988a) assumed that denitrification would produce 0.4 moles of N_2 per mole of cellulose (CH_2O) consumed; D. Grbic-Galic, however, pointed out that the ideal yield during denitrification is actually 0.2 $\text{N}_2/\text{CH}_2\text{O}$ when the inclusion of N_2 in biomass is included. (Grbic-Galic assumed that the composition of cellular material is $\text{C}_5\text{H}_7\text{O}_2\text{N}$, and that 0.08 moles of cells are produced per mole of CH_2O .)

Finally, it might be possible to measure the N_2 -production rates of any halophilic or halotolerant denitrifiers identified by the experiments described above. For realistic rate experiments, however, cellulosic materials would have to be used as the substrate instead of glucose. Because the microbial hydrolysis of cellulose, the rate limiting step under these conditions, would probably be extremely slow, it might only be possible to determine upper limits for the denitrification rate.

During the preceding discussion, the STG assumed that denitrification or NO_3^- reduction would not occur until the drums rupture and the repository resaturates. The participants based this assumption on their belief that cellulosic materials and NO_3^- -bearing sludges are not usually stored in the same drums. Microbial use of NO_3^- as an electron acceptor would thus be impossible until brine provides a medium through which NO_3^- could diffuse to the cellulose. We will attempt to determine whether or not cellulose and sludges are stored separately as we continue our development of the nonradioactive waste inventory.

REFERENCES

- Brush, L. H., and D. R. Anderson (1988a). Potential Effects of Chemical Reactions on WIPP Gas and Water Budgets. Memo to distribution dated 3/28/1988, Sandia National Laboratories, Albuquerque, NM.
- Brush, L. H., and D. R. Anderson (1988b). First Meeting of the WIPP PA Source-Term Group. Memo to distribution dated 10/27/1988, Sandia National Laboratories, Albuquerque, NM.
- Clements, T. L., Jr., and D. E. Kudera (1985). TRU Waste Sampling Program: Volume II - Gas Generation Studies. EGG-WM-6503, Idaho National Engineering Laboratory, Idaho Falls, ID.
- Haberman, J. H., and D. J. Frydrych (1988). Corrosion Studies of A216 Grade WCA Steel in Hydrothermal Magnesium-Containing Brines. In M. J. Apter and R. E. Westerman, Editors, Scientific Basis for Nuclear Waste Management XI. Symposium held November 30 - December 1, 1987. Boston, Massachusetts, U.S.A., Materials Research Society, Pittsburgh, PA, pp. 761-772.
- Molecke, M. A. (1979). Gas Generation From Transuranic Waste: Data Summary and Interpretation. SAND79-1245, Sandia National Laboratories, Albuquerque, NM.

PARTICIPANTS

Rip Anderson
Division 6334
Sandia National Laboratories
Albuquerque, NM 87185
505 844 6553

Larry Brush
Division 6334
Sandia National Laboratories
Albuquerque, NM 87185
505 844 9998 or 846 2799

Jim Butler
Division of Applied Sciences
Harvard University
Cambridge, MA 02138
617 495 2845

A. J. Francis
Department of Applied Science
Brookhaven National Laboratory
Upton, NY 11973
516 282 4534

Dunja Grbic-Galic
Environmental Engineering and Science
Department of Civil Engineering
Stanford University
Stanford, CA 94305
415 723 3668

Janos Lanyi
Department of Physiology and Biophysics
University of California at Irvine
Irvine, CA 92717
714 856 7150

Dennis Powers
Star Route
Box 87
Anthony, TX 79821
915 877 2417

Wendell Weart
Department 6330
Sandia National Laboratories
Albuquerque, NM 87185
505 844 4855

Bill White
101 E. Greene St.
Carlsbad, NM
505 887 8246

Distribution:

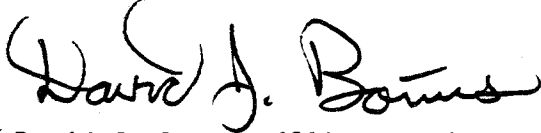
J. N. Butler, Harvard University
G. R. Choppin, Florida State University
P. E. Drez, IT Corporation
A. J. Francis, Brookhaven National Laboratory
D. Grbic-Galic, Stanford University
B. King, IT Corporation
J. K. Lanyi, UC Irvine
D. Powers, Anthony, TX
J. Myers, IT Corporation
1511 D. F. McTigue
6233 J. L. Krumhansl
6233 C. L. Stein
6300 R. W. Lynch
6322 N. N. Brown
6322 M. M. Warrant
6300 W. D. Weart
6331 A. R. Lappin
6331 R. L. Beauheim
6331 D. J. Borns
6331 P. B. Davies
6331 S. J. Lambert
6331 K. L. Robinson
6331 M. D. Siegel
6332 L. D. Tyler
6332 R. Beraun
6332 B. M. Butcher
6332 R. V. Matalucci
6332 M. A. Molecke
6332 D. E. Munson
6332 E. J. Nowak
6332 T. M. Torres
6333 T. M. Schultheis
6334 D. R. Anderson
6334 S. G. Bertram-Howery
6334 K. F. Brinster
6334 L. H. Brush
6334 M. S. Y. Chu
6334 L. S. Gomez
6334 R. Guzowski
6334 R. L. Hunter
6334 M. G. Marietta
6334 R. P. Recharad
6334 A. K. Rutledge

A.4 Dilatancy and Fracturing in the Disturbed Rock Zone
and Its Contribution to the Total Observed Closure
in WIPP Excavations

by D.J. Borns and J.C. Stormont

date: 7 October 1988

to: Distribution



from: David J. Borns, 6331 and John C. Stormont, 6332

subject: Dilatancy and Fracturing in the Disturbed Rock Zone and its contribution to the total observed closure in WIPP excavations

Evidence for Dilatancy

The hydrologic and mechanical properties of the host rock alter concentrically around excavations at the WIPP site in response to the excavation (Borns and Stormont, 1988). This zone of rock has become known as the the Disturbed Rock Zone (DRZ). Portions of the DRZ are thought to be dilatant (Stormont et al., 1987). Dilatancy as used in this memo refers to the the volumetric strain that results from the opening of microfractures (Brace et al., 1966). The objective of this memo is to report on the observation of dilatancy from recent in situ studies at the WIPP site and suggest possible consequences of the volume change associated with dilatancy on other studies at WIPP such as reconciling observed closure with predictive models. The concept of dilatancy and fracture-induced volume change should be integral to any model of the repository system and rock deformation at the WIPP site.

Since 1986, we have completed several hydrologic and geophysical studies of the bedded halites and anhydrites adjacent to the underground excavations at WIPP. Measurements of gas flow, apparent resistivity, and seismic velocity indicate that the porosity of the host rock increase significantly within the DRZ (e.g., gas porosity increases from 0.001 to 0.010 [Stormont et al., 1967]; resistivity increase from 100 ohm-m to 1000 ohm-m, [Borns and Stormont, 1988]; compressional velocities decrease by greater than 10% [Skokan et al., 1988b]; and seismic attenuation is measured in the DRZ [Holcomb, 1988]). The 10^4 increase in gas flow rates within the DRZ indicates that the changes in hydrologic and geophysical properties are not just due to desaturation but also require an increase in fracture porosity. The change in porosity (primarily dilatant volume increase) is accommodated by displacement of the excavation surface inwards (Figure. 1) and contributes to the observed closure. It is noted that multiple mechanisms contribute to the observed closure, but for the remainder of this memo we will focus on the contribution of dilatancy and fracturing to observed closure and reconciling in situ measurements with modelling. We will address the magnitudes of this component of closure in the following sections.

Component of Closure Due to Dilatancy

Using for example the increase (0.001 to 0.010) in gas porosity inferred from the gas-flow testing program (Stormont et al., 1987) and the increase (0.02 to 0.04) in porosity inferred from by seismic velocity (Skokan et al., 1988b), we can proceed to calculate the increment of closure due to dilatancy. [The reader is reminded that these methods are not designed to directly measure porosities, and therefore, the porosities are not determined as precisely one may wish. The various methods do indicate changes in porosity that are within an order of magnitude for the various methods and show the possible ranges for porosities within the DRZ.] The calculation assumes a thickness for the zone of dilatancy (1 or 2 m from gas flow tests and seismic surveys), a cylindrical and isotropic room configuration (Figure. 1). The resulting calculations are based on the following equation:

$$\delta = r_0 \pm \frac{1}{2(\Delta\phi - 1)} \sqrt{(2r_0(\Delta\phi - 1))^2 + 4(2(\Delta\phi - 1))\Delta\phi(R^2 - r_0^2)}$$

where:

- ϕ_0 = the initial porosity of the host rock
- ϕ = the porosity of the rock volume in which dilatancy has occurred
- $\Delta\phi = \phi - \phi_0$ (the change in porosity due to dilatancy)
- r_0 = the initial radius of the circular excavation
- DRZ = the thickness of the dilatant rock zone
- $R = r_0 + \text{DRZ}$ (the outer radius of the dilatant rock zone)
- δ = the radial increment of closure due to dilatancy

Assuming dilatancy in one radial dimension, we have calculated dilatant components of closure for rooms with a radius of 4 m (e.g., Room D) and 5 m (e.g., SPDV Rooms) as in the following table:

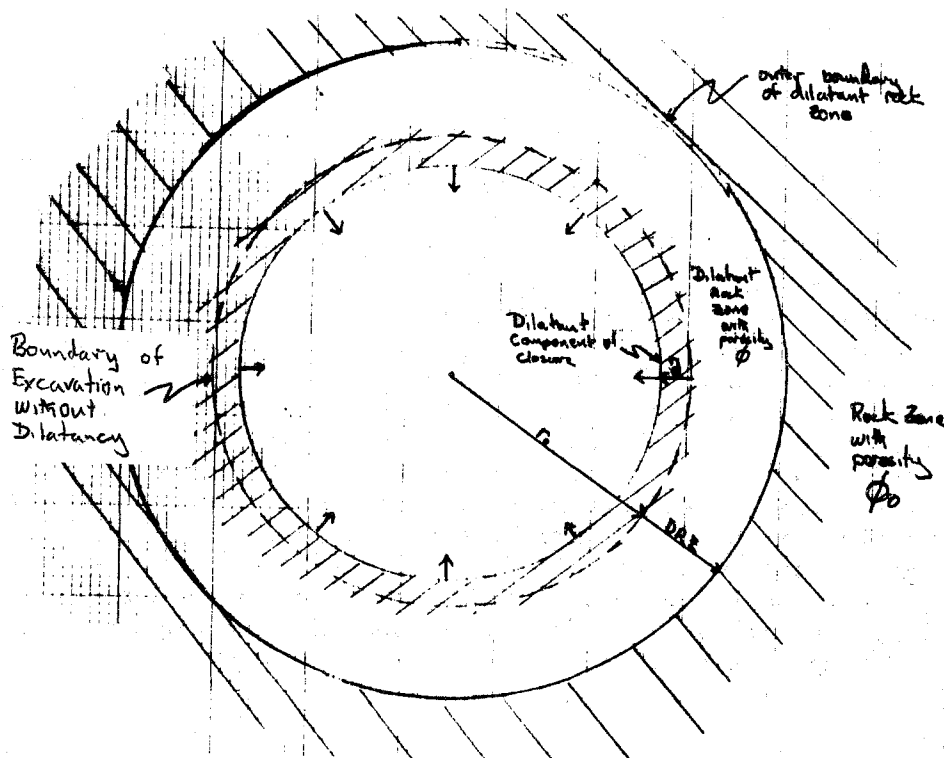


Figure 1. Schematic of Dilatant Zone and Closure

TABLE 1. INCREMENT OF CLOSURE (2θ) IN RESPONSE TO DILATANCY

r_0 Initial Room Radius in meters	DRZ thickness of dilatant zone in meters	$\Delta\phi$ change in porosity	2θ dilatant closure in meters
4*	2	0.009 ^a	0.046
5**	2	0.009 ^a	0.044
5	2	0.02 ^{b,c}	0.098
4	1	0.009	0.020
5	1	0.009	0.020
5	1	0.020	0.044

*: radius comparable to Room D in the experimental area

** : radius comparable to SPDV rooms

a: porosity change calculate from gas-flow tests

b: porosity change calculated from apparent resistivity surveys

c: porosity change calculated from 10% reduction in compressional velocity

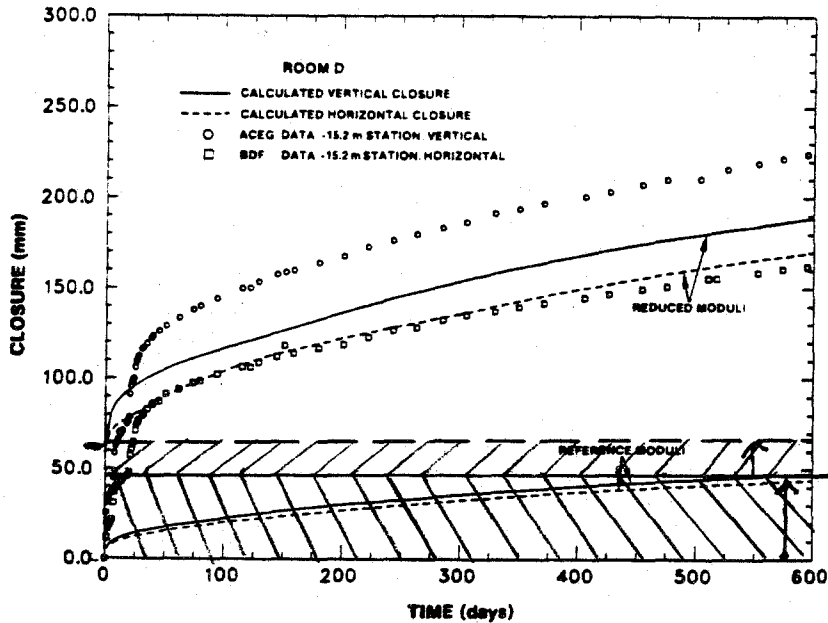
$\Delta\phi = (0.02)$ for both b and c, but calculated independently.

The calculated closure due to dilatancy for both an experimental room (4 m radius) and a SPDV room (5 m radius) is approximately 4.5 cm (1.8 in) for a zone of dilatancy 2 m thick and 2.0 cm (0.8 in) for a dilatant zone 1 m thick. These components are of same magnitude as the early time closure (see Figure 2.; Munson et al. 1987, and GFDAR, 1988).

The development of microfracturing around an excavation in salt may develop very early from the day of ecavation onward (Dussealt et al., 1987) in response to accelerated strain rates around the opening. The decreases in seismic velocities around older excavations show that the fracturing increases with time associated with further increase in porosity (e.g. ϕ increase from 0.2 to 0.4 from resistivity surveys). The increased porosity will lead to a further increment of closure (a 10% velocity decrease indicates an change in porosity $\phi = 0.02$).

Effects of Microscopic Fractures on Observed Closure

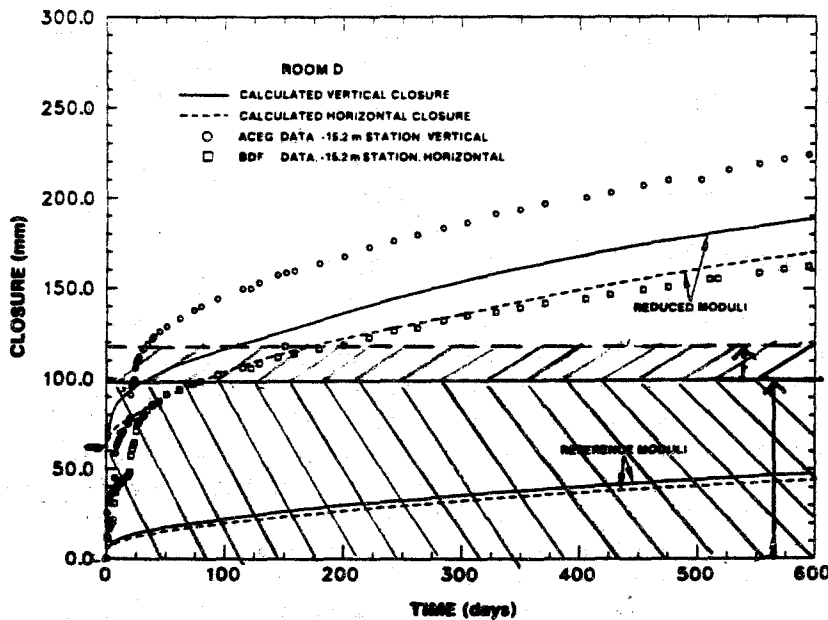
Within 4 years of excavation, 100% of the 10 m wide rooms in the WIPP facility exhibit fractures around the opening (Borns and Stormont, 1988; GFDAR, 1988). In the narrower rooms, the fracture frequency is increasing with time and is expected to eventually reach 100% of the area. The minimum aperture fracture that is apparent to the naked eye is 2 mm. Therefore, we will use 2 mm as a minimum amount of fracture opening per individual fracture. Mapping (Borns, 1985; Borns and Stormont, 1988; GFDAR, 1988) of fractures that develop around a WIPP opening indicate a minimum distribution of fractures within zone 2 m from the excavation surface as: 6 fractures in the floor and 2 fractures each in both of the ribs and the back. These fractures would contribute (using a 2 mm opening) 1.8 cm of vertical closure and 0.8 cm of horizontal closure--Remember, these values are a minimum, since minimum values for both fracture density and aperture were assumed.



Calculated and measured long-time vertical closures in Room D.

$\Delta\phi = 0.009$
 as calculated
 from gas-flow test

~~~~~ observed fracture  
 opening (1.8 cm)  
 dilatancy  
 (46 cm)



Calculated and measured long-time vertical closures in Room D.

$\Delta\phi = 0.02$   
 as calculated  
 from resistivity  
 and seismic survey

~~~~~ observed fracture  
 opening (1.8 cm)
 dilatancy
 (9.8 cm)

Figure 2: Comparison of Dilatant Component of Closure and Observed Closure in Room D (Munson et al, 1987)

Conclusions and Recommendations

Gas-flow tests, electromagnetic and seismic surveys conducted in the WIPP facility indicate zones of increased porosity around underground excavations. The increased porosity implies a volume increase during deformation associated with dilatant strain. The volume increase within the DRZ gives a component of closure with significant magnitude to affect the total observed closure (especially at early times). Dilatant volume increase and its contribution to closure may provide a natural phenomena that accounts for a significant portion of the difference between calculated and observed closure.

References:

- Borns, D. J., 1986. Marker Bed 139: A study of drillcore from a systematic array, Sandia Report, SAND85-0023
- Borns, D. J., and Stormont, J. C., 1988. An interim report on excavation effect studies at the Waste Isolation Pilot Plant: The delineation of the disturbed rock zone, Sandia Report, SAND87-1375
- Brace, W. F., Paulding, B. W., and Scholz, C., Dilatancy in the fracture of crystalline rocks, J. Geophys. Res., 71, 3939-3953
- Dusseault, M. B., Rothenburg, L., and Mraz, D. Z., 1987, The design of openings using multiple mechanism viscoplastic law,
- Holcomb, D. J., 1988. Cross-hole measurements of velocity and attenuation to detect a disturbed zone in salt at the Waste Isolation Pilot Plant, in Cundall, P. A., Sterling, and Starfield, A. M., eds., Rock Mechanics: Proceedings of the 29th U. S. Symposium, 633-640
- Munson, D. E., Torres, T. M., and Jones, Robert L., 1987, Pseudostrain representation of multipass excavations in salt, 28th US Symposium on Rock Mechanics, 853-872
- GFDAR, 1988, Geotechnical Field Data and Analysis Report: July 1986-June 1987, Waste Isolation Pilot Plant, US DOE, DOE/WIPP 87-017
- Skokan, C. K., Pfeifer, M. C., Keller, G. V., and Andersen, H. T., 1988, Studies of electrical methods for characterizing salt properties at the WIPP site, New Mexico
- Skokan, C., Starrett, J., and Andersen, H. T., 1988, Final Report: Feasibility study of seismic tomography to monitor underground pillar integrity at the WIPP site. Sandia Report, SAND88-7096
- Stormont, J. C., Petersen, E. W., and Lagus, P. L., 1987, Summary of and Observations about WIPP Facility Horizon flow measurements through 1986, Sandia Report, SAND87-0176

A.5 Numerical Brine Flow Modeling to an Isolated WIPP Disposal Room

by R. Beraun

date: March 23, 1988

to: Distribution



from: R. Beraun, 6332

subject: Numerical Brine Flow Modeling to an Isolated WIPP Disposal Room

INTRODUCTION

Efforts have been directed toward developing tools for approximating the movement of brine into WIPP excavations from WIPP rock salt. D. F. McTigue [1] has analytically provided some very simple calculational tools for assessing the brine fluxes that might be expected from a Darcy flow mechanism. A series of transient two-dimensional numerical models have been developed as part of these efforts. The results of the numerical calculations of brine inflow into a room in a panel assembly has been presented in a previous memorandum [2]. This memorandum discusses the results of the transient two-dimensional numerical finite element modeling efforts performed to determine the amount of brine accumulated into an isolated WIPP disposal room. The calculations were performed for a range of matrix permeability values ($k \approx 1.0 \times 10^{-21} - 1.0 \times 10^{-20} m^2$) in combination with two initial pressures conditions, hydrostatic and lithostatic. The physics, algorithm, assumptions, material properties, boundary and initial conditions are similar to those corresponding to the case of brine flow to a room in a panel assembly. A detailed discussion has been documented in previous memoranda [2,3].

An independent set of calculations for the case of brine accumulation in an isolated disposal room has been conducted by L. C. Sanchez (Organization 6322) at our request. His findings, documented in a memorandum [6], show good agreement, even though his set of solutions were performed with much different mesh representations.

DISCUSSION

Throughout the modeling, the system was assumed to start at a uniform hydrostatic ($6.0 \times 10^6 Pa$) or lithostatic ($15.0 \times 10^6 Pa$) pressure. Because of the large geometrical dimensions associated with the model, the specification of impermeable boundary conditions to all exterior element boundaries is a good approximation of the real situation. The mesh is a two-dimensional cartesian finite element mesh that was generated by the PATRAN-G [4] finite element graphics package. Upon completion of the mesh, it was translated to the equivalent finite difference network approach for solving Q/TRAN. Figure 1 shows the mesh of the isolated room used in the brine flow computations. Because of symmetry, only a fourth of the room was modeled. A total of 1712 four-node, isoparametric, quadrilateral

elements were used. A very fine grid size (relative to overall dimensions) is used in the repository proximity to accommodate the steep pressure differential away from the room surface walls through a few meters into the formation.

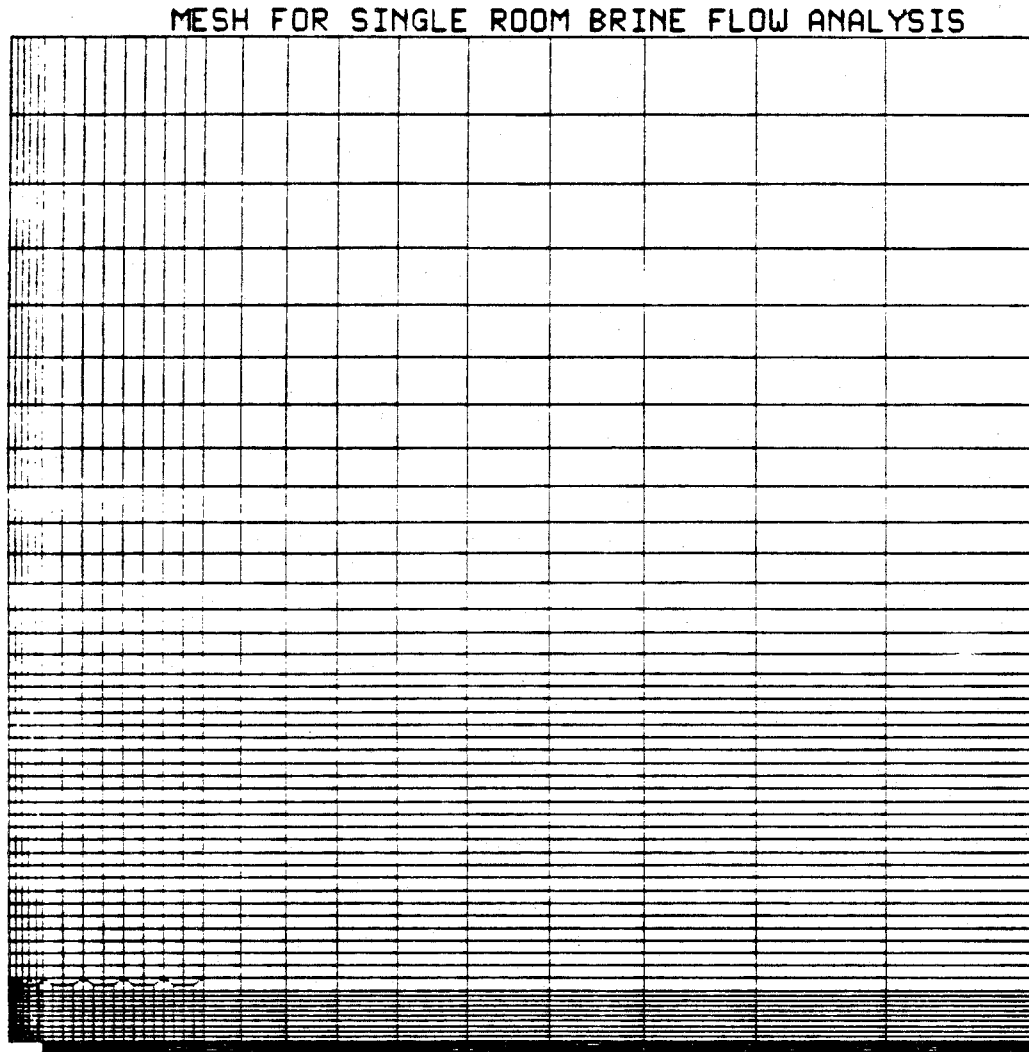


Figure 1: Finite Element Mesh of Room Configuration.

The results found for these conditions are summarized in Figures 2 through 8. Essentially, four different cases were considered; a combination of each of the matrix permeability (k) values (1.0×10^{-21} , $1.0 \times 10^{-20} m^2$) and either hydrostatic or lithostatic initial pressure condition formed a case. Figures 2 and 3 depict the volumetric flow rate per unit length as a function of time computed at the repository walls. The curves on Figure 2 show that for a hydrostatic initial pressure condition, the brine flow rate decreases asymptotically from 1.85×10^{-11} to $9.3 \times 10^{-12} m^3/s.m$ and from 1.06×10^{-10} to $6.46 \times 10^{-11} m^3/s.m$ for matrix permeability values of 1.0×10^{-21} , and $1.0 \times 10^{-20} m^2$ respectively. The curves on Figure 3 represent brine flow rates for the case where the initial pressure condition was lithostatic, these rates decreased also asymptotically from 4.67×10^{-11} to $2.35 \times 10^{-11} m^3/s.m$ for a medium permeability of $1.0 \times 10^{-21} m^2$, and from 2.68×10^{-10} to $1.63 \times 10^{-10} m^3/s.m$ for a medium permeability value of $1.0 \times 10^{-20} m^2$. Figures 4 and 5 present time history curves for the cumulative volume per unit room length for all the cases considered in this study. More significant results found in this study are presented in Figures 6 and 7 which depict the total brine accumulated in an isolated disposal room as a function of time. The curves in Figure 6 are brine cumulative volumes for a hydrostatic initial pressure condition. For a matrix permeability value of $1.0 \times 10^{-21} m^2$, brine volumes of $3.71 m^3$ and $6.54 m^3$ are found at the end of 100 and 200 years respectively; the corresponding values for a matrix permeability of $1.0 \times 10^{-20} m^2$, are 23.63 and $43.0 m^3$. The curves depicted in Figure 7 summarize similar results for the cases where the initial pressure condition is lithostatic; for a matrix permeability of $1.0 \times 10^{-21} m^2$, cumulative volumes of 9.37 and $16.5 m^3$ are found at the end of 100 and 200 years respectively; the corresponding values for a matrix permeability of $1.0 \times 10^{-20} m^2$, are 59.66 and $108.73 m^3$.

The results stated above, are summarized in Table 1 for easy reference. These results were compared with those obtained from an independent set of calculations conducted by L. C. Sanchez (Organization 6322) at our request. His findings, documented in a memorandum [6], show good agreement, even though his set of solutions were performed with much different mesh representations. Table 2 summarizes this comparison.

Table 1: Summary of Results for Cumulative Volumes at 100 and 200 years

| Initial Pressure | Brine Cumulative Volume (m^3) | | | |
|------------------|-----------------------------------|--------------------|--------------------|--------------------|
| | 100 years | | 200 years | |
| | $k = 10^{-21} m^2$ | $k = 10^{-20} m^2$ | $k = 10^{-21} m^2$ | $k = 10^{-20} m^2$ |
| Hydrostatic | 3.712 | 23.63 | 6.535 | 43.0 |
| Lithostatic | 9.373 | 59.66 | 16.50 | 108.73 |

Table 2: Comparison with Reference [6] (Isolated Room Case)

| Time
years | Brine Cumulative Volume per Unit Length (m^3/m) | |
|---------------|---|----------------------|
| | Reference [6]* | Present Calculation* |
| 50 | 0.392 | 0.356 |
| 100 | 0.699 | 0.653 |
| 150 | 0.984 | 0.928 |
| 200 | 1.254 | 1.189 |

*These results correspond to the case where the initial pressure was lithostatic and the matrix permeability was $k = 10^{-20} m^2$.

Finally, the results found in this study which correspond to brine flow to an isolated disposal room, were compared with those corresponding to brine flow to a room in a panel assembly, this comparison is presented in Figure 8. Approximately 1.5 times more brine would be accumulated for an isolated room case than for a room in panel assembly. Cumulative volumes of 60 and 43 m^3 are found for the isolated room and room in a panel case respectively at the end of 100 years. The results shown in this figure indicate that the presence of adjacent rooms does in effect decrease the total brine flow into a room.

REFERENCES

1. McTigue, D. F., "Brine Flow to a Mined Room," Memorandum to Distribution, October, 1987.
2. Beraun, R., "Brine Flow Numerical Modeling for the WIPP Disposal Rooms," Memorandum to Distribution, January, 1988.
3. Beraun, R., "Fluid Flow - Heat Transfer Equivalence," Memorandum to Distribution, February, 1988.
4. PDA Engineering INC, "PATRAN-G User's Guide Volume I and II," Santa Ana, California, 1980.
5. Rockenbach, F. A., "Q/TRAN," PDA Engineering INC, Santa Ana, California, May 1986.
6. Sanchez L. C., "Comparative Calculations Performed to Confirm Previous Calculations Used to Predict Brine Inflow to the WIPP Site," Memorandum to J. M. Freedman, March, 1988.

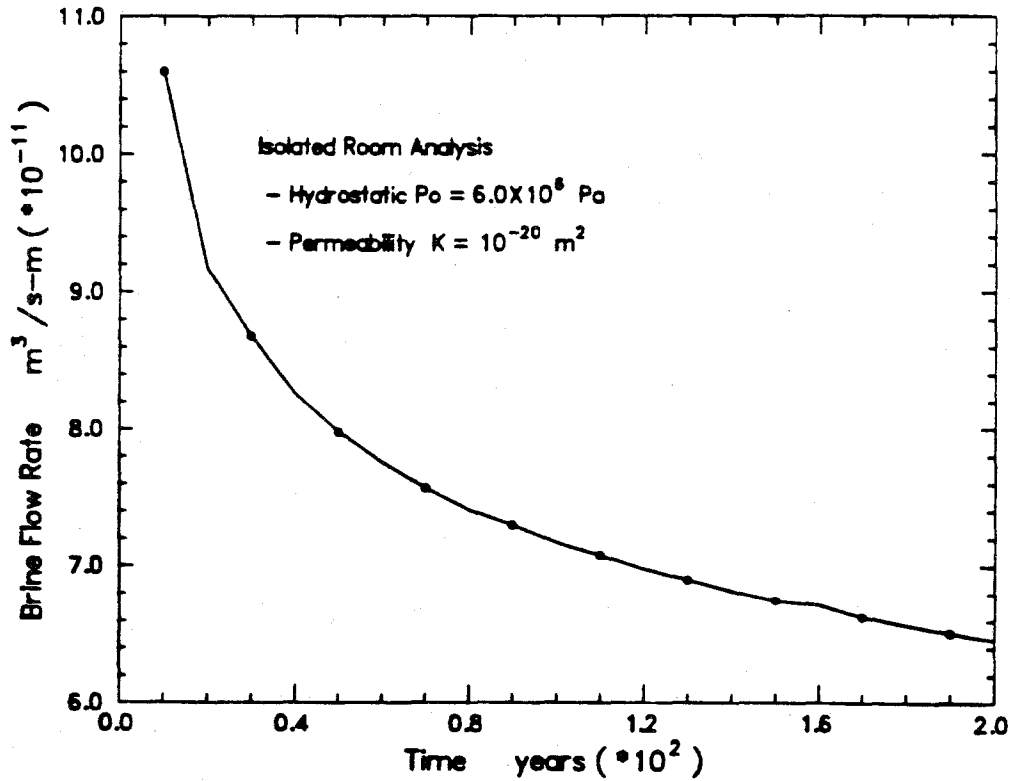
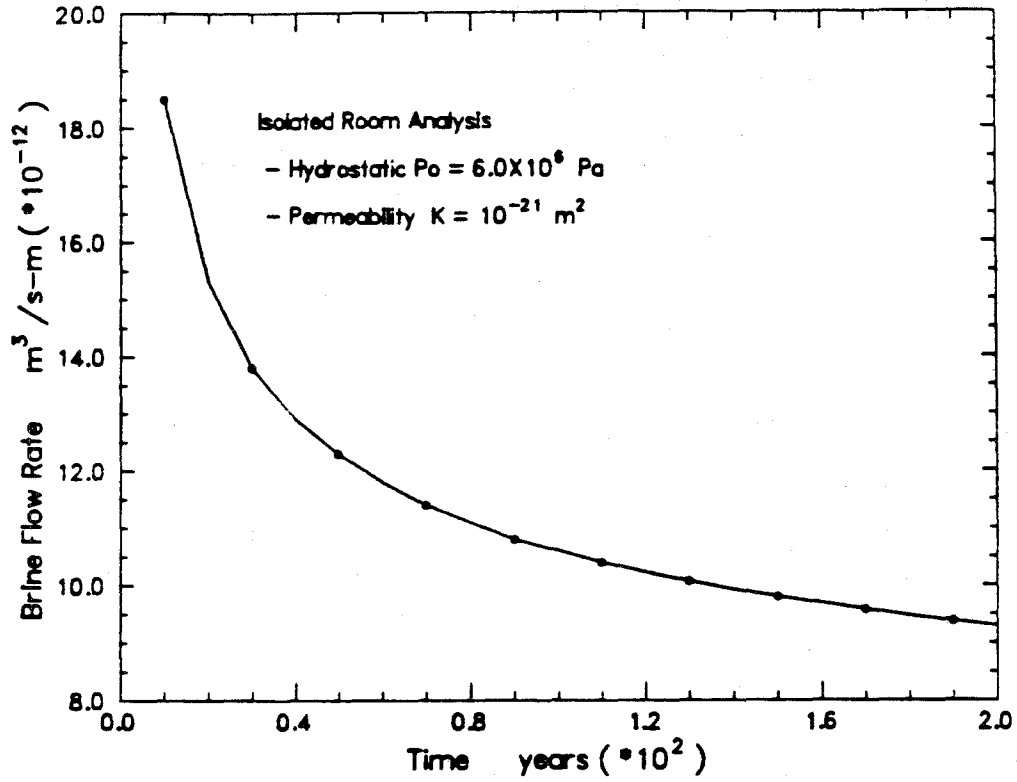


Figure 2: Volumetric Flow Rate per Room Length (Hydrostatic Case).

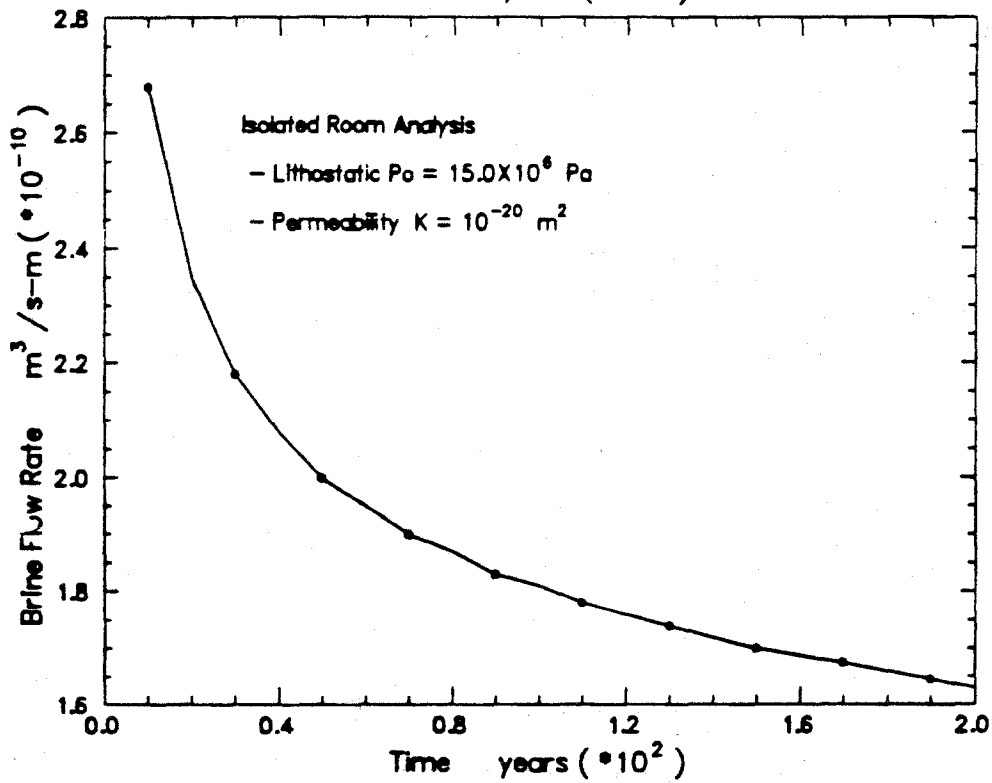
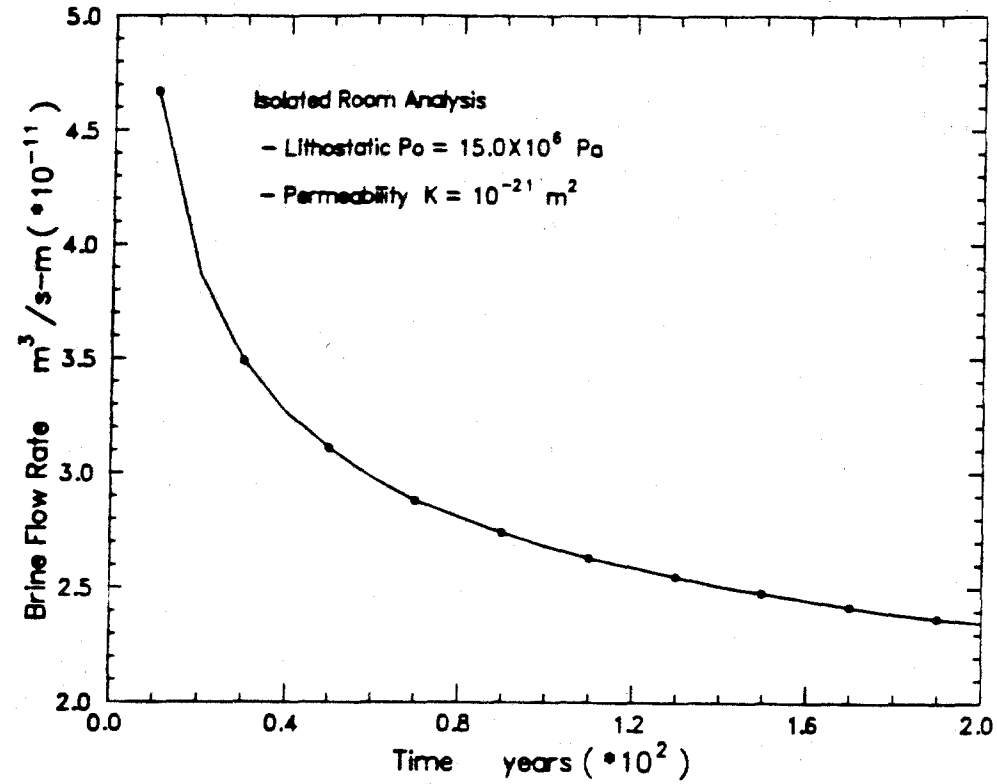


Figure 3: Volumetric Flow Rate per Room Length (Lithostatic Case).

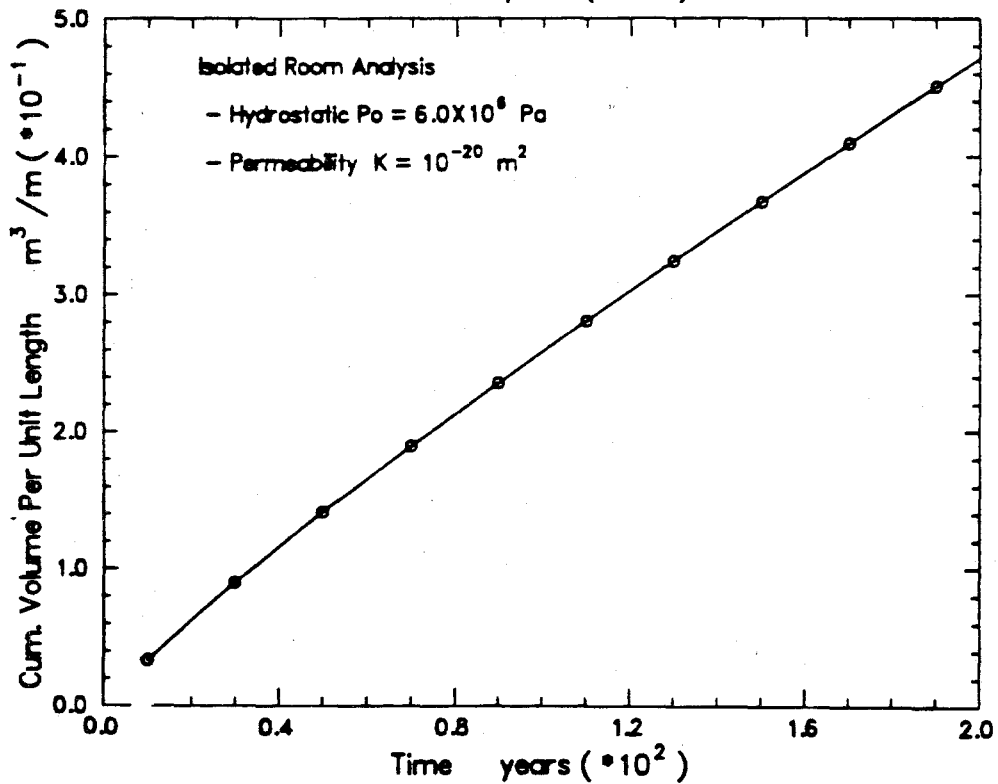
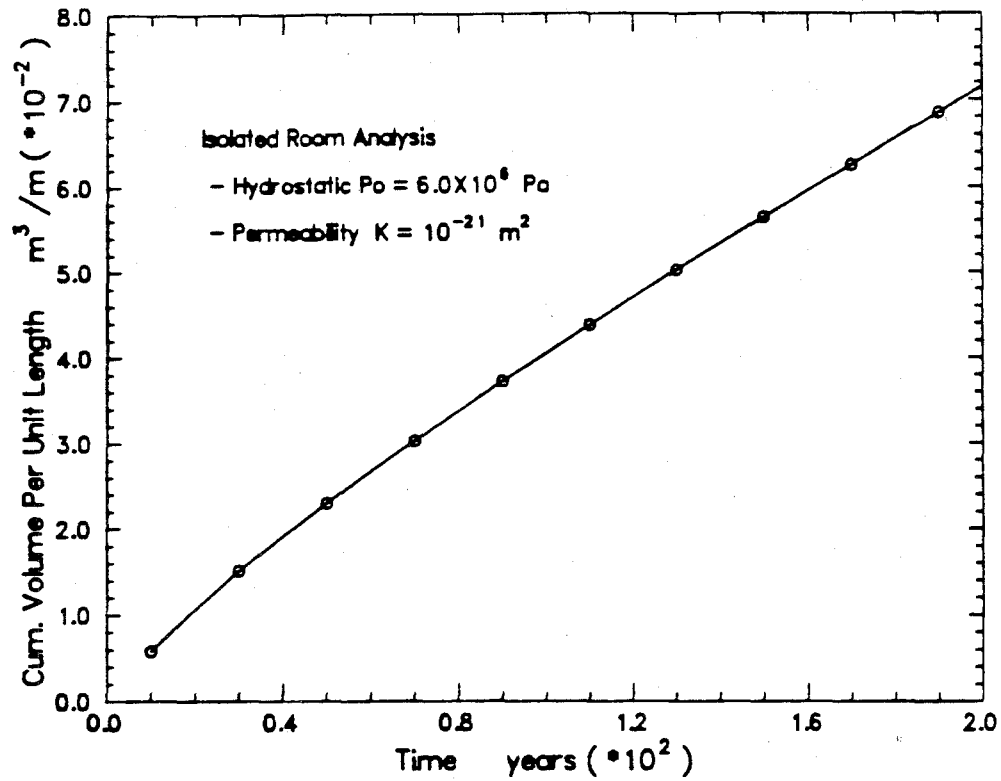


Figure 4: Cum. Volume per Room Length (Hydrostatic Case).

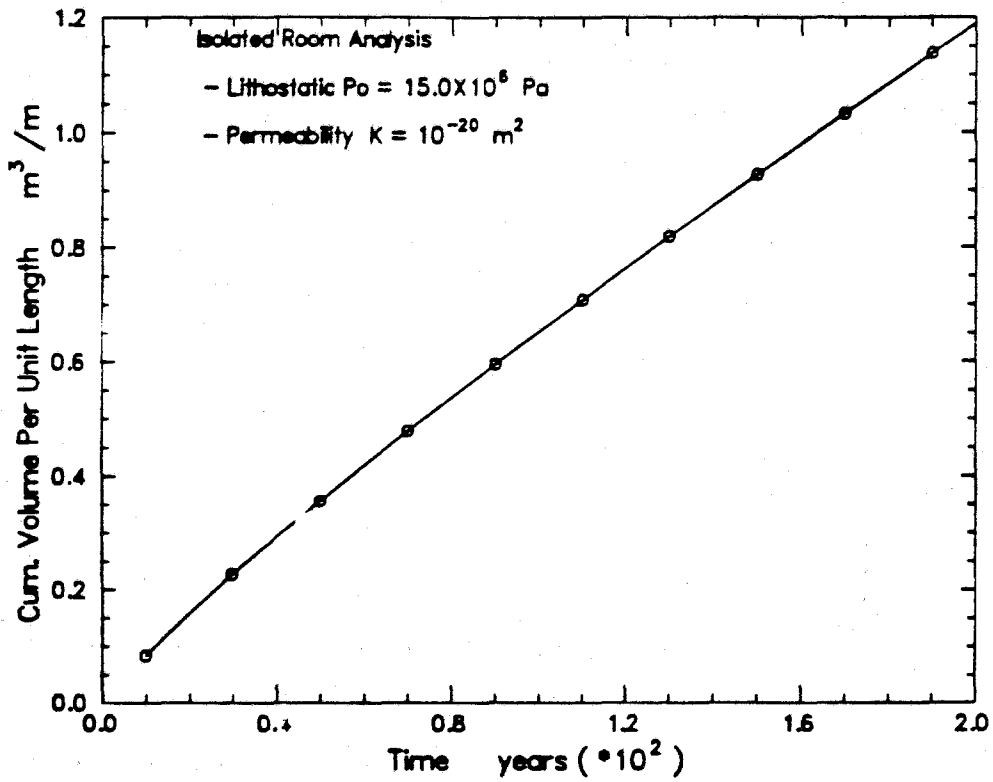
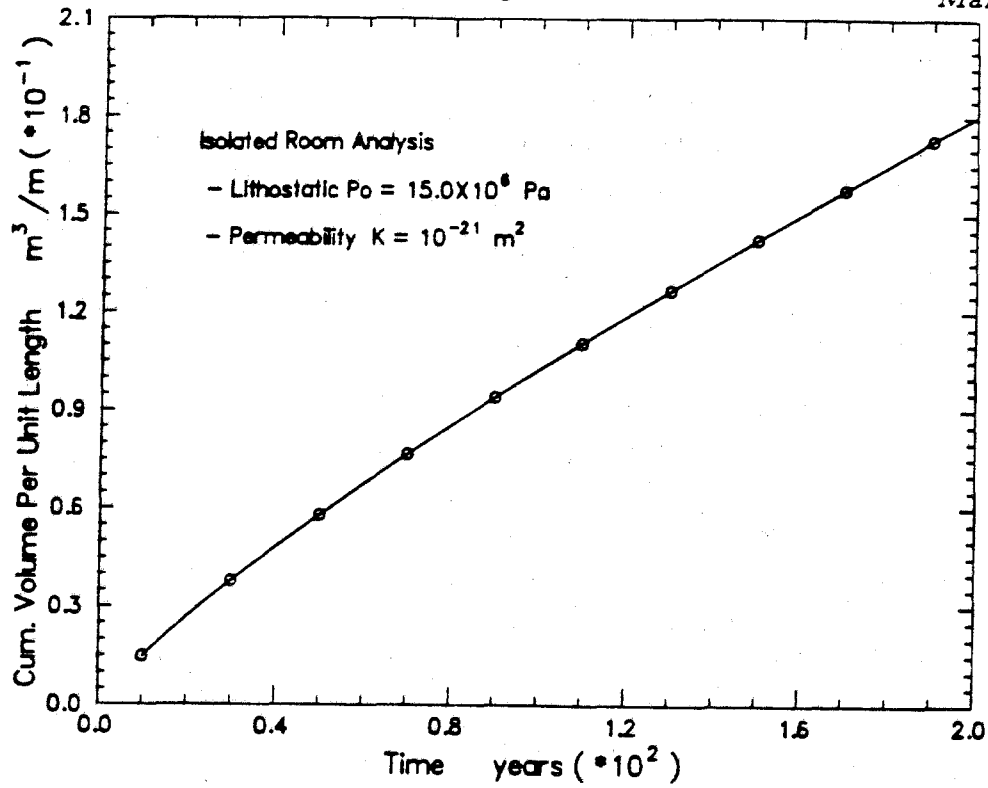


Figure 5: Cum. Volume per Room Length (Lithostatic Case).

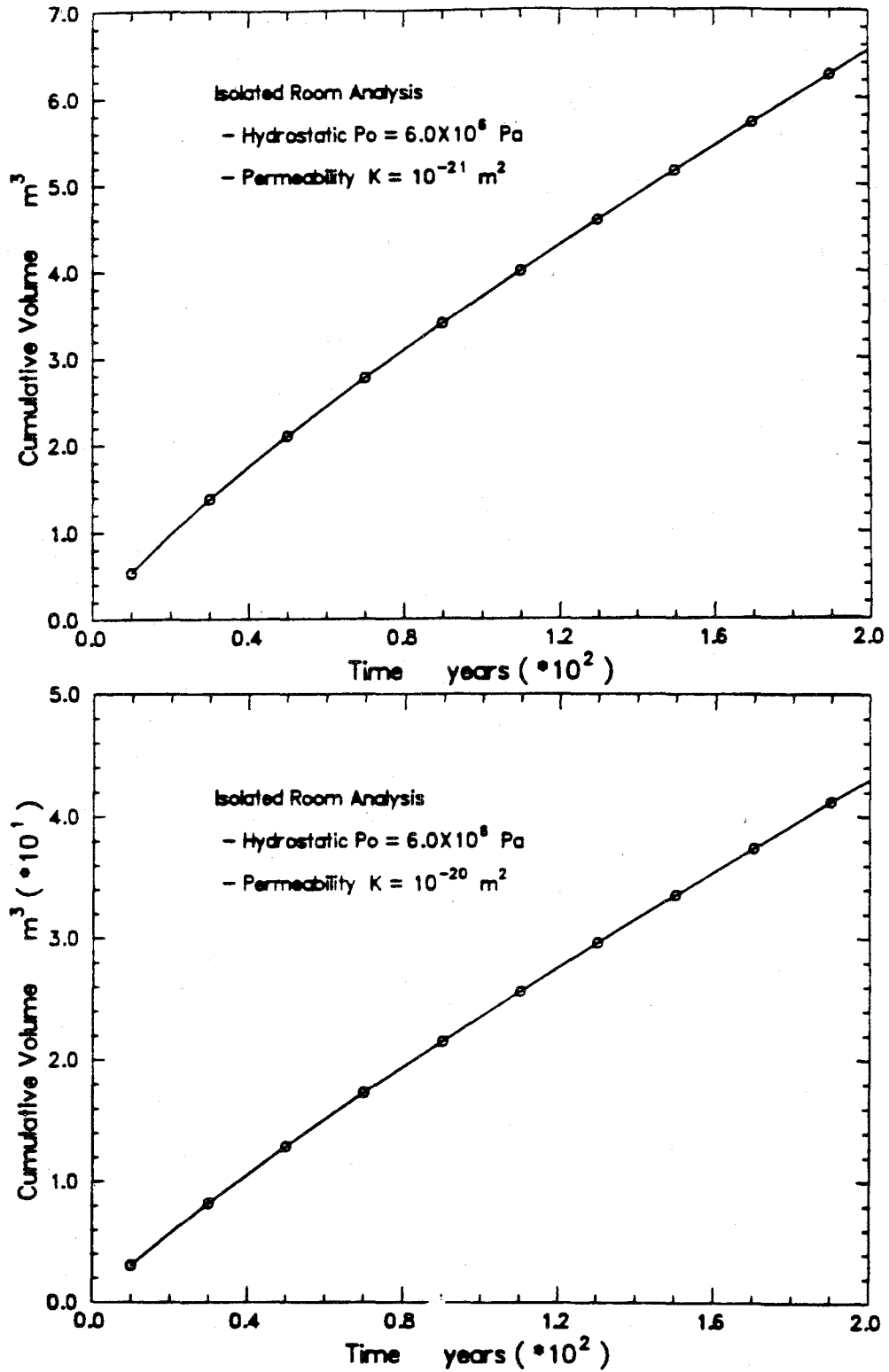


Figure 6: Cumulative Brine Volume (Hydrostatic Case).

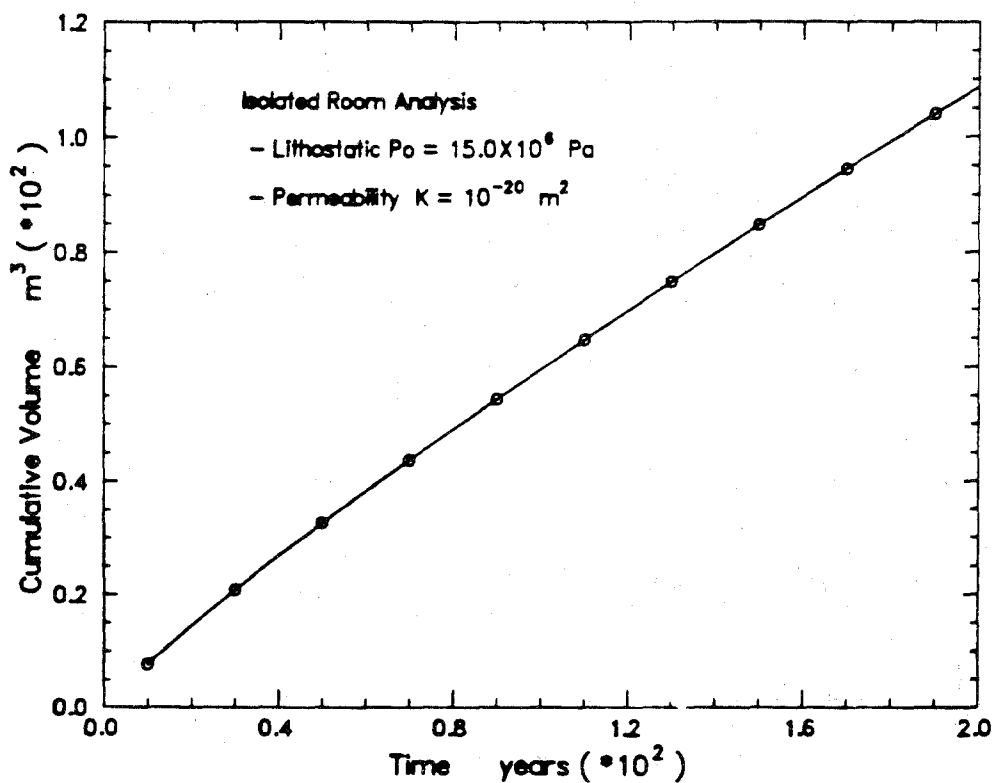
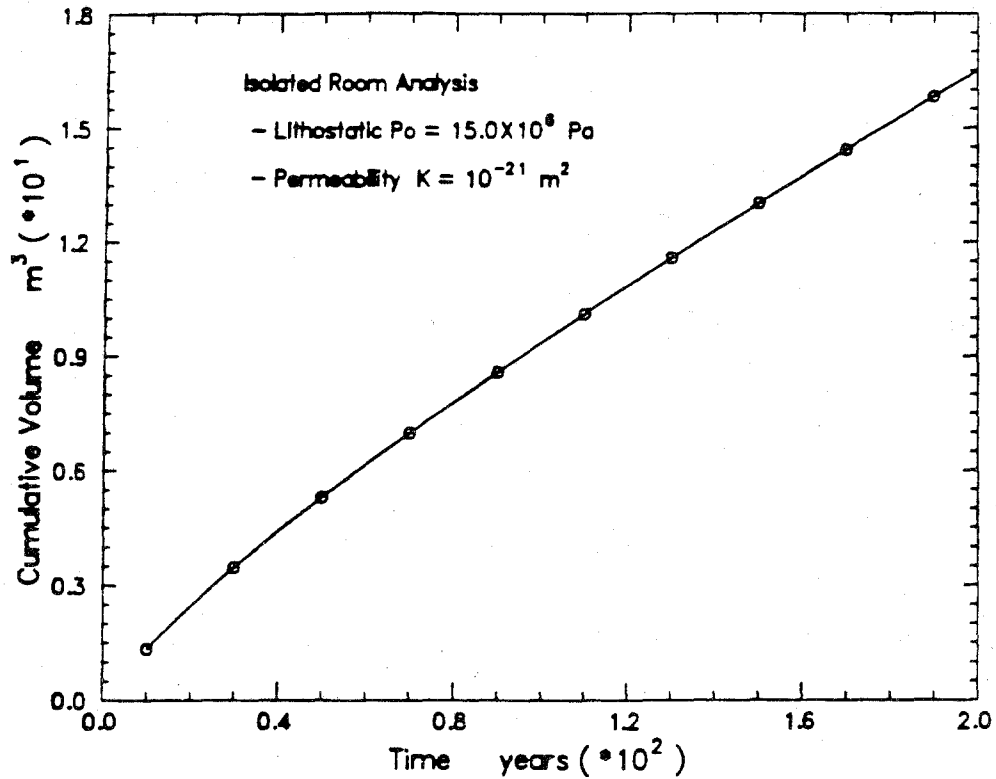


Figure 7: Cumulative Brine Volume (Lithostatic Case).

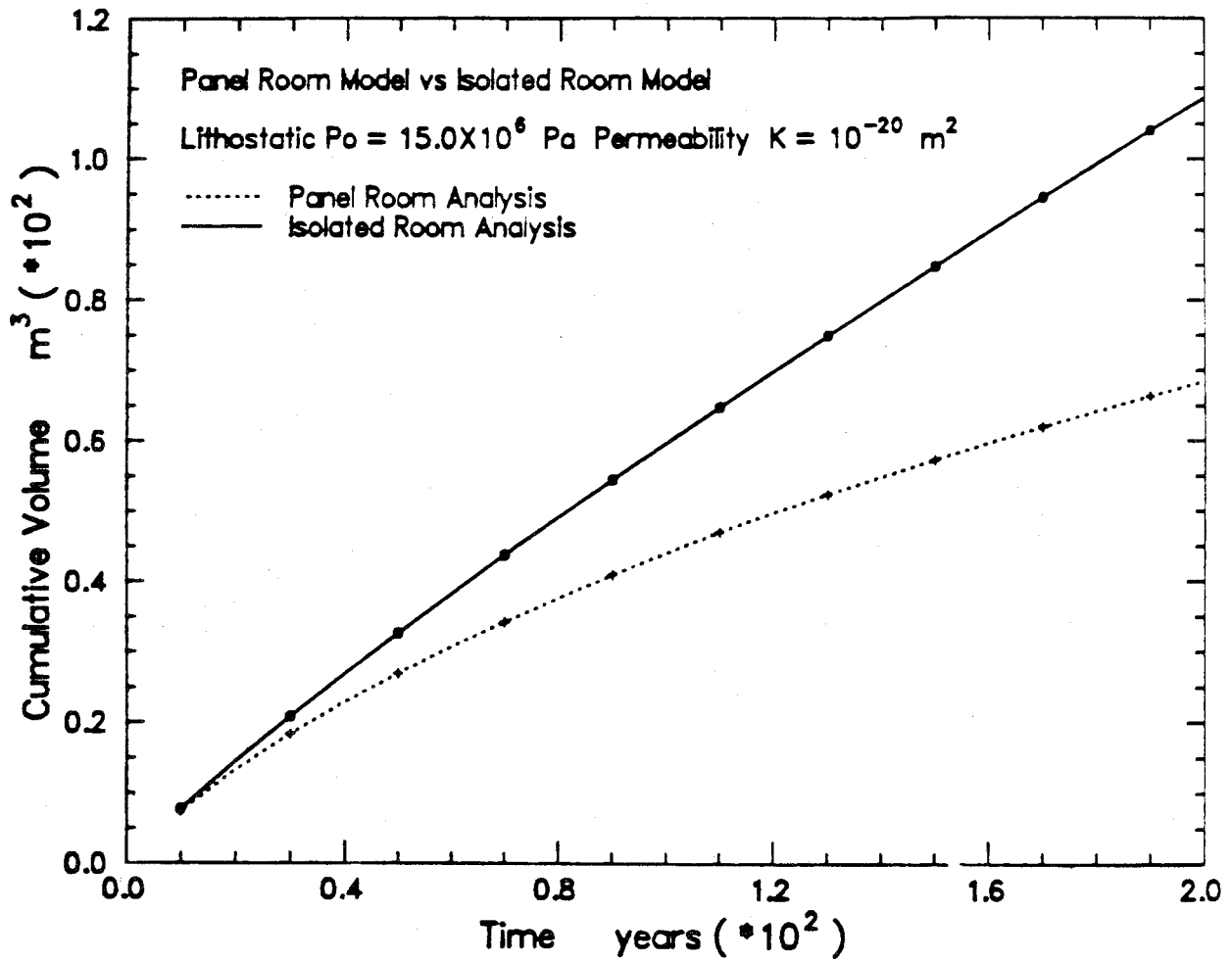


Figure 8: Panel Room Model vs Isolated Room Model (Lithostatic Case).

Copy to:

1510 J. W. Nunziato
1511 D. F. McTigue
6300 R. W. Lynch
6330 W. D. Weart
6331 A. R. Lappin
6332 L. D. Tyler
6332 Staff
6334 D. R. Anderson

A.6 Brine Flow to a Mined Room

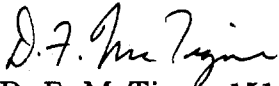
by D.F. McTigue

Sandia National Laboratories

Albuquerque, New Mexico 87185

date: October 21, 1987

to: Distribution



from: D. F. McTigue, 1511

subject: Brine Flow to a Mined Room

Introduction

The expected total volume of brine flow to rooms in the WIPP before closure is a critical issue in performance assessment. There exist a few field measurements that indicate the brine flux to various boreholes scattered around the WIPP site [1, 2]. These data are invaluable as a measure of "ground truth," but they are not sufficient by themselves to answer the performance assessment questions at hand. The estimation of brine inflow cannot be divorced entirely from physical models. For example, one does not know from the measurements how to extrapolate the brine flux to long times, because the data necessarily are restricted to very short time scales relative to the performance assessment period. Perhaps more important is the observation that measurements made in boreholes of roughly the same size reveal nothing about the scaling of flux with cavity dimension.

It is perhaps worthwhile to illustrate the last statement with a concrete example. Measurements of the pre-heating flow to 0.38 m radius boreholes in Rooms A1 and B [1] indicated integrated fluxes of the order of 10 g/day fresh water. Correcting for the volume change when collecting pure water only and dividing by the borehole vertical wall area of 7.4 m², this corresponds to a brine flux of 1.5×10^{-6} m/day. Fluxes of the same order of magnitude have been noted in numerous smaller (0.02-0.06 m radius) boreholes monitored over a two year period in the WIPP site [2]. Consider the result if one simply extrapolates these measurements without putting them in the context of a particular model. A room 4 m × 10 m × 91 m (13 ft × 33 ft × 300 ft) has a total surface area of 2628 m². A period of 200 years is 73000 days. Thus, one might conclude that the cumulative volume of brine in the room after 200 years is the product of the measured flux from a small borehole, the surface area of the room, and the total time: 288 m³ brine, about 8% of the pre-closure room volume (3640 m³). An even more dramatic result will emerge if one assumes that the vertical boreholes simply intercepted flow otherwise destined for Rooms A1 and B, so that the appropriate borehole area to use for the flux calculation is the *cross-section*, 0.46 m². This assumption yields a volume of brine equal to the pre-closure room volume after only 157 years.

Various postulated mechanisms or models of brine transport, however, will give very dif-

ferent results. For example, classical Darcy flow will result in a wall flux that scales like a^{-1} , where a is the dimension of the cavity (see eq. 18). The experimental boreholes have a radius of 0.38 m, while the 4 m \times 10 m room has an effective radius of 4.5 m. Thus, the flux to the room might be expected to be only 10% of that to the relatively small borehole. The difference between hundreds of cubic meters of brine and tens of cubic meters may be quite critical.

The purpose of this memo is to provide some very simple tools with which to assess, in an order-of-magnitude sense, the brine fluxes that might be expected from a Darcy flow mechanism. These results have appeared before in various guises, but it appears that there is a need for the more direct and easily applied summary attempted here. It is emphasized that the Darcy-flow model is not sacred; other plausible mechanisms of brine transport may be posed. Also, of course, the linearized model neglects phenomena such as spatially varying permeability that are expected to prevail in the WIPP [3]. However, it does appear to be roughly consistent, again in an order-of-magnitude sense, with measurements in the WIPP site [1-5]. The existing field measurements are invaluable in this context; they provide a check on any model posed, as well as a means to infer unknown material properties.

Darcy Flow Model

The calculations presented in this memo are based on the assumption of Darcy flow in the host salt. This model has been discussed extensively in a recent report [1]. Classical assumptions about transient Darcy flow lead to a governing equation for the fluid pore pressure that takes the form of a diffusion equation. It is emphasized that the use of the word "diffusion" in this context does *not* imply any mechanistic relation to molecular diffusion of a chemical species in a fluid, diffusion of defects through a crystal lattice, *etc.* The "diffusion" of fluid in a porous medium is simply a statement of conservation of mass for the fluid, along with some assumptions about the interaction (*e.g.*, drag force) between the fluid and solid and the material response (*e.g.*, compressibility) of the constituents.

It is further emphasized that the assumptions for the material response that lead to the classical, linear diffusion model for pore fluid are quite special. In particular, it is worth noting that inelasticity in the volumetric deformation of the porous matrix may change the character of the fluid flow equation. Little is known about the inelastic *volumetric* response of rock salt; the creep modeling program has focused almost exclusively on the *deviatoric* response. It is almost certain that the salt does exhibit some inelastic dilatation, due, say, to the opening of microcracks along grain boundaries in response to the tensile stress normal to mined faces.

With full cognizance of these limitations, the following developments are based on the linear diffusion model for pore fluid. The capacitance, or "storage," of the salt is due to elastic compressibility of the bulk salt, individual mineral grains, and the brine.

Boundary and Initial Conditions

It is assumed that the mined room introduces surfaces at zero (atmospheric) pressure into a region initially at some uniform value. One might expect that the initial pressure is bounded between hydrostatic (for the depth beneath the water table) and lithostatic (for the repository depth). The variation of hydrostatic or lithostatic pressure with depth is negligible within a few tens of meters of the repository. More detailed discussion of the initial condition, including the effect of the altered mean stress field due to the presence of a cavity, is given in [1]. For simplicity, the initial pressure in the following is taken to be hydrostatic:

$$p_0 = 6.0 \times 10^6 \text{ Pa}; \quad (1)$$

the choice of lithostatic initial pressure would simply increase the calculated fluxes and volumes by a factor of about two. The cumulative flux is evaluated at 200 years:

$$t = 6.31 \times 10^9 \text{ s}. \quad (2)$$

Properties

The brine diffusivity, here denoted c , can be estimated by two fundamentally different means. First, one can invoke particular mechanisms of "storage" of fluid mass due to pressure changes, model these mechanisms, and make independent determinations of the necessary material properties. This is the approach taken to date; the assumptions of elastic salt and brine, Darcy flow, *etc.* leads to an explicit form for the diffusivity c as a function of the compressibilities of the porous matrix, the mineral grains, and the brine, as well as the permeability and brine viscosity [1]. It has been estimated previously, based on independent measurements of the mechanical properties of salt [*e.g.*, 6], that the diffusivity for WIPP salt is

$$c \simeq (1.1 \times 10^{14})k \text{ m}^2/\text{s}, \quad (3)$$

where k is given in units of m^2 . The permeability has been measured independently in gas pressure-decay tests [3, 4], and, while widely varying, often falls in the range

$$k \simeq 10^{-21} - 10^{-20} \text{ m}^2 \quad (4)$$

(1–10 nanodarcy). It should be stressed that these estimates are subject to improvement from more detailed modeling and field measurements. However, they appear to be consistent with the flux data considered to date. The brine viscosity at 28 °C is

$$\mu = 1.6 \times 10^{-3} \text{ Pa} \cdot \text{s}; \quad (5)$$

this value was used in calculating (3).

A second approach to the determination of the diffusivity c is to make no explicit assumptions about mechanisms, but rather to adopt the diffusion model as a purely phenomenological theory. The diffusivity can then be determined from, say, measurements of the

decay rate of the brine flux in a simple configuration. Ideally, one would hope that the value of c determined in this fashion is in general agreement with that determined by modeling a particular mechanism of storage. This, of course, would provide some confidence that the model may have captured the essential processes.

At present, little has been done along these lines. All calculations performed in a previous report [1] and in this memo utilize the elasticity model discussed above, and thus arrive at a value for the diffusivity based on independent knowledge of the salt and brine properties (eq. 3). A worthwhile exercise will be to make a careful study of the *transient* behavior of the brine flows measured in both unheated [2] and heated [3] boreholes in the WIPP to obtain empirical values for the brine diffusivity, c . Preliminary estimates based on these data appear to be consistent with (3)-(4).

1-D Flow to an Isolated Room

The first case considered is one-dimensional flow to an isolated room. This represents the case in which there is no vertical flow, perhaps because of impermeable, horizontal clay seams (Fig. 1). The flow can spread outward without bound because there are no adjacent rooms.

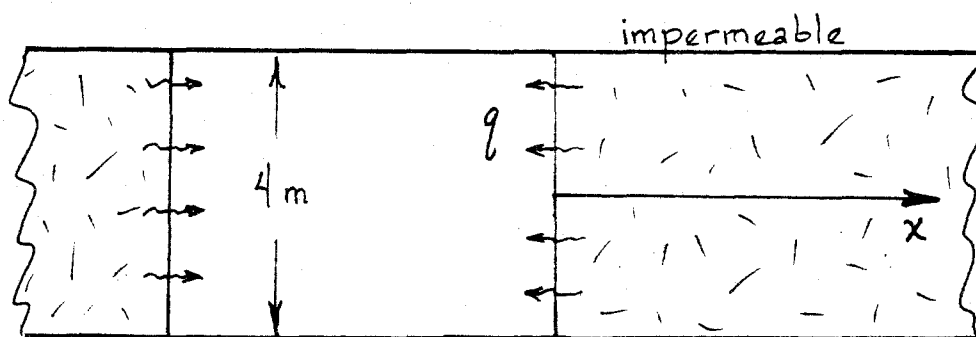


Figure 1. Geometry for lateral flow to an isolated room.

This problem is exactly analogous to the cooling of a plane half-space, and the pressure profile takes the well-known form:

$$p = p_0 \operatorname{erf} \left(\frac{x}{2\sqrt{ct}} \right), \quad (6)$$

where p_0 is the initial pressure, x is the distance away from the wall, and c is the brine diffusivity. The flux at the wall (e.g., in units of $(\text{m}^3/\text{s})/\text{m}^2$) is determined from (6) using Darcy's law:

$$|q(0, t)| = \frac{kp_0}{\mu\sqrt{\pi ct}}, \quad (7)$$

where k is the permeability, and μ is the brine viscosity. The cumulative flux (e.g., in units

of m^3/m^2) is obtained from (7) by integration:

$$Q(t) = \frac{2kp_0}{\mu\sqrt{\pi c}} t^{1/2}. \tag{8}$$

The cumulative volume of brine is determined by multiplying (8) by the area of the vertical side walls of the room.

Sample Calculation

The vertical side-wall area for the model room is

$$A_1 = 728 \text{ m}^2. \tag{9}$$

Thus, for 1-D flow from an unbounded domain, equation (8) predicts a cumulative volume

$$V(k = 10^{-21} \text{ m}^2) = 0.73 \text{ m}^3, \tag{10}$$

$$V(k = 10^{-20} \text{ m}^2) = 2.33 \text{ m}^3. \tag{11}$$

1-D Flow to a Room in an Array

The next case considered is for one-dimensional flow to one room among an array of similar rooms separated by pillars of finite width. In this case, the pressure disturbance can spread

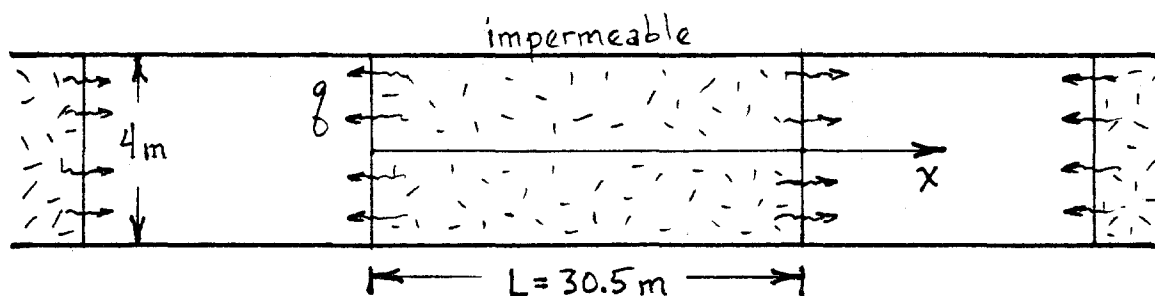


Figure 2. Geometry for lateral flow in an array of rooms.

only to the centerline of the pillar, where it must be symmetric because of flow to the next room. This problem simply looks like the cooling of a finite slab, and the solution is again well known:

$$p = p_0 4 \sum_{n=0}^{\infty} \frac{\sin \lambda_n x}{\lambda_n L} \exp(-c \lambda_n^2 t), \tag{12}$$

where L is the thickness of the pillar between rooms and $\lambda_n L = (2n + 1)\pi$. The flux at the wall is again obtained from Darcy's law by differentiation of (12):

$$|q(0, t)| = \frac{kp_0}{\mu L} 4 \sum_{n=0}^{\infty} \exp(-c \lambda_n^2 t). \tag{13}$$

The cumulative flux is again obtained by integration of (13):

$$Q(t) = \frac{kp_0L}{\mu c} 4 \sum_{n=0}^{\infty} \frac{1 - \exp(-c\lambda_n^2 t)}{(\lambda_n L)^2}, \quad (14)$$

and the total volume is again obtained by multiplying by the vertical area of the side walls.

Sample Calculation

For 1-D flow from a finite domain between rooms, using A_1 from above (9) and

$$L = 30.5 \text{ m}, \quad (15)$$

equation (14) gives:

$$V(k = 10^{-21} \text{ m}^2) = 0.37 \text{ m}^3, \quad (16)$$

$$V(k = 10^{-20} \text{ m}^2) = 0.37 \text{ m}^3. \quad (17)$$

These values are identical because the drainage process is essentially complete after 200 years even at the lower diffusivity. This is apparent from evaluation of the characteristic time, $(L/2)^2/c$, which takes the value 2.1×10^9 s (67 years) for $k = 10^{-21}$ and 2.1×10^8 s (6.7 years) for $k = 10^{-20}$. Also note that the cumulative flux is significantly less than for the unbounded region because there is simply less fluid to draw upon.

1-D Radial Flow to an Isolated Tunnel

The third configuration considered is for flow to a circular tunnel without interaction with adjacent tunnels. In contrast to the foregoing cases, this model accounts for flow from

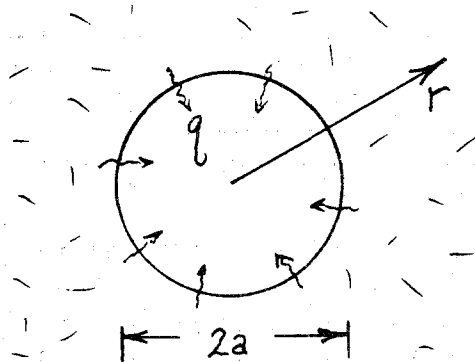


Figure 3. Geometry for radial flow to an isolated tunnel.

above and below the tunnel. It neglects, of course, the effects of the rectangular shape of the room, but those effects damp out for later time. These results have been discussed in a recent report [1]. The flux to the tunnel is given by:

$$|q(0, t)| = \frac{kp_0}{\mu a} \frac{4}{\pi^2} \int_0^{\infty} \frac{\exp(-u^2 ct/a^2) du}{J_0^2(u) + Y_0^2(u) u}, \quad (18)$$

where a is the radius, and $J_0(\zeta)$ and $Y_0(\zeta)$ are zero-order Bessel functions of the first and second kind, respectively. The cumulative flux is:

$$Q(t) = \frac{kp_0a}{\mu c} \frac{4}{\pi^2} \int_0^\infty \frac{1 - \exp(-u^2 ct/a^2)}{J_0^2(u) + Y_0^2(u)} \frac{du}{u^3} \tag{19}$$

The total volume of brine is determined by multiplying by the area of the tunnel walls (vertical side walls, floor, and ceiling for an equivalent rectangular room).

Sample Calculation

The circumference of the model room is 28 m; thus, the effective radius of an equivalent circular tunnel is

$$a = 4.5 \text{ m}, \tag{20}$$

and the appropriate area is the sum of the side-wall, floor, and ceiling areas:

$$A_2 = 2548 \text{ m}^2. \tag{21}$$

Equation (19) then gives,

$$V(k = 10^{-21} \text{ m}^2) = 6.7 \text{ m}^3, \tag{22}$$

$$V(k = 10^{-20} \text{ m}^2) = 40.6 \text{ m}^3. \tag{23}$$

These values are an order of magnitude greater than those for the 1-D (lateral flow only) unbounded case (10-11) because of drawing on a larger volume of material due to radial spreading and because of allowing flow through the larger surface area that includes the floor and ceiling.

Steady Radial Flow to a Line Sink

The last configuration considered is for steady flow to a line sink. This implies that, at sufficiently long time, the pressure field does not relax to zero everywhere as implied by the

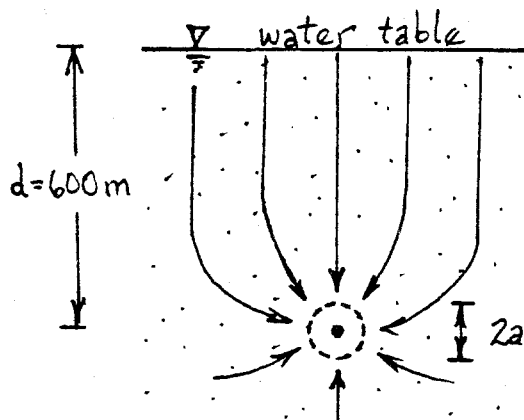


Figure 4. Geometry for steady flow to a line sink.

diffusion model, but approaches a steady-state condition where the far-field is hydrostatic and there is recharge at the water table. In this case, for $a/d \ll 1$, the flux at the room walls is given by [1]:

$$|q_{\text{wall}}| = \frac{k p_0}{\mu a} \frac{-1}{\ln(a/2d)}, \quad (24)$$

and the cumulative flux is obtained simply by multiplying $|q_{\text{wall}}|$ by the wall area and total time of interest.

Sample Calculation

The WIPP facility horizon is about 600 m below the water table, *i.e.*,

$$d = 600 \text{ m}. \quad (25)$$

Equation (24), along with (20), (21), and (25), then gives

$$V(k = 10^{-21} \text{ m}^2) = 2.6 \text{ m}^3, \quad (26)$$

$$V(k = 10^{-20} \text{ m}^2) = 26.3 \text{ m}^3. \quad (27)$$

Summary

Results from the highly idealized models considered here are collected in Table 1.

Table 1. Summary of Results for Cumulative Volume at 200 years.

| Model | Equation | Cumulative Volume (m ³) | |
|-------------------|----------|-------------------------------------|----------------------------|
| | | $k = 10^{-21} \text{ m}^2$ | $k = 10^{-20} \text{ m}^2$ |
| Lateral semi-inf. | [8] | 0.7 | 2.3 |
| Lateral finite | [14] | 0.4 | 0.4 |
| Radial | [19] | 6.7 | 40.6 |
| Line sink | [24] | 2.6 | 26.3 |

The models considered yield results that span a range from a few tenths to a few tens of cubic meters of brine after 200 years. These values embody a good deal of uncertainty, including the models themselves and the coefficients adopted. However, the general approach is defensible; it invokes plausible mechanisms, it can be checked over short time scales by comparison with field measurements, and the coefficients can be estimated from independent tests in the laboratory and field. The general scheme can be refined, using available tools, to account for more complex geometries, two- and three- dimensional effects, spatially varying properties, *etc.*

References

1. Nowak, E. J., and McTigue, D. F., "Interim Results of Brine Transport Studies in the Waste Isolation Pilot Plant (WIPP)," SAND87-0880, May 1987.
2. Deal, D. E., and Case, J. B., "Brine Sampling and Evaluation Program; Phase I Report," IT Corporation Report, DOE-WIPP-87-008, June 15, 1987.
3. Peterson, E., Lagus, P., Brown, J., and Lie, K., "WIPP Horizon *In Situ* Permeability Measurements Final Report," SAND85-7166, January 1987.
4. Stormont, J. C., Peterson, E. W., and Lagus, P. L., "Summary of and Observations About WIPP Facility Horizon Flow Measurements Through 1986," SAND87-0176, May 1987.
5. Peterson, E. W., Lagus, P. L., and Lie, K., "WIPP Horizon Free-Field Fluid Transport Observations," SAND87-7164, in review, October 1987.
6. Krieg, R. D., "Reference Stratigraphy and Rock Properties for the Waste Isolation Pilot Plant (WIPP) Project," SAND83-1908, 1984.

DFM:1511

Copy to:

1510 J. W. Nunziato
1511 D. K. Gartling
1512 J. C. Cummings
1513 D. W. Larson
1520 C. W. Peterson
1530 L. W. Davison
1550 R. C. Maydew
6330 W. D. Weart
6331 A. R. Lappin
6332 L. D. Tyler
6332 J. G. Arguello
6332 R. Beraun
6332 D. E. Munson
6332 E. J. Nowak
6332 J. C. Stormont
6334 D. R. Anderson
6334 L. H. Brush
6334 J. P. Hickerson
6334 M. G. Marietta

A.7 Darcy Model for Brine Inflow to the WIPP;
Evaluation of Data from the IT Brine Sampling Program

date: January 8, 1988

to: Distribution



from: D. F. McTigue, 1511

subject: Darcy Model for Brine Inflow to the WIPP; Evaluation of Data from the IT Brine Sampling Program

Introduction

Recent work [e.g., 1, 2] has suggested that observed brine transport in the WIPP may be dominated by Darcy flow, *i.e.*, flow of intergranular brine due to pressure gradients. This suggestion is supported by order-of-magnitude calculations that show that the flow rates measured in both unheated and heated boreholes are consistent with the proposed driving mechanisms and with independently determined material properties.

The purpose of this memo is to extend the data base upon which speculation about Darcy flow is built. In particular, flow rates monitored in eighteen boreholes by Deal and Case [3] are examined in the context of the Darcy flow model. The object is to determine whether the flow rates measured in scattered locations throughout the WIPP over a two-year period are consistent with the Darcy flow model and with results from the *in situ* moisture release experiments considered previously [1].

Data Reduction

Deal and Case [3] monitored 54 drillholes throughout the WIPP, most of them for about 500 days. They show graphical results for the time histories of the total flux for 20 holes. The flow rates to two of the holes, BX02 and DH37, fell essentially to zero after 600 days. The flow rates to the remaining 18 holes at the end of the reporting period are considered here (Table 1). Hole A1X02 exhibited a nearly monotonic decay in flow rate for nearly 400 days, but then experienced a steady increase in flow rate. The value entered in Table 1 for A1X02 hole corresponds to the value at the end of the period of declining rate. The recorded flow rates represent the integrated flux over the borehole surface areas, and are recorded in Table 1 in units of liters per day, *i.e.*, a volume flow rate.

Deal and Case [3] also report the dimensions of the holes, so that it is simple to calculate the vertical wall area of each. These, too, are recorded in Table 2. The average Darcy flux (or "Darcy velocity") for each hole is easily calculated by dividing the integrated volume flux by the total borehole area. This step is not taken here because the comparison can be misleading. If the flow does occur by a Darcy mechanism, then the Darcy velocity is

expected to scale inversely with the borehole radius. Thus, the appropriate measure for a hole-to-hole comparison in this context is the product of the Darcy flux and the borehole radius. This value appears in the fifth column of Table 1, labeled qa .

The products of the Darcy flux times borehole radius, which are proportional to the total flow rates per unit length of borehole, center around $3 \times 10^{-12} \text{ m}^2/\text{s}$; the maximum value is in hole NG252, at $2.1 \times 10^{-10} \text{ m}^2/\text{s}$.

Radial Darcy Flow

A highly idealized model was introduced previously [1] to investigate the order-of-magnitude agreement of observed fluxes with the proposed Darcy flow mechanism. In particular, it was assumed that mined faces and boreholes introduce zero-pressure surfaces into a region of porous salt in which the brine is initially at hydrostatic pressure. (It is easy to argue that the initial pressure may be as large as lithostatic, but this changes the initial conditions only by a factor of about two. The uncertainty in the permeability is expected to be much greater.) In this case, the Darcy flux, q , to a circular borehole scales in the following fashion [1]:

$$q \sim \frac{kp_0}{\mu a}, \quad (1)$$

where k is the permeability, p_0 is the initial pressure, μ is the brine viscosity, and a is the borehole radius. This factor is multiplied by a time-dependent function of order unity that represents the decay of the flux as the pressure disturbance propagates away from the hole. The characteristic time over which this decay takes place, t_0 , is given by:

$$t_0 = \frac{a^2}{c}, \quad (2)$$

where c is the fluid diffusivity. For elastic rock, the fluid diffusivity scales like:

$$c \sim \frac{kK}{\mu}, \quad (3)$$

where K is an elastic modulus for the porous skeleton. For WIPP salt, it has been argued [4] that the appropriate modulus and viscosity yield a diffusivity of the order of

$$c \simeq 1.1 \times 10^{14} k \text{ m}^2/\text{s}, \quad (4)$$

where the permeability is given in units of m^2 .

Previous calculations suggest that the brine diffusivity is of the order of $10^{-7} \text{ m}^2/\text{s}$. For a borehole of radius 0.05 m, then, (2) gives a characteristic time of the order of $2.5 \times 10^4 \text{ s}$, or about seven hours. Therefore, after 500 days, the drillholes in the WIPP can be expected to be in the asymptotic limit of "late" time. In this case, the flux can be approximated by [1]:

$$q = \frac{kp_0}{\mu a} \frac{2}{\ln(4ct/a^2) - 2\gamma}, \quad (5)$$

where $\gamma \simeq 0.57722$ is Euler's constant.

The apparent permeability can be calculated for each drillhole using (5). In particular, it is assumed that the initial pressure is $p_0 = 6.0 \times 10^6$ Pa, corresponding approximately to hydrostatic pressure for a depth of 600 m. The brine viscosity is taken to be 1.6×10^{-3} Pa·s. The time is assumed to be $t = 4.32 \times 10^7$ s (500 days) for every hole. The diffusivity is assumed to be given by (4). Finally, for each drillhole, the flux, q , and the radius, a , are known (Table 1). Thus, the only unknown parameter is the permeability, k . The nonlinear relationship for k represented by (4) and (5) is then easily solved numerically. The results of this exercise are shown in the last column of Table 1. The values shown may be read directly as nanodarcies ($10^{-21} \text{ m}^2 \simeq 1 \text{ nd}$).

Figure 1 shows a histogram of the logarithm of the apparent permeabilities given in Table 1. The mean of the log is -20.45 ($k = 3.5 \times 10^{-21} \text{ m}^2$, or about 3.5 nanodarcy), and the standard deviation is 0.81. Also shown is the lognormal distribution corresponding to these values. It seems reasonable to conclude that these limited data and the highly idealized model suggest a lognormal distribution for the apparent permeability. This is a common observation in other rocks [e.g., 5, p. 80].

Table 1. Observed flow rates for WIPP drillholes [3].

| Hole | Flow Rate
(l/day) | Area
m^2 | Radius
m | qa
m^2/s | k_{app}
$\text{m}^2 (\times 10^{-21})$ |
|-------|----------------------|----------------------|-------------|-------------------------------|--|
| IG202 | 0.014 | 5.20 | 0.0572 | 1.78×10^{-12} | 1.94 |
| IG201 | 0.025 | 5.91 | 0.0572 | 2.80×10^{-12} | 3.24 |
| NG252 | 0.250 | 0.26 | 0.0190 | 2.11×10^{-10} | 445 |
| A1X01 | 0.026 | 4.84 | 0.0508 | 3.16×10^{-12} | 3.83 |
| A1X02 | 0.010 | 5.74 | 0.0508 | 1.03×10^{-12} | 1.07 |
| A2X01 | 0.025 | 4.87 | 0.0508 | 3.02×10^{-12} | 3.64 |
| A2X02 | 0.015 | 5.13 | 0.0508 | 1.72×10^{-12} | 1.92 |
| A3X01 | 0.023 | 4.91 | 0.0508 | 2.75×10^{-12} | 3.28 |
| A3X02 | 0.001 | 4.93 | 0.0508 | 1.19×10^{-13} | 0.08 |
| BX01 | 0.055 | 4.87 | 0.0508 | 6.65×10^{-12} | 8.81 |
| DH36 | 0.250 | 4.38 | 0.0444 | 2.39×10^{-11} | 46.4 |
| DH38 | 0.055 | 4.04 | 0.0444 | 7.02×10^{-12} | 9.62 |
| DH40 | 0.005 | 4.34 | 0.0444 | 5.90×10^{-13} | 0.59 |
| DH42 | 0.030 | 4.35 | 0.0444 | 3.55×10^{-12} | 4.51 |
| DH42A | 0.095 | 3.44 | 0.0444 | 1.42×10^{-11} | 21.0 |
| DH35 | 0.002 | 4.42 | 0.0444 | 2.37×10^{-13} | 0.20 |
| L1X00 | 0.028 | 3.72 | 0.0380 | 3.32×10^{-12} | 4.33 |
| DH215 | 0.004 | 1.22 | 0.0508 | 1.92×10^{-12} | 2.19 |

Comparison to Room A1 and Room B Moisture Release Measurements

Before the heaters were turned on in the instrumented boreholes in Rooms A1 and B, moisture was collected in all four holes for a few days [6]. The integrated mass flow rates were in the range of 5–15 g/day, which, averaged over the borehole area, corresponds to a Darcy flux of $0.85\text{--}2.6 \times 10^{-11}$ m/s. The product of the flux times the borehole radius, $a = 0.38$ m, is then in the range $qa = 3.2\text{--}9.9 \times 10^{-12}$ m²/s. In comparing these values to those calculated from the IT measurements (Table 1), it should be noted that the latter represent flows at much later time ($t \gg t_0$).

The apparent permeability for the moisture-release holes can be calculated in a fashion similar to the approach used above. In this case, however, the flow rates measured in the pre-heating stage do not reflect very late time, and the asymptotic solution (5) is not accurate. Using the full integral solution [1], the same initial condition, $p_0 = 6.0 \times 10^6$ Pa, and $t = 2.1 \times 10^7$ s (8 months), the observed range of fluxes requires permeabilities in the range $k \simeq 2.4\text{--}9.3 \times 10^{-21}$ m². These values are quite consistent with those required to represent the IT data (Figure 1), and, again, are consistent with independently measured *in situ* permeabilities [7].

Summary and Qualifications

The principal results presented in this memo are:

- A highly idealized Darcy flow model for brine transport to drillholes in the WIPP predicts fluxes of the order observed by Deal and Case [3] for permeabilities of the order of a few nanodarcies.
- The permeability values required to represent the drillhole data can be described reasonably well by a lognormal distribution with a logarithmic mean corresponding to 3.5×10^{-21} m², or 3.5 nanodarcy.
- Permeabilities of the appropriate range have been measured in independent field tests [7].
- The pre-heating flow rates measured in boreholes in Rooms A1 and B [1, 6] are also consistent with a permeability of the same order.

These observations must be qualified by a strong reminder that calculations of the sort employed serve only as an order-of-magnitude test of the plausibility and applicability of a mechanistic model concept. The details of the model rest upon a number of assumptions that warrant further investigation.

First, there are assumptions concerning the predominant physical mechanisms. These include:

- *The salt contains an interconnected network of intergranular pore space.* Although

this assumption appears to be consistent with observed brine flow over short time scales (of the order of two years), calculations indicate that the pressure disturbance would have propagated only a few meters. Thus, it is not at all clear that the observed flows yet reflect the response of "undisturbed" salt. This qualification is particularly important when carrying such calculations out to much longer times.

Field tests designed to test this assumption are currently under way. The tests include pressure-decay measurements in boreholes and measurements of the asymptotic pressure in fluid-filled boreholes.

- *The volumetric deformation of the salt is linearly elastic.* This is clearly not so over some length and time scales. For example, it might be expected that the salt undergoes some inelastic dilatation near mined faces as microcracks or grain boundaries open in tension normal to the faces. Such processes affect the initial conditions (*e.g.*, the initial pore pressures would be *reduced* from the undisturbed values by local dilatation), the material properties (*e.g.*, the permeability may increase locally due to the dilatation; *cf.* [7]), and the governing equations (*e.g.*, the divergence of the fluid flux depends, in part, upon the dilatation *rate*; if the material is elastic, the dilatation rate is proportional to the stress rate; if the material is rate-dependent, terms of different form enter).

Second, certain simplifying assumptions are required in order to perform analysis based on any model. For example, in the present case, the geometry of the system is highly idealized; it is assumed that:

- *The brine transport over a two year time scale is dominated by radial flow.* The drillholes monitored in the WIPP are, obviously, of finite length, so that there is also flow to the surface into which the hole is drilled. Thus, two-dimensional effects might be considered. Furthermore, the drillholes penetrate regions already affected by transport processes associated with the presence of the room or drift from which they are drilled. The first effect would tend to weaken the flow to a drillhole because of the presence of alternative paths. The second effect would tend to make the appropriate initial conditions for the drillhole problem inhomogeneous and smaller in magnitude. Also, the far-field boundary conditions become time dependent because of the coupling to the larger scale problem. Effects such as these that tend to weaken to flow imply that larger permeabilities would be required to match the observations. This conclusion is appealing, in that the permeabilities indicated by the above calculations are on the low end of the range independently measured in the WIPP [7].

Numerical analysis can provide an assessment of the importance of two-dimensional and, if necessary, three-dimensional effects. Such an effort is currently under way.

- *The model neglects complex interactions with the state of stress in the salt.* The model treated to date does account for the coupling of the fluid pressure field to the state of stress in the rock [1]. The effect of a circular hole on a far-field hydrostatic

stress field was included in the early analysis, and affects the initial condition on the pressure. The configuration of the WIPP, of course, is much more complex, and the analysis summarized above does not account for the interaction of adjacent excavations, to cite one example. Deal and Case [3] note that the large excursion in the flow rate to hole DH215 is correlated with nearby mining activity. Such effects are embodied in the model treated to date, but have been omitted from the simple analysis performed.

Finally, it is cautioned that field observations should be evaluated carefully for their relevance to the problem at hand. For example:

- *No account has been taken for anomalous circumstances such as drillholes that penetrate known fractures.* Table 1 and Figure 1 indicate one strikingly large apparent permeability, corresponding to hole NG252. Deal and Case [3] describe flow into this hole from observed fractures, probably associated with stress relief due to the mining. If this is so, the hole accumulates flow to a much greater surface area than that assumed in compiling Table 1. The same volume flow rate, averaged over a much larger area accounting for the fracture area, would move the anomalous flux value toward the more commonly observed rates.

References

1. Nowak, E. J., and McTigue, D. F., Interim Results of Brine Transport Studies in the Waste Isolation Pilot Plant (WIPP), Sandia National Laboratories Technical Report, SAND87-0880, May 1987.
2. McTigue, D. F., and Nowak, E. J., Brine Transport in the Bedded Salt of the Waste Isolation Pilot Plant (WIPP): Field Measurements and a Darcy Flow Model, *Scientific Basis of Nuclear Waste Management*, Materials Research Society, in press December 1987.
3. Deal, D. E., and Case, J. B., Brine Sampling and Evaluation Program; Phase I Report, IT Corporation Technical Report, DOE-WIPP-87-008, June 1987.
4. McTigue, D. F., Brine Flow to a Mined Room, memo to Distribution, October 21, 1987.
5. de Marsily, G., *Quantitative Hydrogeology*, Academic Press, New York, 1986.
6. Nowak, E. J., Preliminary Results of Brine Transport Studies in the Waste Isolation Pilot Plant (WIPP), Sandia National Laboratories Technical Report, SAND86-0720, May 1986.

7. Peterson, E., Lagus, P., Brown, J., and Lie, K., WIPP Horizon *In Situ* Permeability Measurements, Final Report, SAND85-7166, prepared for Sandia National Laboratories by S-Cubed, La Jolla, CA, January 1985.

DFM:1511:dfm

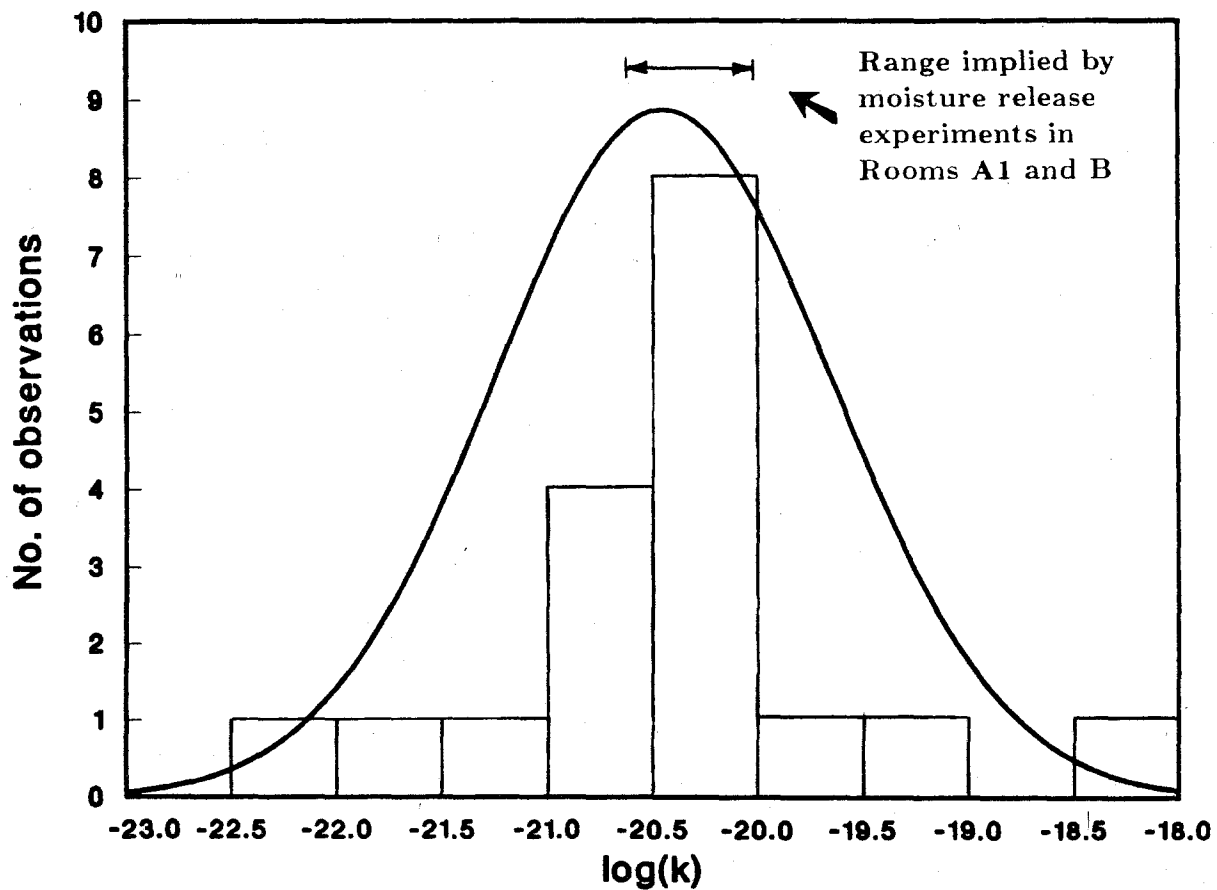


Figure 1. Histogram of apparent permeabilities for drillholes monitored by Deal and Case [3], based on the radial Darcy flow model. Also shown is the lognormal distribution with the same mean and standard deviation. Range of permeabilities implied by pre-heating flow rates observed in Room A1 and Room B moisture release experiments indicated for comparison.

Copy to:

1510 J. W. Nunziato
1511 D. K. Gartling
1512 J. C. Cummings
1513 D. W. Larson
1520 C. W. Peterson
1530 L. W. Davison
1550 R. C. Maydew
6330 W. D. Weart
6331 A. R. Lappin
6332 L. D. Tyler
6332 J. G. Arguello
6332 R. Beraun
6332 D. E. Munson
6332 E. J. Nowak
6332 J. C. Stormont
6334 D. R. Anderson
6334 L. H. Brush
6334 J. P. Hickerson
6334 M. G. Marietta

A.8 Increased Permeability Near Storage Rooms:
Effect on Brine Inflow Computed With a Darcy Model

by D.F. McTigue

Sandia National Laboratories

Albuquerque, New Mexico 87185

date: June 1, 1988

to: Distribution



from: D. F. McTigue, 1511

subject: Increased Permeability Near Storage Rooms: Effect on Brine Inflow Computed With a Darcy Model

Introduction

Much attention has been directed recently to the possible accumulation of large volumes of brine in WIPP storage rooms before creep closure is complete. Slow brine seepage is observed currently in drifts and boreholes [e.g., 1, 2]. One interpretation is that it represents Darcy flow, driven by far-field pressure between hydrostatic and lithostatic toward mined faces at atmospheric pressure [e.g., 3-6]. In this context, the permeability of the salt is a critical parameter in any model predictions. Permeabilities measured in various tests in the salt exhibit a very wide range of values [e.g., 6], spanning several orders of magnitude. Nonetheless, it can be argued on the basis of the more reliable permeability measurements that the permeability of undisturbed salt a few meters away from the drift walls is consistently in the neighborhood of 1-10 nanodarcy. Much higher values are observed within the first few meters of the walls, rising as high as 1 microdarcy [e.g., 6, 7].

These observations suggest that an assessment be made of the influence on brine inflow of a zone of enhanced permeability due to stress relief and creep near the walls of the WIPP storage rooms. The purpose of this memo is to present some highly idealized model calculations for radial flow toward a circular tunnel with a very large increase in permeability near the wall. A reasonable permeability variation is chosen based on *in situ* measurements. The nonlinear initial-value problem for the pore pressure is solved numerically, and the cumulative brine volume is calculated for a design storage room.

Model Description

A simple model for transient, one-dimensional, radial flow in a porous medium results in a nonlinear diffusion equation for the fluid pressure [e.g., 5]:

$$C \frac{\partial p}{\partial t} = \frac{1}{r} \frac{\partial}{\partial r} \left[r \frac{k(r)}{\mu} \frac{\partial p}{\partial r} \right], \quad (1)$$

where C is the capacitance, p is the pressure, k is the permeability, μ is the fluid viscosity, and r is the radial coordinate. It is assumed that the permeability, k , may vary with radial

position. For C constant, (1) can be written:

$$\frac{\partial p}{\partial t} = \frac{1}{r} \frac{\partial}{\partial r} \left[r c(r) \frac{\partial p}{\partial r} \right], \quad (2)$$

where

$$c(r) = \frac{k(r)}{\mu C} \quad (3)$$

is the fluid diffusivity.

It is assumed that the initial pressure is uniform, at some value p_0 :

$$p(r, 0) = p_0. \quad (4)$$

At the wall of the circular tunnel of radius a , the pressure is taken to be atmospheric:

$$p(a, t) = 0, \quad (5)$$

and, in the far field, the pressure is assumed to remain at its initial value:

$$\lim_{r \rightarrow \infty} p(r, t) = p_0. \quad (6)$$

Numerical Analysis

In the form of (2) and (4)–(6), it is difficult to treat the boundary condition at infinity numerically. Thus, it is convenient to introduce a change of variable that maps the semi-infinite domain onto a finite region. Let

$$\eta = 1 - \exp \left[-\zeta \left(\frac{r}{a} - 1 \right) \right], \quad (7)$$

where ζ is a “stretch factor.” Clearly, η has the attractive properties that $\eta = 0$ at $r = a$ and $\eta = 1$ as $r \rightarrow \infty$. The stretch factor, ζ , can be chosen appropriately for the length scale over which the pressure field varies at the time of interest. For example, consider a discretization of the region from $\eta = 1$ to $\eta = 0$ into 80 equal segments. The 81st node is located at $\eta = 1$, which corresponds to $r \rightarrow \infty$. The 80th node is at $\eta = 0.9875$. For $\zeta = 10$, this corresponds to $r/a = 1.44$; for $\zeta = 1$, $r/a = 5.38$; for $\zeta = 0.1$, $r/a = 44.82$; for $\zeta = 0.01$, $r/a = 439.20$. Under the change of variable, equations (2) and (4)–(6) become

$$\frac{\partial p}{\partial t} = \frac{\zeta^2(1-\eta)}{a^2[\zeta - \ln(1-\eta)]} \frac{\partial}{\partial \eta} \left\{ c(\eta)[\zeta - \ln(1-\eta)](1-\eta) \frac{\partial p}{\partial \eta} \right\}, \quad (8)$$

$$p(\eta, 0) = p_0. \quad (9)$$

$$p(0, t) = 0, \quad (10)$$

$$p(1, t) = p_0. \quad (11)$$

Equations (8)–(11) are solved by a numerical method known as the “method of lines,” in which the spatial gradients are resolved by centered differences, leaving a set of coupled, first-order differential equations in time. These are solved in turn by a library ODE solver using an implicit, backward-differentiation scheme [8].

Equation (8) can be written for each computational node i in the form

$$\frac{\partial p_i}{\partial t} = -\frac{1}{C} \frac{\zeta(1-\eta_i)}{a[\zeta - \ln(1-\eta_i)]} \left(\frac{\partial}{\partial \eta} \{[\zeta - \ln(1-\eta)]q\} \right)_i, \quad (12)$$

where the flux q is given by:

$$q = -\frac{k(\eta)}{\mu} \frac{\zeta(1-\eta)}{a} \frac{\partial p}{\partial \eta}. \quad (13)$$

The fluxes are computed at the midpoint nodes so that (12) is approximated by the centered difference form:

$$\frac{dp_i}{dt} \approx -\frac{1}{C} \frac{\zeta(1-\eta_i)}{a[\zeta - \ln(1-\eta_i)]} \left\{ \frac{[\zeta - \ln(1-\eta_{i+1/2})]q_{i+1/2} - [\zeta - \ln(1-\eta_{i-1/2})]q_{i-1/2}}{\Delta \eta} \right\}, \quad (14)$$

and the fluxes (13) are also given by the centered difference approximation:

$$q_{i+1/2} \approx -\frac{k_{i+1/2}}{\mu} \frac{\zeta(1-\eta_{i+1/2})}{a} \left(\frac{p_{i+1} - p_i}{\Delta \eta} \right). \quad (15)$$

The initial condition (9) is given by

$$\left. \begin{aligned} p_1(0) &= 0, \\ p_i(0) &= p_0, \quad i = 2, N \end{aligned} \right\}, \quad (16)$$

and the boundary conditions (10, 11) are accommodated by specifying

$$\frac{dp_1}{dt} = 0, \quad (17)$$

$$\frac{dp_N}{dt} = 0, \quad (18)$$

where N is the number of nodes.

Results

Numerical calculations were performed for several cases (Table 1) in order to investigate the effect of increased permeability in the near-field region. Results are shown here in the form of cumulative brine volume as a function of time for a tunnel with surface area (excluding end walls) equivalent to a design storage room 3 m × 10 m × 91 m (effective radius 4.5 m).

As a reference case, a simulation was carried out for *uniform* permeability and initial pressure. A permeability of $k = 10^{-21} \text{ m}^2$ (1 nanodarcy) was chosen for this calculation, and the diffusivity for this and successive calculations was taken to be [9]:

$$c = (1.1 \times 10^{14})k. \quad (19)$$

The initial pressure was taken to be 15 MPa, corresponding to lithostatic pressure at the repository depth. An exact, analytical solution to this problem is available [*e.g.*, 5], and was evaluated as a check on the numerical scheme. The analytical solution is shown in Figure 1 as Case 1; the numerical solution is indicated as Case 2. The numerical simulation underestimates the cumulative volume at early time, probably because of error in resolving the steep near-wall pressure gradient. After 200 years, the error is small; the cumulative volume is calculated to be about 17 m^3 .

Case 3 treats a very large increase in permeability near the tunnel wall. The variation chosen is based on a crude fit to the *situ* permeability measurements of Peterson, *et al.* [7] (Figure 3). The permeability is assumed to fall off exponentially away from the wall, reaching a far-field value at some distance L :

$$\left. \begin{aligned} k(x) &= k_{\infty} \exp[\lambda(L-x)], & x \leq L \\ k(x) &= k_{\infty}, & x > L \end{aligned} \right\}, \quad (20)$$

where x is the (radial) distance away from the wall and λ is a constant that fixes the magnitude of the permeability increase at the wall. In the present case, the permeability at the wall is assumed to be three orders of magnitude higher (10^{-18} m^2 or $\sim 1 \mu\text{d}$) than the far-field value ($\lambda = 0.6908$), and to fall off to the far-field value 10 m from the wall ($L = 10.0 \text{ m}$) (Figure 2).

After 200 years, this enormous increase in near-wall permeability results in a cumulative brine volume of about 26 m^3 , an increase of about 50% over the uniform cases (Cases 1 and 2). This relatively small difference reflects the fact that, at later time, the flow is controlled by the far-field properties.

It is also of interest to assess the effect of a variable initial pressure distribution. In particular, it can be anticipated that dilatation of the salt in the disturbed zone near the repository will tend to reduce the initial pressure. Thus, consistent with the above argument for the permeability increase near the wall, it is assumed for Case 4 (Table 1) that the initial pressure drops exponentially to zero at the wall over the same length scale L that characterizes the permeability increase:

$$\left. \begin{aligned} p_0(x) &= p_{\infty} \left\{ \frac{\exp(\lambda L) - \exp[\lambda(x-L)]}{\exp(\lambda L) - 1} \right\}, & x \leq L \\ p_0(x) &= p_{\infty}, & x > L \end{aligned} \right\}, \quad (21)$$

Results for this calculation are shown in Figure 1, and are indistinguishable from those with the same permeability variation but uniform initial pressure (Case 3). This is because, with the very large near-wall permeability, the pressure in Case 3 near the wall relaxes so fast that it very quickly looks much like the initial condition for Case 4.

Table 1. Permeability and initial pressure distributions for four cases (Figure 2).

| | Perm.
dist. | k_{wall}
(m ²) | k_{∞}
(m ²) | Init. p
dist. | p_{wall}
(MPa) | p_{∞}
(MPa) |
|----------------|----------------|---------------------------------|-----------------------------------|--------------------|---------------------|-----------------------|
| Case 1 (exact) | uniform | 10^{-21} | 10^{-21} | uniform | 15 | 15 |
| Case 2 (num.) | uniform | 10^{-21} | 10^{-21} | uniform | 15 | 15 |
| Case 3 (num.) | variable | 10^{-18} | 10^{-21} | uniform | 15 | 15 |
| Case 4 (num.) | variable | 10^{-18} | 10^{-21} | variable | 0 | 15 |

Summary

Numerical simulations have been carried out to investigate the effect of a large increase in permeability near the walls of a waste storage room. The increased permeability reflects the "damage" to the salt in the disturbed zone due to stress relief and creep closure. The brine flow calculations assume a Darcy flow mechanism, with the initial pressure lithostatic (15 MPa) and far-field permeability 10^{-21} m² (1 nanodarcy). The principal results are:

- Available *in situ* permeability measurements are reasonably well represented by an exponential increase near the walls. The model calculations presented here assume the far-field permeability is reached 10 m from the walls, and the near-wall increase is three orders of magnitude over the far-field value.
- For the conditions assumed, an increase in the near-wall permeability of three orders of magnitude results in a 50% increase in the cumulative brine volume after 200 years, suggesting that the flow at late time is controlled by the far-field properties.
- A sharply reduced initial pressure field in the near-wall region (Case 4) has virtually no effect on the cumulative brine volume over 200 years.

References

1. Stein, C. L., and Krumhansl, J. L., Chemistry of Brines in Salt From the Waste Isolation Pilot Plant (WIPP) Facility, Southeastern New Mexico: a Preliminary Investigation, SAND85-0897, Sandia National Laboratories, Albuquerque, NM, March 1986.
2. Deal, D. E., and Case, J. B., Brine sampling and evaluation program; Phase I, IT Corporation Technical Report, DOE-WIPP-87-008, June 1987.
3. Bredehoeft, J. D., Pore fluid regime - WIPP repository, Memo to Members of the WIPP Panel, February 27, 1986.

4. McTigue, D. F., Brine flow under hydrostatic pressure, Memo to Distribution, April 14, 1986.
5. Nowak, E. J., and D. F. McTigue, Interim Results of Brine Transport Studies in the Waste Isolation Pilot Plant (WIPP), **SAND87-0880**, Sandia National Laboratories, Albuquerque, NM, May 1987.
6. Bredehoeft, J. D., Will salt repositories be dry?, *EOS - Transactions, American Geophysical Union*, **69**, March 1, 1988, 121&131.
7. Peterson, E., Lagus, P., Brown, J., and Lie, K., WIPP Horizon *In Situ* Permeability Measurements Final Report, **SAND85-7166**, January 1987.
8. Champine, L. F., and H. A. Watts, DEPAC — Design of a User Oriented Package of ODE Solvers, **SAND79-2374**, Sandia National Laboratories, Albuquerque, NM, September 1980.
9. McTigue, D. F., and E. J., Nowak, Brine transport in the bedded salt of the Waste Isolation Pilot Plant (WIPP): field measurements and a Darcy flow model, *Scientific Basis for Nuclear Waste Management*, Materials Research Society, in press, 1988.

DFM:1511

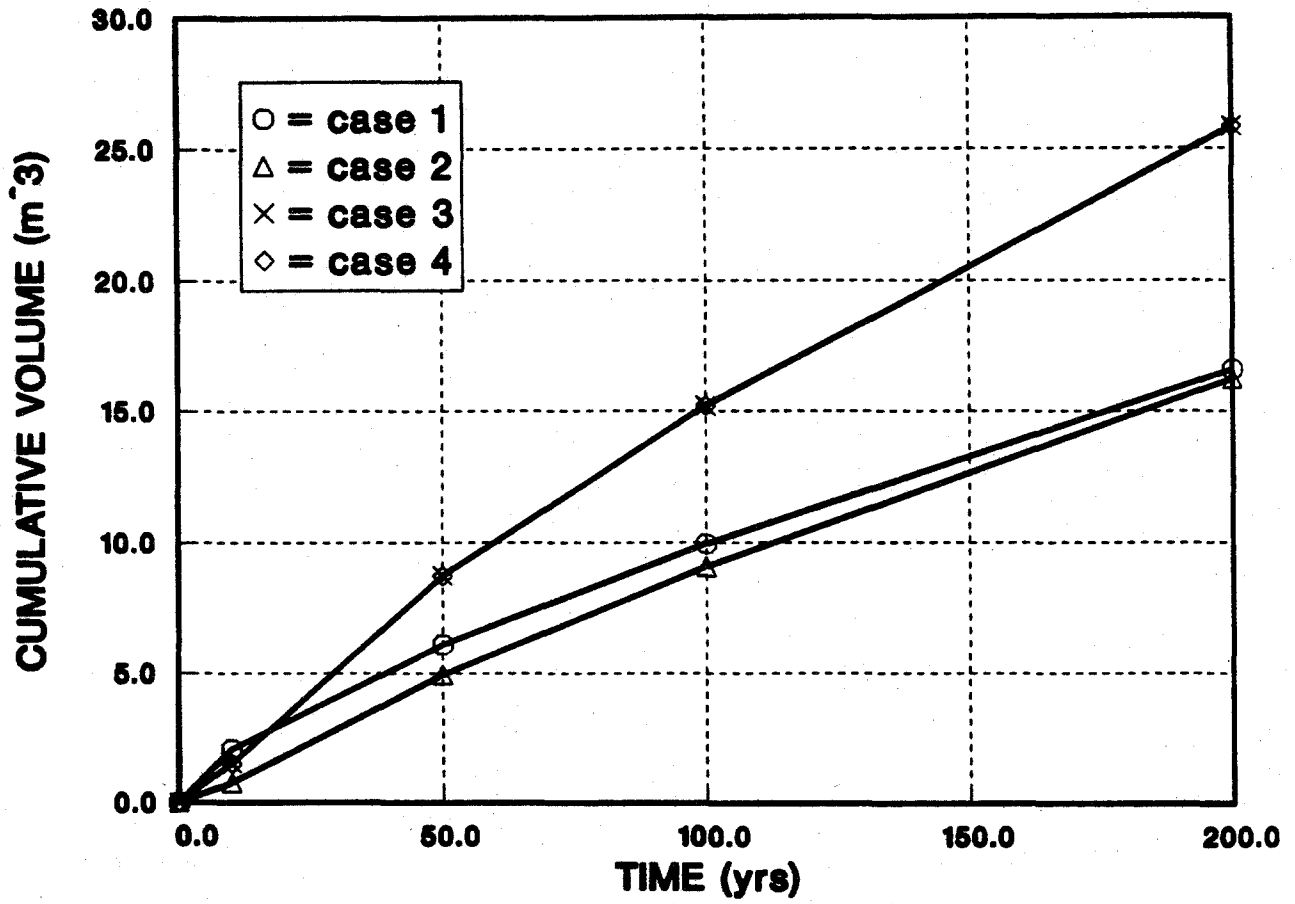


Figure 1. Cumulative volume vs. time for a design storage room; four cases defined in Table 1.

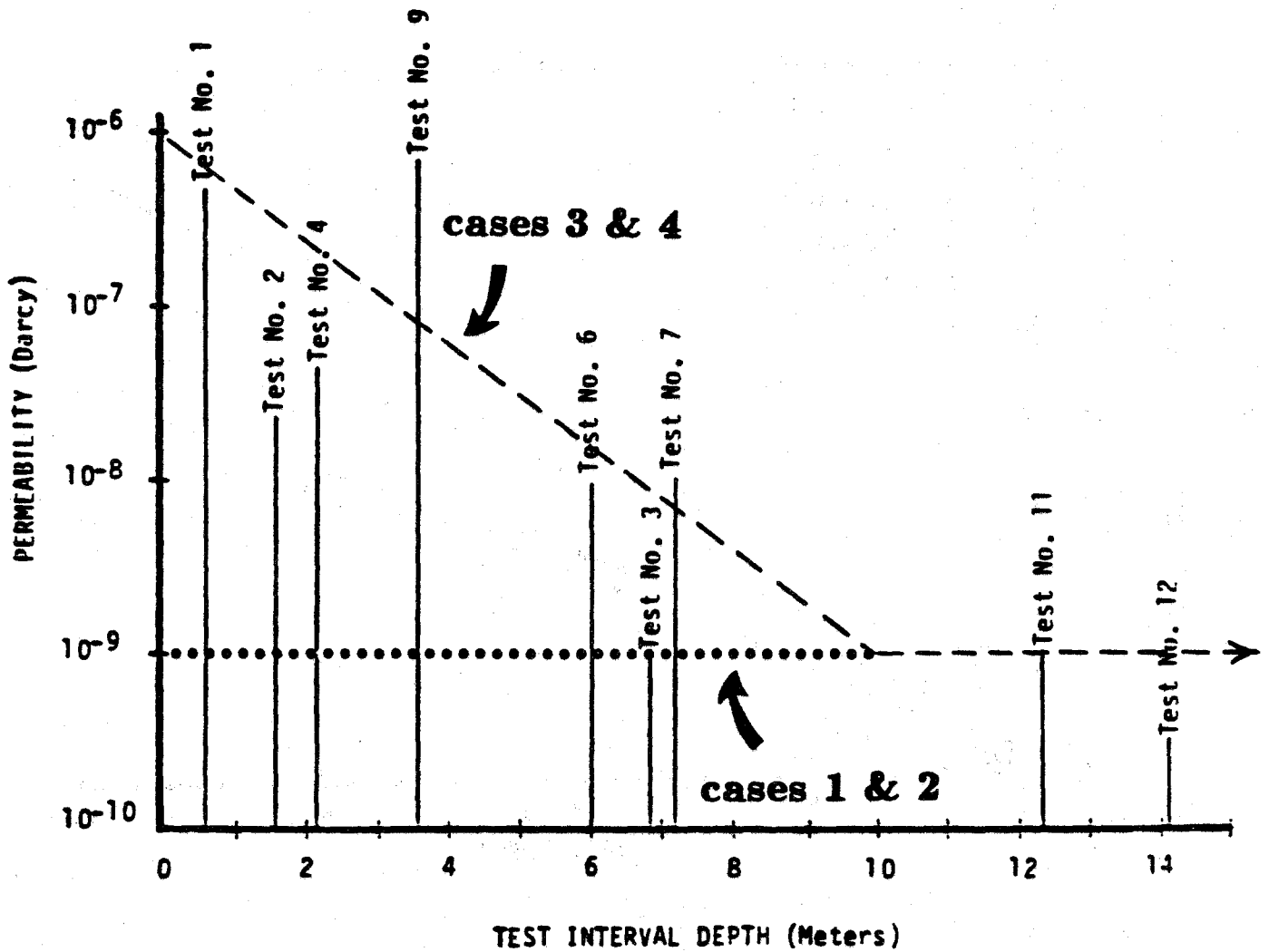


Figure 2. Model permeability variation (eq. 20) superimposed on *in situ* measurements by Peterson, *et al.* [7].

Copy to:

1510 J. W. Nunziato
1511 D. K. Gartling
1511 D. F. McTigue (day file)
1512 J. C. Cummings
1513 D. W. Larson
1520 L. W. Davison
1530 W. Herrmann (acting)
1550 C. W. Peterson
6331 A. R. Lappin
6331 R. L. Beauheim
6331 P. B. Davies
6332 L. D. Tyler
6332 R. Beraun
6332 B. M. Butcher
6332 E. J. Nowak
6332 J. C. Stormont
6334 D. R. Anderson
6334 M. S. Y. Chu

A.9 Preliminary Quantitative Estimates of TRU Waste and Waste
Containers to be Emplaced in the WIPP:

by P. Drez



April 4, 1989

Project No. 301269.02.02

Wendall Weart
Department Manager 6330
Sandia National Laboratory
Albuquerque, New Mexico 87185-5800

Preliminary Quantitative Estimates of TRU Waste and Waste Containers
to be Emplaced in the Waste Isolation Pilot Plant: To Support
Calculations for the Supplemental Environmental Impact Statement

Dear Wendall:

This letter summarizes data provided to Rob Rechard and Larry Brush during the last two months in support of the Supplemental Environmental Impact Statement (SEIS). The data has been derived from two sources:

- Data from the Performance Assessment (PA) Data Base that was initiated as a task under our consulting agreement with Sandia National Laboratory in support of PA. The current computer data base has not been totally checked against the data sheets submitted by the waste generator and storage sites, but these initial numbers are not expected to change any after the quality control procedures are finished.

All data provided in this letter, other than that quoted from Hank Batchelder of Westinghouse, comes from the PA data base.

- Hank Batchelder provided estimates of number of drums and boxes which are expected to be emplaced in the Waste Isolation Pilot Plant (WIPP) through year 2013 from Revision 4 of the Integrated Data Base (IDB). The estimates of the number of boxes were further refined by Hank to differentiate between standard waste boxes (SWB), old metal boxes (4 ft x 4 ft x 7 ft), and old wooden boxes (4 ft x 4 ft x 7 ft).

The data provided to Rob Rechard and Larry Brush is summarized below:

- Revision 4 of IDB:
 - Number of total drums to be shipped to WIPP: 385,000; each drum has an approximate volume of 0.21 m³.
 - Number of SWBs to be shipped to WIPP: 13,500, each SWB has an approximate volume of 63 ft³ or 1.78 m³.
 - Number of old (4 ft x 4 ft x 7 ft) boxes to be shipped to WIPP: 6000, each with an approximate volume of 3.2 m³.

Regional Office

5301 Central Avenue, N.E. • Suite 700 • Albuquerque, New Mexico 87108 • (505) 262-8800

IT Corporation is a wholly owned subsidiary of International Technology Corporation

Wendall Weart

2

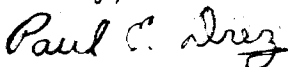
April 4, 1989

- Approximately 4,500 of the old boxes are wooden.
- Approximately 1,500 of the old boxes are metal, which may or may not contain wooden liners.
- PA Data Base:
 - Total weight of celluloseics to be shipped to WIPP:
 - Total paper: 3.28×10^6 kg
 - Total cloth: 2.53×10^5 kg
 - Total treated lumber: 6.66×10^4 kg
 - Total untreated lumber: 5.67×10^4 kg
 - Total plywood: 9.34×10^4 kg
 - Total weight of rubber to be shipped to WIPP:
 - Total Neoprene: 1.37×10^5 kg
 - Total Hypalon: 1.18×10^5 kg
 - Total surgeon's gloves: 5.91×10^5 kg (see note below)
 - Total weight of lead to be shipped to WIPP: 1.30×10^6 kg
 - Total weight of steel to be shipped to WIPP: 5.11×10^6 kg
 - Total weight of iron to be shipped to WIPP: 3.0×10^6 kg.

The total weight estimate for surgeon's gloves is suspect. This estimate is based on information provided by the generator and storage sites, but it would be easy for sites to overestimate the weight of surgeon's gloves in the waste since gloves occupy such a large volume/kg. The generator and storage sites will be queried about this possible overestimation in the next data update later this year.

I hope that this information has been useful in support of the SEIS calculations. Remember that the estimates are based on the first round of data submitted by the waste generator and storage sites. These numbers will probably change in future revisions, but do represent the best estimates of TRU waste to be sent to WIPP, since this data was provided by the sites. Please do not hesitate to contact me at 262-8800 if any additional information is needed.

Sincerely,



Paul E. Drez
Senior Technical Associate

c: H. Batchelder, Westinghouse Carlsbad
L. Brush, SNL
J. Hart, IT Albuquerque
J. Myers, IT Albuquerque
R. Rechard, SNL

APPENDIX B. SPECIFICATIONS FOR THE WIPP SEAL SYSTEM

B.1 Dimensions of Shaft- and Repository-Seal Components

The design height and width or diameter for drifts and shafts have been chosen as the final-state dimensions of the reconsolidated crushed-salt seal components. Two competing processes will determine the final dimensions of the seals. Creep closure causes drift and shaft walls to move inward. Simultaneously, fractures may develop in the disturbed rock zone (DRZ), enlarging the effective excavation size by separating slabs or fragments from the host rock. These slabs or fragments will also be reconsolidated by continuing creep closure.

The expected width for the seal in Marker Bed 139 is equal to the design width of the overlying drift. Gas-flow measurements detected no increased gas flow in MB 139 under the pillars on either side of a WIPP drift (Stormont et al., 1987; Borns and Stormont, 1988). A length of 30 m (Stormont, 1988) has been chosen for the reconsolidated salt component and for the Marker Bed 139 seal component of all drift- and panel-seal systems.

The expected height of the final column of reconsolidated crushed-salt seal material in the lower portion of each shaft is 200 m. This height was calculated using a model for a baseline case that is the best current representation of expected reconsolidation behavior in a WIPP shaft (Nowak and Stormont, 1987). The model was derived from an analysis of crushed-salt reconsolidation that took into account the potential retardation of reconsolidation by inflowing brine and the effect of expected shaft-closure rates. Leakage of brine past the upper seal system and brine seepage from the Salado Fm. during reconsolidation could reduce this column height to 100 m (Nowak and Stormont, 1987). Therefore, the expected range in height for reconsolidated salt is 100 to 200 m.

Dimensions of the crushed-salt seal components in the shafts and main access drifts:

Column of reconsolidated crushed-salt seal material in the C&SH Shaft
diameter: 3.7 m (12 feet) (DOE, 1986, Ch. 7)
length: 200 m (range: 100 m to 200 m)

Column of reconsolidated crushed-salt seal material in the Waste Shaft
diameter: 6.1 m (20 feet) (DOE, 1986, Ch. 8)
length: 200 m (range: 100 m to 200 m)

Column of reconsolidated crushed-salt seal material in the Exhaust Shaft
diameter: 4.6 m (15 feet) (DOE, 1986, Ch. 9)
length: 200 m (range: 100 m to 200 m)

Column of reconsolidated crushed-salt seal material in the Air Intake Shaft
diameter: 6.1 m (20 feet) (Bechtel National Inc., 1987)
length: 200 m (range: 100 m to 200 m)

Reconsolidated crushed-salt seal material in the E300 Access Drift
height: 3.7 m (12 feet) (DOE, 1988b)
width: 4.3 m (14 feet) (DOE, 1988b)
length: 30 m

Reconsolidated crushed-salt seal material in the E140 Access Drift
height: 3.7 m (12 feet) (DOE, 1988b)
width: 7.6 m (25 feet) (DOE, 1988b)
length: 30 m

Reconsolidated crushed-salt seal material in the W30 Access Drift
height: 3.7 m (12 feet) (DOE, 1988b)
width: 4.3 m (14 feet) (DOE, 1988b)
length: 30 m

Reconsolidated crushed-salt seal material in the W170 Access Drift

height: 3.7 m (12 feet) (DOE, 1988b)
width: 4.3 m (14 feet) (DOE, 1988b)
length: 30 m

Dimensions of the seal-system components in MB 139:

MB 139 seal-system component in the E300 Access Drift

height: 0.1 m
width: 4.3 m (14 feet) (DOE, 1988b)
length: 30 m

MB 139 seal-system component in the E130 Access Drift

height: 0.1 m
width: 7.6 m (25 feet) (DOE, 1988b)
length: 30 m

MB 139 seal-system component in the W30 Access Drift

height: 0.1 m
width: 4.3 m (14 feet) (DOE, 1988b)
length: 30 m

MB 139 seal-system component in the W170 Access Drift

height: 0.1 m
width: 4.3 m (14 feet) (DOE, 1988b)
length: 30 m

APPENDIX C. STANDARD DRILLING PROCEDURES USED IN THE DELAWARE BASIN

Some understanding of drilling practices that may be used in the future is necessary for an evaluation of Case II. The calculations in this report assume that: drilling will be for gas and oil; standard drilling procedures now in use will be continued into the future; future drillers will observe all regulations currently imposed by federal and state agencies; and the drillers will have no prior knowledge of the presence of the repository.

Drilling for oil and gas has two main objectives: to drill the hole to the production zone as quickly and economically as possible and to install casing from the reservoir to the surface for well production. The procedures used to accomplish these objectives are fairly well standardized in the drilling industry. When drilling for oil or gas, particularly in the area around the WIPP site, there is always the possibility of encountering a blowout or lost-circulation zone. Therefore, the drilling companies are prepared to handle any of these conditions by responding in a relatively short time.

If a company is drilling an exploratory oil or gas well, the operation uses a standard rotary drill rig with a mud circulation system. The only differences between drilling for oil and gas depend on the depth of the well and the size of casing used. The normal depth for an oil well in the Delaware Basin near the WIPP site ranges from 1,200 to 1,800 m (4,000 to 6,000 ft), but gas-well depths usually exceed 3,000 m (10,000 ft). Consequently, oil wells normally have a standard 41.3-cm (16 1/4-in.) drilled hole to the top of salt, to accommodate 34.0-cm (13 3/8-in.) steel casing, and gas wells normally have a standard 45.7-cm (18-in.) drilled hole, to accommodate 35.6-cm (14-in.) casing. The drilling fluid normally used is a salt-based drilling fluid consisting of bentonite and saturated brine, with a weight of about 10 lbs/gallon or a pressure of 52 psi per 30 m (100 ft) of hole.

The normal procedure is to drill the hole to the base of the Rustler Fm. (the top of salt) and set casing, called a salt string. The use of this casing is dictated by the State Engineer Office, because the WIPP site is

located in a closed ground-water basin, and all hydrocarbon wells are required to protect the aquifers in the basin. In this case the Culebra Dolomite is the aquifer so designated. After the hole has been drilled and the casing placed in the hole, the casing is cemented from bottom to top with an API Class C grout (intended for use in oil and gas wells from surface to a depth of 2,400 m (8,000 ft) and having a sulfate resistance). After casing is set, the drilling company drills either a standard 31.1-cm (12 1/4-in.) hole, if drilling to the shallower depth for oil, or a 35.6-cm (14-in.) hole, if the target depth is for gas. In either case, saturated brine weighing 10 lbs/gallon or providing 52 psi per 30 m (100 ft) of depth is normally used.

According to the assumptions specified in Case II, it is during this phase of drilling, when the drill hole is below the repository, that it intercepts a brine reservoir. When the drilling company intercepts the brine reservoir, they will probably get gas flow to the surface, at which time they will add weight to the drilling fluid (usually barite), increasing the weight to stop the flow from the reservoir. The weight could increase to as much as 16 lbs/gallon or 80 psi per 30 m (100 ft) of hole. A drilling company probably would not stop and plug the drill hole after encountering the brine reservoir. Geopressured brine-reservoir encounters are not uncommon in normal drilling operations, and the drillers would probably cement or case off the brine and continue drilling the hole to the target horizon. Eventually, if the assumptions laid out at the beginning of this appendix hold, any borehole through the repository and brine reservoir will consist of several cement and sand plugs emplaced in casing or wallrock.

In the Delaware Basin in and around the WIPP site, the Oil and Gas Commission controls plugging for abandonment (Oil Conservation Commission, 1952). Because the WIPP site is located in the potash enclave, recommended plugging procedures would provide for protection of the potash horizon from foreign fluids. This could be accomplished by sealing off the brine reservoir with cement grout (usually capped by a plug of at least 60 m (200 ft) of cement grout). About 15 m (50 ft) of sand is emplaced above the grout, and weighted drilling fluid is emplaced to ~60 m (~200 ft) below the potash horizon, where another plug extends through the potash horizon. A second sand plug is emplaced, followed by weighted drilling mud to within ~60 m (~200 ft)

of the top of the salt section, where another plug of cement grout is emplaced. When the base of the casing is reached, the driller might either continue the grout to the surface or provide weighted mud to the surface, where a cap and abandonment marker are placed.

After the plug has been emplaced, the length of time that the plug and casing remain intact and the permeability of the deteriorated plug are of concern to the calculations here. Most cementing companies suggest that the cement plugs should last for at least 100 years; so should the casing. Estimates of plug permeabilities (Table C-1) are based on limited data (Christensen and Petersen, 1981; Buck, 1985; Bush and Piele, 1986; Scheetz et al., 1986). These permeabilities depend strongly on the host rock or substrate in which the plug is emplaced (e.g., clean versus chemically altered steel casing or anhydrite versus halite). There are no data on deteriorated plugs or borehole closure. The values in Table C-1 are derived by calculating permeabilities of an unconsolidated sand with various grain sizes (Freeze and Cherry, 1979). Most experimental studies of plug-borehole interactions extend for hundreds of days or less. With time, the plug and borehole may: (1) attain very low permeabilities similar to the host salt in response to closure or salt precipitation; (2) be filled and propped by fluid until the fluid can migrate out through the formation or through the plugs; or (3) remain propped by debris and sand placed in the borehole by plugging and subsequent decay of the borehole wall. These three possibilities are discussed in the following three paragraphs.

First, predicting the attainment of very low permeabilities in response to borehole closure in the halite portion is now difficult. A borehole that intercepts a brine reservoir in the Castile Fm. must be ~1,000 m (~3,300 ft) in length, about half of which is in halite. Fuenkajorn and Daemen (1988) state that transient creep models do not adequately predict laboratory simulations of borehole closure. The difficulty in modeling borehole closure reflects the variations in intrinsic parameters (e.g., the local distribution of intracrystalline gaps and air voids), which play more of a role in deformation than transient creep. The salt portions of the borehole will eventually close, but current constitutive law models are not adequate to predict when.

Table C-1. Specifications for Gas and Oil Exploratory Boreholes

| <u>Parameter</u> | <u>Value</u> | <u>Units</u> |
|--|-------------------|----------------|
| Drilled diameter | | |
| - in Rustler Fm. (oil well) | 0.413 | m |
| (gas well) | 0.457 | m |
| - in Salado and Castile Fms., (oil well) | 0.311 | m |
| (gas well) | 0.356 | m |
| Borehole plugs | | |
| - lengths | 60 | m |
| - locations: (i) above brine reservoir | | |
| (ii) below potash zone | | |
| (iii) below Rustler Fm. | | |
| Effective borehole permeability | | |
| - open-borehole period | infinite | |
| - plug in Castile Fm. | 10 ⁻¹⁵ | m ² |
| - plugs in Salado Fm. | 10 ⁻¹⁸ | m ² |
| - for times greater than 150 years | | |
| - Case IIA | 10 ⁻¹² | m ² |
| - Cases IIB, IIC, and IID | 10 ⁻¹¹ | m ² |

Second, the fluid filling a borehole will attain a pressure approaching the radial pressure of the the closing borehole. The borehole will remain propped open by fluid unless the permeability of the wall rock of the borehole or the plug system above is adequate to allow the fluid to migrate and reduce the pressure in the borehole.

Finally, debris and sand may prop the hole open. As stated above, a 1000-m borehole into a brine reservoir will have nearly 500 m of non-salt wall rock. If plugs are emplaced in the salt section, another 120 m of the borehole will be filled with non-salt material. As the plugs degrade, the remaining salt-walled portion of the borehole will fill with sand and cementitious debris. This debris will have different mechanical properties than salt and will resist closure and recementation. The resulting borehole will have the permeability of a sand with various grain-size fractions.

In oil-well drilling, it is usually desirable to confine formation fluids to their sources. This is especially important when drilling near the WIPP site, because New Mexico Oil Conservation Commission Order Number R-3221 (OCC, 1967a, 1967b) prohibits disposing of or uncontrolled flow of oil-field brines on the surface. In the rotary system of drilling, the circulation-fluid column effectively prevents fluid flow to the surface so long as the fluid density and column height are sufficient to develop a hydrostatic pressure greater than the formation pressure exposed at the well bore. An adequate fluid column is the primary element affecting well control. Blowout prevention is the second line of defense; its primary function is to preserve the fluid column or to confine well fluids to the borehole until an effective fluid column can be restored. This is accomplished by using surface equipment called "blowout preventers" (BOP's) either to close in the well or to completely restrict the flow of fluids from the well, pending re-establishment of a column of drilling fluid of sufficient density to restrict further influx of formation fluid.

BOP requirements are a function of risk exposure and degree of protection required. The American Petroleum Institute (API) classification of BOP's is based on pressure ratings. The BOP used is normally selected based on the highest pressure expected in the area; drillers are usually conservative in their selection.

If a high-pressure zone is encountered during a drilling operation, and an uncontrolled "kick" (a flow of formation fluid to the wellbore) occurs, the well will "blow out" (uncontrolled well or formation fluid flow to the surface). In these situations, the BOP will be closed, usually hydraulically through an accumulator, within one to one and a half minutes. This action closes the control-gate valves, all the pipe rams, and the annular preventor and retains a 9.6-MPa (200 psi) pressure above the acceptable precharge pressure, sealing off the flow (International Association of Drilling Contractors, 1974). After this operation, the density of the drilling fluid in the pits is increased enough to restrict further influx of formation fluid. The amount of fluid lost to the surface (mud pits) is a function of the time required to close the BOP's and the amount of unbalanced pressure in the fluid column.

In the unlikely possibility of failure of the BOP, the only method of restricting flow from the well is to add weight to the drilling mud, pumping it down the well bore until the unbalanced pressure is overcome. This operation could take from one half hour to several hours depending on the unbalanced pressure encountered and the availability of mud-weighting materials.

APPENDIX D. NUMERICAL APPROACH TO CALCULATIONS
DESCRIBING UNDISTURBED PERFORMANCE

D.1 Computer Model and Input

D.1.1 NEFTRAN

The computer code NEFTRAN (Longsine et al., 1987; Campbell et al., 1981) is used for numerical simulation of steady-state flow and transport in Cases IA and IB (Section 6.1). NEFTRAN simulates ground-water flow and radionuclide transport in a computationally efficient manner. Longsine et al.'s (1987) and Campbell et al.'s (1981) thorough description of NEFTRAN is excerpted here. The brief presentation here relates only those features of the code used in the analysis of Case I.

NEFTRAN assumes that flow and radionuclide transport

...take place along discrete one-dimensional legs or paths. These legs are assembled to form a multidimensional network representing the flow field. NEFTRAN requires pressure boundary conditions to solve the flow equations and these conditions must be specified as part of the input These boundary conditions as well as the flow network are defined from detailed flow fields predicted by flow models in codes such as SWIFT II [Longsine et al., 1987, p. 1].

The boundary conditions can also be defined from idealized conceptual models, as in the present application.

The generalized flow network allows the user to set up any idealized flow network in the vicinity of a repository. A distributed velocity method (DVM) is applied over the entire length of the migration path, using an average velocity for each isotope calculated from the isotopic velocities in all legs. This method allows transport of multiple radionuclide chains in a single run.

NEFTRAN contains a generalized network capability that allows the user to set up any network by specifying the number of legs and junctions, the junctions bounding each leg, and the junctions where boundary conditions are specified. Longsine et al. (1987, pp. 4-11) discuss NEFTRAN in the following excerpt:

. . . the driving force for fluid flow through a leg is a pressure gradient. The underlying assumption for the flow network to represent a flow system is conservation of mass at each junction. This principle can be expressed mathematically as

$$\sum_{\ell} M_{\ell} = 0 \quad [D-1]$$

where ℓ is the summation index over all legs connected at the given junction, and M_{ℓ} is the mass flow rate for the ℓ^{th} leg in units of mass per unit time [See Table D-1 for the Appendix D.1 nomenclature]

If the ℓ^{th} leg is bounded by Junctions $\ell 1$ and $\ell 2$, the mass flow rate in the leg is defined by

$$M_{\ell} = \gamma_{\ell} K_{\ell} A_{\ell} \left[\frac{(P_{\ell 1} - P_{\ell 2})}{Z_{\ell} \gamma_{\ell} g} + \frac{(E_{\ell 1} - E_{\ell 2})}{Z_{\ell}} \right] \quad [D-2]$$

where A_{ℓ} is the cross-sectional area, K_{ℓ} is the hydraulic conductivity, $E_{\ell i}$ is the elevation of the i^{th} junction, g is the acceleration of gravity, $P_{\ell i}$ is the pressure at the i^{th} junction, Z_{ℓ} is the length of the leg, and γ_{ℓ} is the fluid density. . . . The hydraulic conductivity is weighted as

$$K_{\ell} = K'_{\ell} \left[\frac{\mu_f}{\mu_{\ell}} \right] \left[\frac{\gamma_{\ell}}{\gamma_f} \right] \quad [D-3]$$

to account for the effects of brine concentration on the flow. In [Equation D-3], K'_{ℓ} is the fresh-water hydraulic conductivity for the ℓ^{th} leg, μ_f and γ_f are the respective viscosity and density of fresh water at -20°C , [and] μ_{ℓ} and γ_{ℓ} are the respective actual viscosity and density in the ℓ^{th} leg. . . .

The determination of γ_{ℓ} and μ_{ℓ} in [Equation D-3] follows from input on relative brine concentration for the ℓ^{th} leg ℓ and the equations presented in the NWFT/DVM Users Manual In reality, water density and viscosity are functions of temperature, pressure and brine concentration. However, . . . water density and viscosity are represented as functions of brine concentration only. The resulting equations . . . [for] density and viscosity for the fluid in the ℓ^{th} leg are

$$\gamma_{\ell} = \gamma_f + C_{b\ell} [\gamma_s - \gamma_f] \quad [D-4]$$

and

$$\mu_{\ell} = \mu_f [1.0 + 0.0219 C_{b\ell} W_b \gamma_{\ell}] \quad [D-5]$$

where $C_{b\ell}$ = relative brine concentration in the ℓ^{th} leg,

$$0 \leq C_{b\ell} \leq 1;$$

Table D-1. Nomenclature Used in Appendix D.1 (after Longsine et al., 1987, pp. xiv ff.)

| | |
|--------------------|---|
| A_ℓ | cross-sectional area for ℓ^{th} leg |
| C_{b_ℓ} | relative brine concentration in the ℓ^{th} leg |
| $E_{\ell i}$ | elevation of the i^{th} junction in the ℓ^{th} leg |
| D | dispersion coefficient |
| \underline{e} | vector of junction elevations and known boundary pressures in flow equations |
| K_ℓ | hydraulic conductivity in the ℓ^{th} leg |
| K'_ℓ | hydraulic conductivity for fresh water in the ℓ^{th} leg |
| M_ℓ | mass flow rate in ℓ^{th} leg |
| \underline{p} | vector of unknown junction pressures in flow equations |
| $P_{\ell i}$ | pressure at the i^{th} junction of the ℓ^{th} leg |
| $P(v)$ | velocity distribution for an ensemble of particles |
| Q_ℓ | volumetric flow rate in ℓ^{th} leg |
| $R_{k\ell}$ | retardation coefficient for the k^{th} species in the ℓ^{th} leg |
| $S(x, t)$ | source of "injected" particles |
| TS_i | time spent in a time interval as the i^{th} species |
| $v_{f\ell}$ | average fluid velocity for the ℓ^{th} leg |
| $\bar{v}_{k\ell}$ | average velocity for the k^{th} species in the ℓ^{th} leg |
| \bar{v}_f | average fluid velocity |
| $v_m(1, \dots, p)$ | average velocity for particles that begin a time interval as species 1 and end as species p |
| W_b | weight fraction of salt in saturated brine |

| | |
|----------------------|---|
| Z_ℓ | length of the ℓ^{th} leg |
| α_ℓ | dispersivity in ℓ^{th} leg |
| Δt | time interval |
| γ_f | fluid density for fresh water |
| γ_s | fluid density for salt-saturated brine |
| $\underline{\Theta}$ | matrix of coefficients in the flow equations |
| θ_ℓ | components of matrix $\underline{\Theta}$ in flow equations |
| λ_i | decay-rate constant for i^{th} species |
| μ_ℓ | fluid viscosity in ℓ^{th} leg |
| μ_f | reference fluid viscosity |
| ϕ_ℓ | porosity in ℓ^{th} leg |
| ρ | density of an ensemble of particles |

W_b = the weight fraction of salt in saturated brine; and
 γ_s = the density of salt-saturated brine. . . .

Equation [D-2] is a statement of Darcy's law in which the total head difference is given by the sum of dynamic pressure and elevation differences. This equation typically has three unknowns; M_ℓ , $P_{\ell 1}$, and $P_{\ell 2}$ unless either Junction $\ell 1$ or Junction $\ell 2$ has been specified as a boundary junction. For each junction in the network Equation [D-2] is written and [D-2] substituted for M_ℓ . This eliminates the mass flow rates as unknowns leaving only the junction pressures to be determined.

Applying (D-1) to a boundary junction, substituting (D-2) for M_ℓ with $\theta_\ell = A_\ell K_\ell / Z_\ell g$, and repeating this process for every junction in the network results in a matrix equation of the form

$$\underline{\theta} \underline{p} = \underline{e} \tag{D-6}$$

where $\underline{\theta}$ is a matrix of coefficients containing functions of $\theta_\ell = A_\ell K_\ell / Z_\ell g$, \underline{p} is a vector of unknown pressures, and \underline{e} is a vector of junction elevations and

boundary pressures. Longsine et al. (1987, pp. 14-15) continue the discussion in the following excerpt:

After solving for the junction pressures, NEFTRAN calculates the mass flow rate in each leg using [D-2] and divides it by the corresponding density to give the volumetric flow rate. The volumetric flow rate is used to obtain the fluid velocity (Longsine et al., 1987, p. 10).

The average interstitial fluid velocity for the ℓ^{th} leg, $v_{f\ell}$, is given by

$$v_{f\ell} = \frac{Q_{\ell}}{A_{\ell} \cdot \phi_{\ell}} \quad [\text{D-7}]$$

where ϕ_{ℓ} is the porosity of the leg and Q_{ℓ} is the volumetric flow rate. . . .

Let $\ell = 1, 2, \dots, n$ be the number of legs along a given radionuclide migration path. NWFT/DVM . . . uses the weighted average fluid velocity \bar{v}_f over the migration path given by

$$\bar{v}_f = \frac{\sum_{\ell=1}^n Z_{\ell}}{\sum_{\ell=1}^n \frac{Z_{\ell}}{v_{f\ell}}} \quad [\text{D-8}]$$

for the transport simulation such that it preserves total migration time. The result of this approach is to combine all legs into a single one-dimensional segment having average properties. This has been shown to be adequate provided all legs in the migration path represent porous media.

The migration path may also represent fractures with no matrix diffusion under certain circumstances (Section 3.4.3).

The distributed velocity method (DVM), a direct simulation technique used in NEFTRAN, is discussed by Campbell et al. (1981, pp. 15-18):

Like other direct simulation methods, it can simulate either convective- or dispersive-dominated regimes. Unlike other direct simulation techniques, DVM can treat radionuclide chains of arbitrary length and distribution coefficients. However, DVM does introduce some numerical dispersion. Nevertheless, one can control such dispersion . . . and still retain the efficiency required for risk analysis.

The thinking underlying DVM is as follows: Consider a receiver point located at x and donor points located at some typical coordinate x' . Taking the density of an ensemble of particles at

time t' to be $\rho(x', t')$, the density $\rho(x, t)$ at x for $t > t'$ may be determined by introducing a velocity distribution.

The concept here is that, due to heterogeneity of the flow field, . . . a number of alternate paths exist for migration of particles from x' to x . Such paths may be characterized by a continuum of migration times and average velocity components v in the direction of flow. The distribution of such velocities is $P(v)$. Thus for the donor point x' , only those particles with average velocity $v = (x - x') / (t - t')$ arrive at point x at time t' . The density of particles at point x may therefore be obtained by summing over all possible donor points in the following manner:

$$\rho_0(x, t) = \int_{-\infty}^{\infty} dv P(v) \rho(x - v\Delta t, t - \Delta t) \quad [D-9]$$

where

$$\Delta t = t - t'.$$

For convenience, $P(v)$ is represented as a function of velocity only. However, it is certainly possible for P to be a function of other variables such as position x or time increment Δt .

[Equation D-9] gives the propagation of the initial conditions, at time t' , to time t . If, in addition, a source $S(x, \tau)$ is included, then an integration over "injection" time must be performed in addition to an integration over velocity.

$$\rho(x, t) = \rho_0(x, t) + \int_{t'}^t d\tau \int_{v_1}^{v_0} dv P(v) S(x', \tau) \quad [D-10]$$

where $x' = x - v(t - \tau)$. If $S(x', \tau)$ is nonzero only for

$$x_0 \leq x' \leq x_1$$

then the velocity limits for the source term of [Equation D-10] are

$$v_0 = (x - x_0) / (t - \tau) \quad [D-11]$$

and

$$v_1 = (x - x_1) / (t - \tau) \quad [D-12]$$

For example, sources may arise by decay of a radioactive parent. The spatial location of the source (i.e., the radioactive parent) is time dependent.

$P(v)$ can be specialized to a Gaussian form that is appropriate for the treatment of dispersion. This step defines the relation between $P(v)$ and the

Green's Function for the one-dimensional convective dispersion equation with dispersion coefficient, $D = \alpha(\bar{v})$, where α is the dispersivity. The spatial Green's Function for this problem can be rewritten as a function of velocity. This Green's Function in velocity space can be interpreted as a Gaussian form. Writing the complementary solution again for the density of particles allows this Green's Function in velocity space to be directly identified with $P(v)$. This identification is a specialization of the DVM to Fickian dispersion and is used in NEFTRAN. According to Longsine et al. (1987, pp. 17-18),

In NEFTRAN . . . every species can have a different retardation factor in every leg of the migration path . . . [and the average species] velocity for each leg [is treated] separately. For the k^{th} species in the ℓ^{th} leg, the mean species velocity caused by dispersion in the leg is

$$\bar{v}_{k\ell} = v_{f\ell}/R_{k\ell} . \quad [D-13]$$

. . . NEFTRAN maintains a mean velocity for each species and calculates distributed velocities about the mean in each leg.

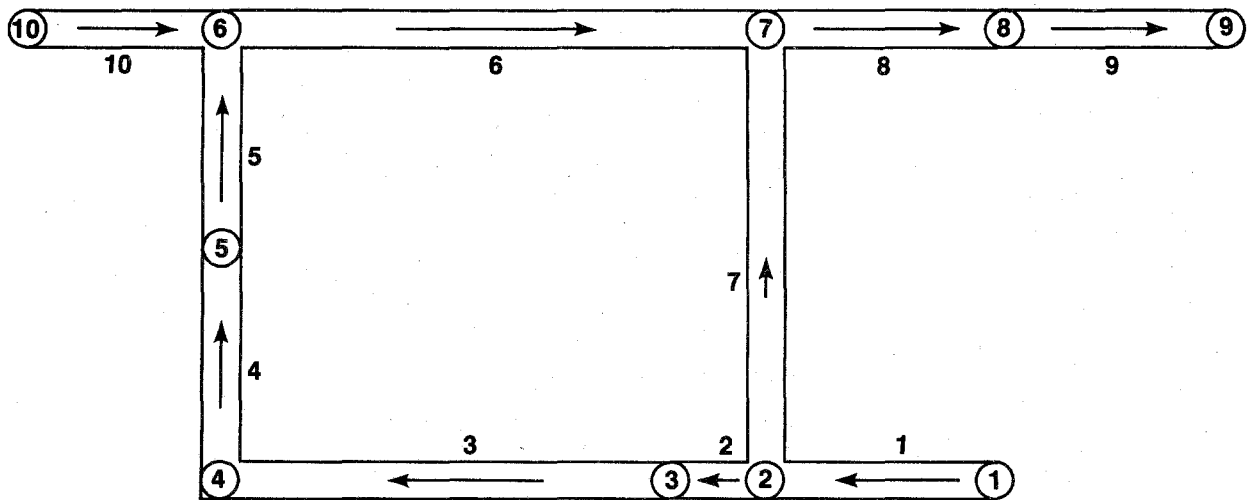
. . . for particles beginning a time step as a parent species and ending the time step as a daughter, NEFTRAN calculates the average velocity achieved by weighting species velocities with the average time spent as each species:

$$v_m(1, \dots, \rho) = \frac{1}{\Delta t} \sum_{i=1}^P TS_i v_i . \quad [D-14]$$

D.1.2 Generalized Network for the Undisturbed Case

The generalized flow network shown in Figure D-1 mimics the possible flowpaths described in Section 6.1. Arrows indicate flow direction along each leg, circled numbers are nodes, and uncircled numbers are legs. Legs 1 and 10 are included to establish continuous flow in the network for MB 139 and the Culebra Dolomite.

The path composed of legs 1, 2, and 3 represents flow through MB 139. Leg 2 simulates the grouted seal in the marker bed that underlies the panel seal. Leg 3 simulates the direct path through MB 139 from that seal to the bottom of the shafts. It is assumed that this path underlies only the excavations, not the pillars. Leg 4 simulates the consolidated lower shaft seals from the repository horizon to -200 meters up the shaft, as described in Section 4.9.



TRI-6330-67-0

Figure D-1. Numerical flow-network input for simulation of Cases IA and IB. Node 2 is the boundary between the waste panel and MB 139. Node 3 is the end of the MB 139 seal. Node 4 is the bottom of the shaft; Node 5 is the top of reconsolidated salt in the shaft; and Node 6 is the top of the shaft in the Culebra Dolomite. Nodes 10, 6, 7, 8, and 9 separate portions of Culebra Dolomite with slightly different hydrologic properties. Node 9 is the hypothetical stock well. Nodes 1 and 10 are input nodes in the repository and Culebra Dolomite.

This leg represents the waste shaft, which has the largest diameter of the four shafts. Leg 5 simulates the poorly consolidated upper shaft seal system. Legs 6, 8, and 9 simulate the path through the Culebra Dolomite to the hypothetical stock-well location (Section 5.3). The conductivities used in Legs 6, 8, and 9 for the Culebra Dolomite are the same as those used by LaVenue et al. (1988). Legs 2 through 6, 8, and 9 represent the transport path from the panels through MB 139, shafts, and Culebra Dolomite to the stock well. This path was used for Cases 1A and 1B.

Leg 7 simulates flow directly from the panel to the Culebra Dolomite through the Salado Fm. Another NEFTRAN run is used to calculate transport along this path and then to the stock well along Legs 8 and 9.

Calculations for transport were performed for the path described from Node 2 to Node 9 through Nodes 3 through 8 for both expected and degraded conditions, using data given in Tables D-2, D-3, and D-4. A single NEFTRAN run provides output at one node, not at intermediate nodes. Because arrival times for the least retarded radionuclide were very long, calculations were performed first for transport to the top of the shaft at the Culebra Dolomite (Node 6), second for transport to the top of the lower shaft seal (Node 5), and third for transport to the base of the shaft (Node 4).

D.2 Recommended Radionuclide-Distribution Coefficients for the Repository Seals, Drifts, and Shafts

D.2.1 Introduction

Radionuclide distribution coefficients (K_d) are used in transport codes to calculate the partitioning of radioelements between the ground water and rock. The definition, underlying assumptions, and limitations of the use of K_d 's to estimate radionuclide retardation are reviewed in Section 3.3.4. As discussed there, a K_d value cannot be extrapolated with confidence to physicochemical conditions that differ from those under which the data were obtained. In addition, the use of a K_d to calculate radionuclide partitioning is valid only if chemical equilibrium exists among all aqueous species containing the

Table D-2. Numerical Parameters Input to NEFTRAN for Case IA

| | <u>Permeability (m²)</u> | <u>Porosity</u> | <u>Length of Path (m)</u> | <u>Cross-Sectional Area of Path (m²)</u> |
|---------------------------------------|-------------------------------------|-------------------|---------------------------|---|
| MB 139 Seal
(Leg 2) | 4 x 10 ⁻¹⁹ | 0.03 | 30 | 0.76 |
| MB 139
(Leg 3) | 3 x 10 ⁻⁷ ^a | 1.00 ^a | 366 | 0.76 |
| Lower Shaft
(Leg 4) | 10 ⁻²⁰ | 0.05 | 200 | 29.2 |
| Upper Shaft
(Leg 5) | 10 ⁻¹² | 0.20 | 200 | 29.2 |
| Culebra
(Leg 6) | 5 x 10 ⁻¹⁵ | 0.16 | 430 | 800 |
| Culebra
(Leg 8) | 5 x 10 ⁻¹⁴ | 0.16 | 1030 | 800 |
| Culebra
(Leg 9) | 5 x 10 ⁻¹³ | 0.16 | 3450 | 800 |
| Salado host rock
(Leg 7) | 3 x 10 ⁻²¹ | 0.001 | 400 | 8030 |
| Dispersivity (m) | | 15.2 | | |
| Solubility Limit of Radionuclides [M] | | 10 ⁻⁶ | | |
| Pressure at Repository (Mpa) | | 14.8 | | |
| Pressure at Culebra (Mpa) | | 1.0 | | |

a. An effective hydraulic conductivity was derived for the fractures in MB 139 using $K = b^2 \rho g / 12 \mu$ with b = fracture aperture, ρ = fluid density, and μ = fluid viscosity. A fracture aperture of 2 mm was used, and to be consistent with the treatment of flow through fractures in NEFTRAN a porosity of 1.0 was used.

Table D-3. Numerical Parameters Input to NEFTRAN for Case IB

| | <u>Permeability (m²)</u> | <u>Porosity</u> | <u>Length of Path (m)</u> | <u>Cross-Sectional Area of Path (m²)</u> |
|--|-------------------------------------|------------------|---------------------------|---|
| MB 139 Seal
(Leg 2) | 4 x 10 ⁻¹⁷ | 0.03 | 30 | 0.76 |
| MB 139
(Leg 3) | 3 x 10 ⁻⁷ | 1.00 | 366 | 0.76 |
| Lower Shaft
(Leg 4) | 10 ⁻¹⁸ | 0.05 | 200 | 29.2 |
| Upper Shaft
(Leg 5) | 10 ⁻¹² | 0.20 | 200 | 29.2 |
| Culebra
(Leg 6) | 5 x 10 ⁻¹⁵ | 0.07 | 430 | 800 |
| Culebra
(Leg 8) | 5 x 10 ⁻¹⁴ | 0.07 | 1030 | 800 |
| Culebra
(Leg 9) | 5 x 10 ⁻¹³ | 0.07 | 3450 | 800 |
| <u>Dispersivity (m)</u> | | 15.2 | | |
| <u>Solubility Limit of Radionuclides [M]</u> | | 10 ⁻⁴ | | |
| <u>Pressure at Repository (Mpa)</u> | | 14.8 | | |
| <u>Pressure at Culebra (Mpa)</u> | | 1.0 | | |

Table D-4. Retardation Factors for Use In Cases IA and IB

| Path | Retardation Factor | | Grain Density
Assumed ρ_R
(g/cm ³) |
|--------------------------------|--------------------|--------------------------|---|
| MB 139 Seal | 1.0 | for all
radionuclides | -- |
| MB 139 ^a | 4.7 | Pu, Th | -- |
| | 1.93 | Am | |
| | 1.04 | U, Np, Ra, Pb | |
| Lower Shaft ^b | 5.16 | Pu, Am, Th | 2.19 |
| | 1.42 | Np | |
| | 1.04 | U, Ra, Pb | |
| Upper Shaft ^b | 1.74 | Pu, Am, Th | 1.84 |
| | 1.07 | Np | |
| | 1.007 | U, Ra, Pb | |
| Salado Host Rock ^b | 231.0 | Pu, Am, Th | 2.30 |
| | 24.0 | Np | |
| | 3.3 | U, Ra, Pb | |
| Culebra ^c (Case IA) | 1497.0 | Pu, Th | 2.85 |
| | 2994.0 | Am | |
| | 16.0 | U, Np, Pb, Ra | |
| Culebra ^c (Case IB) | 3787.0 | Pu, Th | 2.85 |
| | 7574.0 | Am | |
| | 39.0 | U, Np, Pb, Ra | |

- a. Using the K_a values of anhydrite in MB 139 of Table D-5. The retardation factor is calculated as $R_a = 1 + aK_a$, where a, the surface-area-to-volume ratio of the parallel fractures, is 10 cm^{-1} .
- b. Using the K_d values of crushed salt of Table D-5. The retardation factor is calculated as $R = 1 + 0.001 \rho_R K_d \phi / (1 - \phi)$.
- c. Using the K_d values of Table E-1.

solute, if reversible linear sorption is the dominant process controlling exchange of the solute between the ground water and the rock, and if transport of the solute by particulates is insignificant.

It is not now possible to test the validity of these assumptions with respect to radioelement transport within the repository seals, drifts, and shafts. In the repository, solution chemistry will be dominated by the composition of Salado brines, leachates from the waste, concrete, and steel drums, and the products of anaerobic microbial degradation. Fluids in contact with the waste will contain high concentrations of salts and unknown amounts of organic sequestering agents and radionuclides. As discussed in Sections 4.5 and 4.6, very large uncertainties exist in the predicted Eh, pH, concentrations of radionuclides and organics, and partial pressure of CO₂. Solutions from the waste panels will be modified by interactions with the solids along transport paths through the drifts and shafts. It is likely that water chemistry will vary both spatially and temporally along potential radionuclide transport paths; therefore, aqueous speciation may vary and the amount of sorption would be expected to deviate considerably from the amount calculated from any single K_d value. The available data do not allow assessment of the degree of equilibria among the aqueous species containing the radionuclides or between the rock and the aqueous radionuclide species under potential release scenarios. Mixing of waters from the Castile Fm. with fluids within the repository could lead to precipitation of some mineral phases and dissolution of others. Both processes will alter the solution chemistry and could provide mechanisms for radionuclide retardation (coprecipitation) or migration (colloid formation or dissolution of previously deposited radionuclides).

The choice of "recommended" K_d values for the transport calculations within the repository required a large number of subjective assumptions that cannot be supported rigorously. The following section recommends and explains the values used here. The conceptual basis for estimating K_d's in simple systems over a wide range of chemical conditions was outlined in Section 3.3.4. The K_d values given below are considered to be realistic in light of available data; however, research in progress may produce results that will invalidate the logic and recommendations presented below.

D.2.2 Estimated K_d Values

This analysis assumes that the important sorbing substrates in the shafts and drifts will be Salado clay present in the crushed salt used to backfill the drifts. If radionuclides are transported within Marker Bed 139 beneath the drifts, then sorption is assumed to occur along fractures in the anhydrite in the marker bed. Within the Salado Fm., no consideration is given to the relatively minor phases such as polyhalite, magnesite, or quartz that are known to be present.

A review of the literature revealed that K_d values are available for only a limited portion of the spectrum of chemical conditions that can be reasonably hypothesized for the repository. In particular, there were very few data for several of the actinides, radium, and lead in contact with anhydrite in the presence of high Mg-brines containing organic ligands. The K_d data that were examined included those for several reference clays in WIPP A and B brines in inorganic systems (Nowak, 1980), similar data on WIPP clay, dolomite, and anhydrite in WIPP brines A and B (Serne et al., 1977; Dosch and Lynch, 1978; Dosch, 1981), and data from experiments using organic leachates from aerobic degradation of WIPP waste in WIPP brine B with Culebra Dolomite (Paine, 1977; Dosch, 1979). Additional K_d values were obtained from a review of data reported by Tien et al. (1983). Table 3-14 summarizes the relevant data and experimental conditions.

The following procedure was used to obtain the recommended K_d values. Initial ranges of values (Table 3-14) were obtained for chemical conditions that encompassed or were similar in some way to those expected in the WIPP repository. Data from parametric studies or theoretical calculations for simple well-constrained systems (Section 3.3.4) were used to estimate the magnitude of the change in the K_d that might be related to differences between the actual experimental conditions and the conditions postulated for the repository. A set of conservative, realistic K_d 's was selected by considering the effects of unfavorable chemical conditions on the K_d 's listed in Table 3-14. As discussed below, it is possible that under some extreme conditions the K_d 's will be close to zero; however, there is evidence that some sorption

will occur for all radionuclides. Therefore, in this report the K_d 's are assumed not to be zero.

The estimated K_d values are listed in Table D-5. For the drifts and seals, the values for clay must be multiplied by a utilization factor of 0.001 for use in a porous-medium transport equation to account for dilution of the clay by crushed salt and the possibility that fluid flow will be diverted away from the clay particles in the reconsolidated salt. The utilization factor for clay in the Salado horizons above the facility is assumed to be 0.01, based solely on the relative proportions of salt and halite. Sorption in the anhydrite beds will probably occur primarily on the faces of fractures. A surface-area-based distribution coefficient, K_a , was calculated for use in a transport equation for fracture-dominated flow. The definitions of the utilization factor for the clay and the surface-based retardation factor (Section 3.3.4) were derived by Neretnieks (1980) and Neretnieks and Rasmuson (1984).

D.2.3 Extrapolation of Experimental Data to Obtain Recommended K_d Values

In general, the recommended K_d values in Table D-5 are lower than those listed in Table 3-14. Many of the K_d 's reported in the literature for the actinides are in the range of 10,000 to 100,000 mL/g. The significance of such high values is discounted. The K_d 's were calculated solely from the loss of radioactivity from solution; small errors in the measurement of a trace amount of radionuclide remaining in solution could lead to large errors in the calculated K_d . Review of experimental procedures used to obtain the values suggests that the results could be compromised by unrecognized precipitation; this error would lead to high K_d 's that would overestimate the extent of sorption. This kind of error could be especially important for data from WIPP Brines A and B. Preliminary saturation-index calculations by Melfi (1985) indicated that Brine A may be supersaturated with respect to calcite (CaCO_3) and that Brine B may be supersaturated with respect to gypsum ($\text{CaSO}_4 \cdot 2\text{H}_2\text{O}$). These calculations are not conclusive, however, because of possible inconsistencies in the thermodynamic data base used by Melfi. In addition, the extent to which actinides or fission products can be incorporated into the crystal structures of either of these minerals has not been determined.

Table D-5. Recommended K_d Values for Modeling Radionuclide Transport in Drifts, Seals, and Marker Bed 139

| <u>Substrate</u> | <u>Pu</u> | <u>Am</u> | <u>Cm</u> | <u>U</u> | <u>Np</u> | <u>Ra</u> | <u>Th</u> |
|--|-------------------|-----------|-----------|----------|-------------------|-----------|-----------------------|
| Clay ¹ in
Crushed Salt
and Salado
(mL/g) | 100 | 100 | 100 | 1 | (10) ² | (1) | (100) |
| Anhydrite in
MB 139
(mL/g) | 100 | 25 | 25 | (1) | (1) | (1) | (100) |
| Anhydrite in
MB 139
(K_a^3 in mL/m ²) | 3.7×10^3 | 925 | (925) | (37) | (37) | (37) | (3.7×10^3) |

1. The value given is for pure clay. The effective K_d of interstitial clay in a crushed salt porous medium is assumed to be $0.001 \times K_d$ as discussed in the text.
2. All values in parentheses are estimated from K_d 's from similar homologous elements.
3. Calculated assuming original K_d data were from a monodisperse suspension with particle density $\rho = 3 \times 10^6$ g/m³; radius $r = 3.7 \times 10^{-5}$ m and surface area $SA = 2.7 \times 10^{-2}$ m²/g as $K_a = K_d(\text{mL/g})/SA (\text{m}^2/\text{g}) = K_d r \rho/3$. Values are converted to units of cm by multiplying by a factor of 10^{-4} m²/cm².

Estimation of K_d 's is limited by the uncertainties in the course of the future chemical evolution of the repository and requires consideration of large ranges of pH, Eh, organic content, and carbonate content of the ground waters. These possible variations in solution chemistry could result in order-of-magnitude changes of the K_d 's from the values obtained in the experimental studies listed in Table 3-14. Evaluation of the magnitude of these changes requires several assumptions about the nature of sorption reactions occurring on the substrates.

This report assumes that only the clay, anhydrite, and salt components of the Salado Fm. will come into contact with the radionuclides during transport.

None of the elements are considered to sorb onto the halite ($K_d = 0$). The sorption of trace metals onto salt-like minerals such as anhydrite is poorly understood; the paucity of relevant data precludes extrapolation of sorption behavior to physicochemical conditions that differ from those specifically examined in the experimental studies (Table 3-14). As discussed below, some qualitative extrapolations are made based solely on the predicted aqueous speciation of the radionuclides.

Qualitative predictions about the surface properties of the clays in the Salado Fm. over a wide range of physicochemical conditions are possible. The Salado Fm. contains a complex mixture of clay minerals, including a mixed chlorite-saponite phase, illite, chlorite, and serpentine (Bodine, 1978; Krumhansl, 1988). As discussed in Section 3.3.4, this report assumes that the actinides could be adsorbed onto mixed-layer clays by both fixed-charge ion-exchange sites and surface hydroxyl groups (Kent et al., 1988). Section 3.3.4 uses available data and calculations from studies of simple, well-constrained iron oxyhydroxide systems to evaluate the possible variations in the extent of actinide sorption onto the hydrolysis sites as a result of changes in carbonate complexation, ionic strength, competition for sorption sites by other cations such as Mg^{+2} and Ca^{+2} , and organic complexation. Figures 3-20 to 3-23 show the results of calculations relevant to clays within the repository and the Culebra Dolomite.

In Section 3.3.4, the effect of competition among radionuclides and cations such as Mg^{+2} for the fixed-charge sites was evaluated from data describing the sorption behavior of montmorillonite. Figure 3-24 shows the partitioning of uranium between solution and montmorillonite under oxidizing conditions in systems containing cations that compete with the actinides for the sorption sites on the clay. The figure shows that uranium will displace Na^+ and K^+ from sorption sites but that Ca^{+2} and Mg^{+2} are preferentially sorbed instead of uranium onto the montmorillonite. Thus, uranium and the other actinides may not sorb strongly onto the fixed-charge sites of Salado clays in the calcium- and magnesium-rich solutions that could be present in the repository.

The redox speciation of radioelements in the repository after closure is not known. As discussed in other sections of this report, microbial degradation of organic material contained in the waste will probably consume all available oxygen, and anoxic conditions may prevail. Reduction of the radioelements to lower oxidation states is likely under these conditions; however, the rates of the redox reactions are not known, and the speciation at any given time cannot be predicted with the available data. The K_d values in Table 3-14 were obtained under oxic conditions. The sorption behavior of the radioelements under anoxic conditions cannot be extrapolated with these data. Some field studies of radionuclide partitioning between soils, solutions, and organic matter suggest that the K_d 's of the radioelements in their lower oxidation states will be lower than those of the oxidized forms (Choppin and Allard, 1985).

D.2.4 Explanation of Recommended K_d Values

The data for simple systems discussed above suggest that the amount of sorption of actinides onto either clays or sulfates present in the repository could be several orders of magnitude less than that suggested by the K_d data listed in Table 3-14. The reasons for the K_d values chosen for each element are given below.

Plutonium. K_d values for plutonium are decreased by 2 to 3 orders of magnitude from the values in Table 3-14 because of the potential effect of carbonate complexation.

Americium. K_d values for americium are decreased by factors of 3 to 1000 from values listed in the table because of the potential effects of organic complexation. For example, Swanson (1986) found that moderate concentrations (4×10^{-6} to 10^{-4} M) of EDTA significantly decreased Am sorption onto kaolinite and montmorillonite. The magnitude of this effect was a function of the pH and concentrations of EDTA, Ca, Mg, and Fe in solution.

Curium. K_d values for curium were decreased by factors of 3 to 100 from the values listed in Table 3-14, based on the assumption of behavior similar to Am.

Uranium and Neptunium. In general, low K_d 's for uranium and thorium have been measured in waters relevant to the WIPP repository. As shown in Figures 3-22 through 3-24, the K_d of uranium depends strongly on the pH, concentration of competing ions, and the extent of complexation by carbonate and organic ligands. A low value ($K_d = 1$) has been assumed in this report to account for these effects. Theoretical calculations (Leckie, 1989) and arguments based on similarities in speciation, ionic radii, and valence (Chapman and Smellie, 1986) suggest that the behavior of neptunium will be similar to that of uranium.

Thorium. There are very few data for thorium under conditions relevant to the WIPP. Thorium K_d values were estimated from data for plutonium, a reasonable homolog element (Krauskopf, 1986). Data describing sorption of Th onto kaolinite (Riese, 1982) suggest that high concentrations of Ca and Mg will prevent significant amounts of sorption onto clays in the repository. Stability constants for organo-thorium complexes suggest that organic complexation could be important in the repository and may inhibit sorption (Langmuir and Herman, 1980).

Radium and Lead. There are very few sorption data for radium and lead under conditions relevant to the WIPP. K_d values in Table D-5 were estimated by assuming homologous Ra-Pb behavior (cf. Tien et al., 1983). Data from Riese (1982) suggest that Ra will sorb onto clays but that high concentrations of Ca and Mg will inhibit sorption. Langmuir and Riese (1985) presented theoretical and empirical arguments that suggest that Ra will be coprecipitated in calcite, gypsum, and anhydrite in solutions close to saturation with respect to these minerals.

D.2.5 Conclusion

The extent of sorption of radioelements onto clays in the backfill of the repository, the anhydrite of Marker Bed 139, or the Salado Fm. cannot now be predicted with certainty because of uncertainties in the expected chemical environment of the rooms and the lack of relevant empirical K_d and thermodynamic data. A set of K_d values has been recommended based on a review of K_d data obtained in systems that are similar in some way to the conditions

assumed for the WIPP repository and from insights gained from theoretical calculations of radionuclide behavior in simple, well-constrained systems. Many of the available K_d 's are large ($>10,000$) and have been interpreted as indicating significant sorption under specific experimental conditions. Precipitation of evaporite minerals from the solutions (WIPP brines A and B) may have occurred, however, leading to spuriously high K_d values. Moreover, within the range of solution compositions that are possible for the repository after closure, theoretical calculations suggest that there are conditions under which the K_d for any of the elements considered here could drop to very low values (<1). The recommended K_d values represent a compromise between empirical data showing that sorption will occur under some physicochemical conditions relevant to the WIPP repository and theoretical calculations suggesting that many factors can decrease the extent of sorption significantly under other conditions that are possible for the WIPP.

APPENDIX E. NUMERICAL APPROACH TO CALCULATIONS DESCRIBING RADIONUCLIDE
TRANSPORT AFTER HUMAN INTRUSION

E.1 Numerical Implementation of Post-Plugging Analysis

E.1.1 Modeling Approach

The analysis of Case II uses the SWIFT II computer code to simulate the release of fluid from a hypothetical brine reservoir connected by a borehole to the Culebra Dolomite, to simulate the flow field within the Culebra, and to simulate transport of contaminants in the fractured Culebra Dolomite. SWIFT II and the code modifications required to simulate a brine-reservoir breach are described in Sections E.1.2 and E.1.3. LaVenue et al. (1988) described in detail the most recent ground-water flow model of the Culebra Dolomite, which incorporates field data collected until about October 1987. Reeves et al. (1987) discussed the use of double-porosity algorithms to simulate transport in the fractured Culebra Dolomite. Model-input parameters and model results for Case II are presented in Appendix E.2 and Chapter 7.0.

E.1.2 General Description of SWIFT II

SWIFT II (Sandia Waste Isolation, Flow and Transport Code) is a fully transient, three-dimensional code that solves the coupled equations for single-phase flow and transport in porous and fractured geologic media. The processes simulated include fluid flow, heat transport, dominant-species miscible displacement (brine), and trace-species miscible displacement (radionuclide chains).

The first three processes are coupled by fluid density and viscosity. Together they provide the velocity field required to model the fourth process. SWIFT II, a code that has been continuously developed and maintained since 1975, is supported by comprehensive documentation and extensive testing. Reeves et al. (1986a, 1986b) discussed the theory, implementation, and data input of the code and the basic limitations of the method. Using a total of 36 different problems, Finley and Reeves (1981), Ward et al. (1984), Reeves et

al. (1986c), and SKI (1984) compared model results with analytic solutions, field data, and results of other codes. SWIFT II is one of the most extensively verified codes for analysis of radioactive-waste transport in ground water in current use.

E.1.3 Implementation of Brine-Reservoir and Borehole Submodels

E.1.3.1 Model Configuration. Figure E-1 illustrates a brine-reservoir breach. It shows a borehole passing through the repository and connecting a brine reservoir to the Culebra Dolomite. LaVenue et al. (1988) described in detail the most recent model of the Culebra Dolomite. These authors used the SWIFT II code to calibrate a steady-state flow field. The analysis of Case II uses the transmissivity distribution from the Culebra model of LaVenue et al. (1988), considering the pressurized brine reservoir analytically as a source term.

When described in terms of its initial and hydraulic properties, the brine-reservoir submodel assumes the following form:

$$Q = A_Q + B_Q \delta p \quad (E-1)$$

where δp is the change in pressure within the Culebra source block m (i.e., the block where the breach well penetrates the Culebra Dolomite) during time-step Δt . Quantity Q is the volumetric rate of water injection into block m during time-step Δt . A_Q and B_Q are flow-rate parameters defined by Equations E-25 and E-26. Q , like A_Q and B_Q , is assumed to be constant during Δt , but varies as a function of time step to reflect depletion of the brine reservoir.

The development of the brine-reservoir submodel is described below. First, influence functions P_I and W_I are introduced to characterize pressure and flow rate, respectively, at the borehole-reservoir interface. Second, brine-reservoir response is described in terms of P_I and its time derivative P_I' . Finally, the Culebra Dolomite and the reservoir are coupled to obtain a Culebra source term of the form specified in Equation E-1.

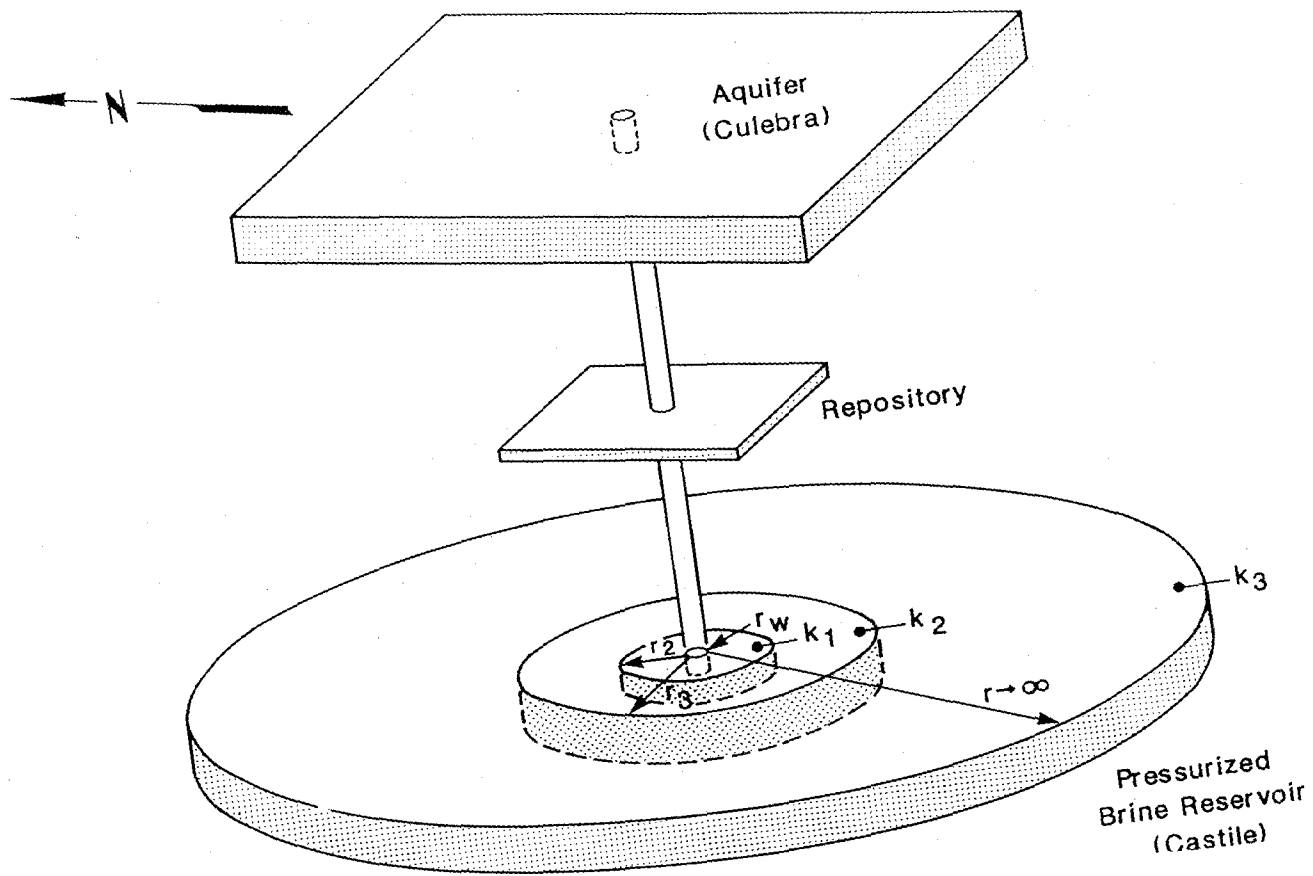


Figure E-1. Schematic diagram of the brine-reservoir-breach release simulation.

E.1.3.2 Influence Functions. Van Everdingen and Hurst (1949) identified two basic influence functions that may be used to determine pressure drawdown and flow rate at a borehole-reservoir interface. One, denoted W_I , corresponds to a constant-pressure condition at $r = r_w$ (Figure E-1). It is called the terminal-pressure influence function. The other, P_I , corresponds to a constant-rate condition at the radius of the well ($r = r_w$). It is called the terminal-rate influence function. Functions P_I and W_I provide basic functions that may be superimposed to obtain general solutions.

Both P_I and W_I are derived from a dimensionless flow equation assumed to have the cylindrically symmetric form

$$\frac{1}{r_D} \frac{\partial}{\partial r_D} \left(k_D r_D \frac{\partial \Delta p}{\partial r_D} \right) = \frac{\partial \Delta p}{\partial t_D} \quad (E-2)$$

where Δp is the pressure drawdown.

For well radius r_w , porosity ϕ , total compressibility c , viscosity μ , and reference permeability k_0 , the dimensionless quantities of Equation E-2 are defined as follows:

$$r_D = r/r_w, \quad t_D = t/t_w, \quad t_w = \phi c r_w^2 / k_0, \quad \text{and } k_D = k/k. \quad (E-3)$$

For a homogeneous system, the reference permeability k_0 is set equal to k . This yields $k_D = 1$, recovering the form of the flow equation as expressed by Van Everdingen and Hurst (1949).

The initial condition assumes a state of equilibrium in the borehole and the reservoir:

$$\Delta p(r_D, t_D = 0) = 0. \quad (E-4)$$

The boundary condition at the wellbore-reservoir interface distinguishes the two influence functions. For P_I ,

$$\frac{\partial \Delta p}{\partial r_D} (r_D = 1, t_D) = -1 . \quad (E-5)$$

For W_I ,

$$\Delta p(r_D = 1, t_D) = 1 . \quad (E-6)$$

For P_I , the dimensionless solution Δp_D of Equation E-2, evaluated at the wellbore interface, yields the constant-rate influence function directly:

$$P_I = \Delta p(r_D = 1, t_D) . \quad (E-7)$$

For W_I , the dimensionless flow rate at the wellbore interface is given by $\partial \Delta p_D / \partial r_D (r_D=1, t_D)$. Integration over dimensionless time yields the constant-pressure influence function

$$W_I = \int_0^{t_D} \left[\frac{\partial \Delta p}{\partial r_D} \right]_{r_D=1} dt_D . \quad (E-8)$$

Assuming homogeneity, Van Everdingen and Hurst (1949) derived analytic expressions for P_I and W_I . Frick and Taylor (1962) tabulated these functions. As a default option, SWIFT II offers an internally specified set of Frick-and-Taylor tables for a homogeneous, infinite system ($1 \leq r_D \leq \infty$). Observations indicate, however, that brine reservoirs at the WIPP site have heterogeneous hydraulic properties. As discussed in Section 3.4.3, WIPP-12 observations indicate that a region with a relatively high permeability k_1 , located near the well, serves as a collection area for a larger region possessing a lower permeability k_2 (Figure E-1).

Section 3.4.3 interprets the WIPP-12 brine-reservoir test data to indicate two regions with permeabilities k_1 and k_2 surrounding the borehole. For conservatism, a third region with a very low permeability k_3 is assumed to provide an effectively infinite source of pressurized brine (Figure E-1). Its distance $r > r_3$ is sufficiently great, however, and its permeability k_3 , equal to the permeability of the intact rock, sufficiently small that it does not participate within the time scale of observations from the WIPP-12 field

testing. For the three zones of the brine reservoir, the dimensionless permeability function assumes the form

$$k_D(r_D) = \begin{cases} k_1/k_0 & 1 \leq r_D \leq r_{D2} \\ k_2/k_0 & r_{D2} < r_D \leq r_{D3} \\ k_3/k_0 & r_D > r_{D3} \end{cases} \quad (E-9)$$

Radii r_w , r_2 , and r_3 are specified in Figure E-1. Equation E-9 uses their dimensionless counterparts $r_D = r/r_w$, $r_{D2} = r_2/r_w$, and $r_{D3} = r_3/r_w$. For this heterogeneous system, the reference permeability has been arbitrarily set to $k_0 = k_1$. Assuming heterogeneous properties makes analytic analysis somewhat difficult. Consequently, this study uses the numerical algorithms of the GTFM model (Pickens et al., 1987) to generate the desired influence functions. A table of these functions provides input for SWIFT II.

E.1.3.3 Generalized Brine-Reservoir Response. Influence function W_I represents the total flow in response to a pressure drop of unity. If the pressure drop at the wellbore $\Delta p_w = \Delta p_w(r_D=1)$ is constant, but differs from unity, then the flow rate is $\Delta p_w W_I$. If Δp_w varies as a function of time, then the principle of superposition (Carslaw and Jaeger, 1959, pp. 30-32) yields the cumulative fluid flow:

$$W_D(t_D) = \int_0^{t_D} \Delta p_w'(\lambda) W_I(t_D - \lambda) d\lambda \quad (E-10)$$

where Δp_w denotes pressure drop at the wellbore-reservoir interface and the prime denotes differentiation with respect to the argument. Multiplication by $W_w = 2\pi\Delta z\phi cr_w^2$ converts W_D to a dimensioned quantity.

If it were used directly in a numerical algorithm, Equation E-10 would require frequent integrations from zero to the current time t_D , an inconvenience for the numerical algorithm. Recognizing this deficiency, Carter and Tracy (1960) approximated Equation E-10 with a form better suited for numerical computations. They assumed a linear variation within a given time step $t_D^n \leq t_D \leq t_D^{n+1}$:

$$W_D^{n+1} = W_D^n + Q_D(t_D - t_D^n) \quad (E-11)$$

where a superscript denotes the time level and Q_D denotes an average rate of flow during the time step. Multiplication by $Q_w = 2\pi\Delta z(k/\mu)$ converts Q_D to a dimensioned quantity.

Carter and Tracy (1960) evaluated the flow rate Q_D by equating the right-hand sides of Equations E-10 and E-11. Treating quantities evaluated at time level n as constants, they used a step-function Laplace transform with respect to t_D to obtain

$$s\overline{\Delta p_w} \overline{W_I} = [(W_D^n - Q_D t_D^n)/s] + [Q_D/s^2] \quad (E-12)$$

where s is the Laplace-transform variable, and the bars denote transformed quantities. With Equation E-12, the analysis of Carter and Tracy becomes approximate. The identity $1/s^2 = s\overline{P_I} \overline{W_I}$ (Van Everdingen and Hurst, 1949, p. 316) allows one to solve for $\overline{\Delta p_w}$. Performing an inverse Laplace transform and solving the resulting equation for Q_D yields

$$Q_D = (\Delta p_w^{n+1} - W_D^n P_I^{n+1}) / (P_I^{n+1} - t_D^n P_I^{n+1}) \quad (E-13)$$

Equation E-13 is close to the desired form of Equation E-1. It gives flow rate as a function of the pressure drop Δp_w at the wellbore. Injection volume W may be accumulated numerically as a function of time, and P_I and P_I' may be evaluated from tables. Equation E-13, however, applies only to the brine reservoir; a description of the hydraulic coupling to the Culebra Dolomite is lacking. This coupling is presented below.

E.1.3.4 Reservoir-Borehole-Aquifer Coupling. Introducing dimensioned quantities W and Q for the volume and the rate injected into the Culebra Dolomite, and a subscript b when necessary to distinguish brine-reservoir quantities, Equation E-13 may be rewritten in the form

$$Q = A_I + B_I \Delta p_{bw} \quad (E-14)$$

where

$$A_I = -(Q_w/W_w)W_I^{n_P' n+1}/(P_I^{n+1} - t_{D I}^{n_P' n+1}) \quad (E-15)$$

and

$$B_I = Q_w/(P_I^{n+1} - t_{D I}^{n_P' n+1}) \quad (E-16)$$

Equations E-14 to E-16 describe the pressure response of the brine reservoir.

To characterize the borehole, the analysis assumes a finite transmissibility T_w arising from plugs or rubble. Borehole flow is governed by the equilibrium condition

$$Q = T_w(p_{bw} - p_w - \rho_s g \Delta h) \quad (E-17)$$

Saturated brine of density ρ_s is assumed to occupy the wellbore with a vertical distance Δh separating the centers of the Culebra Dolomite and brine reservoir.

Defining the static pressure difference $\Delta p_o = p_{bo} - \rho_s g \Delta h - p_o$, Equation E-17 may be written in terms of the pressure drops of brine reservoir Δp_{bw} and aquifer Δp_w :

$$Q = T_w(\Delta p_w - \Delta p_{bw} - \Delta p_o) \quad (E-18)$$

For the pressurized release to be considered here, Δp_w is inherently negative and Δp_{bw} inherently positive.

To characterize the hydraulic coupling to the Culebra Dolomite, the analysis focuses on the grid-block m assumed to be penetrated by the wellbore. The pressure p of this grid block, as determined by the finite-difference method, represents an average over the pore volume V of the block. It is influenced by several factors, including the pore volume of the block, its transmissive connections to neighboring blocks, and the hydraulic connection between wellbore and grid block. To characterize the latter, the analysis assumes the following relation:

$$Q = M(p_w - p) . \quad (E-19)$$

This equation indicates a proportionality between the flow rate and pressure drop between the wellbore and the grid-block center.

Mobility M is given by the equation

$$M = 2\pi(\mu_o/\mu)(K/\rho_o g)\Delta z/\ln(r_1/r_w) \quad (E-20)$$

where K is the hydraulic conductivity of the grid block and Δz is the thickness of the Culebra Dolomite. Parameters ρ_o and μ_o are reference values of density and viscosity, used to convert hydraulic conductivity to permeability. Quantities ρ and μ vary as functions of the average salinity of the fluid in the grid block.

The distance r_1 of Equation E-20 refers to the Culebra Dolomite and should not be confused with a radius (cf. Equation E-9), used to characterize the permeability distribution of the brine reservoir. After defining Δr as a pseudo-grid-block radius, $\Delta r = (\Delta x \Delta y / \pi)^{1/2}$, and after determining the average pressure of the cone of influence in the Culebra Dolomite over the range $r_w \leq r \leq \Delta r$, Reeves et al. (1986a, pp. 26-27) defined r_1 as the radius at which the pressure of the cone of influence equals the average pressure:

$$\ln(r_1/r_w) = r_w(1 + \Delta r/r_w)[\ln(\Delta r/r_w) - 1]/(\Delta r - r_w). \quad (E-21)$$

Interpreting Equation E-19 in terms of the pressure drop between the wellbore pressure and the block-averaged pressure, Equations E-20 and E-21 provide a consistent definition of mobility as the hydraulic conductance from the wellbore radius to the radius of the average pressure. Stated in terms of pressure drops below static pressure, Equation E-19 assumes the form

$$Q = M(\Delta p - \Delta p_w) . \quad (E-22)$$

Equations E-14, E-18, and E-22 provide a set of three equations in the three unknowns Δp_w , Δp_{bw} , and Q . Solved simultaneously, they yield the desired relations. For the flow rate injected into the Culebra Dolomite, the relation is

$$Q = [A_I + B_I(\Delta p_o + \Delta p)]T/(T + B_I) . \quad (E-23)$$

Quantity T represents the net transmissibility due to borehole-aquifer coupling:

$$T^{-1} = T_w^{-1} + M^{-1} . \quad (E-24)$$

The well skin of the brine reservoir is assumed to be of a sufficiently high permeability relative to T_w and M that it may be neglected in Equation E-24.

Expressed in terms of the incremental change δp for time-step n, the pressure drop becomes $\Delta p = \Delta p^n - \delta p$, and the flow rate Q can be expressed in the form of Equation E-1, where

$$A_Q = [A_I + B_I(\Delta p_o + \Delta p^n)]T/(T + B_I) \quad (E-25)$$

and

$$B_Q = -TB_I/(T + B_I) . \quad (E-26)$$

Equations E-1, E-25, and E-26 represent the desired result. For grid-block m and time-step n, SWIFT II determines δp through an implicit solution for the flow field in the Culebra Dolomite. It determines flow rate Q from Equation E-1.

E.1.4 Assumptions About Repository Interactions and Source Term

The physical and radiological characteristics of the repository source term are discussed in Chapter 4.0. The implementation of this source term in the context of Case II is described below, and Case II variations in the source are summarized in Table 1-2.

For Case IIA, the hydraulic conductivity of the waste panel (1×10^{-6} m/s) (Table 4-7) is assumed to be high enough to allow circulation of all Castile brine through the waste prior to continuing up the borehole. This circulation is assumed to be limited to a single waste panel, which

contains seven rooms and two long access drifts that are filled with waste and backfill. During this circulation, the brine is assumed to dissolve waste to the solubility limit of 1×10^{-6} molar for the radionuclide constituents and of 116 mg/L for stable lead. Brine inflow from the Salado Fm. provides a second, smaller source of fluid passing through the repository and carrying dissolved waste up the borehole. The long-term brine-inflow rate has been conservatively estimated to be $1.3 \text{ m}^3/\text{yr}$ for a single waste panel (Section 4.3.2).

For Case IIB, waste precompaction is expected to reduce the hydraulic conductivity of the waste panel to $1 \times 10^{-11} \text{ m/s}$ (Section 4.11 and Table 4-10). The assumed hydrologic impact of the reduced panel permeability is that brine from the Castile Fm. no longer passes through the waste and that the only source of contaminated fluid entering the borehole is brine from the Salado Fm. Case IIB assumes the same brine-inflow rate to the borehole that was used in Case IIA ($1.3 \text{ m}^3/\text{yr}$). This assumption may be overly conservative for Case IIB, because the reduced hydraulic conductivity of the waste panel should also reduce the brine-inflow rate to the borehole. The magnitude of the reduction has not been analyzed. The Salado brine in Case IIB is assumed to dissolve waste up to the specified solubility limits or until all mass for a given waste constituent is dissolved. The specified solubility limits for Case IIB are 1×10^{-4} molar for radionuclides and 116 mg/L for stable lead (Table E-1). Case IIB also assumes degraded geosphere transport.

Case IIC assumes a combination of degraded geosphere transport and increased radionuclide solubility, without waste precompaction. Part of the degraded geosphere transport is an increase in borehole permeability from $1 \times 10^{-12} \text{ m}^2$ in Case IIA to $1 \times 10^{-11} \text{ m}^2$ in Cases IIB and IIC (Table E-2 and Appendix C). This increase in borehole permeability causes a corresponding increase in flow from the Castile brine reservoir. In Case IIB, brine from the Castile Fm. does not pass through the waste; in Case IIC, all Castile brine is assumed to pass through the waste panel prior to continuing up the borehole. Like Cases IIA and IIB, Case IIC assumes that brine from the Salado Fm. also passes through the waste at a rate of $1.3 \text{ m}^3/\text{yr}$. In Case IIC, brine passing through the waste is assumed to dissolve waste up to the specified solubility limits or until all mass for a given waste constituent is

Table E-1. Specifications for Repository Parameters Used in Case II Simulations

| <u>Parameter</u> | <u>Symbol</u> | <u>Base Case</u> | <u>Units</u> |
|--|---------------|-----------------------|--------------|
| Soluble radionuclide concentration for each decay-chain member i | | | |
| - Cases IIA and IID | C_s | 1×10^{-6} | molar |
| | C_s | 2.4×10^{-7} | kg/kg |
| - Cases IIB and IIC | C_s | 1×10^{-4} | molar |
| | C_s | 2.4×10^{-5} | kg/kg |
| Soluble stable-Pb concentration | | | |
| - in repository | C_s | 1.16×10^2 | mg/L |
| | C_s | 1.16×10^{-4} | kg/kg |
| - in Culebra | C_s | 5.4×10^1 | mg/L |
| | C_s | 5.4×10^{-5} | kg/kg |
| Mass in initial waste inventory | M_i | reported in Table E-4 | g |
| Mass of waste in contact with circulating fluids after borehole is plugged | - | $M_i/8$ | g |
| Fluid loading from repository to the borehole (q) | | | |
| - in Cases IIA, IIB, and IIC | | 1.3 | m^3/yr |
| - in Case IID | | 0.1 | m^3/yr |

NOTE: Based on the specified radionuclide solubilities expressed as molarity, solubility values expressed as kg/kg have about a 6% range. Because of the large uncertainty in molarity values, a single solubility value for all radionuclides was used in numerical simulations.

Table E-2. Specifications for Intrusion Borehole for Case II Simulations

| <u>Parameter</u> | <u>Value</u> | <u>Units</u> |
|--|----------------|--------------|
| Borehole UTM location at center | 613324 | m E |
| of southwestern waste panel | 3581146 | m N |
| Altitudes | | |
| - ground surface | 1033 | m |
| - center of Culebra | 825 | m |
| - Rustler-Salado contact | 783 | m |
| - center of waste panel | 381 | m |
| - Salado-Castile contact | 181 | m |
| - center of brine reservoir | 109 | m |
| Drilled diameter | | |
| - in Rustler (oil well) | 0.413 | m |
| (gas well) | 0.457 | m |
| - in Salado and Castile (oil well) | 0.311 | m |
| (gas well) | 0.356 | m |
| Hole diameters used in numerical analysis | | |
| - Cased inside diameter of average hole in Rustler | 0.326 | m |
| - diameter of average borehole in Salado and Castile | 0.334 | m |
| Borehole plugs | | |
| - lengths | 60 | m |
| - locations: (i) above brine reservoir | | |
| (ii) below potash zone | | |
| (iii) below Rustler | | |
| Effective borehole permeability | | |
| - open-borehole period | infinite | |
| - plug in Castile 10-15 | m ² | |
| - plugs in Salado 10-18 | m ² | |
| - for times greater than 150 years | | |
| - Case IIA 10-12 | m ² | |
| - Cases IIB, IIC, and IID 10-11 | m ² | |

dissolved. The specified solubility limits for Cases IIB and IIC are 1×10^{-4} molar for radionuclides and 116 mg/L for stable lead (Table E-1). The higher solubility is used to examine the effects of the uncertainty in radionuclide solubilities (Section 4.2).

Case IID assumes engineered modifications similar to Case IIB, except that in Case IID Salado brine inflow has been scaled to a single room rather than to an entire panel, resulting in an inflow rate of $0.1 \text{ m}^3/\text{yr}$ (Section 4.3.2). As in Case IIB, these modifications are assumed to effectively eliminate the circulation of Castile brine through the waste. Case IID also assumes the same 1×10^{-6} -molar solubility limit used in Case IIA, and assumes the same degraded Culebra transport properties used in Cases IIB and IIC.

The implementation of the repository source term for Case II involves two important additional assumptions. First, the characterization of waste transport solely in the form of dissolved species assumes that colloid formation and transport and particulate transport are insignificant. There is insufficient information available to evaluate the potential importance of these processes. Second, Case II assumes that all waste-generated gas is passively vented from the system. Because this case describes a single borehole penetrating an entire waste panel, the system may behave heterogeneously, with gas produced in a distant part of the panel providing an additional driving force for moving fluid up the borehole. Because of the limitations of the current flow and transport models that have been implemented for WIPP, this process cannot be evaluated quantitatively at this time.

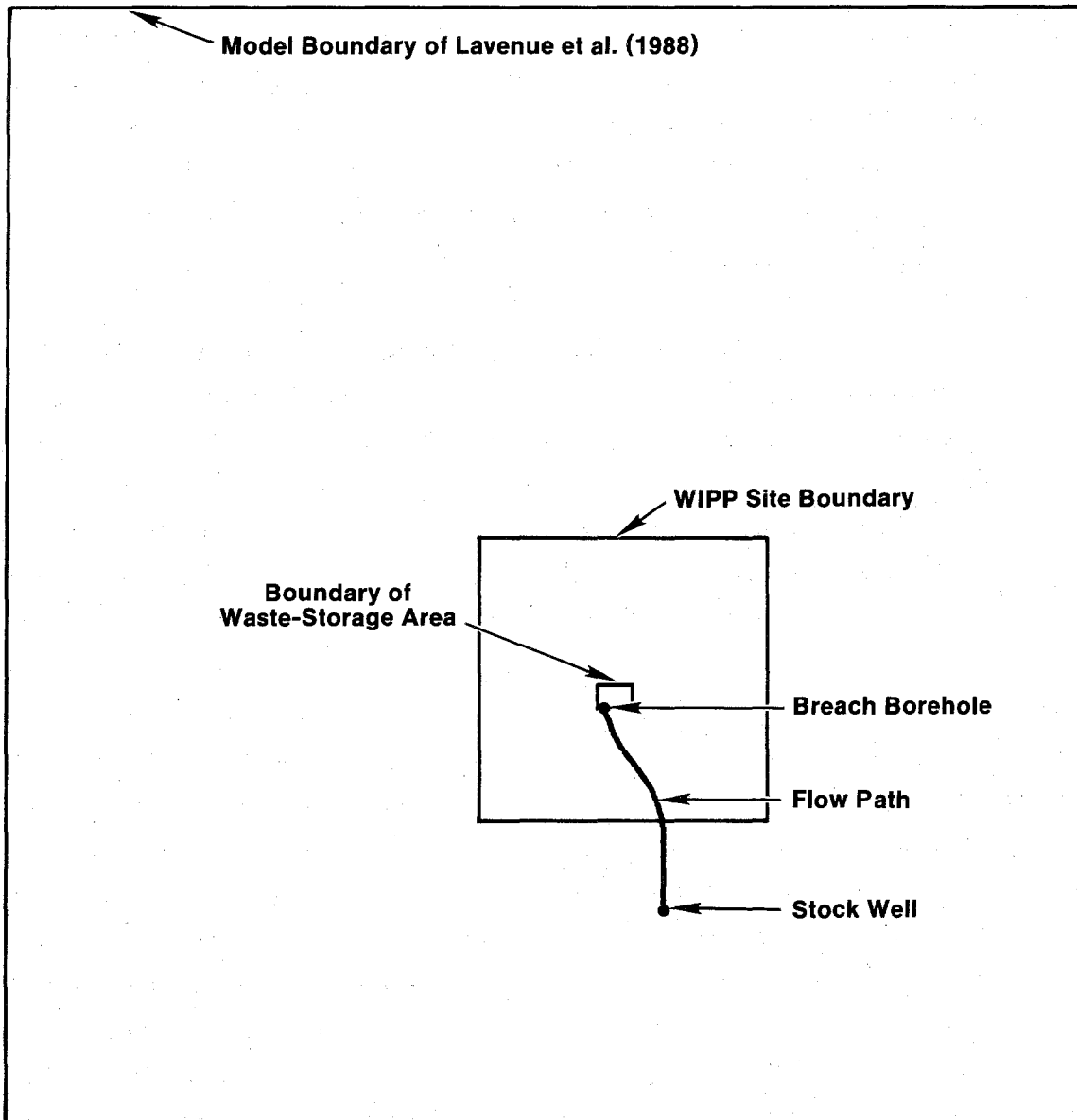
E.1.5 Implementation of Flow and Transport in the Culebra

The solution strategy consists of two distinct steps. The first step, solution of the flow equation, couples brine-reservoir and borehole submodels (Section E.1.3) to the calibrated Culebra ground-water flow model of LaVenue et al. (1988). The objective of this step is to obtain the rate of fluid release from the brine reservoir to the Culebra Dolomite, considering the time-varying degradation of the borehole plugs (Section E.2.2) and the depressurization of the brine reservoir.

The second step, solution of the transport equation, uses the rate of fluid release, the SWIFT II waste-leaching submodel, and the boundary conditions to simulate the release of radionuclide chains and stable Pb to the Culebra Dolomite. Here the objective is to calculate centerline concentrations of the waste plume, and for this purpose, a one-dimensional stream tube is appropriate. The following discussion elaborates on several aspects of the transport approach, including the stream tube, the source block, and lateral dispersion.

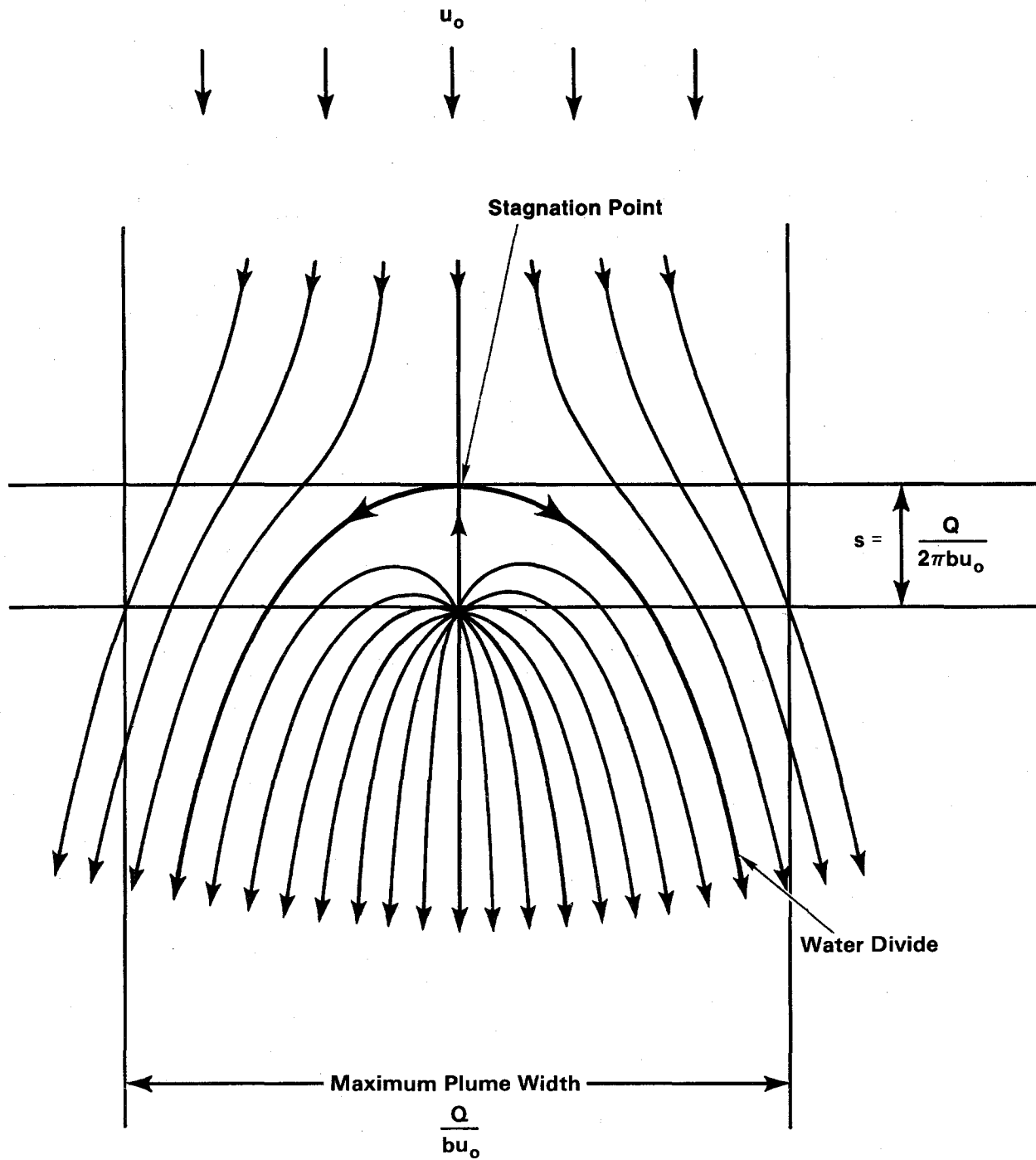
E.1.5.1 Use of a Stream Tube to Calculate Transport. To calculate transport, the numerical model assumes that the steady-state flow field and brine-density distribution of LaVenue et al. (1988) is disturbed insignificantly by the release. To justify this approach, particle travel times in the Culebra Dolomite from the release point to the stock-well location have been calculated for three flow fields, corresponding to steady-state, Case IIA, and Case IIB/IIC/IID conditions. By definition, particle travel times are calculated using the Darcy velocities and a selected porosity. The processes of dispersion, matrix diffusion, and sorption are not included. The calculated particle travel times assumed fracture-dominated transport to assess the maximum transport impact of the transient brine-reservoir perturbations to the undisturbed Culebra flow field. The particle travel time for the undisturbed, steady-state flow simulation differs by about 2% from the Case IIA particle travel time and about 7% from the Case IIB, IIC, and IID travel times. Thus, a release from the breach borehole to the Culebra Dolomite will form a plume, the centerline of which will coincide with the transport pathway illustrated in Figure E-2. The numerical model calculates transport along this centerline using a stream tube. Constructed as described in Appendix B of Reeves et al. (1987), the stream tube yields the same spatial variations in velocity along the transport pathway as the flow model of LaVenue et al. (1988).

Figure E-3 represents an idealized contaminant plume formed as the result of point-source injection at constant rate Q into a unidirectional flow field, which has Darcy velocity u_0 and aquifer thickness b . The stream-tube concept, based on undisturbed flow, can be contrasted with the disturbed flow field (Figure E-3). The latter describes a release of brine-reservoir fluids to the



TRI-6330-71-0

Figure E-2. Model area, WIPP-site boundary, breach-borehole and stock-well locations, and transport pathway.



TRI-6330-68-0

Figure E-3. Schematic illustration of streamlines in a unidirectional flow field perturbed by an injection well (after Bear, 1972).

Culebra Dolomite, focusing on the streamlines near the borehole. These streamlines diverge from the point of release and, at distance, become parallel to the direction of natural ground-water flow.

The streamlines of the injected fluids form a plume of contaminated water of width $2w$ from flow divide to flow divide, as illustrated in Figure E-3 and defined by the relation

$$2w = Q/bu_0 \quad . \quad (E-27)$$

Asymptotically, the flux within the plume equals that of the natural ground-water u_0 . The distance s that separates the points of release and stagnation is defined by the relation

$$s = Q/2\pi bu_0 \quad . \quad (E-28)$$

This distance also provides a measure of the spatial extent of the region in which fluid velocities differ significantly from u_0 . The maximum rate of fluid release Q_{\max} calculated for the borehole and the natural ground-water velocity u_0 calculated by LaVenue et al. (1988) at the point of release (i.e., the borehole) yield stagnation-point distances (Table E-3) for Cases IIA, IIB, IIC, and IID. A comparison of the 7.8- to 69.6-m range of stagnation-point distances at 75 years with the 4840-m distance from the point of release to the stock well indicates that the region of disturbed velocities is small relative to the overall scale for solute transport, thus supporting the assumption of a negligibly disturbed steady-state flow field.

The plume width reaches a maximum when the borehole plugs have fully degraded to the permeability of a rubble-filled borehole (Table E-3). Plume width also varies with distance from the point of release. It decreases monotonically with time from the time of complete degradation of the borehole plugs to 10,000 years (Table E-3). For the numerical calculations, the stream-tube width is chosen to be small relative to plume width. The stream-tube width varies from $\Delta w = 2.87$ m at the point of release to $\Delta w = 0.99$ m at the stock well in order to recreate a velocity distribution that is consistent

Table E-3. Characterization of the Waste Plume Within the Culebra Dolomite from Point of Release to Stock Well

| | <u>Case IIA</u> | <u>Cases IIB and IIC</u> | <u>Case IID</u> |
|---|------------------------------|------------------------------|------------------------------|
| Distance from release to stagnation point | | | |
| - at 75 years | 7.8 m | 69.6 m | 68.8 m |
| - at 10,000 years | 5.6 m | 4.7 m | 3.8 m |
| Theoretical plume width at 75 years | | | |
| - near release point | 49.2 m | 437 m | 432 m |
| - at stock well | 21.1 m | 188 m | 186 m |
| Theoretical plume width at 10,000 years | | | |
| - near release point | 35.2 m | 29.3 m | 24.0 m |
| - at stock well | 15.1 m | 12.5 m | 10.3 m |
| Centerline concentration reduction factor at stock well (Section E.1.5.2) | 37 | 4.2 | 4.3 |
| Brine-reservoir discharge rate [Q] | | | |
| - at 75 years | 9.89 m ³ /yr | 98.1 m ³ /yr | 98.1 m ³ /yr |
| - at 10,000 years | 6.69 m ³ /yr | 1.3 m ³ /yr | 5.35 m ³ /yr |
| Salado brine-inflow rate [q] | 1.3 m ³ /yr | 1.3 m ³ /yr | 0.1 m ³ /yr |
| Source dilution Factor [(Q+q)/q] | | | |
| - at 75 years | * | 76* | 980 |
| - at 10,000 years | * | 5.1* | 55 |
| Darcy velocity in Culebra | | | |
| - at release point | 9.36 x 10 ⁻¹⁰ m/s | 9.36 x 10 ⁻¹⁰ m/s | 9.36 x 10 ⁻¹⁰ m/s |
| - at stock well | 2.18 x 10 ⁻⁹ m/s | 2.18 x 10 ⁻⁹ m/s | 2.18 x 10 ⁻⁹ m/s |

*Source dilution factor only applies to Case IIB and IID

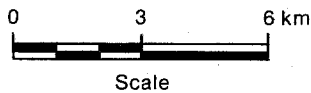
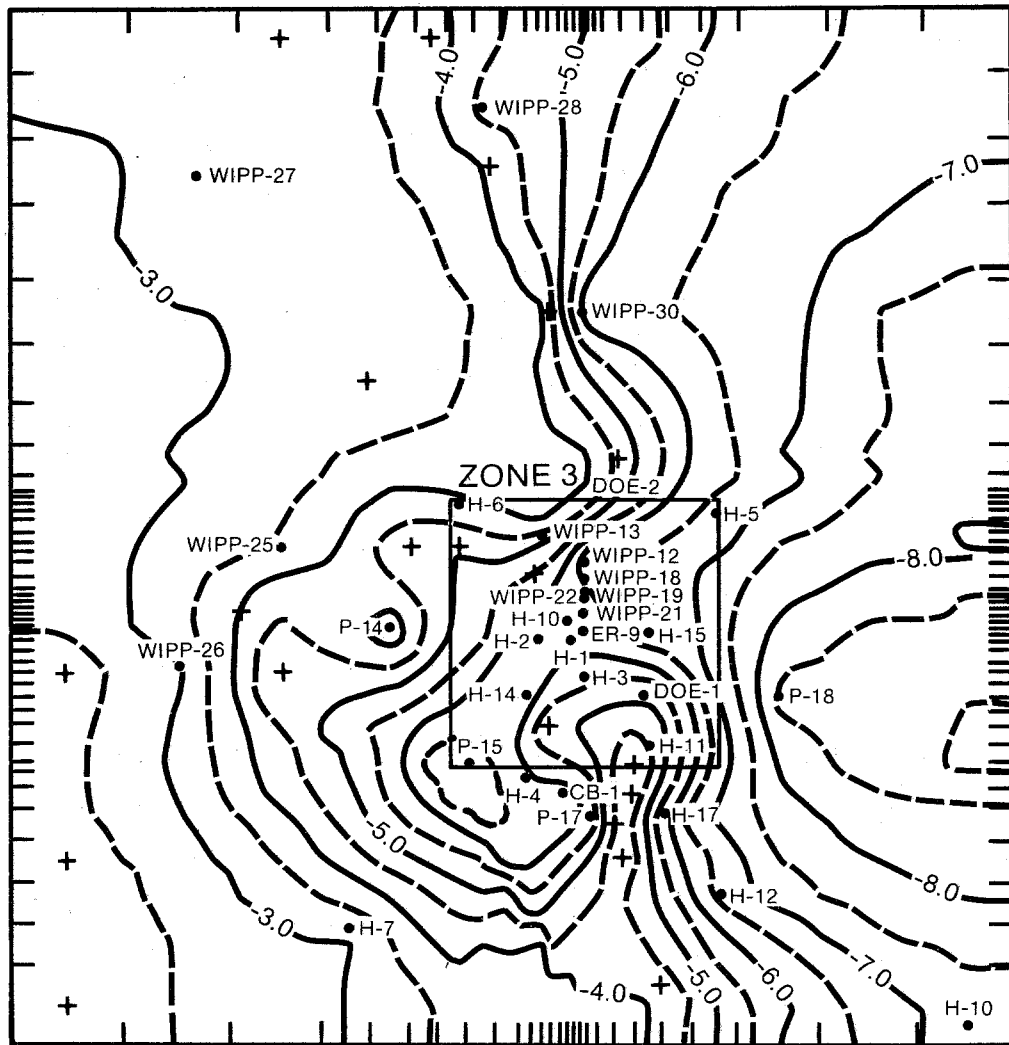
NOTE: All times referenced above correspond to times in the SWIFT II simulation. Because fluid release is negligible while borehole plugs are assumed to be intact, simulations begin at the start of the degradation of the plugs. Time 75 years corresponds to the time at which borehole permeability reaches that of a rubble-filled borehole.

with the velocity distribution along the particle path (Figure E-2) determined using the flow model.

E.1.5.2 Lateral Dispersion. The stream-tube approach used for modeling transport in Case II neglects the effect of lateral dispersion and overestimates solute concentration along the plume centerline. The evaluation of concentration reduction by lateral dispersion entails two main issues. First, can lateral dispersion occur during transport in the Culebra Dolomite? Second, can the concentration reduction by lateral dispersion be rigorously quantified? This section briefly discusses the occurrence of lateral dispersion in the Culebra Dolomite and provides a quantitative evaluation of concentration reduction at the plume centerline by lateral dispersion.

Dispersion in the Culebra. The Culebra Dolomite is an 8-m-thick unit fractured to varying degrees (Section 3.3.1). Where the transmissivity (T) of the Culebra Dolomite is less than $1 \times 10^{-6} \text{ m}^2/\text{s}$, few or no open fractures are observed in cores and the hydraulic response is that of a single-porosity medium (Beauheim, 1987a, 1987b, 1987c). Where transmissivities are between 1×10^{-6} and $1 \times 10^{-4} \text{ m}^2/\text{s}$, open fractures are observed in cores and the hydraulic response is that of a double-porosity medium on the 30-m scale of the 3-hole hydropads. A large portion of the Case II travel path from the breach well to the stock well passes through a zone of relatively high transmissivity ($T > 1 \times 10^{-6} \text{ m}^2/\text{s}$) inferred by model calibration (Haug et al. 1987; LaVenue et al., 1988) (Figure E-4) and by the recent results of the H-11 pumping test (LaVenue et al., 1989). The Culebra Dolomite is known to be fractured at H-3, which is located just south of the waste panels and close to the travel path (Beauheim, 1987a). Therefore, it is likely that much of the contaminant transport in Case II takes place in fractured portions of the Culebra Dolomite.

Lateral dispersion is a form of mixing that results from: velocity variations on the scale of individual flow channels; velocity variations between neighboring flow channels caused by variations in channel size and surface roughness; and solute spreading caused by tortuosity, branching, and interfingering of flow channels. Lateral dispersion in the Culebra Dolomite will be controlled to a large degree by fracture heterogeneity; that is, by



+ PILOT POINT

TRI-6330-75-0

Figure E-4. Calibrated transmissivity distribution from LaVene et al.'s (1988) ground-water flow model of the Culebra Dolomite.

factors such as fracture density, orientation, aperture variation, and degree of fracture interconnection. The detailed characteristics of fracturing along the transport pathway are unknown, but a variety of fracture configurations can be postulated based primarily on the character of fracturing observed in the WIPP shafts (Holt and Powers, 1984, 1986, 1988). Possible fracture configurations may include: irregular fracturing that connects many of the vugs within some stratigraphic units in the Culebra Dolomite; dominantly horizontal fracturing associated with bedding planes, lithologic variations, or unloading stresses; and local brecciation of the lowermost unit within the Culebra. Flow and transport through any of these fracture configurations would be conducive to dispersion processes that would spread a contaminant plume laterally. In spite of the observed fracturing in the WIPP shafts, Culebra transmissivity is low ($T < 1 \times 10^{-6} \text{ m}^2/\text{s}$) at all of the shafts. Therefore, it is likely that the number of fractures or fracture apertures increases southeast of the shafts, consistent with the increase in transmissivity in that direction.

Another approach to lateral dispersion is to postulate what type of fracturing could produce relatively high transmissivity while inhibiting lateral dispersion. The one fracture configuration that might do both would be vertical or near vertical fractures that are widely spaced, relatively isolated, and continuous over horizontal distances on the order of kilometers. No geologic mechanism for producing fractures with these characteristics in the WIPP area is known (Section 3.3.1), and vertical fractures with these characteristics are considered unlikely.

Various fracture configurations conducive to lateral mixing processes during transport are present in the Culebra Dolomite, and geologic mechanisms that could produce a fracture configuration in turn producing relatively high transmissivities while inhibiting lateral dispersion are unknown. Therefore, lateral dispersion is considered a probable transport process in the Culebra Dolomite.

Although lateral dispersion most likely is active in the Culebra Dolomite, field measurement of the lateral dispersivity is extremely difficult, and values for this parameter should be considered highly uncertain. The

magnitude of lateral dispersion is generally considered to be related to longitudinal dispersivity (Section E.2.4.7). Reported ratios of longitudinal to transverse dispersivity range from 5 to 100 (de Marsily, 1986) and 10 to 20 (Bear and Verruijt, 1987).

Concentration Reduction by Lateral Dispersion. The effect of lateral dispersion on concentration along the plume centerline can be approximated using an analytic "reduction factor." Plume-centerline concentrations, when divided by this factor (≥ 1), are corrected for the effects of lateral dispersion.

The theory of Carslaw and Jaeger (1959) can be used to define a reduction factor β by the relation:

$$\beta = 1/\text{erf}[w/2^{1/2}\sigma] \quad (\text{E-29})$$

where w is the plume half width, $\sigma = (2\alpha_T x)^{1/2}$ is the "standard deviation," α_T is the transverse dispersivity, and x is the transport distance measured from the point of release. Because the reduction factor β is a function of transport distance, it cannot be applied to correct for dispersion effects along a concentration profile along the transport pathway. Near the point of release, $\beta \rightarrow 1$, indicating no appreciable reduction in the centerline concentration. At the stock well, assuming a transverse dispersivity of 10 m (10% of the value adopted for longitudinal dispersivity) gives a "standard deviation" of $\sigma = 311$ m.

The reduction factor varies with time, depending on the release rate from the reservoir. The plume has a theoretical width from flow divide to flow divide that reaches a maximum width at early time when the flow rate is also at its maximum value. The use of equation E-29 to calculate the reduction factor as a function of time would overestimate its value at the stock well, because this factor is based on a specific theoretical plume width corresponding to a specific time and ignores the effect of larger actual plume widths at preceding times. To avoid this problem, early-time reduction factors corresponding to maximum theoretical plume widths have been calculated, resulting in values of 37 for Case IIA, 4.2 for Cases IIB and IIC,

and 4.3 for Case IID (Table E-3). The use of these correction factors for reducing the simulated concentrations at the stock well is conservative, because the actual effects of lateral dispersion will be greater as the theoretical plume width decreases and the plume disperses longitudinally. A more accurate estimate of concentrations at the stock well could not be determined without expanding the dual-porosity transport simulation to two dimensions, which was beyond the scope of these calculations.

E.1.5.3 Source-Block Considerations. To minimize the complexities of the transport problem, the transport model uses a relatively simple geometry. It consists of a one-dimensional stream-tube model of the Culebra Dolomite with a single source block to characterize the brine reservoir, repository panel, and borehole. The stream tube's requirement of a constant rate of fluid injection was reconciled with the brine reservoir's time-dependent rate of injection into the Culebra Dolomite by considering two of the effects of a time-varying injection rate upon transport.

First, the time-variable rate of injection could alter contaminant concentrations. For Cases IIA and IIC, contaminant concentrations remain constant (prior to source depletion), because these cases assume that the brine-reservoir fluids have free access to the waste stored in one panel, and that, regardless of the flow rate, concentrations remain fixed at the solubility limit as long as there is sufficient mass present. For some radionuclides, the initial mass present is insufficient to bring concentrations to the solubility limit. In Cases IIB and IID, contaminant concentrations vary with time, because steady-state brine inflow from the Salado Fm. dissolves waste and then mixes with brine-reservoir fluids in the borehole, thereby diluting concentrations to levels consistent with the time-dependent flow from the brine reservoir. In all cases, the source block can accurately reproduce the desired concentrations. For Case IIA, contaminant concentrations remain constant as discussed above. For Cases IIB and IID, time-variable concentrations are preprocessed from known flow components using a stand-alone source model, and the resulting concentrations are imposed as time-dependent boundary conditions. For Case IIC, the SWIFT II waste-leach submodel tracks the depletion of the inventory and maintains solubility limits until total depletion occurs.

The second effect of a time-varying injection rate is that the plume width may be altered. Table E-1 indicates that, between the end of plug degradation and 10,000 years, a significant change occurs near the point of release; however, only the width of the stream tube, Q/bu_0 , varies directly with the rate of injection Q . A specific injection ΔQ into a fixed width Δw does not vary with time. Thus, the centerline stream tube, of width Δw , receives a constant rate of injection, as required.

E.2 Input Parameters for Post-Plugging Analysis

E.2.1 Brine-Reservoir Parameters

A Castile brine reservoir is assumed to extend beneath a portion of the WIPP repository (Section 3.4). Because of the close proximity of the WIPP-12 brine occurrence and the hydrologic data available for it, the parameter values used to characterize a brine reservoir for Case II simulations are based primarily on information from WIPP-12. These parameters include

- P_i initial reservoir pressure,
- b reservoir thickness,
- T reservoir transmissivity,
- ρ_f reservoir fluid density,
- r_b effective distance to the reservoir boundary,
- ϕ reservoir porosity, and
- α reservoir compressibility.

As discussed in Section 3.4.3, interpretations of flow and buildup data from the WIPP-12 brine reservoir indicate that the reservoir is heterogeneous (Popielak et al., 1983). As a result of these interpretations, the hypothetical brine reservoir has been modeled as consisting of three separate parts. In this section, base-case values for each of the parameters listed above are derived from the available data on WIPP-12 (D'Appolonia, 1982, 1983; Popielak et al., 1983) and the interpretation presented in Section 3.4.3. Uncertainty ranges about these base-case values have been derived from the WIPP-12 test interpretations and from limited data on some twelve other wells

that have penetrated brine reservoirs in the Castile Fm. in the vicinity of the WIPP site. Because data on eleven of these brine occurrences are limited, the parameter range is derived in most cases from the WIPP-12 and ERDA-6 data. The parameter ranges are presented for discussion only and are not used in any of the Case II simulations. Table E-4 summarizes the base-case and range values for brine-reservoir parameters.

E.2.1.1 Initial Reservoir Pressure. Two types of data are considered to be best suited for determining initial reservoir pressure. The first is the earliest buildup data recorded after encountering the brine reservoir, and the second is the longest buildup data recorded. A complete summary of the activities performed at WIPP-12 is presented in Table 3-18.

The first buildup period after brine was encountered in WIPP-12 that has a record of pressure versus time is activity 12.03 (D'Appolonia, 1982) (Table 3-18). Prior to this buildup, WIPP-12 had experienced two flow periods separated by a buildup period. The preferred method of analysis of activity WIPP-12.03 is a Horner analysis, which yields a static formation pressure. For this buildup, a Horner buildup analysis could not be performed because a pseudoproducing time that met the criteria set forth in Horner's approximation (Lee, 1982) could not be calculated. Instead, the maximum buildup pressure attained during the 1.43-day buildup was selected, corresponding to a pressure of 1.5 MPa at the surface. This is a good choice for static reservoir pressure, because the buildup was nearly instantaneous and a very limited volume of reservoir fluid had been produced. This pressure corresponds to a reservoir pressure of 12.7 MPa when extrapolated to the center of the brine reservoir at WIPP-12 (918.8 m BGS; Section E.2.1).

The longest buildup period followed Flow Test 3. The flow sequence was 7.0 days in length, followed by a buildup period lasting 278.4 days. For this test, the Horner method was appropriate. By extrapolating to a Horner time equal to one, an undisturbed reservoir pressure of 1.4 MPa was obtained. This corresponds to an initial pressure of 12.6 MPa at the reservoir center depth of 918.8 m BGS.

Table E-4. Parameter Base-Case and Range Values Selected for the Hypothetical Brine Reservoir (same as Table 3-19) (see Figure E-1 for locations)

| Parameter | Symbol | Base Case | Range | Units |
|--|----------|---------------------|--|----------|
| Initial pressure | P_i | 12.7 | 7.0 to 17.4 | MPa |
| Effective thickness | b | 7.0 | 7.0 to 24.0 | m |
| Transmissivity of inner zone | T_i | 7×10^{-4} | 7×10^{-6}
to 7×10^{-2} | m^2/s |
| Distance inner/intermediate zone contact | r_2 | 300 | 100 to 900 | m |
| Transmissivity of intermediate zone | T_o | 7×10^{-6} | 7×10^{-8}
to 7×10^{-2} | m^2/s |
| Distance to intermediate/outer zone contact | r_3 | 2000 | 30 to 8600 | m |
| Transmissivity of outer zone or intact Castile | T_m | 1×10^{-11} | constant | m^2/s |
| Fluid density | ρ_f | 1240 | constant | kg/m^3 |
| Porosity | ϕ | 0.005 | 0.001 to 0.01 | |
| Compressibility of medium | α | 1×10^{-9} | 1×10^{-10}
to 1×10^{-8} | 1/Pa |

These pressures are not the highest recorded at the WIPP-12 wellhead. In 1980, when WIPP-12 extended only through the first 12 m of the Castile Fm., pressures at the surface as high as 3.3 MPa were monitored (Sandia National Laboratories and D'Appolonia, 1982). This surface pressure corresponds to a pressure of 14.5 MPa at a depth representative of the brine reservoir 85 m into the Castile Fm. After extensive testing of the brine reservoir at WIPP-12, the reservoir was sealed by a cement plug set above a bridge plug in Anhydrite III of the Castile between the depths of 848.6 and 906.2 m BGS. After the plug was set, pressures were again monitored at the surface as high as 2.1 MPa, which exceeds the highest surface pressure (1.43 MPa) monitored when the reservoir was open to the borehole.

In an effort to determine the source of the high pressures being monitored at the surface, a testing program was initiated in August 1985. This testing program established that the Castile plug was being bypassed and that pressure-buildup tests performed above the reservoir plug were dominated by the brine reservoir. The testing program also confirmed, however, that the brine reservoir was not able to produce the high pressures monitored at the surface. Testing of the Salado Fm. and the upper Castile failed to locate the source(s) of these high pressures (Beauheim, 1987a, 1987b). Beauheim concluded that the source of high pressure was of low flow capacity and depleted quickly.

For this modeling study, the base-case reservoir pressure is taken from the highest pressure monitored during the testing of the brine reservoir at WIPP-12, which is equivalent to a pressure of 12.7 MPa at the reservoir center. Of the 13 wells in the northern Delaware Basin that have encountered brine reservoirs, only four, including WIPP-12, have been tested adequately to estimate the formation pressure. These pressures range from 12.6 to 14.3 MPa (Popielak et al., 1983) at formation depth. Minimum pressures for nine other wells have been estimated based upon the minimum pressure needed to allow flow at the surface. From these nine estimates, minimum formation pressures range from 7.0 to 17.4 MPa. The range of initial reservoir pressures for this study is 7.0 to 17.4 MPa. The base-case value considered representative of the WIPP-12 reservoir is equal to 12.7 MPa at reservoir depth.

E.2.1.2 Reservoir Thickness. In most cases, the brine reservoirs encountered in the Castile Fm. are located in the lower portion of the uppermost anhydrite unit present at that location. The uppermost anhydrite unit at WIPP-12 is Anhydrite III, which is locally 96.6 m thick (Popielak et al., 1983). At well WIPP-12, the brine reservoir was encountered at the base of Anhydrite III and appears to be limited to a small fractured zone.

Anhydrite III at WIPP-12 was mapped by coring, caliper logs, acoustic televiewer logs, neutron logs, and spinner logs (Popielak et al., 1983). A review of these observations identified seven megascopic fractures in Anhydrite III. All of these fractures were found to be high angle with dips ranging from 70 degrees to vertical. Only two showed any evidence of brine

production, as identified by the spinner log conducted by the USGS (D'Appolonia, 1982). The uppermost brine-producing fracture (fracture C) extends from 916.2 to 917.1 m BGS. The lowermost brine-producing fracture (fracture D) extends from 919.0 to 921.1 m BGS. These depths are taken from the acoustic televiewer log. The spinner log defined the interval from which nearly 100% of the flow was coming as between 916.2 to 921.4 m BGS, which correlates well with both the caliper log and the acoustic televiewer log (Popielak et al., 1983; D'Appolonia, 1982).

Because the reservoir is heterogeneous and composed of high-angle fractures, its thickness is difficult to define from borehole reconnaissance at a single location. The base-case effective thickness of the reservoir is estimated to be 7 m and to occur between 915.3 and 922.3 m BGS. The center of the reservoir is taken to be located at a depth of 918.8 m BGS, which is the center of the interval that produces nearly all of the inflow (D'Appolonia, 1982). All downhole pressures will be referenced from the depth 918.8 m BGS. The adopted base-case effective thickness of 7 m can be considered a minimum thickness. From the center of the reservoir to the base of anhydrite III is ~12.0 m. The maximum effective thickness will be considered 24 m centered at 918.8 m BGS. Because the product of hydraulic conductivity and thickness (transmissivity) cannot be reduced in the reservoir characterization analyses (Section 3.4.3), sensitivity calculations are performed upon transmissivity. The variation in transmissivity caused by thickness uncertainty is less than the variation in transmissivity caused by uncertainty in hydraulic conductivity. As a result, total variation in formation transmissivity is driven by hydraulic conductivity variation, as described in the following section.

E.2.1.3 Reservoir Transmissivity. The WIPP-12 reservoir is modeled as two separate, concentric zones of fractured rocks with different transmissivities. As discussed in Section 3.4.3, the matrix was not considered to contribute to the hydraulic response of the brine reservoir during testing because of the large time constant of the matrix relative to the short duration of the flow periods. Because Case II simulates very long flow periods in the brine reservoir, the matrix is expected to contribute to the reservoir response and is modeled by attaching an infinite low-

transmissivity medium to the peripheral edge of the modeled region (Carter and Tracy, 1960; Reeves et al., 1986a). This medium represents the intact Castile Anhydrite III. Popielak et al. (1983) determined that the intact matrix had a hydraulic conductivity $< 2 \times 10^{-19} \text{ m}^2$. Assuming a thickness of 7 m, the transmissivity of the matrix is $\sim 1 \times 10^{-11} \text{ m}^2/\text{s}$. The transmissivity of the matrix is at least 6 to 8 orders of magnitude less than the base-case transmissivity of the inner and intermediate zones. For this study, the peripheral medium has been assigned a constant transmissivity of $1 \times 10^{-11} \text{ m}^2/\text{s}$.

From hydraulic interpretations presented in Section 3.4.3, it was determined that the inner region of the reservoir can be modeled as a cylindrical zone having a transmissivity of $7 \times 10^{-4} \text{ m}^2/\text{s}$ and extending out from the well to an effective radius of 300 m. The remainder of the reservoir is interpreted to have a lower transmissivity, $7 \times 10^{-6} \text{ m}^2/\text{s}$, and to extend out to a radial distance of 2000 m. These values are interpreted from WIPP-12 testing and are considered base-case values for the hypothetical brine reservoir. The transmissivities of these two are estimated to range, somewhat arbitrarily, by two orders of magnitude from the base-case values. The only Castile brine reservoir transmissivity data available for comparison with these base-case values and ranges were given by Popielak et al. (1983), who calculated transmissivities from as low as $1.6 \times 10^{-9} \text{ m}^2/\text{s}$ at ERDA-6 to as high as $8 \times 10^{-4} \text{ m}^2/\text{s}$ at WIPP-12.

E.2.1.4 Reservoir Fluid Density. Brine from the WIPP-12 brine reservoir has an average total dissolved solids of 328,000 mg/L, as determined from 13 laboratory analyses of water samples taken at the wellhead (Popielak et al., 1983). The average specific gravity, determined in the field and based on 59 analyses, is 1.215. In addition to these traditional analyses, four borehole-pressure-gradient surveys were performed at WIPP-12 as part of the hydraulic testing program from 1982 to 1983. These pressure-gradient surveys showed gradients ranging from 0.0121 to 0.0123 MPa/m, with an average of 0.0122 MPa/m. This average gradient corresponds to an average fluid density of $1240.6 \text{ kg}/\text{m}^3$. For this study, the base-case brine-reservoir fluid density is taken to be $1241 \text{ kg}/\text{m}^3$. This parameter is not varied, and therefore a representative range is not defined.

E.2.1.5 Reservoir Boundary. Because brine-reservoir encounters in the Castile Fm. are isolated (Figure 3-26), the reservoirs must be limited, with some outer boundary beyond which hydraulic communication is minimal. Methods used to infer the limits of brine reservoirs in the Castile Fm. are varied. One method is to look at an areal view of wells penetrating the Castile Fm. and identify which wells did and did not encounter a brine reservoir (Figure 3-26). When a well that encountered a brine reservoir is surrounded by wells that did not, the distance of the latter wells from the brine-reservoir well represents a maximum radius for the reservoir boundary. For example, WIPP-12 is surrounded by four wells in the immediate locality that did not encounter brine in the Castile Fm. These four wells are ~2 to 3 km from WIPP-12. Therefore, based upon the assumption that WIPP-12 is located at the center of the reservoir and the reservoir is circular in extent, the WIPP-12 reservoir may have at most a 2000-m radius. By using this logic, most brine reservoirs in the Castile Fm. in the northern Delaware Basin could be expected to have radii varying from ~800 to 3200 m. Other reservoir geometries are possible, but they have not been used in this analysis.

The most recent investigation that may be used in delineating the extent of the brine reservoir at WIPP-12 is a time-domain electromagnetic survey (TDEM) performed on the land surface over the waste-emplacement panels (The Earth Technology Corporation, 1988). This study suggests that a low-resistivity body, interpreted as a brine reservoir, exists within the Castile Fm. under portions of the waste-emplacement panels. If one assumes that this brine may be connected to the WIPP-12 brine reservoir, then the reservoir could have a boundary located some 1600 to 2000 m from the well.

Another method of inferring the reservoir extent at WIPP-12 is to estimate the total bulk volume of the reservoir using the concept of storativity of an elastic aquifer. The storage coefficient is defined as the volume of water removed from a vertical column of aquifer of height m and unit basal area when the head declines by one unit (Domenico, 1972). The equation for the storage coefficient can be written as

$$S = b \rho g (\alpha + \phi \beta) \quad (E-30)$$

where b is aquifer thickness, ρ is fluid density, g is the acceleration of gravity, α is the compressibility of solids, ϕ is the porosity, and β is the compressibility of the fluid. Domenico (1972) showed that the amount of water released from storage for a given head decline over an area A is equal to

$$\Delta V = S A \Delta h \quad (E-31)$$

where Δh is the given head decline. Equation E-31 can be expanded to

$$\Delta V = \rho g (\alpha + \phi \beta) (b A) \Delta h \quad (E-32)$$

where the product $(b A)$ is equal to the bulk volume of the aquifer (V_b) over which the unit decline in head has occurred and from which water has subsequently been released. Knowing that pressure is equal to the product $(\rho g \Delta h)$, and solving for the bulk volume of the aquifer, Equation E-29 can be expressed as

$$V_b = \Delta V / (\alpha + \phi \beta) \Delta P. \quad (E-33)$$

Therefore, if one knows the total compressibility of an aquifer and the total pressure change (ΔP) that has occurred as a result of a known fluid volume release (ΔV), one can estimate the total bulk volume of the aquifer. This calculation assumes that the pressure change has been uniform over the total bulk volume and that no mass has been transferred across the aquifer boundaries. By assuming a total thickness and a reservoir geometry, one can estimate the distance to the reservoir boundary.

From the time of initial penetration of the brine reservoir at WIPP-12 to the end of Flow Test 3, a volume of 36,935 m³ was produced from the reservoir. The residual pressure drop measured at the wellbore at the end of a 278.4-day shut-in was 0.23 MPa. For the range of total compressibility adopted (Section E.2.1), Equation E-30 estimates a range in aquifer bulk volume of 1.66 x 10⁷ to 1.66 x 10⁹ m³. Assuming the brine reservoir is a right circular cylinder with a range in effective thickness from 7 to 24 m (Section E.2.1), the estimated reservoir radius ranges from 460 to 8600 m. Popielak et al. (1983) reported that at the ERDA-6 reservoir, the production of 262.3 m³ of reservoir

fluid resulted in a change in pressure in the aquifer of 0.36 MPa. Using the same ranges of compressibility and effective thickness as above, the range in aquifer bulk volume at ERDA-6 is estimated to be 7.32×10^4 to 7.32×10^6 m³. This corresponds to a range in estimated reservoir radius of 30 to 560 m.

The final method considered here for identifying reservoir boundaries or large-scale heterogeneities is hydraulic-test interpretation. The hydraulic data do not provide evidence to accurately define the outer boundary location for the WIPP-12 brine reservoir. However, the fact that the reservoir did not recover to static pressure during 278 days of buildup following Flow Test 3 suggests that a boundary may have been encountered in the volume of rock stressed during the testing activities at WIPP-12. Further interpretation of the WIPP-12 testing is presented in Section 3.4.3.

The potential range of reservoir radii is based on the minimum and maximum estimates calculated using the various methods described above. This range is from 30 to 8600 m (Table E-4). The minimum and maximum estimates, and therefore range, of reservoir radii come from the calculation based upon estimating the total reservoir bulk volume. The large variation in these estimates comes from the two-order-of-magnitude range in the uncertainty of total aquifer compressibility. It is not considered probable that any of these brine reservoirs have radii as great as 8600 m. The base-case reservoir radius, taken from the hydraulic interpretations presented in Section 3.4.3, is 2000 m (Table E-4). Because for long flow periods the hydraulic response of the reservoir is a product of the coupled matrix-fracture diffusivities, a Carter-Tracy boundary condition, simulating a semi-infinitely distant model boundary, is attached to the peripheral edge of the modeled region. This boundary condition represents the low-permeability anhydrite matrix, which is considered homogeneous and infinite.

E.2.1.6 Reservoir Porosity. Porosity determinations were made on the reservoir anhydrite through geophysical logging and laboratory tests. Neutron-porosity, gamma-density, and acoustic logs were used to estimate total porosity within Anhydrite III of the Castile Fm. Estimates of porosity from these logs ranged from 0 to 5 percent (Popielak et al., 1983). Laboratory porosity determinations were performed on two intact pieces of core from

Anhydrite III. The first piece (from 858 m BGS) had a porosity of 0.8%, and the second piece (from 916.5 m BGS) had a porosity of 0.2% (Popielak et al., 1983).

The brine occurrence appears to be associated with a zone of secondary porosity resulting from deformation fracturing of the brittle anhydrites. A medium such as this is often characterized by very low secondary porosities and high transmissivities. Because there is no accurate means of estimating secondary porosity for this medium, the modeling will adopt the same range of secondary porosity of 0.1 to 1.0 percent that was used by Popielak et al. (1983). The base-case value of porosity is chosen to be 0.5%.

E.2.1.7 Reservoir Compressibility. In this study, the specific storage is calculated using the classical hydrogeologic representation where the medium compressibility is normalized with respect to the bulk volume (Narasimhan and Kanehiro, 1980). The medium compressibility (α) for a triaxial system can be defined as the inverse of the bulk modulus (B) of the rock

$$\alpha = (1 / B) . \quad (E-34)$$

The bulk compressibility of Anhydrite III was estimated using values of the bulk modulus determined from acoustic logs that were run in WIPP-12. Popielak et al. (1983) reported that the values of bulk modulus for Anhydrite III vary from 3.45×10^{10} to 6.89×10^9 Pa. This represents a compressibility range of 2.9×10^{-11} to 1.45×10^{-10} Pa⁻¹. These values are considered representative of the intact anhydrite. The medium compressibility of a fractured or jointed rock is generally an order of magnitude higher than that of a non-fractured rock (Freeze and Cherry, 1979). Freeze and Cherry (1979) gave a range for medium compressibility for a fractured or jointed rock of 1×10^{-8} to 1×10^{-10} Pa⁻¹. This study adopts this range for compressibility and takes 1×10^{-9} Pa⁻¹ to be the base-case value (Table E-4).

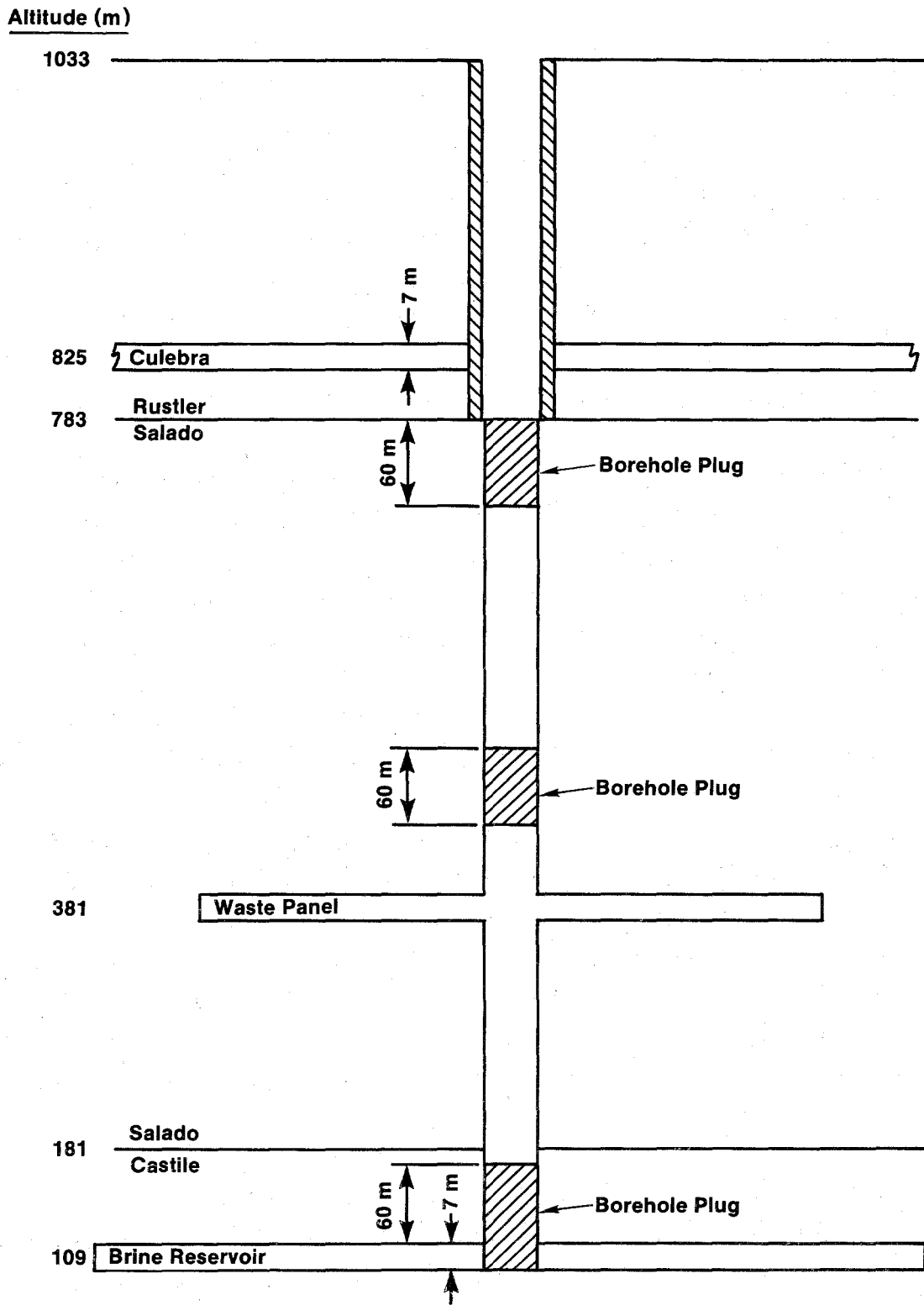
E.2.2 Borehole Parameters

For the Case II simulations, a borehole is assumed to be drilled through the repository and to encounter a brine reservoir within the Castile Fm. The probable continuation of the borehole to the Bell Canyon Fm. or beyond is ignored in the Case II simulations (Section 7.1). Expected drilling procedures and conditions and subsequent borehole plugging are discussed in Appendix C. This section discusses the borehole location and properties used in the simulations. Parameters are summarized in Table E-2.

The borehole is assumed to be drilled through the center of the southwestern waste panel. This is a conservative assumption, because travel times in the Culebra Dolomite calculated using the ground-water flow model of LaVenue et al. (1988) are shortest between the southwestern corner of the waste-storage area and off-site locations such as the stock well (Appendix E.2.4 and Section 5.3).

Altitudes at the borehole for the ground surface and Rustler units are based on the H-3 hydropad, because of its close proximity. The altitude for the center of the repository at the Waste Handling Shaft is taken from Bechtel (1985). The altitude of the Salado-Castile contact at the borehole location was interpolated between WIPP-12 and Cabin Baby-1. The altitude of the center of the brine reservoir was interpolated from the Anhydrite III elevations at WIPP-12 and Cabin Baby-1 and the relative position of the brine reservoir in Anhydrite III at WIPP-12. A schematic representation of the borehole showing altitudes and thicknesses of the various units of interest is shown in Figure E-4.

Borehole-diameter specifications for oil and gas wells are 0.413 m (16-1/4 in.) and 0.457 m (18 in.), respectively, between ground surface and the top of the Salado Fm., and 0.311 m (12-1/4 in.) and 0.356 m (14 in.), respectively, below the top of the Salado Fm. Details of the expected conditions for the drilling, casing, and borehole-plugging events are discussed in Appendix C. The positions of the 60-m-long borehole plugs are shown schematically in Figure E-5.



TRI-6330-69-0

Figure E-5. Schematic illustration of intrusion borehole after plug emplacement.

In the SWIFT II simulations, the borehole hydraulic conductance between the brine reservoir and the Culebra Dolomite is used in modeling the hydraulic coupling of the two aquifers (Section E.1.3). The hydraulic conductance is defined in terms of a transmissibility T_w by the relation

$$T_w = kA/L \quad (E-35)$$

where k is the effective borehole permeability, A is the borehole cross-sectional area, and L is the length of the plugs or rubblized borehole zones. Because borehole diameters differ in exploratory oil and gas wells, an average cross-sectional area for these two well diameters was used. An effective borehole hydraulic conductance was calculated as a harmonic average, using the appropriate borehole or plug lengths with specific permeabilities and cross-sectional areas. For modeling, the plugs are assumed to remain intact for the first 75 years after placement, and then the borehole transmissibility is assumed to increase linearly in magnitude until 150 years, when the effective borehole permeability is equal to 10^{-12} m² for Case IIA and 10^{-11} m² for Cases IIB, IIC, and IID. This time-varying transmissibility is implemented in a step-wise manner with equal increments to the transmissibility at 75, 100, 125, and 150 years.

E.2.3 Repository Source-Term Parameters

The repository, the room and panel layout of the waste-storage area, and the waste inventories are described in Chapter 4.0. Parameter specifications necessary for quantifying the source term for the Case II simulations using SWIFT II (Tables E-5 and E-1) are discussed briefly below.

Simulations were performed for four radioactive-decay chains (²⁴⁰Pu, ²³⁹Pu, ²³⁸Pu, and ²⁴¹Am) and for stable lead for 10,000 years. The initial total waste inventory for the decay-chain members of interest and stable lead in the repository is presented in Table E-5.

For Cases IIA, IIB, and IIC, the mass of waste in one panel was assumed to be exposed to circulating fluids. For Case IID, the mass of waste in one room was assumed to be exposed to circulating fluids (Sections 4.3.2 and 7.3.1). The concentration of the waste species in these fluids is constrained by their

Table E-5. Specification of Waste Radionuclide Species and their Initial ($t = 0$) Mass Inventory (Including Stable Lead) in the Repository for the Case II Simulations.

| <u>Decay Chain or
Waste Species</u> | <u>Radio-
nuclide</u> | <u>Half Life
(years)</u> | <u>Inventory*
(g)</u> |
|---|---------------------------|------------------------------|---------------------------|
| 240Pu → 236U | 240Pu | 6.54 x 10 ³ | 4.76 x 10 ⁵ |
| | 236U | 2.34 x 10 ⁷ | 0 |
| 239Pu | 239Pu | 2.41 x 10 ⁴ | 6.93 x 10 ⁶ |
| 238Pu → 234U → 230Th → 226Ra
→ 210Pb | 238Pu | 87.7 | 2.31 x 10 ⁵ |
| | 234U | 2.44 x 10 ⁵ | 0 |
| | 230Th | 7.7 x 10 ⁴ | 0 |
| | 226Ra | 1.6 x 10 ³ | 0 |
| | 210Pb | 22.3 | 0 |
| 241Am → 237Np → 233U → 229Th | 241Am | 4.32 x 10 ² | 2.26 x 10 ⁵ |
| | 237Np | 2.14 x 10 ⁶ | 1.14 x 10 ⁴ |
| | 233U | 1.59 x 10 ⁵ | 8.15 x 10 ⁵ |
| | 229Th | 7.43 x 10 ³ | 0 |
| Stable Pb | n.a. | n.a. | 1.33 x 10 ⁹ |

Note: n.a. means not applicable

*The best estimates for the inventory in grams for the Pu isotopes is given in Table 4-2b. When simulations for Case II began, those values had not been selected as the best estimates, and the values in this table were used in the Case II calculations.

solubilities. For the radionuclides, the solubility was assumed to be 1×10^{-6} molar for Cases IIA and IID and 1×10^{-4} molar for Cases IIB and IIC. The solubility of stable Pb in the repository fluids was defined as 116 mg/L. All fluids entering the borehole from the waste panel had concentrations at these values except as modified by radioactive decay and the total mass available in one panel. For Pb, the solubility in the Culebra ground water was specified to be 54 mg/L.

Calculations of brine inflow (Section 4.3.2) indicate a conservative, steady-state values of 1.3 m³/yr for one panel and 0.1 m³/yr for one room. In

the Case II simulations, this flux is added to the flux from the brine reservoir to the Culebra Dolomite. As a consequence of the different specified hydrologic properties of the rooms for Cases IIA, IIB, IIC, and IID (Section E.1.4), the mass loading to the borehole differs for each case. For Cases IIA and IIC, all fluid flowing from the brine reservoir is assumed to access the waste mass in one panel; in Cases IIB and IID, fluid from the brine reservoir does not come into contact with the waste in the panel. In Cases IIA, IIB, and IIC, 1.3 m³/yr of Salado brine that has been in contact with the waste mass enters the borehole and flows to the Culebra Dolomite. In Case IID, 0.1 m³/yr of Salado brine that has come into contact with the waste mass enters the borehole and flows to the Culebra Dolomite.

E.2.4 Culebra Parameters

A fractured porous medium is assumed to exist along the travel path between the borehole and the stock well. The flow path, the stock-well location, and the solute-transport properties of the Culebra Dolomite are discussed briefly below. Reeves et al. (1987) also discussed fracturing in the Culebra Dolomite and its effect on hydraulic and tracer tests. The base-case and range parameter values for the Culebra Dolomite are summarized in Table E-6. The range values are presented for discussion and were used only in Cases IIB, IIC, and IID. For Cases IIB, IIC, and IID, end values of the range were selected to provide more rapid or longer-distance solute transport.

A double-porosity medium, for which data are limited, is assumed along the travel path. Base-case and range parameter values are documented using available data, but must be considered uncertain.

E.2.4.1 Regional Flow Field. Section 3.3.5 reviews the hydrologic modeling for the Culebra Dolomite near the WIPP site. The Culebra groundwater-flow model by LaVenue et al. (1988) is the most recent one available for estimating the Darcy-velocity distribution in the regional flow field and for determining the travel path from the breach borehole to the stock well. The model calibration included hydrologic data available by about October 1987. The model was calibrated to undisturbed head conditions only and not to the large-scale multipad pumping tests that have been performed at the WIPP site.

Table E-6. Parameter Base-Case and Range Values Selected for the Culebra Dolomite (Case II)

| Parameter | Symbol | Base Case | Range | Units |
|------------------------------|-----------|------------------------|--|--------------------|
| UTM location of stock well | - | 614682
3576690 | n.a.
n.a. | mE
mN |
| Free-water diffusivity | D' | 1 x 10 ⁻⁶ | 5 x 10 ⁻⁷
to
9 x 10 ⁻⁵ | cm ² /s |
| - Radionuclides - Case IIA | D' | 1 x 10 ⁻⁶ | n.a. | cm ² /s |
| - Cases IIB, IIC,
and IID | D' | 5 x 10 ⁻⁷ | n.a. | cm ² /s |
| - Stable Pb - Case IIA | D' | 4 x 10 ⁻⁶ | n.a. | cm ² /s |
| - Cases IIB, IIC,
and IID | D' | 2 x 10 ⁻⁶ | n.a. | cm ² /s |
| Matrix tortuosity | θ' | 0.15 | 0.03 to 0.5 | |
| - Case IIA | θ' | 0.15 | n.a. | |
| - Cases IIB, IIC, and IID | θ' | 0.03 | n.a. | |
| Matrix-block length | 2L' | 2.0 | 0.25 to 7.0 | m |
| - Case IIA | 2L' | 2.0 | n.a. | m |
| - Cases IIB, IIC, and IID | 2L' | 7.0 | n.a. | m |
| Matrix porosity | ϕ' | 0.16 | 0.07 to 0.30 | |
| - Case IIA | ϕ' | 0.16 | n.a. | |
| - Cases IIB, IIC, and IID | ϕ' | 0.07 | n.a. | |
| Fracture porosity | ϕ | 1.5 x 10 ⁻³ | 1.5 x 10 ⁻⁴
to
1.5 x 10 ⁻² | |
| Longitudinal dispersivity | α | 100 | 50 to 300 | m |
| Fracture flux | u | see note | n.a. | m/s |
| Grain density | ρ_R | 2.82 | 2.78 to 2.86 | g/cm ³ |

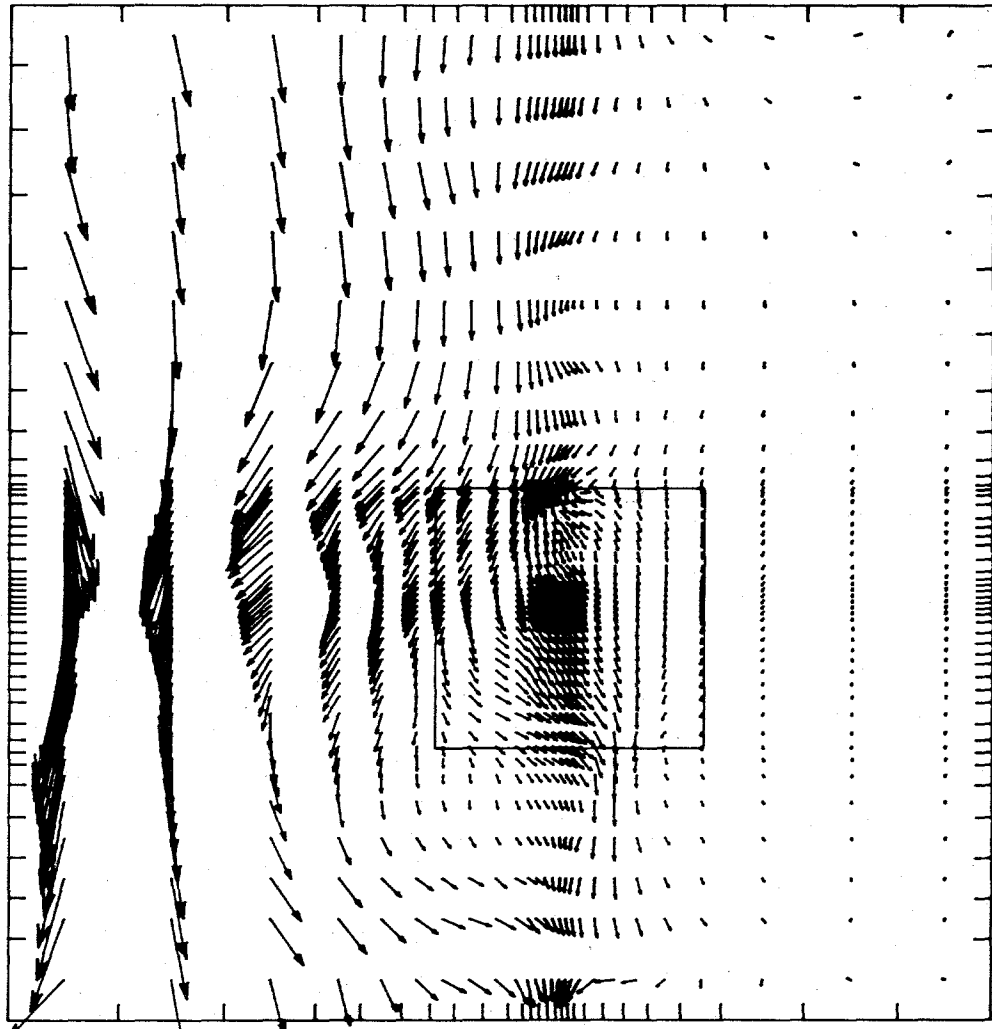
Table E-6. Parameter Base-Case and Range Values Selected for the Culebra Dolomite (Case II) (continued)

| <u>Parameter</u> | <u>Symbol</u> | <u>Base Case</u> | <u>Range</u> | <u>Units</u> |
|----------------------------------|----------------|------------------|--------------|--------------|
| Matrix distribution coefficient | | | | |
| - Case IIA: Pu | K _d | 50 | - | mL/g |
| Am | K _d | 200 | - | mL/g |
| U | K _d | 1 | - | mL/g |
| Np | K _d | 1 | - | mL/g |
| Th | K _d | 50 | - | mL/g |
| Ra | K _d | 0.1 | - | mL/g |
| Pb | K _d | 0.1 | - | mL/g |
| - Cases IIB, IIC,
and IID: Pu | K _d | 25 | - | mL/g |
| Am | K _d | 100 | - | mL/g |
| U | K _d | 1 | - | mL/g |
| Np | K _d | 1 | - | mL/g |
| Th | K _d | 25 | - | mL/g |
| Ra | K _d | 0.05 | - | mL/g |
| Pb | K _d | 0.05 | - | mL/g |

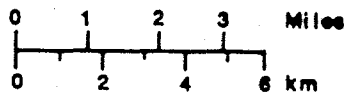
NOTE: n.a. means not applicable. The Culebra ground-water flow model presented in LaVenue et al. (1988) was used for calculating fluxes and determining flow paths. The transient fracture flux along the flow path from the release point in the Culebra Dolomite to the off-site stock well is calculated through hydraulic coupling of the brine reservoir, borehole region, and Culebra.

LaVenue et al. (1988) presented full details on the calibrated Culebra transmissivity distribution and steady-state head distribution. The simulated regional Darcy-flow velocities from the LaVenue et al. (1988) Culebra model are shown in Figure E-6. The field hydrologic program since October 1987, and continuing Culebra ground-water flow modeling are discussed in Section 3.3.5.

As discussed in Section E.2.2, the borehole is assumed to be drilled through the center of the southwestern waste panel (Figure 1-2). A particle-tracking code was used to define the flow path for transport from this release location to a hypothetical stock well. As discussed in Section 5.3, the location of the stock well was selected based on two constraints: the well is assumed to lie on a flow path from the breach borehole and must be located in an area where the water is potentially sufficiently fresh to support stock.



DARCY-VELOCITY VECTORS



Darcy-Velocity Vector Scale

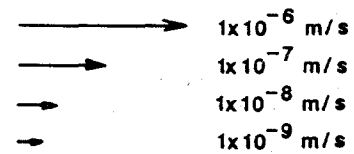


Figure E-6. Simulated flow field (Darcy velocities) for the Culebra Dolomite under undisturbed conditions (after LaVenue et al., 1988).

The UTM coordinates of the breach borehole and stock well are presented in Tables E-2 and E-6, respectively, and their locations are illustrated, along with the transport path in the Culebra Dolomite, in Figure E-2.

E.2.4.2 Free-Water Diffusivity. Values of free-water diffusion coefficients (i.e., the coefficient of diffusion of a given solute in a solution) are required to calculate diffusive fluxes of radionuclides in the Culebra matrix and to determine whether a porous-medium assumption is valid for fractured media (Erickson et al., 1986). Table E-7 lists the coefficients recommended in this report. Ranges of values of the diffusion coefficients estimated at infinite dilution or obtained in experimental studies are also given (Brush, 1988; Li and Gregory, 1974). Experimental data were obtained with granitic ground waters and sodium bentonite (Torstenfelt et al., 1982).

The measured values are lower than those estimated at infinite dilution from the Nernst expression (Li and Gregory, 1974). The experimental values were obtained from apparent diffusion coefficients in sediments and required assumptions about retardation factors for the radionuclides, porosity, and tortuosity. Considerable but unquantifiable uncertainty, therefore, is associated with all the values of the actinide diffusion coefficients reported in the literature.

Extrapolation of the diffusion coefficients measured in the studies listed above to the range of conditions assumed for the Culebra Dolomite introduces another degree of unquantifiable uncertainty. Some data suggest that diffusion coefficients for divalent cations (alkaline earth chlorides, transition metal chlorides) decrease by a factor of 2 with increasing ionic strength over the range 0 to 6 M (Miller, 1982). There are few data, however, to guide predictions of radionuclide diffusion coefficients in the brines that might result from mixing Culebra water with fluids from the repository. Interactions between the radionuclides and other solutes will change the free-water diffusion coefficient in ways that are too complex to predict. Miller (1982) and Anderson (1981) discussed the effect of coupled salt fluxes on the diffusion coefficient in multicomponent systems.

Table E-7. Estimated Free-Water Diffusion Coefficients for Radionuclide Transport in the Matrix of the Culebra Dolomite (cm²/s)

| Element | Recommended Diffusion Coefficients | | | Range of Values in Literature ¹ |
|---------|------------------------------------|-------------------------|--|---|
| | I, IIA | IIB, IIC, IID | | |
| Pu | 1 x 10 ⁻⁶ | 5 x 10 ⁻⁷ | | 4.8 x 10 ⁻⁷ - (3 x 10 ⁻⁶) |
| Am | 1 x 10 ⁻⁶ | 5 x 10 ⁻⁷ | | 5.3 x 10 ⁻⁷ - (3 x 10 ⁻⁶) |
| Cm | (1 x 10 ⁻⁶) | (5 x 10 ⁻⁷) | | no data; use data for Am |
| U | 1 x 10 ⁻⁶ | 5 x 10 ⁻⁷ | | 1.1 x 10 ⁻⁶ - <u>4.3 x 10⁻⁶</u> |
| Np | 1 x 10 ⁻⁶ | 5 x 10 ⁻⁷ | | 5.2 x 10 ⁻⁷ - (3 x 10 ⁻⁶) |
| Ra | 1 x 10 ⁻⁶ | 5 x 10 ⁻⁷ | | <u>7.5 x 10⁻⁶</u> |
| Pb | 4 x 10 ⁻⁶ | 2 x 10 ⁻⁷ | | <u>8 x 10⁻⁶</u> |
| Th | 1 x 10 ⁻⁶ | 5 x 10 ⁻⁷ | | 5 x 10 ⁻⁷ - <u>1.53 x 10⁻⁶</u> |

1. Data from estimated values of Brush (1988) and Higgo et al. (1987) (indicated by parentheses); values calculated from the Nernst expression by Li and Gregory (1974) (underlined); and measurements by Torstenfelt et al. (1982) (all others). Temperature dependence has not been considered for the recommended values.

Transport calculations with SWIFT-II require that all radionuclides within the same decay chain have the same diffusion coefficient. The recommended diffusion coefficient for the actinides and radium in Cases I and IIA (1 x 10⁻⁶) is near the middle of the ranges obtained from the literature. A separate chain was run for Pb to allow the use of a higher diffusion coefficient. This value (4 x 10⁻⁶) was based on the single reported literature value and a reduction factor of 50% to account for the high salinity in the Culebra Dolomite. For Cases IIB, IIC, and IID, all the Case IIA values (with the exception of U and Np) were arbitrarily reduced by 50% to represent "degraded" properties of the Culebra Dolomite. No uncertainties can be assigned to these values. Case I and II diffusion coefficients are summarized in Table E-6.

The base-case and range values for free-water diffusivity that have been selected for this study are substantially lower than those used by Reeves et al. (1987) for two reasons: (1) the previous study did not specifically address the radioactive decay-chain members identified here, and (2) the much higher salinities that are a result of flow from the Salado and Castile Fms. can reduce the free-water diffusivity as much as a factor of two.

E.2.4.3 Matrix Porosity. Laboratory porosity determinations have been performed on 82 core samples from 15 borehole or hydropad locations at and surrounding the WIPP site (Table E-8). Porosity has been determined by the Boyles's Law technique using helium or air for all samples and by the water-resaturation technique for 30 samples. Excellent correlation was obtained between porosity values from the two techniques. From the 82 samples with porosity measurements using the Boyle's Law technique, an average porosity of 15.2% was obtained, with a range of ~3 to 30 percent. Core samples from the H-3 and H-11 hydropads, which are the two hydropads closest to the offsite pathway, had average porosities of 19.8% (6 samples) and 16.2% (10 samples). Porosities ranged from ~17 to 24 percent for the H-3 hydropad and ~10 to 30 percent for the H-11 hydropad.

Matrix-porosity values derived from diffusion experiments performed by Sandia National Laboratories using Culebra Dolomite samples range from 1.1 to 8.7%. The porosities calculated from the diffusion experiments, termed diffusion-porosity values, are lower than those measured by Boyle's Law or mercury-porosimetry techniques. These values lie at the lower end of the range representative of the Culebra matrix (Tables E-6 and E-8). Possible explanations for the differences between values measured by different techniques include sample heterogeneity, incomplete resaturation of previously dried samples, and deviations of actual pore geometry from the idealized model assumed in simple versions of Fick's First Law of Diffusion for solute migration in a porous rock. In general, the samples used in the diffusion measurements are fine-grained dolomites free from large cracks and are chosen for mineral homogeneity and structural competence. No claim has been made that these samples are representative of the Culebra Dolomite in general nor for the transferability of these results to field-scale transport.

Table E-8. Summary of Porosities Measured in Culebra Core Samples

| <u>Well</u> | <u>Sample Identification Number</u> | <u>Porosity Determination (%)</u> | |
|-------------|-------------------------------------|-----------------------------------|---------------------------|
| | | <u>Helium or Air</u> | <u>Water Resaturation</u> |
| H-2a | -1 | 11.6 | 11.3 |
| H-2a | -2 | 12.2 | |
| H-2b | 1-1 | 14.1 | |
| H-2b | 2-1, 3-1 | 15.4 | |
| H-2b | 1-2 | 11.8 | |
| H-2b | 2-2, 3-2 | 10.3 | |
| H-2b1 | -1F | 10.5 | |
| H-2b1 | -1 | 8.2 | 8.8 |
| H-2b1 | -2 | 14.2 | |
| H-2b1 | -3 | 15.3 | 15.8 |
| H-3b2 | 1-3 | 18.8 | |
| H-3b2 | 1-4 | 16.8 | |
| H-3b3 | 2-3, 3-3 | 18.0 | |
| H-3b3 | 2-4, 3-4V | 20.2 | |
| H-3b3 | 1-6 | 24.4 | |
| H-3b3 | 2-5, 3-5 | 20.5 | |
| H-4b | 1-9 | 29.7 | |
| H-4b | 2-6, 3-6V | 20.8 | |
| H-5b | -1 | 12.5 | |
| H-5b1 | -1A | 13.0 | |
| H-5b1 | -1B | 15.6 | |
| H-5b1 | -2 | 22.8 | 23.7 |
| H-5b1 | -2F | 24.8 | |
| H-5b1 | -3 | 13.3 | 12.8 |
| H-6b | 2-7 | 10.8 | |
| H-6b | 2-8 | 11.6 | |
| H-6b | 1-7 | 10.7 | |
| H-6b | 1-8 | 25.5 | |
| H-7b1 | -1 | 17.7 | 18.1 |
| H-7b1 | -1F | 14.9 | |
| H-7b1 | -2A | 20.6 | |
| H-7b1 | -2B | 27.8 | |
| H-7b2 | -1 | 15.9 | 14.8 |
| H-7b2 | -2 | 11.8 | 12.9 |
| H-7c | -1A | 12.5 | 12.9 |
| H-7c | -1B | 16.5 | |
| H-7c | -1C | 13.4 | |
| H-7c | -1F | 13.8 | |
| H-10b | -1 | 8.9 | |
| H-10b | -2 | 11.5 | 11.7 |
| H-10b | -2F | 6.6 | |
| H-10b | -3 | 11.2 | 10.6 |
| H-11 | -1 | 15.5 | 15.3 |
| H-11 | -2 | 10.5 | 11.3 |
| H-11 | -2F | 10.4 | |

Table E-8. Summary of Porosities Measured in Culebra Core Samples (continued)

| <u>Well</u> | <u>Sample Identification Number</u> | <u>Porosity Determination (%)</u> | |
|-------------|-------------------------------------|-----------------------------------|---------------------------|
| | | <u>Helium or Air</u> | <u>Water Resaturation</u> |
| H-11b3 | -1 | 30.3 | 27.5 |
| H-11b3 | -1F | 22.3 | |
| H-11b3 | -2 | 9.9 | 10.3 |
| H-11b3 | -2F | 12.3 | |
| H-11b3 | -3 | 13.0 | 12.6 |
| H-11b3 | -4 | 15.2 | |
| H-11b3 | -4F | 22.4 | |
| W-12 | -1A | 2.8 | |
| W-12 | -1B | 11.4 | |
| W-12 | -2 | 11.6 | 11.9 |
| W-12 | -2B | 12.6 | |
| W-12 | -2F | 13.5 | |
| W-12 | -3 | 13.4 | 13.0 |
| W-13 | -1 | 14.3 | 15.2 |
| W-13 | -2 | 21.9 | 22.6 |
| W-13 | -2F | 26.0 | |
| W-13 | -3A | 17.9 | |
| W-13 | -3B | 9.7 | |
| W-25 | -1 | 11.5 | 12.0 |
| W-26 | -1 | 12.4 | 12.2 |
| W-26 | -1F | 11.2 | |
| W-26 | -2 | 12.6 | 12.6 |
| W-26 | -3 | 12.7 | |
| W-28 | -1A | 14.2 | |
| W-28 | -1B | 13.0 | |
| W-28 | -2 | 18.7 | 18.8 |
| W-28 | -3 | 17.0 | 16.9 |
| W-28 | -3F | 17.9 | |
| W-30 | -1 | 12.8 | 12.4 |
| W-30 | -2 | 15.0 | 15.2 |
| W-30 | -3A | 17.6 | |
| W-30 | -3B | 14.9 | 13.9 |
| W-30 | -3F | 14.9 | |
| W-30 | -4 | 23.9 | |
| AEC-8 | -1 | 7.9 | 8.6 |
| AEC-8 | -1F | 12.2 | |
| AEC-8 | -2 | 10.9 | 10.6 |

Number of Samples = 82
 Average = 15.2%
 Standard Deviation = 5.3%
 Range = 2.8 to 30.3%

For transport along the off-site pathway in the Culebra, a base-case matrix porosity of 16%, the average of available core measurements (Table E-8), has been chosen for the Case IIA simulations. For Cases IIB, IIC, and IID, a matrix porosity of 7% has been selected as a lower-end value. Although lower values have been measured or derived, an average lower value of 7% along the flow path is considered most representative (Table E-6).

E.2.4.4 Matrix Tortuosity and Grain Density. Tortuosity values for dolomite are not available. A review of the literature does permit an estimate of a potential range. Bear (1972), in his review of unconsolidated media, gave values ranging from 0.3 to 0.7. De Marsily (1986) reported tortuosities varying from 0.1 for clay to 0.7 for sand. Barker and Foster (1981) reported diffusion coefficients for Cl^- in chalk samples that indicate tortuosities of 0.02 to 0.17. Katsube et al. (1986) calculated tortuosity values from 0.02 to 0.19 from diffusion experiments on crystalline-rock samples. Diffusion experiments performed by Sandia National Laboratories on a limited number of Culebra core samples yielded tortuosities in the range of 0.03 to 0.09.

Matrix-tortuosity estimates for the Culebra Dolomite were calculated based on formation-factor and matrix-porosity determinations on 15 core samples. The values range from 0.03 to 0.33 with an average value of 0.14 (Table E-9).

For the Case IIA simulations, a base-case matrix tortuosity of 0.15 was selected as representative. This value was also used in regional-scale transport simulations (Reeves et al., 1987). A lower-end estimate of 0.03 for matrix tortuosity was selected for Case IIB, IIC, and IID simulations to investigate the effects of decreased diffusion into the matrix.

Grain density was determined for 73 core samples from 15 borehole or hydropad locations. The values ranged from 2.78 to 2.84 g/cm^3 with an average of 2.82 g/cm^3 and standard deviation of 0.02. A value of 2.82 g/cm^3 was chosen as the base-case value for all simulations.

E.2.4.5 Fracture Porosity. Estimates of fracture porosity can be obtained by interpreting tracer tests conducted at sites exhibiting double-

Table E-9. Summary of Formation Factors and Calculated Tortuosities from Culebra Core Samples

| Well | Identification Number | Helium Porosity (%) | Formation Factor | Calculated Tortuosity |
|---------|-----------------------|---------------------|------------------|-----------------------|
| H-2b1 | -1F | 10.5 | 326.77 | 0.03 |
| H-5b1 | -2F | 24.8 | 12.20 | 0.33 |
| H-7b1 | -1F | 14.9 | 73.49 | 0.09 |
| H-7c | -1F | 13.8 | 79.61 | 0.09 |
| H-10b | -2F | 6.6 | 406.78 | 0.04 |
| H-11 | -2F | 10.4 | 94.82 | 0.10 |
| H-11b3 | -1F | 22.3 | 36.35 | 0.12 |
| H-11b3 | -2F | 12.3 | 101.93 | 0.08 |
| H-11b3 | -4F | 22.4 | 32.74 | 0.14 |
| W-12 | -2F | 13.5 | 47.30 | 0.16 |
| W-13 | -2F | 26.0 | 13.26 | 0.29 |
| W-26 | -1F | 11.2 | 68.77 | 0.13 |
| W-28 | -3F | 17.9 | 26.30 | 0.21 |
| W-30 | -3F | 14.9 | 31.49 | 0.21 |
| AEC-8 | -1F | 12.2 | 90.09 | 0.09 |
| AVERAGE | | 15.6% | 96.13 | 0.14 |
| RANGE | | 6.6 - 26.0% | | 0.03 - 0.33 |

porosity transport behavior. Tracer tests have been performed at the H-2, H-3, H-4, H-6, and H-11 hydropads at the WIPP site. Of these, the tests conducted at the H-3, H-6, and H-11 hydropads appear to demonstrate fracture-transport behavior, as evinced by rapid tracer breakthrough between wells on at least one flow path at each hydropad site. Detailed test interpretations have been reported only for the H-3 hydropad (Kelley and Pickens, 1986).

A first estimate of fracture porosity can be calculated from the convergent-flow tracer tests by the relation

$$\phi = Q t_p / \pi r_t^2 b \quad (E-36)$$

where ϕ is the fracture porosity, Q is the discharge rate at the pumping well, t_p is the time to reach the peak concentration, r_t is the distance between the tracer-addition and pumping wells, and b is the aquifer thickness.

The time to reach the peak concentration is used for this estimate, because this time is assumed to be representative of the average transport rate between the tracer-addition and pumping wells. Although the time to reach the peak concentration also depends on longitudinal dispersivity and diffusive losses to the matrix, this approach provides a first estimate of fracture porosity for calibrating the tracer-breakthrough curves.

The calculated fracture porosities for the flow paths exhibiting the strongest fracture control are 2×10^{-3} and 1×10^{-3} for the H-3 and H-11 hydropads, respectively. These porosities are based on the assumption of isotropic fracture distribution, which may not be valid for some portions of the Culebra Dolomite. Because H-3 and H-11 are closest to the off-site transport pathway, an average value of 1.5×10^{-3} was selected as the base-case fracture porosity (Table E-6). This value was used for all Case II simulations.

E.2.4.6 Matrix-Block Length. The fractured Culebra Dolomite is assumed in this study to consist of three orthogonal fracture sets that define rectilinear matrix units. Both horizontal and vertical (or near vertical) fracture sets have been observed in core samples, shaft excavations, and outcrops (Kelley and Pickens, 1986). The matrix-block sizes are expected to vary spatially across the WIPP site. However, because matrix-block-size data are so few, the effects of this variability cannot be assessed. Therefore, this study analyzes double-porosity effects using an equivalent block size assumed to be applicable over the entire length of the travel path.

A fracture spacing range from 0.5 to 2.4 m has been interpreted for the two travel paths at the H-3 hydropad (Kelley and Pickens, 1986). Although detailed interpretations have not been completed for the H-11 hydropad tracer test, preliminary evaluation of the breakthrough curves suggests matrix-block sizes in the range of 0.8 to 3 m. A base-case value of 2 m is selected for matrix-block length, with a range of 0.25 to 7 m. There is no physical significance to the value of 7 m chosen as the upper limit for fracture spacing. It simply corresponds to a representative measured thickness for the Culebra Dolomite. The base-case matrix-block size of 2 m has been selected for Case IIA, and the upper end matrix-block size of 7 m has been selected for

Case IIB, IIC, and IID simulations (Table E-6) to investigate the effects of fracture spacing.

E.2.4.7 Longitudinal Dispersivity. A review of the literature for various tracer-test scales and contaminant-plume sizes (e.g., Lallemand-Barres and Peaudecerf, 1978; Pickens and Grisak, 1981) suggests that, up to moderate travel distances of 500 to 1,000 m, longitudinal dispersivity can be expressed as a function of the mean travel distance of the solute. Longitudinal dispersivity ranges from several to 10 percent of the travel-path length. Although longitudinal dispersivity is assumed to be directly related to the mean travel distance of the solute, longitudinal dispersivity is not expected to increase beyond some maximum or asymptotic value. This study adopts a longitudinal dispersivity of 100 m.

E.2.4.8 Matrix and Fracture Distribution Coefficients (K_d 's). Radionuclide distribution coefficients (K_d) are used in transport codes to calculate the partitioning of radioelements between the ground water and rock. The definition, underlying assumptions, and limitations of the use of a K_d to estimate radionuclide retardation have been reviewed in Section 3.3.4. As discussed in that section, a K_d value cannot be extrapolated with confidence to physicochemical conditions that differ from those under which the data were obtained. In addition, the use of a K_d to calculate radionuclide partitioning is valid only if: chemical equilibrium exists among all aqueous species containing the solute; reversible, linear sorption is the dominant process controlling exchange of the solute between the ground water and the rock; and transport of the solute by particulates is insignificant. Most of these assumptions inherent in the use of a K_d (Section 3.3.4) are not valid for radioelement transport in the Culebra Dolomite. Water chemistry varies both spatially and temporally along potential radionuclide flow paths (Sections 3.3.2 and 3.3.3; Siegel and Lambert, 1989); therefore, aqueous speciation may vary and the amount of sorption would be expected to deviate considerably from the amount calculated using any single K_d value. The available data do not allow assessment of the degree of equilibria among the aqueous species containing the radionuclides or between the rock and the aqueous radionuclide species under potential release scenarios. In addition, mixing of waters from the repository with ground water in the Culebra Dolomite could lead to

precipitation of some mineral phases and dissolution of others. Both processes would alter the solution chemistry and could provide mechanisms for radionuclide retardation (coprecipitation) or migration (colloid formation or dissolution of previously deposited radionuclides).

Recommended K_d Values. The procedure used to obtain the recommended K_d values is described in Section 3.3.4. The recommended K_d values are listed in Tables E-10 to E-12. Sorption by the dolomite matrix was the only type of retardation considered in the radionuclide transport calculations (Chapter 7.0 and Appendix E). Table E-10 contains K_d values appropriate for calculations of radionuclide retardation in the matrix of the Culebra Dolomite. Supplemental data are given in Tables E-11 and E-12. These tables contain radionuclide distribution coefficients for the clays that are dispersed within the matrix and that line the fractures in the aquifer.

No K_d data are available describing the uptake of Ra or Pb onto dolomite. This report assumes that these elements would sorb onto clay particles within the matrix (comprising ~3% by weight). To account for this fraction of the matrix participating in sorption, a utilization factor of 0.01 was assumed for the Culebra Dolomite, as discussed in Section 3.3.4. The K_d 's for Ra and Pb in Table E-10 were obtained by multiplying the K_d 's for these elements for clays in Table E-11 by a factor of 0.01.

Sorption within the fractures was not considered in the Culebra transport calculations. Data in Tables E-11 and E-12, however, could be used to estimate the additional amount of radionuclide retardation provided by the fracture linings, using equations in Section 3.3.4.

Distribution coefficients, K_d , and a corresponding mass-specific surface area, a_m , have been estimated for clay minerals in the dolomite fractures. For Case IIA, the K_d values range from 10 mL/g for U, Np, Pb, and Ra to 200 mL/g for Pu and Th and 300 mL/g for Am. For Cases IIB and IIC, the K_d values range from 1 mL/g for U and Np to 5 mL/g for Pb and Ra and 100 mL/g for Pu, Am, and Th. The surface area is estimated to be $a_m = 50 \text{ m}^2/\text{g}$. Distribution coefficients are converted to an area-specific form using the relation $K_a = K_d/a_m$. This form emphasizes the importance of the fracture surface area in

Table E-10. Estimated Matrix K_d Values for Transport Calculations in the Culebra Dolomite (mL/g)

| <u>Case</u> | <u>Pu</u> | <u>Am</u> | <u>Cm</u> | <u>U</u> | <u>Np</u> | <u>Pb,Ra</u> | <u>Th</u> |
|----------------------------|-----------|-----------|-----------|----------|-----------|--------------|-----------|
| Case I | 100 | 200 | (200) | 1 | (1) | (1) | (100) |
| Case IIA | 50 | 200 | (200) | 1 | (1) | (0.1) | (50) |
| Cases IIB, IIC,
and IID | 25 | 100 | (100) | 1 | (1) | (0.05) | (25) |

Table E-11. Estimated K_d Values for Clays of the Culebra Dolomite (mL/g)

| <u>Case</u> | <u>Pu</u> | <u>Am</u> | <u>Cm</u> | <u>U</u> | <u>Np</u> | <u>Pb,Ra</u> | <u>Th</u> |
|----------------------------|-----------|-----------|-----------|----------|-----------|--------------|-----------|
| Case I | 300 | 500 | (500) | 10 | (10) | (100) | 300 |
| Case IIA | 200 | (300) | (300) | 10 | (10) | (10) | (200) |
| Cases IIB, IIC,
and IID | (100) | (100) | (100) | (1) | (1) | (5) | (100) |

() = value poorly constrained by available data; estimated by assumption of similar behavior to homolog element.

Table E-12. Estimated K_a Values for Transport Calculations in the Fractures of the Culebra Dolomite (mL/m²)^a

| <u>Case</u> | <u>Pu</u> | <u>Am</u> | <u>Cm</u> | <u>U</u> | <u>Np</u> | <u>Pb,Ra</u> | <u>Th</u> |
|----------------------------|-----------|-----------|-----------|----------|-----------|--------------|-----------|
| Case I | 6 | 10 | (10) | 0.2 | (0.2) | 2 | 6 |
| Case IIA | 6 | (6) | (6) | 0.2 | (0.2) | (0.2) | (6) |
| Cases IIB, IIC,
and IID | (2) | (2) | (2) | (0.02) | (0.02) | (0.1) | (2) |

a. Values are converted to units of cm by multiplying by factor of 10^{-4} cm²/m².

determining the net amount of sorption. After conversion, the distribution coefficients K_a for Case IIA range from 2×10^{-5} to 6×10^{-4} cm, and those for Cases IIB, IIC, and IID range from 2×10^{-6} to 2×10^{-4} cm.

The volume-specific fracture-surface area a_v of the fractured rock enters the retardation factor R_a by the relation $R_a = 1 + K_a a_v / \phi$, where ϕ is the fracture porosity. The surface area a_v is difficult to estimate. Mineral-surface alterations and fracture-fill materials can drastically influence this quantity. Measurements are insufficient at this time to permit a confident estimate, and, consequently, this report has adopted a conservative approximation. Assuming that a smooth surface separates fractures and matrix, the volume-specific fracture-surface area may be written $a_v = 3(1-\phi)/L'$, where $2L'$ is the fracture separation. The first quantity on the right-hand side represents a geometric factor. Its value (3) indicates a spherical model of the rock matrix. Had the model described plane parallel fractures of separation $2L'$, then the geometric factor would have been unity.

The smooth-surface assumption for the fracture surface area permits the calculation of fracture retardations. For Case IIA, where $2L' = 2$ m, fracture retardations R_a range from 1.04 for U, Np, Pb, and Ra to 2.20 for Am, and for Cases IIB, IIC, and IID, where $2L' = 7$ m, from 1.001 for U and Np to 1.114 cm for Pu, Am, and Th. Compared with the retardation factors R for the matrix, such values indicate negligible sorption within the fractures. Consequently, the analysis has assumed $K_a = 0$ and $R_a = 1$ for all species in all Case II simulations.

Rationale for Choices of Recommended K_d Values. In general, the recommended K_d values are lower than those listed in Tables 3-14 and 3-15. Many of the K_d 's reported in the tables for the actinides are in the range of 10,000 to 100,000 mL/g. The significance of such high values is discounted for the reasons given in Appendix D.2.3.

The uncertainties in the composition of water in the Culebra Dolomite that will be produced by mixing fluids from the repository and aquifer require that large ranges of pH, Eh, organic content, and carbonate content of the ground waters be considered in choosing K_d values. These possible variations in

solution chemistry could result in order-of-magnitude changes of the K_d 's from the values obtained in the experimental studies listed in Tables 3-14 and 3-15.

The data for simple systems discussed in Section 3.3.4 suggest that the amount of sorption of actinides onto either clays or dolomite of the Culebra Dolomite could be several orders of magnitude less than that suggested by the K_d data in Tables 3-14 and 3-15 because of these changes in solution composition. Although it is possible that under some extreme conditions, the K_d 's will be close to zero (see Figures 3-20 to 3-23), there is evidence that some sorption will occur; therefore, the K_d 's were assumed not to be zero. In general, it was assumed that K_d 's in Case II would be lower than those in Culebra waters (Case I), and that K_d 's for clays would be higher than those for dolomite. The K_d 's for Case IIA were chosen to represent conditions under which the solution chemistry is dominated by the influx of inorganic salts from the Salado and Castile Fms. K_d values in Cases IIB, IIC, and IID include the additional effects of organic ligands, which form complexes that do not sorb. The K_d values chosen for each element are explained further below.

Plutonium, Americium, and Curium. K_d values for plutonium are decreased from the values in Tables 3-14 and 3-15 because of the potential effect of carbonate complexation and competition for sorption sites by competing cations. K_d values for americium are decreased from values listed in the tables because of the potential effects of organic complexation and competition. K_d values for curium were decreased from the values listed in Tables 3-14 and 3-15 based on the assumption of behavior similar to Am and Eu.

Uranium and Neptunium. In general, low K_d 's for uranium and neptunium have been measured in waters relevant to the WIPP. Low values ($K_d = 1$ or 10) have been assumed here to account for the possible effects of complexation and competition.

Thorium. There are very few data for thorium under conditions relevant to the WIPP. Thorium K_d values were estimated from data for plutonium, a reasonable homolog element (Krauskopf, 1986). Data describing sorption of Th onto kaolinite (Riese, 1982) suggest that high concentrations of Ca and Mg

will prevent significant amounts of sorption onto clays in the repository. Stability constants for organo-thorium complexes suggest that organic complexation could inhibit sorption (Langmuir and Herman, 1980).

Radium and Lead. There are no data describing sorption of radium or lead onto dolomite under conditions relevant to the WIPP. For this report, sorption in the dolomite matrix was assumed to occur on trace amounts of clay. Some data (Riese, 1982; Tien et al., 1983) suggest that Ra will sorb onto clays but that high concentrations of Ca and Mg will inhibit sorption. Langmuir and Riese (1985) presented theoretical and empirical arguments that suggest that Ra will be coprecipitated in calcite and gypsum in solutions close to saturation with respect to these minerals. Under certain mixing ratios, this mechanism may retard radium migration in the Culebra Dolomite. This report assumes that the behavior of radium and lead would be similar, based on homologous behavior in other environments (Tien et al., 1983).

REFERENCES

- Allison, G.B., 1982. "The Relationship Between ^{18}O and Deuterium in Water in Sand Columns Undergoing Evaporation," Journal of Hydrology, vol. 55, pp. 163-169.
- Allison, G.B., W.J. Stone and M.W. Hughes, 1985. "Recharge in Karst and Dune Elements of a Semi-Arid Landscape as Indicated by Natural Isotopes and Chloride," Journal of Hydrology, vol. 76, pp. 1-25.
- Anderson, D.E., 1981. "Diffusion in Electrolyte Mixtures" in A.C. Lasaga and R.J. Kirkpatrick, eds., Kinetics of Geochemical Processes, Reviews in Mineralogy, Vol. 8, Mineralogical Society of America, pp. 211-261.
- Arguello, J.G., 1988. WIPP Panel Entryway Seal--Numerical Simulation of Seal Composite Iteration for Preliminary Design Evaluation, SAND87-2804. Sandia National Laboratories, Albuquerque, NM.
- Arguello, J.G., and T.Torres, 1988. WIPP Panel Entryway Seal--Numerical Simulation of Seal Component/Formation Interaction for Preliminary Design Evaluation, SAND87-2591. Sandia National Laboratories, Albuquerque, NM.
- Baar, C.A., 1977. Applied Salt-Rock Mechanics 1: The In-Situ Behavior of Salt Rocks. Elsevier, Amsterdam.
- Bachman, G.O., 1980. Regional Geology and Cenozoic History of the Pecos Region, Southeastern New Mexico. U.S. Geological Survey Open-File Report 80-1099.
- Bachman, G.O., 1981. Geology of Nash Draw, Eddy County, New Mexico. U.S. Geological Survey Open-File Report 81-31.
- Bachman, G.O., 1985. Assessment of Near-Surface Dissolution At and Near the Waste Isolation Pilot Plant (WIPP), Southeastern New Mexico, SAND84-7178. Sandia National Laboratories, Albuquerque, NM.
- Bachman, G.O., 1987. Karst in Evaporites in Southeastern New Mexico, SAND86-7078. Sandia National Laboratories, Albuquerque, NM.
- Baes, C.F., III, R.D. Sharp, A.L. Sjoreen, and R.W. Shor, 1984. A Review and Analysis of Parameters for Assessing Transport of Environmentally Released Radionuclides through Agriculture, ORNL-5786. Oak Ridge National Laboratory, Oak Ridge, TN.
- Barker, J.A., and S.S.D. Foster, 1981. "A Diffusion Exchange Model for Solute Movement in Fissured Porous Rock," Quarterly Journal of Engineering Geology, London, vol. 14.
- Barr, G.E., W.B. Miller, and D.D. Gonzalez, 1983. Interim Report on the Modeling of the Regional Hydraulics of the Rustler Fm., SAND83-0391. Sandia National Laboratories, Albuquerque, NM.
- Barrows, L.J., 1982. "WIPP Geohydrology--The Implications of Karst" in R.H. Neill, J.K. Channell, L. Chaturvedi, M.S. Little, K. Rehfeldt, and P.

- Spiegler, 1983: Evaluation of the Suitability of the WIPP Site, EEG-23. New Mexico Environmental Evaluation Group, Santa Fe, NM.
- Barthel, J.M., 1989. "Supercompaction and Repackaging Facility for Rocky Flats Plant Transuranic Waste," Briefing Handout, Rockwell International Rocky Flats Plant, January 1989.
- BDM Corporation, 1978. Consequence Assessment of Radionuclide Release from the WIPP Repository to the Environment, BDM/TAC-78-407-TR. BDM Corporation, Albuquerque, NM.
- Bear, J., 1972. Dynamics of Fluids in Porous Media. American Elsevier Publishing Company, NY.
- Bear, J., and A. Verruijt, 1987. Modeling Groundwater Flow and Pollution. D. Reidel Publishing Company, Dordrecht.
- Beauheim, R.L., 1986. Hydraulic-Test Interpretations for Well DOE-2 at the Waste Isolation Pilot Plant (WIPP) Site, SAND86-1364. Sandia National Laboratories, Albuquerque, NM.
- Beauheim, R.L., 1987a. Analysis of Pumping Tests of the Culebra Dolomite Conducted at the H-3 Hydropad at the Waste Isolation Pilot Plant (WIPP) Site, SAND86-2311. Sandia National Laboratories, Albuquerque, NM.
- Beauheim, R.L., 1987b. Interpretation of the WIPP-13 Multipad Pumping Test of the Culebra Dolomite at the Waste Isolation Pilot Plant (WIPP) Site, SAND87-2456. Sandia National Laboratories, Albuquerque, NM.
- Beauheim, R.L., 1987c. Interpretations of Single-Well Hydraulic Tests Conducted At and Near the Waste Isolation Pilot Plant (WIPP) Site, 1983-1987, SAND87-0039. Sandia National Laboratories, Albuquerque, NM.
- Beauheim, R.L., 1988. Scale Effects in Well Testing in Fractured Media, SAND87-1955C. For presentation at the Fourth Canadian/American Conference on Hydrogeology: Fluid Flow, Heat Transfer, and Mass Transport in Fractured Rocks, Banff, Alberta, Canada.
- Beauheim, R.L., 1989a (in preparation). Interpretations of Single-Well Hydraulic Tests of the Culebra Dolomite Conducted in the Vicinity of the Waste Isolation Pilot Plant (WIPP) Site, 1988-1989, SAND89-0869. Sandia National Laboratories, Albuquerque, NM.
- Beauheim, R.L., 1989b (in preparation). Interpretations of Hydraulic-Interference Tests of the Culebra Dolomite Conducted at the H-2, H-4, H-5, H-6, H-7, and H-9 Hydropads at the Waste Isolation Pilot Plant (WIPP) Site, 1981-1987, SAND89-0870. Sandia National Laboratories, Albuquerque, NM.
- Beauheim, R.L., B.W. Hassinger, and J.A. Klaiber, 1983. Basic Data Report for Borehole Cabin Baby-1 Deepening and Hydrologic Testing, WTDS-TME-020. U.S. Department of Energy, Albuquerque, NM.

- Bechtel National Inc., 1985. Quarterly Geotechnical Data Report, DOE-WIPP-221. U.S. Department of Energy, Carlsbad, NM.
- Bechtel National Inc., 1986. Quarterly Geotechnical Field Data Report, DOE-WIPP-213. U.S. Department of Energy, Carlsbad, NM.
- Bechtel National Inc., 1987. "Construction Contract Package CCP-34C, Development for Air Intake Shaft (AIS)," Waste Isolation Pilot Plant, U.S. Department of Energy, Carlsbad, NM.
- Bell and Murphy and Associates, Inc., 1979. Geophysical Investigation of the Waste Isolation Pilot Plant, Eddy County, New Mexico. Report to the U.S. Department of Energy, Carlsbad, NM.
- Bertram-Howery, S.G., and R.L. Hunter, eds., 1989. Plan for Disposal-System Characterization and Long-Term Performance Evaluation of the Waste Isolation Pilot Plant, SAND89-0178. Sandia National Laboratories, Albuquerque, NM.
- Bertram-Howery, S.G., M.G. Marietta, R.L. Hunter, M.S.Y. Chu, L.H. Brush, R.P. Rechard, and K.F. Brinster, 1989 (in preparation). Forecast of the Comparison to 40 CFR Part 191, Subpart B and Methodology Demonstration for the Waste Isolation Pilot Plant, SAND88-1452. Sandia National Laboratories, Albuquerque, NM.
- Bodine, M.W., 1978. "Clay-Mineral Assemblages from Drill Core of Ochoan Evaporites, Eddy County" in G.S. Austin, ed., Geology and Mineral Deposits of Ochoan Rocks in Delaware Basin and Adjacent Areas, New Mexico Bureau of Mines and Mineral Resources Circ. 159, pp. 21-31.
- Bodine, M.W., B.F. Jones, and S.J. Lambert, 1989. "Normative Analysis of Groundwaters from the Rustler Fm. Associated with the Waste Isolation Pilot Plant (WIPP), Southeastern New Mexico" in M.D. Siegel, S.J. Lambert, and K.L. Robinson, eds., Hydrochemical Studies of the Rustler Fm. and Related Rocks in the WIPP Area, Southeastern New Mexico, SAND88-0196. Sandia National Laboratories, Albuquerque, NM.
- Borns, D.J., 1985. Marker Bed 139: A Study of Drillcore from a Systematic Array, SAND85-0023. Sandia National Laboratories, Albuquerque, NM.
- Borns, D.J., and J.C. Stormont, 1988. An Interim Report on Excavation Effect Studies at the Waste Isolation Pilot Plant: The Delineation of the Disturbed Rock Zone, SAND87-1375. Sandia National Laboratories, Albuquerque, NM.
- Borns, D.J., and J.C. Stormont, 1989. "The Delineation of the Disturbed Rock Zone Surrounding Excavations in Salt," Proceedings of the 30th U.S. Rock Mechanics Symposia, Balkeema.
- Borns, D.J., L.J., Barrows, D.W. Powers, and R.P. Snyder, 1983. Deformation of Evaporites Near the Waste Isolation Pilot Plant (WIPP) Site, SAND82-1069. Sandia National Laboratories, Albuquerque, NM.

- Brace, W.F., B.W. Paulding, and C. Scholz, 1966. "Dilatancy in the Fracture of Crystalline Rocks," Journal of Geophysical Research, vol. 71.
- Brady, B.H.G., and E.T. Brown, 1985. Rock Mechanics for Underground Mining, George Allen and Unwin, London.
- Bredehoeft, J.D., 1988. "Will Salt Repositories be Dry?" EOS, Transactions, American Geophysical Union, vol. 69, no. 9.
- Brookins, D.G., and S.J. Lambert, 1988. "WIPP Site Studies: Secondary Selenite Veins in the Rustler Formation and Dewey Lake Red Beds," Materials Research Society Symp. Proc. Vol. 112, pp. 233-241.
- Brush, L.H., 1988. Feasibility of Disposal of High-Level Radioactive Wastes into the Seabed: Review of Laboratory Investigations of Radionuclide Migration Through Deep-Sea Sediments, SAND87-2438. Sandia National Laboratories, Albuquerque, NM.
- Buck, A.D., 1985. Development of a Sanded Nonsalt Expansive Grout for Repository Sealing Application, Miscellaneous Paper SL-85-6. Department of the Army, Waterways Experimental Station, Vicksburg, MS.
- Bush, D.D., and S. Piele, 1986. A Full Scale Borehole Sealing Test in Salt Under Simulated Downhole Conditions: Volume 1, BMI/ONWI-573(2), Office of Nuclear Waste Isolation, Battelle Memorial Institute, Columbus, OH.
- Butcher, B.M., 1989 (in preparation). Waste Isolation Pilot Plant (WIPP) Simulated Waste Compositions and Properties, SAND89-0372. Sandia National Laboratories, Albuquerque, NM.
- Campbell, J.E., D.E. Longsine, and R.M. Cranwell, 1981. Risk Methodology for Geologic Disposal of Radioactive Waste: The NWFT/DVM Computer Code User's Manual, SAND81-0886, NUREG/CR-2081. Sandia National Laboratories, Albuquerque, NM.
- Campbell, J.E., D.E. Longsine, and M. Reeves, 1986. Risk Methodology for Geologic Disposal of Radioactive Waste: The Distributed Velocity Method of Solving the Convective-Dispersion Equation, SAND80-0717, NUREG/CR-1376, Sandia National Laboratories, Albuquerque, NM.
- Campbell, J.E., P.C. Kaestner, B.S. Langkopf, and R.B. Lantz, 1979. Risk Methodology for Geologic Disposal of Radioactive Waste: The Network Flow and Transport (NWFT) Model, SAND79-1920, NUREG/CR-1190. Sandia National Laboratories, Albuquerque, NM.
- Carrera, J., 1984. "Estimation of Aquifer Parameters Under Transient and Steady State Conditions," Ph.D. Dissertation, Hydrology Dept., U. of Arizona, Tucson, AZ.
- Carrera, J., and S.P. Neuman, 1986. "Estimation of Aquifer Parameters Under Transient and Steady State Conditions: 1) Maximum Likelihood Method Incorporating Prior Information," Water Resources Research, vol. 22, pp. 144-210.

- Carslaw, H.S., and J.C. Jaeger, 1959. Conduction of Heat in Solids, Second Edition, Oxford University Press.
- Carter, R.D., and C.W. Tracy, 1960. "An Improved Method for Calculating Water Influx," Transactions of the Society of Petroleum Engineers, American Institute of Mining Engineers, vol. 219, pp. 415-417.
- Cauffman, T.L., and A.M. LaVenue, (in preparation). Ground-Water Flow Modeling of the Culebra Dolomite at the Waste Isolation Pilot Plant (WIPP) Site, vol. 2, Data Base.
- Channell, J.K., 1982. Calculated Radiation Doses from Radionuclides Brought to the Surface if Future Drilling Intercepts the WIPP Repository and Pressurized Brine, EEG-11. New Mexico Environmental Evaluation Group, Santa Fe, New Mexico.
- Chapman, J.B., 1986. Stable Isotopes in Southeastern New Mexico Groundwater: Implications for Dating Recharge in the WIPP Area, EEG-35. New Mexico Environmental Evaluation Group, Santa Fe, New Mexico.
- Chapman, J.B., 1988. Chemical and Radiochemical Characteristics of Groundwater in the Culebra Dolomite, Southeastern New Mexico, EEG-39. New Mexico Environmental Evaluation Group, Santa Fe, NM.
- Chapman, N.A., and J.A.T. Smellie, 1986. "Natural Analogues to the Conditions around a Final Repository for High-Level Radioactive Waste," Chemical Geology, vol. 55, no. 3/4.
- Chaturvedi, L., and J.K. Channell, 1985. The Rustler Formation as a Transport Medium for Contaminated Groundwater, EEG-32. New Mexico Environmental Evaluation Group, Santa Fe, New Mexico.
- Choppin, G.R., and B. Allard, 1985. "Complexes of Actinides with Naturally Occurring Organic Compounds" in A.J. Freeman and C. Keller, eds., Handbook on the Physics and Chemistry of the Actinides, Elsevier Science Publishing Co., New York, NY.
- Christensen, C.L., and E.W. Petersen, 1981. The Bell Canyon Test Summary Report, SAND80-1375. Sandia National Laboratories, Albuquerque, NM.
- Clark, J.W., W. Viessman, M.J. Hammer, 1977. Water Supply and Pollution Control. IEP--A Dun-Donnelley Publisher, New York, NY.
- Clements, T.L., Jr., and D.E. Kudera, 1985. TRU Waste Sampling Program, Volumes 1 and 2, EGG Report EGG-WM-6503. Idaho National Engineering Laboratory, Idaho Falls, ID.
- Coates, D.F., 1981. "Rock Mechanics Principles, CANMET, Energy Mines and Resources Canada, Ottawa, Monograph 874 Peng, S.S., 1978. Coal Mine Ground Control, John Wiley and Sons, New York, NY.
- Cole, C.R., and F.W. Bond, 1980. Assessment of the Effectiveness of Geologic Isolation Systems, Comparison of INTERA and WISAP Model Application, PNL-3070. Pacific Northwest Laboratory, Richland, WA.

- Cooley, C.H., S.W. Butters, and A.H. Jones, 1978. Gas Permeability of SENM Rock Salt, SAND78-2287. Sandia National Laboratories, Albuquerque, NM.
- Coons W., A. Bergstrom, P. Gnirk, M. Gray, B. Knecht, R. Pusch, J. Steadman, B. Stillborg, M. Tokonami, and M. Vaajasaari, 1987. State-of-the-Art Report on Potentially Useful Materials for Sealing Nuclear Waste Repositories, Stripa Project Report 87-12, Swedish Nuclear Fuel and Waste Management Co., Stockholm, Sweden.
- Cooper, J.B., and V.M. Glanzman, 1971. Geohydrology of Project Gnome Site, Eddy County, New Mexico, U.S. Geological Survey Professional Paper 712-A, U.S. Geological Survey, Washington, D.C.
- Costin, L.S., and W.R. Wawersik, 1980. Creep Healing of Fractures in Rock Salt, SAND80-0392. Sandia National Laboratories, Albuquerque, NM.
- Craig, H., L.I. Gordon, and Y. Horibe, 1963. "Isotopic Exchange Effects in the Evaporation of Water, I: Low-Temperature Experimental Results," Journal of Geophysical Research, vol. 68, pp. 5079-5087.
- D'Appolonia Consulting Engineers, Inc., 1981. Modeling Verification Studies Long-Term Waste Isolation Assessment, Waste Isolation Pilot Plant (WIPP) Project, Southeastern New Mexico. Report for U.S. Department of Energy, Carlsbad, NM.
- D'Appolonia Consulting Engineers, Inc., 1982. Data File Report - ERDA-6 and WIPP-12 Testing. Report for Westinghouse Electric Corporation and the U.S. Department of Energy, Albuquerque, NM.
- D'Appolonia Consulting Engineers, Inc., 1983. Data File Report: ERDA-6 and WIPP-12 Testing, Addendum 2. Report for Westinghouse Electric Corporation and the U.S. Department of Energy, Albuquerque, NM.
- Davies, P.B., 1983. "Assessing the Potential for Deep-Seated Salt Dissolution and Subsidence at the Waste Isolation Pilot Plant (WIPP)." Unpublished manuscript presented at the State of New Mexico Environmental Evaluation Group Conference: "WIPP Site Suitabilities for Radioactive Waste Disposal," Carlsbad, NM, May 12-13, 1983.
- Davies, P.B., 1986. "Pleistocene-to-Present Flow-System Evolution in the Northern Delaware Basin, Southeastern New Mexico--Analysis Using Transient Cross-Sectional Flow Simulations," GSA Abstracts with Program vol. 18, p. 580.
- Davies, P.B., 1987. "Modeling Areal, Variable-Density, Ground-Water Flow Using Equivalent Freshwater Head--Analysis of Potentially Significant Errors," Proc. NWWA Conference on Solving Ground Water Problems with Models, 2, February 10-12, 1987, Denver, CO, pp. 888-903.
- Davies, P.B., 1989 (in press). Variable-Density Ground-Water Flow and Paleohydrology in the Region Surrounding the Waste Isolation Pilot Plant (WIPP), Southeastern New Mexico, U.S. Geological Survey Open-File Report 88-490, U.S. Geological Survey, Albuquerque, NM.

- de Marsily, G., 1986. Quantitative Hydrogeology. Academic Press, New York, NY.
- Deal, D.E., and J.B. Case, 1987. Brine Sampling and Evaluation Program, Phase I Report, DOE-WIPP-87-008. U.S. Department of Energy, Carlsbad, NM.
- Deal, D.E., J.B. Case, R.M. Deshler, P.E. Drez, J. Myers, and J.A. Tyburski, 1989. Brine Sampling and Evaluation Program Phase II Report, DOE-WIPP-87-010. U.S. Department of Energy, Carlsbad, NM.
- Dennehy, K.F., 1982. Results of Hydrologic Tests and Water-Chemistry Analyses, Wells H-6A, H-6B, and H-6C, at the Proposed Waste Isolation Pilot Plant Site, Southeastern New Mexico, U.S. Geological Survey Water-Resources Investigations 82-8, Albuquerque, NM.
- Dennehy, K.F., and J.W. Mercer, 1982. Results of Hydrologic Tests and Water-Chemistry Analyses, Wells H-5A, H-5B, and H-5C, at the Proposed Waste Isolation Pilot Plant Site, Southeastern New Mexico, U.S. Geological Survey Water-Resources Investigations 82-19, Albuquerque, NM.
- Dillon, R.T., R.B. Lantz, and S.B. Pahwa, 1978. Risk Methodology for Geologic Disposal of Radioactive Waste: The Sandia Waste Isolation Flow and Transport (SWIFT) Model, SAND78-1267. Sandia National Laboratories, Albuquerque, NM.
- Dodson, C.R., and M.B. Standing, 1944. "Pressure-Volume-Temperature and Solubility Relations for Natural-gas Water Mixtures, Drill. and Prod. Prac.", American Petroleum Institute.
- Domenico, P.A., 1972. Concepts and Models in Groundwater Hydrology. McGraw-Hill Book Company, New York, NY.
- Dosch, R.G., 1979. "Radionuclide Migration Studies Associated with the WIPP Site in Southern New Mexico" in G. J. McCarthy, ed., Scientific Basis for Nuclear Waste Management. Plenum Publishing Company, New York, NY, vol. 1, pp. 395-398.
- Dosch, R.G., 1981. Solubility and Sorption Characteristics of Uranium (VI) Associated with Rock Samples and Brines/Groundwaters from WIPP and NTS, SAND80-1595. Sandia National Laboratories, Albuquerque, NM.
- Dosch, R.G., and A.W. Lynch, 1978. Interaction of Radionuclides with Geomedia Associated with the Waste Isolation Pilot Plant (WIPP) in New Mexico, SAND78-0297. Sandia National Laboratories, Albuquerque, NM.
- Drever, J.I., 1982. The Geochemistry of Natural Waters. Prentice Hall, pp. 78-89.
- Driscoll, F.G., 1986. Groundwater and Wells. Johnson Division, St. Paul, MN.
- Dusseault, M.B., L. Rothenburg, and D.Z. Mraz, 1987. "The Design of Openings Using Multiple Mechanism Viscoplastic," 28th US Symposium on Rock Mechanics, pp. 633-642.

- Eisenbud, M., H. Petrow, R.T. Drew, F.X. Roser, G. Kegel, and T.L. Cullen, 1964. "Naturally Occurring Radionuclides in Foods and Waters from the Brazilian Areas of High Radioactivity" in J.A.S. Adams and W.M. Lowder, eds., The Natural Radiation Environment, University of Chicago Press, Chicago, IL.
- Elnaggar, H.A., G.M. Karadi, and R.J. Krizek, 1974. "Non-Darcian Flow in Clay Soils" in R.B. Dowdell, and H.W. Stoll, eds., Flow, Its Measurement and Control In Science and Industry, vol. 1, Instrument Society of America, Pittsburgh, Pa.
- Erickson, K.L., M.S.Y. Chu, M.D. Siegel, and W. Beyeler, 1986. "Approximate Methods to Calculate Radionuclide Discharges for Performance Assessment of HLW Repositories in Fractured Rock" in R.G. Post, ed., Waste Management 86, vol. 2, University of Arizona, pp. 377-386.
- Evans, G.V., R.L. Otlet, R.A. Downing, R.A. Monkhouse, and G. Rae, 1979. "Some Problems in the Interpretation of Isotope Measurements in United Kingdom Aquifers," Proceedings of the International Symposium on Isotope Hydrology, Int. Atomic Energy Agency STI/PUB 493, vol. 2, Vienna, pp. 679-706.
- Eyler, L.L., and N.J. Lombardo, 1982. "Analytical Modeling of Large Particle Coal Transport" in E. Hayied, Slurry Transportation and Pneumatic Handling," Winter Annual Meeting, ASME, Phoenix, AZ, November 14-19, 1982, The American Society of Mechanical Engineers, New York, NY, 1982.
- Ezrokhi, L.L., 1952. "Viscosity of Aqueous Solutions of the Individual Salts of Seawater Systems," Journal of Applied Chemistry USSR, vol. 25, pp. 917-926.
- Finley, N.C. and M. Reeves, 1981. SWIFT Self-Teaching Curriculum: Illustrative Problems to Supplement the User's Manual for the Sandia Waste-Isolation Flow and Transport Model (SWIFT), NUREG/CR-1968, SAND81-0410, Sandia National Laboratories, Albuquerque, NM.
- Freeze, R.A., and J.A. Cherry, 1979. Groundwater. Prentice-Hall, Inc., Englewood Cliffs, NJ.
- Frick, T.C., and R.W. Taylor, eds., 1962. Petroleum Production Handbook, vol. II, Society of Petroleum Engineers of AIME.
- Fuenkajorn, K., and J.J.K. Daemen, 1988. Borehole Closure in Salt, NUREG/CR-5243, UniversityS. Nuclear Regulatory Commission, Washington, D.C.
- Garrels, R.M., and C.L. Christ, 1965. Solutions, Minerals, and Equilibria, Freeman, Cooper, and Co., San Francisco, CA.
- Gonzalez, D.D., 1983. Ground Water Flow in the Rustler Fm., Waste Isolation Pilot Plant (WIPP), Southeast New Mexico (SENM): Interim Report, SAND82-1012. Sandia National Laboratories, Albuquerque, NM.

- Griswold, G.B., 1977. Site Selection and Evaluation Studies of the Waste Isolation Pilot Plant (WIPP), Los Medanos, Eddy County, New Mexico, SAND77-0946. Sandia National Laboratories, Albuquerque, NM.
- Haberman, J.H., and D.J. Frydrych, 1988. "Corrosion Studies of A216 Grade WCA Steel in Hydrothermal Magnesium-containing Brines" in M. J. Apted and R. E. Westerman, eds., Scientific Basis for Nuclear Waste Management XI, Materials Research Society, Pittsburgh, PA.
- Haug, A., V.A. Kelley, A.M. LaVenue, and J.F. Pickens, 1987. Modeling of Ground-Water Flow in the Culebra Dolomite at the Waste Isolation Pilot Plant (WIPP) Site, SAND86-7167. Sandia National Laboratories, Albuquerque, NM.
- Hausner, H.H., and M. Kumar Mal, 1982. Handbook of Powder Metallurgy, Chemical Publishing Co., Inc.
- Hayes, K.F., C. Papelis, and J.O. Leckie, 1988. "Modeling Ionic Strength Effects on Anion Adsorption at Hydrous Oxide/Solution Interfaces," Journal of Colloid and Interface Science, vol. 125, pp. 717-726.
- Healy, J.W., 1974. Proposed Interim Standard for Plutonium in Soils, LA-5483-MS pp. 7-76. Los Alamos Scientific Laboratory, Los Alamos, NM.
- Helgeson, H.C., 1968. "Evaluation of Irreversible Reactions in Geochemical Processes Involving Minerals and Aqueous Solutions--I. Thermodynamic Relations," Geochimica et Cosmochimica Acta, vol. 32, pp. 853-877.
- Higgo, J.J., L.V.C. Rees, T.G. Coles, and D.S. Cronan, 1987. Diffusion of Radionuclides Through Deep-Sea Sediments, DOE/RW87.053. Department of the Environment, London, UK.
- Hiss, W.L., 1976. "Stratigraphy and Ground-Water Hydrology of the Capitan Aquifer, Southeastern New Mexico and West Texas," Ph.D. Dissertation, University of Colorado, Boulder, CO.
- Holcomb, D.J., and M. Shields, 1987. Hydrostatic Creep Consolidation of Crushed Salt with Added Water, SAND87-1990. Sandia National Laboratories, Albuquerque, NM.
- Holt, R.M., and D.W. Powers, 1988. Facies Variability and Post-Depositional Alteration Within the Rustler Formation in the Vicinity of the Waste Isolation Pilot Plant, Southeastern New Mexico, DOE/WIPP-88-004. U.S. Department of Energy, Carlsbad, NM.
- Holt, R.M., and D.W. Powers, 1986. Geotechnical Activities in the Exhaust Shaft, DOE-WIPP-86-008. U.S. Department of Energy, Carlsbad, NM.
- Holt, R.M., and D.W. Powers, 1984. Geotechnical Activities in the Waste Handling Shaft, WTSD-TME-038. U.S. Department of Energy, Carlsbad, NM.
- Holt, R.M., D.W. Powers, R.L. Beauheim, and M.E. Crawley, 1989 (in preparation). Conceptual Hydrogeological Model of the Rustler Formation

- in the Vicinity of the Waste Isolation Pilot Plant Site, Southeastern New Mexico, SAND89-0862, Sandia National Laboratories, Albuquerque, NM.
- Hunter, R.L., 1985. A Regional Water Balance for the Waste Isolation Pilot Plant (WIPP) Site and Surrounding Area, SAND84-2233. Sandia National Laboratories, Albuquerque, NM.
- Hunter, R.L., 1989 (in preparation). WIPP Performance Assessment: Scenarios for Analysis and Further Screening, SAND88-0050. Sandia National Laboratories, Albuquerque, NM.
- ICRP, 1959. "Report of the ICRP Committee II on Permissible Dose for Internal Radiation," International Commission on Radiological Protection. ICRP Publication 2, Pergamon Press, New York, NY.
- ICRP, 1975. Report of the Task Group on Reference Man: Anatomical, Physiological, and Metabolic Characteristics, Pergamon Press, New York, NY.
- ICRP, 1977. Annals of the ICRP, ICRP Publication 26, Recommendations of the International Commission on Radiological Protection. Pergamon Press, New York, NY.
- ICRP, 1979. Annals of the ICRP, ICRP Publication 30, Limits for Intake of Radionuclides by Workers. Pergamon Press, New York, NY.
- INTERA Environmental Consultants, Inc., 1978. Radiological Waste Storage Analysis, Consultant's report prepared for Sandia Laboratories, INTERA, Houston, TX.
- International Association of Drilling Contractors, Rotary Drilling Committee, 1974, IADC Drilling Manual, ninth edition.
- Isaacson, R.E., L.E. Brownell, R.W. Nelson, and E.L. Roetman, 1974. "Soil-Moisture Transport in Arid Site Vadose Zones," Proc. International Symposium on Isotope Hydrology, 1973, Int. Atomic Energy Agency (Vienna), p. 97-114.
- Jackson, K.J., and T.J. Wolery, 1985. "Extension of the EQ3/6 Computer Codes to Geochemical Modeling of Brines" in C.M. Jantzen, J.A. Stone, and R.C. Ewing, eds., Scientific Basis for Nuclear Waste Management VIII, Symposium held November 26-29, 1984, Boston, MA, U.S.A., Materials Research Society Symposia Proceedings, Vol. 44, Materials Research Society, Pittsburgh, PA.
- Katsube, T.J., T.W. Melnyk, and J.P. Hume, 1986. Pore Structure from Diffusion in Granitic Rocks, Technical Record TR-381, Atomic Energy of Canada, Ltd.
- Kaufman, D.W., ed., 1960. Sodium Chloride, the Production and Properties of Salt and Brine, Monograph no. 145, American Chemical Society, Washington, DC, p. 612.
- Kelley, V.A., and J.F. Pickens, 1986. Interpretation of the Convergent-Flow Tracer Tests Conducted in the Culebra Dolomite at the H-3 and H-4

- Hydropads at the Waste Isolation Pilot Plant (WIPP) Site, SAND86-7161. Sandia National Laboratories, Albuquerque, NM.
- Kent, D.B., V.S. Tripathi, N.B. Ball, and J.O. Leckie, 1988. Surface-Complexation Modeling of Radionuclide Adsorption in Subsurface Environments, NUREG/CR-4807, SAND86-7175. Sandia National Laboratories, Albuquerque, NM.
- Krauskopf, K.B., 1986. "Thorium and Rare-Earth Metals as Analogs for Actinide Elements," Chemical Geology, vol. 55, pp. 323-336.
- Krieg, R.D., 1984. Reference Stratigraphy and Rock Properties for the Waste Isolation Pilot Plant (WIPP) Project, SAND83-1908. Sandia National Laboratories, Albuquerque, NM.
- Krumhansl, J., 1988. Personal communications reported in Technical Progress Report for month ending November 30, 1988, Waste Isolation Pilot Plant, Waste Management Technology Department, Sandia National Laboratories, Albuquerque, NM.
- Kutilek, M., 1972. "Non-Darcian Flow of Water in Soils--Laminar Region, a Review" in Int. Assoc. for Hydraulic Res., ed., Fundamentals of Transport Phenomena in Porous Media, Elsevier Publishing Company, New York, NY.
- Lallemand-Barres, and P. Peaudecerf, 1978. "Recherche des Relations Entre les Valeurs Mesurées de la Dispersivité Macroscopique d'un Milieu Aquifère, Ses Autres Caractéristiques et ales Conditions de Mesure. Etude Bibliographique," Rech. Bull. Bur. Geol. Min. Sér. 2, Sec. III, 4-1978, pp. 277-284.
- Lambe, T.W., and R.V. Whitman, 1979. Soil Mechanics. John Wiley & Sons, New York, NY.
- Lambert, S.J., 1978. "Geochemistry of Delaware Basin Ground Waters" in G.S. Austin, ed., Geology and Mineral Deposits of Ochoan Rocks in Delaware Basin and Adjacent Areas, NM Bur. Mines & Min. Res. Circ. 159, Socorro, NM, pp. 33-38.
- Lambert, S.J., 1983. Dissolution of Evaporites in and around the Delaware Basin, Southeastern New Mexico and West Texas, SAND82-0461. Sandia National Laboratories, Albuquerque, NM.
- Lambert, S.J., 1987. Feasibility Study: Applicability of Geochronologic Methods Involving Radiocarbon and Other Nuclides to the Groundwater Hydrology of the Rustler Formation, SAND86-1054. Sandia National Laboratories, Albuquerque, NM.
- Lambert, S.J., 1989. "Isotopic Constraints on the Rustler and Dewey Lake Groundwater Systems" in M.D. Siegel, S.J. Lambert, and K.L. Robinson, eds., Hydrogeochemical Studies of the Rustler Formation and Related Rocks in the WIPP Area, Southeastern New Mexico, SAND88-0196. Sandia National Laboratories, Albuquerque, NM.

- Lambert, S.J., and D.M. Harvey, 1987. Stable-Isotope Geochemistry of Groundwaters in the Delaware Basin of Southeastern New Mexico, SAND87-0138. Sandia National Laboratories, Albuquerque, NM.
- Lambert, S.J., and J.A. Carter, 1984. Uranium-Isotope Disequilibrium in Brine Reservoirs of the Castile Fm., Northern Delaware Basin, Southeastern New Mexico, I: Principles and Methods, SAND83-0144. Sandia National Laboratories, Albuquerque, NM.
- Lambert, S.J., and J.A. Carter, 1987. Uranium-isotope Systematics in Groundwaters of the Rustler Formation, Northern Delaware Basin, Southeastern New Mexico, SAND87-0388. Sandia National Laboratories, Albuquerque, NM.
- Lambert, S.J., and J.W. Mercer, 1978. Hydrologic Investigations of the Los Medanos Area, Southeastern New Mexico, SAND77-1401. Sandia National Laboratories, Albuquerque, NM.
- Lambert, S.J., and K.L. Robinson, 1984. Field Geochemical Studies of Groundwaters in Nash Draw, Southeastern New Mexico, SAND83-1122. Sandia National Laboratories, Albuquerque, NM.
- Langmuir, D., and A.C. Riese, 1985. "The Thermodynamic Properties of Radium," Geochimica et Cosmochimica Acta, vol. 49, pp. 1593-1601.
- Langmuir, D., and J.S. Herman, 1980. "The Mobility of Thorium in Natural Waters at Low Temperatures," Geochimica et Cosmochimica Acta, vol. 44, pp. 1753-1766.
- Lappin, A. R., 1988. Summary of Site-Characterization Studies Conducted From 1983 Through 1987 at the Waste Isolation Pilot Plant (WIPP) Site, Southeastern New Mexico, SAND88-0157. Sandia National Laboratories, Albuquerque, NM.
- LaVenue, A.M., A. Haug, and V.A. Kelley, 1988. Numerical Simulation of Ground-Water Flow in the Culebra Dolomite at the Waste Isolation Pilot Plant (WIPP) Site: Second Interim Report, SAND88-7002. Sandia National Laboratories, Albuquerque, NM.
- LaVenue, A.M., B.S. RamaRao, and M. Reeves, 1989 (in preparation). Ground-Water Flow Modeling of the Culebra Dolomite at the Waste Isolation Pilot Plant (WIPP) Site, Vol. 1. Model Calibration, Vol. 2. Data Base, SAND89-7068/1, SAND89-7068/2. Sandia National Laboratories, Albuquerque, NM.
- Leckie, J.O., 1989. "Simulations of Distribution Coefficients Using Surface Complexation Models," Appendix C in M.D. Siegel, ed., Progress in Development of a Methodology for Geochemical Sensitivity Analysis for Performance Assessment: Volume 2. Speciation, Sorption, and Transport in Fractured Media, Letter Report to the U.S. Nuclear Regulatory Commission.
- Lee, W.J., 1982. Well Testing. SPE Textbook Series Vol I, Society of Petroleum Engineers of AIME, New York, NY.

- Li, Y., and S. Gregory, 1974. "Diffusion of Ions in Seawater and in Deep-Sea Sediments," Geochimica et Cosmochimica Acta, vol. 38, pp. 703-714.
- Long, J.C.S., J.S. Remer, C.R. Wilson, and P.A. Witherspoon, 1982. "Porous Media Equivalents for Networks of Discontinuous Fractures," Water Resources Research, vol. 18, no. 3.
- Longsine, D.E., E.J. Bonano, and C.P. Harlan, 1987. User's Manual for the NEFTRAN Computer Code, NUREG/CR-4766, SAND86-2405. Sandia National Laboratories, Albuquerque, NM.
- Lowenstein, T.K., 1987. Post-Burial Alteration of the Permian Rustler-Formation Evaporites, WIPP Site, New Mexico, EEG-36. New Mexico Environmental Evaluation Group, Santa Fe, New Mexico.
- Lynch, A.W., and R. G. Dosch, 1980. Sorption Coefficients for Radionuclides on Samples from the Water-Bearing Magenta and Culebra Members of the Rustler Formation, SAND80-1064. Sandia National Laboratories, Albuquerque, NM.
- Martin, W.E. and S.G. Bloom, 1976. "Plutonium Transport and Dose Estimation Models," Transuranium Nuclides in the Environment, Symposium Proceedings, San Francisco, 1975, STI/PUB/410. International Atomic Energy Agency, Vienna.
- Maslov, V.I., K.I. Maslova, and I.N. Verkhovshaya, 1967. "Characteristics of the Radioecological Groups of Mammals and Birds of Biocoenoses with High Natural Radiation" in B. Aberg and F.P. Hungate, eds., Radiological Concentration Processes, Pergamon Press, New York, NY.
- Matalucci, R.V., C.L. Christensen, T.O. Hunter, M.A. Molecke, and D.M. Munson, 1982. Waste Isolation Pilot Plant (WIPP) Research and Development Program: In Situ Testing Plan, SAND81-2628. Sandia National Laboratories, Albuquerque, NM.
- McCave, I.N. "Particulate Size Spectra, Behavior, and Origin of Nepheloid Layers Over the Nova Scotian Continental Rise," Journal of Geophysical Research, vol. 88, (C 12), pp. 7647-7666.
- McTigue, D.F., and E.J. Nowak, 1987. "Brine Transport in the Bedded Salt of the Waste Isolation Pilot Plant (WIPP): Field Measurements and a Darcy Flow Model" in M.J. Apted and R.E. Westerman, eds., Materials Research Society Symposium Proceedings: Scientific Basis for Nuclear Waste Management XI, Materials Research Society, Pittsburgh, PA, pp. 209-218.
- Meijer, A.J., J.L. Lolcama, and F.J. Pearson, 1987. "Consistency of Densities and Chemical Compositions of Water Samples from the Culebra Dolomite," Appendix E in A. Haug, V.A. Kelley, A.M. LaVenue, and J.F. Pickens, Modeling of Ground-Water Flow in the Culebra Dolomite at the Waste Isolation Pilot Plant (WIPP) Site: Interim Report, SAND86-7167. Sandia National Laboratories, Albuquerque, NM.
- Melfi, J.F., 1985. "A Geochemical Model for Radionuclide Speciation in High Ionic Strength Solutions," Master's Thesis, U. of New Mexico, Albuquerque, NM.

- Mercer, J.W., 1983. Geohydrology of the Proposed Waste Isolation Pilot Plant Site, Los Medanos Area, Southeastern New Mexico. U.S. Geological Survey Water Resources Investigation 83-4016.
- Mercer, J.W., and B.R. Orr, 1979. Interim Data Report on the Geohydrology of the Proposed Waste Isolation Pilot Plant Site, Southeastern New Mexico. USGS Water-Resources Investigations 79-98, U.S. Geological Survey, Albuquerque, NM.
- Mercer, J.W., P. Davis, K.F. Dennehy, and C.L. Goetz, 1981. Results of Hydrologic Tests and Water-Chemistry Analyses, Wells H-4A, H-4B, and H-4C at the Proposed Waste Isolation Pilot Plant Site, Southeastern New Mexico. U.S. Geological Survey Water-Resources Investigations 81-36, Albuquerque, NM.
- Mercer, J.W., R.L. Beauheim, R.P. Snyder, and G.M. Fairer, 1987. Basic Data Report for Drilling and Hydrologic Testing of Drillhole DOE-2 at the Waste Isolation Pilot Plant (WIPP) Site, SAND86-0611. Sandia National Laboratories, Albuquerque, NM.
- Mericle, L.W. and R.P. Mericle, 1965. "Biological Discrimination of Differences in Natural Background Radiation Level," Rad. Bot., vol. 5, pp. 475-492.
- Miller, D.G., 1982. Estimation of Tracer Diffusion Coefficients of Ions in Aqueous Solution, UCRL-53319. Lawrence Livermore National Laboratory, Livermore, CA.
- Molecke, M.A., 1976. "Revised Representative Brines/Solutions for WIPP Experimentation," memo to distribution dated 10/08/76. Sandia National Laboratories, Albuquerque, NM.
- Molecke, M.A., 1979. Gas Generation from Transuranic Waste Degradation: Data Summary and Interpretation, SAND79-1245. Sandia National Laboratories, Albuquerque, NM.
- Molecke, M.A., 1983. A Comparison of Brines Relevant to Nuclear Waste Experimentation, SAND83-0516. Sandia National Laboratories, Albuquerque, NM.
- Morgan, H.S., C.M. Stone, and R.D. Krieg, 1986. Evaluation of WIPP Structural Modeling Capabilities Based on Comparisons with South Drift Data, SAND85-0323. Sandia National Laboratories, Albuquerque, NM.
- Morgan, H.S., 1987. "TRU Storage Room Calculation with Stratigraphy," SNL memorandum to D.E. Munson, Sandia National Laboratories, Albuquerque, NM.
- Mraz, D., 1980. "Plastic Behavior of Salt Rock Utilized in Designing a Mining Method, CIM Bulletin, vol. 73, pp. 11-123.
- Munson, D.E., and A.F. Fossum, 1986, "Comparison Between Predicted and Measured South Drift Closures at WIPP Using a Transient Creep Model for Salt," Proc. 27th U.S. Symp. on Rock Mechanics, Soc. of Mining Engineers, Littleton, CO, pp. 931-939.

- Munson, D.E., A.F. Fossum, and P.E. Senseny, 1989. "Approach to First Principles Model Prediction of Measured WIPP In Situ Room Closure in Salt," Proc. 30th University S. Rock Mechanics Symposium, at the University of West Virginia, June 19-22, 1989, to be published by A. A. Balkema, Rotterdam, Netherlands.
- Muskat, M., 1949. Physical Principles of Oil Production, McGraw-Hill Book Company, Inc.
- Myers, J., P. James, and P. Drez, 1989. "The Redox State of the Culebra Member of the Rustler Formation" in M. D. Siegel, S.J. Lambert, and K.L. Robinson, eds., Hydrogeochemical Studies of the Rustler Formation and Related Rocks in the WIPP Area, Southeastern New Mexico, SAND88-0196. Sandia National Laboratories, Albuquerque, NM.
- Narasimhan, T.N., and B.Y. Kanehiro, 1980. "A Note on the Meaning of Storage Coefficient," Water Resources Research, vol. 16, no. 2.
- National Council on Radiation Protection and Measurements, 1984. Radiological Assessment: Predicting the Transport, Bioaccumulation, and Uptake by Man of Radionuclides Released to the Environment, NCRP Report No. 76. National Council on Radiation Protection and Measurements, Bethesda, MD.
- National Research Council on the Waste Isolation Pilot Plant, 1984. Review of the Scientific and Technical Criteria for the Waste Isolation Pilot Plant (WIPP), DOE/DP/48015-1. National Academy Press, Washington, DC.
- Nativ, R., and D.A. Smith, 1987. "Hydrogeology and Geochemistry of the Ogallala Aquifer, Southern High Plains," Journal of Hydrology, vol. 1.
- Neill, R.H., J.K. Channell, L. Chaturvedi, M.S. Little, K. Rehfeldt, and P. Spiegler, 1983. Evaluation of the Suitability of the WIPP Site, EEG-23. New Mexico Environmental Evaluation Group, Santa Fe, New Mexico.
- Neretnieks, I., 1980. "Diffusion in the Rock Matrix: An Important Factor in Radionuclide Retardation?" Journal of Geophysical Research, vol. 85, pp. 217-253.
- Neretnieks, I., and A. Rasmuson, 1984. "An Approach to Modeling Radionuclide Migration in a Medium with Strongly Varying Velocity and Block Sizes along the Flow Path," Water Resources Research, vol. 20, pp. 1823-1836.
- Neuzil, C.E., 1986. "Groundwater Flow in Low-Permeability Environments," Water Resources Research, vol. 22, pp. 1163-1195.
- New Mexico Oil Conservation Commission, 1967a. Order of the Commission, Case No. 3551, Order No. R-3221. Oil Conservation Commission, Santa Fe, NM.
- New Mexico Oil Conservation Commission, 1967b. Order of the Commission, Case No. 3644, Order No. R-3221-A. Oil Conservation Commission, Santa Fe, NM.
- New Mexico Oil Conservation Commission, 1952. Order of the Commission, Case No. 308, Order No. R-98-A. Oil Conservation Commission, Santa Fe, NM.

- Niou, S., and J. Pietz, 1987. A Statistical Inverse Analysis of the H-3 Hydropad Pumping Test. Report for Westinghouse Electric Corp., Management and Operating Contractor for the Waste Isolation Pilot Plant, Carlsbad, NM.
- Nowak, E.J., 1980. Radionuclide Sorption and Migration Studies of Getters for Backfill Barriers, SAND79-1110. Sandia National Laboratories, Albuquerque, NM.
- Nowak, E.J., 1986. Preliminary Results of Brine Migration Studies in the Waste Isolation Pilot Plant (WIPP), SAND86-0720. Sandia National Laboratories, Albuquerque, NM.
- Nowak, E.J., and D.F. McTigue, 1987. Interim Results of Brine Transport Studies in the Waste Isolation Pilot Plant (WIPP), SAND87-0880. Sandia National Laboratories, Albuquerque, NM.
- Nowak, E.J., and J.C. Stormont, 1987. Scoping Model Calculations of the Reconsolidation of Crushed Salt in WIPP Shafts, SAND87-0879. Sandia National Laboratories, Albuquerque, NM.
- Nowak, E.J., D.F. McTigue, and R. Beraun, 1988. Brine Inflow to WIPP Disposal Rooms: Data, Modeling, and Assessment, SAND88-0112. Sandia National Laboratories, Albuquerque, NM.
- Oak Ridge National Laboratory, 1988. Integrated Data Base for 1988: Spent Fuel and Radioactive Waste Inventories, Projections, and Characteristics, DOE/RW-0006, Rev. 4, Oak Ridge, TN.
- Olsen, H.W., 1966. "Darcy's Law in Saturated Kaolinite," Water Resources Research, vol. 2, no. 2.
- Osmond, J.K., and J.B. Cowart, 1976. "The Theory and Uses of Natural Uranium Isotopic Variations in Hydrology," Atomic Energy Review, vol. 14, pp. 621-679.
- Paine, R.T., 1977. Chemistry Related to the Wipp Site, Draft Final Report, Sandia Contract GTK/07-1488. Chemistry Department, University of New Mexico, Albuquerque, NM.
- Papelis, C., K. Hayes, and J. Keckie, 1988. HYDRAQL: A Program for the Computation of Chemical Equilibrium Composition of Aqueous Batch Systems Including Surface-Complexation Modeling of Ion Adsorption at the Oxide/Solution Interface, Stanford Technical Report no. 306, Stanford University, Stanford, CA.
- Peterson, E.W., P.L. Lagus, and K. Lie, 1987a. WIPP Horizon Free Field Fluid Transport Characteristics, SAND87-7164. Sandia National Laboratories, Albuquerque, NM.
- Peterson, E.W., P.L. Lagus, and K. Lie, 1987b. Fluid Flow Measurements of Test Series A and B for the Small Scale Seal Performance Tests, SAND87-7041. Sandia National Laboratories, Albuquerque, NM.

- Peterson, E.W., P.L. Lagus, R.D. Broce, and K. Lie, 1981. In Situ Permeability Testing of Rock Salt, SAND81-7073. Sandia National Laboratories, Albuquerque, NM.
- Pfeiffer, M.C., 1987. "Multicomponent Underground DC Resistivity Study at the Waste Isolation Pilot Plant, Southeast New Mexico," T-3372, M.S. Thesis., Colorado School of Mines, Golden, CO.
- Pickens, J.F., and G.E. Grisak, 1981. "Scale-Dependent Dispersion in a Stratified Granular Aquifer," Water Resources Research, vol. 17, pp. 1191-1211.
- Pickens, J.F., G.E. Grisak, J.D. Avis, D.W. Belanger, and M. Thury, 1987. "Analysis and Interpretation of Borehole Hydraulic Tests in Deep Boreholes: Principles, Model Development, and Applications," Water Resources Research, vol. 23, pp. 1341-1375.
- Pinder, G.F., 1974. Galerkin Finite-Element Models for Aquifer Simulation. Princeton University Water Resources Program, Dept of Civil Engineering, Dept of Geological and Geophysical Science, Princeton University, Princeton, NJ.
- Plummer, L.N., 1984. "Geochemical Modeling: A Comparison of Forward and Inverse Methods" in B. Hitchon and E.I. Wallick, eds., Proc. First Canadian/American Conference on Hydrogeology. Practical Applications of Ground Water Geochemistry, Banff, Alberta, Canada, June 22-26, 1984, National Water Well Association, Worthington, OH.
- Plummer, L.N., D.L. Parkhurst, G.W. Fleming, and S.A. Dunkle, 1988. PHROPITZ-A Computer Program Incorporating Pitzer's Equations for Calculation of Geochemical Reactions in Brines, U.S. Geological Survey Water-Resources Investigation Report 88-4153.
- Popielak, R.S., R.L. Beauheim, S.R. Black, W.E. Coons, C.T. Ellingson, and R.L. Olsen, 1983. Brine Reservoirs in the Castile Fm., Waste Isolation Pilot Plant (WIPP) Project, Southeastern New Mexico, TME-3153. U.S. Department of Energy, Carlsbad, NM.
- Powers, D.W., S.J. Lambert, S.E. Shaffer, L.R. Hill, and W.D. Weart, 1978. Geological Characterization Report for the Waste Isolation Pilot Plant (WIPP) Site, Southeastern New Mexico, SAND78-1596. Sandia Laboratories, Albuquerque, NM.
- Prausnitz, J.M., 1969. Molecular Thermodynamics of Fluid-Phase Equilibria, Prentice-Hall, Inc., Englewood Cliffs, NJ.
- Pusch, R., 1980. Swelling Pressure of Highly Compacted Bentonite, KBS Project 15:05 Technical Report 80-13, Division Soil Mechanics, University of Lulea, Lulea 1980-08-20.
- Ramey, D.S., 1985. Chemistry of Rustler Fluids, EEG-31. New Mexico Environmental Evaluation Group, Santa Fe, NM.

- Randall, W.S., M.E. Crawley, and M.L. Lyon, 1988. 1988 Annual Water Quality Data Report for the Waste Isolation Pilot Plant, DOE/WIPP-88-006. U.S. Department of Energy, Carlsbad, NM.
- Reeves, M., D.S. Ward, N.D. Johns, and R.M. Cranwell, 1986a. Data Input Guide for SWIFT II, the Sandia Waste-Isolation Flow and Transport Model for Fractured Media, Release 4.84, SAND83-0242, NUREG/CR-3162. Sandia National Laboratories, Albuquerque, NM.
- Reeves, M., D.S. Ward, N.D. Johns, and R.M. Cranwell, 1986b. Theory and Implementation for SWIFT II, The Sandia Waste-Isolation Flow and Transport Model for Fractured Media Release 4.84, SAND83-1159, NUREG/CR-3328. Sandia National Laboratories, Albuquerque, NM.
- Reeves, M., D.S. Ward, P.A. Davis, and E.J. Bonano, 1986c. SWIFT II Self-Teaching Curriculum: Illustrative Problems for the Sandia Waste-Isolation Flow and Transport Model for Fractured Media, SAND84-1586, NUREG/CR-3925. Sandia National Laboratories, Albuquerque, NM.
- Reeves, M., V.A. Kelley, and J.F. Pickens, 1987. Regional Double-Porosity Solute Transport in the Culebra Dolomite: An Analysis of Parameter Sensitivity and Importance at the Waste Isolation Pilot Plant (WIPP) Site, SAND87-7105. Sandia National Laboratories, Albuquerque, NM.
- Reeves, M., V.A. Kelley, and J.F. Pickens, 1989 (in preparation). Regional Double-Porosity Solute Transport in the Culebra Dolomite Under High-Pressure-Release Conditions : An Analysis of Parameter Sensitivity and Importance at the Waste Isolation Pilot Plant (WIPP) Site, SAND89-7069. Sandia National Laboratories, Albuquerque, NM.
- Register, J.K., 1981. Brine Pocket Occurrences in the Castile Formation, Southeastern New Mexico, TME 3080. U.S. Department of Energy, Carlsbad, NM.
- Reisenauer, A.E., 1979. Variable Thickness Transient Groundwater Flow Model (VTT). Formulation, User's Manual and Program Listings, PNL-3160-1,2,3. Pacific Northwest Laboratory, Richland, WA.
- Remson, I., 1984. "Hydrogeologic Overview of the Nuclear Waste Isolation Program," 25th Symposium on Rock Mechanics.
- Richey, S.F., 1986. Hydrologic-Test Data from Wells at Hydrologic-Test Pads H-7, H-8, H-9, and H-10 Near the Proposed Waste Isolation Pilot Plant Site, Southeastern New Mexico, U.S. Geological Survey Open-File Report 86-413, Albuquerque, NM.
- Richey, S.F., 1987a. Preliminary Hydrologic Data for Wells Tested in Nash Draw, Near the Proposed Waste Isolation Pilot Plant Site, Southeastern New Mexico, U.S. Geological Survey Open-File Report 87-37, Albuquerque, NM.
- Richey, S.F., 1987b. Water-Level Data from Wells in the Vicinity of the Waste Isolation Pilot Plant, Southeastern New Mexico, U.S. Geological Survey Open-File Report 87-120, Albuquerque, NM.

- Riese, A.C., 1982. "Adsorption of Radium and Thorium onto Quartz and Kaolinite: A Comparison of Solution/Surface Equilibria Models," Ph.D. Thesis, Colorado School of Mines, Golden, CO.
- Robinson, K.L., 1988. Analysis of Solutes in Groundwaters from the Rustler Formation at and Near the WIPP Site, SAND86-0917. Sandia National Laboratories, Albuquerque, NM.
- Robinson, T.W., and W.B. Lang, 1938. "Geology and Ground-Water Conditions of the Pecos River Valley in the Vicinity of Laguna Grande de la Sal, New Mexico," 12th and 13th Biennial Reports. New Mexico State Engineer, Santa Fe, NM, pp. 77-100.
- Sanchez, A.L., J.W. Murray, and T.H. Sibley, 1985. "The Adsorption of Plutonium IV and V on Goethite," Geochimica et Cosmochimica Acta, vol. 49, pp. 2297-2307.
- Sandia Laboratories, 1979. Summary of Research and Development Activities in Support of Waste Acceptance Criteria for WIPP, SAND79-1305. Sandia Laboratories, Albuquerque, NM.
- Sandia National Laboratories and D'Appolonia Consulting Engineers, Inc., 1982. Basic Data Report for Drillhole WIPP 12 (Waste Isolation Pilot Plant--WIPP), SAND82-2336. Sandia National Laboratories, Albuquerque, NM.
- Sarganum, A., P. Riley, K. Arulanandan, and R.B. Krone, 1973. "Physical-Chemical Factors in Erosion of Cohesive Soils," Proceedings of the American Society of Civil Engineers, Journal of Hydraulic Division, vol. 99, pp. 555-558.
- Saulnier, G.J., Jr., 1987. Analysis of Pumping Tests of the Culebra Dolomite Conducted at the H-11 Hydropad at the Waste Isolation Pilot Plant (WIPP) Site, SAND87-7124. Sandia National Laboratories, Albuquerque, NM.
- Saulnier, G.J., Jr., and J.D. Avis, 1988. Interpretation of Hydraulic Tests Conducted in the Waste-Handling Shaft at the Waste Isolation Pilot Plant (WIPP) Site, SAND87-7001. Sandia National Laboratories, Albuquerque, NM.
- Scheetz, B.E., P.H. Licastro, and D.M. Roy, 1986. A Full Scale Borehole Sealing Test in Anhydrite Under Simulated Downhole Conditions, Volumes 1 and 2, BMI/ONWI-573(2). Office of Nuclear Waste Isolation, Battelle Memorial Institute, Columbus, OH.
- Serne, R.J., D. Rai, M.J. Mason, and M. Molecke, 1977. Batch K_d Measurements of Nuclides to Estimate Migration Potential at the Proposed Waste Isolation Pilot Plant in New Mexico, PNL-2448. Pacific Northwest Laboratories, Richland, WA.
- Sewards, T., M.L. Williams, K. Keil, S.J. Lambert, and C.L. Stein, 1989. "Mineralogy of the Culebra Dolomite" in M.D. Siegel, S.J. Lambert, and K.L. Robinson, eds., Hydrogeochemical Studies of the Rustler Formation and Related Rocks in the WIPP Area, Southeastern New Mexico, SAND88-0196. Sandia National Laboratories, Albuquerque, NM.

- Siegel, M.D., and S.J. Lambert, 1989. "Summary of Hydrogeochemical Constraints on Groundwater Flow in the Rustler Formation" in M.D. Siegel, S.J. Lambert, and K.L. Robinson, eds., Hydrogeochemical Studies of the Rustler Formation and Related Rocks in the WIPP Area, Southeastern New Mexico, SAND88-0196. Sandia National Laboratories, Albuquerque, NM.
- Siegel, M.D., ed. 1989. Progress in Development of a Methodology for Geochemical Sensitivity Analysis for Performance Assessment: Volume 2. Speciation, Sorption and Transport in Fractured Media, Letter Report to the U.S. Nuclear Regulatory Commission.
- Siegel, M.D., K.L. Robinson, and J. Myers, 1989. "Solute Relationships in Groundwaters from the Culebra Member of the Rustler Formation near the WIPP Site, Southeastern, New Mexico" in M.D. Siegel, S.J. Lambert, and K.L. Robinson, eds., Hydrogeochemical Studies of the Rustler Formation and Related Rocks in the WIPP Area, Southeastern New Mexico, SAND88-0196. Sandia National Laboratories, Albuquerque, NM.
- Siegel, M.D., S.J. Lambert, and K.L. Robinson, eds., 1989. Hydrogeochemical Studies of the Rustler Formation and Related Rocks in the WIPP Area, Southeastern New Mexico, SAND88-0196. Sandia National Laboratories, Albuquerque, NM.
- Siegel, M.D., S.L. Phillips, J.O. Leckie, and W.R. Kelly, 1989. "Development of a Methodology of Geochemical Sensitivity Analysis for Performance Assessment" (SAND87-1133C) in B.E. Buxton, ed., Proceedings of the Conference on Geostatistical Sensitivity, and Uncertainty Methods for Ground-Water Flow and Radionuclide Transport Modeling, Battelle Press.
- Sjaardema, G.D., and R.D. Krieg, 1987. A Constitutive Model for the Consolidation of WIPP Crushed Salt and Its Use in Analyses of Backfilled Shaft and Drift Configurations, SAND87-1977. Sandia National Laboratories, Albuquerque, NM.
- SKI (STATENS KAERNKRAFTINSPEKTION Swedish Nuclear Power Inspectorate), 1984. INTRACOIN International Nuclide Transport Code Intercomparison Study, SKI 84 Final Report Level 1:3.
- Snyder, R.P., 1985. Dissolution of Halite and Gypsum, and Hydration of Anhydrite to Gypsum, Rustler Fm., in the Vicinity of the Waste Isolation Pilot Plant, Southeastern New Mexico, U.S. Geological Survey Open-File Report 85-229, Denver, CO.
- Soil Conservation Service, 1971. Soil Survey of Eddy Area, New Mexico. U.S. Government Printing Office, Washington, D.C.
- Skokan, C., J. Starrett, and H.T. Andersen, 1988. Final Report: Feasibility Study of Seismic Tomography to Monitor Underground Pillar Integrity at the WIPP Site, SAND88-7096. Sandia National Laboratories, Albuquerque, NM.
- Soudek, A., 1984. "Binary and Ternary Ion Exchange on Sodium Montmorillonite for Application to Backfill in Nuclear Waste Disposal," Master's Thesis, Chemical Engineering, University of California, Berkeley, CA.

- Stein, C.L., 1985. Mineralogy in the Waste Isolation Pilot Plant (WIPP) Facility Stratigraphic Horizon, SAND85-0321. Sandia National Laboratories, Albuquerque, NM.
- Stein, C.L., and J.L. Krumhansl, 1986. Chemistry of Brines in Salt from the Waste Isolation Pilot Plant (WIPP), Southeastern New Mexico: A Preliminary Investigation, SAND85-0897. Sandia National Laboratories, Albuquerque, NM.
- Stein, C.L., and J.L. Krumhansl, 1988. "A Model for the Evolution of Brines in Salt from the Lower Salado Formation, Southeastern New Mexico," Geochimica et Cosmochimica Acta, vol. 52.
- Stensrud, W.A., M.A. Bame, K.D. Lantz, T.L. Cauffman, J.B. Palmer, and G.J. Saulnier, Jr. 1988a. WIPP Hydrology Program, Waste Isolation Pilot Plant, Southeastern New Mexico, Hydrologic Data Report #6, SAND87-7166. Sandia National Laboratories, Albuquerque, NM.
- Stensrud, W.A., M.A. Bame, K.D. Lantz, J.B. Palmer, and G.J. Saulnier, Jr., 1988b. WIPP Hydrology Program, Waste Isolation Pilot Plant, Southeastern New Mexico, Hydrologic Data Report #7, SAND88-7014. Sandia National Laboratories, Albuquerque, NM.
- Stormont, J.C., 1988. Preliminary Seal Design Evaluation for the Waste Isolation Pilot Plant, SAND87-3083. Sandia National Laboratories, Albuquerque, NM.
- Stormont, J.C., and J.G. Arguello, 1988. Model Calculations of Flow Through Shaft Seals in the Rustler Formation, SAND87-2859. Sandia National Laboratories, Albuquerque, NM.
- Stormont, J.C., E.W. Peterson, and P.L. Lagus, 1987. Summary of and Observations about WIPP Facility Horizon Flow Measurements through 1986, SAND87-0176. Sandia National Laboratories, Albuquerque, NM.
- Streltsova, T.D., 1988. Well Testing in Heterogeneous Formations, Exxon Monograph, John Wiley and Sons, Inc., New York, NY.
- Sutherland, H.J., and S. Cave, 1978. Gas Permeability of SENM Rock Salt, SAND78-2287. Sandia National Laboratories, Albuquerque, NM.
- Swanson, J.L., 1986. Organic Complexant-Enhanced Mobility of Toxic Elements in Low-Level Wastes: Final Report, NUREG/CR-4660, PNL-4965-10. Pacific Northwest Laboratory, Richland, WA.
- Swartzendruber, D., 1962. "Non-Darcy Flow Behavior in Liquid-Saturated Porous Media," Journal of Geophysical Research, vol. 67, no. 13.
- The Earth Technology Corporation, 1988. Final Report for Time Domain Electromagnetic (TDEM) Surveys at the WIPP Site, SAND87-7144. Sandia National Laboratories, Albuquerque, NM.
- Tien, P.L., F.B. Nimick, A.B. Muller, P.A. Davis, R.V. Guzowski, L.E. Duda, and R.L. Hunter, 1983. Repository Site Data and Information in Bedded

- Salt: Palo Duro Basin, Texas, SAND82-2223, NUREG/CR-3129. Sandia National Laboratories, Albuquerque, NM.
- Till, J.E. and H.R. Meyer, 1983. Radiological Assessment: A Textbook on Environmental Dose Analysis, NUREG/CR-3332. U.S. Nuclear Regulatory Commission, Washington, DC.
- Torstenfelt, B., H. Kipatsi, K. Anderson, B. Allard, and University Olofsson, 1982. "Transport of Actinides Through a Bentonite Backfill" in W. Lutze, ed., Scientific Basis for Radioactive Waste Management V, Elsevier Science Publishing Co., New York, NY, pp. 659-668.
- Trescott, P.C., G.F. Pinder, and S.P. Larson, 1976. Finite-Difference Model for Aquifer Simulation in Two Dimensions with Results of Numerical Experiments, U.S. Geological Survey Techniques of Water-Resources Investigations, Book 7, Chapter C1, U.S. Government Printing Office, Washington, D.C.
- Tsunashima, A., G.W. Brindley, and M. Bastovanov, 1981. "Adsorption of Uranium from Solutions by Montmorillonite; Compositions and Properties of Uranyl Montmorillonites," Clays and Clay Minerals, vol. 29, pp. 10-16.
- Tyler, L.D., R.V. Matalucci, M.A. Molecke, D.E. Munson, E.J. Nowak, and J.C. Stormont, 1988. Summary Report for the WIPP Technology Development Program for Isolation of Radioactive Waste, SAND88-0844. Sandia National Laboratories, Albuquerque, NM.
- Uhland, D.W. and W.S. Randall, 1986. 1986 Annual Water Quality Data Report for the Waste Isolation Pilot Plant, DOE-WIPP-86-006. U.S. Department of Energy, Carlsbad, NM.
- UNC, 1988. "Report on the Analysis of 20 Samples from Nine WIPP Project Wells," UNC Technical Services, Inc., unpublished report prepared for Sandia National Laboratories, Albuquerque, NM.
- Uhland, D.W., W.S. Randall and R.C. Carrasco, 1987. 1987 Annual Water Quality Data Report for the Waste Isolation Pilot Plant, DOE-WIPP-87-006. U.S. Department of Energy, Carlsbad, NM.
- United Nations, 1972. Ionizing Radiation: Levels and Effects. A Report of the United Nations Scientific Committee on the Effects of Atomic Radiation, United Nations, New York, NY.
- U.S. Department of Energy, 1985. "Committed Dose Equivalent Tables for U.S." in J.P. Corley, ed., Population Dose Calculations, Pacific Northwest Laboratory, U.S. Department of Energy/EH Office of Operational Safety, Washington, DC.
- U.S. Department of Energy, 1983. Preliminary Design Validation Report. Bechtel National, Inc., San Francisco, CA.
- U.S. Department of Energy, 1980a. Final Environmental Impact Statement, Waste Isolation Pilot Plant, DOE/EIS-0026. Vols 1-2, U.S. Government Printing Office, Washington, D.C.

- U.S. Department of Energy, 1980b. Waste Isolation Pilot Plant Safety Analysis Report, Vols. 1-5, U.S. Department of Energy.
- U.S. Department of Energy, 1986. Waste Isolation Pilot Plant Design Validation Final Report, DOE-WIPP-86-010, prepared by the U.S. Department of Energy, WIPP Project Office, Carlsbad, NM.
- U.S. Department of Energy, 1988a. Internal Dose Conversion Factors for Calculation of Dose to the Public, DOE/EH-0071. U.S. Department of Energy, Washington, DC.
- U.S. Department of Energy, 1988b. Geotechnical Field Data and Analysis Report, DOE-WIPP-87-017. U.S. Department of Energy, Carlsbad, NM.
- U.S. Department of Energy, 1989. Waste Isolation Pilot Plant Compliance Strategy for 40 CFR 191, DOE-WIPP-86-013. U.S. Department of Energy, Carlsbad, NM.
- U.S. Department of Energy and State of New Mexico, 1981, as modified. Agreement for Consultation and Cooperation Between the U.S. Department of Energy and the State of New Mexico on the Waste Isolation Pilot Plant, modified 11/30/84, 8/4/87, and 3/22/88.
- U.S. Department of Energy, U.S. Department of the Interior, and State of NM, 1981. Stipulated Agreement in the Case of State of New Mexico, ex rel. Jeff Bingaman, Attorney General of the State of New Mexico, vs. The United States Department of Energy et al., Civil Action no. 81-0363 JB, in the United States District Court for the District of New Mexico.
- U.S. Environmental Protection Agency, 1985. "Environmental Standards for the Management and Disposal of Spent Nuclear Fuel, High-Level and Transuranic Radioactive Waste; Final Rule," 40 CFR Part 191, Federal Register, vol. 50, pp. 38066-38089.
- U.S. Nuclear Regulatory Commission, 1976. Regulatory Guide 1.109: Calculation of Annual Doses to Man from Routine Releases of Reactor Effluents for the Purposes of Evaluating Compliance with 10 CFR Part 50, Appendix I, U.S. Nuclear Regulatory Commission, Washington, DC.
- U.S. Public Health Service, 1970. Radiological Health Handbook, U.S. Public Health Service, Rockville, MD.
- Van Devender, T.R., 1980. "Holocene Plant Remains from Rocky Arroyo and Last Chance Canyon, Eddy County, New Mexico," The Southwestern Naturalist, vol. 25, pp. 361-372.
- Van Everdingen, A.F., and W. Hurst, 1949. "Application of the Laplace Transformation to Flow Problems in Reservoirs," Transactions of the Society of Petroleum Engineers, American Institute of Mining Engineers, vol. 186, pp. 305-324.
- Vennart, J., 1981. "Limits for Intakes of Radionuclides by Workers: ICRP 30," Health Physics, vol. 40, pp. 477-484.

- Voss, C.I., 1984. A Finite-Element Simulation Model for Saturated-Unsaturated, Fluid-Density-Dependent Ground-Water Flow with Energy Transport or Chemically Reactive Single-Species Solute Transport. U.S. Geological Survey Water-Resources Investigations Report 84-4369, U.S. Government Printing Office, Washington, DC.
- Ward, D.S., M. Reeves, and L.E. Duba, 1984. Verification and Field Comparison of the Sandia Waste-Isolation Flow and Transport Model (SWIFT), SAND83-1154, NUREG/CR-3316. Sandia National Laboratories, Albuquerque, NM.
- Wawersik, W.R., and C.M. Stone, 1985. Application of Hydraulic Fracturing to Determine Virgin In Situ Stress State Around Waste Isolation Pilot Plant--In Situ Measurements, SAND85-1776. Sandia National Laboratories, Albuquerque, NM.
- Wawersik, W.R., and C.M. Stone, 1986. "Experience with Hydraulic Fracturing Tests for Stress Measurements in the WIPP," Proc. 27th U.S. Rock Mechanics Symposium, at the University of Alabama, Tuscaloosa, 1986, Society of Mining Engineers, Littleton, CO.
- Whicker, F.W., 1980. "Ecological Effects of Transuranics in the Terrestrial Environment" in W.C. Hanson, ed., Transuranic Elements in the Environment, DOE/TIC-22800. U.S. Department of Energy.
- White, F.M., 1974. Viscous Fluid Flow, McGraw Hill, Inc., New York, NY.
- Williamson, C.R., 1979. "Deep-Sea Sedimentation and Stratigraphic Traps, Bell Canyon Formation (Permian) Delaware Basin" in N.M. Sullivan, ed., Guadalupean Delaware Mountain Group of West Texas and Southeast New Mexico, Publication 79-18, Society of Economic Paleontologists and Mineralogists (Permian Basin Section).
- Wimbush, M., 1976. "The Physics of the Benthic Boundary Layer" in I.N. McCave, ed., The Benthic Boundary Layer. Plenum Press, New York, NY.
- Wolery, T.J., 1983. EQ3NR. A Computer Program for Geochemical Aqueous Speciation-Solubility Calculations: User's Guide and Documentation, UCRL-53414. Lawrence Livermore National Laboratory, Livermore, CA.
- Yapp, C. J., 1982. Letter of record from C. J. Yapp to S. J. Lambert, July 13, 1982. Sandia National Laboratories, Albuquerque, NM.

FEDERAL AGENCIES

U.S. Department of Energy, (5)
Office of Civilian Radioactive Waste Management
Attn: Deputy Director, RW-2
Associate Director, RW-10
Office of Program Administration and Resources Management
Associate Director, RW-20
Office of Facilities Siting and Development
Associate Director, RW-30
Office of Systems Integration and Regulations
Associate Director, RW-40
Office of External Relations and Policy

Office of Geologic Repositories
Forrestal Building
Washington, DC 20585

U.S. Department of Energy (203)
Albuquerque Operations Office
Attn: W. J. Arthur III (200)
Bruce G. Twining
J. E. Bickel
R. Marquez, Director Public Affairs Division
P.O. Box 5400
Albuquerque, NM 87185

U.S. Department of Energy
Attn: National Atomic Museum Library
Albuquerque Operations Office
P. O. Box 5400
Albuquerque, NM 87185

U.S. Department of Energy (9)
WIPP Project Office (Carlsbad)
Attn: J. Tillman (4)
A. Hunt
T. Lukow (2)
V. Daub
B. Young
P.O. Box 3090
Carlsbad, NM 88221

U.S. Department of Energy
Research & Waste Management Division
Attn: W. R. Bibb, Director
P. O. Box E
Oak Ridge, TN 37831

U.S. Department of Energy
Richland Operations Office
Nuclear Fuel Cycle & Production Division
Attn: R. E. Gerton
P.O. Box 500
Richland, WA 99352

U.S. Department of Energy (5)
Office of Defense Waste and Transportation Management
Attn: T. B. Hindman----- DP-12
M. Duff ----- DP-123
A. Follett ----- DP-122
C. H. George ----- DP-124
J. Mathur ----- DP-123
Washington, DC 20545

U.S. Department of Energy (2)
Idaho Operations Office
Fuel Processing and Waste Management Division
785 DOE Place
Idaho Falls, ID 83402

U.S. Department of Energy (3)
Savannah River Operations Office
Defense Waste Processing Facility Project Office
Attn: S. Cowan
W. J. Brumley
P.O. Box A
Aiken, SC 29802

U.S. Geological Survey
Branch of Regional Geology
Attn: R. Snyder
MS913, Box 25046
Denver Federal Center
Denver, CO 80225

U.S. Geological Survey
Conservation Division
Attn: W. Melton
P.O. Box 1857
Roswell, NM 88201

U.S. Geological Survey (2)
Water Resources Division
Attn: Cathy Peters
Suite 200
4501 Indian School, NE
Albuquerque, NM 87110

U.S. Nuclear Regulatory Commission (4)
Division of Waste Management
Attn: Michael Bell
Hubart Miller
Jacob Philip
NRC Library
Mail Stop 623SS
Washington, DC 20555

U.S. Department of Energy (3)
Albuquerque Operations Office
Attn: G. Runkle (EHD)
R. M. Ostmeyer*
C. Soden (EHD)
P.O. Box 5400
Albuquerque, New Mexico 87185-5400

U.S. Department of Energy
Attn: Marvin Furman
Richland Operations Office
825 Jadivin Ave.
P.O. Box 550
Richland, WA 99352

U.S. Department of Energy (2)
Deputy Assistant Secretary for Environment, EH-20
Attn: Raymond P. Berube
John Tseng
1000 Independence Ave. SW
Washington, D.C. 20585

U.S. Department of Energy (1)
Nevada Operations Office
Attn: D. Livingston
2753 S. Highland Drive
Las Vegas, NV 87183-8518

U.S. Environmental Protection Agency
Office of Radiation Protection Programs (ANR-460)
Attn: Mark Cotton
Washington, D.C. 20460

U.S. Environmental Protection Agency
Office of Radiation Protection Programs (ANR-460)
Attn: Daniel J. Egan, Jr.
Washington, D.C. 20460

STATE AGENCIES

Environmental Evaluation Group (3)
Attn: Library
Suite F-2
7007 Wyoming Blvd., N.E.
Albuquerque, NM 87109

New Mexico Bureau of Mines and Mineral Resources (2)
Attn: F. E. Kottolowski, Director
J. Hawley
Socorro, NM 87801

NM Department of Energy & Minerals
Attn: Kasey LaPlante, Librarian
P.O. Box 2770
Santa Fe, NM 87501

LABORATORIES/CORPORATIONS

F. A. Donath
The Earth Technology Corporation
3777 Long Beach Blvd.
Long Beach, CA 90807

EG&G Idaho
1955 Fremont Street
Attn: C. Atwood
Idaho Falls, ID 83415

APTEK, Inc.
Attn: B. Lewis
1257 Lake Plaza Drive
Colorado Springs, CO 80906

New Mexico Engineering Research Institute
Attn: R. McCurley
P.O. Box 25
University Station
Albuquerque, New Mexico 87131

Charles R. Hadlock
Arthur D. Little, Inc.
Acorn Park
Cambridge, MA 02140-2390

Kathleen Hain
BDM Corporation
7519 Jones Branch Drive
McLean, VA 22101

Western Water Consultants (1)
Attn: P. A. Rechard
P.O. Box 4128
Laramie, WY 82071

In-Situ Inc. (1)
Attn: S. C. Way
209 Grand Avenue
Laramie, WY 82070

Jacobs Engineering Group, Inc.
Attn: W. Beyeler
5301 Central Avenue, NE
Suite 1700
Albuquerque, New Mexico 87108

Bill Kennedy
Pacific Northwest Laboratory
Battelle Blvd.
P.O. Box 999
Richland, WA 99352

K. K. Wahi
GRAM Incorporated
1709 Moon, NE
Albuquerque, NM 87112

Don Wood
Westinghouse Hanford Company
P.O. Box 1970
Richland, WA 99352

Battelle Pacific Northwest Laboratories (6)
Attn: D. J. Bradley
J. Relyea
R. E. Westerman
S. Bates
H. C. Burkholder
L. Pederson
Battelle Boulevard
Richland, WA 99352

Savannah River Laboratory (6)
Attn: N. Bibler
E. L. Albenisius
M. J. Plodinec
G. G. Wicks
C. Jantzen
J. A. Stone
Aiken, SC 29801

Savannah River Plant
Attn: Richard G. Baxter
Building 704-S
Aiken, SC 29808

George Dymmel
SAIC
101 Convention Center Dr.
Las Vegas, NV 89109

INTERA Technologies, Inc. (7)

Attn: G. E. Grisak
J. F. Pickens
A. Haug
A. M. LeVenue
T. Cauffman
V. Kelley
M. Reeves

Suite #300
6850 Austin Center Blvd.
Austin, TX 78731

INTERA Technologies, Inc.

Attn: Wayne Stensrud
P.O. Box 2123
Carlsbad, NM 88221

IT Corporation (2)

Attn: R. F. McKinney
J. Myers

Regional Office - Suite 700
5301 Central Avenue, NE
Albuquerque, NM 87108

IT Corporation (2)

Attn: D. E. Deal
P.O. Box 2078
Carlsbad, NM 88221

Los Alamos Scientific Laboratory

Attn: B. Erdal, CNC-11
Los Alamos, NM 87545

Oak Ridge National Laboratory (4)

Attn: R. E. Blanko
E. Bondietti
C. Claiborne
G. H. Jenks

Box Y

Oak Ridge, TN 37830

RE/SPEC, Inc.

Attn: W. Coons
P. F. Gnirk

P.O. Box 14984
Albuquerque NM 87191

RE/SPEC, Inc. (7)
Attn: L. L. Van Sambeek
D. B. Blankenship
G. Callahan
T. Pfeifle
J. L. Ratigan
P. O. Box 725
Rapid City, SD 57709

Rockwell International (1)
Attn: C. E. Wickland
Rocky Flats Plant
Golden, CO 80401

Rockwell International (3)
Atomics International Division
Rockwell Hanford Operations
Attn: J. Nelson (HWVP)
P. Salter
W. W. Schultz
P.O. Box 800
Richland, WA 99352

Science Applications International Corporation
Attn: Howard R. Pratt, Senior Vice President
10260 Campus Point Drive
San Diego, CA 92121

Science Applications International Corporation
Attn: Michael B. Gross, Ass't. Vice President
Suite 1250
160 Spear Street
San Francisco, CA 94105

Systems, Science, and Software (2)
Attn: E. Peterson
P. Lagus
Box 1620
La Jolla, CA 92038

Westinghouse Electric Corporation (7)
Attn: Library
W. C. Moffitt
W. P. Poirer
W. R. Chiquelin
V. F. Likar
D. J. Moak
R. F. Kehrman
P. O. Box 2078
Carlsbad, NM 88221

UNIVERSITIES

University of Arizona
Attn: J. G. McCray
Department of Nuclear Engineering
Tucson, AZ 85721

University of New Mexico (2)
Geology Department
Attn: D. G. Brookins
Library
Albuquerque, NM 87131

Pennsylvania State University
Materials Research Laboratory
Attn: Della Roy
University Park, PA 16802

Texas A&M University
Center of Tectonophysics
College Station, TX 77840

Mechanical, Aerospace, and Nuclear Engineering Department
Attn: W. Kastenber
D. Browne
5532 Boelter Hall
University of California
Los Angeles, CA 90024

Department of Civil Engineering
University of Wyoming
Attn: V. R. Hasfurther
Laramie, WY 82071

Department of Geology
University of Wyoming
Attn: J. I. Drever
Laramie, WY 82071

Department of Mathematics
University of Wyoming
Attn: R. E. Ewing
Laramie, WY 82071

Department of Hydrology and Water Resources
University of Arizona
Attn: S. P. Neuman
Tucson, AZ 85721

A. L. Gutjahr
Department of Mathematics
New Mexico Institute of Mining and Technology
Socorro, NM 87801

W. J. Conover
College of Business Administration
Texas Tech University
Box 4319
Lubbock, TX 79409-4319

PERFORMANCE ASSESSMENT PEER REVIEW PANEL

G. Ross Heath
College of Ocean and Fishery Sciences
University of Washington
Seattle, WA 98195

Thomas H. Pigford
Department of Nuclear Engineering
4153 Etcheverry Hall
University of California
Berkeley, CA 94270

Patrick A. Domenico
Geology Department
Texas A & M
College Station, TX 77843-3115

Neville Cook
Rock Mechanics Engineering
Mine Engineering Dept.
University of California
Berkeley, CA 94270

Thomas A. Cotton
4429 Butterworth Place, NW
Washington, DC 20016

Robert J. Budnitz
President, Future Resources Associates Inc.
2000 Center Street
Suite 418
Berkeley, CA 94704

C. John Mann
Department of Geology
245 Natural History Bldg.
1301 West Green Street
University of Illinois
Urbana, IL 61801

Charles D. Hollister
Dean for Studies
Woods Hole Oceanographic Institute
Woods Hole, MA 02543

Benjamin Ross
Disposal Safety, Inc.
Suite 600
1629 K Street NW
Washington, D.C. 20006

LIBRARIES

Thomas Brannigan Library
Attn: Don Dresp, Head Librarian
106 W. Hadley St.
Las Cruces, NM 88001

Hobbs Public Library
Attn: Ms. Marcia Lewis, Librarian
509 N. Ship Street
Hobbs, NM 88248

New Mexico State Library
Attn: Ms. Ingrid Vollenhofer
P.O. Box 1629
Santa Fe, NM 87503

New Mexico Tech
Martin Speere Memorial Library
Campus Street
Socorro, NM 87810

Pannell Library
Attn: Ms. Ruth Hill
New Mexico Junior College
Lovington Highway
Hobbs, NM 88240

Roswell Public Library
Attn: Ms. Nancy Langston
301 N. Pennsylvania Avenue
Roswell, NM 88201

WIPP Public Reading Room
Attn: Lee Hubbard, Head Librarian
Carlsbad Municipal Library
101 S. Halagueno St.
Carlsbad, NM 88220

Government Publications Department
General Library
University of New Mexico
Albuquerque, NM 87131

Information Services Department,
Albuquerque Public Library
501 Copper Avenue NW
Albuquerque, NM 87102

New Mexico Institute of Mining and
Technology Library
Government Documents
Campus Station
Socorro, NM 87801

Public Reading Room
National Atomic Museum
Wyoming Boulevard SE
Kirtland Air Force Base
Albuquerque, NM 87115

Santa Fe Public Library
145 Washington Avenue
Santa Fe, NM 87501

U.S. Department of Energy-ID
Public Reading Room
University Place
1776 Science Center Drive
Idaho Falls, ID 83402

U.S. Department of Energy-RL
Public Reading Room
Hanford Science Center
825 Jadwin Avenue
Richland, WA 99352

U.S. Department of Energy-CH
Public Reading Room
9800 South Cass Avenue
Building 201
Argonne, IL 60439

U.S. Department of Energy-SFO
Public Reading Room
1333 Broadway, 7th Floor
Oakland, CA 94612

U.S. Department of Energy-NV
Public Reading Room
2753 South Highland Street
Las Vegas, NV 89109

U.S. Department of Energy-HQ
Public Reading Room
Room 1E-190, Forrestal Building
1000 Independence Ave. SW
Washington, DC 20585

U.S. Department of Energy-OR
Public Reading Room
Federal Building
200 Administration Road
Oak Ridge, TN 37830

U.S. Department of Energy-SR
FOI Publication/Document Room
Aiken, SC 29802

Denver Public Library
Government Documents Room
Second Floor
1357 Broadway
Denver, CO 80203-2185

Government Publications
Norlin Library
University of Colorado/Boulder
18th and Colorado Streets
Campus Box 184
Boulder, CO 80309

Department of Public Works and Utilities
Westminster City Hall
4800 West 92nd Avenue
Westminster, CO 80030

NATIONAL ACADEMY OF SCIENCES, WIPP PANEL

Dr. Charles Fairhurst, Chairman
Department of Civil and Mineral Engineering
University of Minnesota
500 Pillsbury Dr. SE
Minneapolis, MN 55455

Dr. John O. Blomeke
Route 3
Sandy Shore Drive
Lenoir City, TN 37771

Dr. John D. Bredehoeft
Western Region Hydrologist
Water Resources Division
U.S. Geological Survey (M/S 439)
345 Middlefield Road
Menlo Park, CA 94025

Dr. Karl P. Cohen
928 N. California Avenue
Palo Alto, CA 94303

Dr. Fred M. Ernsberger
250 Old Mill Road
Pittsburgh, PA 15238

Dr. Rodney C. Ewing
Department of Geology
University of New Mexico
200 Yale, NE
Albuquerque, NM 87131

Dr. William R. Muehlberger
Department of Geological Sciences
University of Texas at Austin
P.O. Box 7909
Austin, TX 78712

Dr. Frank L. Parker
Department of Environmental Engineering
Vanderbilt University
Nashville, TN 37235

Dr. D'Arcy A. Shock
233 Virginia
Ponca City, OK 74601

Dr. Peter B. Myers, Staff Director
National Academy of Sciences
Committee on Radioactive Waste Management
2101 Constitution Avenue
Washington, DC 20418

Staff Officer
Board on Radioactive Waste Management
GF462
2101 Constitution Avenue
Washington, D. C. 20418

FOREIGN ADDRESSES

Studiecentrum Voor Kernenergie (1)
Centre D'Energie Nucleaire
Attn:Mr. A. Bonne
SCK/CEN
Boeretang 200
B-2400 Mol
BELGIUM

Atomic Energy of Canada, Ltd. (2)
Whiteshell Research Estab.
Attn:Peter Haywood
John Tait
Pinewa, Manitoba, CANADA
ROE 1L0

Dr. D. K. Mukerjee
Ontario Hydro Research Lab
800 Kipling Avenue
Toronto, Ontario, CANADA
M8Z 5S4

Mr. Jean-Pierre Olivier
OECD Nuclear Energy Agency
Division of Radiation Protection and Waste Management
38, Boulevard Suchet
75016 Paris, FRANCE

Claude Sombret
Centre D'Etudes Nucleaires De La Vallee Rhone
CEN/VALRHO
S.D.H.A. BP 171
30205 Bagnols-Sur-Ceze
FRANCE

Bundesministerium fur Forschung und Technologie
Postfach 200 706
5300 Bonn 2
FEDERAL REPUBLIC OF GERMANY

Bundesanstalt fur Geowissenschaften und Rohstoffe
Attn:Michael Langer
Postfach 510 153
3000 Hannover 51
FEDERAL REPUBLIC OF GERMANY

Hahn-Mietner-Institut fur Kernforschung (1)
Attn:Werner Lutze
Glienicker Strasse 100
100 Berlin 39
FEDERAL REPUBLIC OF GERMANY

Institut fur Tieflagerung (4)
Attn:K. Kuhn
Theodor-Heuss-Strasse 4
D-3300 Braunschweig
FEDERAL REPUBLIC OF GERMANY

Kernforschug Karlsruhe (1)
Attn:K. D. Closs
Postfach 3640
7500 Karlsruhe
FEDERAL REPUBLIC OF GERMANY

Physikalisch-Technische Bundesanstalt
Attn:Peter Brenneke
Postfach 33 45
D-3300 Braunschweig
FEDERAL REPUBLIC OF GERMANY

D. R. Knowles
British Nuclear Fuels, plc
Risley, Warrington, Cheshire WA3 6AS
1002607 GREAT BRITAIN

Shingo Tashiro
Japan Atomic Energy Research Institute
Tokai-Mura, Ibaraki-Ken
319-11 JAPAN

Netherlands Energy Research Foundation ECN (2)
Attn:Tuen Deboer, Mgr.
L. H. Vons
3 Westerduinweg
P.O. Box 1
1755 ZG Petten, THE NETHERLANDS

Svensk Karnbransleforsorjning AB
Attn:Fred Karlsson
Project KBS
Karnbranslesakerhet
Box 5864
10248 Stockholm, SWEDEN

SANDIA INTERNAL

1510 J. W. Nunziato
1511 D. K. Gartling
1511 R. R. Eaton
1511 P. Hopkins
1520 C. W. Peterson
1521 R. D. Krieg
1521 J. G. Arguello
1521 H. S. Morgan
1521 C. M. Stone
1523 J. H. Biffle
1523 D. P. Flanagan
1523 A. P. Gilkey
1524 W. C. Mills-Curran
3141 S. A. Landenberger (5)
3151 W. I. Klein (3)
3154-1 C. L. Ward, (8) for DOE/OSTI
6000 D. L. Hartley
6230 W. C. Luth
6232 W. R. Wawersik
6233 T. M. Gerlach
6233 J. L. Krumhansl
6300 R. W. Lynch
6310 T. O. Hunter
6310 G. E. Barr
6312 F. W. Bingham
6312 R. W. Prindle

6312 M. S. Tierney
 6313 T. Blejwas
 6315 P. C. Kaplan
 6330 W. D. Weart
 6330 V. L. Bruch
 6330 D. P. Garber
 6330 S. Pickering
 6331 A. R. Lappin (50)
 6331 R. L. Beauheim
 6331 D. J. Borns
 6331 P. B. Davies
 6331 S. J. Lambert
 6331 R. Z. Lawson
 6331 K. L. Robinson
 6331 M. D. Siegel
 6332 L. D. Tyler
 6332 R. Beraun
 6332 B. M. Butcher
 6332 B. L. Ehgartner
 6332 M. A. Molecke
 6332 D. E. Munson
 6332 E. J. Nowak
 6332 R. J. Roginski
 6332 J. C. Stormont
 6332 T. M. Torres
 6332 Sandia WIPP Central Files (10)
 6333 T. M. Schultheis
 6334 D. R. Anderson
 6334 S. Bertram-Howery
 6334 K. Brinster
 6334 L. Brush
 6334 M. S. Y. Chu
 6334 L. S. Gomez
 6334 R. Guzowski
 6334 R. L. Hunter
 6334 H. J. Iuzzolino
 6334 M. G. Marietta
 6334 R. R. Rechard
 6334 A. Rutledge
 6334 E. Shepherd
 6400 D. J. McCloskey
 6415 R. M. Cranwell
 6415 J. C. Helton
 6415 R. L. Iman
 6416 M.S.Y. Chu
 7100 C. D. Broyles
 7110 J. D. Plimpton
 7120 M. J. Navratil
 7125 R. L. Rutter
 7125 J. T. McIlmoyle
 7130 J. O. Kennedy
 7133 O. Burchett
 7133 J. W. Mercer
 7135 P. D. Seward
 8524 J. A. Wackerly (SNLL Library)



8232-2/068718



00000001 -



8232-2/068718



00000001 -



8232-2/068718



00000001 -